Lecture Notes in Applied and Computational Mechanics 82

Theodoros Triantafyllidis *Editor*

Holistic Simulation of Geotechnical Installation Processes

Theoretical Results and Applications

Springer

Lecture Notes in Applied and Computational Mechanics

Volume 82

About this Series

This series aims to report new developments in applied and computational mechanics—quickly, informally and at a high level. This includes the fields of fluid, solid and structural mechanics, dynamics and control, and related disciplines. The applied methods can be of analytical, numerical and computational nature.

More information about this series at http://www.springer.com/series/4623

Theodoros Triantafyllidis
Editor

Holistic Simulation of Geotechnical Installation Processes

Theoretical Results and Applications

Springer

Editor
Theodoros Triantafyllidis
Institute of Soil Mechanics and Rock Mechanics
Karlsruhe Institute of Technology
Karlsruhe
Germany

ISSN 1613-7736 ISSN 1860-0816 (electronic)
Lecture Notes in Applied and Computational Mechanics
ISBN 978-3-319-52589-1 ISBN 978-3-319-52590-7 (eBook)
DOI 10.1007/978-3-319-52590-7

Library of Congress Control Number: 2017930143

Printed on acid-free paper

This Springer imprint is published by Springer Nature
The registered company is Springer International Publishing AG
The registered company address is: Gewerbestrasse 11, 6330 Cham, Switzerland

Preface

This textbook summarizes the final results of the research group GEOTECH founded by the German Research Council (DFG) dealing with the holistic consideration of geotechnical installation processes. In this sense, the entire process for the realization of a geotechnical construction project starting from a well-defined initial stress and deformation state is taken into account.

From the engineering practice, it is well known that the installation process of structural elements into the ground may cause strong deformation and stress redistribution in the surrounding soil. Dealing with excavation pits in urban areas, installation processes like piling or anchoring therefore often lead to unexpected displacements of the shoring or neighbouring buildings exceeding those due to the excavation or dewatering of the pit. The assessment of the deformations resulting from geotechnical installation processes is, on the one hand, required from the codes (EC 7) or regulations but on the other hand, validated high-quality prediction simulations are still not available. Suitable numerical methods should be based on realistic and validated highly nonlinear incremental constitutive models for the soils under cyclic/dynamic loading conditions and advanced simulation tools. However, existing models do not offer up to now the required prediction quality.

The main target of the research group is the provision of suitable methods for the simulation of geotechnical installation processes based on fundamental research in order to reliably predict the serviceability state of supporting systems and nearby structures especially with regard to the vibro-installation of piles.

In order to achieve these targets, the research group operates in three levels:

- benchmarking projects with element-like and large-scale model tests for calibration and validation of the developed numerical models
- theoretical fundamental research for the development of high-quality constitutive soil models and contact formulations in combination with efficient numerical implementations and algorithms

– application of the developed theoretical models to boundary value problems with parametric studies of respective geotechnical installation processes and recommendations for further use of the numerical models in practice as well as for the practical optimization of these processes.

In this book, the final research results including not only the demonstrator experiments for pile installation as benchmarks are presented, but also the simulation results of recently developed numerical techniques and constitutive modelling for the description of the nonlinear behaviour of soils under dynamic/cyclic excitation. Furthermore, interesting results are presented associated with the vibro-injection pile installation with multimaterial flow and large material deformations. The presented results can also be used for validation of new techniques or material models in the future.

The contributions of our invited speakers (Prof. R.J. Finno, Prof. M. Taiebat, Prof. W. Fuentes and Prof. T. Schanz) in the final GEOTECH Workshop (23 and 24 February 2017 in Karlsruhe) are very much appreciated and are also included in this volume due to their relevance to the scientific targets of the group.

The editor likes to thank all his colleagues (Prof. Ehlers, Prof. Wriggers, Prof. Savidis, Prof. Rackwitz, Prof. Hettler) and co-workers (Dr. Niemunis, Dr. Osinov, Dr. Huber) for their valuable contributions and their extreme efforts and engagement in order to achieve the high scientific targets of the projects.

Furthermore, I would like to express my thanks to Mrs. Meininger for the organization of all the workshops of the research group GEOTECH and her engagement to make those events pleasant as well as Dr. Vogelsang for the assistance to prepare the book.

Finally, all of us like to express our deep gratitude to DFG (German Research Council) for the generous financial support of this very interesting research topic in geotechnical engineering.

February 2017 Th. Triantafyllidis

Contents

Adaptive Management Evaluation of the SQBRC Excavation

Richard J. Finno[1(✉)], Zhenhao Shi[1], Sangre Kim[1], Nathan Crafton[1], and Daniel Rendell[2]

[1] Department of Civil and Environmental Engineering, Northwestern University, Evanston, USA
r-finno@northwestern.edu
[2] Getec UK, London, UK

Abstract. This paper summarizes the adaptive management approach for controlling ground movements resulting from geotechnical construction activities, and presents the results of such analyses made throughout construction of the excavation for the SQBRC building in Chicago, IL, wherein attendant ground movement was a key design issue. This paper describes the support system, summarizes the performance data collected in real time, and presents the results of the optimizations made during excavation. Optimization of soil parameters based on plane strain analyses made at well-defined excavation stages resulted in reasonable predictions of computed lateral movements at the end of the excavation. Issues related modeling the support system in three dimensional analyses are discussed, and effects of past construction activities and construction operations other than the cycles of excavation and support installation are illustrated. Current limitations of the approach with respect to supported excavations are discussed.

1 Introduction

Uncertainty is the distinguishing feature of geotechnical engineering in that nature leaves behind soil and rock that is variable in composition, extent and behavior. Developments in sensor technology, information technology and numerical analysis allow one to apply the observational approach so that the effects of these uncertainties on design and performance can be minimized. These advances allow a cycle of measurement and prediction update based on observed performance to be made in near real time. However, one must carefully select the monitoring data used as observations and properly numerically simulate construction to minimize the difference between predictions and observed performance. This general approach is termed "adaptive management" and can be employed to predict, monitor and control performance during geotechnical construction. The goal of the approach is to isolate the effects of the soil parameters to update performance predictions, and as such, the construction process must be modeled correctly. After data are collected at early stages of a project, updated parameters form the basis of a new simulation to predict responses at later, and more

T. Triantafyllidis (ed.), *Holistic Simulation of Geotechnical Installation Processes*,
Lecture Notes in Applied and Computational Mechanics 82, DOI 10.1007/978-3-319-52590-7_1

critical, stages of construction. This paper summarizes an adaptive management approach which incorporates real-time monitoring data to allow updating of design predictions based on performance data. Capabilities with respect to supported excavations are described. A case study is summarized to illustrate its application and current limitations.

2 Adaptive Management Approach

Once design criteria for a project have been established, an adaptive management approach can be employed to predict, monitor and control performance during geotechnical construction (e.g., Finno [3,4]). This approach is summarized in Fig. 1. The left hand column represents calculations made during the design and updating phases, and includes for excavation projects finite element simulations of the construction process. In general, observations against which the predictions are compared can be of any type, including deformation, pore water pressure or structural response data in geotechnical applications. The center column represents the optimization needed to update predictions based on the measurements. Ideally, this process works automatically, all data collected in the field is transferred in real time to a host computer where it can be processed into format compatible with the numerical analyses. After data are collected at early stages of a project, updated parameters form the basis of a new simulation to predict responses at later, and presumably more critical, stages of construction.

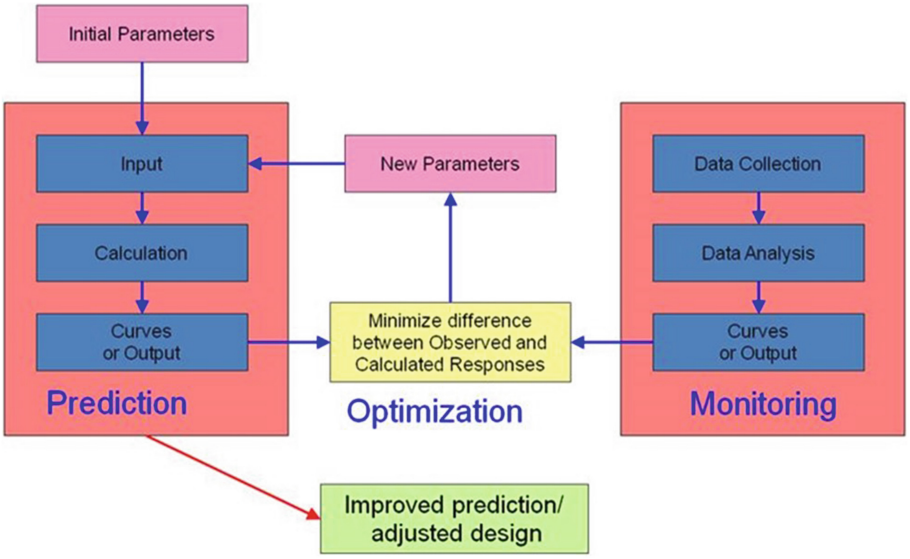

Fig. 1. Adaptive management process

In the work presented herein, the finite element code PLAXIS was the platform for the numerical analyses and the optimization was performed in MATLAB. These codes and the field performance data from the site website were linked via the programming language PYTHON such that the optimization and updated performance predictions were made automatically. Human intervention was only needed to extract the proper data files from the project website.

Successful application of the adaptive management approach depends equally on reasonable numerical simulations of the construction process, the constitutive models employed, the type of monitoring data used as observations, and the optimization techniques used to minimize the difference between predictions and observed performance.

Use of an inverse model provides results and statistics, offers powerful tools for model analysis and, in many instances, expedites the process of adjusting parameter values. A fundamental benefit of inverse modeling is its ability to calculate automatically parameter values that produce the best fit between observed and computed results. The calibration by inverse analysis can be very effective in minimizing the errors between the measured and computed results (e.g., Ou and Tang [13]; Ledesma et al. [11]; Finno and Calvello [6]; Hashash and Finno [9]). However, the convergence of an inverse analysis to an "optimal solution" (i.e. best-fit between computed results and observations) does not necessarily mean that the simulation is satisfactorily calibrated. A geotechnical evaluation of the optimized parameters is always necessary to verify the reliability of the solution. For a model to be considered "reliably" calibrated, both the fit between computed and observed results must be satisfactory (i.e. errors are within desired and/or accepted accuracy) and the best-fit values of the model parameters must be reasonable.

A common method of inverse analysis that has been applied to geotechnics is optimization by the gradient method. This approach employs a local parameter identification of a specific constitutive law. Many of the early evaluations of performance data using this approach were conducted with very simple soil models that severely restricted the ability of the computations to accurately reflect the observed field performance data, irrespective of employing inverse techniques. Clearly, unless the constitutive model has the capability to represent the response of the soil to the particular loading condition, the approach will not be successful.

When applying the optimization technique to field problems, the underlying assumption is that the only uncertainty is the material response, and all other factors are known and contain no errors. When making a prediction of response during design, this is clearly not true. However, if field observations of performance are used to calibrate the model during construction, then the construction procedures are known exactly and this source of uncertainty is removed. Furthermore, the timely collection and screening of the data must be successfully accomplished. For any monitoring system to be fully automated, one must be able to track construction progress so that performance data can be correlated with the excavation activities. An internet accessible weather-resistant video

camera is currently used in practice with some degree of regularity to allow remote visualization of the construction process in real-time, as well as a dated, photographic record of construction (e.g., Finno and Blackburn [5]).

One key issue is the selection of the soil model to be used in the optimization scheme when making an update. If one wants to get reasonable updated predictions of performance at the early stages of excavation, then the constitutive model used to represent the soil behavior in the critical soil strata must represent the behavior at all strain levels. Because one wants to get accurate updates on performance at the early stages of excavation where the deformations and shear strain levels are small, the constitutive model must include this feature of behavior or the optimized parameter will change until the strains are large enough so that further degradation is accurately represented in the model. While we have employed for analyses for the case reported herein the hardening soil model with small strain stiffness (Benz et al. [2]) and a hypoplasticity model for clays (Mašín [12]) as the constitutive model, only the results from the hypoplasticity model will be presented in this paper.

A second key issue deals with the inherent three-dimensional nature of excavation process. Normally, a two-dimensional plane strain model of the excavation is developed so that updated performance predictions can be made at key stages of the project. Such a stage would be when the excavation is made below a tie back or cross-lot brace elevation and the excavated surface is flat so that the plane strain conditions are applicable. However, for real time updates at more times during the excavation, for example, when some parts of the excavation that are deeper than others, a three-dimensional model is required to allow updated predictions at any time during the process. This type of model also is needed if there are adjacent building that have altered the states of stress in the foundation soils that will impact the current excavation. This is the case for the SQBRC excavation reported herein. While these models have been developed, the research regarding them is on-going. Selected results of these analyses are presented to illustrate some the issues with 3-D analyses.

3 Case Study: Louis A. Simpson and Kimberly K. Querry Biomedical Research Center

The excavation for the Louis A. Simpson and Kimberly K. Querry Biomedical Research Center (SQBRC) located on the Chicago campus of Northwestern University required a 43 ft to 59 ft deep excavation to facilitate the construction of a 14 story building with two basement levels. The site is located on a former hospital that was demolished prior to any activities related to the SQBRC began. The hospital included one basement level and was supported on drilled shafts. The shafts were cut off at excavated grade for the new SQBRC structure. The shafts below that level were left in place and not used as part of the new foundation system.

3.1 Subsurface Conditions and Excavation Support System

Idealized soil stratigraphy at the site is presented in Fig. 2. Sidewalk elevation for this site is 14 ft Chicago City Datum (CCD). A primarily granular urban fill was found between 14 ft CCD and −11 ft CCD. A layer of clean beach sand was encountered between −11 ft and −19 ft CCD. Beneath the sand layer are a sequence of increasingly stronger and stiffer clays. The soft to medium clays found between −19 ft to −42 ft CCD and the stiff to very stiff clays between −42 ft to −72 ft CCD are glacially-derived ice margin deposits. Below elevation −72 ft CCD, basal tills consisting of hard clays and clayey silts, locally known as "hardpan" are encountered until Dolomitic limestone is encountered at approximate −140 ft CCD. Ground water was encountered in boreholes between 1 and −1 ft CCD.

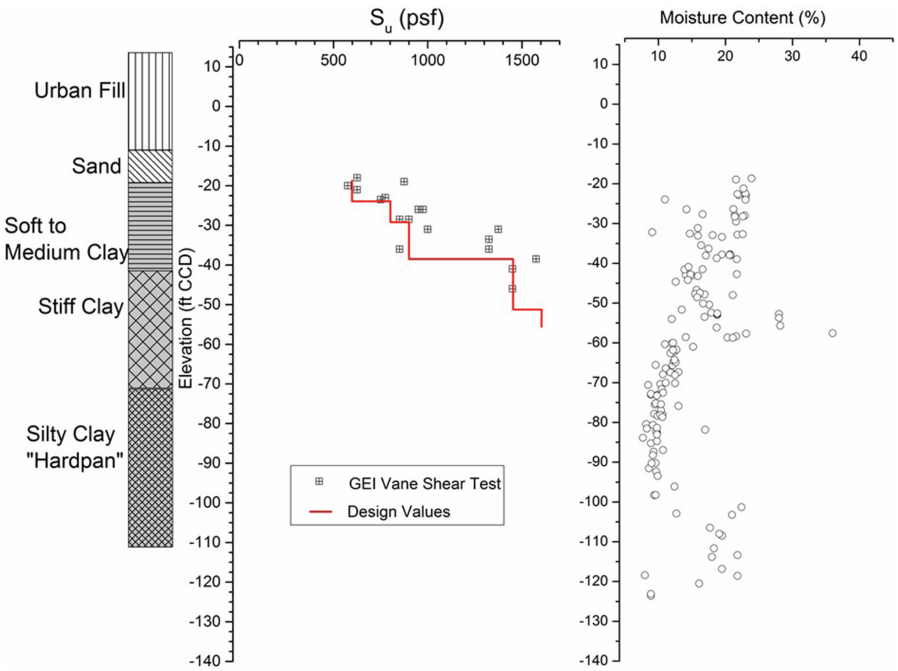

Fig. 2. Subsurface conditions

A section view of the lateral support at the north wall is shown in Fig. 3a and a photo of that location taken as the second level of tiebacks were being installed is shown in Fig. 3b. The earth retention system consisted of driven hot rolled Z-shaped sheet piles with five levels of support on the north, east, and south walls, and soldier pile and lagging on the west side of the site. These levels of support include grouted tiebacks at elev 2 ft CCD North side and 7 ft CCD south side (level 1), diagonal internal braces centered at elev −4 ft CCD

(level 2), grouted tiebacks at elev −20 ft CCD. At a few locations, the wall was braced with grouted tiebacks at elev −27 ft CCD, adjacent to the temporary crane foundations along the north wall and southwest corner of the excavation. Tiebacks on the east side of the site are only present in level 3 and 4 due to the presence of the adjacent Lurie Center and RIC buildings.

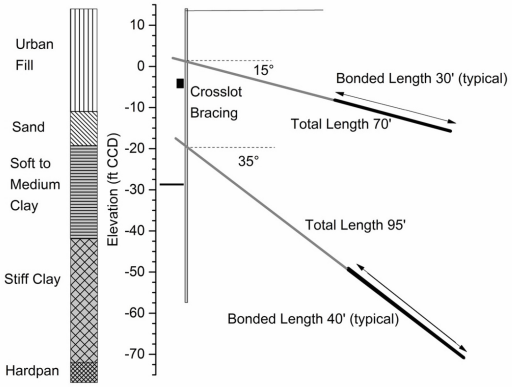

(a)

(b)

Fig. 3. Excavation support system at the north wall of the excavation

Tieback anchors were. 0.6 in. diameter strands in 4 and 6 strand configurations made of 270 ksi steel. Internal braces consisted of 36 in. × 5/8 in. pipe struts which were preloaded using hydraulic jacks to 1/3 of the design load before installing shim plates and welding in place. The longest internal braces

were simply supported against self-weight by a system of piles and connected WF beams (Fig. 3b).

Load from all levels of tiebacks is distributed by the use of wales comprised of two C14x33.9 steel sections connected by welded spacer plates allowing the tieback to pass between them. Loads from the cross lot bracing at level 2 were distributed using 2 W27x281 steel sections as wales. The connections between the walers and the sheet piles were made with spot welds.

The SQBRC structure will be supported by belled drilled shaft foundations. The depth to bottom for these foundations ranged between −80 ft CCD and −85 ft CCD. Shaft sizes ranged from 2.5 to 10 ft in diameter with bell diameters between 6 and 22 ft. Micropiles were installed adjacent the excavation on the south side of the site to support a slab foundation utilized for loading and unloading of heavy construction materials. These micropiles consisted of 7 in. diameter steel pipes extending to elev −85 ft CCD, with a bonded zone starting at elev −55 ft CCD. Grout was injected with pressures between 140 and 350 psi.

3.2 Instrumentation

Instrumentation locations at the site is shown in Fig. 4, plan view of the site which also shows the locations of the adjacent structures, the Lurie Center to the west and the RIC building to the east.

To measure the lateral deflection of the sheeting, shape accel arrays (SAA) were installed at six locations around the site - noted as SAA-1 through SAA-6 on Fig. 4. An SAA is very similar to a traditional inclinometer, but it remains in place throughout the excavation and can be programmed to take readings at specified time intervals. It consists of a number of rigid segments either 1.64 or 1 ft

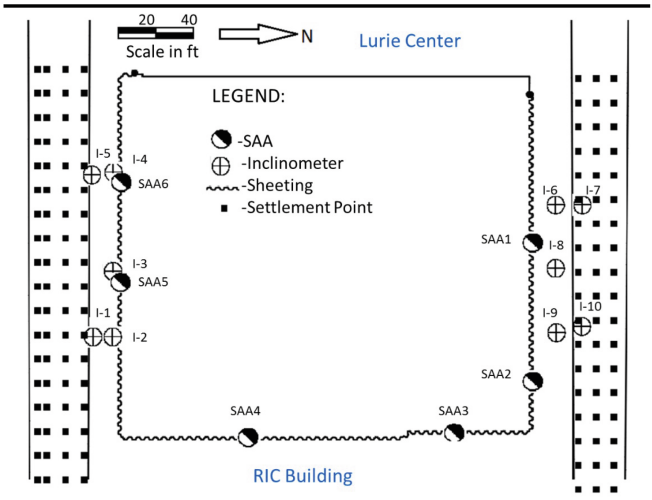

Fig. 4. Site instrumentation plan

long with a diameter of 1 in. Each segment has three temperature-calibrated Micro Electro Mechanical System (MEMS) accelerometers and the segments are connected by flexible joints that can move in any direction but cannot twist. The 3D shape of SAA in a near-vertical casing is determined from static accelerations of X and Y accelerometers. The SAA were installed and initialized after the sheet piles were placed. In addition to the SAAs, 10 conventional slope indicators were installed in the ground adjacent to the north and south sheet pile walls. These devices were initialized prior to any construction activity at the site.

Two robotic total stations were installed on structures off the site influence area to measure deformations of the surrounding structures and the basement wall shared with the Lurie Center. Conventional optical surveys were made of 126 surface settlement points established in the streets to the north and south of the site.

All remotely sensed data was displayed in real time on a project web site. An interface was developed between the automated data presented on the project website developed by Getec and the finite element code used in the optimization process. The field data were linked to the optimization procedure as subsequently described.

3.3 Sequence of Activities

The sequence of activities at the site is summarized in Table 1. The work progressed consistently across the site, until the tieback anchors comprising the

Table 1. Sequence of activities

Task	Dates	Activity
1	11/04/16	Traditional inclinometers installed and initialized
2	11/02/15–2/23/16	Drilled shafts installed
3	02/05/16–2/26/16	Sheet piles installed by vibratory hammer
4	03/04/16	SAAs installed and initialized
5	02/29/16–03/11/16	Excavation to level 1 (0 ft CCD North side of site, 5 ft CCD south side)
6	03/03/16–3/28/16	Installation of level 1 support- tieback Level 1
7	03/25/16–04/01/16	Excavation to level 2 (−7 ft CCD)
8	03/28/16–05/08/16	Installation of level 2 support - cross lot bracing
9	05/09/16–06/09/16	Excavation to level 3 (−22 ft CCD)
10	05/21/16–07/09/16	Installation of support level 3 - tieback level 2
11	06/23/16–09/02/16	Excavation to level 4 (−29 ft CCD)
12	06/25/16–07/29/16	Installation of support level 4 - tieback level 3
13	09/02/16	Excavation to final grade complete (varies −29 ft to −45 ft CCD)
14	08/05/16	Installation of grade beams and foundations begins

Fig. 5. Site activities during task 10

third level of support were prestressed. Activities noted as tasks 11 through 14 occurred simultaneously at various locations at site, primarily as a result of different final excavation grades.

A photograph taken during task 10 is presented in Fig. 5. The photo shows the location of an access ramp at the south wall that was present at various times during the excavation. The presence of this ramp made conditions on the south wall three-dimensional for most of the excavation. As such, the adaptive management procedure was applied to conditions at the north wall during the excavation because the conditions there could be represented as plane strain at the times during construction when the excavated level was level across the entire north wall. Plane strain optimizations were made as several times during construction and the updated predictions were Class A, i.e., true predictions and not back-calculations.

3.4 Summary of Performance

A summary of the lateral wall movements recorded by the two SAA along the north wall during excavation is shown in Fig. 6. In the figure, Level 1 refers to the cantilever stage with excavation to depths 2 ft below the upper level tieback, Level 2 to the excavation below the cross lot bracing, Level 3 to the excavation below the lower tieback level, Level 4 to the excavated grade at the base of the wall and final excavation refers to time when the localized deeper excavation within the center of the site was completed. The general responses in both SAA are similar in that less than 0.15 in. of lateral movements were noted until the excavation had reached the underlying soft clay. Thereafter, the movements increased as the softer clays behind the wall and below the excavation were stressed in response to the excavation unloading. More movement was noted in the center of the excavation at SAA-1, a maximum of 1.6 in., than near the edges at SAA-2, a maximum of 1.4 in. After the cantilever stage, the maximum

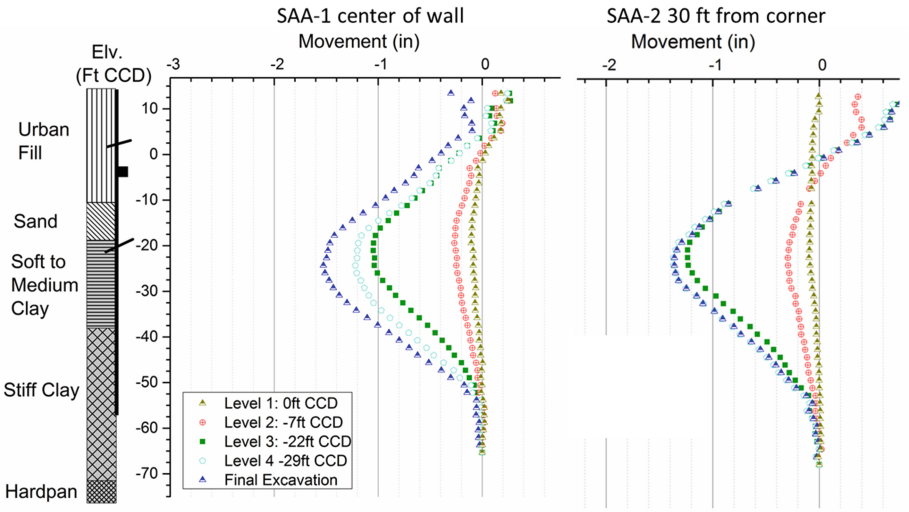

Fig. 6. Lateral wall movements along north end of excavation

movement was located near the excavated surface as excavation proceeded. These trends are typical of excavations in Chicago. Note that the design aimed to limit the lateral movements to 2 in., as required by the City of Chicago to protect utilities buried in the adjacent streets.

A summary of the lateral wall movements recorded by the two SAA along the south wall during excavation is shown in Fig. 7. At SAA-5, movements at only two dates are shown. This is because the access ramp shown on Fig. 5 precluded significant movements until it was removed. However, the movements recorded at SAA-6 were recorded throughout the excavation process and followed the same trends as noted in the north wall. The magnitudes of these movements are a bit larger than observed at the north wall because the deeper excavation in the center of the site was closer to the south wall and because of the impact of micropile installation near SAA-6, as will be discussed. In any case, the maximum lateral movement was 2.5 in., greater than the regulatory requirement of 2 in. However, this movement apparently had no impact on the adjacent utilities.

Micropiles were installed adjacent to the south wall during an 18 day period while the excavation was a constant level of −7 ft CCD and the cross-lot braces were being installed. The movements associated with the micropile installation at SAA-6 are showed in Fig. 8. The micropiles were grouted at pressures that varied between 140 to 300 psi. The maximum lateral movement caused by installing the micropiles was 0.3 in. measured at a SAA that was 3.5 ft from the nearest micropile. The largest movements occurred in the soft clay and negligible movements developed below elev −62 ft CCD, even though the bonded zones of the micropiles was between elev −55 and −85 ft CCD. These movements were localized, as other inclinometers located at greater distances registered negligible

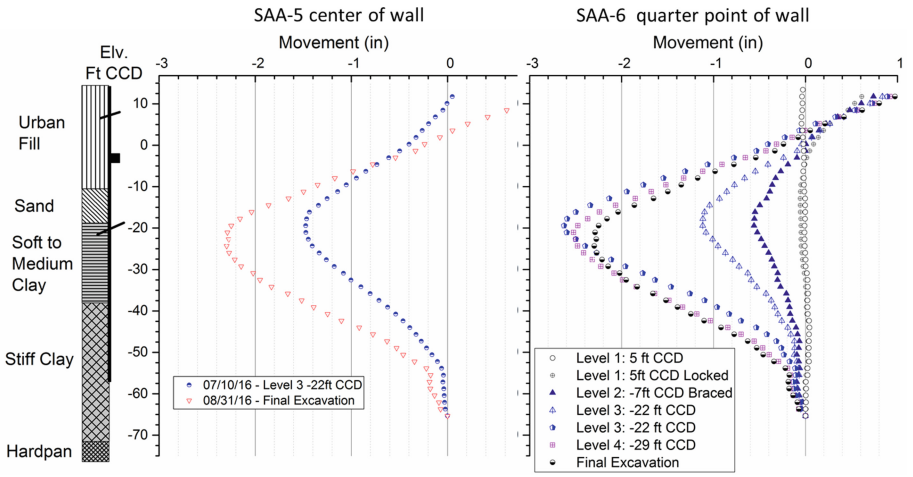

Fig. 7. Lateral wall movements along south end of excavation

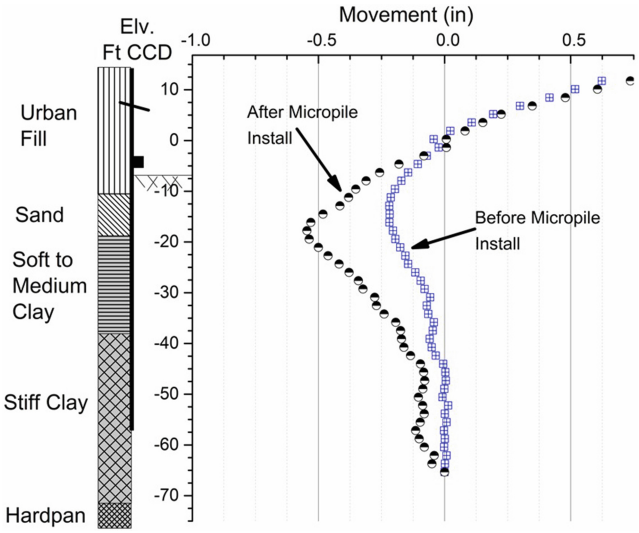

Fig. 8. Lateral movements at SAA-6 caused by micropile installation

movements. However, the installation did contribute to the lateral movements at SAA-6 being larger than those measured near the center of the wall at SAA-5.

The data in Fig. 8 shows the importance of identifying the cause of movements when using the field performance data to optimize soil parameters when applying adaptive management procedures at a project. Unless the micropile installation was explicitly considered in the finite element simulation, then these movements would be incorrectly interpreted as being a result of the excavation process. Optimizations conducted on such a basis would be incorrect.

4 Optimization Assuming Plane Strain Conditions

As is typical, the plane strain model of the excavation was developed so that updated performance predictions can be made at key stages of the project, for example when the excavation is made below a tie back or cross lot elevation and the excavated surface is flat so that the plane strain conditions are strictly applicable. However, there are some parts of the excavation that are deeper than others to accommodate mat foundations where plane strain is not strictly applicable. Also, the sequence of excavating is such that plane strain conditions are met during the process at only a few instance. While it is advantageous to use data collected at several locations to optimize parameters, in this case that was not possible. Specifically, for the plane strain analyses, ideally the SAAs located in the center of both the north and south wall would have been used for the optimization process. However because of the presence of the access ramp in the center of the wall until excavation had reached elev −22 ft CCD at most of the site, the movements were negligible at that location until the latter stages of construction. Updates at that time would have been not nearly as useful to the project team. Consequently, only data collected at the north wall was used in the optimization process during excavation, although as will be seen, the finite element simulation included both walls and the entire excavation.

A 3-D model is required to allow updated predictions at any time during the process, and thus to provide the earliest indication of how well the system is performing in terms of controlling excavation-induced ground movements. Several issues related to such an analysis are discussed herein.

4.1 Constitutive Model

The hypoplasticity clay model developed by Mašín [12] was used in the plane strain analyses to represent the responses of the two clay strata. Unlike models formulated within the elasto-plasticity framework, there is no separation between the elastic and plastic components of strains in the hypo-plasticity model. Important features of the selected model as related to this work include: (1) the basic principles of critical state soil mechanics are incorporated; (2) non-linear small strain stiffness is considered; (3) the anisotropy of very small strain stiffness (i.e., G_0) is reproduced.

Table 2 summarizes the model parameters in the hypo-plasticity model. The p' and e in this table are the mean effective stress and void ratio, respectively. The parameters A_g and n_g are interpolation parameters in the following relation:

$$G_0 = A_g(p')^{n_g} \tag{1}$$

The parameters m_{rat}, R_{max}, β_r and χ control the small strain stiffness degradation with increasing strain.

4.2 Finite Element Mesh

The finite element code PLAXIS was used to make the computations presented herein. Figure 9 shows the finite element mesh in the analysis and idealized soil

Table 2. Model parameters in the hypo-plasticity clay model

Model parameters	Description of its role
λ^*	Slope of the virgin compression line in lnp' vs. $ln(1+e)$ plane
κ^*	Slope of the rebound line in lnp' vs. $ln(1+e)$ plane
N	The value of $ln(1+e)$ on the virgin compression line that corresponds to $p'=1$
ϕ_c	The critical state friction angle
ν_{pp}	The ratio of the bulk modulus in isotropic compression (K_i) and the shear modulus in undrained shear (G_i) for tests starting from the isotropic normally compressed state
A_g and n_g	Interpolation parameters of the very small strain stiffness (G_0)
α_g	The ratio of horizontal and vertical shear stiffness at very small strain
m_{rat}, R_{max}, β_r and χ	Small strain stiffness degradation parameters

stratigraphy for the SQBRC excavation. Note that this section is a north-south section through the site and is not symmetric about its centerline due to the variations in excavation depth. Also, the effects of the building to the east and west of the site on the stress conditions within the clays at the center of the excavation are assumed negligible when considering behavior at the center of the wall.

The fill and sand layers were modeled by Hardening Soil (HS) model (Schanz et al. [15]). The HS model has been proved successful in modeling the fill and sand behavior in the analysis of the Lurie Center excavation (Rechea [14]), located adjacent to the SQBRC excavation. The parameter optimization is conducted in the two clay layers because these two layers govern the excavation-induced ground movement, as noted by the fact that very little lateral movement was observed until the excavation reached these clays.

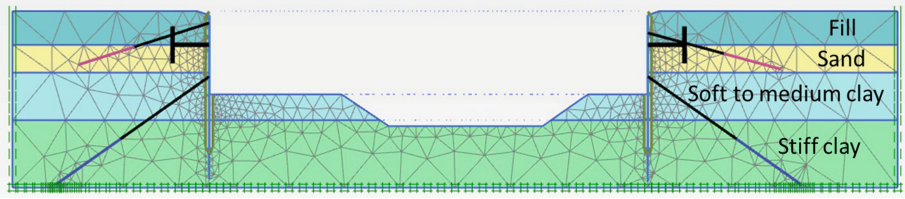

Fig. 9. FEM mesh and soil stratigraphy

4.3 Initial Hypoplasticity Model Parameters

The HS parameters of fill and sand layers were taken directly from those reported by Rechea [14]. For the two clay layers, the parameters λ^*, κ^*, N, ν_{pp}, α_g, m_{rat}, R_{max}, β_r and χ were taken from the values reported by Arboleda-Monsalve [1], which had been used in the numerical analysis of One Museum Park West (OMPW) excavation in the downtown Chicago. In Arboleda-Monsalve's work, the soft to medium clays were modeled as two separate strata, as was the stiff clays. The averaged parameter value among layers were used as the initial values in this work, e.g., the averaged value of λ^* values reported by Arboleda-Monsalve for Blodgett and Deerfield layers were used as the λ^* value for the soft to medium clays in this analysis. The parameter ϕ_c was estimated by matching the undrained shear strength measured by field vane at the SQBRC site. The parameters A_g and n_g were estimated based on in-situ shear wave velocity measured at the sites of OMPW and Ford Center excavations (Finno et al. [7]).

4.4 Parameter Optimization

Optimization is conducted with inverse analysis based on a gradient method. Herein, it is accomplished by coupling the optimization toolbox in MATLAB with the finite element code Plaxis. A program is written in Python to transfer data between Plaxis and MATLAB. A Gauss-Newton method modified by the addition of damping and Marquardt parameters is used to find a best fit between the computed and observed values, as defined by a weighted least-squares objective function, $S(b)$:

$$S(b) = [y - y'(b)]^T w[y - y'(b)] \tag{2}$$

where b is a vector containing values of the soil model parameters to be estimated; y is the vector of the observations being matched by the regression; $y'(b)$ is the vector of the computed values which correspond to observations; w is the weight matrix. The weighting is used to reduce the influence of observations that are less reliable and increase the influence of observations that are more reliable. In this work, a diagonal weight matrix is used. The weight of every observation, w_{ii}, is equal to the inverse of its error variance $w_{ii} = 1/(\sigma_i^2)$.

Optimization-related statistics provide information regarding which parameters can be estimated through optimization with respect to particular field observations and whether certain parameters can be estimated simultaneously. Two statistics used in this work are composited scaled sensitivity (CSS) and parameter correlation coefficient (PCC).

The CSS indicates the sensitivity of computed responses to selected parameters and is defined as:

$$CSS_j = [\Sigma_{j=1}^{ND}(\frac{\partial y_i'}{\partial b_j} b_j w_{ii}^{1/2})^2 / ND]^{1/2} \tag{3}$$

where y_i' is the ith simulated value; b_j is the jth estimated parameter; $\partial y_i'/\partial b_j$ is the sensitivity of the ith estimated value with respect to the jth parameter;

w_{ii} is the weight of the ith observation and ND is the number of observations. The CSS indicate the total amount of information provided by the observations for the estimation of the jth parameter and measure the relative importance of the input parameters being simultaneously estimated. The higher the value of CSS, the higher the likelihood that computed responses could be altered by changing the parameter.

The PCC quantifies the correlation between each pair of parameters and ranges from −1 to 1. When the PCC is close to −1 or 1, the two parameters are highly correlated and cannot be uniquely estimated through optimization. The PCC is computed from the Variance-Covariance matrix, V:

$$V = S^2(X^T wX)^{-1} \tag{4}$$

where S is the objective function value calculated from Eq. 2, X is the sensitivity matrix with $X_{ij} = \partial y_i'/\partial b_j$. Accordingly, the PCC between the ith and jth parameter is given by:

$$PCC_{ij} = \frac{V_{ij}}{\sqrt{V_{i,i}V_{j,j}}} \tag{5}$$

For reasons already discussed, the field observations input into the optimization were the lateral displacement measured by SAA-1. The data presented herein are for the following two stages: (1) excavation to elev −7 ft CCD before the installation of the struts, and, (2) excavation to elev −22 ft CCD before the installation of the second level tiebacks. The former was the first elevation at which optimization was attempted during excavation. The lateral movements at this time were less than 0.25 in. To illustrate the process of optimization, results are presented for the latter case when the excavation reached elevation −7 ft CCD. In this case, optimization was using sets of data in both stages.

Figure 10 shows the computed CSS for soil parameters from the two clay layers. The selected parameters in the figure primarily govern soil's deformability as opposed to strength and failure, because the soil movement surrounding the excavation is the optimization objective. The targeted responses in computing CSS are soil lateral movement at centerline of the north wall of the excavation at two stages, when the excavation had been made to elev −7 ft and −22 ft CCD.

Figure 11 shows the absolute value of computed PCC for the same parameters. In this work, it is assumed that when the absolute value of PCC is equal or greater than 0.9, the corresponding two parameters cannot be optimized simultaneously. For both layers, it is clear that the parameters κ^* and ν_{pp}, R_{max} and χ cannot be optimized together.

To constrain the number of parameters simultaneously optimized and consequently ensure both the effectiveness and efficiency of the optimization, it was decided that each layer has two parameters to be optimized, with one controlling soil small strain stiffness and the other controlling large strain stiffness. At first, the parameters λ^* and R_{max}, κ^* and R_{max} were selected to be optimized for soft to medium stiff clay layer and stiff clay layer, respectively. While possessing the similar sensitivity, the parameter λ^* of soft to medium stiff clay is preferred compared to the parameter κ^*, because further excavation below

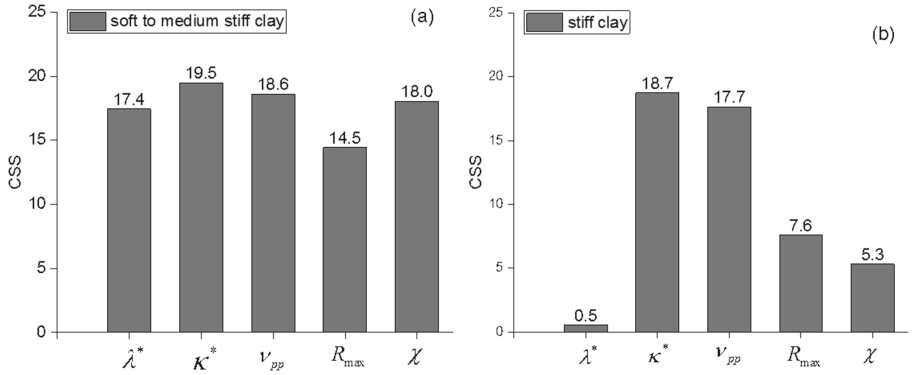

Fig. 10. Composite scaled sensitivity

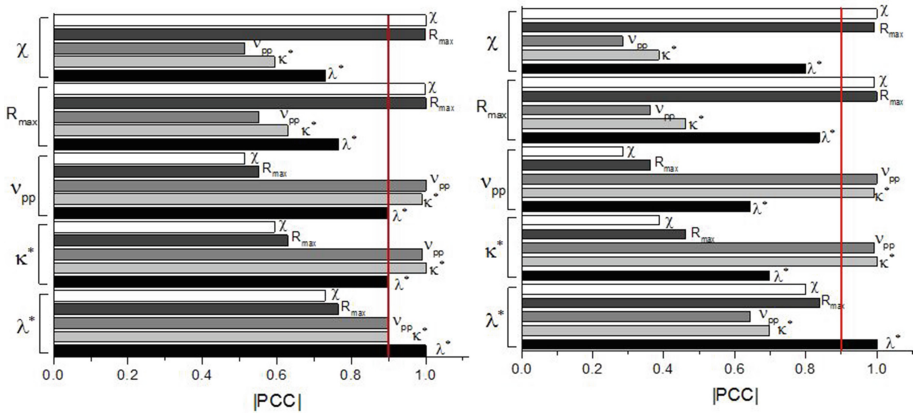

Fig. 11. Parameter correlation coefficient

elev −22 ft CCD is expected to result in more plastic deformation of the layer, which is primarily controlled by the parameter λ^*. It is noteworthy that the results from preliminary optimizations show that the parameter κ^* of stiff clay layer is reduced to significantly smaller value than that reported for other clays (eg., Gudehus et al. [8]), indicative that the soil behavior at the layer is controlled by small strain stiffness. As a result, only the parameter R_{max} is optimized for the stiff clay layer.

Table 3 summarizes the initial and optimized model parameters for the two clay layers when data sets from the two excavation depths are used in the computation. Note that while the three parameters that were optimized changed values, the amount of the correction was relatively small and within normal ranges expected for the parameters.

Table 3. Initial and optimized parameters for the two clay layers

	Soft to medium clay		Stiff clay	
	Initial	Optimized	Initial	Optimized
λ^*	0.06	0.07	0.05	
κ^*	0.012		0.012	
N	0.76		0.64	
ϕ_c	33		35	
ν_{pp}	0.15		0.15	
A_g	14000		37000	
n_g	0.61		0.61	
α_g	1.1		1.1	
m_{rat}	1		1	
R_{max}	5.0 e−5	4.19 e−5	2.4 e−5	4.86 e−5
β_r	0.18		0.18	
χ	1.3		1.3	

4.5 Computations Based on Optimized Paramsseters

The ability of the adaptive management procedure to update performance predictions at the SQBRC is illustrated based on the comparisons of the computed and observed lateral wall movements. Figure 12 shows the computed and observed values at SAA-1 based on the parameters optimized when the excavation was at elev −7 ft CCD (Fig. 12a) and parameters optimized when the excavation was at elev −22 ft CCD (Fig. 12b). The parameters used in the computation in Fig. 12b are those listed in Table 3. In Fig. 12(a), one sees that there is good agreement at when the excavation is at elev. −7 ft CCD, as expected since those data formed the basis of the optimization. However, by the time the excavation reached elev −22 ft CCD, the computed deformations were significantly less that the observed values. However, as one would expect, when both data sets formed the basis of the optimization in 12b, there was good agreement at both stages. One can conclude that there was insufficient information in the data set when the maximum movements were about 0.2 in. to allow optimization. When the next available period of excavation - when the excavation was below the second tieback level at −22 ft CCD - allowed one to use plane strain conditions to adequately represent the loading conditions, the movements were in the clays were large enough and hence contained enough information to permit computed results to adequately represent the observations.

However, this was not a test of the method since the data from the deeper cut was also used in the optimization. Figure 13 shows the comparison between the computed values based on data collected at elev −7 ft and −22 ft CCD for the final excavated conditions. These calculations represent Class A predictions for the final deformations because they were made during excavation. The

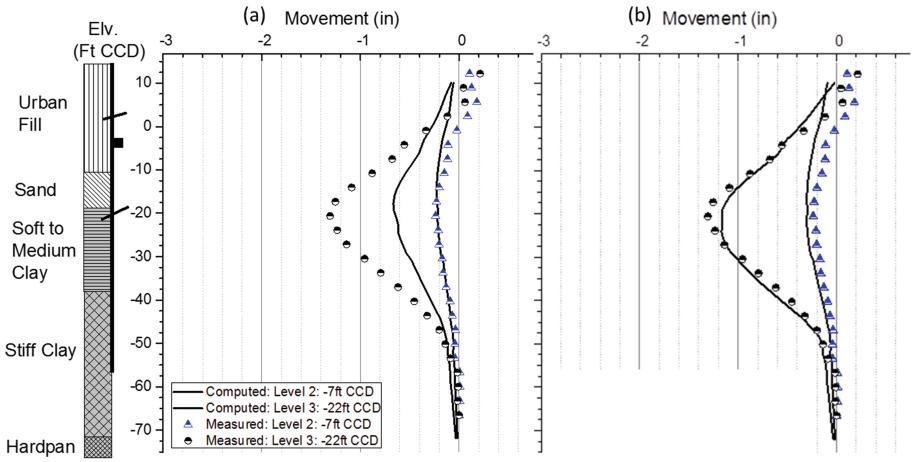

Fig. 12. Computed and observed lateral movements at SAA-1 (a) optimized using data from −7 ft CCD, (b) optimized using data from −7 ft and −22 ft CCD

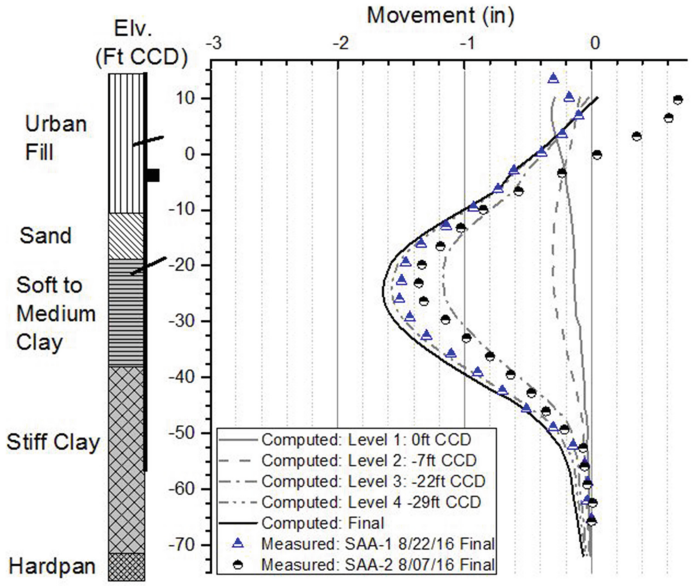

Fig. 13. Computed lateral movements at end of excavation and observed final values along north wall

computed and observed values agree well, in both magnitude and shape of the wall deformations at SAA-1. This shape array was located in the center of the wall and its response reflected plane strain conditions.

Also shown in Fig. 13 is the final deformations measured at SAA-2, located relatively close to the corner of the excavation. As one would expect, these values are smaller than those that developed at mid-length of the wall. Only a 3-D analyses could be expected to match both field data sets with the same set of parameters.

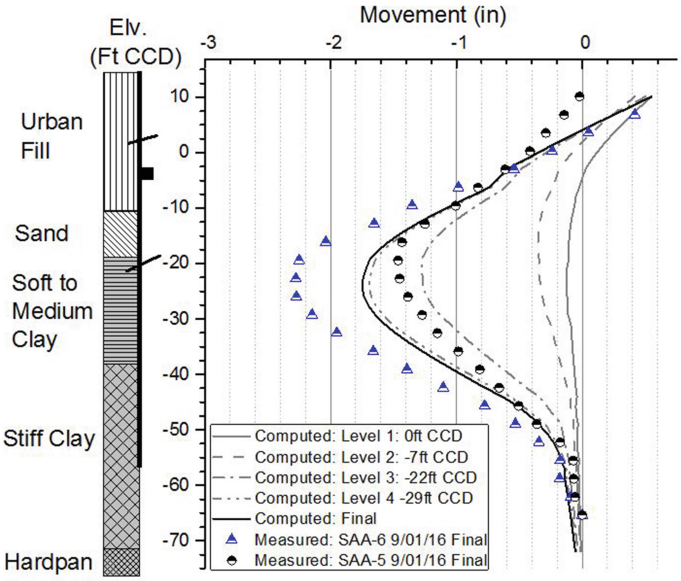

Fig. 14. Computed lateral movements at end of excavation and observed final values along south wall

Figure 14 shows the comparison between computed and observed results at the south wall based on optimization of the center of the north wall. The computed results are derived from the same simulation that produced the results in Fig. 13, since both sides of the excavation were represented in the analysis. The final lateral movements along the south wall measured at SAA-5 (80 ft from the southwest corner of the excavation) and SAA-6 (66 ft from the southwest corner) are shown in the figure.

In this case, the computed deflected shape of the wall agreed well with the observations, but the magnitude did not. Near the center of the wall, computed movements were 0.3 in. (or about 17%) more than the observed maximum values. However, at the quarter point, the computed movements were about 0.6 in. (about 35%) less than the observed maximum value. This discrepancy was due to at least two factors. First, SAA-6 was affected by the installation of the micropiles; recall that the maximum movement caused by their installation was 0.3 in. (Fig. 8). Second, the excavation in the southwest corner of the site adjacent to SAA-6 was 9 ft deeper adjacent to the wall than in the middle of the site,

as was assumed in the plane strain analysis. Thus, while good agreement was not observed in the magnitudes along the south wall, given the limitations of using a plane strain analysis, the parameters shown in Table 3, which were optimized for the conditions when the clays first became significantly stressed, resulted in reasonably computed deformations at both sides of the excavation. It is clear, however, that the detailed performance monitoring is necessary for the adaptive management approach to work well. An automated monitoring system such as that installed at the SQBRC site was very helpful in developing the correlations between construction activities and observed performance.

5 Optimization Assuming 3-D Conditions

There are a number of advantages of implementing a 3-D model to compute deformations when using the adaptive management approach to deep excavations. Several of the more important include:

1. Ability to update predictions at virtually any time, unlike when using plane strain simulations.
2. Ability to explicitly consider the effects of adjacent buildings, especially when working in congested urban environments. The construction of such buildings will alter the stress conditions in the soil at some locations which will be impacted by excavation for a new building.
3. Conceptually being able to explicitly account for variability in the soil conditions.

However, there are drawbacks to such an approach as well. In addition to the practical issue of the much larger size of the problem that must be numerically simulated, representing a support system in 3-D raises some questions as to how to model them. In particular, for the case of a sheet pile wall, the segments are discontinuous laterally, with some undefined rotational stiffness at each segment. The representation of an in-place sheet pile wall, including the effects of wales on the in-plane stiffness, becomes problematic.

Several of these issues are currently being studied, and selected results are presented in this paper to illustrate how these issues can affect the results of an analyses. As mentioned before, the adaptive management approach relies on isolating the effects of the soil response so that rationale updates of performance prediction can be made. When it is applied during construction, the uncertainties associated with how the excavation is actually constructed are eliminated, idealizations in the initial conditions and support system are still made, and these can have an effect on the computed deformations.

In particular, the effects of how the sheet pile wall is represented in the model and the impacts of the construction of an adjacent building, the RIC building in this case, on the computed wall deformations are examined.

5.1 Soil Parameters and Finite Element Mesh

In the analyses presented in this section, the soil response is modeled using the HS model. The parameters are shown in Table 4. Definitions of the parameters are found in the PLAXIS manual and will not be repeated herein for sake of brevity. They are parameters that were developed as part of the preliminary design studies, and are representative of those used in several studies of excavations in Chicago (e.g., Finno and Calvello [6]; Rechea [14]; Finno [3,4]). The results of the analyses presented in this section are used to illustrate variations in response, and as such, as long as the parameters yield reasonable magnitudes of movements, the conclusions drawn will be valid.

Table 4. Hardening Soil parameters for 3-D simulations

Parameter	Fill	Soft to medium clay	Stiff clay
γ_{unsat} (pcf)	115	100	120
γ_{sat} (pcf)	115	120	130
e_{in}	0.5	1	1
$E_{50,ref}$ (psf)	282,000	125,500	1,090,000
$E_{oed,ref}$ (psf)	282,000	87,700	763,000
$E_{ur,ref}$ (psf)	846,000	376,000	3,270,000
m	0.5	0.8	0.85
c'_{ref} (psf)	400	5	5
ϕ (degree)	30	26	32
ψ (degree)	2	0	0
ν'_{ur}	0.2	0.2	0.2
p_{ref} (psf)	2,000	2,000	2,000
R_{inter}	0.5	0.5	0.5
OCR	1	1.4	1.5

The finite element mesh used in the analyses is shown in Fig. 15. The model represents the northeast quarter of the SQBRC excavation. As seen in the figure, the fill and sand strata have been combined into a single layer because relatively small lateral wall movements (less than 0.2 in.) were observed during excavation and hence the element sizes were somewhat larger in this upper layer than in the clays. As suggested on the figure, the wales for the tiebacks and the cross-lot braces were explicitly modeled, as noted in pink. The tiebacks were individually modeled as embedded beams for the grouted anchor and anchor elements for the unbonded length. The cross lot braces were modeled as beam elements and the sheet pile wall was modeled as plate elements. The non-uniform depth of the final excavation level is seen in the figure.

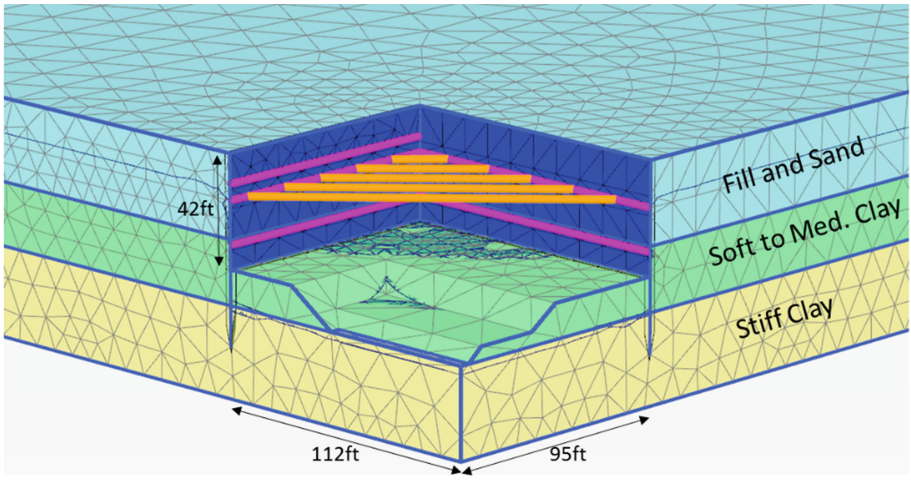

Fig. 15. Finite element mesh for 3-D analyses

5.2 Effect of Sheet Pile Stiffness Assumption

When modeling a sheet pile wall in a plane strain analyses, the parameters required are the Young's modulus and Poisson's ratio of steel, and some geometry parameters, such as cross-sectional area and moment of inertia of the particular steel pile section. When sheet piles have z-shaped cross-sections, the geometry of the sheet-pile wall requires transformation to a representative rectangular cross-sectional geometry for the finite element analysis. This is straightforward in a plane strain simulation, but somewhat problematic in a 3-D analysis. Figure 16 shows the geometric dimensions that are transformed. The z-shaped sheet-pile wall geometry provides a larger moment of inertia against bending in the 2–3 plane (perpendicular to the wall) than in the 1–3 plane (parallel to the wall).

When representing the sheet piles with plates, some transformation is required to account for the Z-shape within the context of a constant cross section of a plate element. The elastic modulus parameters are not traditional Young's Moduli, but rather bending stiffness parameters. The stiffness in bending in the vertical direction, the 2–3 plane in Fig. 16, is calculated as $E_1 I_1$, and the axial stiffness is calculated by $E_1 A_1$. In this case, I_1 and A_1 are the cross-sectional properties in a horizontal cross-section of the rectangular element used to model the wall.

The bending stiffness in the horizontal direction, the 1–3 plane in Fig. 16, depends primarily on the rotational stiffness at the sheeting interlocks. It is recommended in PLAXIS that the moment of the sheet-pile in the horizontal direction is less than the vertical direction by a factor of 20. Bending in the 1–2 plane is not a factor for sheet pile walls, and the wall is relatively stiff (against bending) in that direction.

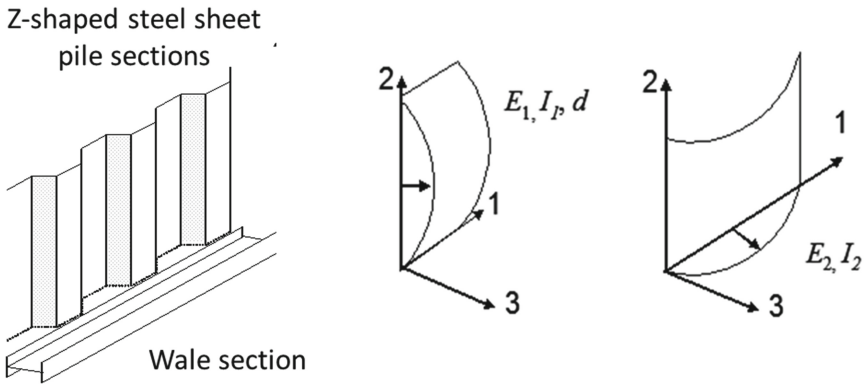

Fig. 16. Schematic of steel sheet pile and bending stiffness notation

However, there is no experimental data to justify the 20-fold reduction of wall stiffness of which the authors are aware. The number is similar to the reduction of E for straight sheet pile sections used in circular cellular cofferdams, where sheets are driven into the ground with the aid of a template and subsequently filled with sand to create the cofferdam cell. In this case, the interlocks are quite loose until filling, and the resulting slack in the system in the tangential direction has been modeled by using a horizontal modulus that has been reduced by 20 to 33 times, primarily on the basis of matching the lateral movements of the cofferdam walls during filling (Kuppusamy et al. [10]).

To illustrate the effects of various E ratio assumptions, a series of simulations were conducted using the mesh shown in Fig. 15. The reductions considered varied from no reduction, and therefore an analysis that is similar to the plane strain condition, and reductions of E in the horizontal direction for bending in the 1–3 plane (Fig. 16) of 5, 10 and 20.

The computed lateral wall movements at the end of excavation are shown in Fig. 17 along the north wall at essentially the same locations as SAA-1 and SAA-2 for the actual SQBRC excavation. As can be seen, the same general pattern of movements is observed in both the center and near the corner of the wall as for the actual excavation (Fig. 6). However, at both locations, the maximum lateral wall movements increase by about 50% as the E reduction ratio increases from 1 to 20. Furthermore, the wall response above the strut location changes significantly as the E reduction ratio increases. The isotropic response is typical of convention observed responses where the top of the wall rotates back after excavation is made below the first support level. In this 3-D case, the wall rotates about the cross lot brace level, rather than the first tieback level. This may be a result of the full moment connection assumed in the finite element simulation of the substantial wales; in the field, the wales were tack welded to the sheeting, and thus full moment connections would not result. The observed responses in Figs. 5 and 6 suggest that the 3-D isotropic response is more akin to the SAA data at the site. However, more study is needed to clarify this issue.

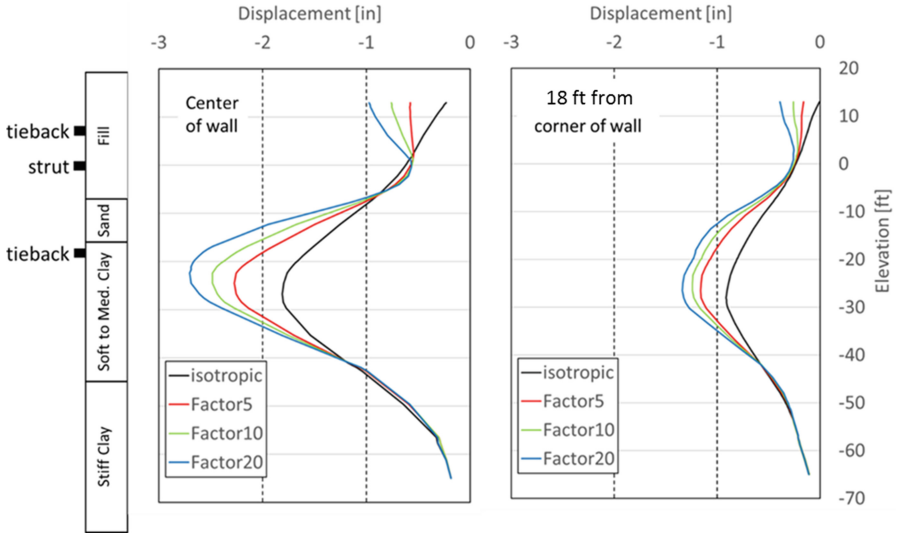

Fig. 17. Effect of sheet pile stiffness variation on computed lateral displacements at center and near corner of north wall

To further illustrate the effects of the E reduction ratio assumption, a plot of the lateral wall movements at the elevation of the maximum movement, about elev −25 ft CCD, along the north wall is shown in Fig. 18. Again one sees that the larger the E reduction ratio, the larger the displacements. Also, the higher E ratio results in larger curvatures in this direction, although the differences among the four cases are not particularly large.

Another factor to consider when modeling a sheet pile wall in a 3-D analysis is how to consider the effects of discontinuous elements, i.e., the wales, which were tack welded to sheet pile wall. The composite section increases the moment capacity in horizontal direction, but by how much? This remains an open question.

5.3 Effect of Modeling the Adjacent RIC Building

The RIC building to the east of the SQBRC excavation was founded on belled drilled shafts founded in the hard clays and included a 14 ft deep basement. As such the stresses in the clays beneath it were less than those to the south and north of the SQBRC excavation. Given that the cross-lot braces were diagonal, loads from the north and south sides of the excavation were likely transmitted to the east wall adjacent to the RIC building. The same is true for the Lurie Center to the west of the excavation which was also supported on belled drilled shafts and had a 42 ft deep basement.

To illustrate the effects of these unbalanced in situ stresses that existed, a 3-D analysis was conducted using the same geometry as shown in Fig. 15, but the

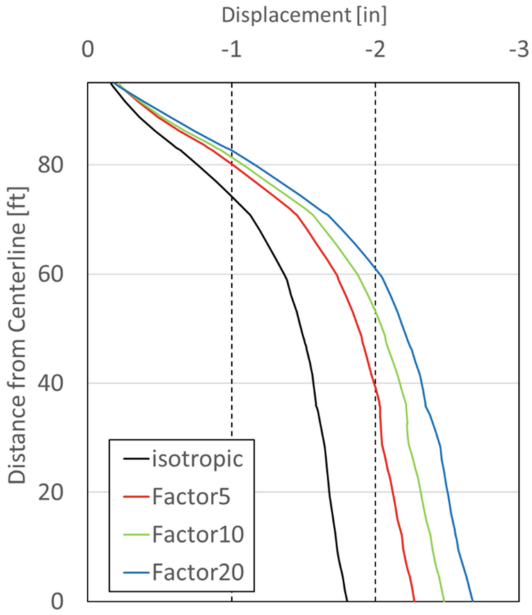

Fig. 18. Effect of sheet pile stiffness assumption on maximum lateral wall movements along north wall

excavation for the RIC building was included in the simulation. In reality, a full 3-D simulation that included simulating both the RIC and Lurie Center excavations would be required, but the size of mesh required for this calculation was too large to allow sufficient resolution for the detailed simulation of the SQBRC excavation. So while the simulation which takes advantage of symmetry about two planes is an approximation of the actual conditions, it does illustrate the effects of the different in situ stresses at various locations around an excavation resulting from adjacent building construction.

The soil parameters used in this analysis were those given in Table 4. Results of the simulation are shown in Fig. 19, a plot of the lateral wall movements of the north and east walls versus depth at the center of each wall. When the RIC structure and excavation explicitly was considered, the results show that maximum lateral wall movements are about 25% larger when the RIC excavation was included.

Apparently, the loads from the north side of the excavation were transferred to the RIC side via the diagonal cross-lot braces because the available stiffness of the soil at the RIC side was reduced by unloading. When the RIC building was not considered, more lateral movement was computed on the east side, as a consequence of the absence of the upper tieback level at the east side (see Fig. 15). It was not needed in the field because of the 14 ft deep basement at the RIC building. This example illustrates that the stress conditions in the soil caused by past construction activities in urban areas may affect computed deformations

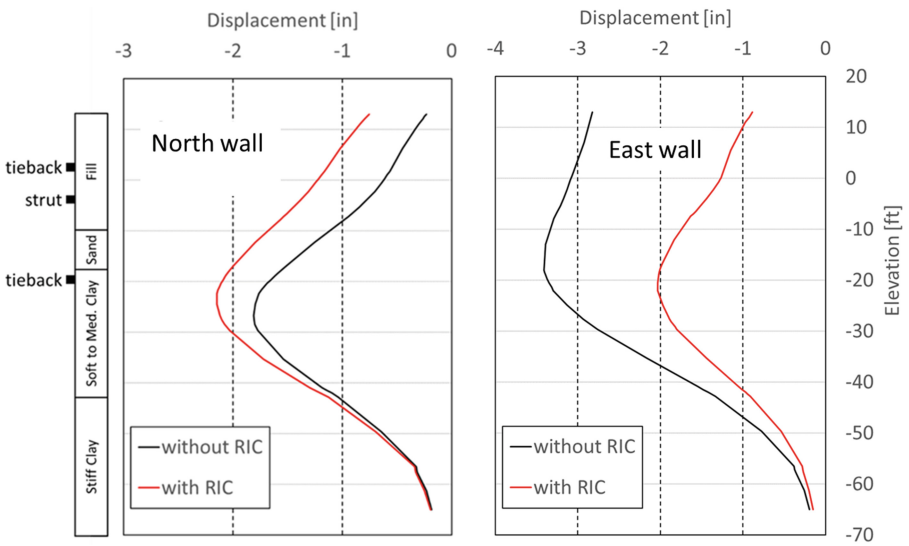

Fig. 19. Effect of the presence of the RIC building on computed wall lateral movements at center of north and east walls

associated with deep supported excavations and that when diagonal braces are used, careful consideration must be given to the in situ stress conditions that may have been affected by past construction.

6 Concluding Remarks

Plane strain modeling resulted in optimization of parameters at a relatively early stage of excavation at the SQBRC site such that lateral wall movements were predicted reasonably well at the end of the project. This was made possible by the automated monitoring system installed at the site, particularly the SAA that autonomously collected lateral wall movements and stored the data in a project web site and access to the project web camera. Construction had to be closely monitored so that times when plane strain conditions were applicable and that activities other than cycles of excavation and bracing that caused ground movements could be identified. When subsurface conditions are similar to those in the Chicago area, significant movements will not develop until the softer clays are stresses by the excavation activities, and as such, these times will represent the earliest that one could reasonably expect optimization to be reliably completed.

However, the full potential of the method will not be realized until optimization can be done based on actual conditions, which many times during an excavation are 3-D in nature. While the capabilities of the 3-D analyses are such that one can adequately model non-uniform excavation and support installation, there are a number of other factors need to be studied further. Two of these issues

have been highlighted herein and included modeling the sheet pile as a three-dimensional support so that the rotational stiffness and the wale-wall connections can be adequately represented and defining the initial stress conditions at the start of construction in a crowded urban setting. Because of uncertainties associated with these issues, one cannot isolate the effects of the constitutive model on the observed deformations. This lack of unambiguity in causes of computed responses currently limits the application of the adaptive management method to well defined excavation stages and center portions of large excavations where past construction activities have been adequately modeled.

Acknowledgements. The excavation support system was designed and constructed by Hayward Baker, Inc. The authors are grateful for their cooperation and would like to thank Mr. Justin Lewis, the project manager, for his help and interest throughout the project. Getec developed and maintained the project web site which provided real time access to the SAA data. The cooperation of Mr. Jay Baehr and Ms. Jo Lemieux-Murphy of Facilities Management at Northwestern University was instrumental in providing unfettered access to data collected by a variety of subcontractors. The funding for the work reported herein was provided by a National Science Foundation grant CMMI-1603060. The support of Dr. Richard Fragaszy is greatly appreciated.

References

1. Arboleda-Monsalve, L.G.: Performance, instrumentation and numerical simulation of One Museum Park West excavation. Ph.D. thesis. Northwestern University, Evanston, IL (2014)
2. Benz, T., Vermeer, P.A., Schwab, R.: A small-strain overlay model. Int. J. Numer. Anal. Methods Geomech. **33**(1), 25–44 (2009)
3. Finno, R.J.: Linking field observations and performance prediction updates during construction. In: Proceedings of the 15th Great Lakes Geotechnical/Geoenvironmental Conference. ASCE, Indianapolis (2008)
4. Finno, R.J.: Use of monitoring data to update performance predictions of supported excavations. In: Proceedings of the International Symposium on Field Measurements in Geomechanics, FMGM 2007, GSP 175. ASCE, Boston (2007)
5. Finno, R.J., Blackburn, J.T.: Automated monitoring of supported excavations. In: Proceedings of the 13th Great Lakes Geotechnical/Geoenvironmental Conference, GPP 3, pp. 1–12. ASCE, Milwaukee (2005)
6. Finno, R.J., Calvello, M.: Supported excavations: the observational method and inverse modeling. JGGE **131**(7), 826–836 (2005). ASCE
7. Finno, R.J., Hiltunen, D.R., Kim, T.: Cross-anisotropy of Chicago glacial clays from field and laboratory data. In: Proceedings of GeoCongress 2012. ASCE, Oakland, March 2012
8. Gudehus, G., Amorosi, A., Gens, A., Herle, I., Kolymbas, D., Mašín, D., Muir Wood, D., Niemunis, A., Nova, R., Pastor, M.: The soil models info project. Int. J. Numer. Anal. Meth. Geomech. **32**(12), 1571–1572 (2008)
9. Hashash, Y.M.A., Finno, R.J.: Development of new integrated tools for predicting, monitoring and controlling ground movements due to excavations. In: Proceedings of the Underground Construction in Urban Environments. ASCE Metropolitan Section Geotechnical Group, New York (2005)

10. Kuppusamy, T., Clough, G.W., Finno, R.J.: Finite element analysis of cofferdam with cell interaction. In: Proceedings of 11th International Conference of Soil Mechanics and Foundation Engineering, San Francisco, CA, vol. 4, pp. 1973–1986 (1985)
11. Ledesma, A., Gens, A., Alonso, E.E.: Estimation of parameters in geotechnical backanalysis-maximum likelihood approach. Comput. Geotech. **18**(1), 1–27 (1996)
12. Mašín, D.: Clay hypoplasticity model including stiffness anisotropy. Géotechnique **64**(3), 232–238 (2014)
13. Ou, C.Y., Tang, Y.G.: Soil parameter determination for deep excavation analysis by optimization. J. Chin. Inst. Eng. **17**(5), 671–688 (1994)
14. Rechea, C.: Inverse analysis techniques for parameter identification in simulation of excavation support systems. Ph.D. thesis, Northwestern University, Evanston, IL (2006)
15. Schanz T., Vermeer P.A., Bonnier P.G.: The hardening soil model-formulation and verification. In: Proceedings of the Plaxis Symposium, Beyond 2000 in Computational Geotechnics, Amsterdam, Balkema, pp. 281–296 (1999)

Stress Paths on Displacement Piles During Monotonic and Cyclic Penetration

Jakob Vogelsang(✉), Gerhard Huber, and Theodoros Triantafyllidis

Institute of Soil Mechanics and Rock Mechanics,
Karlsruhe Institute of Technology, Karlsruhe, Germany
jakob.vogelsang@kit.edu

Abstract. In this contribution, a study on the behavior of instrumented model piles in slow, cyclic penetration tests using a cylindrical full model test set-up is presented. The tests are performed under 1g-conditions in a uniform medium sand. A hydraulic driving system enables a displacement controlled penetration similar to the pile motion during vibro-driving at strongly reduced frequency. The pile instrumentation allows the measurement of shaft and tip force during the driving process. Systematic variation of soil density and displacement amplitude reveals the occurrence of typical stress paths of vibratory pile penetration. By comparison with results from monotonic and vibratory penetration tests, the influence of the penetration mode is deduced. Results from FE simulations applying a hypoplastic soil model help to illustrate the strong requirements and the considerable challenges to obtain realistic simulations of cyclic pile penetration processes. Some hints towards a further numerical modeling of the tests are given.

Keywords: Displacement pile · Monotonic penetration · Cyclic penetration · Vibratory pile driving

1 Vibratory and Cyclic Pile Penetration

Vibratory pile driving bases on the application of a harmonic excitation to a vibrator-pile system in order to facilitate the penetration compared to jacking or impact driving. The pile motion during vibro-penetration is a result of the excitation, the dynamic properties of the pile-vibrator system and the soil response. In practice, the range of applied frequencies is 15 to 50 Hz and typical displacement amplitudes lie within 5–15 mm resulting in penetrations per cycle of vibration of about 1–10 mm [4,15]. Generally speaking, dense cohesionless soils require high displacement amplitudes whereas in loose soil, it is helpful to use high frequencies [15].

The global penetration behavior and the evolution of tip resistance depend qualitatively on the combination of displacement amplitude and penetration per cycle of vibration. However, in cohesionless soils and in the scope of application, the tip resistance is independent of the current penetration velocity. High penetration rates, the so-called fast vibratory driving, is characterized by the reach

T. Triantafyllidis (ed.), *Holistic Simulation of Geotechnical Installation Processes*,
Lecture Notes in Applied and Computational Mechanics 82, DOI 10.1007/978-3-319-52590-7_2

of a limit tip resistance comparable to monotonic penetration resistance. The beneficial effect of eased penetration is obtained for larger ratios of amplitude and penetration per cycle, the so-called slow vibratory pile driving [4,15]. These dependencies are qualitatively well known, although there is still a considerable lack of understanding the soil mechanical processes and of concise prognosis tools for the driving process. Although FE simulations have been shown to be able to qualitatively reproduce the major effects, their systematic and quantitative validation is still under research.

The shaft friction in a given depth depends on the radial stress acting on the pile shaft and the friction coefficient between soil and shaft. It is also independent of shearing velocity for cohesionless soils. While the friction coefficient can be estimated or measured with sufficient accuracy, knowledge about the radial stress distribution is difficult to be obtained. Although it is reasonable to assume a qualitatively increasing stress with depth, simple estimations e.g. done by Dierssen [5] fail to explain the observed mechanisms, notably, the so-called friction fatigue effect: the decreasing radial stress in a given depth with increasing pile penetration [9,11,20]. This degradation of stress along the pile shaft is a function of depth, soil density, number and amplitude of cycles and pile diameter [11,14,20]. The quantitative incorporation of all these effects in numerical simulations is currently not possible.

Laboratory model tests on pile penetration are useful to gain a better understanding of the process and to obtain experimental data for comparison with numerical simulations. However, dealing with vibratory pile penetration, the test results may be influenced by boundary effects and the tests therefore be problematic for numerical simulations. Accounting for the velocity-independence of the soil resistance during vibro-penetration, cyclic penetration tests at strongly reduced frequency are frequently used to overcome some of these limitations and to incorporate major effects of vibratory penetration at the same time [8,11,20]. The cyclic pile motion is now imposed. It can thus be maintained constant throughout a test and is easily varied from test to test. Although e.g. White and Lehane [20] highlight the role of cyclic pile motion, it is interesting to note that a systematic investigation of its influences has not been carried out until now.

The present study tries to contribute to this research in order to close the knowledge gap and to provide valuable experimental data for comparison with numerical simulations. The objective is to investigate whether slow cyclic penetration tests can be used to observe effects similar to vibratory pile driving and to perform a parametric study on the influence of soil density, pile displacement amplitude and penetration depth. The cyclic penetration tests are interpreted with respect to monotonic penetration tests for three different initial densities. A systematic investigation of the process is achieved by application of prescribed cyclic displacement sequences maintained throughout each test. Due to the concentration on slow tests, a wide range of numerical models should be applicable for the simulation of the tests. Some numerical back-calculations of the tests are also given in this paper.

2 Experimental Setup

2.1 Experimental Setup

The basic test setup is schematically illustrated in Fig. 1(a). It is also described in detail in [19]. The model tests are performed in a cylindrical test container of stainless steel. The container has an inner diameter of 0.94 m and a height of 1.45 m measured from the bottom of the container. It is filled with dry sand, thus, the inner dimensions of the test container correspond to the initial sample geometry. An instrumented model pile is penetrated into the sand by means of an actuator unit mounted on top of the container. The actuator unit consists of a loading frame installed with a differential hydraulic actuator allowing a maximum stroke of about 1.2 m. Typical penetration depths reached in the tests are about 1 m. The actuator is operated by a hydraulic aggregate and is equipped with a control valve allowing the application of two-way displacement sequences.

The model pile has a diameter of 50 mm and about 1.4 m length. It is manufactured of a stainless steel tube with 2 mm thickness and has an instrumented pile tip. The tip has an angle of aperture of 60°. The friction angle between pile surface and test sand can be estimated to $12 \div 15°$ based of the results of interface tests [19]. Above the pile head, a 0.46 m long spacer is placed to take advantage of the full cylinder stroke for pile penetration. The spacer is connected to the hydraulic piston.

The ratio of test container and pile diameter is rather small ($d_C/d_{pile} \approx 19$) and the container wall can be considered as rigid. Thus, significant boundary effects are expected in the experiments leading to an increase of penetration resistance compared to free-field conditions, particularly in dense sand [4,19]. However, the tests are comparable between each other and the lateral boundary conditions can be implemented in a numerical model so that the basic requirements for benchmark experiments are fulfilled.

Two types of tests can be performed with the current setup: monotonic and cyclic penetration tests. In monotonic tests, the pile penetration is conducted with a constant velocity of 3 mm/s. Cyclic tests consist of alternating phases of downward motion with approximately 3 mm/s and upward motion with about 5 mm/s. The control valve for the hydraulic actuator is therefore connected to the data acquisition. In the case of cyclic tests, the measurement of pile displacement is sampled and the valve is switched according to the desired sequence of downward and upward pile motion. The amount of downward and upward motion can be prescribed with sufficient accuracy after some calibration procedures. The frequency is in the range of $0.25 \div 1$ Hz leading to moderate accelerations at the pile toe of about 0.2 g max. around the reversal phases of pile motion.

2.2 Instrumentation

At the pile head, the displacement and the head force are measured. A potentiometric cable transducer which is attached to the connection cross bar measures the relative displacement between pile head and loading frame. The load cell for

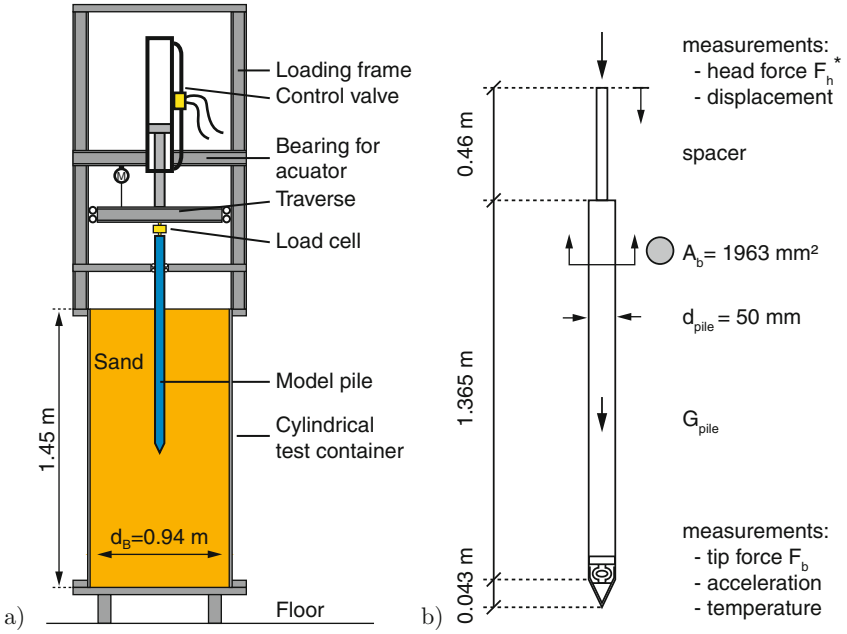

Fig. 1. (a) Basic test setup for the model tests and (b) measurements on the instrumented model pile

the pile head force is self-fabricated and connects the pile head to the traverse. It has a measuring range of 50 kN, a resolution of 0.01 kN and a linearity error smaller than 0.5%.

The pile tip is instrumented with a load cell, an acceleration transducer and a temperature measurement. The load cell (in-house manufacture) is designed for 10 kN maximum load with 0.5% linearity error, Fig. 2. Detailed information about the design and the characteristics of the load cell can be found in [19]. For acceleration, an ICP-transducer and for temperature, a micro PT-100-type sensor are used.

The measurements are recorded using a multichannel system with simultaneous sampling and digital filtering (16 bit, 400 Hz sampling rate and 40 Hz Bessel lowpass filter, 4th order).

Figure 1(b) shows the nomenclature for the measured values that are used for the interpretation in this paper. $u_{y,pile}$ indicates the position of the pile shoulder relative to the initial level of the sand surface, resp. the upper edge of the test container. The overall penetration resistance is named F_h and corresponds to the measured head force F_h^* subtracted by the pile weight G_{pile}. The tip resistance is expressed in terms of the measured tip force F_b and the tip pressure $q_b = F_b/A_b$. The shaft friction force can be calculated as the difference between overall and tip resistance, $F_s = F_h - F_b$.

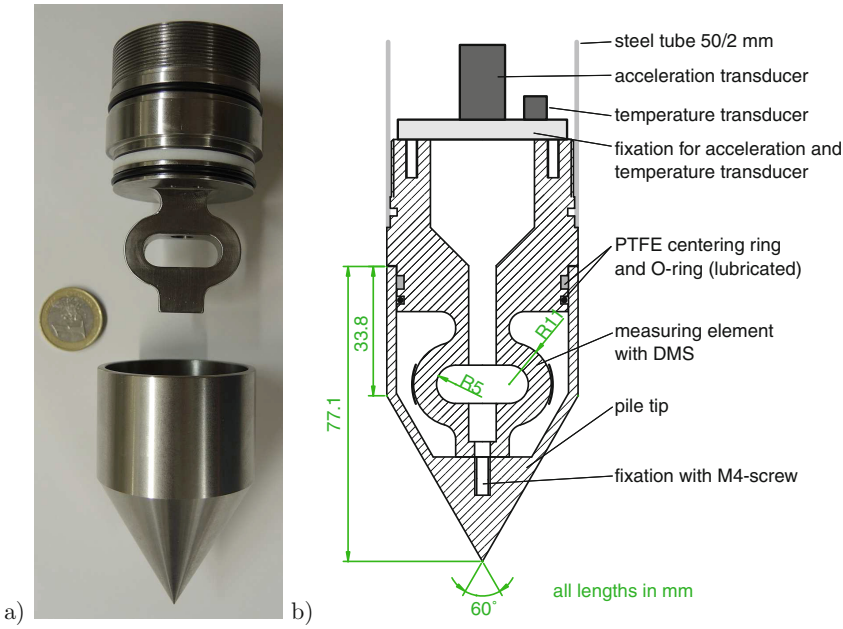

Fig. 2. Self-fabricated instrumented model pile tip: (a) Photo and (b) cross section

2.3 Test Sand and Sample Preparation

A uniform medium quartz sand is used in the present study. The minimum and maximum void ratios are $e_{min} = 0.557$ and $e_{max} = 0.873$. Compared to other studies of the authors [18,19], the test sand has slightly more fine content and different index void ratios, however, it remains very similar. Figure 3 shows a typical grain size distribution determined for the sand of the present series (2016) in comparison with sand of an older charge (2013).

A rainer system is used to pluviate the dry sand into the test container. Different initial densities are achieved by variation of the free fall height and pluviation intensity. Loose samples are prepared using a rigid tube and zero free fall height by building up a soil cone, according to the ASTM Standard [1] or DIN 18126 [6] procedures. As can be seen in Table 1, the achieved relative densities actually are about zero, which proves that the method also works in a larger scale. Medium dense and dense samples are built up in horizontal layers using a diffusor with 0.15 to 0.3 m free fall height and low intensity. High free fall heights and low intensities lead to higher densities [3,19]. A detailed description of the preparation and uniformity control methods is provided by Vogelsang [19].

2.4 Experimental Program

The test series discussed here comprises 9 penetration tests including 3 monotonic (MON) and 6 cyclic tests (CYC). Three different initial densities

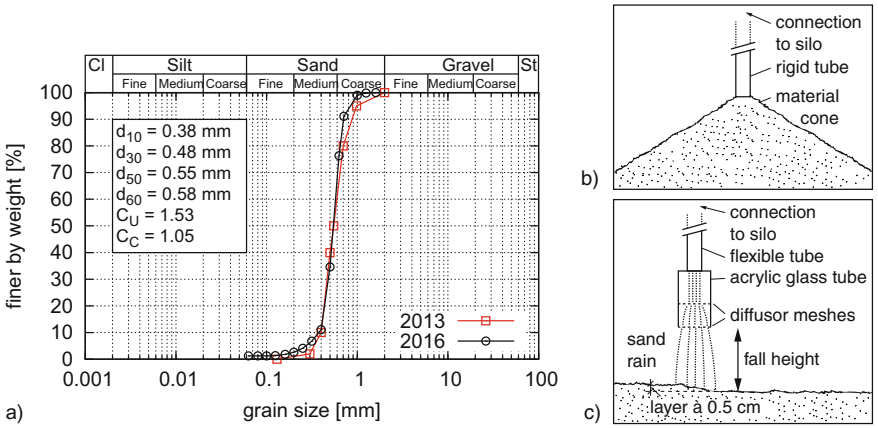

Fig. 3. (a) Grain size distributions of the test sand in comparison with sand from previous studies, (b) sand deposition procedure for loose samples and (c) for medium dense and dense samples.

have been investigated: loose, medium dense and dense. For each density a set consisting of a monotonic test, a cyclic test with small amplitude and a cyclic test with large amplitude has been performed. Information concerning the initial conditions and the performed test paths are given in Table 1.

The designation of the tests follows [19], where also additional test results can be found. The value y_0 corresponds to the initial vertical height of the pile shoulder above the sand surface (Fig. 4 - test start) and in the column $u_{y,pile}$, the test path is characterized. In the case of monotonic penetration, only the maximum penetration depth is given (relative to the pile shoulder). For cyclic tests, the values in brackets describe the performed sequence of downward and upward motion. For the discussion of the test results the variable $u_{y,pile}$ is used

Table 1. Test information for the present study

Test	Date	e_0 [−]	$I_{D,0}$ [−]	Type	y_0 [mm]	$u_{y,pile}$ [mm]
VM-06	15.02.16	0.8655	0.024	MON	35	−1050
VM-07	17.02.16	0.8746	−0.005	CYC	35	−1030 (−10/+4)
VM-10	18.03.16	0.6958	0.561	CYC	67	−1010 (−10/+4)
VM-11	07.04.16	0.6990	0.551	MON	67	−1010
VM-12	13.04.16	0.7019	0.542	CYC	66	−1080 (−5/+1)
VM-15	24.05.16	0.6001	0.864	CYC	69	−635 (−10.3/+4.3)
VM-16	17.06.16	0.6001	0.864	MON	73	−660
VM-17	06.07.16	0.5990	0.867	CYC	74	−630 (−6.9/+3)
VM-20	19.10.16	0.8707	0.007	CYC	74	−1080 (−5/+1)

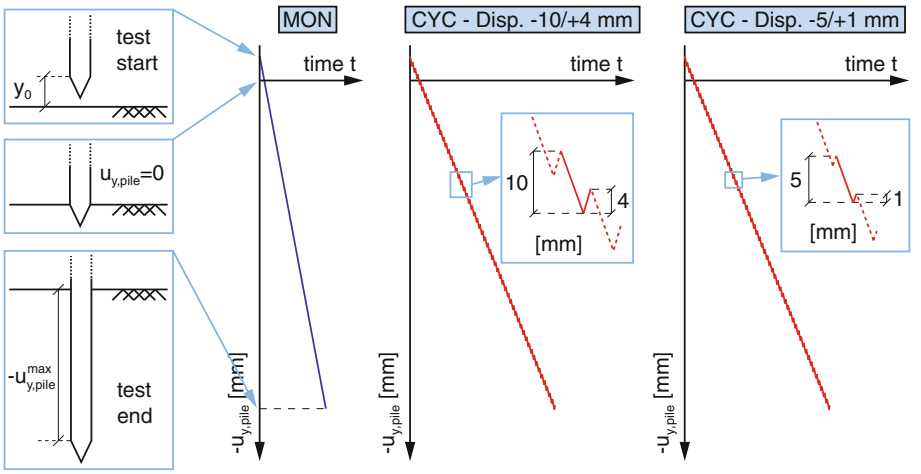

Fig. 4. Schematic illustration of the test paths performed for the present study

indicating the current vertical position of the pile shoulder below the sand surface (negative values for positions below the sand surface).

In the first group of tests, alternations of a penetrative motion of ca. 10 mm and upward motions of about 4 mm are conducted. This displacement sequence will be characterized as cyclic displacement with large amplitude. The other cyclic test path corresponds to penetration phases of about 5 mm and pullout phases of approximately 1 mm. These tests will be named tests with small displacement amplitude. The test paths are schematically illustrated in Fig. 4.

3 Test Results

3.1 Global Penetration Resistance

The first results in Fig. 5 are illustrating the evolution of penetration resistance in monotonic tests. The curves of the three tests will be displayed in the subsequent figures and serve as a reference for the cyclic tests.

It can be seen that the magnitude of penetration resistance changes depending on the initial soil density. The resistance in medium dense sand is about 10 times and in dense sand about 20 times larger than in loose sand. Therefore, in the subsequent figures, individual scales will be used for the different densities.

Apart from the magnitude of measured force, the qualitative shape of the evolution of penetration resistance is density-dependent. According to the description of penetration resistance in sand given by Linder [12], the penetration process can be divided in three important phases. The first phase of penetration resembling to the behavior of shallow foundations cannot be distinguished, probably to the conical pile tip. The two other important phases of penetration can be observed for the tests in loose and medium dense sand: a transition phase

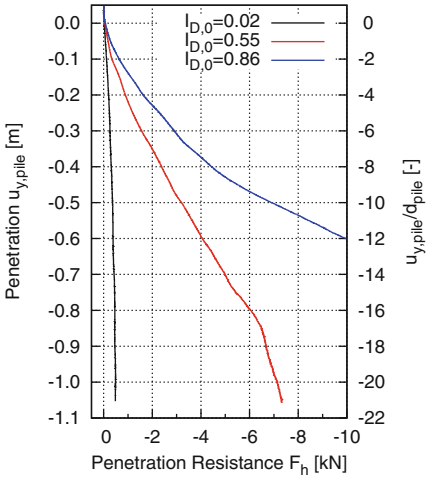

Fig. 5. Comparison of the penetration resistance in monotonic tests

with very slowly increasing resistance and a phase of quasi-constant penetration resistance (Linder [12]). Especially in medium dense sand, the reaching of the third phase of quasi-constant resistance is very marked in a depth of about $16d_{\text{pile}}$. In loose sand, the phase of constant resistance is also very pronounced (better to see in Fig. 6). On the other hand, in dense sand, the transition to the third phase is not reached. The rapidly increasing resistance in dense sand is indicating a strong jamming effect related to the low ratio of container/pile diameter.

Figure 6 shows a comparison of the penetration resistance in cyclic and monotonic penetration tests of the present series. The upper row corresponds to the tests with large amplitude ($\approx -10/+4$ mm) and the lower row to the tests with smaller amplitude ($\approx -5/+1$ mm). The left hand side shows the results in loose sand, the middle those in medium dense and the right hand side the tests in dense sand. This composition is maintained throughout the subsequent figures. The tests in dense sand were only performed to a depth of about 0.65 m because the maximum force of the tip load cell was reached.

Figure 6 shows an alternation of large compressive forces in the penetration phases and slightly positive forces during upward motion. The penetration resistance is composed of tip and shaft force, whereas the pullout force is attributed only to the shaft force. The interpretation of the results is first done based on the envelope curves, in other words the maximum penetration and pullout resistance. Afterwards, the behavior during individual cycles will be considered in detail.

The maximum penetration force in a given depth is clearly related to the monotonic penetration resistance. Thus, the envelope of the penetration force has a similar shape as the monotonic curve. In loose sand, the monotonic resistance is slightly exceeded, probably due to a stronger densification of the material around

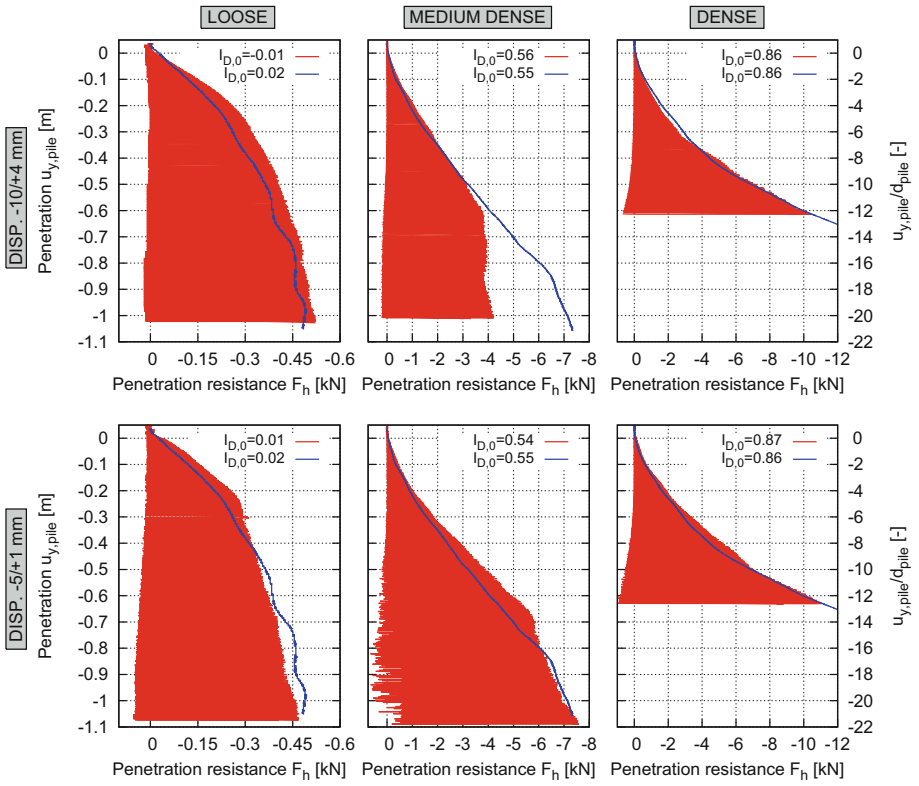

Fig. 6. Comparison of the evolution of global penetration resistance. Large amplitude driving in the upper row and small amplitude driving in the lower row. The columns represent different initial densities from loose to dense.

the pile. Regardless the amplitude, for medium dense and dense sand, above depths of about 0.6 m, the limit value during cyclic penetration is almost equal to the monotonic resistance. In medium dense sand, large penetration depths and amplitudes lead to a significantly lower maximum penetration resistance. In 1 m depth, only about 60% of the monotonic resistance are reached. Whether a similar effect occurs in dense sand remains unclear due to the limitation of penetration depth.

3.2 Evolution of Tip Resistance

The evolution of tip resistance with depth is depicted in Fig. 7. The figure is equally composed as Fig. 6.

In Fig. 7 it can be seen, that generally, the tip force vanishes during upward motion of the pile. The tip force during penetration is similar to the global penetration resistance, indicating that tip resistance is predominant compared to shaft resistance. Globally, similar observations like from Fig. 6 can be drawn.

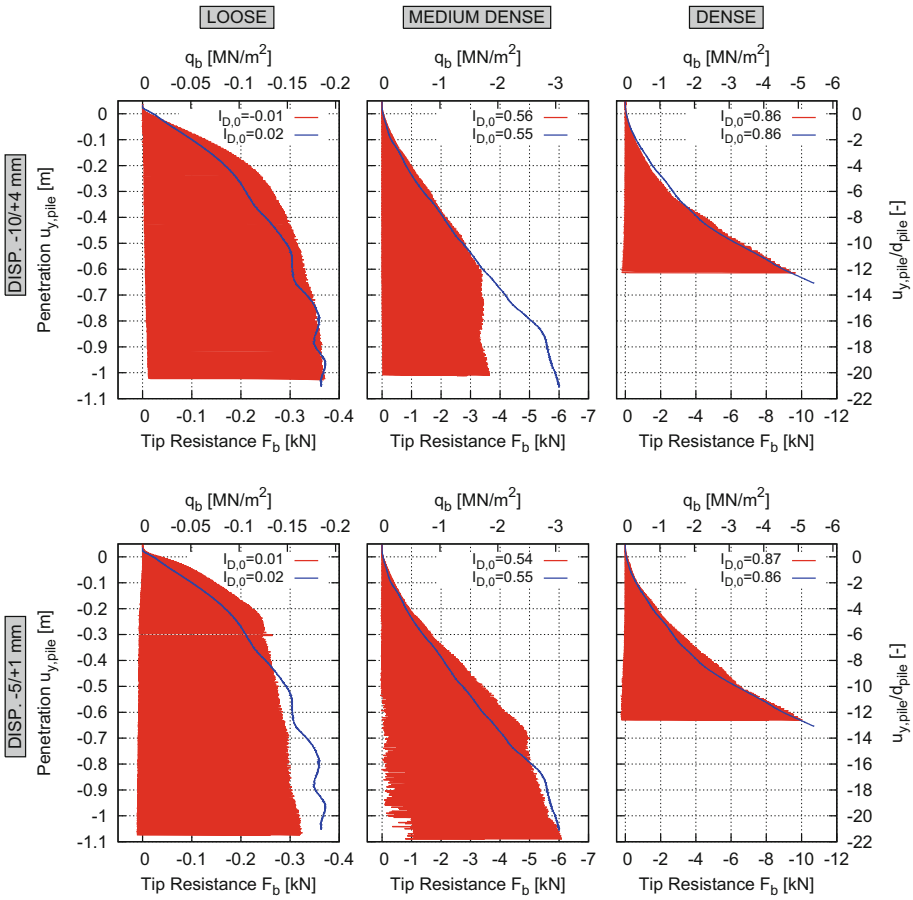

Fig. 7. Comparison of the evolution of tip resistance. Large amplitude driving in the upper row and small amplitude driving in the lower row. The columns represent different initial densities from loose to dense.

The most interesting observation in Fig. 7 is the significant difference between the cyclic tests in medium dense sand. In the case of the larger amplitude, the tip force vanishes during every upward motion of the pile and below 0.6 m the maximum tip resistance development is significantly below the monotonic tip resistance. Contrarily, for smaller upward motion and large penetration depths, the tip force decreases during upward motion, but remains compressive. Furthermore, the maximum tip force developed during penetration is very similar to the monotonic curve. A certain displacement amplitude resulting in a clear stress relief below the pile tip seems to be necessary to facilitate the penetration compared to jacking. For shallow penetration the monotonic resistance is always reached even though the tip force vanishes during upward pile motion. These

observations are in accordance with the in-situ results of Cudmani [4] for small penetration depths.

3.3 Evolution of Shaft Resistance

Similarly to the preceding figures, Fig. 8 shows the evolution of shaft force with penetration depth.

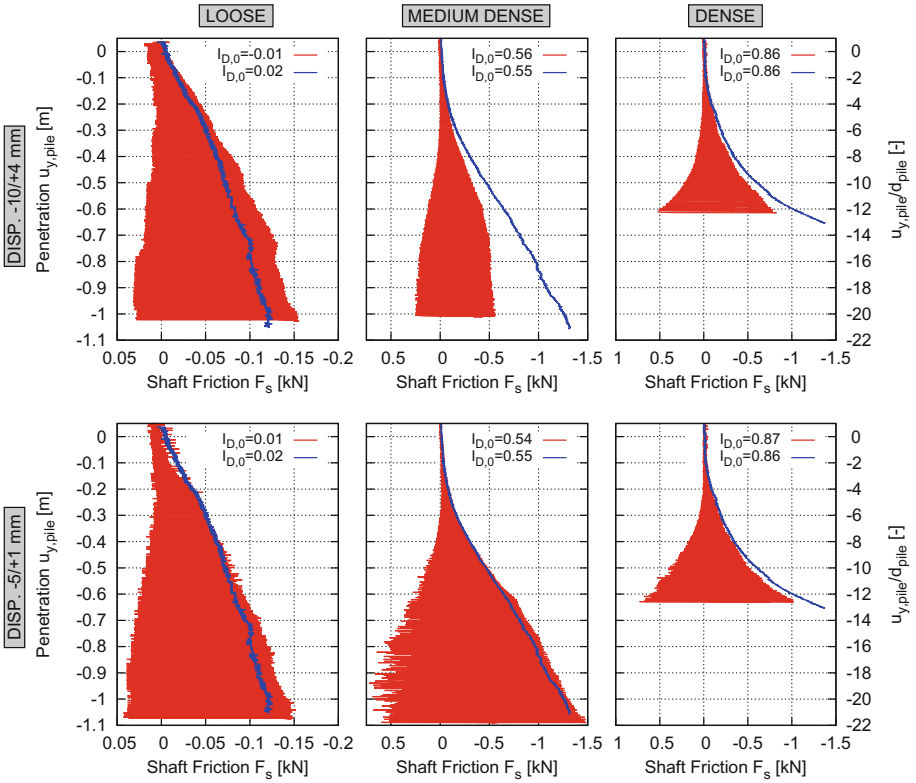

Fig. 8. Comparison of the evolution of shaft resistance. Large amplitude driving in the upper row and small amplitude driving in the lower row. The columns represent different initial densities from loose to dense.

In all tests, more shaft friction is mobilized during penetration compared to the pullout phase. This leads to a more or less pronounced asymmetry of both envelope curves. It is interesting to notice that the shaft friction during upward motion in loose sand is almost negligible indicating very low radial stresses acting on the pile. In these tests, the maximum shaft friction is slightly higher compared to monotonic penetration. A stronger densification due to cyclic penetration can be considered as the cause for this increase of shaft capacity. The tests in medium

dense sand clearly reveal the occurrence of the so-called friction fatigue effect in the case of large amplitude cycling. Throughout the whole test, the maximum shaft friction during penetration is clearly below the monotonic curve. Contrarily, for small amplitudes, the developed maximum resistance almost perfectly corresponds to the monotonic resistance. Even though the amount of upward motion is smaller, more friction is mobilized in the pullout phases compared to the test with large amplitude. This indicates, that the global stress regime acting on the pile is higher for small amplitude cycling and friction fatigue does not occur. In dense sand, friction fatigue does not play a major role although slightly lower shaft friction is observed for large amplitude cycling.

Large amplitudes in combination with medium dense soil conditions seem to be beneficial for the occurrence of friction fatigue [20]. The reason why friction fatigue is not so pronounced in the other tests may be due to the inability of loose sand for arching and the lack of dense sand for significant contraction.

3.4 Cyclic Evolution of Tip Resistance

Figure 9 investigates the cyclic evolution of tip resistance in detail. Therefore, a short section in about 0.5 m penetration depth is depicted.

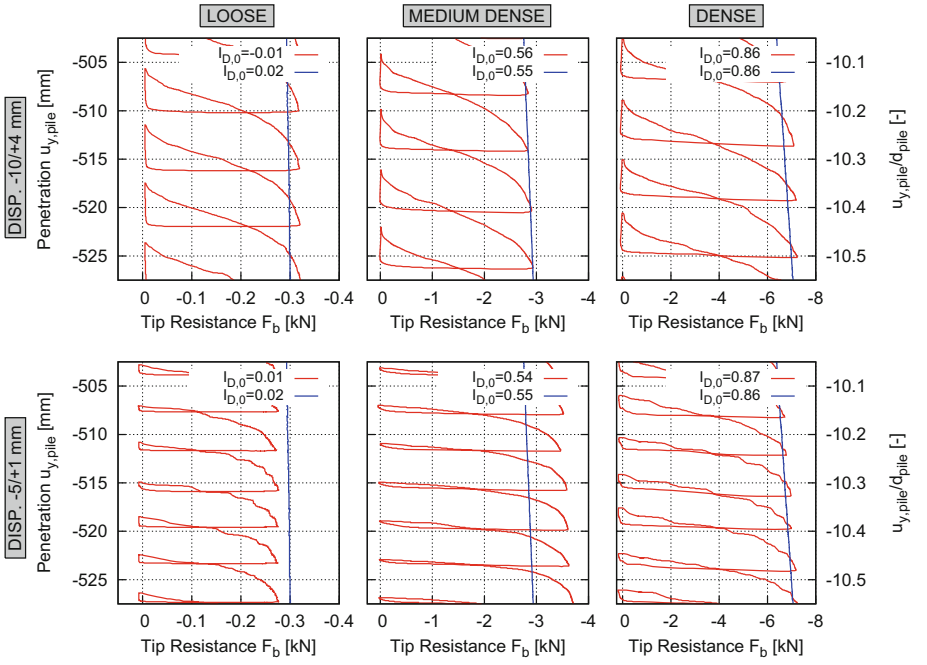

Fig. 9. Comparison of the cyclic evolution of shaft resistance in 0.5 m depth. Large amplitude driving in the upper row and small amplitude driving in the lower row. The columns represent different initial densities from loose to dense.

As it was shown before, the maximum tip force increases with soil density. However, apart from the magnitude of developed force, the evolution of tip resistance is qualitatively similar for all three densities. Its shape depends mainly on the imposed pile motion. Large amplitudes lead to a S-shaped mobilization of tip resistance during the penetration phases. The tip force vanishes after about 0.3 mm of upward pile motion and remains approximately zero throughout the whole pullout phase. In the subsequent penetration phase, the initial stiffness is very low, leading to slow increase of tip resistance. However, a section with zero tip force during penetration as described by Cudmani [4] for vibratory tests is not apparent, see also Sect. 4. This indicates that the pile tip does not lose contact to the sand. Although the tip force also vanishes in the tests with smaller upward motion of the pile, a considerably higher reloading stiffness is observed. Unloading and reloading stiffness are very similar. The tip resistance appears to reach a limit state that lies in the range of the monotonic resistance. In the cyclic test with small amplitude in medium dense sand, the maximum tip resistance exceeds the monotonic test, however, the amount can be explained with local differences of void ratio [19].

Figure 10 shows detailed cycles in a depth of about 1 m for the tests in loose and medium dense sand. The tests in dense sand have not reached this depth and are therefore not shown.

In loose sand, the evolution of tip resistance is similar in 1 m and 0.5 m depth. However, for the tests in medium dense sand, significant differences can be identified. Although the qualitative behavior is comparable to Fig. 9, the maximum tip resistance during penetration with large amplitude is substantially lower compared to the other cyclic test and to the monotonic penetration resistance.

As will be shown in Sect. 4, the observed cyclic patterns of the evolution of tip resistance have marked parallels to the tip resistance measured during vibro-penetration [4]. The measurements obtained with large amplitudes show the characteristics of the so-called cavitational penetration mode while the tests with smaller amplitudes have more similarities with the so-called non-cavitational mode [4]. A combination of large upward displacement and little penetration per cycle seems to be a trigger for the cavitational penetration mode. The non-cavitational mode occurs for small upward displacements and large effective penetration.

3.5 Cyclic Evolution of Shaft Resistance

Figure 11 shows the cyclic evolution of shaft force for the same section as Fig. 9 in a penetration depth of about 0.5 m.

The evolutions of shaft friction in the tests with large amplitudes exhibit an alternation between significant resistance in the penetration phases and very low or slightly positive resistance in the pullout phases. An increase of shaft friction during the first $4 \div 6$ mm of penetration is observed. There seems to occur a strong increase of radial stress acting on the pile in this phase. A limit shaft resistance is reached only in loose and medium dense sand. After the reversal of pile motion, the shaft friction is very low and is only slowly mobilized during

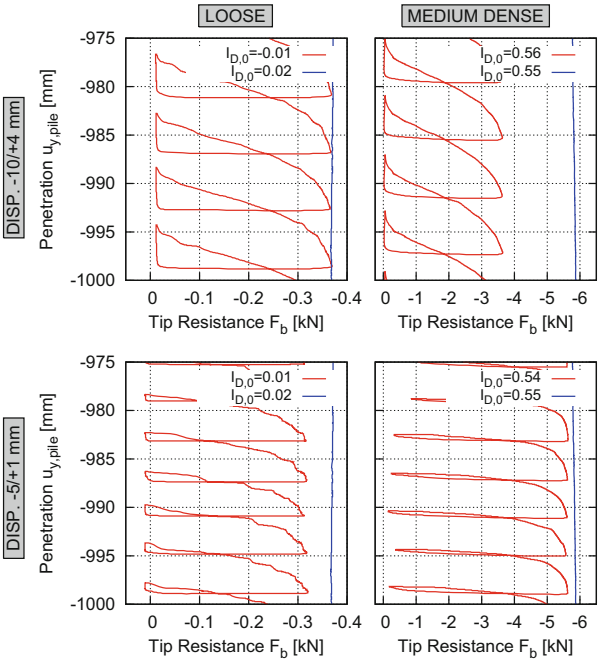

Fig. 10. Comparison of the cyclic evolution of tip resistance in 1 m depth. Large amplitude driving in the upper row and small amplitude driving in the lower row. The columns represent different initial densities from loose to medium dense.

the pullout phase. In the case of loose and medium dense sand, the shaft friction remains very small throughout the whole phase indicating very low stresses acting on the pile.

The penetration phase is qualitatively similar in the tests with smaller amplitude, but the occurring shaft resistance is larger. It is almost equal to the monotonic resistance in medium dense and dense sand. The increase of shaft friction is stronger during the first phase of penetration, thus, the shear stiffness of the soil around the pile is higher compared to the tests with smaller amplitude. The pullout phases reveal more differences between the tests with different amplitudes. Even though the amount of upward motion is lower in the small amplitude tests, more friction is mobilized during the pullout phase. This indicates that the stress relief that was observed in the test with large amplitude does not take place. The stress regime seems to change less during small amplitude cycling and a limit state is not reached in the pullout phase. This observation supports the conclusions by White and Lehane [20] made on the basis of cyclic interface tests with and without shear stress reversal. They found out that friction fatigue is significantly more pronounced in the case of two-way cycling (with shear stress reversal). In the light of these findings, it can

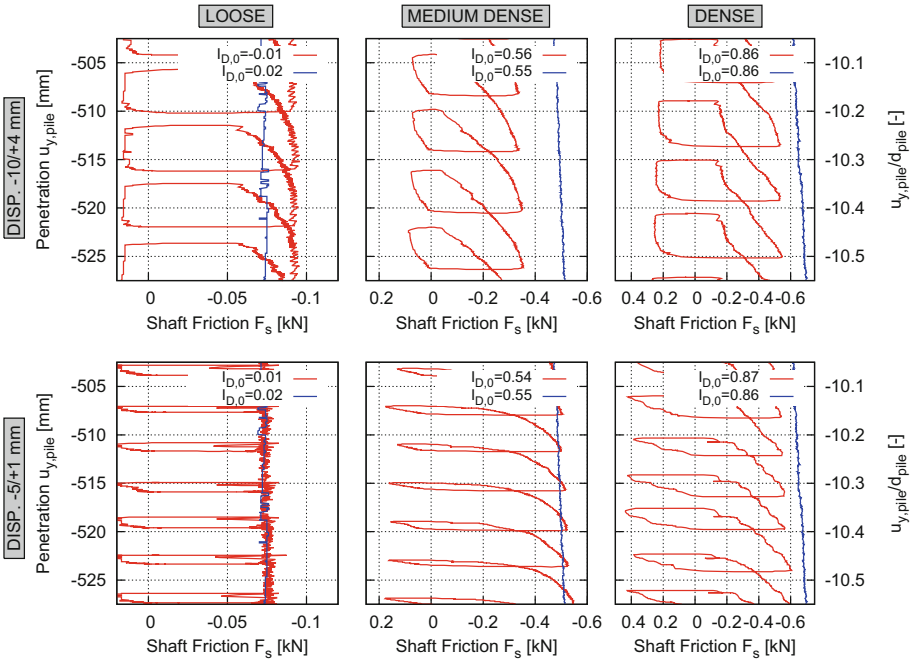

Fig. 11. Comparison of the cyclic evolution of shaft resistance in 0.5 m depth. Large amplitude driving in the upper row and small amplitude driving in the lower row. The columns represent different initial densities from loose to medium dense.

be assumed that the shear stress does not reverse clearly along the whole pile shaft in the small amplitude pile penetration tests presented here.

4 Comparison with Vibratory Tests

The comparison with existing measurements during vibro-driving processes is used in this section to validate the presented model tests with regard to real pile driving and to demonstrate the parallels between cyclic and vibro-driven penetration.

Figure 12 shows some measurements from Cudmani and Huber [4,10] obtained in two types of test series: Fig. 12(a) and (b) during in field tests on a test site near Karlsruhe, Germany and Fig. 12(c) and (d) in calibration chamber tests (CC) using a dry sand that is very comparable to the one used in the present study. The results are displayed in the form chosen for the figures in this paper. Three representative cycles are shown, whereby the second cycle is highlighted. Vertical displacement downwards is negative and the measured tip force is expressed in terms of tip resistance q_b. The pile in the field tests had a length of about 7 m and a diameter of 0.16 m. The pile tip was conical with an opening angle of about 100° [10]. The chosen sections are from a depth of 5 m in

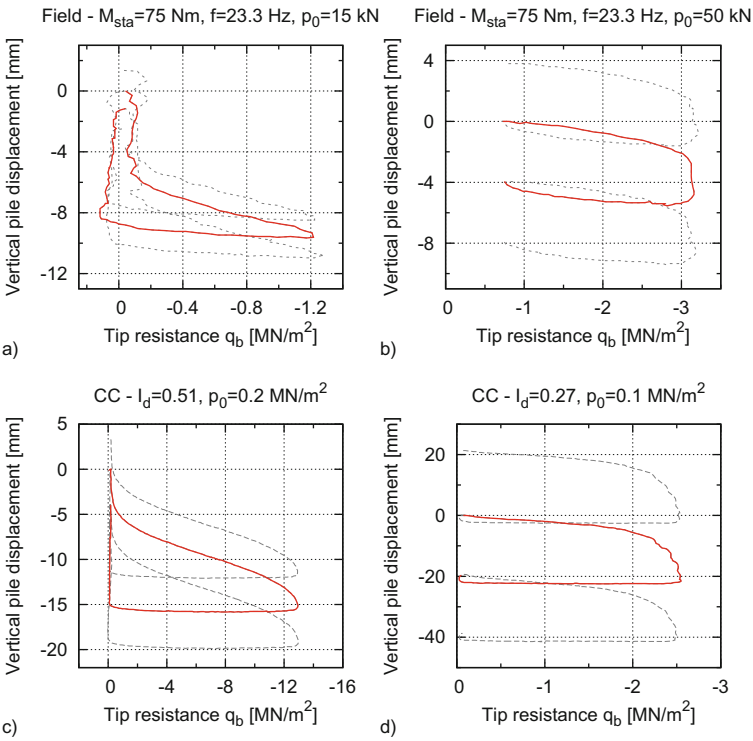

Fig. 12. Measurements during vibratory penetration: (a), (b) field tests and (c), (d) calibration chamber tests (from Cudmani [4] replotted with the sign convention of this paper)

sandy gravel below the ground water table. In Fig. 12(a) and (b) different static driving forces F_0 have been used that result in different penetration modes (the static moment M_{sta} is equal). The model pile for the CC tests was very similar to CPT equipment. The diameter of the model pile was 36 mm and the opening angle of the tip 60°. Both tests have been performed with similar parameters (static force $F_0 = 0.8\,\mathrm{kN}$, frequency $f = 32 - 35\,\mathrm{Hz}$ and coefficient of earth pressure $K = 1$). Two different penetration modes are observed here due to a variation of density and stress level p_0.

Figure 12(a) and (c) reveal the occurrence of the so-called cavitational pile driving mode whereas the results in Fig. 12(b) and (d) correspond to the non-cavitational mode. Although strong parallels are evident between field and calibration chamber measurements, also some differences can be seen. In the field test results shown in Fig. 12(a), the phase with negligible tip resistance at the beginning of each penetration phase is very pronounced compared to Fig. 12(c). Here, the mobilization of tip resistance begins earlier. This may be a consequence of the different tip angles. Considering Fig. 12(b) and (d), the most obvious difference is that the tip pressure does not vanish during the phases of upward

motion in Fig. 12(b), while it actually does in Fig. 12(d). Furthermore, the reach of a limit penetration resistance is more pronounced in Fig. 12(b).

Especially the calibration chamber test results are very similar to those of the quasistatic tests presented in this paper. They demonstrate that in quasistatic tests some important effects of vibro-penetration can be investigated. The evolution of stresses below the pile toe principally depends on the cyclic pile motion. The ratio between penetration per cycle and upward pile motion appears to be an indicator for the occurring penetration mode. Both, the results presented here as well as Cudmani's measurements [4] show that the most frequent penetration mode is the cavitational one.

These observations lead to the statement that for a first validation step for numerical models of vibratory pile driving in granular soils, also quasistatic boundary value problems can be used. Due to the prescribed pile displacement, the implementation of the test paths is very easy and a quantitative comparison can be drawn on the basis of the developed soil resistance.

5 Towards a Numerical Simulation of the Tests

This section serves to give indications towards a successful simulation of the presented test results and to demonstrate the encountered challenges.

5.1 Model Setup and Description of Soil Behavior

Pile penetration processes are usually simulated using the so-called zipper technique that was established systematically by Cudmani [4]. The pile is introduced as a rigid surface in contact with the soil. It possesses a pre-pile that represents an initial cavity in the soil. The rounded pile tip expands this cavity during penetration until the full pile diameter is reached. A similar model is described in more detail in [2] in this book. A schematic illustration of the applied FE model is shown in Fig. 13(a). More details are given in Appendix A.

The classic von Wolffersdorff hypoplasticity [21] in combination with the extension by Niemunis and Herle [13] has been shown for many times to perform well for simulations of monotonic penetration problems [4,7,19]. However, considering cyclic penetration, the model suffers from serious shortcomings. Substantial problems for the model (and most others) arise from the following characteristics:

- Large numbers of cycles
- Spatial and temporal variation of strain amplitudes
- Large changes of the stress level with stresses up to a few MN/m^2 during penetration and negligible stress during upward motion of the pile

A discussion on the shortcomings of the hypoplastic model for typical deformation paths of pile penetration is also provided in [2] in this book. Nevertheless, the model is used here to illustrate the considerable challenges for realistic simulations of cyclic penetration processes. The applied soil parameters are given in Appendix A.

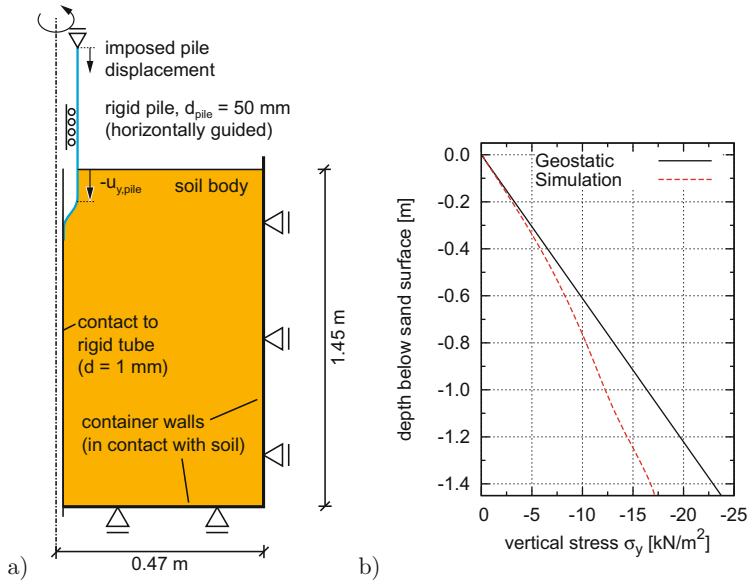

Fig. 13. (a) Schematic illustration of a suitable FE model for the simulation of the tests and (b) calculated initial stress profile in medium dense, dry sand ($I_{D,0} = 0.55$)

5.2 Initial Conditions

In test containers with rigid side walls, the initial stress field in the soil can differ from geostatic conditions due to silo effects. As shown by Vogelsang et al. [17] and Vogelsang [19], a satisfactory estimation of the initial soil stresses can be obtained by FE simulation of the soil deposition. A simple technique using a layered activation of the actual soil weight led to very realistic results. The simulation methods are described in detail in [17, 19].

Figure 13(b) investigates the soil stresses after the soil deposition for the test container used in this study. It shows the calculated stress profile in the center of a medium dense sample. From Fig. 13(b) can be seen that silo effects remain negligible up to a depth of about 0.5 m. Even in 1.1 m depth, which is the maximum depth reached in the pile penetration tests, the influences of silo effects on the initial stress distribution are moderate. With regard to a FE simulation of the subsequent pile penetration, a consideration of silo effects is therefore not of vital importance. A geostatic stress field with $K_0 = 0.4$ should be a good start for simulations of the pile tests. Once this validation step is achieved, a better back-calculation may be obtained when silo effects are considered.

5.3 Test Paths

Applying quasistatic FE formulations, each phase of downward and upward motion can be interpreted as a simulation step with the corresponding constant

displacement velocity. Using a dynamic FE code, such an implementation of the test paths would lead to velocity jumps and singularities of acceleration around the reversal points. These should therefore be smoothed, for example using the smooth step amplitude function in ABAQUS [16]. Another way is to idealize the zigzag test paths of the experiments as a sinusoidal function with a downward trend (like e.g. done in [2]). Applying explicit integration schemes, it may be necessary to shorten the simulation time compared to the physical time scale in order to minimize the computation time [8]. However, it has to be ensured the process remains mostly quasistatic in order to avoid problems arising from the reflecting boundaries.

5.4 Contact Modeling

The steel surface of the pile is rather smooth, so simple contact formulations like the Coulomb friction model should be able to capture the major effects. Based on interface shear tests [19], the friction angle between sand and steel can be estimated to $12 \div 15°$. Another important setting parameter for the contact model is the treatment of the contact behavior in normal direction (separation on/off in ABAQUS [16]). Since a sand-steel interface cannot support tensile stresses, a restriction of the contact kinematics excluding a separation of the contact surfaces is physically not justifiable. However, a separation of the contact in normal direction is not to be expected here due to the steep angle of the tip cone and its exclusion can sometimes be numerically beneficial. In the present case, the simulations turned out to run more stable without a restriction of the contact kinematics. The consequences of this input parameter are illustrated in Fig. 14. It shows a short section of the load-displacement curve for penetration with the $-10/+4$ mm displacement sequence. The deformed FE mesh in the highest point of pile motion during one cycle is shown on the right. As can be seen, a gap forms below the pile tip. In the load curve, the phase without contact below the pile tip can also be recognized during upward and in the first part of the downward

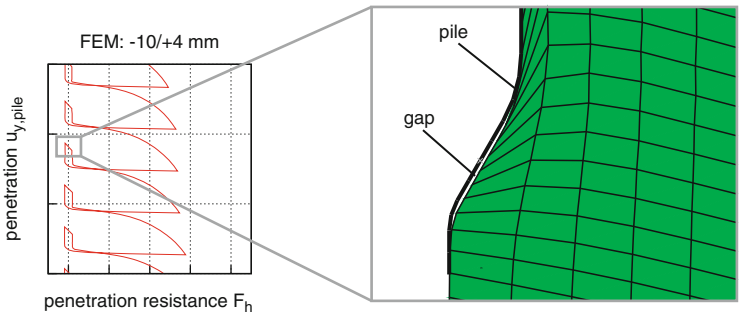

Fig. 14. Load-displacement curve during cyclic penetration and mesh configuration in the highest point of the pile during one cycle

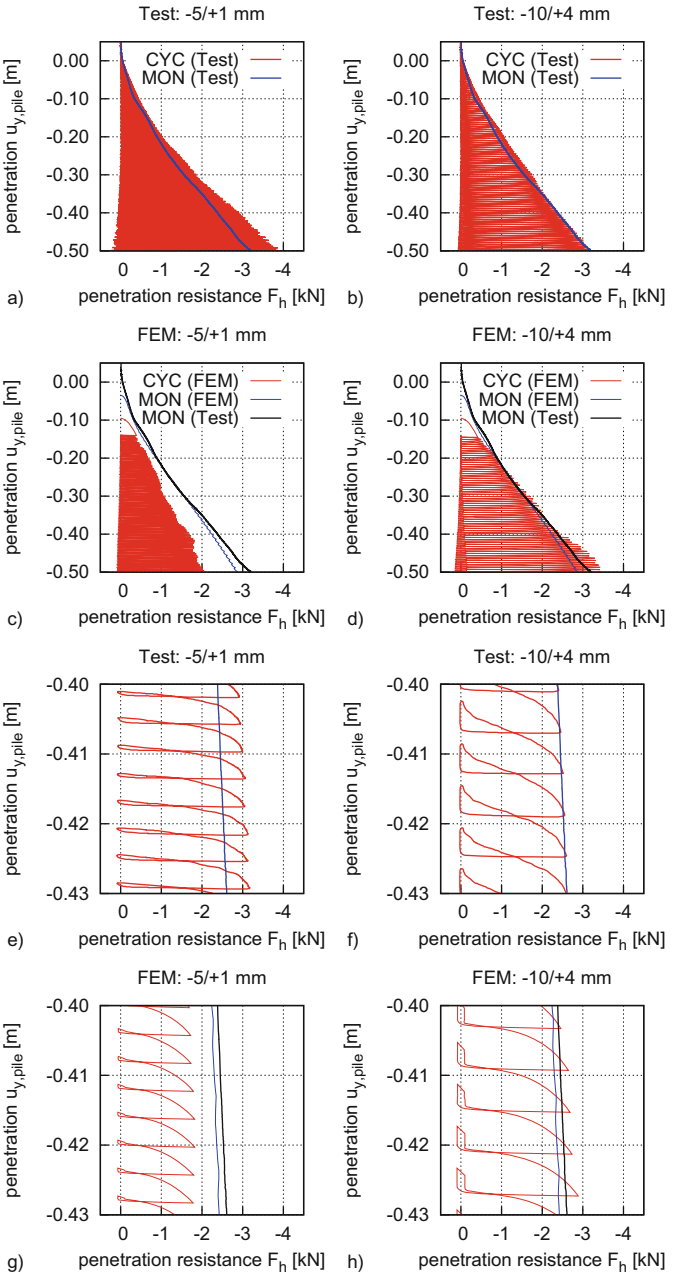

Fig. 15. Comparison of experimental and numerical results of cyclic penetration resistance in medium dense sand: (a)–(d) overview of the first 0.5 m and (e)–(h) detail of cycles in 0.4 m depth. Small amplitude driving in the left column and large amplitude driving in the right column. (ABAQUS/STANDARD with geostatic initial state)

motion. Such phases have not been identified in the experiments and have to be considered as numerical artefacts.

5.5 Some Simulation Results

Figure 15 presents exemplary results from back-calculations of the three model tests in medium dense sand. The simulations concentrate on the first 0.5 m of penetration. The left column corresponds to the cyclic test with small amplitude (−5/+1 mm) and the right column to the one with larger amplitude (−10/+4 mm). The first row, Fig. 15(a) and (b), gives an overview of the experimental results and the second row, Fig. 15(c) and (d), of the simulation results. Figure 15(e)–(h) show details of the cycles in about 0.4 m depth in the same order. Since silo effects are negligible within the first 0.5 m depth, a geostatic initial state was chosen to simplify the simulations.

In both cyclic experiments, the monotonic limit resistance is reached during the first 0.5 m of penetration, Fig. 15(a) and (b). Considering the numerical simulations, this behavior is observed only for the test with −10/+4 mm displacement sequence, Fig. 15(d). The smaller penetration rate (per cycle) of the test with the −5/+1 mm sequence leads to a lower penetration resistance, Fig. 15(c). The detailed presentation of selected cycles reveals that the qualitative behavior of the experiment is better modeled in the case of small upward motion of the pile (−5/+1 mm), Fig. 15(g). The loosening of the soil around the pile tip during large displacement upwards cannot be reproduced by the numerical model, Fig. 15(h). Thus, the stiffnesses during reloading do not differ significantly. As it is demonstrated in [2], these deficits are probably attributed to the performance of the soil model in the occurring deformation paths.

6 Conclusions

Monotonic and cyclic full-model pile penetration tests in dry sand have been carried out to investigate the influence of cyclic penetration on the soil resistance. The tests include some major effects of vibratory pile driving but offer advantages such as an easier systematic investigation of the process and the achievement of very suitable experimental data for model validation purposes.

During cyclic pile penetration, monotonic and cyclic effects on soil resistance are counteracting. Monotonic pile motion tends to increase the stress level around the pile, while superimposed cycling can cause a substantial stress relief. The ratio between upward motion and effective penetration per cycle is an indicator for the developed soil resistance compared to the monotonic resistance. Large ratios lead to a facilitated penetration, whereas by working with low ratios similar stresses than during monotonic penetration are observed. The beneficial effect of cyclic penetration regarding the driveability is most pronounced in medium dense sand in combination with large pile displacement amplitudes.

The observed stress paths during penetration with large amplitude are very similar to the cavitational vibratory penetration mode. Cyclic penetration with

lower amplitude corresponds to the non-cavitational vibratory mode. Friction fatigue along the shaft becomes evident in medium dense sand when large cycles are imposed.

The suitability of commonly used simulation methods [4,7,8] is questionable for cyclic penetration processes, mainly due to deficiencies of most soil models to perform in typical deformation paths. However, the applied FE model with hypoplastic description of the soil behavior is qualitatively capable to reproduce important effects observed in the experiments. The improvement of available soil models is a primary task in order to obtain more realistic simulations of pile penetration processes.

A Details of the FE Model

Details concerning the setup of the numerical model can also be found in [19]. Axisymmetric CAX4 elements are used. The horizontal length of the elements near the symmetry axis is greater than the height in order to reduce mesh distortion problems. An impression of the FE mesh near the pile tip can be received in Fig. 14. In order to ensure a better numerical stability, the first 0.05 m of soil are replaced by a uniformly distributed pressure equivalent to the soil weight. The initial conditions are assumed to be geostatic with $K_0 = 0.37$. The initial void ratio is chosen according to the corresponding experiment (Table 1). The pile penetration begins in 0.1 m depth (position of the pile shoulder with respect to the sand surface). After an initial phase of 30 mm monotonic displacement the cyclic pile motion is prescribed. The increment size corresponds to a pile displacement of about 0.06 mm.

The material parameters used for the simulations are given in Table 2. Note that these differ from the parameters used in [2]. The calibration procedure is described by Vogelsang [19]. The slight differences of the current test sand compared to older charges (see Sect. 2.3) have not been considered during the calibration.

The Coulomb friction model is used to model the interaction between soil and pile resp. soil and side walls. A friction angle of 12° is chosen for the pile-soil and 22° ($\approx 2/3\varphi_c$) for the soil-wall interface.

Table 2. (a) Applied constitutive parameters of the test sand and (b) additional constitutive parameters of the extended hypoplastic model with intergranular strain

a)

$\varphi_c[^\circ]$	h_s [MPa]	e_{c0}	e_{d0}	e_{i0}	α	β	n
33.1	19000	0.865	0.549	1.0	0.1	1.25	0.285

b)

R	m_R	m_T	β_r	χ
5×10^{-5}	2.5	1.25	0.1	4.0

References

1. ASTM Standard D4254-91: Standard test method for minimum index density and unit weight of soils and calculation of relative density. Annual Book of ASTM Standards. ASTM International, West Conshohocken (2006)
2. Chrisopoulos, S., Vogelsang, J., Triantafyllidis, T.: FE simulation of model tests on vibratory pile driving in saturated sand. In: Triantafyllidis, T. (ed.) Holistic Simulation of Geotechnical Installation Processes. LNACM, vol. 82, pp. 124–149. Springer, Cham (2017)
3. Choi, S.-K., Lee, M.-J., Choo, H., Tumay, M.T., Lee, W.: Preparation of a large size granular specimen using a rainer system with a porous plate. Geotech. Test. J. **33**(1), 45–54 (2009)
4. Cudmani, R.O.: Statische, alternierende und dynamische Penetration in nichtbindigen Böden. Dissertation, vol. 152. Publications of the Institute of Soil Mechanics and Rock Mechanics, University of Karlsruhe (2001)
5. Dierssen, G.: Ein bodenmechanisches Modell des Vibrationsrammens in körnigen Böden. Dissertation, vol. 133. Publications of the Institute of Soil Mechanics and Rock Mechanics, University of Karlsruhe (1994)
6. DIN 18126: Bestimmung der Dichte nichtbindiger Böden bei lockerster und dichtester Lagerung. Beuth-Verlag (1996-11)
7. Grabe, J., König, F.: Zur aushubbedingten Reduktion des Drucksondierwiderstands. Bautechnik **81**(7), 569–577 (2004)
8. Henke, S.: Untersuchungen zur Pfropfenbildung infolge der Installation offener Profile in granularen Böden. Habilitation, vol. 29. Publications of the Institute of Geotechnical Engineering and Construction Management, TU Hamburg-Harburg (2013)
9. Hereema, E.P.: Predicting pile driveability: heather as an illustration of the "friction fatigue" theory. In: SPE European Petroleum Conference, London (1978)
10. Huber, G.: Vibrationsrammen: Großmaßstäbliche Versuche. In: Workshop "Vibrationsrammen", Karlsruhe, Germany, pp. 13–30 (1997)
11. Lehane, B.M., White, D.J.: Lateral stress changes and shaft friction for model displacement piles in sand. Can. Geotech. J. **42**, 1039–1052 (2005)
12. Linder, W.-R.: Zum Eindring- und Tragverhalten von Pfählen in Sand. Dissertation, Fachbereich für Bauingenieur- und Vermessungswesen, TU Berlin (1977)
13. Niemunis, A., Herle, I.: Hypoplastic model for cohesionless soils with elastic strain range. Mech. Cohesive Frictional Mater. **2**(4), 279–299 (1997)
14. Rimoy, S.P.: Ageing and axial cyclic loading studies of displacement piles in sand. Dissertation, Department of Civil and Environmental Engineering, Imperial College London (2013)
15. Rodger, A.A., Littlejohn, G.S.: A study of vibratory driving in granular soils. Géotechnique **30**(3), 269–293 (1980)
16. Simulia: Abaqus Users Manual. Version 6.14 (2014)
17. Vogelsang, J., Zachert, H., Huber, G., Triantafyllidis, T.: Effects of soil deposition on the initial stress state in model tests: experimental results and FE simulation. In: Triantafyllidis, T. (ed.) Holistic Simulation of Geotechnical Installation Processes. LNACM, vol. 77, pp. 1–20. Springer, Heidelberg (2015). doi:10.1007/978-3-319-18170-7_1
18. Vogelsang, J., Huber, G., Triantafyllidis, T., Bender, T.: Interpretation of vibratory pile penetration based on digital image correlation. In: Triantafyllidis, T. (ed.) Holistic Simulation of Geotechnical Installation Processes. LNACM, vol. 80, pp. 31–51. Springer, Heidelberg (2016). doi:10.1007/978-3-319-23159-4_2

19. Vogelsang, J.: Untersuchungen zu den Mechanismen der Pfahlrammung. Dissertation, Publications of the Institute of Soil Mechanics and Rock Mechanics, Karlsruhe Institute of Technology, submitted (2017)
20. White, D.J., Lehane, B.M.: Friction fatigue on displacement piles in sand. Géotechnique **54**(10), 645–658 (2004)
21. von Wolffersdorff, P.-A.: A hypoplastic relation for granular materials with a predefined limit state surface. Mech. Cohesive Frictional Mater. **1**, 251–271 (1996)

Contribution to the Non-Lagrangian Formulation of Geotechnical and Geomechanical Processes

Daniel Aubram(✉), Frank Rackwitz, and Stavros A. Savidis

Chair of Soil Mechanics and Geotechnical Engineering,
Technische Universität Berlin (TU Berlin),
Secr. TIB1-B7, Gustav-Meyer-Allee 25, 13355 Berlin, Germany
daniel.aubram@tu-berlin.de

Abstract. Numerical simulations of geomechanical and geotechnical processes, such as vibro-injection pile installation, require suitable algorithms and sufficiently realistic models. These models have to account for large deformations, the evolution of material interfaces including free surfaces and contact interfaces, for granular material behavior in different flow regimes as well as for the interaction of the different materials and phases. Although the traditional Lagrangian formulation is well-suited to handling complex material behavior and maintaining material interfaces, it generally cannot represent large deformation, shear and vorticity. This is because in Lagrangian numerical methods the storage points (nodes resp. material points) move with the local material velocity, which may cause mesh tangling resp. clustering of points. The present contribution addresses the development of models for geotechnical and geomechanical processes by utilizing Eulerian and Arbitrary Lagrangian-Eulerian (ALE) formulations. Such non-Lagrangian viewpoints introduce additional difficulties which are discussed in detail. In particular, we investigate how to track interfaces and to model interaction of different materials with respect to an arbitrarily moving control volume, and how to validate non-Lagrangian numerical models by small-scale experimental tests.

Keywords: Large deformations · Mixture · Granular material · Sand · Volume averaging · Closure model · Interface reconstruction · Eulerian · Multi-material ALE

1 Introduction and Literature Review

1.1 Geotechnical and Geomechanical Processes

During the last decade there has been an increasing interest in gaining broad understanding of the mechanisms associated with geotechnical installation processes, and how they influence the strength and stiffness characteristics of the soil [79,155]. The main objective of the DFG Research Unit FOR 1136 GeoTech

T. Triantafyllidis (ed.), *Holistic Simulation of Geotechnical Installation Processes*,
Lecture Notes in Applied and Computational Mechanics 82, DOI 10.1007/978-3-319-52590-7_3

[156,157], with which the authors collaborate in the context of Subproject 5, is the provision of suitable methods for numerical simulation of such processes in order to predict the deformations of supporting systems and nearby structures.

Geotechnical installation processes, like pile driving, vibro replacement, or pressure grouting, generally involve large deformations and material flow, the evolution of material interfaces including free surfaces and contact interfaces, as well as the dynamical interaction of multiple, physically distinct materials on a hierarchy of spatial scales [14,21,118,141]; see Fig. 1. In particular, the complexity in the behavior of the soil is attributable to its granular nature and internal structure, and to the presence of multiple phases (solid, liquid and gas). The grain-fluid mixture is generally subject to different flow regimes and undergoes changes in phase composition and internal structure depending on the dynamics of the geotechnical process [17,22].

The mechanisms and phenomena associated with geotechnical installation processes, except perhaps for the significance of soil-structure-interaction, are similar to those of geomechanical or geomorphological flows, for example, avalanches and debris flows [87,90,92,130,133], submarine landslides [103,114], and soil liquefaction [97,145]. Although the objectives of geomorphologists and geotechnical engineers in studying these phenomena may be somewhat different, both need reliable continuum mechanical models and validated numerical methods for prediction. Both also agree that multi-phase rather than single-phase or rheological approaches should be applied to capture the complexity of evolving geomaterial behavior [87,91,176].

1.2 Lagrangian Formulation

Geotechnical engineers have been traditionally concerned with accurate determination of soil failure conditions and small deformations that may affect structures. For such situations the Lagrangian formulation of the governing equations (balance equations, constitutive models, etc.) and their discrete counterparts is well-suited because it naturally handles complex material behavior and maintains material interfaces [57,99,144,176]. Lagrangian formulations have also been employed to study large deformation problems in geotechnical engineering [41,49,50,84,109] as well as geomechanical or granular flows [49,90,139]; see also [148].

The discretizations in Lagrangian methods are either mesh-based, like in the finite element method (FEM) [27,174], or point-based, like in the material point method (MPM) [25,150] or smoothed particle hydrodynamics (SPH) [72,105]. The major drawback of Lagrangian approaches is that they cannot represent large deformation, shear and vorticity without serious losses in accuracy and/or efficiency. This is because the storage points (mesh nodes resp. material points) move with the local material velocity, which may cause mesh distortion resp. clustering of points [34,110]; we remark that some point-based methods rely on a spatially fixed background mesh, but the solution variables are attributed to Lagrangian point masses. Severe local deformations may change the topology of the material, e.g. by creating new free surfaces, and thus can hardly be

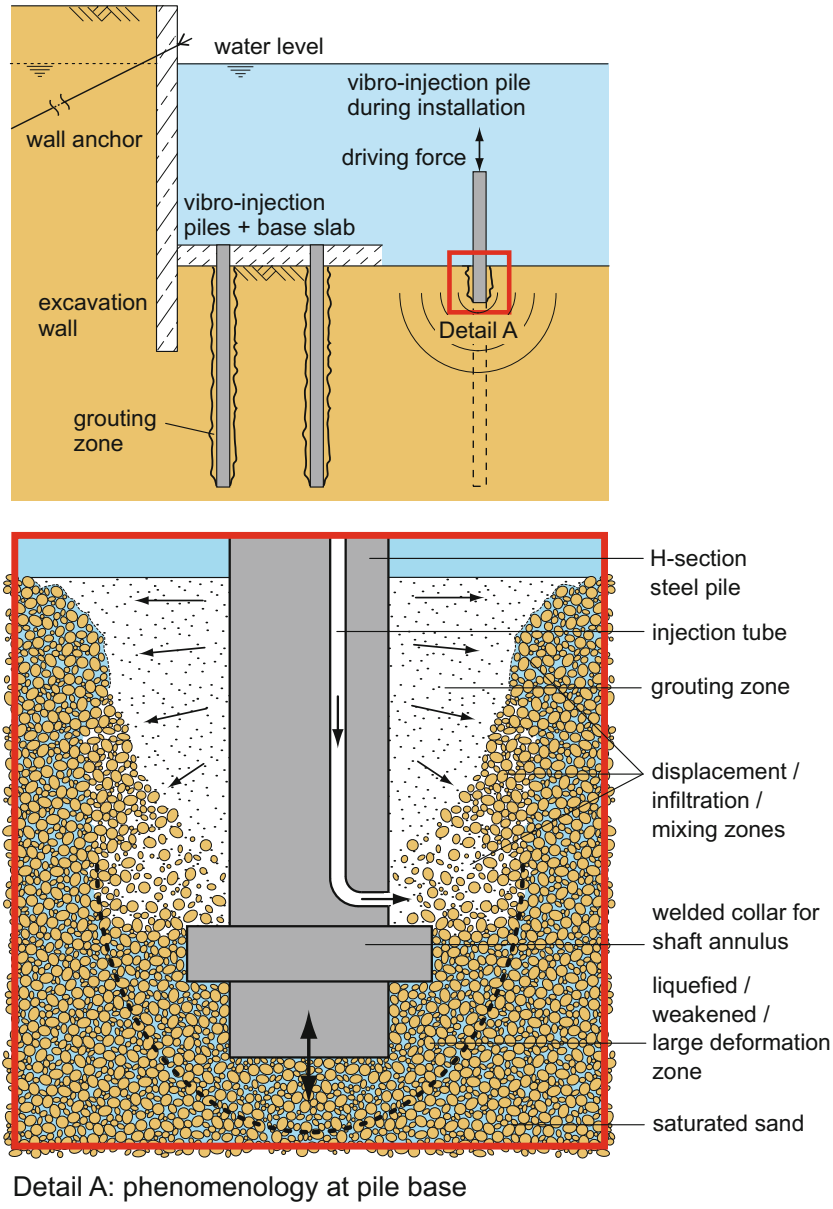

Fig. 1. Schematic of a complex geotechnical process: installation of vibro-injection piles to tie back the base slab of a deep excavation.

addressed by Lagrangian meshes without rezoning (remeshing). In such extreme situations, which are likely to occur in geotechnical and geomechanical processes, calculations slow down or even terminate.

1.3 Non-Lagrangian Formulations

Definitions and Basic Relations. In our research work we pursue a non-Lagrangian approach to overcome the limitations of a Lagrangian calculation. A non-Lagrangian formulation is one where the domain of reference or a control volume moves at a velocity different from the material velocity. The reference domain is an independent continuum made up of reference points, and which is approximated by the computational mesh in numerical simulations. By definition, the mesh topology (connectivity) does not change, which distinguishes non-Lagrangian approaches from those Lagrangian techniques employing manual or automatic rezoning of the mesh.

In a non-Lagrangian approach the reference domain can be fixed in space as in the Eulerian formulation, or may move arbitrarily as in the arbitrary Lagrangian-Eulerian (ALE) formulation [13,14,34]. Figure 2 illustrates the different concepts. The ALE idea has been invented in the 1960–70's [82,160,161]. Accordingly, the spatial description of any scalar, vector or tensor field, q, is related to its referential or ALE description $\hat{q}$ by the composition $\hat{q} = q \circ \Phi$, where Φ is the relative motion that maps reference points onto spatial points currently occupied by the material. The material description Q of the field is obtained from $Q = q \circ \varphi$, where φ is the material motion. Taking the material time derivative of $q = \hat{q} \circ \Phi^{-1}$ leads to the fundamental ALE operator

$$\dot{q} = \frac{\partial \hat{q}}{\partial t} \circ \Phi^{-1} + \boldsymbol{c} \cdot \boldsymbol{\nabla} q, \qquad \text{with} \quad \dot{q} = \frac{\partial Q}{\partial t} \circ \varphi^{-1} \stackrel{\text{def}}{=} h(\ldots). \tag{1}$$

The first term on the right side of the first equation represents the time derivative of q with respect to fixed reference points. The second term, called the convective term, stems from the relative motion between the material and the reference domain and involves the so-called convective velocity $\boldsymbol{c}$. Finally, $h(\ldots)$ is a source or an evolution equation for the field q under consideration.

The Lagrangian and Eulerian formulations are only two special cases of the ALE formulation. In the Eulerian formulation, $\boldsymbol{c} = \boldsymbol{v} = \partial\varphi/\partial t$ represents the material velocity, and $\Phi = \mathrm{id}$, for which (1) reduces to the common material time derivative. On the other hand, if the motion of the reference domain coincides with that of the material (i.e. $\boldsymbol{c} = \boldsymbol{0}$ and $\Phi = \varphi$), then the Lagrangian formulation is obtained. However, in the present work we are concerned with formulations which are essentially non-Lagrangian (Fig. 2).

Advection Algorithms. The change from a Lagrangian to a non-Lagrangian viewpoint introduces two main difficulties: the presence of convective terms in the time derivatives and the problem of tracking material interfaces. The first difficulty is usually resolved either by approximating the convective terms directly, or

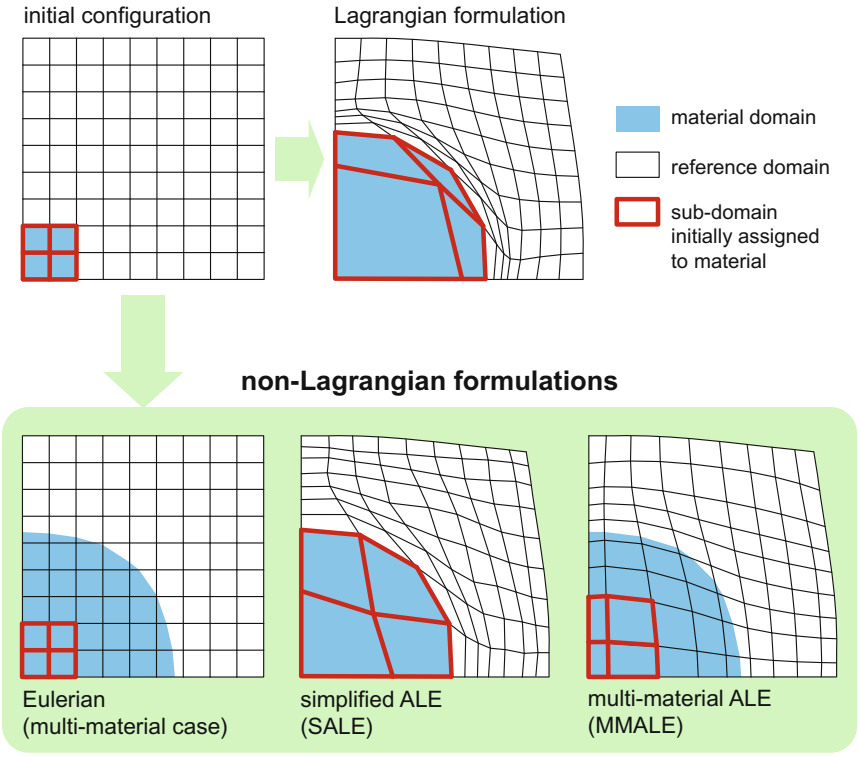

Fig. 2. Schematic of Lagrangian and non-Lagrangian formulations.

by using conservative advection algorithms from computational fluid dynamics (CFD) [80,98]. However, in contrast to ideal or Newtonian fluids the constitutive behavior of soils and other geomaterials is generally path-dependent. Moreover, soil strength as well as geomorphological flows are driven by gravity and friction, which introduces additional source terms in the balance of momentum. One standard approach for solving such problems is to use the operator-splitting resp. fractional-step technique [33,34,52,98]. If an operator-split is applied to the governing equations of the problems under consideration, the convective terms and the source terms are treated in separate equations which are solved sequentially.

Interface Tracking. The second difficulty of tracking interfaces arises because material boundaries (free surfaces or contact interfaces) generally are not aligned with the underlying computational mesh, as they would be in a Lagrangian formulation. Since the mesh motion in ALE methods is arbitrary, it can be defined in such a way that material boundaries are resolved by edges (2d) or faces (3d) of the mesh elements, and elements contain only a single material. This is called a simplified ALE (SALE) formulation [33,34,110]. The drawback

of an SALE formulation is that the range of problems that may be addressed is not much greater than for a pure Lagrangian method because the material boundaries remain Lagrangian in both cases (Fig. 2). Methods that do not share this limitation require techniques for interface tracking [37,88,142].

Interface tracking methods either track the surface, defined by a distance function or parameter representation, or the volume occupied by the material behind the interface. When using volume tracking, the material boundary is reconstructed *ab initio* from the solution data in each mesh element containing two or more materials (so-called multi-material elements). This can be done by employing the densities of Lagrangian marker points, with the disadvantages outlined above, or alternatively, the fractional volume of each material as in volume of fluid (VOF) [59,81,137,138,175] or moment of fluid (MOF) methods [65,66]. ALE formulations using these methods for interface tracking are referred to as full or multi-material ALE (MMALE) formulations [34,110] (Fig. 2).

Application to Geotechnical and Geomechanical Processes. Concerning the modeling of geotechnical and geomechanical processes, several non-Lagrangian approaches are documented in the literature. These may be classified into SALE formulations using direct approximation of the convective terms [121,122,146], SALE formulations using first-order [14,16,19,20,61] and second-order advection algorithms [102,151], and Eulerian formulations using advection algorithms. The order of the advection algorithm refers to the maximum accuracy with which the spatial distribution of the solution variable is approximated. Within the Eulerian approaches, one may distinguish between channel or depth-integrated hydraulic models [60,132,134], two- or three-dimensional full-scale models using free surface tracking [107,108], and multi-material full-scale models using volume tracking by VOF methods [1,12,78].

The models for the soil or debris material employed in these approaches are based on single- or two-phase descriptions ranging between simple rheological models in case of the full-scale Eulerian formulations, plastic or viscoplastic constitutive equations using the Mohr-Coulomb criterion in case of the hydraulic Eulerian formulations, and more or less advanced soil mechanical models in case of the SALE formulations. Yet no full-scale multi-material Eulerian or MMALE formulation is available which models both the complex rate-independent frictional granular material behavior and the multi-phase behavior of the grain-fluid mixture.

1.4 Multi-material Eulerian and MMALE Methods

Multi-material Eulerian and MMALE (Fig. 2) are non-Lagrangian formulations that emerged along with those computational continuum mechanics tools commonly referred to as "hydrocodes" [34,110]. Typical applications include detonation and impact problems, the dynamics of bubbles and droplets, material processing and manufacturing, or astrophysical events. Besides research codes [35,38,69,70] and codes developed at national laboratories for energy and

defense applications [3,59,71,106,112,115,129,165,175], some general purpose commercial codes include multi-material Eulerian or MMALE capabilities as well [58,101]; note that the fixed mesh in coupled Eulerian-Lagrangian (CEL) formulations [40,126,135,154] is in fact multi-material Eulerian. The decisive advantage of an ALE mesh is that the mesh motion can be kept as Lagrangian as possible, resulting in less numerical diffusion and more accurate representation of interfaces compared to a fixed Eulerian mesh.

Three Step Scheme. Implementations commonly use a Lagrange-plus-remap or three step scheme which falls into the category of operator-splitting techniques (see above). The three step scheme divides the incremental solution of the non-linear problem into a Lagrangian step, a rezone step, and remap step (Fig. 3). During the Lagrangian step, the set of equations is solved by accounting for the sources but neglecting the convective terms; cf. (1). The rezone step relocates the nodes either to their original positions (Eulerian limit) or in such a way that mesh distortion is reduced. The remap step finally transfers the solution variables onto the modified mesh by using conservative advection algorithms. Physical time is advanced only during the Lagrangian step, whereas the spatial distributions of the solution variables are fixed during the remap step.

Subcell Closure Models (Mixture Models). The rezone step may give rise to elements which intersect with material interfaces and thus contain a heterogeneous mixture of two or more materials (Fig. 3 right). Because the spatial distribution of the element's degrees of freedom is homogeneous, however, a lack of information arises within such multi-material elements. The main difficulties are to accurately determine the states of the individual material portions and the reaction of the element they will generate [143]. To tackle these difficulties, the heterogeneous mixture is represented as an effective single-phase material

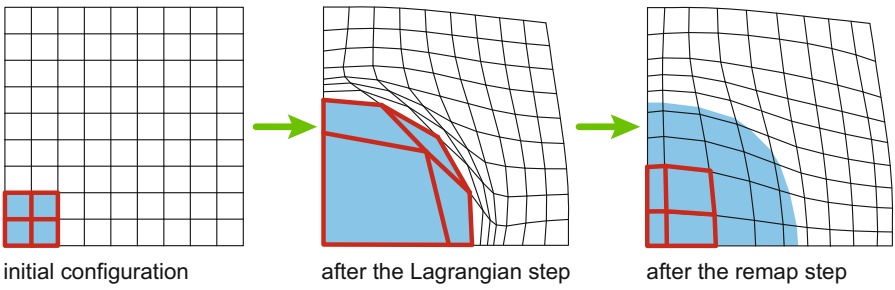

Fig. 3. Illustration of the MMALE three step scheme (rezone step not shown); in the multi-material Eulerian limit the rezoned mesh would be identical to the original mesh. The blue area indicates a material zone whose initial configuration is assigned to an element patch highlighted in red. At the end of a calculational cycle several elements intersect with the interface between blue and white, thus contain a mixture of two materials.

(homogenized mixture). This should be based on reasonable, physically-based mixing rules, referred to as subcell closure models, which can be derived from theories incorporating material volume fraction information [36,51,53,116,117]. However, all available subcell models assume pure, i.e. single-phase homogeneous materials at the outset, thus are not capable of including two-phase coupled response among the different materials of the mixture.

1.5 Large-Scale Modeling of Multi-phase Mixtures

From the previous discussion it can be concluded that adequate non-Lagrangian models for geotechnical or geomechanical processes must account for the dynamical interaction of multiple materials on at least three different length scales [17,21,22]: the scale l_{micro} defined by a typical grain diameter of the granular material (microscale), the scale l_{meso} at which the granular material can be represented as a continuum interacting with other bulk materials (mesoscale), and the scale l_{macro} at which the immiscible mixture of mesoscale continua can be represented as an effective single-phase material (macroscale). The mesoscale is the scale commonly used in soil mechanics, and at which continuum mechanical material models operate, e.g. to reproduce the nonlinear coupled behavior of fluid-saturated sand. The solid grains and the interstitial fluid of the granular material cannot be individually distinguished. The mesoscale also carries the information of interest associated with bulk material deformation and interface evolution. On the other hand, the macroscale is typically defined by a characteristic element length in multi-material Eulerian and MMALE calculations, thus is closely connected the non-Lagrangian formulation.

Our objective is not to describe small-scale details in the multi-phase flow field, but rather large-scale motions and interactions of the materials. Flow details should only be resolved to the extend they effect the mean flow. Upscaling information from lower to higher scales can be achieved by different types of approaches, and each has its advantages and disadvantages [26,56,77]. In both mathematical homogenization [10,67,83] and volume averaging in the sense of Whitaker [131,166–169], the balance equations for mass, momentum, etc., as well as the closure relations (e.g. constitutive equations) are postulated to hold on the small scale. Filtering techniques are then applied to obtain corresponding equations on the large scale at which measurements are often made. On the other hand, the continuum theory of mixtures [46–48,158] makes no small scale assumptions. Instead the system is viewed as overlapping continua with all balance principles postulated on the large scale. The form of the constitutive equations in terms of large scale variables is usually restricted by exploiting the entropy inequality.

A third type of approaches combining principles of the other two is adopted in the present research. Hybrid mixture theory was introduced in [74–77] and has been extended by Cushman and co-workers regarding two [2] and three spatial scales [30,31,119,120]. The basic idea is to apply local volume averaging [45,63,64] to the small scale balance equations and to make the constitutive assumptions needed for closure at the large scale with respect to which averaging

is carried out, that is, for the averaged balance equations. The closure relations can be obtained either by direct postulation of desirable equations, as done in [99] and herein, or based on thermodynamical considerations as in the continuum theory of mixtures.

1.6 Overview and Structure of the Work

This contribution summarizes the work done in Subproject 5 of the DFG Research Unit FOR 1136. The main objective of the subproject is the theoretical and numerical modeling of complex geotechnical processes such as the installation of vibro-injection piles [125,136]; cf. Fig. 1. In previous papers [21,22,141], MMALE has been introduced as the authors preferred modeling framework. The main reasons for this are as follows:

- it can represent large material deformations, shear and vorticity, as well as material interface evolution including topological changes (e.g. new free surfaces are allowed to be created in a natural manner);
- it can incorporate advanced history-dependent constitutive equations and multi-phase behavior of the soil or debris material;
- it can handle interactions of multiple materials without contact elements or specific algorithms;
- it is mass conservative and can be made less numerical diffusive than pure Eulerian formulations;
- it is more versatile than Lagrangian formulations and can be applied in situations where Lagrangian formulations fail.

In accordance with the individual tasks performed to reach the objectives, the paper is structured as follows. Section 2 addresses the continuum mechanical modeling of saturated sand as a compressible grain-fluid mixture by starting with the most general, averaged equations for two-phase media. In Sect. 3, a rigorous theoretical framework is developed based upon the interpretation of geotechnical and geomechanical processes as complex multi-phase flows. This framework allows for the consideration of two-phase coupled behavior of saturated sand as well as for the construction of models for the time evolution of the material volume fractions and averaged (homogenized) properties in multi-material flow situations. The numerical techniques implemented in the Lagrangian step, the rezone step, and the remap of the developed MMALE method are outlined in Sect. 4. In this method, the homogeneous equilibrium model derived from the theoretical framework provides a closed set of equations that holds at each spatial point and at all interfaces (i.e. in single-material as well as in multi-material elements). Section 5 then summarizes the experimental model tests concerned with the vibro-injection pile installation. The main purposes of these tests are the verification of the assumptions underlying the theoretical investigations and the validation of the MMALE computational models. Conclusions and outlook of future work are discussed in Sect. 6.

2 Saturated Sand as a Grain-Fluid Mixture

2.1 Averaged Equations of General Two-Phase Flow

In this section we derive a mathematical model for grain-fluid mixtures with compressible constituents. The starting point are the most general, averaged equations describing conservation of mass and balance of linear momentum, respectively, of non-reacting immiscible two-phase flow [63,64,89]:

$$\frac{\partial \pi^\alpha \rho^\alpha}{\partial t} + \operatorname{div}(\pi^\alpha \rho^\alpha \boldsymbol{v}^\alpha) = 0, \tag{2}$$

$$\frac{\partial \pi^\alpha \rho^\alpha \boldsymbol{v}^\alpha}{\partial t} + \operatorname{div}(\pi^\alpha \rho^\alpha \boldsymbol{v}^\alpha \otimes \boldsymbol{v}^\alpha) = \pi^\alpha \rho^\alpha \boldsymbol{b}^\alpha + \operatorname{div}(\pi^\alpha \boldsymbol{\sigma}^\alpha) + \boldsymbol{\Gamma}^\alpha. \tag{3}$$

The equations are in Eulerian conservation form, thus referring to a fixed modeling domain $\mathcal{D} \subset \mathbb{R}^3$ of the three-dimensional ambient Euclidian space. Each term is generally a function of point $\boldsymbol{x} \in \mathcal{D}$ and time $t \in [0, T] \subset \mathbb{R}$. The superscript $\alpha \in \{\mathrm{s}, \mathrm{f}\}$ indicates the phase, which is either solid or fluid (liquid or gas), and π^α is the α-phase volume fraction with properties

$$\pi^\alpha \in [0, 1], \text{ for all } \alpha, \qquad \text{and} \qquad \sum\nolimits_\alpha \pi^\alpha = 1. \tag{4}$$

Moreover, $\boldsymbol{v}^\alpha$ is the spatial image of the phase α material velocity, ρ^α is the spatial mass density of that phase, $\boldsymbol{b}^\alpha$ is a prescribed body force per unit mass, and $\boldsymbol{\sigma}^\alpha = (\boldsymbol{\sigma}^\alpha)^{\mathrm{T}}$ is the symmetric Cauchy stress. A superscribed T denotes transposition of a second-order tensor, $\otimes$ is the tensor product, and div is the spatial divergence operator. The momentum interfacial transfer term $\boldsymbol{\Gamma}^\alpha$ includes surface drag forces per unit volume generated by the relative motion of the phases. Here we simply assume that both phases move with the same velocity, i.e. $\boldsymbol{v}^{\mathrm{s}} = \boldsymbol{v}^{\mathrm{f}}$, resulting in $\boldsymbol{\Gamma}^{\mathrm{s}} = -\boldsymbol{\Gamma}^{\mathrm{f}} \equiv \boldsymbol{0}$. In fluid-saturated granular material this formalizes locally undrained conditions [99,176].

The stress tensor is usually decomposed into a pressure stress and an extra stress according to [111,159]

$$\boldsymbol{\sigma}^\alpha = -p^\alpha \boldsymbol{I} + \boldsymbol{s}^\alpha, \tag{5}$$

where $\boldsymbol{I}$ is the second-order unit tensor. In general, the changes in pressure stress are related to changes in mass density, whereas the extra stress is related to material deformations. For simplicity, we let $p^\alpha = -\frac{1}{3} \operatorname{tr} \boldsymbol{\sigma}^\alpha$, meaning that the extra stress is deviatoric, i.e. $\boldsymbol{s}^\alpha = \boldsymbol{\sigma}^\alpha_{\mathrm{dev}}$, where tr denotes the trace of a second-order tensor and $\boldsymbol{\sigma}_{\mathrm{dev}} \overset{\mathrm{def}}{=} \boldsymbol{\sigma} - \frac{1}{3}(\operatorname{tr} \boldsymbol{\sigma})\boldsymbol{I}$.

We remark that quantities in (2) and (3) have been averaged with respect to a representative volume element (RVE). Because of $(4)_2$, summation over both phases yields the mixture balance equations

$$\frac{\partial \bar{\rho}}{\partial t} + \operatorname{div}(\bar{\rho} \bar{\boldsymbol{v}}) = 0, \tag{6}$$

$$\frac{\partial \bar{\rho} \bar{\boldsymbol{v}}}{\partial t} + \operatorname{div}(\bar{\rho} \bar{\boldsymbol{v}} \otimes \bar{\boldsymbol{v}}) = \bar{\rho} \bar{\boldsymbol{b}} + \operatorname{div} \bar{\boldsymbol{\sigma}}, \tag{7}$$

respectively. For example, $\bar{\rho} = \sum_\alpha \pi^\alpha \rho^\alpha$.

Provided that the $\boldsymbol{\sigma}^\alpha$ have already been modeled by appropriate constitutive equations, the set (2) and (3) constitutes a system of $2 \cdot 2$ equations in the $3 \cdot 2 - 1$ unknowns π^α, ρ^α, and $\boldsymbol{v}^\alpha$, with $\alpha \in \{\mathrm{s}, \mathrm{f}\}$, where we emphasize that the π^α should only be considered and counted as only one variable because of $(4)_2$. Therefore, the system of equation requires one additional relation for the volume fraction, called the topological closure relation [44,45,51], to close the system. Otherwise the system would be indeterminate.

2.2 Stress Contributions in Granular Material

We consider a cohesionless granular material in which a single fluid fills the interstitial space. Rheologists call this a dense grain-fluid mixture or granular suspension [5], and a common example is saturated sand. Since only two phases are present, we simply define the fluid fraction or porosity through

$$n \overset{\text{def}}{=} \pi^{\mathrm{f}}, \qquad \text{so that} \qquad \pi^{\mathrm{s}} = 1 - n \tag{8}$$

by using $(4)_2$.

Two limiting regimes of dry granular flow are usually considered [9,86,139]: a rate-independent frictional flow regime usually studied in soil mechanics [144,176], and a rate-dependent viscous flow regime where grain inertia and instantaneous grain contacts through collision dominate [23,86,87]. In the intermediate, frictional-collisional flow regime, the contributions of frictional and collisional interactions to the bulk stress of the mixture cannot be clearly distinguished [6–8,93].

Further complexity is introduced by the interstitial fluid in granular materials. Besides the consolidation and liquefaction phenomena well-known in soil mechanics, indirect grain interactions may occur through lubricated contacts [5,6,8,54]. Generally all flow regimes have to be considered in the analysis of geotechnical and geomechanical processes. However, yet no constitutive equation is available which models the mechanical behavior of dense grain-fluid mixture over a wide range of flow conditions and material properties [8].

To account for the different flow regimes, the stress tensors of the solid and fluid phases in grain-fluid mixtures are additively decomposed into a rate-independent frictional part and a rate-dependent viscous part [9,87,93]:

$$\boldsymbol{\sigma}^\alpha \overset{\text{def}}{=} \boldsymbol{\sigma}^\alpha_{\mathrm{fr}} + \boldsymbol{\sigma}^\alpha_{\mathrm{vi}}, \qquad \text{with} \quad \alpha \in \{\mathrm{s}, \mathrm{f}\}. \tag{9}$$

Terzaghi's effective stress [153], $\boldsymbol{\sigma}'_{\mathrm{fr}}$, is introduced as

$$\frac{\boldsymbol{\sigma}'_{\mathrm{fr}}}{1-n} \overset{\text{def}}{=} -(p^{\mathrm{s}} - p^{\mathrm{f}})\boldsymbol{I} + \boldsymbol{s}^{\mathrm{s}}_{\mathrm{fr}} \tag{10}$$

in accordance with [32], so that

$$\frac{p'}{1-n} = p^{\mathrm{s}} - p^{\mathrm{f}}, \tag{11}$$

where $p' \stackrel{\text{def}}{=} -\frac{1}{3}\operatorname{tr}\boldsymbol{\sigma}'_{\text{fr}}$ is the (negative) mean effective stress and $p^{\text{s}} - p^{\text{f}}$ is the excess pressure.

A particular form of the principle of effective stress [144,176] can be derived by combining (10) with an expression of the total stress of the grain-fluid mixture,

$$\bar{\boldsymbol{\sigma}} = (1-n)\boldsymbol{\sigma}^{\text{s}} + n\boldsymbol{\sigma}^{\text{f}}, \tag{12}$$

resulting in

$$\bar{\boldsymbol{\sigma}}_{\text{fr}} = \boldsymbol{\sigma}'_{\text{fr}} - p^{\text{f}}\boldsymbol{I}. \tag{13}$$

We adopt this form for conceptual reasons, while noting that several other versions have been postulated; cf. [96].

If the effective stress for the viscous part is assumed unaffected by fluid stresses, then substitution of (13) and (9) into (12) yields the following representation of the principle of effective stress for a general grain-fluid mixture [92]:

$$\bar{\boldsymbol{\sigma}} = \boldsymbol{\sigma}'_{\text{fr}} + \boldsymbol{\sigma}'_{\text{vi}} + \boldsymbol{\sigma}^{\text{f}}_{\text{fr}} + n\boldsymbol{\sigma}^{\text{f}}_{\text{vi}} = \boldsymbol{\sigma}' - p^{\text{f}}\boldsymbol{I} + n\boldsymbol{s}^{\text{f}}, \tag{14}$$

with $\boldsymbol{\sigma}' = \boldsymbol{\sigma}'_{\text{fr}} + \boldsymbol{\sigma}'_{\text{vi}}$. In terms of pressure stress, the principle (14) reads $\bar{p} = p' + p^{\text{f}}$, where $\bar{p} \stackrel{\text{def}}{=} -\frac{1}{3}\operatorname{tr}\bar{\boldsymbol{\sigma}}_{\text{fr}}$.

2.3 Constitutive Equations

Application of (14) requires models for $\boldsymbol{\sigma}'_{\text{fr}}$, $\boldsymbol{\sigma}'_{\text{vi}}$, p^{f}, and $\boldsymbol{s}^{\text{f}}$. The fluid phase is usually represented as a Newtonian fluid, leading to simple representations of p^{f} and $\boldsymbol{s}^{\text{f}}$. Concerning the frictional part of effective stress, $\boldsymbol{\sigma}'_{\text{fr}}$, a large number of constitutive equations has been proposed for applications in soil mechanics. States of failure can be adequately modeled by models employing the classical Mohr-Coulomb yield condition [176]. Comprehensive constitutive equations that might be applied beyond states of failure fall into the categories of hypoelastoplastic [100,113,128,152] or hypoplastic [73,95,123,164] rate constitutive equations. Significant progress in the development of hypoplasticity has also been achieved in the context of this DFG Research Unit [104,124]. Such equations take the general form

$$\overset{\triangledown}{\boldsymbol{\sigma}}'_{\text{fr}} \stackrel{\text{def}}{=} \mathbf{c}'_{\text{fr}}(\boldsymbol{\sigma}'_{\text{fr}}, n, \boldsymbol{h}) : \boldsymbol{d}, \tag{15}$$

by assuming incompressible constituents. Here $\overset{\triangledown}{\boldsymbol{\sigma}}$ denotes any objective rate of $\boldsymbol{\sigma}$, $\mathbf{c}$ is the fourth-order material tangent tensor, $\boldsymbol{h}$ is a set of history variables other than stress, and $\boldsymbol{d} \stackrel{\text{def}}{=} \frac{1}{2}(\boldsymbol{\nabla v} + (\boldsymbol{\nabla v})^{\text{T}})$ is the spatial rate of deformation tensor.

Constitutive equations for the viscous part of the effective stress, $\boldsymbol{\sigma}'_{\text{vi}}$, are often restricted to particular flow conditions or to narrow ranges of material properties. Common models take the form [87,127]

$$\boldsymbol{\sigma}'_{\text{vi}} \stackrel{\text{def}}{=} \mu' \boldsymbol{d}^{\text{s}}_{\text{dev}}, \tag{16}$$

where μ' is the dynamic shear viscosity. The latter is generally a function of the porosity resp. solid volume fraction and shear rate [23,68,86,87,93,94,127,130].

2.4 Topological Closure and Compressible Constituents

Section 2.1 has revealed that a well-posed model for grain-fluid mixtures requires topological closure, that is, an evolution equation for the fluid volume fraction (porosity). If the material of one phase, say, the solid phase is incompressible, then this missing equation is readily obtained from conservation of mass of that phase. However, an indeterminacy arises for compressible constituents, reflected in the fact that π^α and ρ^α appear in the general Eqs. (2) and (3) only in the form of the product $\tilde{\rho}^\alpha = \pi^\alpha \rho^\alpha$, but not separately.

A Lagrangian formulation is chosen to resolve the aforementioned indeterminacy. First, let the material time derivative of a α-phase-related quantity q^α along the velocity $\boldsymbol{v}^\alpha$ be defined through

$$\dot{q}^\alpha \overset{\text{def}}{=} \frac{\partial q^\alpha}{\partial t} + \boldsymbol{v}^\alpha \cdot \boldsymbol{\nabla} q^\alpha, \qquad \text{with} \quad \alpha \in \{\mathrm{s}, \mathrm{f}\}, \tag{17}$$

where $\boldsymbol{\nabla}$ is the covariant derivative, and $\boldsymbol{v}^\mathrm{s} = \boldsymbol{v}^\mathrm{f} = \bar{\boldsymbol{v}}$, i.e. locally undrained conditions have been assumed. Conservation of mass (2) for the solid phase can then be written in Lagrangian form:

$$\frac{\dot{\tilde{\rho}}^\mathrm{s}}{\tilde{\rho}^\mathrm{s}} = -\operatorname{div} \boldsymbol{v}^\mathrm{s}. \tag{18}$$

with the bulk mass density $\tilde{\rho}^\mathrm{s} = \pi^\mathrm{s} \rho^\mathrm{s} = (1-n)\rho^\mathrm{s}$ of the solid phase.

The decomposition of stress (5) introduces pressure as an independent variable. The pressure change of each phase is related to its change in density through a compression model of the form

$$-\left.\frac{1}{V^\alpha}\frac{\partial V^\alpha}{\partial p^\alpha}\right|_{M^\alpha} = \frac{1}{\rho^\alpha}\frac{\mathrm{d}\rho^\alpha}{\mathrm{d}p^\alpha} \overset{\text{def}}{=} \frac{1}{K^\alpha}, \qquad \text{with} \quad \alpha \in \{\mathrm{s}, \mathrm{f}\}. \tag{19}$$

K^α is the bulk modulus of the α-phase material, $V^\alpha = \pi^\alpha V$ is the volume occupied by phase α within a small Lagrangian control volume V of the mixture, $M^\alpha = \rho^\alpha V^\alpha$ is the mass of that phase volume, and $|_{M^\alpha}$ means that the mass of the α-phase is kept constant along with differentiation.

In a mixture the pressure of each compressible constituent is generally a function of the mass density and volume fraction of that constituent. In particular, the pressure of the solid phase (grains) in granular material does not only depend on the mass density but also on the porosity [28,29]. However, one usually assumes that the Lagrangian control volume occupied by the grain-fluid mixture is a function

$$V = V(p^\mathrm{f}, \bar{p} - p^\mathrm{f}) \tag{20}$$

of the fluid phase pressure and the pressure difference $\bar{p} - p^\mathrm{f} = p'$. Under the assumption that total mass of the solid phase, M^s, is kept fixed, one has

$$\begin{aligned}\left.\frac{\mathrm{d}V}{V}\right|_{M^\mathrm{s}} &= \frac{1}{V}\left.\frac{\partial V}{\partial(\bar{p}-p^\mathrm{f})}\right|_{p^\mathrm{f},M^\mathrm{s}} \mathrm{d}(\bar{p}-p^\mathrm{f}) + \frac{1}{V}\left.\frac{\partial V}{\partial p^\mathrm{f}}\right|_{\bar{p}-p^\mathrm{f},M^\mathrm{s}} \mathrm{d}p^\mathrm{f} \\ &= \frac{1}{V}\left.\frac{\partial V}{\partial \bar{p}}\right|_{p^\mathrm{f},M^\mathrm{s}} \mathrm{d}(\bar{p}-p^\mathrm{f}) + \frac{1}{V}\left.\frac{\partial V}{\partial p^\mathrm{f}}\right|_{\bar{p}-p^\mathrm{f},M^\mathrm{s}} \mathrm{d}p^\mathrm{f} \\ &\overset{\text{def}}{=} -\frac{1}{K_\mathrm{dr}}\,\mathrm{d}(\bar{p}-p^\mathrm{f}) - \frac{1}{K_\mathrm{uj}}\,\mathrm{d}p^\mathrm{f},\end{aligned} \tag{21}$$

where K_dr and K_uj are called the drained bulk modulus and unjacketed bulk modulus of the granular material, respectively, and

$$K_\mathrm{uj} \approx K^\mathrm{s}. \tag{22}$$

By recalling that $M^\mathrm{s} = \rho^\mathrm{s} V^\mathrm{s} = \rho^\mathrm{s}(1-n)V$, Eq. (18) is equivalent to

$$\frac{\mathrm{d}\tilde{\rho}^\mathrm{s}}{\tilde{\rho}^\mathrm{s}} = -\left.\frac{\mathrm{d}V}{V}\right|_{M^\mathrm{s}}. \tag{23}$$

Therefore, replacing in (21) the total differential with the material time derivative yields

$$\dot{\bar{p}} = -K_\mathrm{dr}\,\mathrm{div}\,\boldsymbol{v}^\mathrm{s} + \zeta\,\dot{p}^\mathrm{f}, \tag{24}$$

where $\zeta \overset{\text{def}}{=} 1 - K_\mathrm{dr}/K^\mathrm{s}$ is the Biot-Willis coefficient [42,43,176].

Based on the previous results together with the definition of mean effective stress, (11), we are now able to relate solid and fluid phase pressures, p^s and p^f, to solid phase volumetric deformation. To determine the rate of the solid pressure, we start from the relative volume change $\mathrm{d}V^\mathrm{s}/V^\mathrm{s}|_{(1-n)}$ by keeping solid phase volume fraction constant:

$$\begin{aligned}\left.\frac{\mathrm{d}V^\mathrm{s}}{V^\mathrm{s}}\right|_{1-n} &= -\frac{1}{\rho^\mathrm{s}}\frac{\partial \rho^\mathrm{s}}{\partial p^\mathrm{s}}\mathrm{d}p^\mathrm{s} = -\frac{\mathrm{d}p^\mathrm{s}}{K^\mathrm{s}} = -\frac{1}{K^\mathrm{s}}\left(\frac{\mathrm{d}p'}{1-n} + \mathrm{d}p^\mathrm{f}\right) \\ &= \left(\left.\frac{\mathrm{d}V}{V}\right|_{M^\mathrm{s}} + \frac{\mathrm{d}p^\mathrm{f}}{K^\mathrm{s}}\right)\frac{K_\mathrm{dr}}{(1-n)K^\mathrm{s}} - \frac{\mathrm{d}p^\mathrm{f}}{K^\mathrm{s}} \\ &= \frac{K_\mathrm{dr}}{(1-n)K^\mathrm{s}}\left.\frac{\mathrm{d}V}{V}\right|_{M^\mathrm{s}} - \left(1 - \frac{K_\mathrm{dr}}{(1-n)K^\mathrm{s}}\right)\frac{\mathrm{d}p^\mathrm{f}}{K^\mathrm{s}},\end{aligned} \tag{25}$$

By replacing the total differential with the material time derivative again and rearrange, one obtains

$$\dot{p}^\mathrm{s} = -\frac{K_\mathrm{dr}}{1-n}\,\mathrm{div}\,\boldsymbol{v}^\mathrm{s} + \frac{\zeta - n}{1-n}\,\dot{p}^\mathrm{f}. \tag{26}$$

On the other hand, the assumption of locally undrained conditions, i.e. $\boldsymbol{v}^\mathrm{f} = \boldsymbol{v}^\mathrm{s} = \bar{\boldsymbol{v}}$, allows us to rewrite conservation of mass (2) for the fluid phase as

$$\dot{p}^\mathrm{f} = -\zeta Q\,\mathrm{div}\,\boldsymbol{v}^\mathrm{s}, \qquad \text{with} \quad Q \overset{\text{def}}{=} \left(\frac{\zeta - n}{K^\mathrm{s}} + \frac{n}{K^\mathrm{f}}\right)^{-1}. \tag{27}$$

Substitution of (27) into (24) finally yields a Lagrangian form of (6):

$$\dot{\bar{p}} = -K \operatorname{div} \bar{\boldsymbol{v}}, \tag{28}$$

in which

$$K = K_{\mathrm{dr}} \left(1 + \frac{\zeta^2}{\zeta \dfrac{K_{\mathrm{dr}}}{K^{\mathrm{s}}} + n \left(\dfrac{K_{\mathrm{dr}}}{K^{\mathrm{f}}} - \dfrac{K_{\mathrm{dr}}}{K^{\mathrm{s}}} \right)} \right). \tag{29}$$

Equation (28) in conjunction with the bulk modulus given by (29) holds for arbitrary compositions of saturated grain-fluid mixtures with compressible constituents and homogeneous velocity, that is, undrained conditions. Particular cases included are:

- solid without any pores ($n = 0$, $K_{\mathrm{dr}} = K^{\mathrm{s}}$, $\zeta = 0$), for which $K = K^{\mathrm{s}}$;
- fluid without any solid content ($n = 1$, $K_{\mathrm{dr}} = 0$, $\zeta = 1$), for which $K = K^{\mathrm{f}}$;
- dry granular material ($0 < n < 1$, $K^{\mathrm{f}} \approx 0$), for which $K = K_{\mathrm{dr}}$;
- uniform suspension of zero friction ($K_{\mathrm{dr}} = 0$, $\zeta = 1$), for which $p^{\mathrm{s}} = p^{\mathrm{f}}$ and $K = ((1-n)/K^{\mathrm{s}} + n/K^{\mathrm{f}})^{-1}$, known as Wood's equation [172, p. 327].

In concluding this section, we remark that the definition (11) of mean effective stress resolves the indeterminacy associated with volume fraction evolution in compressible grain-fluid mixtures. This definition provides the missing link between volumetric deformation and changes in solid and fluid pressures. Evolution of volume fraction in two-phase grain-fluid mixtures thus can be associated with solid phase conservation of mass (2) resp. (18) alone:

$$\dot{n} = (1-n) \left(\frac{\dot{p}^{\mathrm{s}}}{K^{\mathrm{s}}} + \operatorname{div} \boldsymbol{v}^{\mathrm{s}} \right), \tag{30}$$

in which $\dot{p}^{\mathrm{s}}$ is given by (26).

3 Mixture Model for Multi-material Interaction

The previous section was concerned with the continuum mechanical modeling of general two-phase, grain-fluid mixtures, of which saturated sand is but one example. It has been shown that if both compressible phases move with the same velocity, representing locally undrained conditions, then the mixture can be equivalently modeled as an effective single-phase, i.e. homogeneous bulk material. In the section that follows, we summarize a rigorous theoretical framework we have developed [17,21,22] to construct macroscopic mixture models for the dynamical interaction of grain-fluid mixtures with multiple other, physically distinct bulk materials, e.g. pure fluids or pure solids. Void, representing empty space or atmosphere, is generally considered as material, and all materials may undergo large deformations. We refer to such a situation as multi-material flow.

3.1 Averaging Procedure

Consider a three-scale system consisting of bulk fluid (F), bulk solid (S), and fluid-saturated granular material (G). The granular material consists of a solid phase (s) and fluid phase (f), and is constituted by an assembly of solid grains, whose typical diameter defines the microscale of the problem, l_{micro}. The grain assembly can be represented by a continuum at the mesoscale l_{meso}, separated from the bulk solid and bulk fluid by sharp interfaces. Moreover, we assume that the multi-material system has a representative volume element (RVE) with characteristic length l_{macro}, the macroscale. The RVE is a sub-domain $\mathcal{H} \subset \mathcal{D}$ of the spatially fixed, i.e. Eulerian modeling domain introduced in Sect. 2.1.

Let $k \in \{\mathrm{S}, \mathrm{F}, \mathrm{G}\} \overset{\mathrm{def}}{=} \{1, \ldots, M\}$ denote the material and $\alpha \in \{\mathrm{s}, \mathrm{f}\} \overset{\mathrm{def}}{=} \{1, \ldots, N\}$ the phase. A particular phase α in a particular material k represents an individual, chemically-independent constituent of the flow and is denoted by αk. Concerning the present situation, $\alpha k \in \{\mathrm{S} \equiv \mathrm{sS}, \mathrm{F} \equiv \mathrm{fF}, \mathrm{sG}, \mathrm{fG}\}$. The intersection of each two constituents is either empty or the shared interface. The indicator function $\chi^{\alpha k} : \mathcal{D} \times [0, T] \to \{0, 1\}$ which picks out the α-phase domain of the k-material domain is defined by

$$\chi^{\alpha k}(\boldsymbol{x}, t) \overset{\mathrm{def}}{=} \begin{cases} 1 & \text{if } \boldsymbol{x} \text{ is in } \alpha k \text{ at time } t, \\ 0 & \text{else.} \end{cases} \tag{31}$$

The point we wish to emphasize is that the indicator function (31) can be represented as the product $\chi^{\alpha k} = \chi^{\alpha} \chi^{k}$ of two independent indicator functions for each material k and each phase α.

As introduced in Sect. 1, our approach employs hybrid mixture theory to upscale information from the microscale to the macroscale. The microscopic balance equations are upscaled by using local volume averaging, and then the closure relations (constitutive equations, etc.) are postulated on the macroscale. To this end, let the subregion of the RVE occupied by the k-material be $\mathcal{H}^k$, and let $\mathcal{H}^{\alpha k}$ be the subregion occupied by the α-phase of the k-material, with $\mathcal{H} = \bigcup_k \mathcal{H}^k = \bigcup_k \bigcup_\alpha \mathcal{H}^{\alpha k}$. Then the $\mathcal{H}$-average of an arbitrary time-dependent spatial microscopic field $q(\boldsymbol{x}, t)$ is defined through

$$\langle q \rangle(\boldsymbol{x}, t) \overset{\mathrm{def}}{=} \frac{1}{H} \int_{\mathcal{H}} q(\boldsymbol{x} + \boldsymbol{y}, t) \, \mathrm{d}v \tag{32}$$

for all $\boldsymbol{x} \in \mathcal{D}$ and $t \in [0, T]$, where $\mathrm{d}v$ is the volume density on $\mathbb{R}^3$, $H \overset{\mathrm{def}}{=} \int_{\mathcal{H}} 1 \, \mathrm{d}v = \mathrm{const}$ is the volume measure of $\mathcal{H}$, and $\boldsymbol{y} \in \mathcal{H}$ is a vector.

Two particular averaged fields frequently used are the volume fractions

$$f^k \overset{\mathrm{def}}{=} \langle \chi^k \rangle = \frac{H^k}{H} \qquad \text{and} \qquad \pi^{\alpha k} \overset{\mathrm{def}}{=} \frac{1}{f^k} \langle \chi^{\alpha k} \rangle = \frac{H^{\alpha k}}{H^k}, \tag{33}$$

where $H^k \overset{\mathrm{def}}{=} \int_{\mathcal{H}^k} 1 \, \mathrm{d}v = \int_{\mathcal{H}} \chi^k \, \mathrm{d}v$ and $H^{\alpha k} \overset{\mathrm{def}}{=} \int_{\mathcal{H}^{\alpha k}} 1 \, \mathrm{d}v = \int_{\mathcal{H}} \chi^{\alpha k} \, \mathrm{d}v$. While f^k is the volume fraction of the k-material with respect to the RVE, $\pi^{\alpha k}$ represents

the macroscale volume fraction of the α-phase intrinsic to the k-material, with $f^k, \pi^{\alpha k} \in [0,1]$. Phase or material overlaps are not allowed, hence

$$\sum\nolimits_k f^k = 1 \qquad \text{and} \qquad \sum\nolimits_\alpha \pi^{\alpha k} = 1 \tag{34}$$

for all $k \in \{1, \ldots, M\}$.

Different macroscopic (i.e. $\mathcal{H}$-averaged) fields can now be defined by employing the previous definitions and the properties (34). Clearly, if q is a microscopic field defined per unit volume, then

$$\langle q \rangle = \sum\nolimits_k f^k q^k = \sum\nolimits_k \sum\nolimits_\alpha f^k \pi^{\alpha k} q^{\alpha k}, \tag{35}$$

with

$$q^k \stackrel{\text{def}}{=} \frac{\langle \chi^k q \rangle}{f^k} \qquad \text{and} \qquad q^{\alpha k} \stackrel{\text{def}}{=} \frac{\langle \chi^{\alpha k} q \rangle}{f^k \pi^{\alpha k}}. \tag{36}$$

Here $\langle q \rangle$ is the volume average of q in the mixture, q^k is the intrinsic k-material average, and $q^{\alpha k}$ is the intrinsic average related to the α-phase in the k-material. Accordingly, if $q = \rho$, for example, is the microscopic spatial mass density, then $\rho^{\alpha k}$ represents the mass of the constituent αk per unit volume of that constituent, $\pi^{\alpha k} \rho^{\alpha k}$ is the mass of the constituent αk per unit volume of the k-material, and $f^k \pi^{\alpha k} \rho^{\alpha k}$ denotes its mass per unit volume of the mixture.

We remark that, in the present approach, each material represents a mixture generally composed of a solid phase and a fluid phase. Hence, we define

$$n^k \stackrel{\text{def}}{=} \pi^{\mathrm{f}k} \tag{37}$$

as the fluid fraction or porosity of material k, with $k \in \{\mathrm{S}, \mathrm{F}, \mathrm{G}\}$; cf. (8). Then the solid fraction is $\pi^{\mathrm{s}k} = 1 - n^k$ by using $(34)_2$. For pure solid ($k = \mathrm{S}$) one has $n^{\mathrm{S}} = 0$, whereas $n^{\mathrm{F}} = 1$ in case of pure fluid ($k = \mathrm{F}$).

3.2 Macroscopic Mixture Model

On the microscale all constituents of the mixture are regarded as continua, governed by the equations of continuum mechanics [111,158,159]. The balance equations are conservation of mass and balance of momentum for the problems under consideration, in conjunction with the interface jump conditions. Each term of the microscopic balance equations is averaged according to the procedure above. Details can be found in [21], and in [63,64] for the case of two scales.

Under the assumption of non-reactive constituents, one obtains the following Eulerian conservation form of α-phase-k-material macroscopic conservation of mass

$$\frac{\partial f^k \pi^{\alpha k} \rho^{\alpha k}}{\partial t} + \operatorname{div}(f^k \pi^{\alpha k} \rho^{\alpha k} \boldsymbol{v}^{\alpha k}) = 0 \tag{38}$$

and macroscopic balance of linear momentum

$$\begin{aligned} &\frac{\partial f^k \pi^{\alpha k} \rho^{\alpha k} \boldsymbol{v}^{\alpha k}}{\partial t} + \operatorname{div}(f^k \pi^{\alpha k} \rho^{\alpha k} \boldsymbol{v}^{\alpha k} \otimes \boldsymbol{v}^{\alpha k}) \\ &= f^k \pi^{\alpha k} \rho^{\alpha k} \boldsymbol{b}^{\alpha k} + \operatorname{div}(f^k \pi^{\alpha k} \boldsymbol{\sigma}^{\alpha k}) + \boldsymbol{\Gamma}^{\alpha k}. \end{aligned} \tag{39}$$

Note that these equations are consistent with the set (2) and (3) for general two-phase media if one sets $\chi^k \equiv 1$ resp. $f^k \equiv 1$ (single material case). As in Sect. 2.1, let us further assume that no momentum is exchanged no matter between which constituents, and that velocity is homogeneous. Clearly,

$$\boldsymbol{\Gamma}^{\alpha k} \equiv \mathbf{0} \qquad \text{and} \qquad \langle \boldsymbol{v} \rangle = \boldsymbol{v}^k = \boldsymbol{v}^{\alpha k}, \tag{40}$$

for all $k \in \{\mathrm{S}, \mathrm{F}, \mathrm{G}\}$ and $\alpha k \in \{\mathrm{S}, \mathrm{F}, \mathrm{sG}, \mathrm{fG}\}$.

Based on (35), summation of (38) and (39) over all phases and all materials finally yield the macroscopic conservation of mass and macroscopic balance of momentum of the mixture:

$$\frac{\partial \langle \rho \rangle}{\partial t} + \operatorname{div} \langle \rho \boldsymbol{v} \rangle = 0, \tag{41}$$

$$\frac{\partial \langle \rho \boldsymbol{v} \rangle}{\partial t} + \operatorname{div} \langle \rho \boldsymbol{v} \otimes \boldsymbol{v} \rangle = \langle \rho \boldsymbol{b} \rangle + \operatorname{div} \langle \boldsymbol{\sigma} \rangle. \tag{42}$$

We emphasize again the consistency between (41) and (6), as well as between (42) and (7) for the case where the mixture represents a single saturated granular material and no other bulk materials. Moreover, Sect. 2 has revealed that grain-fluid mixtures without mass and momentum exchange can be treated as homogeneous bulk material, possessing a single velocity field. Therefore, after adding the superscript G referring to the granular material to the relevant terms of Sect. 2, these terms can be directly substituted into the equations of this section.

After combining the mixture balance principles (41) and (42) with the particularizations made for saturated granular material in Sect. 2, and doing some algebraic manipulation, the following Lagrangian model for geotechnical or geomechanical multi-material flow is obtained [17,21]:

$$\langle \dot{p} \rangle / \langle K \rangle + \operatorname{div} \langle \boldsymbol{v} \rangle = 0 \tag{43}$$

$$\operatorname{div} \langle \boldsymbol{s} - p\boldsymbol{I} \rangle + \langle \rho \boldsymbol{b} \rangle - \langle \rho \rangle \langle \dot{\boldsymbol{v}} \rangle = \mathbf{0}, \tag{44}$$

in which

$$\langle p \rangle = \sum_k f^k p^k = f^{\mathrm{S}} p^{\mathrm{S}} + f^{\mathrm{F}} p^{\mathrm{F}} + f^{\mathrm{G}} \left(p^{\mathrm{G}'} + p^{\mathrm{fG}} \right), \tag{45}$$

$$\langle \boldsymbol{s} \rangle = \sum_k f^k \boldsymbol{s}^k = f^{\mathrm{S}} \boldsymbol{s}^{\mathrm{S}} + f^{\mathrm{F}} \boldsymbol{s}^{\mathrm{F}} + f^{\mathrm{G}} \left(\boldsymbol{s}^{\mathrm{G}'} + n^{\mathrm{G}} \boldsymbol{s}^{\mathrm{fG}} \right), \tag{46}$$

$$\begin{aligned} \langle \rho \rangle &= \sum_k f^k \rho^k \\ &= f^{\mathrm{S}} \rho^{\mathrm{S}} + f^{\mathrm{F}} \rho^{\mathrm{F}} + f^{\mathrm{G}} \left((1 - n^{\mathrm{G}}) \rho^{\mathrm{sG}} + n^{\mathrm{G}} \rho^{\mathrm{fG}} \right), \end{aligned} \tag{47}$$

$$\frac{1}{\langle K \rangle} = \sum_k \frac{f^k}{K^k} = \frac{f^{\mathrm{S}}}{K^{\mathrm{S}}} + \frac{f^{\mathrm{F}}}{K^{\mathrm{F}}} + \frac{f^{\mathrm{G}}}{K^{\mathrm{G}}}, \tag{48}$$

and K^{G} given by (29).

Constitutive equations and compression models must be prescribed for the bulk solid ($\boldsymbol{s}^{\mathrm{S}}$, p^{S}), bulk fluid ($\boldsymbol{s}^{\mathrm{F}}$, p^{F}), granular material ($\boldsymbol{s}^{\mathrm{G}'}$, $p^{\mathrm{G}'}$), and interstitial fluid ($\boldsymbol{s}^{\mathrm{fG}}$, p^{fG}), by using the consistent macroscopic rate of deformation tensor

$$\langle \boldsymbol{d}_k \rangle \stackrel{\text{def}}{=} \langle \boldsymbol{d} \rangle + \frac{\dot{f}^k}{3f^k}\boldsymbol{I} \qquad \text{for each } k \in \{\mathrm{S},\mathrm{F},\mathrm{G}\}. \tag{49}$$

Moreover, in accordance with Sect. 2.4 the evolution of the porosity of the granular material is given by

$$\dot{n}^{\mathrm{G}} = (1-n^{\mathrm{G}})\left(\frac{\dot{p}^{\mathrm{sG}}}{K^{\mathrm{sG}}} + \operatorname{div}\langle \boldsymbol{v}_{\mathrm{G}} \rangle\right), \tag{50}$$

with

$$\dot{p}^{\mathrm{sG}} = -\frac{K^{\mathrm{G}}_{\mathrm{dr}}}{1-n^{\mathrm{G}}}\operatorname{div}\langle \boldsymbol{v}_{\mathrm{G}} \rangle + \frac{\zeta^{\mathrm{G}} - n^{\mathrm{G}}}{1-n^{\mathrm{G}}}\,\dot{p}^{\mathrm{fG}} \tag{51}$$

and $\operatorname{div}\langle \boldsymbol{v}_{\mathrm{G}} \rangle = \operatorname{div}\langle \boldsymbol{v} \rangle + \dot{f}^{\mathrm{G}}/f^{\mathrm{G}}$.

The model is the backbone of our non-Lagrangian numerical method summarized in Sect. 4. Its is important to note that the set of Eqs. (43) and (44) holds at each spatial point and at all interfaces, as well as for zones occupied by a single or multiple bulk materials. All materials that might be present in such processes, either compressible or incompressible, are treated in a unified fashion due to the decomposition of stress (5) used for all constituents.

3.3 Volume Fraction Evolution and Homogeneous Equilibrium

In the mathematical sense of counting equations and unknowns, the above system of equations requires an additional $M-1$ closure relations (for the present case, $M=3$) to become a closed system. It is natural to think of this indeterminacy as being associated with conservation of mass and the evolution of the material volume fractions f^k, with $k \in \{1,\ldots,M\} = \{\mathrm{S},\mathrm{F},\mathrm{G}\}$. The reader is referred to [44,45,51] for a more general discussion of volume fraction closure in two- and multi-phase flow models.

A simple way to obtain topological closure for multi-material flow is to assume constant volume fractions. However, such an assumption is inadequate if material compressibilities differ by several orders of magnitude. In our approach, we achieve closure by assuming homogeneous equilibrium [53,116,149], formalized through

$$p^k = \langle p \rangle \quad \text{and} \quad \boldsymbol{v}^k = \langle \boldsymbol{v} \rangle \quad \text{for all } k \in \{\mathrm{S},\mathrm{F},\mathrm{G}\}. \tag{52}$$

The first assumption of pressure equilibrium between bulk materials is adequate because the speed of sound in each material is large compared with velocities in the problems of interest. In other words, equilibration is infinitely fast such that pressure is continuous across a material interface. The second assumption, $(52)_2$, has already motivated zero momentum exchange between the constituents; see (40). However, it is not generally a reasonable one because equilibration of

velocity differences is driven by drag forces on material interfaces. Using the assumption implies fully bonded materials.

In following [53,116] and using the assumptions (52), we have derived in [17,21] a more realistic closure model reflecting homogeneous equilibrium:

$$\dot{f}^k = f^k \left(\frac{\langle K \rangle}{K^k} - 1 \right) \operatorname{div} \langle \boldsymbol{v} \rangle, \quad \text{for all } k \in \{\mathrm{S}, \mathrm{F}, \mathrm{G}\}. \tag{53}$$

Note that this equation naturally provides for a mixture compression model and a void collapse mechanism: the material with the smallest bulk modulus contributes most to the total volume change.

3.4 Non-Lagrangian Formulation of the Model

Since local volume averaging is defined with respect to a fixed region of space, the Eulerian formulation of the proposed model is natural. Indeed, the Lagrangian form (43) and (44) has been derived from the Eulerian conservation form (41) and (42), respectively, using the material time derivative. The arbitrary Lagrangian-Eulerian (ALE) formulation further generalizes the model. A condensed derivation is given below; for more details, see [13,14].

According to Sect. 1.3, the ALE formulation introduces a reference domain which may move in space at an arbitrary velocity $\boldsymbol{w}$. The relative volume change between the referential coordinate system and the spatial coordinate system is the Jacobian, J, and its rate of change is given by

$$\frac{\partial J}{\partial t} = J \operatorname{div} \boldsymbol{w}. \tag{54}$$

The ALE operator (1) is substituted into the Eqs. (43) and (44), respectively. Multiplication of the resulting equations with J and substitution of (54) gives the ALE conservation form of (43) and (44):

$$\frac{\partial \hat{p} J}{\partial t} + J \operatorname{div}(p \boldsymbol{c}) = J(p - K) \operatorname{div} \boldsymbol{v} \tag{55}$$

$$\frac{\partial \hat{\rho} \hat{\boldsymbol{v}} J}{\partial t} + J \operatorname{div}(\rho \boldsymbol{v} \otimes \boldsymbol{c}) = J(\rho \boldsymbol{b} + \operatorname{div}(\boldsymbol{s} - p \boldsymbol{I})), \tag{56}$$

where

$$\boldsymbol{c} = \boldsymbol{v} - \boldsymbol{w} \tag{57}$$

is the convective velocity. Angle brackets indicating mixture quantities have been dropped for notational brevity.

3.5 Application: Isotropic Compression

Consider a Lagrangian control volume occupied with a mixture of steel (bulk solid), air (bulk fluid), and dry sand. The volume is subjected to quasi-static isotropic compression. Under these conditions only (43) needs to be integrated

in time. A first-order explicit scheme has been implemented for this purpose. The initial volume fractions are set to $f_0^{\mathrm{S}} = 0.4$, $f_0^{\mathrm{F}} = 0.2$, and $f_0^{\mathrm{G}} = 0.4$, respectively, and the initial porosity of the sand is $n_0^{\mathrm{G}} = 0.4$. The sand is chosen to be uniform and fine-grained, with an angle of internal friction $\phi = 32°$. The initial pressure of all constituents is the atmospheric pressure at sea level, $p_{\mathrm{atm}} = 101.0\,\mathrm{kPa}$.

Steel under isotropic compression can be approximated by hypoelasticity [159]. The constant bulk modulus is $K^{\mathrm{S}} = 1.6 \times 10^8\,\mathrm{kPa}$. Moreover, we assume that the compressibility of the bulk air and the air trapped in the sand pores does not change with pressure, so that $K^{\mathrm{F}} = K^{\mathrm{fG}} = p_{\mathrm{atm}} = \mathrm{const}$.

Janbu's power law [173] is employed in order to model nonlinear stiffness of the granular material:

$$E_{\mathrm{s}} \stackrel{\mathrm{def}}{=} C \left(\frac{-\sigma'}{p_{\mathrm{atm}}} \right)^a p_{\mathrm{atm}}, \tag{58}$$

where E_{s} is the confined stiffness of the bulk granular material measured in the confined compression (oedometer) test. σ' is the effective stress component in loading direction and C, a are constants. For uniform fine sand, the values $C = 300$ and $a = 0.6$ are reasonable. Jaky's formula [55] then relates σ' in the oedometer test to the mean effective stress, yielding

$$\sigma' = -\frac{3\langle p \rangle}{1 + 2(1 - \sin\phi)}. \tag{59}$$

Finally, a relationship between E_{s} and the drained bulk modulus of the granular material, $K_{\mathrm{dr}}^{\mathrm{G}}$, can be established by using elasticity theory,

$$K_{\mathrm{dr}}^{\mathrm{G}} = E_{\mathrm{s}} \frac{1 + \nu}{3(1 - \nu)}, \tag{60}$$

in which Poisson's ratio is estimated from $\nu = (1 - \sin\phi)/(2 - \sin\phi)$.

Results are plotted in Fig. 4 and seem to be reasonable. At the beginning of isotropic compression of the mixture, the bulk air is compressed, which does not significantly change the mixture pressure and the porosity of the granular material. The increase in bulk solid and granular material volume fractions is approximately the same due to (53) and the fact that the mixture bulk modulus is relatively low at this stage of compression. Once the bulk air has been completely compressed, mixture pressure increases exponentially because of the power law (58) and continuous compaction of the granular material. This, in turn, gives more weight to the large bulk modulus of steel in evaluating the mixture bulk modulus, (48).

4 Numerical Techniques

The MMALE method developed in the context of Subproject 5 is an extension of our simplified ALE method for plane and axisymmetric problems [14,16,19,20, 140]. The implementation uses the three step scheme introduced in Sect. 1.4 and illustrated in Fig. 3. In this section we present the basic numerical techniques in

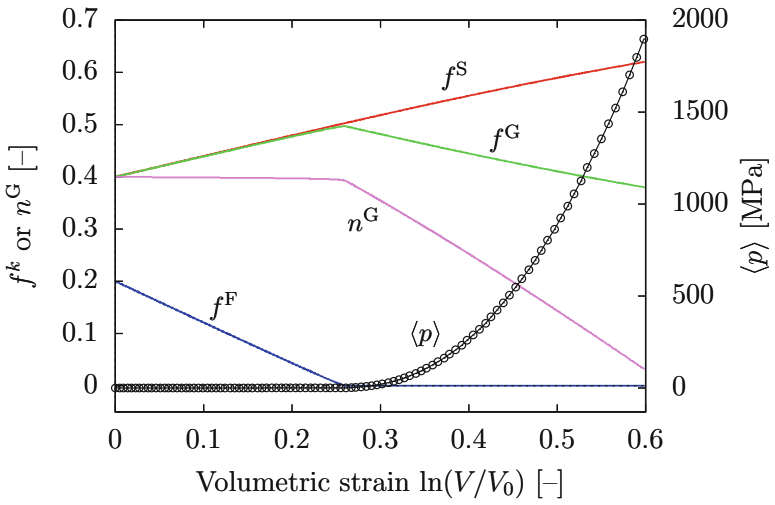

Fig. 4. Example application of the homogeneous equilibrium model: mixture of steel (bulk solid), air (bulk fluid), and dry sand under quasi-static isotropic compression. Evolution of the volume fractions, sand porosity, and mixture pressure. Reprint from [17, p. 97] with permission of Elsevier.

the Lagrangian step, rezone step, and remap step associated with that scheme. Additional details can be found in [18,141].

Let us write the set of Eqs. (55) and (56) in compact form

$$\frac{\partial \hat{q} J}{\partial t} + J \operatorname{div} F = SJ, \tag{61}$$

where $q \in \{\rho \boldsymbol{v}, p\}$, F is the convective flux of q, and S is the source term. Conceptually, the three step scheme splits (61) into two sets of equations which are solved sequentially:

$$\frac{\partial \hat{q} J}{\partial t} = SJ, \qquad \text{(Lagrange)} \tag{62}$$

$$\frac{\partial \hat{q} J}{\partial t} + J \operatorname{div} F = 0. \qquad \text{(remap)} \tag{63}$$

The first set of equations, (62), is associated with $\boldsymbol{c} = \boldsymbol{0}$ resp. $\boldsymbol{v} = \boldsymbol{w}$. Hence, it is equivalent to the set of Eqs. (43) and (44) and formalizes an Lagrangian description of motion. The solution of the second set of equations, (63), is associated with the remap step.

4.1 Lagrangian Step

During the Lagrangian step, the set (43) and (44) subject to prescribed initial conditions and boundary conditions is solved with almost standard finite element

methods [27,99,174,176]. Accordingly, the set of equations is written in a weak form which is discretized in space using finite elements. A two-field mixed element formulation is used which accounts for material and geometric nonlinearities. For a single finite element Ω, the weak form of the governing equations discretized in space can be written in matrix form

$$\boldsymbol{M}^*\ddot{\boldsymbol{y}} + \boldsymbol{C}^*\dot{\boldsymbol{y}} + \boldsymbol{F}^{\text{in}} - \boldsymbol{F}^{\text{ex}} = \boldsymbol{0} \qquad \stackrel{\text{def}}{=} \boldsymbol{\Psi}, \tag{64}$$

in which

$$\begin{aligned}
&\boldsymbol{\Psi} \stackrel{\text{def}}{=} \begin{bmatrix} \boldsymbol{\Psi}^{\boldsymbol{u}} \\ \boldsymbol{\Psi}^{\boldsymbol{p}} \end{bmatrix}, \qquad \boldsymbol{y} \stackrel{\text{def}}{=} \begin{bmatrix} \boldsymbol{u} \\ \boldsymbol{p} \end{bmatrix}, \qquad \boldsymbol{M}^* \stackrel{\text{def}}{=} \begin{bmatrix} \boldsymbol{M} & \boldsymbol{0} \\ \boldsymbol{0} & \boldsymbol{0} \end{bmatrix}, \\
&\boldsymbol{C}^* \stackrel{\text{def}}{=} \begin{bmatrix} \boldsymbol{C} & \boldsymbol{0} \\ \boldsymbol{Q}^{\mathrm{T}} & \boldsymbol{S} \end{bmatrix}, \qquad \boldsymbol{F}^{\text{in}} \stackrel{\text{def}}{=} \begin{bmatrix} \boldsymbol{f}^{\text{in}} - \boldsymbol{Q}\boldsymbol{p} \\ \boldsymbol{0} \end{bmatrix}, \qquad \boldsymbol{F}^{\text{ex}} \stackrel{\text{def}}{=} \begin{bmatrix} \boldsymbol{f}^{\text{ex}} \\ \boldsymbol{0} \end{bmatrix}, \\
&\boldsymbol{M} \stackrel{\text{def}}{=} \int_{\Omega} \boldsymbol{N}_{\boldsymbol{v}}^{\mathrm{T}} \rho \boldsymbol{N}_{\boldsymbol{v}} \, \mathrm{d}v, \qquad \boldsymbol{Q} \stackrel{\text{def}}{=} \int_{\Omega} \boldsymbol{B}^{\mathrm{T}} \boldsymbol{m} \boldsymbol{N}_p \, \mathrm{d}v, \\
&\boldsymbol{S} \stackrel{\text{def}}{=} \int_{\Omega} \boldsymbol{N}_p^{\mathrm{T}} \frac{1}{K} \boldsymbol{N}_p \, \mathrm{d}v, \qquad \boldsymbol{f}^{\text{in}} \stackrel{\text{def}}{=} \int_{\Omega} \boldsymbol{B}^{\mathrm{T}} \boldsymbol{s} \, \mathrm{d}v, \\
&\boldsymbol{f}^{\text{ex}} \stackrel{\text{def}}{=} \boldsymbol{f}^{\boldsymbol{b}} + \boldsymbol{f}^{\boldsymbol{t}} \stackrel{\text{def}}{=} \int_{\Omega} \boldsymbol{N}_{\boldsymbol{v}}^{\mathrm{T}} \rho \boldsymbol{b} \, \mathrm{d}v + \int_{\partial_{\boldsymbol{\sigma}}\Omega} \boldsymbol{N}_{\boldsymbol{v}}^{\mathrm{T}} \boldsymbol{t} \, \mathrm{d}a.
\end{aligned} \tag{65}$$

In the equations, $\boldsymbol{y}$ is the vector of nodal degrees of freedom, including the nodal pressure vector $\boldsymbol{p}$ and nodal displacement vector $\boldsymbol{u}$, $\boldsymbol{M}$ is called the (consistent) mass matrix, $\boldsymbol{Q}$ is the coupling matrix, $\boldsymbol{S}$ is the compressibility matrix, $\boldsymbol{f}^{\text{in}}$ is the vector of internal nodal forces, and $\boldsymbol{f}^{\text{ex}}$ is the vector of applied external nodal forces, consisting of the body forces $\boldsymbol{f}^{\boldsymbol{b}}$ and the surface forces $\boldsymbol{f}^{\boldsymbol{t}}$. Moreover, $\boldsymbol{N}_p$ and $\boldsymbol{N}_{\boldsymbol{v}}$ are the matrices of the interpolation functions for pressure and velocity, respectively, $\boldsymbol{B}$ is the strain operator matrix, and $\boldsymbol{m} = [1, 1, 1, 0]^{\mathrm{T}}$. A damping matrix $\boldsymbol{C}$ has been included for reasons of generality. If $\boldsymbol{C} = \boldsymbol{0}$, then damping is assumed to reside entirely in dissipative material behavior.

We emphasize that the terms in (64) are functions of the current geometry $\boldsymbol{x}$, which is also unknown. However, the current geometry can be determined from the initial geometry and the nodal displacements $\boldsymbol{u}$ due to the Lagrangian formulation. The material time derivative of the displacement is the velocity, that is, $\boldsymbol{v} = \dot{\boldsymbol{u}}$ and $\dot{\boldsymbol{v}} = \ddot{\boldsymbol{u}}$ is the material acceleration.

The continuous time interval of interest, $[0, T] \subset \mathbb{R}$, is partitioned into a sequence of discrete time steps, using an incremental decomposition $t_{n+1} = t_n + \Delta t$. Then, the solution of the semi-discrete weak form (64) is advanced implicitly in time using the Newmark-beta and generalized trapezoidal methods in conjunction with a damped Newton-Raphson method. The final form of the linearized system of equations reads

$$\boldsymbol{K}_{n+1}^{i} d\boldsymbol{y}_{n+1}^{i} = \boldsymbol{r}_{n+1}^{i}, \tag{66}$$

where i denotes the current iteration step, $\boldsymbol{r}^i_{n+1}$ is called the vector of residuals,

$$\begin{aligned}\boldsymbol{K}^i_{n+1} &\stackrel{\text{def}}{=} \begin{bmatrix} \dfrac{\partial \boldsymbol{\Psi}^{\boldsymbol{u}}}{\partial \boldsymbol{u}^i_{n+1}} & \dfrac{\partial \boldsymbol{\Psi}^{\boldsymbol{u}}}{\partial \boldsymbol{p}^i_{n+1}} \\ -\dfrac{1}{a_1}\dfrac{\partial \boldsymbol{\Psi}^{\boldsymbol{p}}}{\partial \boldsymbol{u}^i_{n+1}} & -\dfrac{1}{a_1}\dfrac{\partial \boldsymbol{\Psi}^{\boldsymbol{p}}}{\partial \boldsymbol{p}^i_{n+1}} \end{bmatrix} \\ &= \begin{bmatrix} a_0\boldsymbol{M}^i_{n+1} + a_1\boldsymbol{C}^i_{n+1} + \boldsymbol{D}^i_{n+1} & -\boldsymbol{Q}^i_{n+1} \\ -(\boldsymbol{Q}^i_{n+1})^{\mathrm{T}} & -\frac{a_6}{a_1}\boldsymbol{S}^i_{n+1} \end{bmatrix}\end{aligned} \tag{67}$$

is the effective stiffness matrix,

$$\boldsymbol{D} \stackrel{\text{def}}{=} \int_{\Omega} \boldsymbol{B}^{\mathrm{T}} \mathbf{c} \boldsymbol{B}_{\mathrm{dev}} \, \mathrm{d}v \tag{68}$$

is the material stiffness matrix (ignoring initial stress stiffness), $\boldsymbol{B}_{\mathrm{dev}}$ is the deviatoric strain operator, and a_0, a_1, a_6 are numbers associated with the time integration scheme.

The element type used in the current implementation is the MINI quadrilateral element [24], which is the quadrilateral analogue of the MINI triangle element [11,177]. It is a stabilized quadrilateral using a bilinear approximation of the geometry, displacement, and pressure together with an additional bubble function for the displacement approximation.

Solution of the finite element system of equations (66) requires evaluation of the stress at the quadrature points of the elements in every iteration of every time step. The stress has to be integrated because the constitutive equations are generally given in spatial rate form using objective stress rates; cf. (15). Our current method employs an incrementally objective integration algorithm originally developed by Hughes [85] and improved in [147, Sect. 8.3] in order to ensure exact stress update if the motion over a time step is rigid.

4.2 Rezone Step

After the Lagrangian step, the mesh is rezoned. The rezone step provides the mesh velocity $\boldsymbol{w}$, from which the convective velocity required for remap can be determined in accordance with (57); cf. [14,15] for mesh rezoning resp. smoothing algorithms. If the MMALE method is run in the pure Eulerian mode ($\boldsymbol{w} = \mathbf{0}$ resp. $\boldsymbol{c} = \boldsymbol{v}$), the mesh nodes are relocated to their original positions. In either case the mesh topology remains unchanged.

4.3 Remap Step

The basic equation for the remap is the conservation law (63). Data assumed to be given in the remap step includes both the deformed geometry $\boldsymbol{x}^-$ and rezoned geometry $\boldsymbol{x}^+$ as well as the solution variables q^- obtained after the

Lagrangian step; quantities before and after the remap are marked with $-$ and $+$, respectively.

Due to the structure of (63), the remap takes the form of an advection problem subject to the initial condition $q|_{t=t^-} = q^-$. A finite volume method [14,20,98] is employed for numerical solution. Finite volume methods are conservative because they solve the integral form of a conservation law with respect to a control volume tessellation. In our method the control volume tessellation coincides with the underlying finite element mesh, hence the terms "control volume" and "element" can be used interchangeably. The problem for which we seek an approximate solution can be summarized as

$$\frac{\mathrm{d}}{\mathrm{d}t}\int_{\Omega} q \,\mathrm{d}v + \sum_I \int_{\Gamma_I} q\boldsymbol{c}\cdot\boldsymbol{n}\,\mathrm{d}a = 0 \tag{69}$$

subject to $q|_{t=t^-} = q^-$ and for each element, where Ω is the element domain, Γ_I is the boundary edge starting at local node I, with $\partial\Omega \approx \bigcup_I \Gamma_I$, and $\boldsymbol{n}$ is the unit normal to that edge.

After discretization in space and first-order explicit discretization in time, (69) takes the form

$$q^+ = \frac{q^- V^- - \sum_I \Delta Q_I^-}{V^+}, \qquad \text{with} \quad V^+ = V^- - \sum_I \Delta V_I. \tag{70}$$

Here q^+ is the remapped field under consideration, V^- is the volume of the deformed element in the Lagrangian mesh, V^+ is the element volume in the relocated mesh (i.e. after the remap), ΔV_I is the total volume transported across the edge Γ_I between Ω and the element $\Omega_{\mathrm{adj}(I)}$ adjacent to Γ_I, and ΔQ_I^- represents the transported q-volume across that edge.

For each element, ΔV_I is commonly defined as the volume swept out by the edge Γ_I between the configurations $\boldsymbol{x}^-$ and $\boldsymbol{x}^+$ [39]. Moreover, it is defined positive if the nodes defining the edge are moved further into the element's region, that is, if the transport volume is leaving the element. The transported q-volume ΔQ_I^-, on the other hand, is approximated by using the so-called Godunov flux

$$\begin{aligned}\Delta Q_I^- &\overset{\text{def}}{=} \tfrac{1}{2}\Delta V_I(q^- + q^-_{\mathrm{adj}(I)}) + \tfrac{1}{2}|\Delta V_I|(q^- - q^-_{\mathrm{adj}(I)}) \\ &= \tfrac{1}{2}\Big((q^- + q^-_{\mathrm{adj}(I)}) + \mathrm{sgn}(\Delta V_I)(q^- - q^-_{\mathrm{adj}(I)})\Big)\,\Delta V_I.\end{aligned} \tag{71}$$

Substitution into (70) results in a conservative first-order upwind transport algorithm which corresponds to the classical donor-cell difference scheme [34]. Donor-cell advection is used in many ALE codes because it is simple, stable, conservative, and monotonicity-preserving [33,61,69,70,82,129]. Discussions of this and several other advection algorithms can be found, for example, in [34,80,98].

The pseudocode of a suitable implementation of the donor-cell transport algorithm in the remap step is provided in Algorithm 1, and it uses a procedure outlined in [39]. Note that volume is updated only if the total transported

Algorithm 1. Donor-cell advection algorithm.

Input: V^-, q^-, Lagrangian mesh and rezoned mesh
Output: V^+, q^+ for all elements

1 **forall the** *elements in the mesh* **do**
2 set $V = V^-$ (total volume);
3 set $Q = q^- V$ (q-volume);
4 **forall the** *elements in the mesh* **do**
5 **forall the** *element edges* I **do**
6 calculate total transport volume ΔV_I;
7 **if** $\Delta V_I > 0$ **then**
8 $V \leftarrow V - \Delta V_I$;
9 $V_{\mathrm{adj}(I)} \leftarrow V_{\mathrm{adj}(I)} + \Delta V_I$;
10 $\Delta Q_I^- = q^- \Delta V_I$ (donor-cell assumption);
11 $Q \leftarrow Q - \Delta Q_I^-$;
12 $Q_{\mathrm{adj}(I)} \leftarrow Q_{\mathrm{adj}(I)} + \Delta Q_I^-$
13 **forall the** *elements in the mesh* **do**
14 $V^+ = V$ and $q^+ = Q/V^+$

volume is positive, i.e. a negative transport volume is set to zero, and a volume subtracted from the element is added to element adj(I) adjacent to edge I to avoid double counts. This eliminates half of the remap operations. Higher-order accurate transport algorithms have the same structure as the donor-cell algorithm Algorithm 1, except for the evaluation of q^- occurring in line 10 [39].

4.4 Treatment of Multi-material Elements

One important feature that distinguishes non-Lagrangian from the Lagrangian numerical methods is the presence of multi-material elements (cf. Sect. 1 and Fig. 3 right). These elements require extensions of the Lagrangian step and remap step presented in the previous sections in order to achieve a reasonable accuracy of the overall MMALE method.

Mixture Model in the Lagrangian Step. In the Lagrangian step, the stress and state variables are integrated in time for each individual material. Thereafter, the stress and stiffness for the mixture of materials has to be evaluated and substituted into the respective terms of the system of finite element equations (66). For this purpose, we have developed the framework and homogeneous equilibrium model summarized in Sect. 3 accounting for the two-phase behavior of saturated granular material. We reemphasize that the homogeneous equilibrium model is consistent with the set of equations solved in the Lagrangian step, hence valid for both single- and multi-material elements.

Eulerian and MMALE meshes may consist of elements that partially or completely cover void (empty space or atmosphere); note that void is treated as a

particular bulk fluid in (43) and (44). These elements require special treatment in the implicit Lagrangian step because a stiffness matrix has to be inverted [38]. Void elements practically do not have any stiffness or mass density. Therefore, their nodes remain unconsidered when setting up the finite element system of equations. Elements located at material boundaries are partially filled with void. The stiffness of the mixture inside these elements might be low, causing large displacement increments during the equilibrium iterations. Therefore, the incremental nodal displacements of partially filled elements are uniformly scaled.

Material Subzones Representation in the Remap Step. If an element contains $m > 1$ materials, the remap must be carried out for all variables q of each individual material k, with $k \in \{1, \ldots, m\}$. Application of mixture theory (Sect. 3) then requires that the advected variable is $q^k f^k$, where q^k represents the averaged variable measured per unit volume of the k-material, and f^k is the k-material volume fraction. The generic advection algorithm (70) then takes the form

$$q^{k+} = \frac{q^{k-} f^{k-} V^- - \sum_I \Delta Q_I^{k-}}{f^{k+} V^+} \quad \text{for all } k \in \{1, \ldots, m\}, \tag{72}$$

and with V^+ obtained from $(70)_2$.

For the determination of the transported (advected) volume fraction f^{k+} and the transported q^k-volume ΔQ_I^{k-} across element edges I, the the spatial distribution of the material subzones (subcells) in multi-material elements must be taken into account. Otherwise initially coherent zones would disperse after a few advection steps. The present MMALE method reconstructs and propagates material interfaces element by element by using a volume of fluid (VOF) method. The amount of transported material is defined as the regions swept out by the element edges during mesh rezoning truncated by the interfaces.

Common state-of-the-art VOF methods approximate the interface in each multi-material element by a straight line; see reviews in [37,137]. One of the earliest two-dimensional methods is due to Youngs [175], which forms a basis for the developments of the present research. Our implementation relies on that described in [138] because the original paper provides little detail of the interface reconstruction procedure. Details are presented in [22], so only a few key facts will be repeated here.

A linear interface can be generally described by the Hesse normal form

$$\boldsymbol{n} \cdot \boldsymbol{x} - d = 0, \tag{73}$$

in which $\boldsymbol{x}$ is an arbitrary point on the interface, $\boldsymbol{n}$ is the unit normal on that interface, and d is the line constant. A linear reconstruction of the interface is determined for each element in two steps: (i) estimate $\boldsymbol{n}$, or equivalently, the interface slope and (ii) determine d such that the volume fraction of the material lying behind the interface matches the known value.

The interface slope is estimated based on the volume fraction data in the current element and its neighbors. The location of the material interface is

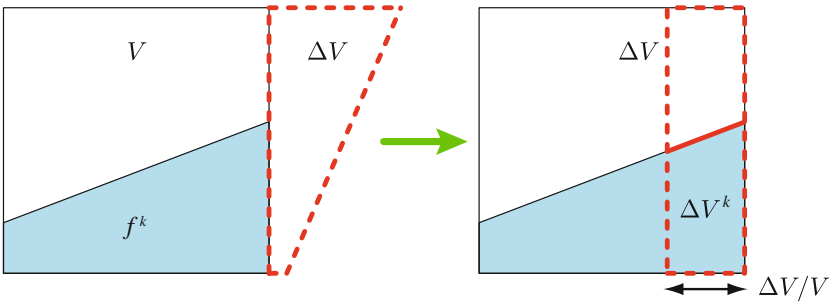

Fig. 5. VOF interface propagation in accordance with [34,175]. The reconstructed interface and the total volume ΔV transported across an element edge are used to calculate the transported material volume $\Delta V^k > 0$.

determined by noting that the truncated element volume behind the interface represents the partial material volume. Volume is conserved, i.e. the right location of the interface has been determined, if the partial volume divided by the element volume matches the given volume fraction data of that element. The matching can be achieved by deriving an explicit expression that relates the truncated element volume to d.

The material transport volumes are usually computed as truncation volumes, as illustrated in Fig. 5. Once the total transport volume across an element edge, ΔV, has been determined, a region having the same amount of volume is created that lies entirely within the element (Fig. 5 right). The k-material transport volume, ΔV^k, is then defined as the set-theoretic intersection of the total transport volume and the material domain behind the reconstructed interface. Finally, the material volume fraction can be updated in accordance with (70), i.e.

$$f^{k+} = \frac{f^{k-}V^- - \sum_I \Delta V_I^k}{V^+}. \tag{74}$$

Once the transported k-material volumes ΔV_I^k are known, the transported q^k-volumes ΔQ_I^{k-} needed for the remap (72) can be determined by an appropriate advection scheme. In case of donor-cell advection (71),

$$\Delta Q_I^{k-} = \tfrac{1}{2}\Big((q^{k-} + q^{k-}_{\mathrm{adj}(I)}) + \mathrm{sgn}(\Delta V_I^k)(q^{k-} - q^{k-}_{\mathrm{adj}(I)})\Big)\,\Delta V_I^k. \tag{75}$$

4.5 Rigid Disk in Uniform Flow Field

To test the VOF reconstruction and propagation algorithms of our method, we consider a rigid circular disk transported in a uniform diagonal velocity field. The problem statement and square mesh are shown in Fig. 6a. Figure 6b depicts the reconstructed interface in the initial configuration and the corresponding distribution of the red material volume fraction. The latter has been obtained by intersecting the circular material domain with the domain enclosed by each

mesh element, resulting in a volume fraction constant in each element. A direct comparison of the original interface and its piecewise linear reconstruction is given in the detailed view of Fig. 7. Note that the fractional element volume on each side of the interface is the same for the original interface and its linear approximation.

The second and third row in Fig. 6 show the material configurations and volume fraction distributions after advecting the material along the diagonal of the computational domain. Figures 6c and d plot the results for the case where the transport algorithm does not account for the geometry of the material subzone in each element. It can be seen that the material loses coherence and disperses during transport (Fig. 6c), leading to a blurred red zone in the volume fraction plot (Fig. 6d). In contrast to that, the shape of the circular disk is retained throughout the calculation if the material distribution is considered in each remap step by using the VOF algorithm (Figs. 6e and f).

5 Experimental Tests

Experimental model tests have been carried out in the context of Subproject 5 to observe the multi-material flow field during vibro-injection pile (RI-pile) installation in sand. This section summarizes the test set-up, measurement concept and experimental program, and discusses some preliminary results. Further details have been presented in a previous paper [141]. Moreover, we refer the reader to the benchmark tests done in the Central Project of the DFG Research Unit, e.g. those reported in [162,163] and in this collection.

5.1 Set-Up and Measurement Concept

The set-up used for the tests is shown in Fig. 8. The main components are a waterproof chamber with glass panel serving as a viewing window, a model pile, and a device for vibratory pile driving. All components are in-house developments. The vibrator consists of two counter-rotating imbalances whose mass and rotational speed are adjustable. The model pile is made up of a 50 mm × 50 mm stainless steel square tube equipped with a welded-on collar at the pile toe and a built-in injection tube. The opening of the injection tube is located directly above the collar (Fig. 8c). Pressurized injection is enabled by a diaphragm pressure vessel.

During the tests the pile was guided alongside the glass panel. The driving and grouting process was digitally filmed through the viewing window using a standard Full HD camcorder. Series of consecutive still images were recorded at 50 Hz with a maximum resolution of 1920 × 1080 pixels. Digital still images of the configurations at the end of the tests were also captured. By analyzing the recorded image sequence using image correlation software, details of the multi-material flow field could be measured without on-sample instrumentation. A MATLAB toolbox based on particle image velocimetry (PIV) [4,14,171], called GeoPIV [170], is used in the present research. PIV tracks the texture within

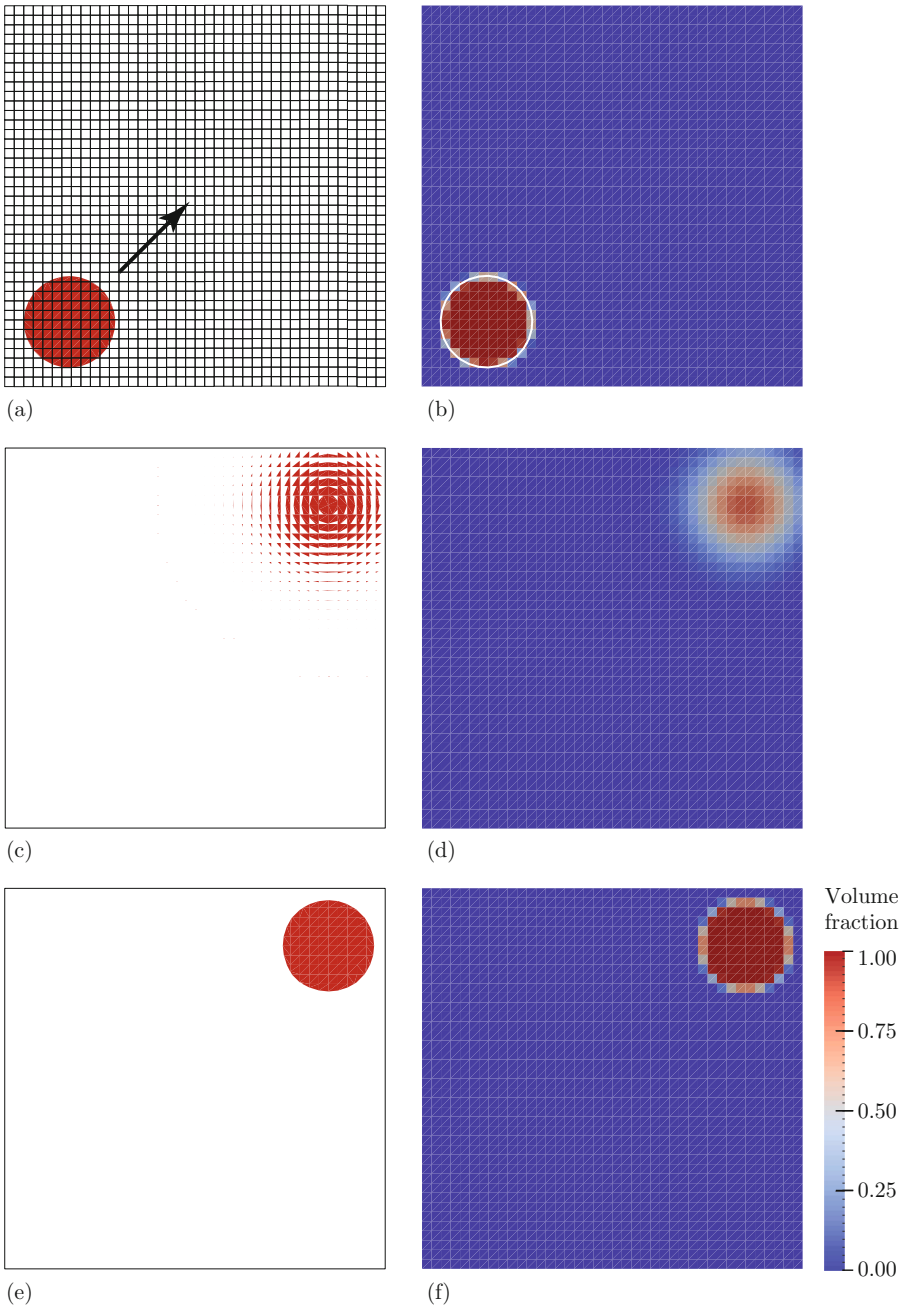

Fig. 6. Transport of a circular disk in uniform flow. (a) Initial configuration and mesh. (b) Initial volume fraction distribution and reconstructed material interface. (c) Final configuration and (d) final volume fraction distribution without interface tracking. (e) Final configuration and (f) final volume fraction distribution using the VOF method.

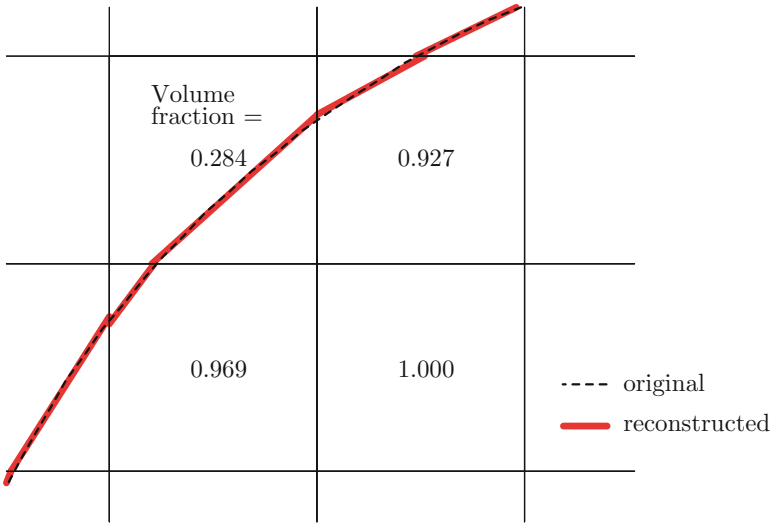

Fig. 7. Detailed view of Fig. 6b. Original interface portion (dashed line) and piecewise linear reconstructed interface (solid red line) which is generally discontinuous across element edges. The material volume fraction in each element matches the original value obtained by intersecting the circle with the element domain.

areas of an image through a sequence of images to determine local incremental displacement vectors. The totality of these displacement vectors represents an incremental displacement field from which an incremental strain field can be obtained through postprocessing.

5.2 Experimental Program

The sand employed in the experimental model tests is a quartz sand with well-rounded to angular grains identified as fine-gravelly coarse Sand (fgrCSa) according to [62]. The limit void ratios are $e_{\min} = 0.482$ and $e_{\max} = 0.779$. Further granulometric properties are listed in [14], in which the same sand was used for quasi-static penetration tests. In all tests the chamber was filled with air dried sand by dry sieve pluviation. Each sand model was prepared in several layers of equal thickness in order to achieve a homogeneous distribution of initial density. Due to geometric constraints of the chamber the initial mean relative density was always larger than 85% (very dense).

Series with a total of 10 tests have been conducted (Table 1). The degree of saturation, the grouting material, the grouting pressure, and the load amplitude of the vibrator were varied between the tests. The vibration frequency was about 20 Hz for all tests and the load amplitude varied between 1.9 kN and 2.56 kN. Two tests were run in air dried sand, whereas the other were carried out in sand which had been water flooded. In three experiments the pile shaft annulus

Fig. 8. Experimental investigation of vibro-injection pile installation. (a) Filled test chamber with glass panel and model pile. (b) Detailed view of the glass panel, pile guide, and model pile. (c) Tapered pile toe with welded-on collar and bolt closing the injection tube. (d) Self-made vibrator with controller (frequency converter). Reprint from [141, p. 117] with permission of Springer.

Table 1. Details of conducted vibro-injection pile (RI-pile) installation tests. Reprint from [141, p. 119] with permission of Springer.

Test ID	Date	Saturation	Grouting material/ Pressurization [bar]	Frequency [Hz]/ Load amplitude [kN][a]
RI-1-D	2011	Air dried	None	20.7/2.56
RI-2-F		Water flooded		20.0/2.39
RI-3-F				20.0/1.90
RI-4-F				
RI-5-B[b]			Bentonite slurry/—[c]	20.0/2.39
RI-6-D	2012	Air dried	None	20.0/2.39
RI-7-B		Water flooded	Bentonite slurry/—[c]	
RI-8-B			Bentonite slurry/1.0	
RI-9-H[b]			Hydraulic binder/3.0	
RI-10-H	2013	Water flooded	Hydraulic binder/3.0	20.0/2.39
D – dry; F – flooded; B – bentonite; H – hydraulic binder				
In all tests the initial mean relative density was >85 % (very dense)				

[a] with respect to the vibrator; the static force (dead weight) varies between the tests
[b] analyzed by using particle image velocimetry
[c] loaded under its own weight

created by the welded-on collar was injected with pigmented bentonite slurry, whereas hydraulic binder was used in two other tests.

5.3 Test Results

All the tests using bentonite slurry injection failed in keeping open the shaft annulus created by the collar at the model pile toe. In contrast to that, the hydraulic binder has a sufficiently high shear resistance to stabilize the shaft annulus while possessing excellent flowability during pressurized grouting. Figure 9 shows two digital photographs of test RI-9-H recorded about half an hour after the pile installation has completed. Although the amount of hydraulic binder infiltration into the pores of the coarse test sand increases with time, it cannot be completely avoided. Therefore, the assumption of impermeable interfaces (zero mass exchange) in the mixture model summarized in Sect. 3 is not always a reasonable one. Despite this, Fig. 9 indicates a clear soil-grout interface which is almost vertical along the pile shaft.

Figure 10 shows the results of a PIV analysis of test RI-9-H using hydraulic binder injection. Figure 10a plots the time history of the vertical displacement of the pile tip. Those configurations where image capturing took place are marked with black squares. During a vibration cycle, however, the pile moves upward and downward. The displacement increments in the soil which occurred during the downward motion of the pile between image 1 and image 2 are displayed in

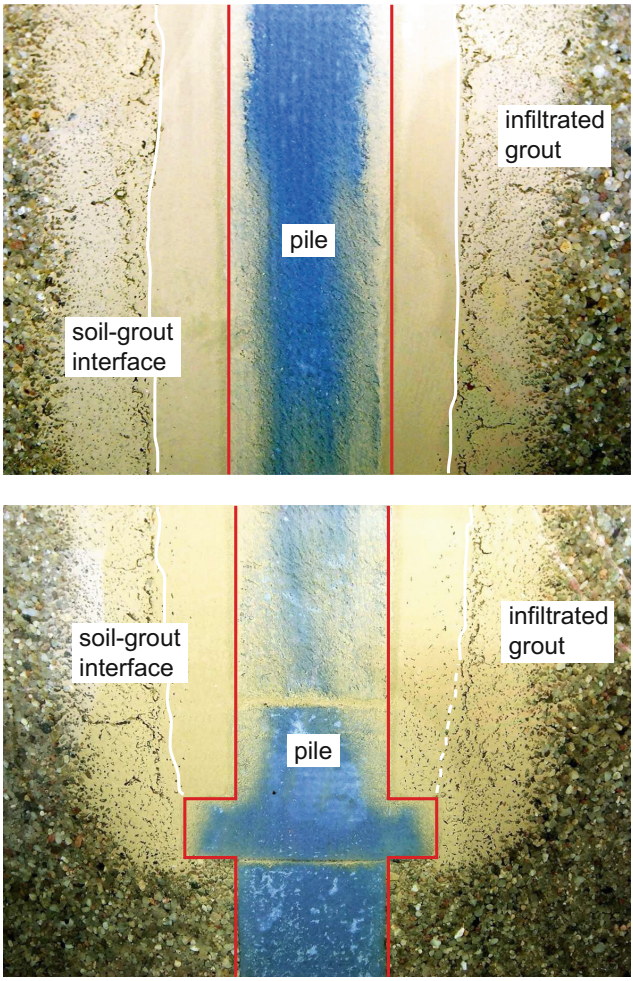

Fig. 9. Digital photograph of the configuration of test RI-9-H (hydraulic binder injection) through the viewing window of the chamber about half an hour after pile installation has completed. Reprint from [141, p. 120] with permission of Springer.

Fig. 10b using vectors with scaled length. It is clearly visible that the soil is not only displaced below the pile toe and underneath the collar in a predominantly vertical direction but also moves downward above the collar. Figure 10c shows the displacement increments due to upward motion of the pile between image 5 and image 6. The vectors above the collar indicate that the soil located at the soil-grout interface is dragged along with the pile motion and displaced in lateral direction.

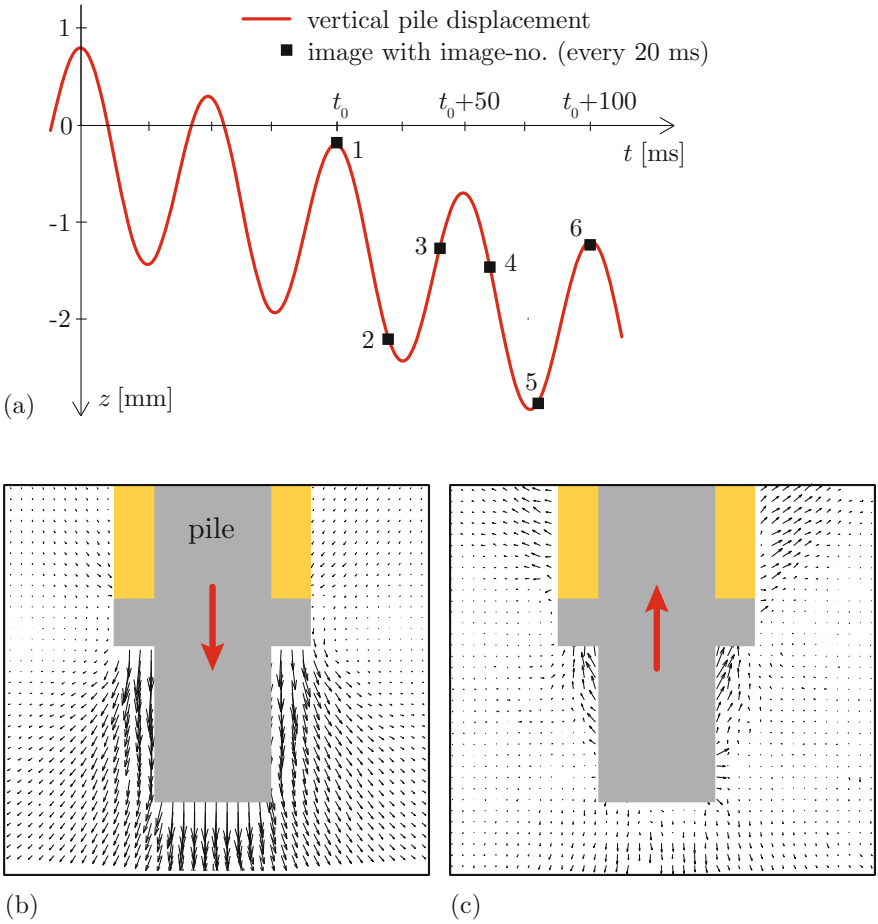

Fig. 10. Results of model test RI-9-H using hydraulic binder injection. (a) Schematic time history of vertical pile displacements. PIV results showing soil displacement increments (b) at downward motion of the pile (image 1 to image 2), and (c) at upward motion of the pile (image 5 to image 6).

6 Conclusions and Outlook

The original objective of Subproject 5 of the DFG Research Unit FOR 1136 GeoTech has been the numerical simulation of vibro-injection pile installation in sand. Our research work within this project, however, has revealed that available methods will not produce reliable results because of two shortcomings: (i) they cannot represent the large deformations and material interface evolution associated with such multi-material flow situations and/or (ii) they cannot accurately reproduce the complex two-phase, coupled behavior of saturated geomaterial. Consequently, we adjusted the focus of our research towards theoretical mod-

eling of geotechnical and geomechanical processes in general, and the development of a numerical tool that consistently employs the advanced models in a non-Lagrangian formulation.

A rigorous theoretical framework has been developed in order to model the geomaterial (saturated sand or debris material) as a general grain-fluid mixture as well as its interaction with multiple other bulk materials such as pure solid and pure fluid on the macroscale. Macroscopic balance principles have been derived from the corresponding balance principles on the microscale by employing local volume averaging as the filtering technique. In contrast to common two-scale theories, the proposed three-scale hybrid mixture approach is able to incorporate both the evolution of bulk material interfaces as well as the two-phase phenomena associated with grain-fluid mixtures. Moreover, the approach allows for the use of phenomenological constitutive models describing grain-fluid mixture response for different flow regimes. Accordingly, the stress tensors have been split into rate-independent and rate-dependent parts, and into a pressure stress and an extra stress. Closure of the mixture model has been achieved by the fundamental assumption of homogenous distributions of pressure and velocity.

To numerically model and simulate geotechnical and geomechanical processes, we have developed a multi-material ALE (MMALE) method. The implementation of the method is based on the common three step scheme, splitting incremental solution into Lagrangian, rezone, and remap steps. MMALE allows material interfaces to flow through the computational mesh, so that multi-material elements may arise which contain two or more materials. The homogeneous equilibrium mixture model derived from the proposed hybrid mixture theory describes the interaction within those multi-material elements in a mechanically consistent way. The donor-cell advection algorithm is used to conservatively remap the solution variables onto the rezoned mesh. To precisely determine the amount of lost or gained material volume, material interfaces are reconstructed and propagated through the mesh by using the VOF technique.

Experimental model tests have been carried out in order to investigate the relevant phenomena of vibro-injection pile installation in sand, an example of a complex geotechnical process. A special model pile and a test chamber with viewing window have been designed and manufactured for this purpose. Image sequences have been recorded through the viewing window during the installation process, which have been subsequently analyzed by using particle image velocimetry. The tests indicate that displacement, infiltration, and mixing occurs along the soil-grout interface due to the dynamical interaction of multiple, physically distinct materials on different spatial scales. The tests also reveal that the grains in a body of sand usually entail adequate image texture for PIV analysis, but not the grouting material unless it would be seeded with marker particles.

Future work will focus on the application of the the MMALE method in conjunction with the proposed mixture model to specific geotechnical and geomechanical processes. The developed modeling framework is unique on national as well on international level and offers great potential for future research. The latter is motivated by the assumptions and restrictions associated with

the present research. For example, the incorporation of mass and momentum transfer between the constituents would be of great practical relevance because geomechanical problems are often driven by local drainage and consolidation phenomena as well as by contact constraints.

Nomenclature

Operators and Special Notations

$\cdot, :, \otimes$	single contraction, double contraction, tensor product
$\langle\cdot\rangle$	spatial average
$\dot{(\cdot)}, \dot{(\cdot)}^{\alpha}$	material time derivative, of an α-related field
$\hat{(\cdot)}$	referential, ALE description
$(\cdot)^{\alpha k}$	αk-intrinsic average
$\overset{\triangledown}{(\cdot)}$	objective rate
$\boldsymbol{\nabla}(\cdot)$	covariant derivative, gradient
$\partial(\cdot)$	boundary, partial derivative
$\mathrm{div}(\cdot)$	divergence
$\Delta(\cdot)$	increment
$\mathrm{tr}(\cdot)$	trace of a second-order tensor

Superscripts and Subscripts

$-, +$	associated with Lagrangian step, remap step
adj	adjacent
dev	deviator of a second-order tensor
dr	drained
f, fG	fluid phase, in granular material
fr	frictional (rate-independent) contribution
F	bulk fluid; $\mathrm{F} \equiv \mathrm{fF}$
G	fluid-saturated granular material
$', \mathrm{G}'$	related to effective stress in granular material
k	k-material; $k \in \{\mathrm{S}, \mathrm{F}, \mathrm{G}\} = \{1, \ldots, M\}$
$n, n+1$	associated with time t_n, t_{n+1}
s, sG	solid phase, in granular material
S	bulk solid; $\mathrm{S} \equiv \mathrm{sS}$

T	transpose of a tensor
uj	unjacketed
vi	viscous (rate-dependent) contribution
α	α-phase; $\alpha \in \{\mathrm{s}, \mathrm{f}\} = \{1, \ldots, N\}$
αk	α-phase in k-material; $\alpha k \in \{\mathrm{S}, \mathrm{F}, \mathrm{sG}, \mathrm{fG}\}$

Latin Symbols

$\boldsymbol{b}, \boldsymbol{b}^{\alpha k}, \langle \boldsymbol{b} \rangle$	body force per unit mass
$\boldsymbol{B}$	strain operator matrix
$\boldsymbol{c}$	convective velocity
$\mathbf{c}$	fourth-order material tangent tensor
$\boldsymbol{C}$	damping matrix
d	line constant
$\boldsymbol{d}, \boldsymbol{d}^k$	spatial rate of deformation
$\mathrm{d}a, \mathrm{d}v$	surface area density, volume density
$\boldsymbol{D}$	material stiffness matrix
$\mathcal{D}$	modeling domain in the ambient space
$f, f^k, f^{\alpha k}$	volume fractions, of k, αk
$\boldsymbol{f}^{\mathrm{in}}, \boldsymbol{f}^{\mathrm{ex}}$	vector of internal, external nodal forces
$\boldsymbol{f}^{\boldsymbol{b}}, \boldsymbol{f}^{\boldsymbol{t}}$	vector of body, surface forces
$H, H^k, H^{\alpha k}$	volume measures of $\mathcal{H}$, $\mathcal{H}^k$, $\mathcal{H}^{\alpha k}$
$\mathcal{H}$	representative volume element (RVE)
$\mathcal{H}^k, \mathcal{H}^{\alpha k}$	portions of k, αk in $\mathcal{H}$
I	local node, vertex, edge
$\boldsymbol{I}$	second-order unit tensor
J	Jacobian
$K, K^k, K^{\alpha k}, \langle K \rangle$	bulk modulus
$\boldsymbol{K}$	effective stiffness matrix
$l_{\mathrm{micro}}, l_{\mathrm{meso}}, l_{\mathrm{macro}}$	microscale, mesoscale, macroscale
M	mass, number of materials in the mixture
$\boldsymbol{M}$	mass matrix
n, n^k, n^{G}	fluid fraction, porosity
$\boldsymbol{n}$	normal on interface
N	number of phases in the mixture

$\boldsymbol{N}_p, \boldsymbol{N}_{\boldsymbol{v}}$	matrix of the interpolation functions
$p^{\alpha k}, p^k, \langle p \rangle$	pressure
$p', p^{\mathrm{G}'}$	mean effective stress
$\boldsymbol{p}$	nodal pressure vector
$q, q^k, q^{\alpha k}$	generic spatial field
$\boldsymbol{Q}$	coupling matrix
$\boldsymbol{r}$	vector of residuals
$\boldsymbol{s}^k, \boldsymbol{s}^{\alpha k}, \langle \boldsymbol{s} \rangle$	extra stress
$\boldsymbol{S}$	compressibility matrix
t	time
$\boldsymbol{u}$	nodal displacement vector
$\boldsymbol{v}, \boldsymbol{v}^k, \boldsymbol{v}^{\alpha k}, \langle \boldsymbol{v} \rangle$	spatial velocity
V	volume, of an element
$\boldsymbol{w}$	mesh velocity
$\boldsymbol{x}$	point in the ambient space
$\boldsymbol{y}$	vector of nodal degrees of freedom

Greek Symbols

Γ_I	edge, element edge
$\boldsymbol{\Gamma}^{\alpha k}$	rate of momentum supply via $\partial \mathcal{H}^{\alpha k}$
$\Delta Q_I, \Delta Q_I^k$	total transported q-volume, transported q^k-volume
$\Delta V_I, \Delta V_I^k$	total transport volume, material transport volume
ζ	Biot-Willis coefficient
μ	dynamic shear viscosity
$\pi^{\alpha k}$	volume fraction of α with respect to $\mathcal{H}^k$
$\rho, \rho^k, \rho^{\alpha k}, \langle \rho \rangle$	spatial mass density
$\boldsymbol{\sigma}, \boldsymbol{\sigma}^k, \boldsymbol{\sigma}^{\alpha k}, \langle \boldsymbol{\sigma} \rangle$	(Cauchy) stress
$\boldsymbol{\sigma}', \boldsymbol{\sigma}^{\mathrm{G}'}$	effective stress
$\chi^k, \chi^\alpha, \chi^{\alpha k}$	indicator function
Ω	element domain, control volume

Acronyms

ALE	Arbitrary Lagrangian-Eulerian
CFD	Computational Fluid Dynamics
FEM	Finite Element Method
MMALE	Multi-Material Arbitrary Lagrangian-Eulerian
MPM	Material Point Method
MOF	Moment Of Fluid
PIV	Particle Image Velocimetry
RVE	Representative Volume Element
SPH	Smoothed Particle Hydrodynamics
VOF	Volume Of Fluid

Acknowledgments. The authors gratefully acknowledge the financial support by the German Research Foundation (DFG; Grant SA 310/26-2) as part of the DFG Research Unit FOR 1136. The authors are also grateful to their colleagues in this research unit for collaboration and for helpful discussions.

References

1. Abadie, S., Morichon, D., Grilli, S., Glockner, S.: Numerical simulation of waves generated by landslides using a multiple-fluid Navier-Stokes model. Coast. Eng. **57**, 779–794 (2010)
2. Achanta, S., Cushman, J.H., Okos, M.R.: On multicomponent, multiphase thermomechanics with interfaces. Int. J. Eng. Sci. **32**(11), 1717–1738 (1994)
3. Addessio, F.L., Baumgardner, J.R., Dukowicz, J.K., Johnson, N.L., Kashiwa, B.A., Rauenzahn, R.M., Zemach, C.: CAVEAT: a computer code for fluid dynamics problems with large distortion and internal slip. Report LA-10613-MS-REV. 1 (revised edition), Los Alamos National Laboratory, Los Alamos, USA (1990)
4. Adrian, R.J.: Particle-imaging techniques for experimental fluid mechanics. J. Annu. Rev. Fluid Mech. **23**, 261–304 (1991)
5. Ancey, C., Coussot, P., Evesque, P.: A theoretical framework for granular suspensions in a steady simple shear flow. J. Rheol. **43**(6), 1673–1699 (1999)
6. Ancey, C., Evesque, P.: Frictional-collisional regime for granular suspension flows down an inclined channel. Phys. Rev. E **62**(6), 8349–8360 (2000)
7. Ancey, C.: Dry granular flows down an inclined channel: experimental investigations on the frictional-collisional regime. Phys. Rev. E **65**, 011304 (2001)
8. Ancey, C.: Plasticity and geophysical flows: a review. J. Nonnewton. Fluid Mech. **142**, 4–35 (2007)
9. Anderson, K.G., Jackson, R.: A comparison of the solutions of some proposed equations of motion of granular materials for fully developed flow down inclined planes. Ind. Eng. Chem. Fundam. **241**, 145–168 (1992)

10. Arbogast, T., Douglas, J., Hornung, U.: Derivation of the double porosity model of single phase flow via homogenization theory. SIAM J. Math. Anal. **21**(4), 823–836 (1990)
11. Arnold, D.N., Brezzi, F., Fortin, M.: A stable finite element for the Stokes equations. Calcolo **21**(4), 337–344 (1984)
12. Assier-Rzadkiewicz, S., Mariotti, C., Heinrich, P.: Numerical simulation of submarine landslides and their hydraulic effects. J. Waterw. Port Coast. Ocean Eng. **123**(4), 149–157 (1997)
13. Aubram, D.: Differential geometry applied to continuum mechanics. Veröffentlichungen des Grundbauinstitutes der Technischen Universität Berlin, vol. 44, Shaker Verlag, Aachen (2009). http://dx.doi.org/10.14279/depositonce-2185
14. Aubram, D.: An arbitrary Lagrangian-Eulerian method for penetration into sand at finite deformation. Veröffentlichungen des Grundbauinstitutes der Technischen Universität Berlin, vol. 62. Shaker Verlag, Aachen (2013). http://dx.doi.org/10.14279/depositonce-3958
15. Aubram, D.: Optimization-based smoothing algorithm for triangle meshes over arbitrarily shaped domains. arXiv e-prints, 1410.5977 [cs.NA] (2014). http://arxiv.org/abs/1410.5977
16. Aubram, D.: Development and experimental validation of an Arbitrary Lagrangian-Eulerian (ALE) method for soil mechanics. Geotechnik **38**(3), 193–204 (2015). http://dx.doi.org/10.1002/gete.201400030
17. Aubram, D.: Homogeneous equilibrium model for geomechanical multi-material flow with compressible constituents. J. Nonnewtonian Fluid Mech. **232**, 88–101 (2016). http://dx.doi.org/10.1016/j.jnnfm.2016.04.001
18. Aubram, D.: A multi-material Eulerian method for large deformation and free surface flow of geomaterials (in preparation)
19. Aubram, D., Rackwitz, F., Savidis, S.A.: An ALE finite element method for cohesionless soil at large strains: computational aspects and applications. In: Benz, T., Nordal, S. (eds.) Proceedings 7th European Conference on Numerical Methods in Geotechnical Engineering (NUMGE), pp. 245–250. CRC Press, Boca Raton (2010)
20. Aubram, D., Rackwitz, F., Wriggers, P., Savidis, S.A.: An ALE method for penetration into sand utilizing optimization-based mesh motion. Comput. Geotech. **65**, 241–249 (2015). http://dx.doi.org/10.1016/j.compgeo.2014.12.012
21. Aubram, D., Rackwitz, F., Savidis, S.A.: Vibro-injection pile installation in sand: part i—interpretation as multi-material flow. In: Triantafyllidis, T. (ed.) Holistic Simulation of Geotechnical Installation Processes. LNACM, vol. 77, pp. 73–102. Springer, Heidelberg (2015). doi:10.1007/978-3-319-18170-7_5
22. Aubram, D., Savidis, S.A., Rackwitz, F.: Theory and numerical modeling of geomechanical multi-material flow. In: Triantafyllidis, T. (ed.) Holistic Simulation of Geotechnical Installation Processes. LNACM, vol. 80, pp. 187–229. Springer, Heidelberg (2016). doi:10.1007/978-3-319-23159-4_10
23. Bagnold, R.A.: Experiments on a gravity-free dispersion of large solid spheres in a Newtonian fluid under shear. Proc. R. Soc. Lond. Ser. A **225**, 49–63 (1954)
24. Bai, W.: The quadrilateral 'mini' element for the stokes problem. Comput. Methods Appl. Mech. Eng. **143**, 41–47 (1997)
25. Bardenhagen, S.G., Brackbill, J.U., Sulsky, D.: The material-point method for granular materials. Comput. Methods Appl. Mech. Eng. **187**, 529–541 (2000)
26. Bedford, A., Drumheller, D.S.: Theories of immiscible and structured mixtures. Int. J. Eng. Sci. **21**(8), 863–960 (1983)

27. Belytschko, T., Liu, W.K., Moran, D.: Nonlinear Finite Elements for Continua and Structures. Wiley, Chichester (2000)
28. Bennethum, L.S.: Compressibility moduli for porous materials incorporating volume fraction. J. Eng. Mech. **132**, 1205–1214 (2006)
29. Bennethum, L.S.: Theory of flow and deformation of swelling porous materials at the macroscale. Comput. Geotech. **34**, 267–278 (2007)
30. Bennethum, L.S., Cushman, J.H.: Multiscale, hybrid mixture theory for swelling systems-I, balance laws. Int. J. Eng. Sci. **34**(2), 125–145 (1996)
31. Bennethum, L.S., Cushman, J.H.: Multiscale, hybrid mixture theory for swelling systems-II, constitutive theory. Int. J. Eng. Sci. **34**(2), 147–169 (1996)
32. Bennethum, L.S., Weinstein, T.: Three pressures in porous media. Transp. Porous Media **54**, 1–34 (2004)
33. Benson, D.J.: An efficient, accurate, simple ALE method for nonlinear finite element programs. Comput. Methods Appl. Mech. Eng. **72**, 305–350 (1989)
34. Benson, D.J.: Computational methods in Lagrangian and Eulerian hydrocodes. Comput. Methods Appl. Mech. Eng. **99**, 235–394 (1992)
35. Benson, D.J.: A multi-material Eulerian formulation for the efficient solution of impact and penetration problems. Comput. Mech. **15**, 558–571 (1995)
36. Benson, D.J.: A mixture theory for contact in multi-material Eulerian formulations. Comput. Methods Appl. Mech. Eng. **140**, 59–86 (1997)
37. Benson, D.J.: Volume of fluid interface reconstruction methods for multi-material problems. Appl. Mech. Rev. **55**(2), 151–165 (2002)
38. Benson, D.J.: An implicit multi-material Eulerian formulation. Int. J. Numer. Meth. Eng. **48**, 475–499 (2000)
39. Benson, D.J.: Momentum advection on unstructured staggered quadrilateral meshes. Int. J. Numer. Meth. Eng. **75**, 1549–1580 (2008)
40. Benson, D.J., Okazawa, S.: Contact in a multi-material Eulerian finite element formulation. Comput. Methods Appl. Mech. Eng. **193**, 4277–4298 (2004)
41. Beuth, L., Wieckowski, Z., Vermeer, P.A.: Solution of quasi-static large-strain problems by the material point method. Int. J. Numer. Anal. Meth. Geomech. **35**, 1451–1465 (2011)
42. Biot, M.A.: General theory of three-dimensional consolidation. J. Appl. Phys. **12**, 155–164 (1941)
43. Biot, M.A., Willis, D.G.: The elastic coefficients of the theory of consolidation. J. Appl. Mech. **24**, 594–601 (1957)
44. Bouré, J.A.: Two-phase flow models: the closure issue. Multiphase Science and Technology **3**(1–4), 3–30 (1987)
45. Bouré, J.A., Delhaye, J.M.: General equations and two-phase flow modeling section 1.2. In: Hetsroni, G. (ed.) Handbook of Multiphase Systems. Hemisphere Publishing Corporation (1982)
46. Bowen, R.M.: Theory of mixtures. In: Eringen, A.C. (ed.) Continuum Physics. Vol. III: Mixtures and EM Field Theories, part I. Academic Press, New York (1976)
47. Bowen, R.M.: Incompressible porous media models by use of the theory of mixtures. Int. J. Eng. Sci. **18**(9), 1129–1148 (1980)
48. Bowen, R.M.: Compressible porous media models by use of the theory of mixtures. Int. J. Eng. Sci. **20**(6), 697–735 (1982)
49. Bui, H.H., Fukagawa, R., Sako, K., Ohno, S.: Lagrangian meshfree particles method (SPH) for large deformation and failure flows of geomaterial using elastic-plastic soil constitutive model. Int. J. Numer. Anal. Meth. Geomech. **32**, 1537–1570 (2008)

50. Carter, J.P., Booker, J.R., Davis, E.H.: Finite deformation of an elasto-plastic soil. Int. J. Numer. Anal. Meth. Geomech. **1**, 25–43 (1977)
51. Chang, C.H., Ramshaw, J.D.: Dynamical evolution of volume fractions in multi-pressure multiphase flow models. Phys. Rev. E **77**, 066305 (2008)
52. Chorin, A.J., Hughes, T.J.R., McCracken, M.F., Marsden, J.E.: Product formulas and numerical algorithms. Commun. Pure Appl. Math. **31**, 205–256 (1978)
53. Colella, P., Glaz, H.M., Ferguson, R.E.: Multifluid algorithms for Eulerian finite difference methods (1997). (unpublished manuscript)
54. Coussot, P., Ancey, C.: Rheophysical classification of concentrated suspensions and granular pastes. Phys. Rev. E **59**(4), 4445–4457 (1999)
55. Craig, R.F.: Craig's Soil Mechanics, 7th edn. E & FN Spon, London (2007)
56. Cushman, J.H., Bennethum, L.S., Hu, B.X.: A primer on upscaling tools for porous media. Adv. Water Resour. **25**, 1043–1067 (2002)
57. Das, B.M.: Advanced Soil Mechanics, 3rd edn. Taylor & Francis, Boca Raton (2008)
58. Dassault Systèmes: Abaqus Analysis User's Guide, Version 6.14 (2014)
59. DeBar, R.B.: Fundamentals of the KRAKEN code. Technical report UCID-17366, Lawrence Livermore Laboratory, Livermore, USA (1974)
60. Denlinger, R.P., Iverson, R.M.: Flow of variably fluidized granular masses across three-dimensional terrain. Numerical predictions and experimental tests. J. Geophys. Res. **106**(B1), 553–566 (2001)
61. Di, Y., Yang, J., Sato, T.: An operator-split ALE model for large deformation analysis of geomaterials. Int. J. Numer. Anal. Meth. Geomech. **31**, 1375–1399 (2007)
62. DIN EN ISO 14688–1: Geotechnische Erkundung und Untersuchung – Benennung, Beschreibung und Klassifizierung von Boden – Teil 1: Benennung und Beschreibung. Beuth Verlag, Berlin, January 2003 (German Code)
63. Drew, D.A.: Mathematical modeling of two-phase flow. Annu. Rev. Fluid Mech. **15**, 261–291 (1983)
64. Drew, D.A., Passman, S.L.: Theory of Multicomponent Fluids. Springer, New York (1999)
65. Dyadechko, V., Shashkov, M.: Moment-of-fluid interface reconstruction. Report LA-UR-05-7571, Los Alamos National Laboratory, Los Alamos, USA (2005)
66. Dyadechko, V., Shashkov, M.: Reconstruction of multi-material interfaces from moment data. J. Comput. Phys. **227**, 5361–5384 (2008)
67. Emeriault, F., Cambou, B., Mahboubi, A.: Homogenization for granular materials: non reversible behaviour. Mech. Cohesive-Frictional Mater. **1**, 199–218 (1996)
68. Forterre, Y., Pouliquen, O.: Flows of dense granular media. Annu. Rev. Fluid Mech. **40**, 1–24 (2008)
69. Freßmann, D.: On single- and multi-material arbitrary Lagrangian-Eulerian approaches with application to micromechanical problems at finte deformations. Dissertation, Fachbereich Bauingenieur- und Vermessungswesen, Universität Hannover, Germany (2004)
70. Freßmann, D., Wriggers, P.: Advection approaches for single-and multi-material arbitrary Lagrangian-Eulerian finite element procedures. Comput. Mech. **39**, 153–190 (2007)
71. Galera, S., Breil, J., Maire, P.-H.: A 2D unstructured multi-material Cell-Centered Arbitrary Lagrangian-Eulerian (CCALE) scheme using MOF interface reconstruction. Comput. Fluids **46**, 237–244 (2011)
72. Gingold, R.A., Monaghan, J.J.: Smoothed particle hydrodynamics: theory and application to non-spherical stars. Mon. Not. R. Astron. Soc. **181**, 375–389 (1977)

73. Gudehus, G.: A comprehensive constitutive equation for granular materials. Soils Found. **36**(1), 1–12 (1996)
74. Hassanizadeh, M., Gray, W.G.: General conservation equations for multi-phase systems: 1, averaging procedure. Adv. Water Resour. **2**, 131–144 (1979)
75. Hassanizadeh, M., Gray, W.G.: General conservation equations for multi-phase systems: 2, mass, momenta, energy, and entropy equations. Adv. Water Resour. **2**, 191–203 (1979)
76. Hassanizadeh, M., Gray, W.G.: General conservation equations for multi-phase systems: 3, constitutive theory for porous media flow. Adv. Water Resour. **3**, 25–40 (1980)
77. Hassanizadeh, M., Gray, W.G.: Mechanics and thermodynamics of multiphase flow in porous media including interphase boundaries. Adv. Water Resour. **13**(4), 169–186 (1990)
78. Heinrich, P.: Nonlinear water waves generated by submarine and aerial landslides. J. Waterw. Port Coast. Ocean Eng. **118**(3), 249–266 (1992)
79. Hicks, M.A., Dijkstra, J., Lloret-Cabot, M., Karstunen, M. (eds.): Installation Effects in Geotechnical Engineering. CRC Press, London (2013)
80. Hirsch, C.: Numerical Computation of Internal and External Flows, Vol. 1: Fundamentals of Computational Fluid Dynamics, 2nd edn. Butterworth-Heinemann, Burlington (2007)
81. Hirt, C.W., Nichols, B.D.: Volume of Fluid (VOF) method for the dynamics of free boundaries. J. Comput. Phys. **39**, 201–225 (1981)
82. Hirt, C.W., Amsden, A.A., Cook, J.L.: An arbitrary Lagrangian-Eulerian computing method for all flow speeds. J. Comput. Phys. **14**, 227–253 (1974)
83. Hornung, U.: Homogenization and Porous Media. Springer, New York (1997)
84. Hu, Y., Randolph, M.F.: A practical numerical approach for large deformation problems in soil. Int. J. Numer. Anal. Meth. Geomech. **22**, 327–350 (1998)
85. Hughes, T.J.R.: Numerical implementation of constitutive models: rate-independent deviatoric plasticity. In: Nemat-Nasser, S., Asaro, R.J., Hegemier, G.A. (eds.) Theoretical Foundation for Large-Scale Computations for Nonlinear Material Behavior, pp. 29–63. Martinus Nijhoff Publishers, Dordrecht (1984)
86. Hutter, K., Rajagopal, K.R.: On flows of granular materials. Continuum Mech. Thermodyn. **6**, 81–139 (1994)
87. Hutter, K., Svendsen, B., Rickenmann, D.: Debris flow modeling: a review. Continuum Mech. Thermodyn. **8**, 1–35 (1996)
88. Hyman, J.M.: Numerical methods for tracking interfaces. Physica D **12**, 396–407 (1984)
89. Ishii, M., Hibiki, T.: Thermo-Fluid Dynamics of Two-Phase Flow, 2nd edn. Springer, LLC (2011)
90. Iverson, R.M.: The physics of debris flows. Rev. Geophys. **35**(3), 245–296 (1997)
91. Iverson, R.M.: The debris-flow rheology myth. In: Rickenmann, D., Chen, C.L. (eds.) Debris-Flow Hazards Mitigation: Mechanics, Prediction, and Assessment, pp. 303–314. Millpress, Rotterdam (2003)
92. Iverson, R.M., Denlinger, R.P.: Flow of variably fluidized granular masses across three-dimensional terrain, 1. Coulomb mixture theory. J. Geophys. Res. **106**(B1), 537–552 (2001)
93. Johnson, P.C., Jackson, R.: Frictional-collisional constitutive relations for granular materials, with application to plane shearing. J. Fluid Mech. **176**, 67–93 (1987)
94. Jop, P., Forterre, Y., Pouliquen, O.: A constitutive law for dense granular flows. Nature **441**, 727–730 (2006)

95. Kolymbas, D.: Introduction to Hypoplasticity. A.A. Balkema, Rotterdam (2000)
96. Lade, P.V., de Boer, R.: The concept of effective stress for soil, concrete and rock. Géotechnique **47**, 61–78 (1997)
97. Lade, P.V., Yamamuro, J.A. (eds.): Physics and Mechanics of Soil Liquefaction. A.A. Balkema, Rotterdam (1999)
98. LeVeque, R.J.: Finite Volume Methods for Hyperbolic Problems, 3rd edn. Cambridge University Press, Cambridge (2002)
99. Lewis, R.W., Schrefler, B.A.: The Finite Element Method in the Static and Dynamic Deformation and Consolidation of Porous Media, 2nd edn. Wiley, Chichester (1998)
100. Li, X.S.: A sand model with state-dependent dilatancy. Géotechnique **52**(3), 173–186 (2002)
101. Livermore Software Technology Corporation (LSTC): LS-DYNA Keyword User's Manual, Vol. I, R8.0. Livermore Software Technology Corporation (LSTC) (2015)
102. Liyanapathirana, D.S.: Arbitrary Lagrangian Eulerian based finite element analysis of cone penetration in soft clay. Comput. Geotech. **36**, 851–860 (2009)
103. Locat, J., Lee, H.J.: Submarine landslides: advances and challenges. Can. Geotech. J. **39**, 193–212 (2002)
104. Loges, I., Niemunis, A.: Neohypoplasticity—estimation of small strain stiffness. In: Triantafyllidis, T. (ed.) Holistic Simulation of Geotechnical Installation Processes. LNACM, vol. 77, pp. 163–180. Springer, Heidelberg (2015). doi:10.1007/978-3-319-18170-7_9
105. Lucy, L.B.: A numerical approach to the testing of the fission hypothesis. Astron. J. **82**, 1013–1024 (1977)
106. Luttwak, G., Rabie, R.L.: The multi material arbitrary Lagrangian Eulerian code MMALE and its application to some problems of penetration and impact. Technical report LA-UR-85-2311, Los Alamos National Laboratory, Los Alamos, New Mexico, USA (1985)
107. Ma, G., Shi, F., Kirby, J.T.: Shock-capturing non-hydrostatic model for fully dispersive surface wave processes. Ocean Model. **43–44**, 22–35 (2012)
108. Ma, G., Kirby, J.T., Shi, F.: Numerical simulation of Tsunami waves generated by deformable submarine landslides. Ocean Model. **69**, 146–165 (2013)
109. Mabsout, M.E., Tassoulas, J.L.: A finite element model for the simulation of pile driving. Int. J. Numer. Meth. Eng. **37**, 257–278 (1994)
110. Mair, H.U.: Review: hydrocodes for structural response to underwater explosions. Shock Vibr. **6**, 81–96 (1999)
111. Malvern, L.E.: Introduction to the Mechanics of a Continuous Medium. Prentice Hall Inc., New Jersey (1969)
112. Mandell, D.A., Adams, T.F., Holian, K.S., Addessio, F.L., Baumgardner, J.R., Mosso, S.J.: MESA: a 3-D computer code for armor/anti-armor applications. Report LA-UR-89-1851, Los Alamos National Laboratory, Los Alamos, USA (1989)
113. Manzari, M.T., Dafalias, Y.F.: A critical state two-surface plasticity model for sands. Géotechnique **47**(2), 255–272 (1997)
114. Masson, D.G., Harbitz, C.B., Wynn, R.B., Pedersen, G., Løvholt, F.: Submarine landslides: processes, triggers and hazard prediction. Philos. Trans. R. Soc. Lond. Ser. A **364**, 2009–2039 (2006)
115. McGlaun, J.M., Thompson, S.L.: CTH: a three-dimensional shock wave physics code. Int. J. Impact Eng. **10**, 351–360 (1990)
116. Miller, G.H., Puckett, E.G.: A high-order Godunov method for multiple condensed phases. J. Comput. Phys. **128**, 134–164 (1996)

117. Miller, D.S., Zimmerman, G.B.: An algorithm for time evolving volume fractions in mixed zones in Lagrangian hydrodynamics calculations. Russ. J. Phy. Chem. B **3**, 117–121 (2009)
118. Moseley, M.P., Kirsch, K. (eds.): Ground Improvement, 2nd edn. Spon Press, New York (2004)
119. Murad, M.A., Bennethum, L.S., Cushman, J.H.: A multi-scale theory of swelling porous media: I, application to one-dimensional consolidation. Transp. Porous Media **19**, 93–122 (1995)
120. Murad, M.A., Cushman, J.H.: Multiscale flow and deformation in hydrophilic swelling porous media. Int. J. Eng. Sci. **34**(3), 313–338 (1996)
121. Nazem, M., Sheng, D., Carter, J.P.: Stress integration and mesh refinement for large deformation in geomechanics. Int. J. Numer. Meth. Eng. **65**, 1002–1027 (2006)
122. Nazem, M., Sheng, D., Carter, J.P., Sloan, S.W.: Arbitrary Lagrangian-Eulerian method for large-strain consolidation problems. Int. J. Numer. Anal. Method Geomech. **32**(9), 1023–1050 (2008)
123. Niemunis, A., Herle, I.: Hypoplastic model for cohesionless soils with elastic strain range. Mech. Cohesive-Frictional Mater. **2**, 279–299 (1997)
124. Niemunis, A., Tavera, C.E.G., Wichtmann, T.: Peak stress obliquity in drained and undrained sands, simulations with neohypoplasticity. In: Triantafyllidis, T. (ed.) Holistic Simulation of Geotechnical Installation Processes. LNACM, vol. 80, pp. 85–114. Springer, Heidelberg (2016). doi:10.1007/978-3-319-23159-4_5
125. Nikolinakou, M.A., Whittle, A.J., Savidis, S.A., Schran, U.: Prediction and interpretation of the performance of a deep excavation in Berlin sand. J. Geotech. Geoenviron. Eng. **137**(11), 1047–1061 (2011)
126. Noh, W.F.: CEL: a time-dependent, two-space-dimensional, coupled Eulerian-Lagrange code. In: Alder, B. et al. (ed.) Methods in Computational Physics, Advances in Research and Applications, vol. 3: Fundamental Methods in Hydrodynamics, pp. 117–179. Academic Press, New York and London (1964)
127. Passman, S.L., Nunziato, J.W., Bailey, P.B., Reed, K.W.: Shearing motion of a fluid-saturated granular material. J. Rheol. **30**(1), 167–192 (1986)
128. Pastor, M., Zienkiewicz, O.C., Chan, A.H.C.: Generalized plasticity and the modelling of soil behaviour. Int. J. Numer. Anal. Method Geomech. **14**, 151–190 (1990)
129. Peery, J.S., Carroll, D.E.: Multi-material ALE methods in unstructured grids. Comput. Methods Appl. Mech. Eng. **187**, 591–619 (2000)
130. Pitman, E.B., Le, L.: A two-fluid model for avalanche and debris flows. Philos.Trans. R. Soc. Lond. Ser. A **363**, 1573–1601 (2005)
131. Plumb, O.A., Whitaker, S.: Dispersion in heterogeneous porous media, 1. local volume averaging and large-scale averaging. Water Resour. Res. **24**(7), 913–926 (1988)
132. Pudasaini, S.P.: A general two-phase debris flow model. J. Geophys. Res. **117**, F03010 (2012)
133. Pudasaini, S.P., Hutter, K.: Avalanche Dynamics: Dynamics of Rapid Flows of Dense Granular Avalanche. Springer, Heidelberg (2007)
134. Pudasaini, S.P., Wang, Y., Hutter, K.: Modelling debris flows down general channels. Nat. Hazards Earth Syst. Sci. **5**, 799–819 (2005)
135. Qiu, G., Henke, S., Grabe, J.: Application of a coupled Eulerian-Lagrangian approach on geomechanical problems involving large deformations. Comput. Geotech. **38**, 30–39 (2011)
136. Rackwitz, F., Savidis, S.A.: Numerische Untersuchungen zum Tragverhalten von Zugpfählen in Berliner Sand. Bauingenieur **79**(9), 375–383 (2004). (in German)

137. Rider, W.J., Kothe, D.B.: Reconstructing volume tracking. J. Comput. Phys. **141**, 112–152 (1998)
138. Rudman, M.: Volume-tracking methods for interfacial flow calculations. Int. J. Num. Meth. Fluids **24**(7), 671–691 (1997)
139. Savage, S.B., Hutter, K.: The motion of a finite mass of granular material down a rough incline. J. Fluid Mech. **199**, 21–24 (1989)
140. Savidis, S.A., Aubram, D., Rackwitz, F.: Arbitrary Lagrangian-Eulerian finite element formulation for geotechnical construction processes. J. Theoret. Appl. Mech. **38**(1–2), 165–194 (2008)
141. Savidis, S.A., Aubram, D., Rackwitz, F.: Vibro-injection pile installation in sand: part ii—numerical and experimental investigation. In: Triantafyllidis, T. (ed.) Holistic Simulation of Geotechnical Installation Processes. LNACM, vol. 77, pp. 103–131. Springer, Heidelberg (2015). doi:10.1007/978-3-319-18170-7_6
142. Scardovelli, R., Zaleski, S.: Direct numerical simulation of free-surface and interfacial flow. Annu. Rev. Fluid Mech. **31**, 567–603 (1999)
143. Shashkov, M.: Closure models for multimaterial cells in arbitrary Lagrangian-Eulerian hydrocodes. Int. J. Num. Methods Fluids **56**(8), 1497–1504 (2008)
144. Schofield, A.N., Wroth, C.P.: Critical State Soil Mechanics. McGraw-Hill, New York (1968)
145. Seed, R.B., Cetin, K.O., Moss, R.E.S., Kammerer, A.M., Wu, J., Pestana, J.M., Riemer, M.F., Sancio, R.B., Bray, J.D., Kayen, R.E., Faris, A.: Recent advances in soil liquefaction engineering: a unified and consistent framework. Technical report EERC 2003–06, University of California, Berkeley, California, USA (2003)
146. Sheng, D., Nazem, M., Carter, J.P.: Some computational aspects for solving deep penetration problems in geomechanics. Comput. Mech. **44**, 549–561 (2009)
147. Simo, J.C., Hughes, T.J.R.: Computational Inelasticity. Springer, Heidelberg (1998)
148. Soga, K., Alonso, E., Yerro, A., Kumar, K., Bandara, S.: Trends in large-deformation analysis of landslide mass movements with particular emphasis on the material point method. Géotechnique **66**(3), 248–273 (2016)
149. Stewart, H.B., Wendroff, B.: Two-phase flow: models and methods. J. Comput. Phys. **56**, 363–409 (1984)
150. Sulsky, D., Zhou, S.-J., Schreyer, H.L.: Application of a particle-in-cell method to solid mechanics. Comput. Phys. Commun. **87**, 236–252 (1995)
151. Susila, E., Hryciw, R.D.: Large displacement FEM modelling of the cone penetration Test (CPT) in Normally consolidated sand. Int. J. Numer. Anal. Meth. Geomech. **27**, 585–602 (2003)
152. Taiebat, M., Dafalias, Y.F.: SANISAND: simple anisotropic sand plasticity model. Int. J. Numer. Anal. Meth. Geomech. **32**, 915–948 (2008)
153. Terzaghi, K.: Theoretical Soil Mechanics. Wiley, New York (1943)
154. Tho, K.K., Leung, C.F., Chow, Y.K., Swaddiwudhipong, S.: Eulerian finite-element technique for analysis of jack-up spudcan penetration. Int. J. Geomech. **12**, 64–73 (2012)
155. Triantafyllidis, T. (ed.): Numerical Modelling of Construction Processes in Geotechnical Engineering for Urban Environment. CRC Press, London (2006)
156. Triantafyllidis, T. (ed.): Holistic Simulation of Geotechnical Installation Processes: Numerical and Physical Modelling. LNACM, vol. 77. Springer, Heidelberg (2015). http://dx.doi.org/10.1007/978-3-319-18170-7
157. Triantafyllidis, T. (ed.): Holistic Simulation of Geotechnical Installation Processes: Benchmarks and Simulations. LNACM, vol. 80. Springer, Heidelberg (2016). http://dx.doi.org/10.1007/978-3-319-23159-4

158. Truesdell, C., Toupin, R.A.: Encyclopedia of physics. In: Flugge, S. (ed.) Bd. III/1: The Classical Field Theories, pp. 226–793. Springer, Heidelberg (1960)
159. Truesdell, C., Noll, W.: The Non-Linear Field Theories of Mechanics, 3rd edn. Springer, Heidelberg (2004)
160. Trulio, J.G., Trigger, K.R.: Numerical solution of the one-dimensional hydrodynamic equations in an arbitrary time-dependent coordinate system. Report UCRL-6522, Lawrence Radiation Laboratory, University of California, Livermore, USA (1961)
161. Trulio, J.G.: Theory and structure of the AFTON codes. Report AFWL-TR-66-19, Air Force Weapons Laboratory, Kirtland Air Force Base, New Mexico, USA (1966)
162. Vogelsang, J., Huber, G., Triantafyllidis, T.: Requirements, concepts, and selected results for model tests on pile penetration. In: Triantafyllidis, T. (ed.) Holistic Simulation of Geotechnical Installation Processes. LNACM, vol. 80, pp. 1–30. Springer, Heidelberg (2016). doi:10.1007/978-3-319-23159-4_1
163. Vogelsang, J., Huber, G., Triantafyllidis, T., Bender, T.: Interpretation of vibratory pile penetration based on digital image correlation. In: Triantafyllidis, T. (ed.) Holistic Simulation of Geotechnical Installation Processes. LNACM, vol. 80, pp. 31–51. Springer, Heidelberg (2016). doi:10.1007/978-3-319-23159-4_2
164. von Wolffersdorff, P.-A.: A hypoplastic relation for granular materials with a predefined limit state surface. Mech. Cohesive-Frictional Mater. **1**, 251–271 (1996)
165. Weseloh, W.N., Clancy, S.P., Painter, J.W.: PAGOSA physics manual. Report LA-14425-M, Los Alamos National Laboratory, Los Alamos, USA (2010)
166. Whitaker, S.: Flow in porous media I: a theoretical derivation of Darcy's law. Trans. Porous Media **1**, 3–25 (1986)
167. Whitaker, S.: Flow in porous media II: the governing equations for immiscible, two-phase flow. Trans. Porous Media **1**, 105–125 (1986)
168. Whitaker, S.: Flow in porous media III: deforming media. Trans. Porous Media **1**, 127–154 (1986)
169. Whitaker, S.: The Method of Volume Averaging. Kluwer Academic Publishers, Dordrecht (1999)
170. White, D.J., Take, W.A.: GeoPIV: Particle Image Velocimetry (PIV) software for use in geotechnical testing. Technical report CUED/D-SOILS/TR322, Geotechnical and Environmental Research Group, University of Cambridge, UK (2002)
171. White, D.J., Take, W.A., Bolton, M.D.: Soil deformation measurement using Particle Image Velocimetry (PIV) and photogrammetry. Géotechnique **53**(7), 619–631 (2003)
172. Wood, A.B.: A Textbook of Sound. The Macmillan Company, New York (1930)
173. Wood, D.M.: Soil Mechanics: A One-Dimensional Introduction. Cambridge University Press, Cambridge (2009)
174. Wriggers, P.: Nonlinear Finite Element Methods. Springer, Heidelberg (2008)
175. Youngs, D.L.: Time-dependent multi-material flow with large fluid distortion. In: Morton, K.W., Baines, M.J. (eds.) Numerical Methods for Fluid Dynamics, pp. 273–285. Academic Press, London (1982)
176. Zienkiewicz, O.C., Chan, A.H.C., Pastor, M., Schrefler, B.A., Shiomi, T.: Computational Geomechanics - With Special Reference to Earthquake Engineering. Wiley, Chichester (1999)
177. Zienkiewicz, O.C., Taylor, R.L.: The Finite Element Method, Volume 1: The Basis, 5th edn. Butterworth-Heinemann, Oxford (2000)

Experimental Investigation of Vibratory Pile Driving in Saturated Sand

Jakob Vogelsang(✉), Gerhard Huber, and Theodoros Triantafyllidis

Institute of Soil Mechanics and Rock Mechanics,
Karlsruhe Institute of Technology, Karlsruhe, Germany
jakob.vogelsang@kit.edu

Abstract. An experimental study using half-model tests to investigate the vibro-penetration of piles in saturated sand is presented. In the tests, a model pile with half-circular cross section is penetrated along an observation window by means of a vibrator. The use of a high speed camera and a sophisticated image acquisition system enables the observation of the penetration process with sufficient temporal and spatial resolution. A consistent evaluation of pile head and toe motion is achieved using a combined interpretation of acceleration measurements and Digital Image Correlation (DIC) analysis. The application of DIC to evaluate cyclic soil deformations reveals the relation of typical displacement patterns in the soil and characteristic phases of pile penetration. Pore water pressure measurements at two fixed locations show the dependence of pore water pressure evolution on the penetration mode and soil density. The extensive measurements allow an improved interpretation of the typical penetration modes during vibratory pile driving.

Keywords: Vibratory pile penetration · Pile driving · Digital image correlation

1 Introduction

Thorough research on complex processes like vibratory pile driving should be based on numerical simulations with validated material models, field studies and not least on the laboratory investigation using model tests. Numerical simulations provide the potential to solve complicated problems, for example towards a consideration of the effects of vibro-driving on adjacent structures. However, the numerical modeling of pile driving and related processes is still under research. Most of the existing models are based on simplifying assumptions and a systematic validation has not been carried out until now. They are therefore not established in the engineering community. Without an objective and quantitative comparison with experimental data, a high level of acceptance will not be achieved. To perform these benchmarks, high-quality experiments capturing the significant effects of pile driving are needed.

The suitability of field tests as benchmark experiments is limited due to the poor knowledge and observability of the underground conditions including soil

T. Triantafyllidis (ed.), *Holistic Simulation of Geotechnical Installation Processes*,
Lecture Notes in Applied and Computational Mechanics 82, DOI 10.1007/978-3-319-52590-7_4

state. Nevertheless, important achievements have been made on the basis of field tests [2,3,6,7]. Model tests can overcome some limitations of field studies and have therefore been extensively used to investigate vibratory pile driving in the laboratory. Rodger and Littlejohn [9] summarized and interpreted important experiences from practice and were able to identify the fundamental penetration modes. O'Neill et al. [8], Wong [20] and Wong et al. [21] concentrated their laboratory studies on the driveability and the bearing capacity of vibro-driven piles in granular soil. They have demonstrated the existence of an optimum frequency of about 20 Hz regarding the penetration velocity that seems to be independent of soil density (for the used vibrator-pile-soil system). Cudmani [6] and Cudmani et al. [5] used calibration chamber tests to investigate the influencing factors on the occurrence of two different penetration modes: the so-called cavitational and non-cavitational vibratory pile driving. The consideration of higher vibration modes, e.g. described by Vielsack and Storz [14], is not within the scope of this study. All these investigations contribute to an improved knowledge and a better comprehension of the mechanics of vibratory pile driving. However, without information about the soil deformations in vicinity to the pile toe, the soil mechanical interpretation of many test results has to remain hypothetical and therefore often qualitative and superficial [15].

Digital Image Correlation (DIC) techniques have been shown to be very useful to obtain information about the soil deformation occurring in model tests. For the application of DIC, the test setup has to provide an observation window to visualize the soil in the region of interest. In the case of pile penetration tests, a half-model pile is driven into a soil body along the observation window. Monotonic penetration processes have been studied in detail by many researchers, e.g. [1,18,19]. When it comes to cyclic or vibratory processes, only very few experimental results including DIC measurements exist [10,16]. The reliable evaluation and the synchronization with other measurements are much more difficult and very high frame rates are required to capture the cyclic and dynamic pile and soil motion. A first attempt for the evaluation of cyclic soil behavior during vibro-penetration has been made in [16] proving the benefit but also the challenges of these evaluations.

In this contribution, experiences and results from a series of vibratory pile penetration tests are described. A half model that enables the evaluation of cyclic soil motion around the penetrating model pile is used for this purpose. First results of similar model tests have been presented in [16], however, the occurring pile penetration was very limited in these tests. Now, penetration depths of about 15 pile diameters are reached. Additionally, an enhanced instrumentation is applied, enabling also the evaluation of pore water pressures in vicinity to the pile. Due to these improvements, the model tests provide new insights into vibratory pile driving processes and the soil behavior near to penetrating piles.

2 Description of the Experiments

2.1 Experimental Setup

The test setup is also extensively described in [16,18], therefore, only the most important aspects are briefly summarized here. The test container has a half-circular base area and an acrylic glass front sheet, see schema in Fig. 1. It is used as an observation window in the intended symmetry plane of the problem. During the sample preparation and the test, the container is reinforced with two steel beams attached outside to minimize deflection. The test container is filled with saturated soil and a model pile with almost half-circular cross section is vibrated into the soil along the observation window. Two LED spotlights with constant intensity and with very low IR-content give a good, uniform illumination without heating-up the test container.

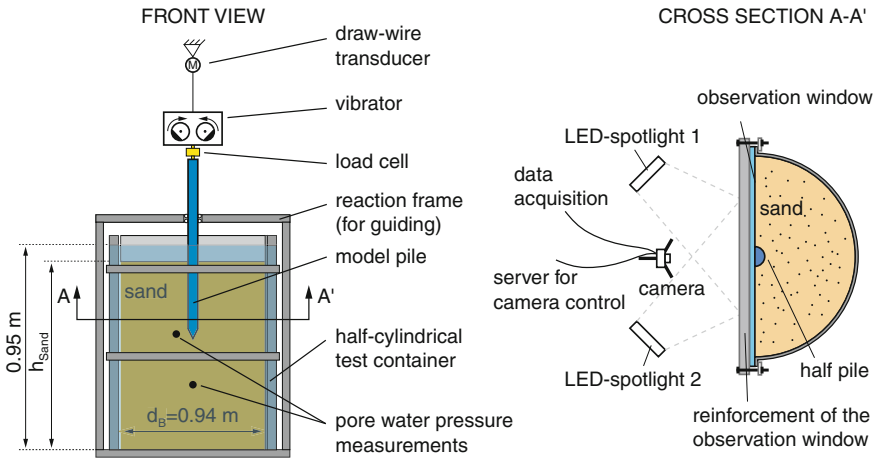

Fig. 1. Basic test setup for the vibratory pile tests

Contrary to [16], in this study, a pile with almost half-conical tip has been used, see Fig. 2(a). Figure 2(b) summarizes important characteristics of the pile-vibrator system used here.

2.2 Test Sand, Sample Preparation and Uniformity Control

A uniform medium quartz sand is used as test material. An extensive characterization of the sand is provided by Vogelsang [18]. A very similar sand has been used in other studies of the authors [16]. Important properties and some remarks on specific characteristics of the current test sand can be found in [17] in this book.

The same preparation methods as described in [16] have been applied for the present test series. The dry sand is pluviated into deaerated water by means of

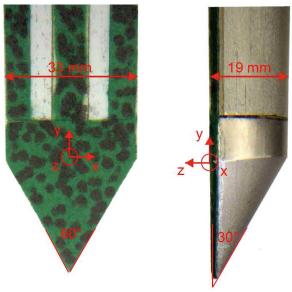

a)

b)

mass vibrator	m_{vib}	g	6594
frequency range		Hz	0-50
static moment	M_{sta}	kgm	0.00533
mass load cell	m_{LC}	g	660
mass pile	m_{pile}	g	627
total mass	m_{dyn}	g	7881
stiffness load cell	c_{LC}	kN/mm	100
stiffness pile	EA/L_{pile}	kN/mm	8.51
length pile	L_{pile}	m	0.97
cross section	A_b	mm^2	493.6

Fig. 2. (a) Pile tip and (b) characteristics of the pile-vibrator system used

a diffusor system. A subsequent densification is achieved through hammer blows against the container walls leading to a liquefaction and reconsolidation of the sample [18]. Contrary to [16], the model pile is not pre-installed during the sand deposition procedure.

CPT results verifying the sample uniformity are also included in [16]. The achieved sample quality is shown to fulfill the high requirements that have to be established for model pile penetration tests.

2.3 Experimental Program and Procedures

The test series described here contains three tests that have been performed under similar conditions. Information concerning the tests is shown in Table 1. Three different initial densities for the sand ranging from medium dense to dense have been investigated. An explanation of the symbols and the nomenclature for the pile toe region is provided in the end of the paper.

Table 1. Information on the three vibratory tests of this study.

Test	Date	h_{sand} [m]	e_0 [-]	$I_{D,0}$ [%]	S_r [-]	y_0 [mm]	f [Hz]	$u_{y,pile,max}$ [mm]
VIB-HM-04	19.07.16	0.808	0.6478	71	1	−129	25.0	−481
VIB-HM-05	08.08.16	0.787	0.6127	82	1	−116	25.0	−466
VIB-HM-06	17.08.16	0.837	0.6923	53	1	−157	25.0	−509

After the sand deposition, the pile is placed and fixed at the desired position and the horizontal guidings for the pile to be driven are installed. The vertical position of the pile tip is a few mm above the sand surface. Then the fixation of the pile is released and the pile penetrates into the sand by a few pile diameters due to the weight of the pile-vibrator system. In Table 1, the value y_0 indicates

the initial vertical position of the pile shoulder relative the sand surface. Beginning from this configuration, the vibrations are applied with a frequency of 25 Hz. $u_{y,pile}$ is used for the vertical position of the pile shoulder with respect to the initial sand surface, $u_{y,pile,max}$ is the maximum penetration depth reached in the test (negative for penetration). The vibrations are stopped when the pile head reaches the upper guiding, thus, the maximum vertical travel of the pile is about −350 mm corresponding to about $u_{y,pile,max} = -500$ mm depth of the pile tip ($\approx -15 d_{pile}$).

2.4 Measurements and Image Acquisition System

The instrumentation used in the present test series is slightly enhanced compared to [16] and is described in detail in [18]. The following measurements have been recorded:

- Pile head force between pile and vibrator using a load cell of type HBM Type U2A with 10 kN measuring range
- Mean pile head displacement with potentiometric draw-wire sensor
- Acceleration at the pile head using a PCB 321 A02 ICP sensor with ±50 g measuring range
- The pore water pressures at two stationary locations in the plane of the observation window applying GE UNIK 5000 transducers hydraulically connected to the location of measurement (20 kN/m^2 measuring range, for details see [18])
- Eccenter position using a light barrier system indicating the sign of the resulting vertical excitation force
- Digital images of a soil region with approximately 200 × 125 mm^2 in 0.5 m depth with a frame rate of 300 fps
- Synchronization signal during image capturing

The image acquisition system and the synchronization with the other measurements is schematically illustrated in Fig. 3. The maximum image rate is 352 fps with 2048×1088 pixels. Here, 300 fps are used. The continuous data rate is about 750 MB/s (monochrome images with 8-bit depth). The image resolution corresponds approximately to 0.1 mm/pixel resp. 5 pixel per mean grain. A frame drawn on the inner observation window around the outer edges of the region of interest enables the determination of the scale, an exact rotation of the image with respect to the vertical axis and a distortion control. Depending on the applied excitation frequency, the image rate provides between 10 and 15 images per cycle of vibration (here 12 with $f = 25$ Hz) which is sufficient to reproduce the cyclic displacements. To handle the high image rate, high speed interfaces, an adapted video grabber and a server with 120 GB RAM are used. This equipment enables a continuous data transfer to the hard disc array to record a complete vibratory test.

For a synchronization of the other measurements and the image series, the camera is connected to the data acquisition system. A signal for the times at which an image was captured is recorded. A LED bar code that is placed near

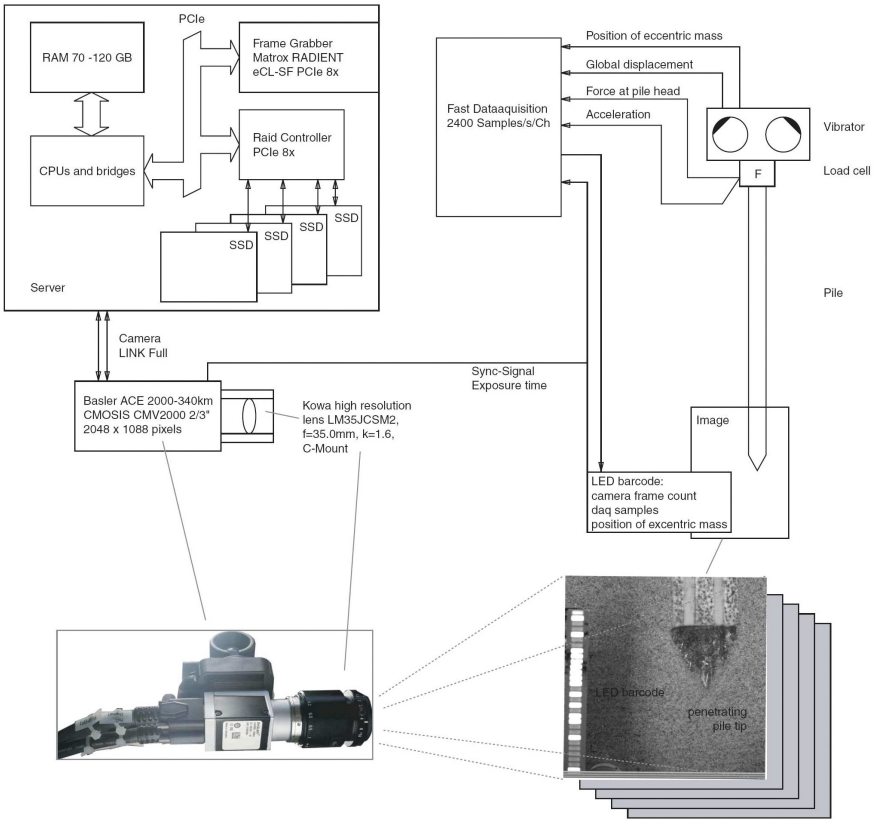

Fig. 3. Data and image acquisition system

to the image border facilitates the synchronization of measurements and captured images. It provides information about the data and image samples and the position of the eccentric masses.

2.5 Test Evaluation

The penetration velocity, the force-displacement curve, the evolution of pore water pressures and the occurring soil displacements are the basis of the interpretation of the tests.

Displacement of the Pile-Vibrator System. The displacements of the pile-vibrator system are evaluated using two different approaches accounting for the non-perfect rigidity of the pile:

– By analyzing the image series using Digital Image Correlation (see next paragraph). This evaluation is possible for the region of the pile toe in the test

section where it is visible in the images. It allows the determination of the total pile toe displacements (trend and cycles) with a sampling rate equal to the image rate. The pile displacements can be described easily e.g. in terms of splines-functions (*Python* [11]). By differentiating twice, the accelerations of the pile toe can be estimated and accounted for in the interpretation [11]. A synchronization with the force measurement enables of determination of the load-displacement behavior of the pile (see also [16]).

– The mean pile head displacement is measured by a potentiometer attached to a wire-drum. During strong accelerations of the pile, a vibration of the drum can sometimes not be prevented. The mean pile displacement is therefore calculated as the moving average over one vibration period of the drum. For short time periods, the cyclic pile head displacements are evaluated by two times integration of the measured acceleration. A trapezoidal rule is used for this purpose and a possible drift is subtracted to obtain the pure cyclic displacements.

Soil Reaction Force. The measured pile head force F_h results primarily from the soil reaction force but also contains the inertia force of the pile. This force is subtracted from the head force in order to evaluate the net soil reaction force (plus a probably occurring friction between observation window and pile). Note, that the soil reaction is understood as a total force and comprises effective soil resistance and pore water pressures. It is assumed that pile and vibrator undergo the same accelerations and that the measurement at the vibrator can be taken as representative for the pile also. For the evaluation of the inert mass, the pile mass and 90% of the load cell mass are considered which corresponds approximately to the mass below the measuring element.

Digital Image Correlation (DIC). The DIC evaluation is performed using the software JPIV [13] and a subsequent summation and strain calculation procedure. The JPIV settings and their physical meaning are given in Table 2. Evaluation methods and theoretical framework are extensively described by Vogelsang [18]. The test evaluation presented here concentrates on the cyclic pile-soil interaction. Similar evaluations like in [16] are used therefore, considering short test sections when the pile reaches a depth of about 0.5 m. For the evaluation of the load-displacement curve, the pile toe displacements are tracked

Table 2. JPIV settings used in the present study

Pass	Test [pixel]	Patch [mm]	Width/Height [$\times d_{50}$]	Interrogation window [pixel]	Width/Height [mm]
1	64	≈ 8	≈ 15	128	≈ 16
2	32	≈ 4	≈ 7	64	≈ 8
3	32	≈ 4	≈ 7	64	≈ 8

and synchronized with the force measurements. Incremental displacement fields in the soil evaluated during a representative cycle are used to analyze the soil behavior.

3 Description of the Experimental Results

3.1 Typical Test Results

Figure 4 shows some typical test results obtained for three selected cycles in test VIB-HM-05 with dense sand ($I_{D,0} = 0.82$). The second cycle is highlighted. At the beginning of this cycle, the pile shoulder is located about 0.42 m below the sand surface, which corresponds to the configuration where the point of the pile tip passes the vertical level of the lower pore water pressure transducer PWD_1. This test section will be analyzed in detail later on in comparison with the two other tests.

The test results verify that the penetration behavior is quasi stationary and the consideration of individual cycles is admissible for the interpretation.

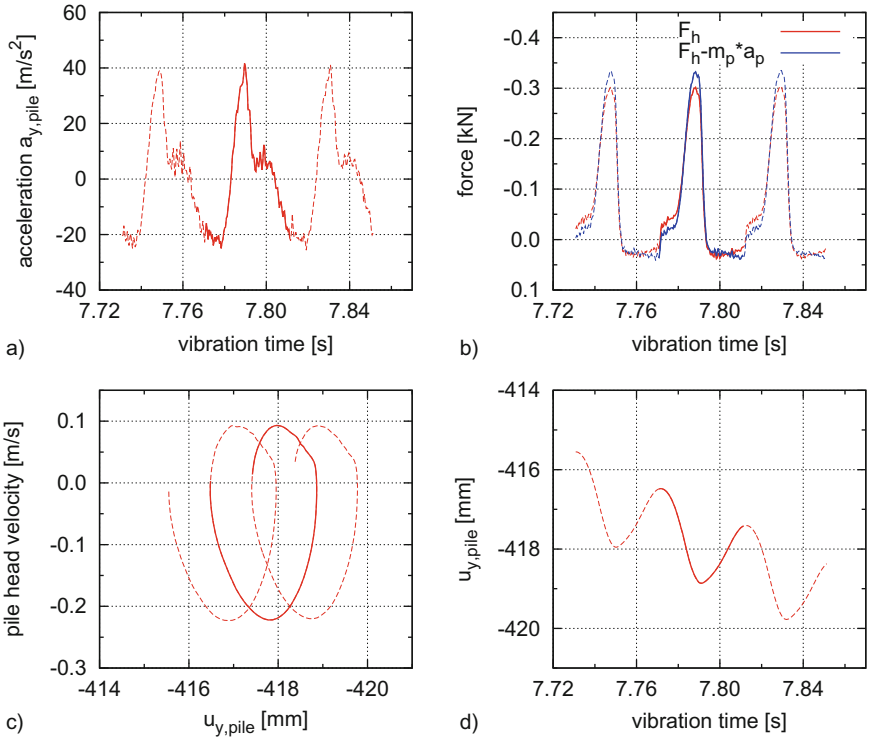

Fig. 4. Typical test results of VIB-HM-05 ($I_{D,0} = 0.82$): time history of (a) acceleration and (b) head force F_h and soil reaction force $F_h - m_p \cdot a_p$, (c) phase diagram and (d) evolution of pile head displacement ($m_p = m_{pile}$, $a_p = a_{y,pile}$)

The measured head force pulsates and increases strongly in the penetration phases. Assuming that the pile undergoes the same accelerations as the vibrator, the soil reaction force can be calculated from the pile head force taking into account the inertial force of the pile, Fig. 4(b). It is slightly higher than the pile head force in the penetration phases and stays constantly small and positive during upward pile motion. This positive force is probably attributed to shaft friction and friction between pile and observation window. The cyclic pile head velocity and displacement are calculated from the measured acceleration as described above. The pile displacement is approximately sinusoidal with downward trend, Fig. 4(c) and (d), except after the end of the penetration phase where a slight kink is observed in the phase diagram due to the sharp impact, Fig. 4(c). The described behavior does not qualitatively change throughout the test. Similarities and differences to the other tests will be discussed in the next paragraphs.

3.2 Global Penetration Behavior

Figure 5 compares the evolution of pile motion with depth for all three tests. Figure 5(a) shows the mean penetration velocity calculated by differentiation of the mean pile head displacement. Figure 5(b) depicts the pile head displacement amplitude obtained by integrating the acceleration signal twice.

The mean penetration velocity decreases strongly with depth. As expected, penetration occurs faster with decreasing relative density. The calculated pile head amplitude is slightly larger than the calculated free amplitude of the pile-vibrator system, probably due to the non-rigidity of the pile. It is interesting to see that the displacement amplitude increases noticeably with depth for the tests VIB-HM-05 ($I_{D,0} = 0.82$) and VIB-HM-06 ($I_{D,0} = 0.53$) while it is approximately constant in test VIB-HM-04 ($I_{D,0} = 0.71$). The decrease of the

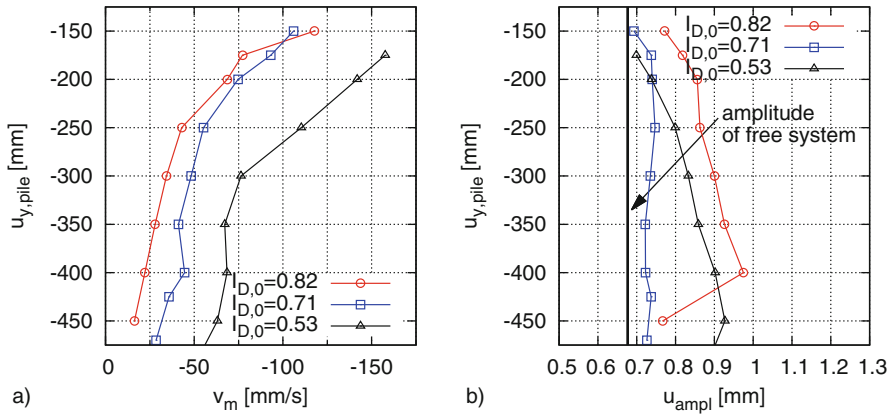

Fig. 5. Evolution of (a) mean penetration velocity v_m and (b) displacement amplitude u_{ampl} at the pile head with penetration depth for the three tests

displacement amplitude towards the end of test VIB-HM-05 is maybe a result of cables touching the guiding of the pile and impeding the pile displacement.

3.3 Cyclic Penetration Behavior

Figure 6 shows the cyclic penetration behavior of the pile for three selected cycles. The second cycle is highlighted and taken as a representative cycle. The current penetration depths differ slightly due to different initial sand heights but the position with respect to the container bottom is equal and the point of the pile tip is at the same vertical level as the lower pore water pressure transducer, see illustration in Fig. 6(d).

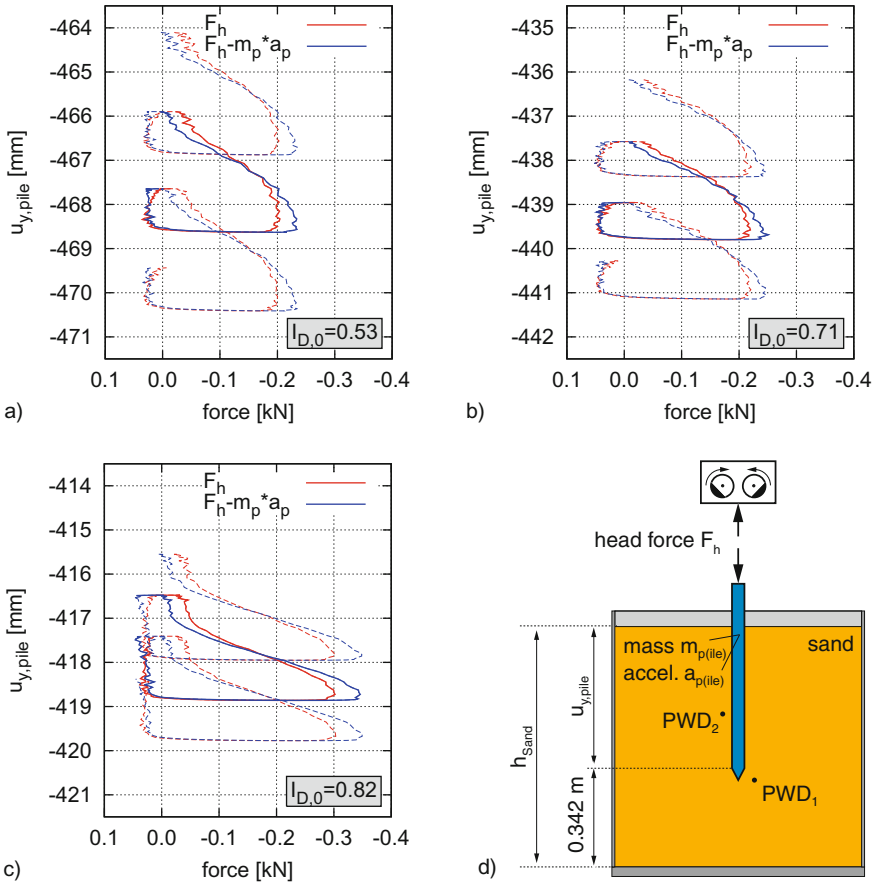

Fig. 6. Cyclic evolution of head force F_h and soil reaction force $F_h - m_p \cdot a_p$ for (a) VIB-HM-06 ($I_{D,0} = 0.53$), (b) VIB-HM-04 ($I_{D,0} = 0.71$, (c) VIB-HM-05 ($I_{D,0} = 0.82$) and (d) illustration of the current configuration

The maximum penetration resistance increases with relatively density but the differences are not so pronounced as could be expected for the investigated density range. The reach of a limit resistance can only be observed in Fig. 6(a) for the test with the lowest density. Only test VIB-HM-05 in Fig. 6(c) resembles clearly to the so-called cavitational penetration mode described by Cudmani [6] and is therefore chosen afterwards for the interpretation of the penetration mechanism. The test reveals a very low reloading stiffness in the penetration phase. For the first 0.5 mm, the penetration resistance remains very small. Subsequently, the penetration resistance increases roughly linearly without reaching a limit state. The measured force during upward pile motion is small and results probably from friction along the shaft between pile and soil and between pile and observation window. The other two tests cannot be associated clearly with this penetration mode although they provide some of the described characteristics. In VIB-HM-06, the initial penetration phase with very low stiffness is less pronounced and furthermore, a limit state seems to be reached towards the end of the penetration phase, Fig. 6(a). The force-displacement curve of test VIB-HM-04 is similar but due to the smaller penetration per cycle a limit state is not reached, Fig. 6(b). None of the tests can be identified as penetration in the non-cavitational mode.

3.4 Evolution of Pore Water Pressure

The permeability of the test sand is rather high ($\approx 1.5 \cdot 10^{-3}$ m/s for medium density), however, this does not completely prevent a build-up of pore water pressures. Typical evolutions of pore water pressure at the two measurement locations is shown in Fig. 7(a) exemplary for test VIB-HM-05 ($I_{D,0} = 0.82$). PWD_1 is the lower and PWD_2 is the upper pressure transducer. The marked configurations I–IV will be used for the interpretation. Figure 7(b) illustrates the positions of the pile tip with respect to the pore water pressure measurements in the configurations I–IV.

The pore water pressures oscillate around the hydrostatic pressure without significant trend. A slight build-up of mean pore water pressure is observed when the pile tip approaches the pressure transducer, but only about 0.5 kN/m^2 maximum. The pore water pressure amplitudes increase with approaching pile tip and decrease rapidly when the pile tip has passed the location of measurement. This behavior was observed in all tests. The maximum amplitudes are always reached when the point of the pile tip is located at the same vertical level as the pore water pressure measurement location, Detail I and III in Fig. 7(b). When the pile shoulder reaches this level, the amplitude has already decreased significantly. The envelopes of pore water pressures were similar in the other tests and are therefore not presented here.

The evolutions of excess pore water pressure at PWD_1 are shown in detail in combination with the pile displacement in Fig. 8. The same test sections as above have been used. The left vertical axis corresponds to the pore water pressure measurement while the right axis is used for the pile displacement. The dashed vertical lines indicate the reversal points of pile motion. An alternative presentation of the results eliminating time by plotting the pore water pressure

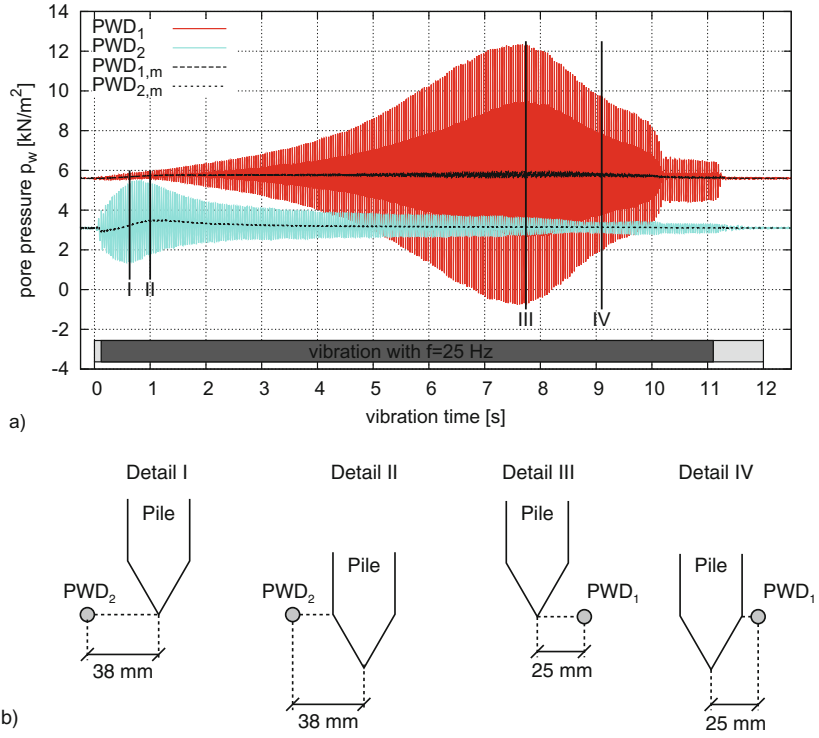

Fig. 7. Typical evolutions of pore water pressures at two stationary locations PWD_1 and PWD_2 during vibro-penetration in VIB-HM-05 ($I_{D,0} = 0.82$): (a) Measurements and (b) position of the pile toe with respect to the locations of measurement for the configurations I–IV

evolution depending on the pile displacement is shown in Fig. 9. In the left column, the alternating part of the displacements $u_{y,pile,zm}$ (zero mean) and in the right column the total displacements are used. The arrows indicate the curve sense.

Only in the case of VIB-HM-04 which has a density lying between those of the two other tests, the pore water pressure oscillates with a frequency corresponding to the excitation mainly. In the two other tests, the pore water pressure evolutions apparently contain the double excitation frequency. Towards the end of the penetration phases, in all tests, negative excess pore water pressures can be seen. During upward pile motion, primarily positive excess pore water pressures occur. In the tests VIB-HM-06 ($I_{D,0} = 0.53$) and VIB-HM-05 ($I_{D,0} = 0.82$), a change of positive and negative excess pore water pressures is observed in each penetration and pullout phase resulting in an evolution with double excitation frequency. Towards the end of upward pile motion the pore water pressure tends to approach the hydrostatic level.

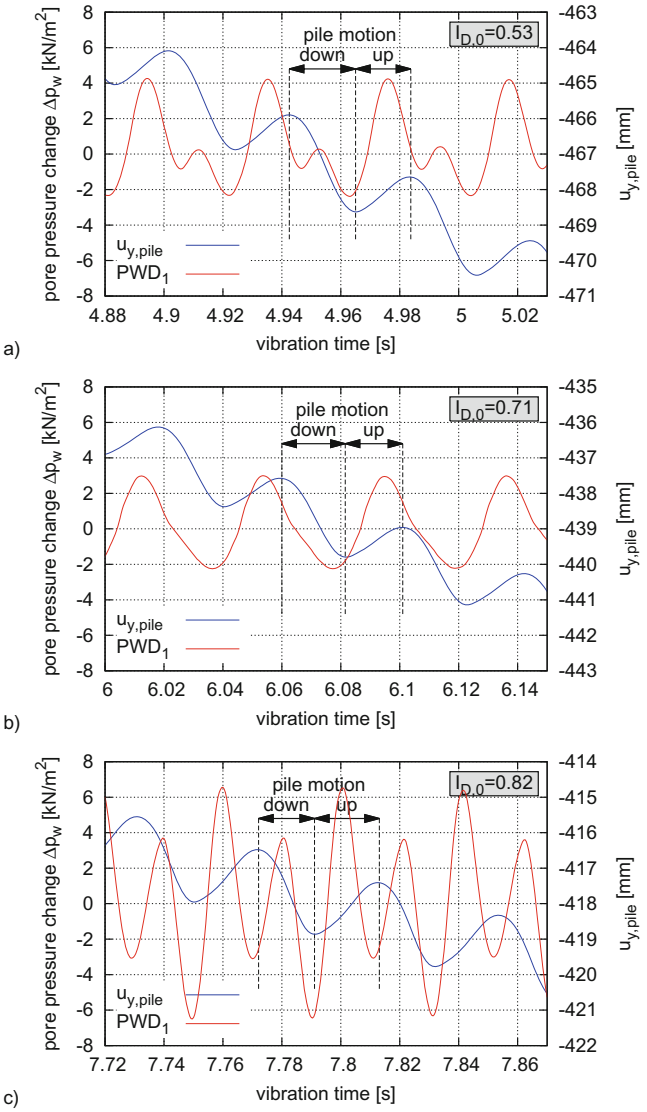

Fig. 8. Pore water pressure changes with respect to the initial hydrostatic pressure at PWD_1 in representative test sections: (a) VIB-HM-06 ($I_{D,0} = 0.53$), (b) VIB-HM-04 ($I_{D,0} = 0.71$), (c) VIB-HM-05 ($I_{D,0} = 0.82$)

Intuitively, one would expect excess pore water pressures during penetration and negative excess pore water pressures during upward pile motion. The observed behavior can only be explained with the volumetric soil behavior. Negative excess pore water pressures in the penetration phases have to be considered as an indicator for a phase with dilative soil behavior around the pile tip.

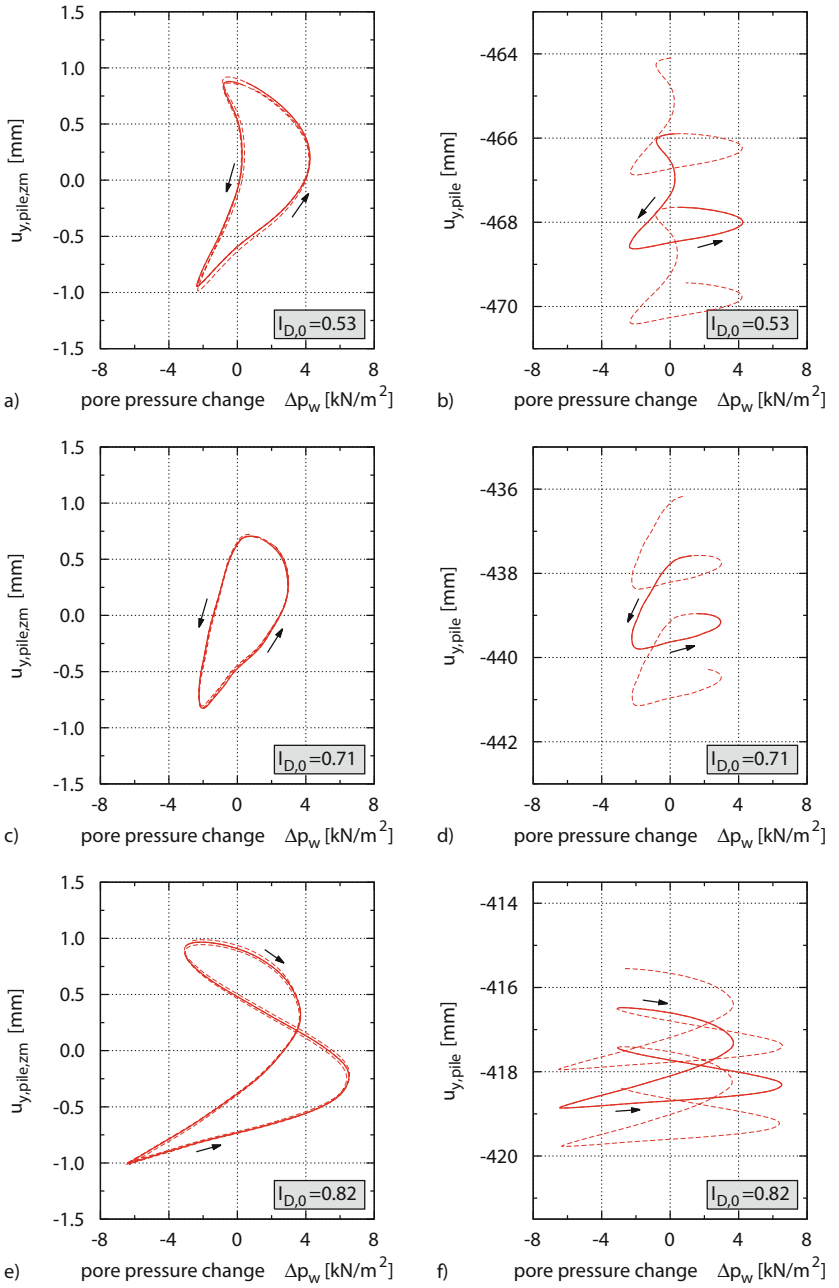

Fig. 9. Pore water pressure changes with respect to the initial hydrostatic pressure at PWD_1 depending on the alternating pile displacement $u_{y,pile,zm}$ (zero mean, left column) and total pile displacement $u_{y,pile}$ (right column) in representative test sections: (a), (b) VIB-HM-06 ($I_{D,0} = 0.53$), (c), (d) VIB-HM-04 ($I_{D,0} = 0.71$), (e), (f) VIB-HM-05 ($I_{D,0} = 0.82$)

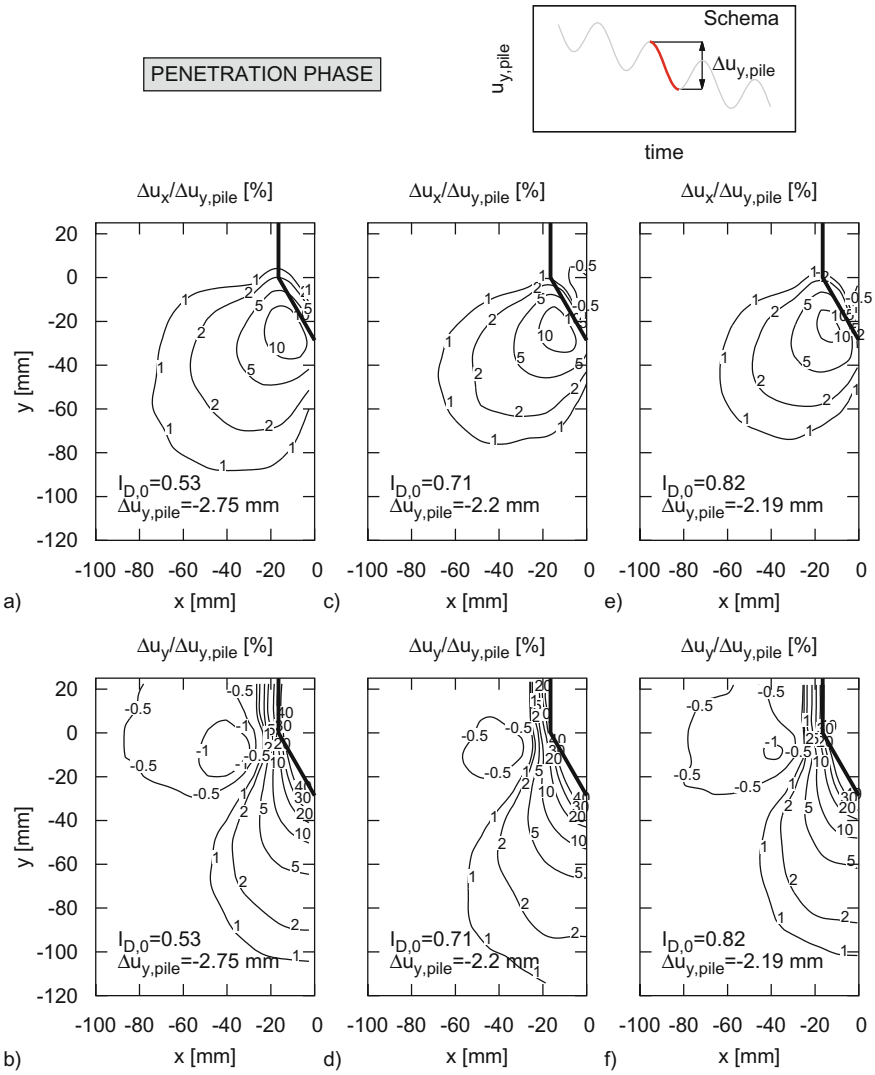

Fig. 10. Normalized incremental displacement fields obtained from DIC analysis for the penetration phase of the representative cycle: (a), (b) VIB-HM-06 ($I_{D,0} = 0.53$), (c), (d) VIB-HM-04 ($I_{D,0} = 0.71$) and (e), (f) VIB-HM-05 ($I_{D,0} = 0.82$)

On the other hand, excess pore water pressure during upward motion indicates contractancy.

From cyclic triaxial tests on medium dense and dense sand, it is well known that a double alternation of contractancy and dilatancy occurs if the shear deformation amplitude is sufficiently large. After reversals of deformation, the soil exhibits contractancy before the phase transformation line is reached and the

behavior switches to dilative regime. Regarding pile driving, the cyclic deformation is superimposed by a monotonic portion (penetration). The phase transformation line is therefore almost always reached in the penetration phase. During upward pile motion, the occurring deformations are sometimes not sufficient for a mobilization of dilatancy. Results of triaxial tests reproducing deformation paths that are considered to be typical for cyclic pile penetration are given in [4] in this book.

3.5 Incremental Displacement Fields

Figure 10 compares the incremental displacement fields for the penetration phase of the representative cycle obtained with DIC for the three tests. The upper row shows the horizontal displacements Δu_{x} while the lower row contains the vertical displacements Δu_{y}. Every column stands for one test. As shown above, the pile motion differs between the three tests. In order to achieve comparability, the incremental soil displacements are therefore normalized with the incremental pile displacement $\Delta u_{\mathrm{y,pile}}$ during the penetration phase. The position of the pile tip in the initial configuration of the penetration phase is indicated in thick black line. The evaluation was performed for the left half of the symmetric problem. On the right side, the pressure transducer oscures the view on the sand and exhibits a DIC analysis.

Despite different densities and amounts of pile penetration, the displacement fields remain qualitatively similar. Laterally below the pile tip a soil zone is displaced outwards with maximum horizontal displacement of 10% of the vertical pile displacement. The whole soil volume affected has a width of about four pile diameters (here considered as the region with horizontal displacements larger than 1% of the vertical pile displacement). It appears to decrease slightly with increasing density which may indicate more confined conditions. The main vertical displacements are directed downwards. Beside the pile shoulder, a small zone with upward displacements can be identified. Directly below the pile tip, the largest vertical displacements reach about 40% of the pile displacements. Taking again 1% of $\Delta u_{\mathrm{y,pile}}$ as a criterion, the soil zone subjected to vertical displacements extends to a depth of roughly three pile diameters measured from the pile shoulder. The results are in good accordance with the measurements published in [16].

Similar observations can be made considering the phase of upward pile motion. The displacements are mainly in opposite direction of the penetration phase. The extension of the affected soil zone is also similar for the three densities. Again, the horizontal displacements are smaller in dense sand, Fig. 11(e). Compared to the pile displacement, the vertical soil displacements are the largest in the case of VIB-HM-04, Fig. 11(d). This indicates that the short phase of upward motion in this test is qualitatively different compared to the other tests.

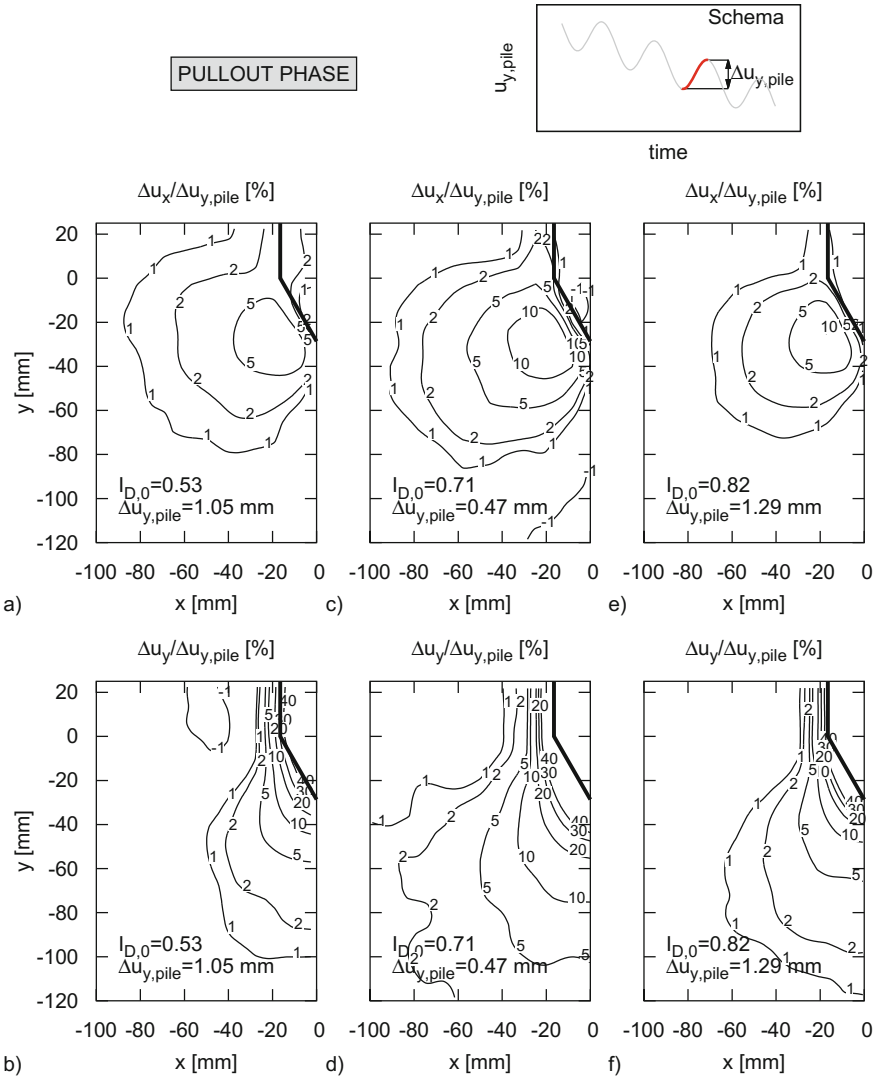

Fig. 11. Normalized incremental displacement fields obtained from DIC analysis for the pullout phase of the representative cycle: (a), (b) VIB-HM-06 ($I_{D,0} = 0.53$), (c), (d) VIB-HM-04 ($I_{D,0} = 0.71$) and (e), (f) VIB-HM-05 ($I_{D,0} = 0.82$)

4 Interpretation of the Penetration Mechanism

This paragraph summarizes the most important findings and tries to give an overview of the mechanism of pile penetration. The representative cycle of VIB-HM-05 is chosen due to the similitude to the so-called cavitational pile penetration mode [5,6].

Figure 12 shows a combination of results from DIC together with measurements on the pile and pore water pressure measurements for the penetration phase. Figure 12(a)–(d) contain the DIC measurements. Now, the incremental displacement fields are calculated for four sections: both, penetration and pullout phase are split into two sections each. The following characteristic curve points are used: (1) the beginning of penetration, (2) the maximum of pore water pressure in the penetration phase, (3) the beginning of upward pile motion, (4) the maximum of pore water pressure in the pullout phase and (5) the end of upward pile motion. Again, the incremental displacements are normalized with the pile displacement occurring in the corresponding section. Figure 12(e) and (f) provide the (already known) force-displacement curve and the combined illustration pore water pressure evolution and pile displacement. The curve points indicating the evaluated sections are marked. Figure 13 is equivalent to Fig. 12 but for the pullout phase.

A comparison of the Fig. 12(a), (b) and (c), (d) reveals that the deformation mechanism is qualitatively changing during the penetration phase. At the beginning of penetration from 1 to 2, only very localized deformations occur in direct vicinity to the pile tip, Fig. 12(a), (b). This corresponds to the section with very low soil resistance, Fig. 12(e), and excess pore water pressure build-up, Fig. 12(f). Cudmani [5,6] assumes that pile and soil have separated during upward pile motion leading to the formation of a gap below the pile toe and that this gap has to be closed in the first phase of penetration. However, even in the highest positions of the pile during the cycles, an opening of a gap has not been observed here. The section is rather seen as a consolidation phase for the soil directly below the pile tip. In the second section of the penetration phase from 2 to 3, a more extended deformation mechanism has developed. In [18] it is shown that the deformations occurring in this section are similar to those during monotonic pile penetration. Consequently, the section comprises the increase of soil resistance, Fig. 12(e), and a tendency for negative pore water pressures (dilative soil behavior), Fig. 12(f).

Like for the penetration phase, the split of the pullout phase also shows a different behavior in the two sections. Globally, the displacements are in opposite direction compared to the penetration phase. The beginning of upward motion from 3 to 4 is like a reflection of the end of penetration (2 to 3). One difference is that in the outer regions, vertical displacements downwards (against the pile motion) are observed. The end of upward motion from 4 to 5 corresponds more to the opposite of phase 1 to 2. The soil reaction force does not significantly change from 4 to 5, Fig. 13(e), but Fig. 13(f) shows that the excess pore water pressure changes from positive to negative in this phase. Whether this effect is a result of the transition from contractive to dilative soil behavior or of the extraction of pile volume can not be clarified. Although the differences between the two sections of the pullout phase are less pronounced as in the penetration phase, the combined interpretation of DIC and pore water pressure measurements reveals a qualitatively different behavior.

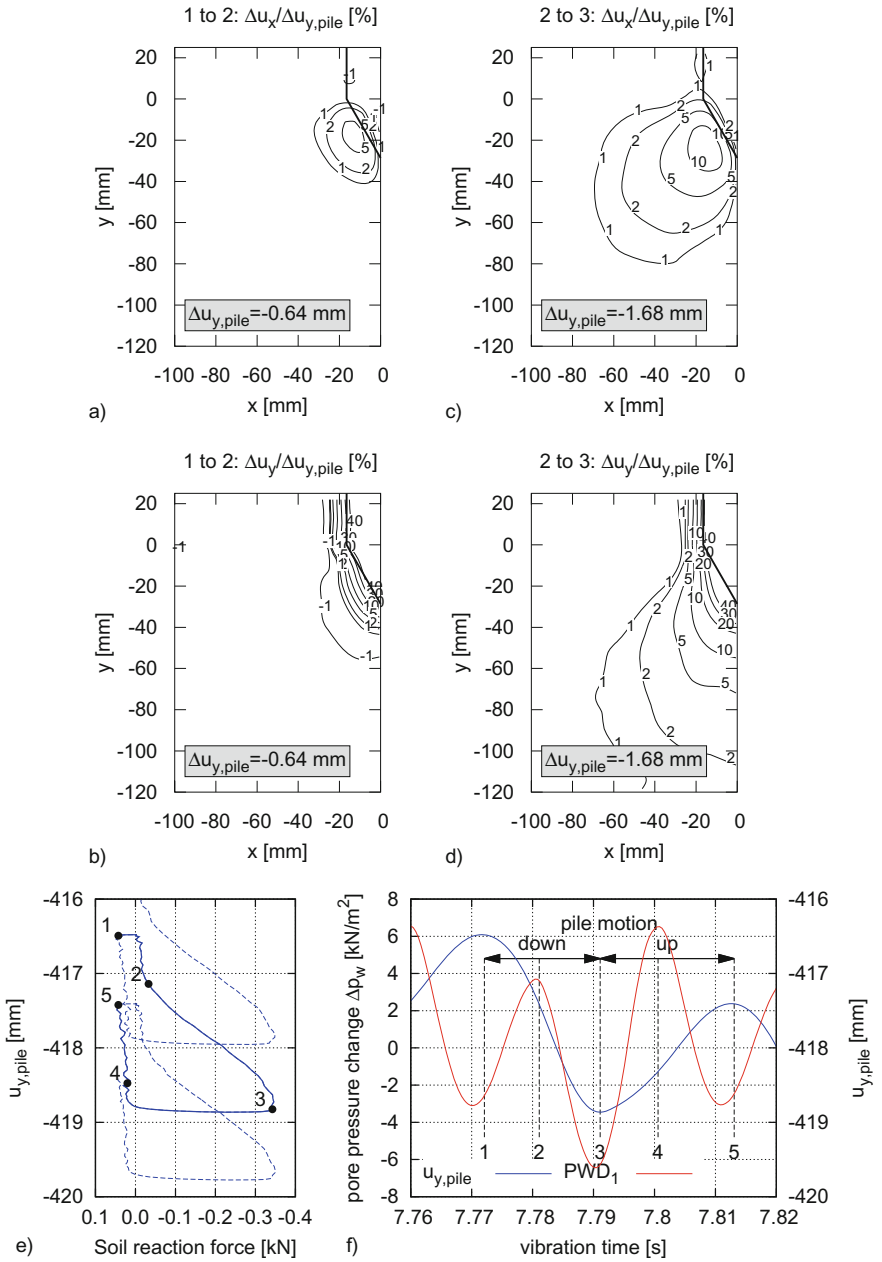

Fig. 12. (a)–(d) Normalized incremental displacement fields obtained from DIC analysis in the penetration phase of the representative cycle of test VIB-HM-05 ($I_{D,0} = 0.82$), (e) force-displacement curve and (f) pore water pressure evolution

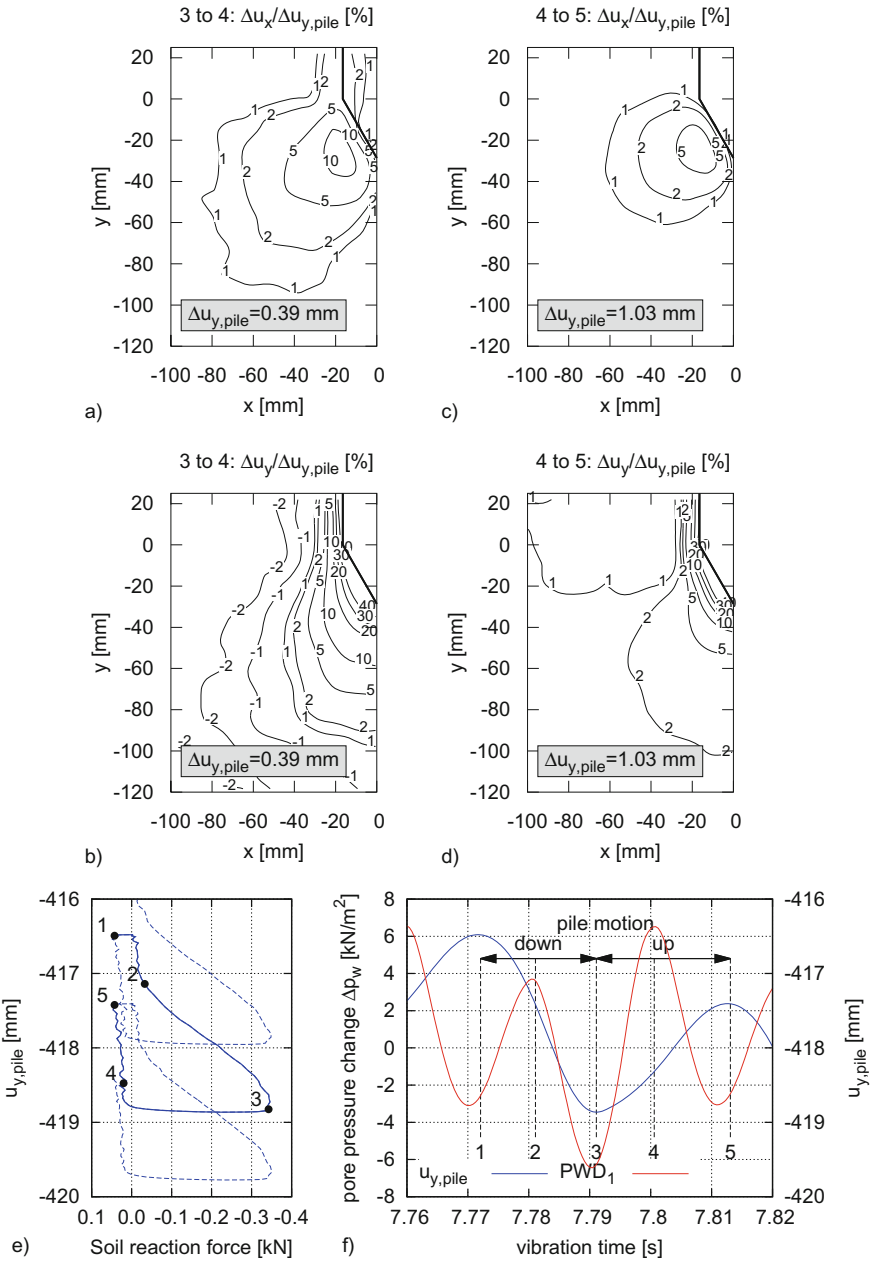

Fig. 13. (a)–(d) Normalized incremental displacement fields obtained from DIC analysis in the pullout phase of the representative cycle of test VIB-HM-05 ($I_{D,0} = 0.82$), (e) force-displacement curve and (f) pore water pressure evolution

The results globally support the interpretation of vibratory pile driving given in [16]. Vogelsang et al. [17] and Vogelsang [18] show that the evolution of cyclic soil resistance is mainly a result of the cyclic pile motion. Of course, a pore water pressure buildup in cohesionless soil is only possible in a vibratory test. A comparable dynamic pore water pressure evolution is reported by Triantafyllidis [12] for pile driving processes in an excavation pit. Due to the similarity with other laboratory experiments as well as with observations from practice, the tests are considered to provide a realistic insight into the typical mode of vibratory pile penetration and should be used for model validation purposes.

5 Conclusions

The penetration behavior of a vibro-driven pile is determined by the excitation (frequency, static and dynamic driving force), the dynamic properties of the vibrator-pile-soil system and the soil state (density, stress level and degree of saturation). The penetration velocity decreases with depth (increasing stress level) and density. A clear link between soil density and amplitude of pile motion could not be observed.

Although the evolution of pore water pressures near to the pile is not governing the penetration behavior in the presented tests, its measurement is very useful for the test interpretation. Pore water pressures appear to be an indicator for the volumetric soil behavior around the pile. Depending on the mean penetration velocity and the displacement amplitude of the pile in combination with the soil density, the pore water pressures either oscillate with same frequency as the excitation or are subject to a frequency doubling. A frequency doubling is considered to indicate a double alternation of contractancy and dilatancy in the soil during each excitation period.

The most commonly encountered penetration mode, so-called cavitational pile penetration, occurs for large displacement amplitudes with respect to moderate penetration velocities. The soil surrounding the pile has to provide the potential for the mobilization of dilatancy. After the reversals of pile motion, the soil behaves contractant. The mobilization of soil resistance is accompanied by dilative soil behavior.

As a next step, the experimental results presented here will be compared with numerical back-calculations. The FE techniques presented in [4] of this book will be applied for the simulations. In this context, emphasize will be given on the performance of different soil models to capture the observed volumetric soil behavior.

Notation

Forces are displayed in mechanical sign convention. Downward displacements are defined as negative. Horizontally, the center line of the pile corresponds to the origin of the coordinate system. The used terminology for the pile toe region is illustrated in Fig. 14(a). Pile toe is used in general for the lower end of the

pile, pile tip for the tapered region (if existent). Some important symbols are explained in Fig. 14(b).

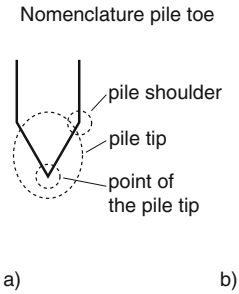

x, y	cartesian coordinates in the observation plane
y_0	initial vertical position of the pile shoulder
u_y, v_y, a_y	vertical displacement, velocity and acceleration
u_x	horizontal displacement (in observation plane)
$u_{y,pile}$	vertical position pile shoulder below sand surface
u_{ampl}	vertical pile displacement amplitude
F_h	pile head force
h_{sand}	sand height
d_{pile}	pile diameter
A_b	pile cross section
f	vibration frequency
p_w	pore water pressure

Fig. 14. (a) Nomenclature for the pile toe region and (b) notation used in the paper

Acknowlegdements. The work presented in this paper was supported by the German Research Foundation (DFG) as part of the research project "Central project of the researchers group FOR 1136 with demonstrator experiments". The authors acknowledge the financial support.

References

1. Arshad, M.I., Tehrani, F.S., Prezzi, M., Salgado, R.: Experimental study of cone penetration in silica sand using digital image correlation. Géotechnique **64**(7), 551–559 (2014)
2. Chow, F.C.: Field measurements of stress interactions between displacement piles in sand. Ground Eng. **28**(6), 36–40 (1995)
3. Chow, F.C., Jardine, R.J., Nauroy, J.F., Brucy, F.: Time-related increases in the shaft capacities of driven piles in sand. Géotechnique **47**(2), 353–361 (1997)
4. Chrisopoulos, S., Vogelsang, J., Triantafyllidis, T.: FE simulation of model tests on vibratory pile driving in saturated sand. In: Triantafyllidis, T. (ed.) Holistic Simulation of Geotechnical Installation Processes. LNACM, vol. 82, pp. 124–149. Springer, Cham (2017)
5. Cudmani, R.O., Huber, G., Gudehus, G.: Zyklische und dynamische Penetration nichtbindiger Böden. Workshop "Boden unter fast zyklischer Beanspruchung", Bochum (2000)
6. Cudmani, R.O.: Statische, alternierende und dynamische Penetration in nichtbindigen Böden. Dissertation, Publications of the Institute of Soil Mechanics and Rock Mechanics, vol. 152. University of Karlsruhe (2001)
7. Huber, G.: Vibrationsrammen: Großmaßstäbliche Versuche. Workshop Vibrationsrammen, Karlsruhe (1997)
8. O'Neill, M.W., Vipulanandan, C., Wong, D.: Laboratory modeling of vibro-driven piles. J. Geotech. Eng. **116**(8), 1190–1209 (1990)

9. Rodger, A.A., Littlejohn, G.: A study of vibratory pile driving in granular soils. Géotechnique **30**(3), 269–293 (1980)
10. Savidis, S.A., Aubram, D., Rackwitz, F.: Vibro-injection pile installation in sand: part II - numerical and experimental investigation. In: Triantafyllidis, T. (ed.) Holistic Simulation of Geotechnical Installation Processes - Numerical and Physical Modelling, pp. 103–131. Springer, Cham (2015)
11. SciPy community: SciPy reference guide - release 0.13.0 (2013)
12. Triantafyllidis, Th: Neue Erkenntnisse aus Messungen an tiefen Baugruben am Potsdamer Platz in Berlin. Bautechnik **75**(3), 133–154 (1998)
13. Vennemann, P.: JPIV-software package for particle image velocimetry (2007). http://www.jpiv.vennemann-online.de
14. Vielsack, P., Storz, M.: Dynamics of vibratory pile driving. In: Workshop "Vibrationsrammen", pp. 3–12. Karlsruhe (1997)
15. Viking, K.: The vibratory pile installation technique. In: Holeyman et Rocher-Lacoste, G. (ed.) TRANSVIB 2006, Editions du LCPC, pp. 65–82. Paris (2006)
16. Vogelsang, J., Huber, G., Triantafyllidis, T., Bender, T.: Interpretation of vibratory pile penetration based on digital image correlation. In: Triantafyllidis, T. (ed.) Holistic Simulation of Geotechnical Installation Processes - Benchmarks and Simulations, pp. 31–51. Springer, Cham (2016)
17. Vogelsang, J., Huber, G., Triantafyllidis, T.: Stress paths on displacement piles during monotonic and cyclic penetration. In: Triantafyllidis, T. (ed.) Holistic Simulation of Geotechnical Installation Processes. NNACM, vol. 82, pp. 29–52. Springer, Cham (2017)
18. Vogelsang, J.: Untersuchungen zu den Mechanismen der Pfahlrammung. Dissertation, Publications of the Institute of Soil Mechanics and Rock Mechanics, Karlsruhe Institute of Technology (2017, submitted)
19. White, D.J., Bolton, M.D.: Displacement and strain paths during plane-strain model pile installation in sand. Géotechnique **54**(6), 375–397 (2004)
20. Wong, D.: Driveability and load transfer characteristics of vibro-driven piles. Dissertation, Department of Civil and Environmental Engineering, University of Houston (1988)
21. Wong, D., O'Neill, M.W., Vipulanandan, C.: Modelling of vibratory pile driving in sand. Int. J. Num. Anal. Methods Geomech. **16**, 189–210 (1992)

FE Simulation of Model Tests on Vibratory Pile Driving in Saturated Sand

Stylianos Chrisopoulos(✉), Jakob Vogelsang, and Theodoros Triantafyllidis

Institute of Soil Mechanics and Rock Mechanics,
Karlsruhe Institute of Technology, Karlsruhe, Germany
stylianos.chrisopoulos@kit.edu

Abstract. The present study reports the extensive comparison of model tests with numerical simulations of vibro-driven pile installation in saturated sand. The purpose of the study is to validate existing simulation techniques and to investigate the ability of those to reproduce effects experimentally observed during pile installation. A limited number of cycles has been considered and the focus is placed on the cyclic evolution of soil deformations and stresses. Two axisymmetric FE models have been developed for the simulation of model tests. In the first, the pile-soil interaction is modeled in a simplified way by applying a sinusoidal displacement boundary condition at the soil-pile interface close to the pile toe. The second model simulates the performed model tests more realistically by including the pile-oscillator system. The **u**-p formulation has been adopted in both models for the dynamic analysis of fluid-saturated solids with nonzero permeability. A hypoplastic constitutive model with intergranular strain has been selected to describe the mechanical behavior of the soil. The soil displacements and the evolution of pile resistance are compared. The good agreement between the results confirms that the pile installation process can be satisfactory reproduced numerically.

Keywords: Saturated sand · Vibratory pile driving · Model tests

1 Introduction

Vibratory pile driving involves substantial stress redistribution in the underground. Especially in water-saturated soil, the installation process can lead to a significant reduction of the effective stresses and thus to soil shear stiffness degradation around the pile. Adjacent foundations and structures might therefore be subjected to inadmissible deformations and also the load-bearing behavior of a vibro-driven pile is strongly influenced by the installation process. Hence, there is a strong need for the development of appropriate calculation approaches and numerical methods to quantify the mentioned phenomena, not only from a researchers perspective but also from a practical point of view.

Difficulties concerning a realistic numerical simulation of vibratory pile penetration arise from the description of pile-soil interaction and the complicated deformation process in the soil around the pile, including large monotonic as well

T. Triantafyllidis (ed.), *Holistic Simulation of Geotechnical Installation Processes*,
Lecture Notes in Applied and Computational Mechanics 82, DOI 10.1007/978-3-319-52590-7_5

as cyclic deformations with alternating phases of very high and very low stress regime. The interaction of soil and pore fluid in water-saturated conditions leads to considerable additional challenges. Therefore, suitable modeling techniques and constitutive models have to fulfill very high requirements. Although there are several numerical studies simulating the pile driving process in saturated soil [6–8,12,21], most of them rely on simplifications and rough assumptions. Additionally, due to the fact that a validation of these methods has not been carried out, a reliable prediction of the effects of pile penetration is currently difficult and questionable.

A key issue of the simulation of vibratory pile driving below the groundwater table is the dynamic analysis of fluid-saturated solids with nonzero permeability. However, for example the commonly used finite-element program ABAQUS does not provide a built-in procedure for these types of simulations. Consequently, vibratory pile driving is often simulated in dry sand although in situ the penetration depths mostly reach the groundwater. If the presence of pore water is considered, its influence is either reduced to the buoyancy force [6–8] or locally undrained conditions are assumed [21]. In order to tackle this problem, a user-defined finite element has been used in the present study. The element is based on the **u**-p formulation and has been proposed and validated in [4].

In the present study, model tests on vibro-driven pile installation in saturated sand are compared with numerical simulations. The model validation is carried out based on the back-calculation of an exemplary test sequence that has already been extensively evaluated [19]. In this first validation step, a limited number of cycles has been considered, in order to justify the application of an implicit dynamic FE-formulation in combination with a hypoplastic constitutive soil model. Two axisymmetric FE models have been developed for the simulation of model tests, see Fig. 1.

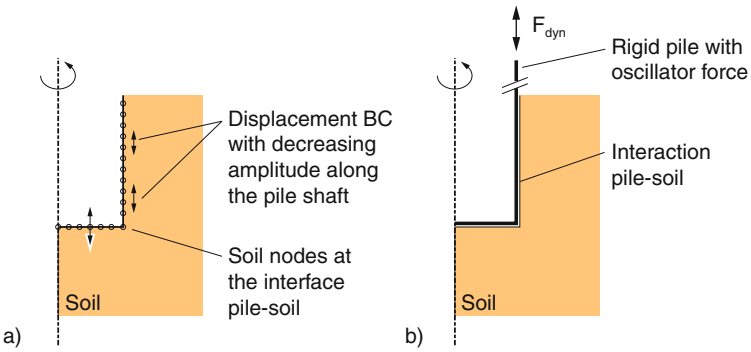

Fig. 1. (a) Simplified and (b) enhanced modeling technique

The simplified model has been developed in order to validate a simplified simulation technique, proposed in recent numerical studies [4,15,21]. Therein, the

pile-soil interaction is modeled by introducing a prescribed sinusoidal displacement boundary condition at the soil-pile interface. The maximum displacement amplitude is applied at the pile toe, while the amplitude vanishes along the pile shaft. The dynamic BVP is solved with zero and finite soil permeability. Firstly, the influence of soil permeability on the solution is investigated based on the numerical results. Subsequently, experimental and numerical results are compared based on the occurring soil displacements and displacement amplitudes.

The enhanced model overcomes some of the limitations of the first model by including the pile-oscillator system and a contact definition between soil and pile. Pile and oscillator are modeled as rigid bodies and vibrate due to a prescribed dynamic load at the oscillator. This setup enables the comparison of the penetration behavior of the pile between experiment and simulation. A detailed comparison of cyclic soil deformations is also provided in this paper. Accounting for the experiences with the simplified model, the second dynamic BVP is solved only for finite soil permeability.

2 Model Test Concept

The experimental set-up and the instrumentation for the model tests was developed by Vogelsang et al. [19], see also [20]. It is illustrated schematically in Fig. 2. The test container has a half cylindrical base area and a plane acrylic glass front sheet, which is used as an observation window for the measurement of the soil displacements around the pile using Digital Image Correlation (DIC) technique. A similar test set-up is used by Savidis et al. [16], Tehrani et al. [17] and Arshad et al. [1].

The model pile has an almost half-circular cross-section with a diameter of 33 mm and a flat-ending pile toe. The front and side view of the pile are shown in Fig. 2. The front part of the pile is covered by a combination of felt and PTFE (Teflon)-stripes, in order to minimize the friction between pile and observation window. Assuming that the friction between sand and wall is also low, the simplified consideration of a radially symmetric geometry of the model seems to be justified.

In the tests, the pile is pre-installed in a certain depth before it is subjected to vibrations for a short time period of a few seconds. During the test preparation, the dry sand is pluviated into water while the pile is already fixed in its initial position. A description of the test preparation methods and a discussion on sample homogeneity are given in [19,20]. It is intended to keep the pile penetration as low as possible. Therefore, the pile-oscillator system is suspended by a compensation spring that reduces the static driving force. The stress level in the soil due to gravity is very low and might be problematic for the calibration parameters used in the numerical simulation of the model tests. A moderately elevated stress level is achieved by application of a uniformly distributed load with a magnitude of 2 kN/m^2 on the ground surface.

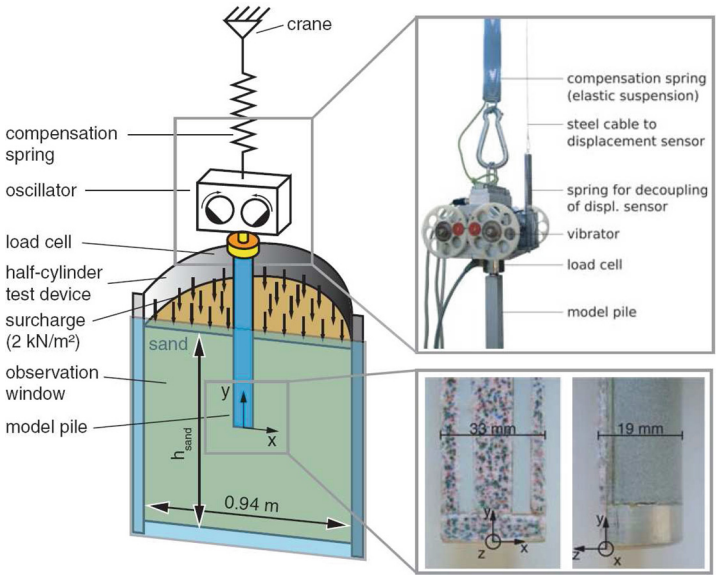

Fig. 2. Set-up of the experiments with detail photos of the pile-oscillator system and the pile toe

During the model tests, the region of interest around the pile toe is filmed with a high-speed camera providing approximately 15 images per cycle of vibration. The video files are then decomposed into individual images. The occurring deformations are evaluated using the Particle Image Velocimetry software JPIV [18] and a subsequent summation and strain calculation procedure [19,20]. In the test sequence evaluated here, the other measurements concern the pile head force and the global penetration. They are recorded with a frequency of 2400 Hz. A detailed description of the measurement methods and the evaluation procedures can be found in [20].

3 Test Material, Constitutive Model and Soil Parameters

A poorly graded medium quartz sand with sub-rounded grains has been used in the model tests. It is referred to in the literature as Karlsruhe Sand. Some important properties of the sand are given in Table 1. An extensive characterization of the material can be found in [20]. In the numerical simulations, the hypoplasticity constitutive model according to von Wolffersdorff [25] extended by the intergranular strain concept proposed by Niemunis and Herle [14] has been used to describe the granular soil behavior. The hypoplastic parameters of Karlsruhe sand, used in the present study are depicted in Table 2. The parameter set has been proposed for the test sand in [24] and has also been used for numerical simulations of vibro-penetration in [2,21].

Table 1. Properties of Karlsruhe Sand

Mean grain size	d_{50}	[mm]	0,55
Coefficient of uniformity	U	[-]	1,5
Critical friction angle	φ_c	[°]	32,8
Min. void ratio	e_{min}	[-]	0,549
Max. void ratio	e_{max}	[-]	0,851

Table 2. (a) Constitutive parameters of Karlsruhe Sand and (b) additional constitutive parameters of the extended hypoplastic model with intergranular strain

a)

φ_c[°]	h_s [MPa]	e_{c0}	e_{d0}	e_{i0}	α	β	n
32.8	5800	0.866	0.568	0.953	0.13	1.05	0.28

b)

R	m_R	m_T	β_r	χ
1×10^{-4}	5.0	5.0	0.2	1.0

The permeability coefficient k was determined by laboratory tests [2,20] and can be estimated for a given porosity n using Eq. 1, which corresponds to the Kozeny/Carman equation [3,11].

$$k(n) = \frac{1}{308} \frac{\gamma_w}{\eta_w} \frac{n^3}{(1-n)^2} d_w^2 \tag{1}$$

with γ_w the specific weight and $\eta_w = 1.37 \cdot 10^{-3}$ kN s/m^2 the dynamic viscosity of the water and $d_w = 0.5$ mm the effective grain size.

4 Simplified Finite Element Model

The radially symmetric FE-model with the initial and boundary conditions is shown in Fig. 3. The dimensions of the model are selected to coincide with the geometry of the model test. Figure 3(c) shows a detail of the FE-mesh at the pile toe vicinity. The size of the finite elements amounts about 1.5 mm near the pile and 25 mm at the outer boundary of the model. As in the experiment, a constant distributed load with a magnitude of 2 kN/m^2 is applied to the ground surface in order to avoid inadmissible tensile effective stresses and ensure better numerical stability. In order to approximate the influence of the side walls on the model test, no normal displacement and no shear stresses are selected at the outer boundary of the numerical model. A possibly occurring friction between sand and outer wall is thus neglected. As previously mentioned, the soil displacements occurring in the model test are evaluated near the pile toe with the Digital Image Correlation (DIC). The measured values are imposed as a time-varying boundary condition at the soil-pile interface of the FE model (see Fig. 3d), corresponding to the vibration of the pile. Consequently, the vertical displacement u_y is prescribed

by means of a composite function, which decomposes into a cyclic part due to pile vibration and a trend due to pile penetration:

$$u_y(t) = v_m\ t - u_{ampl}\left[1 - \cos(2\pi f t)\right], \tag{2}$$

with v_m the mean penetration velocity, u_{ampl} the pile displacement amplitude, f the vibration frequency and t the time from the beginning of vibration. This displacement boundary condition is imposed with the maximum amplitude u_{ampl} at the pile bottom and 5 mm upwards along the pile shaft. Subsequently, follows a 20 mm long transition zone in which the amplitude decreases linearly down to zero, see Fig. 3(c). The horizontal displacement at the soil-pile interface is set to zero. Concerning the pore water boundary conditions, the pore water pressure at the top surface is set to zero, while the other boundaries are taken to be impermeable.

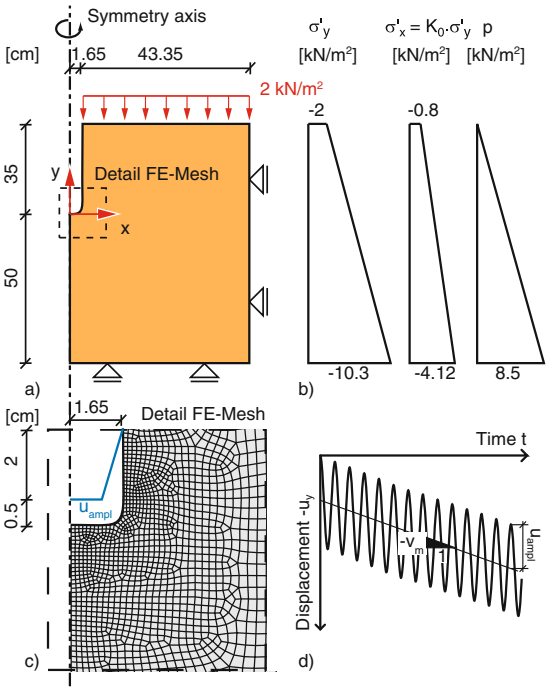

Fig. 3. Simplified FE model: (a) Geometry and boundary conditions, (b) initial conditions, (c) detail of the FE-mesh in the vicinity of pile toe and (d) prescribed displacement boundary condition at pile toe

The initial soil stresses are considered to be geostatic with the coefficient of earth pressure at rest K_0, calculated according to Jaky [10]:

$$K_0 = 1 - sin(\varphi'_p) = 0.4 \tag{3}$$

with $\varphi_p^{'} = 37^\circ$ corresponding approximately to the peak friction angle of the test sand for the given density. The initial distribution of the pore water pressure is assumed to be hydrostatic with the water level lying at the ground surface. The initial distribution of pore fluid pressure and effective stress components are illustrated schematically in Fig. 3b. The soil is considered to be fully saturated ($S_r = 1$) with the compression modulus of the fluid taken to be constant and equal to the bulk modulus of the pure water, $K_f = 2.2$ GPa. The initial density is taken from the model test, with $e_0 = 0.691$ corresponding to a medium dense sand with $I_{D,0} = 0.53$. The initial intergranular strain tensor components are set to zero.

The dynamic BVP has been solved with the FE-Software ABAQUS/STANDARD both with $k = 0$ and $k = 1.5 \cdot 10^{-3}$ m/s soil permeability, the last chosen accordingly to Eq. 1. As in [15], the simulation with $k = 0$ is performed using CAX4 elements available in ABAQUS/STANDARD by introducing the pore water pressure as an internal variable in the constitutive model. For the dynamic analysis of fluid-saturated solids with nonzero permeability the axisymmetric $u8p4$ `UEL`, presented and validated in [4], is used. The dynamic calculation is carried out with the implicit HHT integration schema [9] for the duration of 1 s. The time increment is taken to be constant and equal to 10^{-4} s, which corresponds to approximately 425 increments per cycle of vibration. In case of finite permeability, additional viscous stresses have been used for better numerical treatment of the dynamic step, as proposed in [4], with the values of viscosity coefficients λ and μ (see Eq. 5 in [4]), chosen small enough in order not to strongly influence the numerical solution. Furthermore, in order to avoid positive (tensile) mean effective stress in the soil, the small-stress correction according to [4] has been used.

Some important parameters of the simulation are summarized in Table 3.

Table 3. Parameters for the simulation of the model test

h_{sand} (m)	e_0 (−)	$I_{D,0}$ (%)	u_{ampl} (mm)	v_m (mm/s)	f (Hz)	K_0 (-)	K_f (GPa)	S_r (-)	k (m/s)
0.85	0.691	53	0.5	−11	23.5	0.4	2.2	1	0/0.0015

4.1 Observations from FE Simulations

In the present section, the interest is focused on the influence of soil permeability on the solution of the boundary value problem. The main target is placed on the cyclic evolution of stresses in the vicinity of the pile toe due to the pile vibration. Since the instrumentation of model tests does not allow stress measurements in the soil, a validation of these observations based on the present model experiment is not possible. Consequently, in this section only numerical simulation results will be presented.

Figures 4 and 5 show the distributions of mean effective stress near the pile toe after 10 and 23.5 cycles (at the end of simulation, $t = 1\,\mathrm{s}$), obtained from the solution of the numerical simulation calculated with $k = 0$ (Fig. 4) and $k = 1.5 \cdot 10^{-3}$ m/s (Fig. 5). The red area in the figures corresponds to a low-stress zone, in which the mean effective stress lies between 0 and -0.5 kPa, i.e. does not exceed 15% of the initial value at the pile toe level.

In the locally undrained case ($k = 0$), the mean effective stress is reduced close to the pile toe to nearly zero after several cycles of vibration. The low-stress zone is approximately circular and extends over an area of about two pile diameters after 1 s of vibration. For $k = 1.5 \cdot 10^{-3}$ m/s, a low-stress zone is only generated at the pile shaft above the pile shoulder. Throughout the entire simulation time, the area beneath the pile toe is subjected to a quasi-stationary change between large effective stress during pile penetration and small effective stress during upward pile motion.

This behavior is demonstrated in Fig. 6(a), where the evolution of mean effective stress at Point A (see Figs. 4 and 5) is plotted for the two different permeabilities. Point A is located about two pile diameters below the pile toe at a horizontal distance of a half pile radius from the symmetry axis. For $k = 1.5 \cdot 10^{-3}$ m/s, the mean effective stress decreases slightly and oscillates with an amplitude of circa 1 kPa, while it vanishes after several cycles of vibration in the case of $k = 0$ m/s. For $k = 1.5 \cdot 10^{-3}$ m/s, due to the consolidation process, the average pore water pressure does not increase during the vibration but oscillates slightly about its initial value, see Fig. 6(b). In the case of zero permeability, the displacement trend downwards leads to a gradual increase of the mean pore water pressure during the vibration without reaching an asymptotic state. For a great number of cycles, the accumulation of pore water pressure during pile penetration can lead to unrealistic pore pressure gradients.

Figure 7 shows the calculated displacement vectors in the soil after 1 s of vibration in the vicinity of the pile toe for the two investigated soil permeabilities. For $k = 0$, a significant zone with circular displacement paths about a stationary point, located in the low-stress zone, is observed. Similar to the observations in [15], the circular zone shows a significant accumulation of permanent displacements. Its existence is related to the assumption of locally undrained conditions in the soil. The rotation disappears for the solution with high soil permeability, as can be seen in Fig. 7 (right). For $k = 1.5 \cdot 10^{-3}$ m/s the direction of the soil displacements is almost gravitational. A comparable behavior occurs in the model tests, where no rotational zones were observed and the direction of the soil displacements is found to be almost in the gravitational direction (see Fig. 9 in the following section).

In the case of a finite permeability, the dynamic excitation is accompanied by a consolidation process in the soil. Figure 8 shows the calculated distribution of void ratio after 1 s of vibration. The initial void ratio is $e_0 = 0.691$ ($I_{D,0} = 0.53$) and corresponds to the light blue color in the figure. As can be seen from Fig. 8, there is a narrow zone with dilative behavior along the pile shaft and directly beneath the pile toe. Here, the soil behavior is governed by the large monotonic

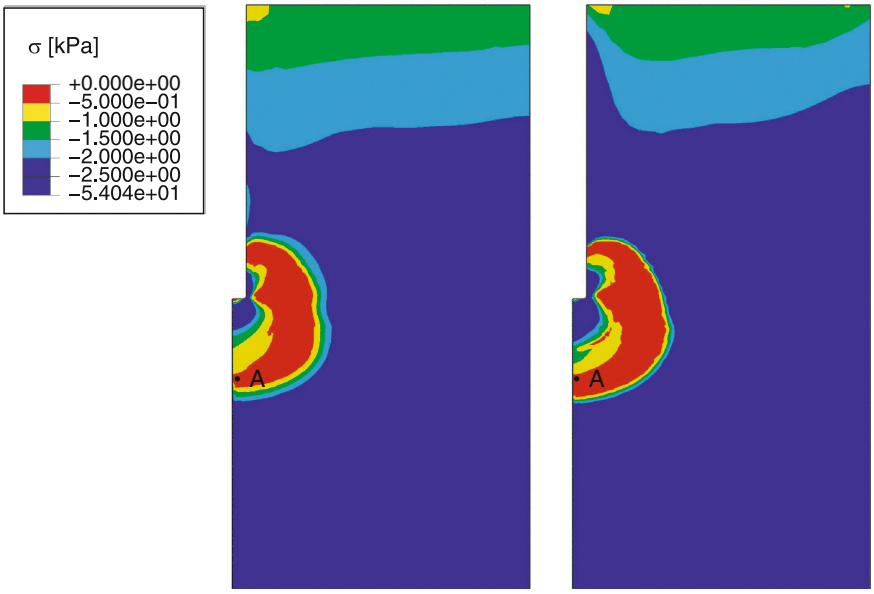

Fig. 4. Mean effective stress near the pile toe after 5 cycles (left) and 23.5 cycles (right) for $k = 0$

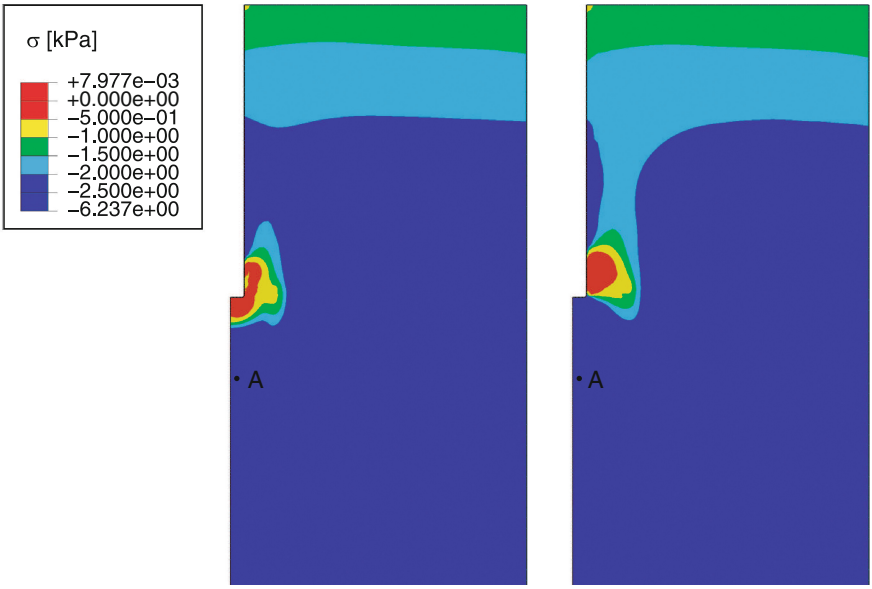

Fig. 5. Mean effective stress near the pile toe after 5 cycles (left) and 23.5 cycles (right) for $k = 1.5 \cdot 10^{-3}$ m/s

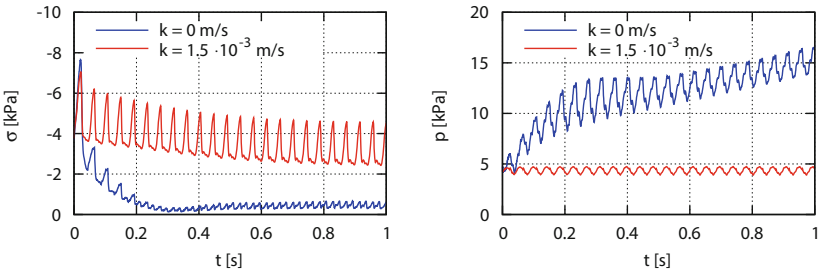

Fig. 6. (a) Mean effective stress (σ) and (b) pore pressure (p) at Point A (see Figs. 4 and 5) as functions of time for $k = 0$ m/s and for $k = 1.5 \cdot 10^{-3}$ m/s

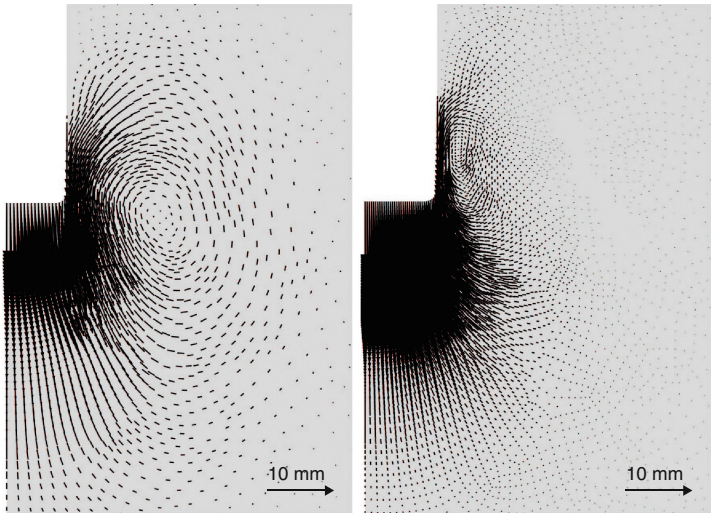

Fig. 7. Displacement vectors near to the pile toe after 1 s of vibration for $k = 0$ (left) and $k = 1.5 \cdot 10^{-3}$ m/s (right)

deformation due to the displacement trend downwards. Outside of this area, the cyclic deformation predominates, leading to an approximately circular soil compaction zone. The strongest densification occurs beneath the pile toe.

Figure 8 proves rather significant volume changes and thus, partly drained conditions in the soil. Based on these observations, the assumption of locally undrained conditions with almost constant void ratio cannot be justified. This consequence is also supported by the experimental observation of free particles that move cyclically within the soil skeleton due to water flow.

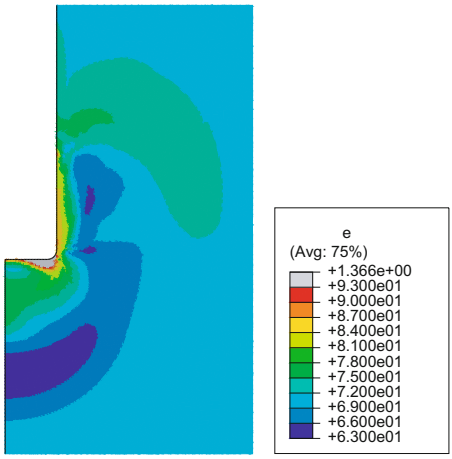

Fig. 8. Void ratio near to the pile toe after 1 s of vibration for $k = 1.5 \cdot 10^{-3}$ m/s

4.2 Comparison of FE- and Experimental Results

In this paragraph, the experimental results are compared with the simulations using the simplified FE model. Figure 9 shows the isolines of horizontal (a–c) and vertical (d–f) displacements after 1 s of vibration. The experimental results are depicted in the left column, the central column corresponds to the FE solution with undrained conditions and on the right hand side, the FE solution with $k = 1.5 \cdot 10^{-3}$ m/s is shown.

Beneath the pile toe, the horizontal displacements concentrate in a zone located below the pile shoulder in all three cases, Fig. 9(a)–(c). The soil is pushed outwards due to the imposed downward displacement at the pile-soil interface. The maximum values reach about 2 mm which corresponds to ca. 17% of the vertical pile displacement (12 mm after 1 s of vibration) resp. about 6% of the pile diameter (33 mm). The zone that is horizontally displaced is considerably larger in the case of undrained conditions. The experimental results lie somewhere in between the two FEM solutions but resemble more the drained solution. Above the pile toe, neither the experimental results nor the FEM solution with $k = 1.5 \cdot 10^{-3}$ m/s show significant horizontal displacements. Contrarily, for undrained conditions a clear motion towards the pile shaft is observed there.

The vertical displacements below the pile toe near to the symmetry axis are similar, Fig. 9(d)–(f). They remain greater than 50% of the vertical pile displacement up to about one pile diameter below the pile toe. However again, the undrained solution appears to slightly overestimate the occurring displacements for larger depths. Although a satisfactory agreement between the three solutions is observed beneath the pile toe, the existence of the zone with rotational displacement paths in the locally undrained case leads to a zone beside the pile toe with upward soil motion. As can be seen in Fig. 9(e) and (f), the model test results and the FEM results with $k = 1.5 \cdot 10^{-3}$ m/s show a global trend for settlements.

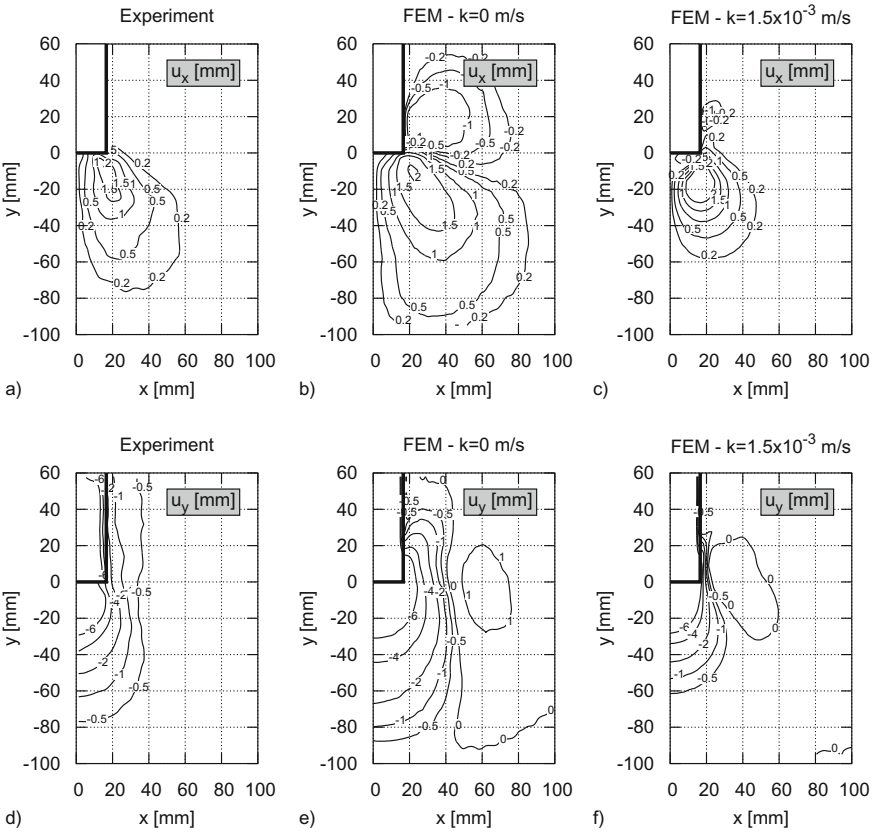

Fig. 9. (a)–(c) Horizontal and (d)–(e) vertical displacement fields after 1 s of vibration obtained in the model test (left), by the numerical simulations with $k = 0$ m/s (middle) and $k = 1.5 \cdot 10^{-3}$ m/s (right)

Figure 10 shows the fields of horizontal and vertical displacement amplitudes after 0.5 s of vibration. The figure is composed in the same way as Fig. 9.

The largest horizontal amplitudes occur below the pile shoulder and reach values up to 0.05 mm. The vertical amplitudes are about one magnitude larger, with 0.4 mm in the direct pile toe vicinity. The amplitude field calculated for partially drained conditions ($k = 1.5 \cdot 10^{-3}$ m/s) is in almost perfect agreement with the experimental results. The occurring amplitudes as well as the affected soil region are very similar, except for the very small vertical amplitudes in the outer regions. The FE solution obtained with undrained soil conditions shows a significant overestimation of the soil region subjected to vibrations. Moreover, the large displacement amplitudes above the pile toe and in the outer zones cannot be identified in the other results. It can be stated that the assumption of locally undrained conditions leads to a qualitative disagreement with experimental observations and numerical results with finite soil permeability.

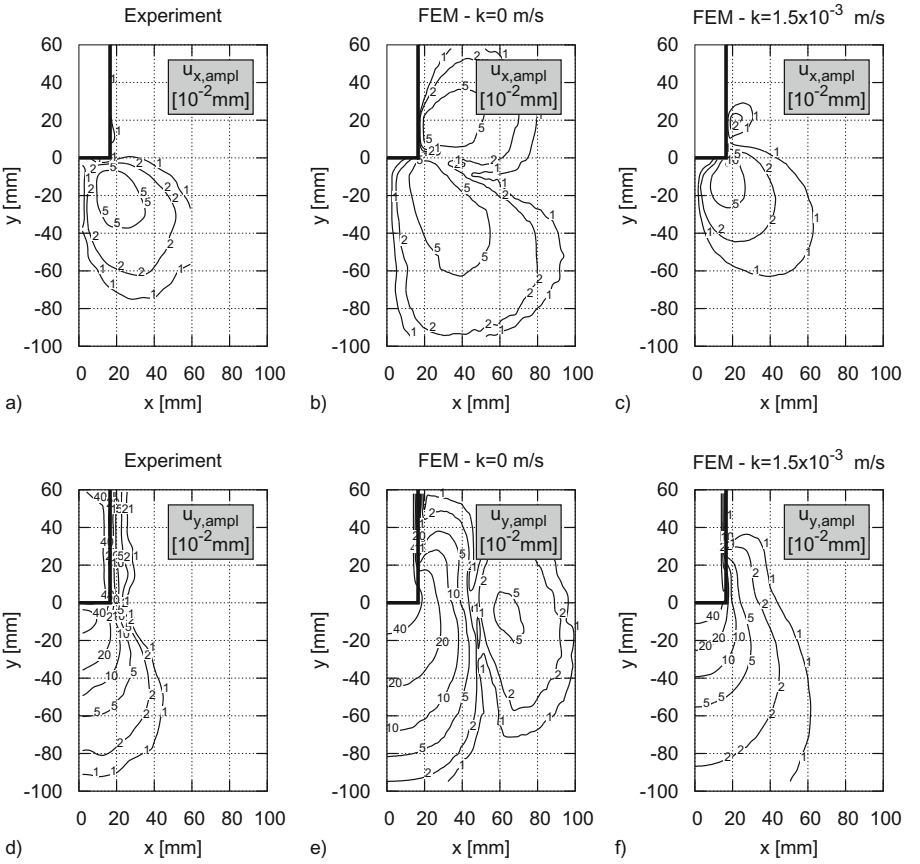

Fig. 10. (a)–(c) Horizontal and (d)–(e) vertical displacement amplitude fields after 0.5 s of vibration obtained in the model test (left), by the numerical simulations with $k = 0$ m/s (middle) and $k = 1.5 \cdot 10^{-3}$ m/s (right)

Although very satisfactory results are obtained from the solution with $k = 1.5 \cdot 10^{-3}$ m/s, the simplified FE model demands a knowledge of the experimental results at the pile-soil interface. Consequently, only limited conclusions can be drawn for the vibratory pile driving process, particularly for in situ conditions. Furthermore, important aspects such as the evolution of pile resistance during the pile installation process cannot be investigated. For a better understanding of the process, a second, enhanced FE-model is described in the following section.

5 Enhanced FE-Model

The enhanced model is also radially symmetric and includes not only the soil body but also the pile-oscillator system, as can be seen in Fig. 11. The model

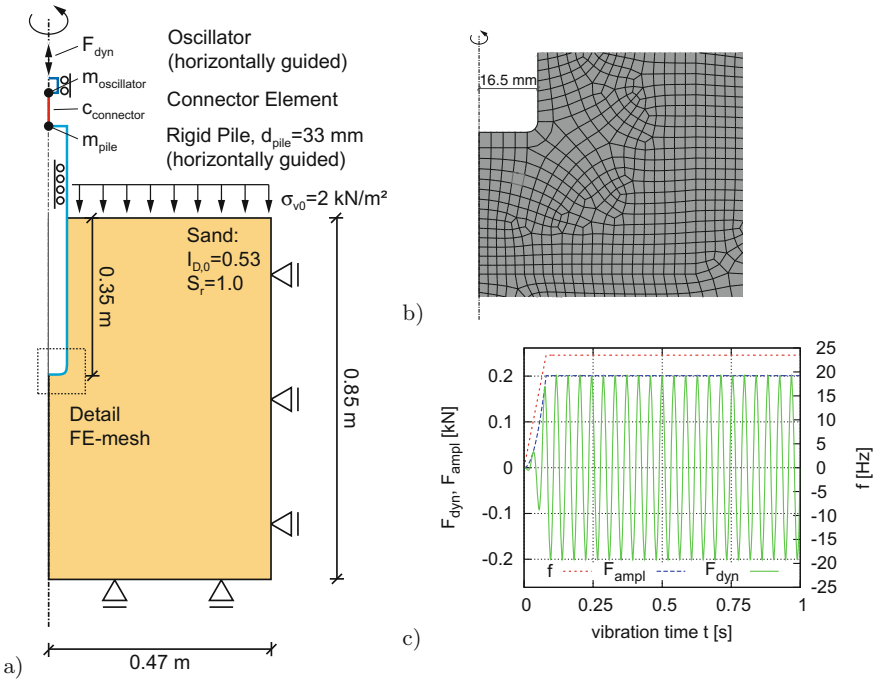

Fig. 11. Enhanced FE model: (a) Geometry and boundary conditions, (b) detail of the FE-mesh in the vicinity of pile toe and (c) evolution of the prescribed point load at oscillator

dimensions correspond to those of the simplified model. The pile and the oscillator are assumed to be horizontally guided rigid bodies, each with its own mass defined in the related reference point. The pile is connected to the oscillator with a 1-D connector element, which represents the load cell in model test. This model setup enables the output of the force at the location of force measurement in the experiment.

Figure 11(b) shows the FE mesh in the pile toe vicinity. The FE mesh in the soil is similar to the one of the simplified FE model, except directly beside and under the pile toe. The first row of elements in this region is rather coarse (size of elements about 6 mm) in order to reduce mesh distortion problems during the simulation of pile penetration. A frictionless node-to-surface contact formulation [5] has been used for the pile-soil interaction. A separation of the contact in the normal direction is excluded, since the opening of a gap filled with void (air) is physically not justified. Like in the simplified model, a constant distributed load with 2 kN/m^2 magnitude is applied to the ground surface and the normal displacement and the shear stresses at the outer boundaries are taken to be zero. At the pile toe and along the pile shaft the contact to the pile forms the boundary condition for the soil. The hydraulic boundary conditions as well

as the initial conditions and material parameters for the soil body are the same as those in the simplified FE model.

The calculation is performed in ABAQUS/STANDARD with $k = 1.5 \cdot 10^{-3}$ m/s and consists of three steps: In the first step, pile and oscillator are fixed and the initial geostatic equilibrium is calculated. In the second step, pile and oscillator are set free in vertical direction and move slightly downwards due to their own weight without the existence of inertia forces. The last step is a dynamic calculation step, where the excitation is applied as a prescribed dynamic excitation of the oscillator. The evolution of the load is shown in Fig. 11(c). In the experiment, the oscillator reaches the full vibration frequency and thus, the oscillating force after about two vibration periods. This behavior is approximated in the FE model. The dynamic calculation step was carried out according the implicit HHT integration schema with a constant time increment of 10^{-4} s. Similar to the simplified model, the small stress correction and small viscous stresses have been used.

For the comparison of the FE results ("full" model) and the model test results (almost "half" model), the masses of oscillator and pile as well as the force amplitude and the connector element stiffness are scaled by the ratio of the cross-sections of full- and half pile (scaling factor equal to 1.73). Thereby remains the free amplitude of the pile-oscillator system unchanged and the dynamic behavior of the total system is only slightly influenced. The results are compared based on the occurring soil reaction force. This force is the result of the pile head force subtracted by the inertia force of the pile. It also includes pore pressures effects. Comparability between the force measurements and simulation results is achieved by division by the cross-section of the pile. The result is named as related soil reaction force:

$$(F_H - m_{pile}\ a_{pile})/A_b \tag{4}$$

with F_H the pile head force, m_{pile} and a_{pile} the mass and acceleration of the pile and A_b the pile cross-section at the toe. It should already be noted here that in the experiment, F_H also includes system friction between pile and front sheet.

Some important parameters of the simulation with the enhanced model are summarized in Table 4.

Table 4. Parameters for the simulation of the model test with the enhanced model

h_{sand} (m)	e_0 (−)	$I_{D,0}$ (%)	m_{pile} (kg)	$m_{oscillator}$ (kg)	$c_{connector}$ (kN/mm)	f (Hz)	K_0 (-)	K_f (GPa)	S_r (-)	k (m/s)
0.85	0.691	53	2.25	11.4	173	23.5	0.4	2.2	1	0.0015

5.1 Comparison of Numerical and Experimental Results

The pile penetration behavior is compared in Fig. 12. Figure 12(a) shows the evolution of measured and calculated pile displacements. Figure 12(b) depicts in

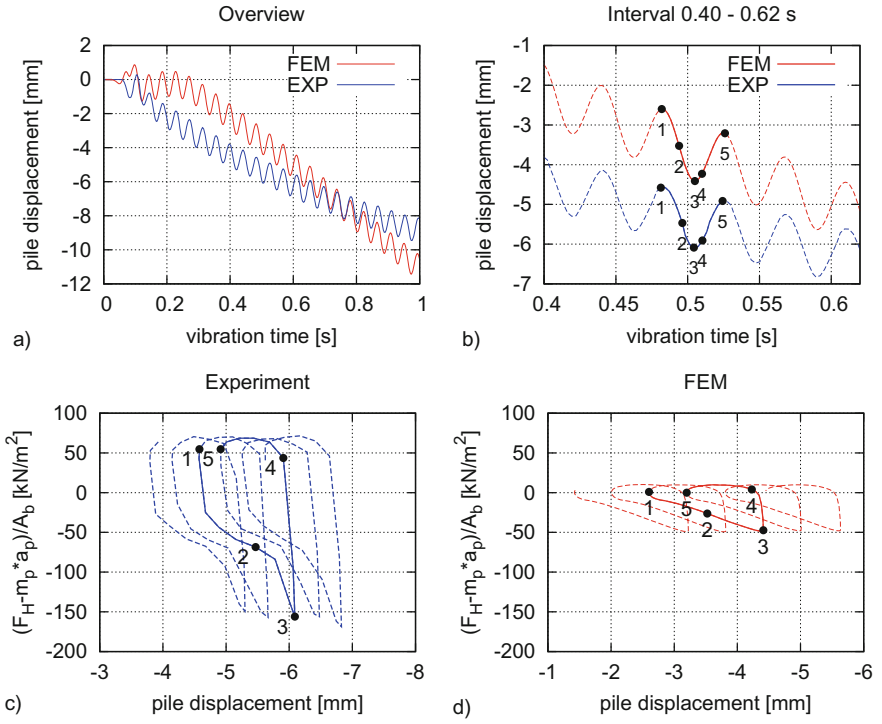

Fig. 12. (a) Evolution of measured and calculated pile displacements during the pile vibration, (b)–(d) detailed analysis of the section from 0.4 to 0.6 s: (b) evolution of pile displacement (c) related soil reaction force during pile penetration for the model test and (d) for the FE- simulation ($m_p = m_{pile}$ and $a_p = a_{pile}$)

detail the time period from 0.4 to 0.62 s of Fig. 12(a). The cycle at about 0.5 s is selected as a representative cycle for the comparison of the results and is marked with five points. The measured and calculated related soil reaction force during pile penetration is compared in Fig. 12(c) and (d).

Apart from the first cycles a qualitatively similar behavior is observed in Fig. 12(a). After about 0.3 s, a quasi-steady state is reached with approximately constant mean penetration velocity. The oscillation amplitude is also similar, which indicates a successful transmission between the "full" simulation model and the "half" experimental model. However, the pile penetrates faster in the simulation than in model test. The penetration per cycle amounts about 0.65 mm in the simulation, while it is only 0.4 mm in the test.

The cycles of the force-displacement curves in Fig. 12(c) and (d) differ in shape and size between simulation and model test. Although the penetration per cycle is greater in the simulation, the maximum mobilized soil reaction force is only about a third of that in the experiment. Moreover, the characteristic S-shape of the evolution of penetration resistance in the test as described in

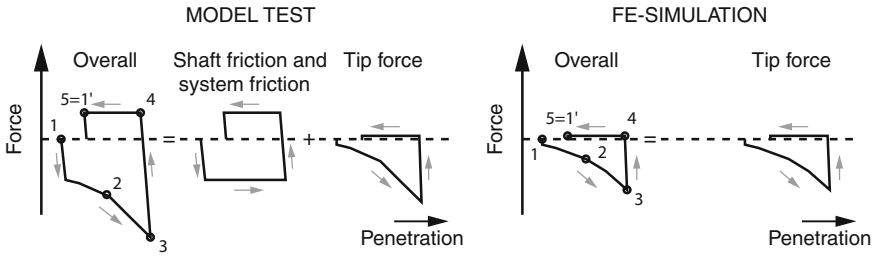

Fig. 13. Schematic explanation of the characteristics of the force curve in the model test and the numerical simulation

[19,20] is not evident in the simulation. The numerical model fails to reproduce the large force amplitude between the marked points 2 and 4. In the experiment, this difference is a result of the pile shaft friction and the friction between pile and front sheet. These effects are excluded in the numerical simulation. However, it can be assumed, that this simplification at least partly causes the observed differences in terms of penetration rate, see Fig. 12(a). Subtracting frictional influences from the experimental soil reaction force leads to a more realistic force amplitude compared to the simulation (see the schematic explanation Fig. 13). However, there is still a difference in the mobilized soil resistance.

In order to prove the above explanation, we introduce a dashpot feature in the FE model, Fig. 14. The dashpot connects the pile to the ground, thus, the

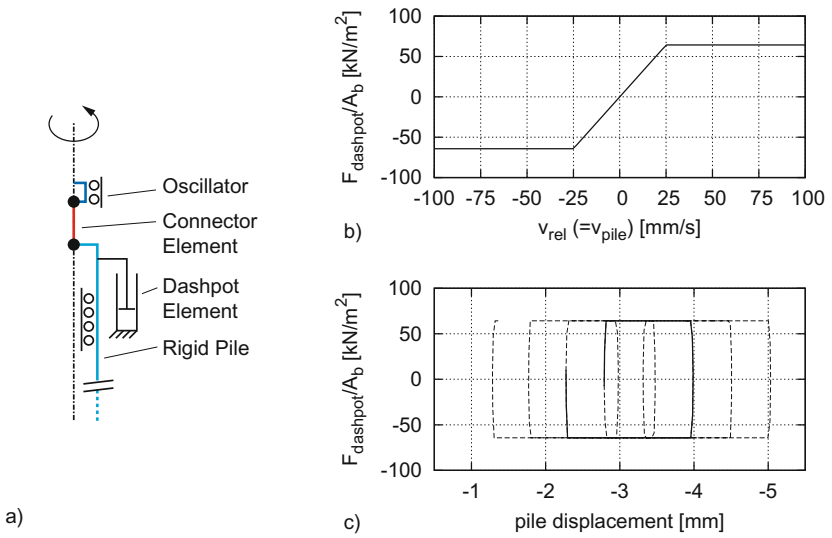

Fig. 14. (a) Dashpot element attached to the pile to substitute system friction effects, (b) characteristic curve and (c) related force-displacement curve of the dashpot

pile velocity v_{pile} corresponds to the relative velocity v_{rel}. The characteristic curve of the dashpot and the resulting force-displacement relationship for the simulated test are given in Fig. 14. Due to the velocity-based definition of the characteristic curve, immediately before the reversal points of pile motion, the resulting force differs slightly from a typical friction model.

It should be noted that by modeling the dashpot, it is not intended to propose a universal model to substitute the shaft friction. Shaft friction depends on the normal stresses acting on the shaft and the ultimate shaft friction is usually not constant throughout the process. However, it has been experimentally observed that system friction predominates in the present case and that its limit value is relatively constant. This system friction influences the penetration behavior of the pile. The purpose of the dashpot feature here is to achieve a better comparability between experiment and simulation by introducing effects that are not incorporated in the numerical model.

Figure 15 shows the comparison of experimental and numerical results like Fig. 12, but with the dashpot. The penetration behavior in the simulation is now more similar to the experiment, indicating a beneficial performance of the dashpot. Also the evolution of penetration resistance is reproduced better. However,

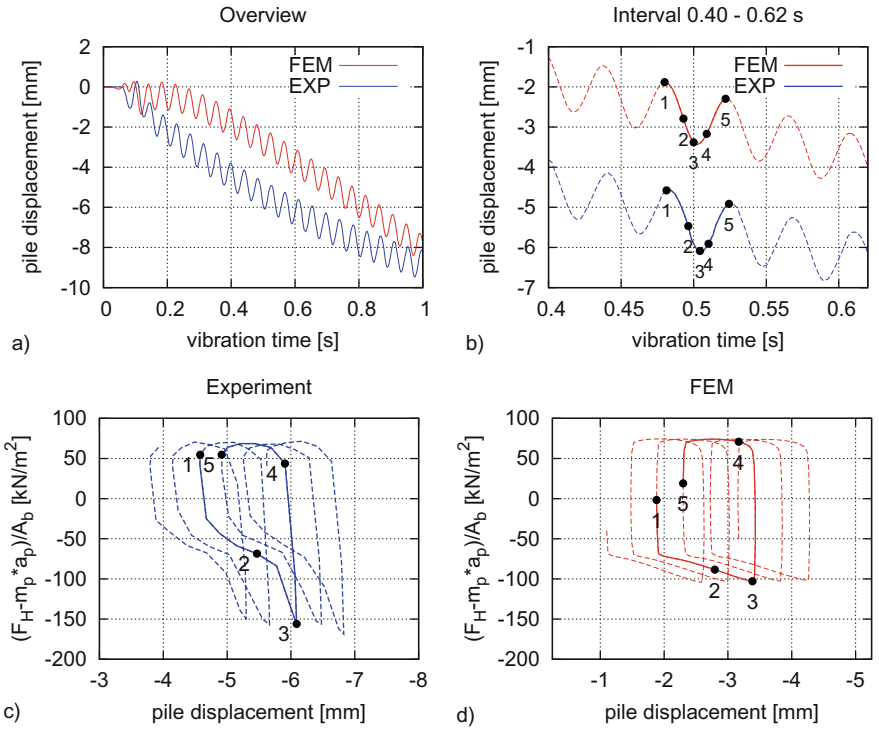

Fig. 15. The same as in Fig. 12 for the solution with the dashpot ($m_p = m_{pile}$ and $a_p = a_{pile}$)

the strong increase of pile resistance between the points 2 and 3 is still missing in the simulation. The reason for this discrepancy will be discussed later on.

Figures 16 and 17 compare the measured and calculated incremental displacement fields near the pile toe for the representative cycle (highlighted cycle in Fig. 15). Figure 16 presents the results during the penetration phase and Fig. 17 during the phase of the upward pile motion. Both phases are divided into two sections between the marked points $1 \div 2$ and $2 \div 3$ respectively $3 \div 4$ and $4 \div 5$, see Fig. 15(b). The images on the left show the horizontal displacements whereas the vertical displacements are depicted in the images on the right. The left part of each image illustrates the experimental results and the right the results obtained from the FE simulation. As can be seen in Fig. 15(b), the displacement amplitudes are almost identical and thus a direct comparison of the displacement fields is possible.

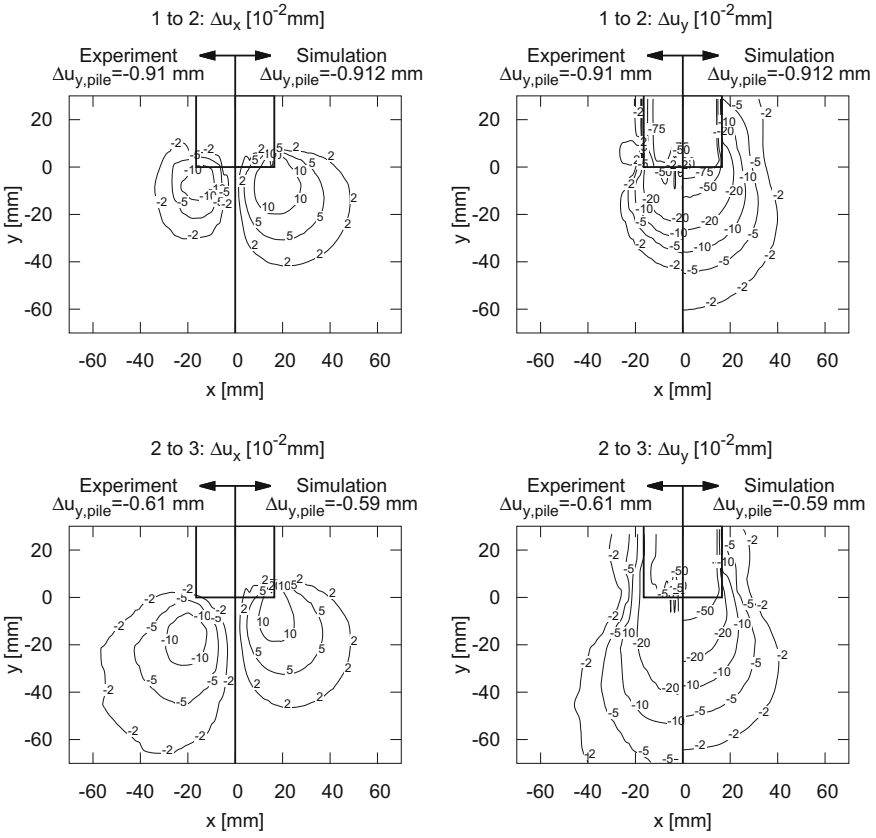

Fig. 16. Comparison of incremental displacement fields for the representative cycle during the penetration phase $1 \div 2$ (above) and $2 \div 3$ (below). The horizontal displacements (left) and the vertical (right) are shown in the images. The left part of each image depicts the experimental results and the right the FE-simulation.

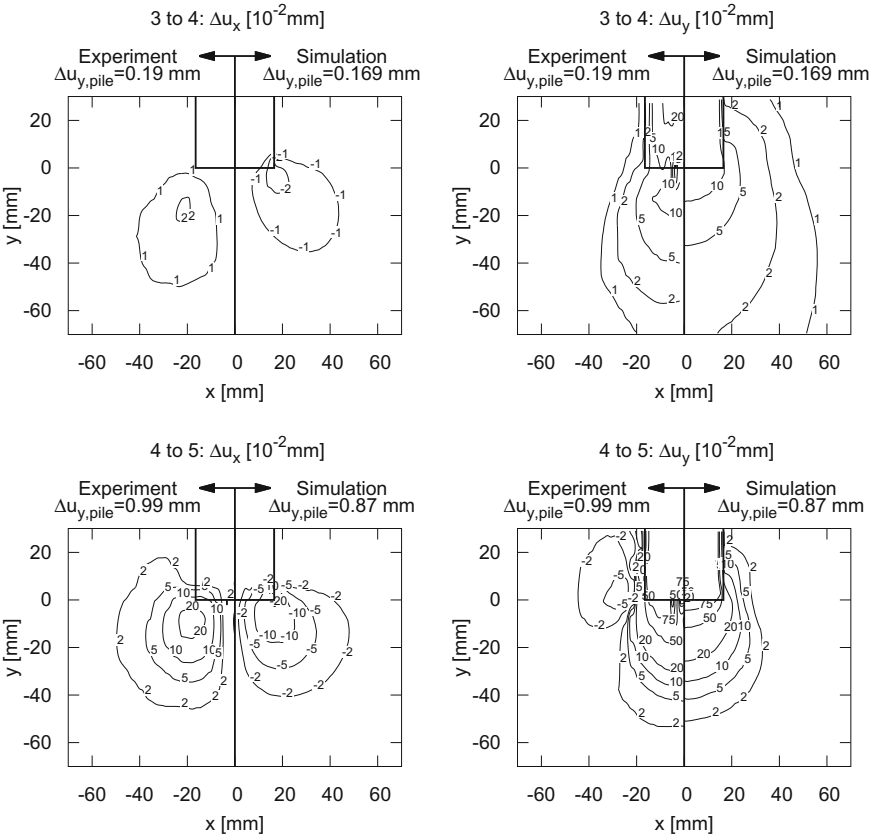

Fig. 17. Comparison of incremental displacement fields for the representative cycle during during the upward pile motion phase $3 \div 4$ (above) and $4 \div 5$ (below). The horizontal displacements (left) and the vertical (right) are shown in the images. The left part of each image depicts the experimental results and the right the FE-simulation.

Comparing the images, the following observations can be made:

- Phase $1 \div 2$: There is a good agreement between numerical and experimental results. Both reveal soil displacements directed away from pile toe in a spherical area of about two pile diameters. However, compared with the model test the numerical simulation overestimates the soil displacements.
- Phase $2 \div 3$: The soil displacements are qualitatively similar to Phase $1 \div 2$. In the experiment, a deeper and larger zone of the soil is affected compared to the first phase of penetration. The numerical results do not exhibit significant differences to the preceding phase.
- Phase $3 \div 4$: Due to the sharp decrease of tip pressure after the reversal of pile motion, a slight uplift and horizontal soil movement towards the pile is

observed. The vertical displacement field is similar to the previous phase $2 \div 3$, but inversed. Model test and simulation results are in good agreement.
– Phase $4 \div 5$: The deformation mechanism corresponds to the Phase $1 \div 2$ in opposite direction. Directly below the pile toe, the soil is moved to the symmetry axis following the vertical motion of the pile. The simulation reproduces this mechanism qualitatively and quantitatively with almost perfect agreement.

For the sake of brevity, the incremental displacement fields obtained from the simulations without the dashpot feature are not presented here. However, it should be noted that they are also in very good accordance with the experimental results.

Figure 18 illustrates the logarithmic volumetric soil deformation ε_{vol} depending on the pile displacement for the representative cycle (see Fig. 15) for two selected locations around the pile toe (named element A and C following the nomenclature in [19]). Element A is located below the pile toe while element C lies slightly beside, see Fig. 18(a). In Fig. 18(b)–(e), the experimental results are compared with the results obtained from the numerical simulation. The procedure for the calculation of volumetric strain in the experiment has been presented in [19]. The volumetric strains are set to zero at the beginning of the highlighted cycle.

Experiment and simulation show a considerable oscillation of volumetric strain, which proves the presence of at least partially drained conditions in the soil. At element A, the largest amplitude of volumetric strain is observed. In the model test, the peak-to-peak amplitude amounts 1.7% at element A resp. only 0.5% at element C. The numerical simulation clearly underestimates the changes of volumetric strain (0.5% at element A and 0.25% at C).

The numerical simulation reproduces the contractant soil behavior during Phase 1–2 but fails to mobilize dilatancy, that is experimentally observed towards the end of the downward pile motion (Phase 2–3). The dilatant phase in the experiment corresponds to the phase with strong increase of penetration resistance (between the points 2 and 3 in Fig. 15(c)) and results in a deeper and larger deformation mechanism (see Phase 2–3 in Fig. 16). On the other hand, the lack of dilatancy in the simulation leads to the almost linear increase of soil resistance during the downward pile motion (Fig. 15(d)) and very similar incremental displacement fields for the two penetration phases (Fig. 16). During the upward pile motion, generally a volume increase is observed, which is more pronounced in the experiment. However, in the experiment, at element C the reversal of pile motion is accompanied by a strain reversal and a slight contractant soil behavior (between points 3 and 4 in Fig. 18(d)), which is not evident in the simulation.

The inability of simulation to reproduce the effects mentioned above is related with the ineffective performance of the hypoplastic constitutive model to describe some issues of cyclic soil behavior. Important deficiencies of the applied hypoplastic model will be discussed in the following paragraph based on element tests.

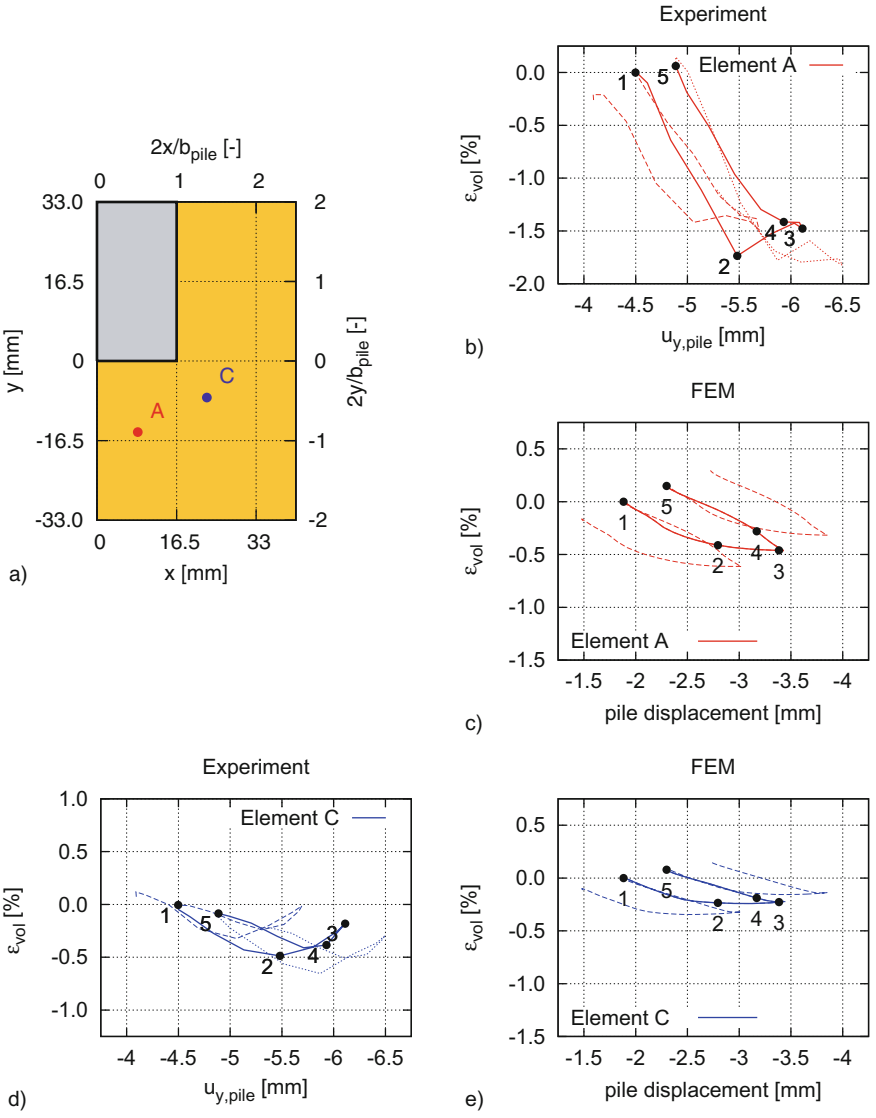

Fig. 18. (a) Volumetric strain plotted versus the pile displacement for the representative cycle (see Fig. 15b) at three selected points: (a) Location of the selected points, (b)–(d) experimental and numerical results at the selected points

5.2 Hypoplasticity in Cyclic Triaxial Element Tests

Two cyclic drained triaxial tests have been carried out and are recalculated in element tests via the software ABAQUS/STANDARD. The two triaxial tests imitate typical loading paths of pile penetration. In both tests (named Triax A and Triax B), a large monotonic deformation is interrupted by phases of

unloading, in Triax A without and in Triax B with shear stress reversal. The tested sand was initially medium dense and the initial void ratios similar. The conducted test paths are:

– Triax A: alternation of monotonic triaxial compression of $\Delta\varepsilon_1 = -4\%$ followed by unloading to $q = 0$
– Triax B: repetition of cycles consisting of a monotonic triaxial compression of $\Delta\varepsilon_1 = -4\%$ and a monotonic triaxial extension of $\Delta\varepsilon_1 = 2\%$

For the back-calculations, the same hypoplastic model and parameters as described in Chap. 3 have been used. Figure 19 shows a comparison of test and simulation results.

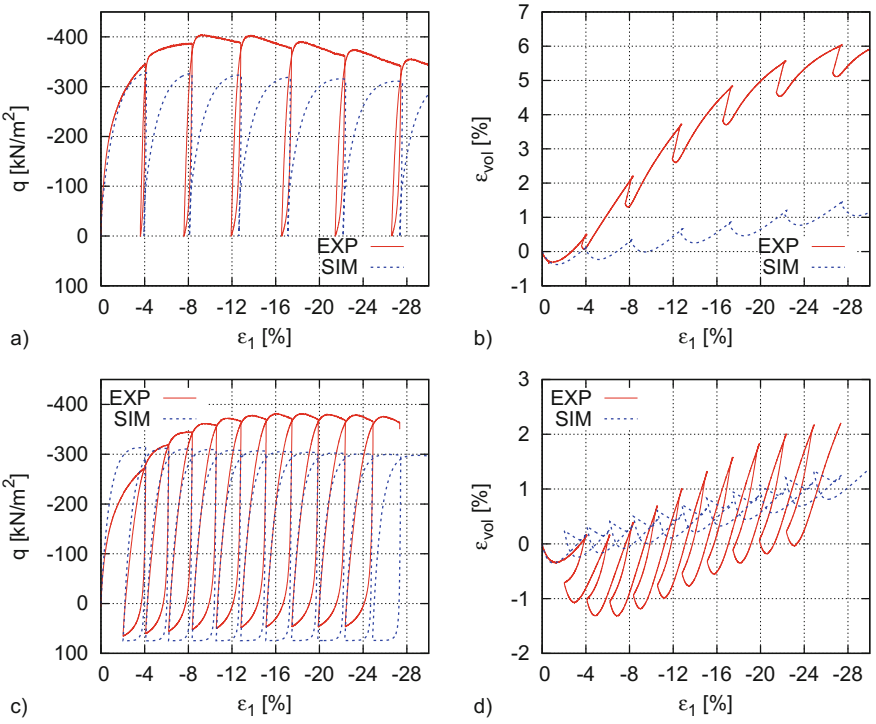

Fig. 19. Back calculation of drained cyclic triaxial tests: (a), (b) Triax A ($e_0 = 0.654$, $I_{D,0} = 0.66$) and (c), (d) Triax B ($e_0 = 0.668$, $I_{D,0} = 0.62$)

Both experiments show a global trend to dilatancy due to the large monotonic portion of the deformation. Cyclic deformation without shear stress reversal in Triax A leads to stronger dilatancy than it is the case in Test B with shear stress reversal. The unloading phases are associated with significant contractant material behavior, which is more pronounced in Test B (with shear stress

reversal). During reloading, the material continues to contract slightly before a strong mobilization of dilatancy is observed. The volumetric strain amplitudes are about 0.5% for Triax A and 1% for Test B respectively. The reloading stiffness is lower in Test B than in Triax A.

Comparison with back-calculations reveal considerable problems for hypoplasticity to realistically reproduce the test results. The most important shortcomings of the hypoplastic model are a lack of contractancy during unloading, a too long phase of contractant behavior during reloading and too weak mobilization of dilatancy subsequently. Similar shortcomings have been observed and described by Niemunis et al. [13] and Wichtmann [23]. From these deficiencies arise the major problems of the numerical simulation to reproduce the experimental observations, such as the evolution of pile resistance and the penetration velocity (see Fig. 15). Recently developed constitutive models, like neohypoplasticity [13], aim to improve the described deficiencies of the commonly used hypoplasticity model. There is reasonable hope that by implementation of a better description of soil behavior within the FE framework of the present study, enhanced simulations of vibro-penetration can be achieved.

6 Closing Remarks

Vibratory pile driving in saturated soil has been intensely studied by means of Finite Element simulations with help of a user-defined element in the framework of an **u**-p formulation. A simplified and an enhanced model have been developed and used to back-calculate model test results.

The simplified solution technique proposed in [4,15,21], regardless its rough simplifications with the prescribed sinusoidal displacement boundary condition, can be used to study the soil deformations around a vibrating pile if the considered time period and the occurring pile penetration is limited. The assumption of zero soil permeability affects the numerical solution and leads to results that have not been confirmed by experimental observations, notably the formation of a zone with rotational displacement patterns around the pile toe and an unrealistic build-up of pore water pressure. Consequently, the assumption of locally undrained conditions in the soil seems to be inappropriate for the numerical simulation of vibratory pile driving. The solution with the actual soil permeability achieves to reproduce adequately the soil deformations in the vicinity of the pile during the vibratory pile driving process.

The good agreement between the results of the enhanced FE-model and the model test confirms that the pile installation process can be satisfactory reproduced numerically. The differences observed in the developed pile resistance and penetration velocity do not originate from the numerical method, but rather from the inability of the hypoplastic model to describe adequately the soil behavior for the occurring deformation paths.

As a next validation step, the developed enhanced FE model will be applied for the simulation of new vibratory tests, presented in [22] in this book. These experiments include also large pile penetration effects and provide an improved instrumentation to enable pore pressure measurements.

Acknowledgments. The study was financed by the Deutsche Forschungsgemeinschaft as part of the Research Unit FOR 1136 'Simulation of geotechnical construction processes with holistic consideration of the stress strain soil behaviour', Subproject 6 'Soil deformations close to retaining walls due to vibration excitations'.

References

1. Arshad, M.I., Tehrani, F.S., Prezzi, M., Salgado, R.: Experimental study of cone penetration in silica sand using digital image correlation. Géotechnique **64**(7), 551–569 (2014)
2. Bender, T.: Numerische und experimentelle Simulation der Vibrationsrammung von Pfählen in wassergesättigtem Sand. Diploma thesis. Institute of Soil Mechanics and Rock Mechanics, Karlsruhe Institute of Technology (2015)
3. Carman, P.C.: Permeability of saturated sands, soils and clays. J. Agric. Sci. **29**, 263–273 (1937)
4. Chrisopoulos, S., Osinov, V.A., Triantafyllidis, T.: Dynamic problem for the deformation of saturated soil in the vicinity of a vibrating pile toe. In: Triantafyllidis, T. (ed.) Holistic Simulation of Geotechnical Installation Processes. Benchmarks and Simulations, pp. 53–67. Springer, Cham (2016)
5. Dassault Systèmes Simulia: Abaqus Analysis User's Manual. Version 6.14 Documentation (2014)
6. Grabe, J., Mahutka, K.-P.: Finite-Elemente-Analyse zur Vibrationsrammung von Pfählen. Bautechnik **82**(9), 632–640 (2005)
7. Grabe, J., Henke, S., Schümann, B.: Numerical simulation of pile driving in the passive earth pressure zone of excavation support walls. Bautechnik Special issue 2009 - Geotechnical Engineering, pp. 40–45 (2009)
8. Henke, S.: Influence of pile installation on adjacent structures. Int. J. Numer. Anal. Meth. Geomech. **34**, 1191–1210 (2010)
9. Hilber, H.M., Hughes, T.J.R., Taylor, R.L.: Improved numerical dissipation for time integration algorithms in structural dynamics. Earthq. Eng. Struct. Dyn. **5**, 283–292 (1977)
10. Jaky, J.: The coefficient of earth pressure at rest. J. Soc. Hung. Architects Eng. **78**(22), 355–358 (1944)
11. Kozeny, J.: Über kapillare Leitung des Wassers im Boden. In: Sitzungsbericht der Akademie der Wissenschaften, Wien, vol. 136, no. 2a, pp. 271–306 (1927)
12. Mahutka, K.-P., König, F., Grabe, J.: Numerical modelling of pile jacking, driving and vibratory driving. In: Triantafyllidis, T. (ed.) Numerical Modelling of Construction Processes in Geotechnical Engineering for Urban Environment, pp. 235–246. Taylor & Francis, London (2006)
13. Niemunis, A., Grandas, C., Wichtmann, T.: Peak stress obliquity in drained and undrained sands. Simulations with neohypoplasticity. In: Triantafyllidis, T. (ed.) Holistic Simulation of Geotechnical Installation Processes. Benchmarks and Simulations, pp. 85–114. Springer, Cham (2016)
14. Niemunis, A., Herle, I.: Hypoplastic model for cohesionless soils with elastic strain range. Mech. Cohesive-Frictional Mater. **2**(4), 279–299 (1997)
15. Osinov, V.A., Chrisopoulos, S., Triantafyllidis, T.: Numerical study of the deformation of saturated soil in the vicinity of a vibrating pile. Acta Geotech. **8**, 439–446 (2013)

16. Savidis, S.A., Aubram, D., Rackwitz, F.: Vibro-injection pile installation in sand: part II - numerical and experimental investigation. In: Triantafyllidis, T. (ed.) Holistic Simulation of Geotechnical Installation Processes. Numerical and Physical Modelling, pp. 149–162. Springer, Cham (2015)
17. Tehrani, F.S., Han, F., Salgado, R., Prezzi, M., Tovar, R.D., Castro, A.G.: Effect of surface roughness on the shaft resistance of non-displacement piles embedded in sand. Géotechnique **66**(5), 386–400 (2016)
18. Vennemann, P.: JPIV-software package for Particle Image Velocimetry (2007). http://www.jpiv.vennemann-online.de
19. Vogelsang, J., Huber, G., Triantafyllidis, T., Bender, T.: Interpretation of vibratory pile penetration based on Digital Image Correlation. In: Triantafyllidis, T. (ed.) Holistic Simulation of Geotechnical Installation Processes. Benchmarks and Simulations, pp. 53–67. Springer, Cham (2016)
20. Vogelsang, J.: Untersuchungen zu den Mechanismen der Pfahlrammung. Dissertation. Publications of the Institute of Soil Mechanics and Rock Mechanics, Karlsruhe Institute of Technology, submitted (2017)
21. Vogelsang, J., Chrisopoulos, S.: Experimentelle und numerische Untersuchungen zum Vibrationsrammen in nichtbindigem Boden. Technical papers of the special session "Forum for young geotechnical engineers", Baugrundtagung, Berlin, vol. 33, pp. 195–202 (2014)
22. Vogelsang, J., Huber, G., Triantafyllidis, T.: Experimental investigation of vibratory pile driving in saturated sand. In: Triantafyllidis, T. (ed.) Holistic Simulation of Geotechnical Installation Processes. LNACM, vol. 82, pp. 101–123. Springer, Cham (2017)
23. Wichtmann, T.: Soil behaviour under cyclic loading - experimental observations, constitutive description and applications. Habilitation, vol. 181. Publications of the Institute of Soil Mechanics and Rock Mechanics, Karlsruhe Institute of Technology (2016)
24. Wienbroer, H.: Umlagerung von Sand durch Wechselbeanspruchung. Dissertation, vol. 174. Publications of the Institute of Soil Mechanics and Rock Mechanics, Karlsruhe Institute of Technology (2011)
25. von Wolffersdorff, P.-A.: A hypoplastic relation for granular materials with a predefined limit state surface. Mech. Cohesive-Frictional Mater. **1**, 251–271 (1996)

Some Aspects of the Boundary Value Problems for the Cyclic Deformation of Soil

Vladimir A. Osinov

Institute of Soil Mechanics and Rock Mechanics,
Karlsruhe Institute of Technology, Karlsruhe, Germany

Abstract. Some geotechnical installation processes such as vibratory pile driving or vibro-compaction of soils are characterised by a wide strain amplitude range in the soil, from several per cent and higher in the vicinity of the vibration source to vanishingly small amplitudes in the far field. The gradual accumulation of residual stresses and deformations after each small-amplitude cycle plays in such processes as important a role as large-amplitude cyclic deformation. The numerical simulation of such processes faces, among other difficulties, the necessity to model simultaneously large- and small-amplitude cyclic deformation with a large number of cycles. This imposes stringent requirements on the constitutive model. A problem of the large-amplitude vertical vibration of a pile in saturated soil, which belongs to the problems with a wide strain amplitude range, was solved earlier with two constitutive models: an incremental hypoplasticity model and a high-cycle accumulation model. Using this problem as an example, the present paper discusses the solution approaches and numerical and constitutive aspects of the problem, with particular attention to the accumulation effects in hypoplasticity.

Keywords: Cyclic deformation · Hypoplasticity · Pile vibration

1 Introduction

Boundary value problems for the cyclic deformation of soil can be classified into two groups according to the number of cycles to be modelled: low-cycle problems, in which the number of cycles does not exceed several tens, and high-cycle problems with a larger number of cycles up to tens of thousands or more. A wide area of applications for low-cycle problems is the modelling of earthquake-induced soil deformation. Many cyclic soil deformation processes related to geotechnical engineering are high-cycle processes, e.g. vibratory or impact pile driving or vibro-compaction of soils. The modelling of such processes is often restricted to a relatively small number of cycles and is thus reduced to the solution of a low-cycle problem.

Along with the number of cycles, each cyclic deformation problem is characterised by a range of strain amplitudes. The mechanical behaviour of soils under cyclic loading is strongly dependent on the strain amplitude. We will restrict

T. Triantafyllidis (ed.), *Holistic Simulation of Geotechnical Installation Processes*,
Lecture Notes in Applied and Computational Mechanics 82, DOI 10.1007/978-3-319-52590-7_6

ourselves to granular soils such as sand whose skeleton is commonly assumed to exhibit rate-independent constitutive behaviour. For small strain amplitudes below 10^{-5}, the response of soil to cyclic loading may with good accuracy be considered as linearly elastic. For higher amplitudes, the behaviour of soil becomes plastic with a residual stress after a closed deformation cycle and a residual deformation after a closed stress cycle. In some cases such as earthquake-related problems, the assumed elastic range may be extended to higher strain amplitudes up to 10^{-4}. On the other hand, permanent changes in stresses or deformations may need to be taken into account even for small strain amplitudes of the order of 10^{-5} if the changes accumulate over a large number of cycles. The accumulation effects become stronger with increasing amplitude.

Some high-cycle processes such as vibratory pile driving or deep vibratory compaction involve a wide range of strain amplitudes from several per cent and higher in the vicinity of the vibration source to vanishingly small amplitudes in the far field. The deformation in the near-field is additionally complicated by the large-strain flow of the soil caused by the pile penetration or the soil compaction. The weak accumulation effects at strain amplitudes of 10^{-4} to 10^{-3} at distances of one to a few metres from the pile or vibrator play an important role, as they determine the ultimate changes in the soil state (stresses and density) at these distances. The wide amplitude range together with the necessity to correctly reproduce the accumulation effects for a large number of cycles impose stringent requirements which can hardly be satisfied by any of the existing constitutive models.

Incremental plasticity models allow us to calculate an arbitrary deformation path and any number of cycles. Solving problems with many cycles entails high computational costs, as each cycle has to be computed incrementally with a large number of strain increments. The maximum size of the strain increment is limited by the accumulation of numerical errors in the residual stresses or deformations after each cycle. However, if the weak accumulation effects in the problem under study are important, the main difficulty in solving the problem for a large number of cycles is not the long computing time but the inaccuracy of the incremental model in regard to the weak accumulation effects. Constitutive models of another type, so-called explicit cyclic models, consider the stresses and deformations as explicit functions of the number of cycles and are calibrated directly on high-cycle tests. For this reason, they are more accurate in describing the accumulation effects than incremental models. A disadvantage of explicit models, which restricts their use, is that they are inapplicable to strain amplitudes over 10^{-3}.

In this paper we consider the problem of the vibration of a pile in saturated granular soil solved earlier in [1,10,11]. A spherically symmetric approximation to this problem for the vicinity of the pile toe was studied in [7,8]. If the pile displacement amplitude is large enough, the pile vibration problem belongs to the class of problems with a wide strain amplitude range and a large number of cycles. The problem was solved with two constitutive models of different types: an incremental hypoplasticity model and an explicit high-cycle model. In the

present paper, using this problem as an example, we discuss the solution approach, some numerical aspects and some features of the constitutive models. The large-amplitude pile vibration problem is of interest in connection with the simulation of vibratory pile driving. The problem of vibratory pile driving involves additional numerical difficulties, as compared to pure pile vibration without penetration. The difficulties arise, in particular, from the pile-soil contact conditions and the mesh distortion. These questions are beyond the scope of the present paper.

The low-cycle pile vibration problem with the hypoplasticity model is described in Sect. 2. To judge whether the hypoplasticity model is appropriate for the high-cycle problem as well, in Sect. 3 we present examples of how the model reproduces the accumulation effects at small strain amplitudes. This issue has not been addressed in the literature so far. Sections 4 and 5 outline the explicit cyclic model and its use in the high-cycle pile vibration problem. Section 5 also discusses numerical aspects of solving the high-cycle problem with the explicit model.

2 Low-Cycle Pile Vibration Problem

The problem of the vertical vibration of a cylindrical closed-ended pile in saturated soil has been solved in [1] in a two-dimensional axisymmetric formulation with the finite-element program Abaqus/Standard. A user-defined finite element has been constructed to enable the solution of the dynamic problem with nonzero soil permeability. The same problem with locally undrained conditions is studied in [10]. The objective of the studies was to find permanent stresses and stress amplitudes in the vicinity of the pile toe. The problem is solved for a few tens of cycles with fine spatial and temporal discretization. The soil is modelled as a two-phase medium consisting of a solid skeleton and a pore fluid. The dynamic problem with nonzero soil permeability [1] is formulated in the u-p approximation [19,20] neglecting the difference in the accelerations of the solid and fluid phases. The behaviour of the solid skeleton is modelled by the hypoplasticity theory with intergranular strain [3]. The constitutive equations for the effective-stress tensor $\boldsymbol{\sigma}$ and for the intergranular-strain tensor $\boldsymbol{\delta}$ are written as

$$\dot{\boldsymbol{\sigma}} = \mathbf{F}\left(\dot{\boldsymbol{\varepsilon}}, \boldsymbol{\sigma}, \boldsymbol{\delta}\right), \tag{1}$$

$$\dot{\boldsymbol{\delta}} = \mathbf{S}\left(\dot{\boldsymbol{\varepsilon}}, \boldsymbol{\delta}\right) \tag{2}$$

with tensor-valued functions $\mathbf{F}$ and $\mathbf{S}$, where $\boldsymbol{\varepsilon}$ is the deformation tensor, and the dot stands for the time derivative. The constitutive functions $\mathbf{F}$ and $\mathbf{S}$ can be found in the original paper [3] or in [5,6,9]. The vertical vibration of the pile is simulated by prescribing time-harmonic displacement of the soil with given amplitude and frequency at the pile-soil interface. Non-reflecting boundary conditions available in Abaqus are prescribed at the outer boundary of the computational domain to minimize wave reflections.

A typical solution to the low-cycle pile vibration problem is shown in Fig 1. The figure shows the distribution of the mean effective stress around the pile

toe after 20 cycles of vibration. The cyclic deformation of the soil caused by the pile vibration results in the formation of a zone with low effective stress around the toe. The absolute value of the mean effective stress in the darkest area in Fig. 1 does not exceed 1 kPa, or 2% of the initial stress (−50 kPa at the toe depth). This low-stress zone, which may also be viewed as a liquefaction zone, appears around the pile toe after the first several cycles of vibration and grows slowly with time. The low-stress zone is formed with both zero and nonzero permeability of up to 10^{-3} m/s. The difference between the two cases is in the pore pressure evolution. The reduction of the mean effective stress in the locally undrained case is accompanied by the build-up of the pore pressure, so that the total stress in the low-stress zone remains approximately at the same level. An increase in the pore pressure in the high-permeability case is weaker because of the pore pressure dissipation. As a result, the total stress in the low-stress zone becomes smaller in absolute value compared with the initial stress.

Owing to the large strain amplitudes in the immediate vicinity of the pile toe, the major changes in the stress state, from the initially homogeneous stresses to what is shown in Fig. 1, occur during the first 10–20 cycles. The size of the low-stress zone then slowly increases with the number of cycles. The question arises as to how to solve the high-cycle problem and thus to trace the further evolution of the stress state. Obviously, one possibility is to continue the calculations for a larger number of cycles. As mentioned in Introduction, the main difficulty in this case is not the long computing time but the question of whether the constitutive model correctly reproduces the weak accumulation effects which determine the growth of the low-stress zone in our problem or the ultimate soil density in a vibro-compaction problem. This question is discussed in the next Section in relation to the hypoplasticity model.

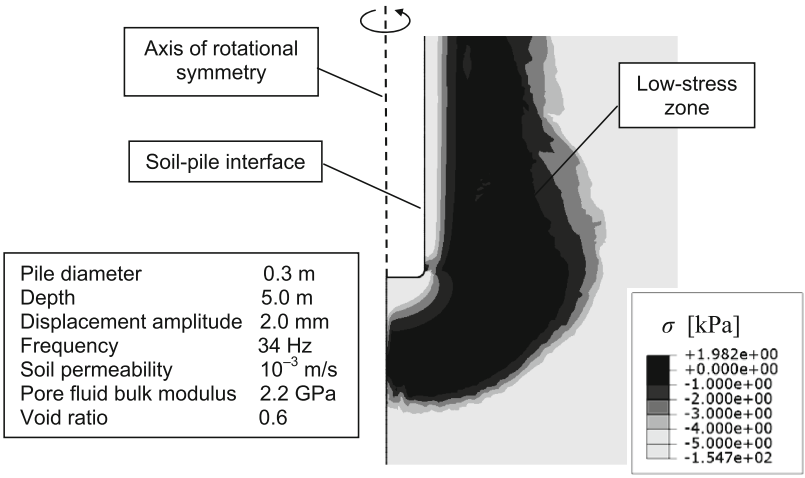

Fig. 1. Mean effective stress in saturated sand around the pile toe after 20 cycles of vibration calculated with the hypoplasticity model [1]

3 Accumulation Effects in Hypoplasticity

The versions of hypoplasticity in which stresses and density are the only state variables (e.g. [2,18]) are known to be unsuitable for the modelling of multi-cycle deformation because of excessive ratcheting. An additional state variable called intergranular strain [3] substantially improves the ability of the theory to model cyclic deformation. Although most attention in the development of the extended version with intergranular strain was paid to the adequate description of the stiffness, the accumulation effects are qualitatively correct: drained cyclic shearing results in the gradual compaction of the soil, while undrained shearing results in the effective-stress reduction. This stimulated the use of the intergranular-strain version of hypoplasticity for the numerical modelling of processes with multi-cycle deformation including vibratory pile driving, deep vibratory compaction and earthquake-induced soil liquefaction (see references in [10]). However, *quantitative* analyses of the accumulation effects are still missing in the literature.

A common drawback of incremental plasticity models regarding cyclic deformation is that it is problematic, if at all possible, to calibrate a given model with respect to the accumulation effects at small to medium strain amplitudes for a large number of cycles and, at the same time, to preserve the correct constitutive behaviour at large amplitudes. The accumulation effects depend on many factors such as the applied strain or stress amplitude, the relative soil density, the current stress state and the cyclic deformation history.

The set of constitutive parameters of the extended version of hypoplasticity with intergranular strain consists of two groups. The first group includes the basic parameters involved in both the basic version without intergranular strain [18] and the extended version [3]. The second group includes additional intergranular-strain parameters involved in the extended version only. The basic parameters are determined from element tests with monotonic deformation. The proper estimation of the additional parameters requires cyclic tests, which are more complicated and time consuming. For this reason, the additional parameters are often estimated otherwise or taken from the original paper [3]. Problems in the determination of the intergranular-strain parameters may cause additional inaccuracy of the model.

Here we will discuss the applicability of the hypoplasticity theory with intergranular strain to the modelling of high-cycle deformation with several hundred cycles and moderate strain amplitudes in the range between 10^{-4} and 10^{-3}. Emphasis in the examples presented below will be placed on the accumulation effects rather than on the incremental stiffness. The hypoplasticity model will be compared with the high-cycle accumulation model discussed below in Sect. 4. Since the cyclic model is calibrated directly on multi-cycle tests, the curves obtained with this model will be used here as benchmark curves. For the comparison of the two models to be possible, we will take a soil (sand L12 from [17]) for which both models have been calibrated [13].

Example 1. The first example deals with the densification of dry soil caused by cyclic shearing. This type of deformation is closely related, for instance, to

the modelling of deep vibratory compaction. Figure 2 shows the results of cyclic simple shearing with the initial relative density $I_D = 0.2$, the initial stresses $\sigma_{11} = -100\,\text{kPa}$, $\sigma_{22} = \sigma_{33} = -70\,\text{kPa}$, $\sigma_{12} = \sigma_{13} = \sigma_{23} = 0$, and the strain amplitude $\gamma_{12} = 10^{-3}$. The stress component σ_{11} is kept constant during the deformation. A salient feature of the compaction with a constant strain amplitude observed in experiments is the strong decrease in the compaction rate with increasing density. This feature is well reproduced by the cyclic model. In contrast, the hypoplasticity model shows little influence of the current density on the compaction rate. Although the model predicts the existence of a densest state in which the compaction terminates, this state is reached too fast because of too high compaction rates at medium and high densities. The weak dependence of the compaction rate on the density is found to be an inherent characteristic of the present version of hypoplasticity, rather than being a consequence of an improper choice of the intergranular-strain parameters. This drawback may lead to the considerable overestimation of the final density in the numerical simulation of compaction processes with a large number of cycles.

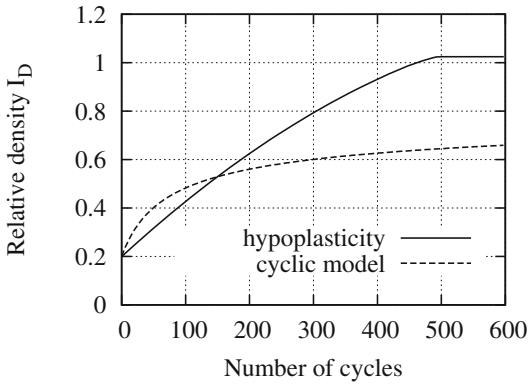

Fig. 2. Densification of dry sand during cyclic simple shearing with a strain amplitude of 10^{-3}

Example 2. The fact that the influence of the density on the densification of dry soil in the hypoplasticity model is weak suggests that the effective-stress reduction in saturated soil under undrained conditions may also depend only slightly on the density. This conjecture turns out to be true. Figure 3 shows the mean effective stress σ after 300 cycles of pure shearing calculated with the two models for sand L12. The initial stress state is hydrostatic with the mean stress $\sigma_0 = -100\,\text{kPa}$. The stress in the figure is shown as a function of the strain amplitude for two relative densities. The degree of the effective-stress reduction obtained with hypoplasticity increases with increasing amplitude up to the total vanishing of the effective stress for sufficiently large amplitudes. However, in contrast to the cyclic model, there is no dependence of the effective-stress reduction on the density. The curves for the dense and loose soils practically coincide,

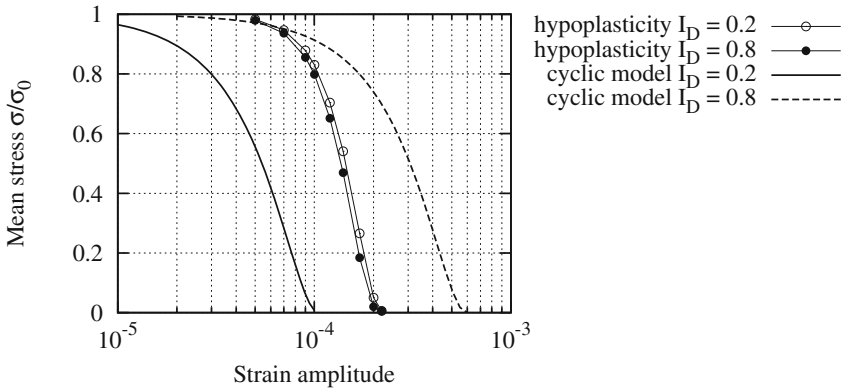

Fig. 3. Mean effective stress in saturated soil after 300 cycles of pure shearing as a function of the strain amplitude

which is inconsistent with experimental observations. It is likely that this model, when used for the high-cycle pile vibration problem for saturated soil, will give the same rate of growth of the low-stress zone for dense and loose soils.

Example 3. Another deficiency of the extended version of hypoplasticity manifests itself when monotonic deformation is superimposed on small-amplitude cyclic deformation. The model is such that small-amplitude cyclic deformation makes the intergranular strain tensor nearly zero in norm (much smaller than a certain value). This remains true if the average deformation tensor changes slowly with the number of cycles. If the intergranular strain tensor is zero, the model reduces to hypoelasticity, i.e. incrementally linear elasticity with stress-dependent stiffness. The change in the average stress is then dictated by the monotonic part of the deformation according to the hypoelastic response. If the monotonic part of the deformation has a deviatoric component, the model can produce arbitrarily high principal-stress ratios and tensile stresses.

This property of the model is illustrated in Fig. 4 by a strain-controlled triaxial test in which the deformation components ε_1 and $\varepsilon_2 = \varepsilon_3$ oscillate with amplitudes of 8×10^{-5} and 4×10^{-5}, respectively, and also have monotonic constituents (Fig. 4a). The monotonic part of the deformation has a deviatoric and a tensile volumetric components. Such deformation is expected to result in the gradual reduction and eventual vanishing of the stress. Calculations show that the monotonic and the purely cyclic deformation paths applied individually produce the correct stress responses: the stress components tend to zero. However, this is not the case for the superposition of the two paths. The stresses calculated with the parameters of sand L12 are shown in Fig. 4b. The stress σ_1 does tend to zero in the beginning but then crosses the zero axis and becomes positive. The stress σ_2 begins to increase in absolute value already after the first several cycles. The stress evolution in the present example depends on the intergranular-strain parameters and can be such that much more cycles are needed for the wrong

trend to become noticeable. Figure 4c shows the result obtained with the parameters of Karlsruhe sand used in [1,8,10]. The stresses in Fig. 4c decrease in absolute value during the first few tens of cycles, but the trend then turns to that shown in Fig. 4b as the number of cycles increases.

The drawback illustrated in Fig. 4 escaped attention until recently and was revealed in the solutions to the boundary value problems of the cyclic deformation of saturated soil with finite permeability [8]. The monotonic volumetric expansion of the soil skeleton due to pore water flow together with the applied cyclic loading may result in a deformation path similar to that shown in Fig. 4a. An ad hoc approach that eliminates the above drawback of the constitutive model is proposed in [8]. It is known from numerical experiments that the original version of hypoplasticity without intergranular strain does not produce unlimited stress ratios – at least, for coaxial deformation. In the approach proposed in [8], the original and extended versions of hypoplasticity are combined using a weight function. The function is chosen in such a way that the extended version continuously turns to the original one if the increasing principal-stress ratio exceeds a certain threshold. Alternatively, tensile stresses and unlimited principal-stress ratios could be eliminated by the small-stress correction and the projection of the stress state on a bounding surface, as described in Sect. 4 for the high-cycle model.

The examples presented in this Section show that the use of an incremental constitutive model – in our case, hypoplasticity – for the solution of a high-cycle problem with small to medium strain amplitudes may lead to substantial errors in permanent stresses and deformations. An alternative way is to use an explicit cyclic model.

4 High-Cycle Accumulation Model

While incremental plasticity models describe any deformation path, so-called explicit cyclic models are developed specially for the simulation of cyclic deformation. Stresses and deformations in these models are understood as average quantities that change gradually with the number of cycles due to small-amplitude cyclic deformation. The models are called 'explicit' because the average stresses and deformations are considered as explicit functions of the number of cycles. In this paper we will deal with the application of the high-cycle accumulation model for granular soils elaborated in [4,12]. The constitutive parameters of the model control directly the dependence of the accumulation effects on the strain amplitude, the current density, the stress state and the cyclic deformation history. The model has been calibrated by cyclic element tests on various sands with a large number of cycles (up to 10^5) [14–17].

The constitutive equation for the stress tensor in the cyclic model is written in rate form with respect to the number of cycles treated as a real number. If the soil is deformed with a constant frequency, the constitutive equation can be written in terms of temporal rates:

$$\dot{\boldsymbol{\sigma}} = \mathsf{E}(\boldsymbol{\sigma}) : (\dot{\boldsymbol{\varepsilon}} - \dot{\boldsymbol{\varepsilon}}^{acc}), \tag{3}$$

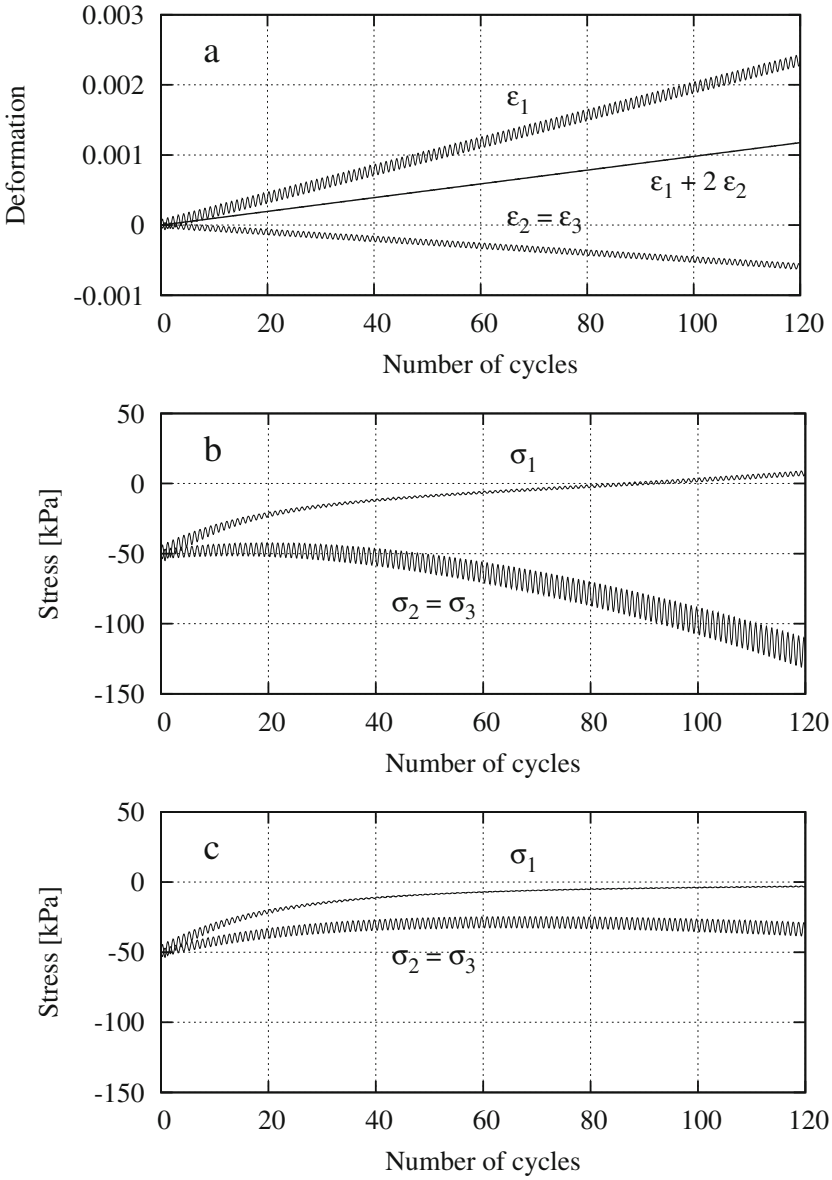

Fig. 4. Strain-controlled cyclic triaxial test calculated with the hypoplasticity model with a hydrostatic initial state and a relative density of 0.8. (a) Deformation components, (b) stress components for sand L12, (c) stress components for Karlsruhe sand

where $\boldsymbol{\sigma}$ is the average stress tensor (the effective stress in the case of saturated soil), $\boldsymbol{\varepsilon}$ is the average deformation tensor of the skeleton, and $\mathsf{E}(\boldsymbol{\sigma})$ is a stress-dependent stiffness tensor. The tensor $\dot{\boldsymbol{\varepsilon}}^{acc}$ entering the constitutive equation is a strain accumulation rate which is a function of a scalar strain amplitude ε^{amp}, the void ratio, the stress tensor and the cyclic deformation history (see [4,7,12,14,17] for detail). The determination of the strain amplitude ε^{amp} as a function of space and time, when solving a high-cycle problem, constitutes a separate boundary value problem which is independent of the cyclic model. The scalar strain amplitude ε^{amp} is determined from the amplitudes of the individual components of the strain tensor corresponding to the cyclic deformation. Equation (3) has been calibrated by the comparison of the results of drained and undrained cyclic tests [15,16]. The tensor E is taken as in an isotropic elastic solid with a fixed Poisson ratio and a pressure-dependent bulk modulus

$$K(\sigma) = A\, p_{atm}^{1-n}\, (-\sigma)^n, \tag{4}$$

where σ is the mean stress and A, p_{atm}, n are parameters.

The use of equations (3), (4) for the solution of boundary value problems requires two corrections. The first correction should prevent the possible unlimited growth of the principal-stress ratio caused by the hypoelastic response (3). The correction in [8,11] is made by projecting the stress state on a given bounding surface in the stress space if the stress state falls outside the surface. The bounding surface corresponds to the Matsuoka-Nakai yield condition with a given friction angle. The projection is made in the direction to the hydrostatic axis in such a way that the mean stress does not change. Equation (3) then becomes

$$\dot{\boldsymbol{\sigma}} = \mathsf{E}(\boldsymbol{\sigma}) : (\dot{\boldsymbol{\varepsilon}} - \dot{\boldsymbol{\varepsilon}}^{acc}) + \dot{\boldsymbol{\sigma}}^{cor} \tag{5}$$

with a correction term $\dot{\boldsymbol{\sigma}}^{cor}$.

The second correction to (3), (4) is necessary if the mean stress σ approaches zero. This may be the case in saturated soil subjected to cyclic deformation, either because of low soil permeability or in the presence of tensile deformation of the skeleton due to pore water flow. It can be shown that if $0 < n < 1$ in (4), which is the case for granular soil, the mean stress σ reaches zero after a finite number of cycles. Zero σ and, as a consequence, zero skeleton stiffness make a boundary value problem ill-posed. The small-stress correction proposed in [11] is made through the multiplication of (4) by a factor which depends on σ:

$$K(\sigma) = A\, p_{atm}^{1-n}\, (-\sigma)^n \left[1 - \exp\left(-\frac{\sigma}{\sigma_\zeta}\right)\right]^{\zeta - n}, \tag{6}$$

with a parameter $\zeta > 1$ and a reference stress $\sigma_\zeta < 0$. With $\zeta > 1$, the mean stress σ, if it decreases in absolute value, approaches zero asymptotically with the number of cycles. At the same time, (6) turns into (4) if $\sigma/\sigma_\zeta \gg 1$.

5 High-Cycle Boundary Value Problem

The high-cycle accumulation model has two attractive advantages over incremental models in relation to the numerical solution of boundary value problems

with a large number of cycles. First, this model, when properly calibrated, is much more accurate in the description of the accumulation effects, and second, it enables us to calculate a large number of cycles in a relatively short computing time. A crucial disadvantage, which substantially restricts the application of the model, is that it is invalid for large strain amplitudes over 10^{-3}. This is not a drawback of this particular model, but rather an intrinsic property of any explicit model based on the concept of gradually changing average stresses and deformations. This restriction does not allow the high-cycle model to be directly employed for the solution of the pile vibration problem considered in this paper because of large strain amplitudes in the vicinity of the pile.

The problem of vibration-induced soil deformation can be solved with the high-cycle model by excluding the zone of large strain amplitudes from the computational domain with the help of an auxiliary boundary [7,8,11], as illustrated in Fig. 5. The main difficulty in this approach is the specification of boundary conditions at the auxiliary boundary. The location of the auxiliary boundary and the boundary conditions may be deduced from the solution to the low-cycle problem solved with an incremental model for the whole domain prior to the high-cycle problem [8,11]. The low-cycle solution also provides an initial stress state for the high-cycle problem.

The solution of the high-cycle problem with the cyclic accumulation model consists in the concurrent solution of two coupled boundary value problems, called here the first and the second problems. A calculation step between times t and $t + \Delta t$ begins with the determination of the scalar strain amplitude field $\varepsilon^{amp}(\mathbf{x}, t)$ as a function of space at time t. Finding this strain amplitude constitutes the *first* boundary value problem. As mentioned on Sect. 4, this problem is independent of the cyclic model and may be solved with any suitable constitutive model in a dynamic or quasi-static formulation, depending on the physical

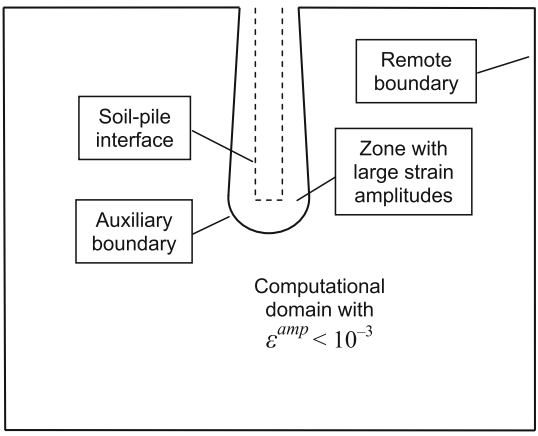

Fig. 5. Computational domain with an auxiliary boundary around the pile for the high-cycle problem

problem under study. For pile vibration studied in [7,8,11], the first boundary value problem is solved for an elastic medium in the dynamic steady-state formulation for time-harmonic displacements and stresses with spatially inhomogeneous soil stiffness. The stiffness is determined from the current effective stress through an assumed relation which is also independent of the cyclic model. The steady-state problem is solved with a given pressure or displacement amplitude at the auxiliary boundary (stress-controlled and displacement-controlled cases, respectively). The remote boundary is made transparent for outgoing waves by non-reflecting boundary conditions. They are exact in the spherically symmetric problem [7,8] and approximate in the two-dimensional case [11].

The scalar strain amplitude determines the tensorial strain accumulation rate $\dot{\boldsymbol{\varepsilon}}^{acc}(\mathbf{x}, t)$ required for the constitutive equation (3). Assuming this rate to be constant on the interval Δt, the effective stress, the pore pressure and the void ratio at time $t + \Delta t$ are found from the *second* boundary value problem – a quasi-static deformation problem for a fluid-saturated porous solid with the constitutive equation (3) for the skeleton. The auxiliary boundary in [7,8,11] is taken to be impermeable with zero displacements. The boundary conditions at the remote boundary correspond to the conditions at infinity. After the new stress state at time $t + \Delta t$ has been found, the next step begins with the first boundary value problem with the new stiffness. In order to reduce the computing time, it may be reasonable to check the effective stress changes and to update the strain amplitude field by solving the first boundary value problem only if the changes exceed a certain threshold. If the stress changes are too small, the old strain amplitude field may be taken for the next step.

The solution scheme for the high-cycle problem as two coupled boundary value problems has been implemented in [7,8,11]. The problem for the vicinity of a pile toe has been solved in [7,8] in a spherically symmetric approximation. The study in [11] is aimed at finding permanent stress changes near a concrete wall caused by the large-amplitude vibration of a pile. The influence of the pile is simulated by a spherically symmetric vibration source with a constant pressure amplitude σ_a (stress-controlled problem) placed at a distance L from the wall, as illustrated in Fig. 6. This approximation reduces the original three-dimensional pile-wall problem to a two-dimensional axisymmetric problem.

A feature of the steady-state problem in the stress-controlled case is a resonance-like increase in the strain amplitude (called resonance for brevity) at a certain spatial distribution of the effective stress. The resonance has been observed in both the spherically symmetric and the two-dimensional axisymmetric problems. No resonance occurs in the displacement-controlled case, since the strain amplitude is controlled by the displacement amplitude at the boundary. The resonance is accompanied by an abrupt increase in the size of the low-stress zone and may also result in an abrupt change in the stress state at a fixed spatial point if the low-stress zone covers this point during the resonance. This is illustrated in Fig. 7, which shows the mean effective stress near the concrete wall for the problem in Fig. 6. The effective stress changes gradually until the instant of resonance and then falls quickly to a smaller or nearly zero value. The

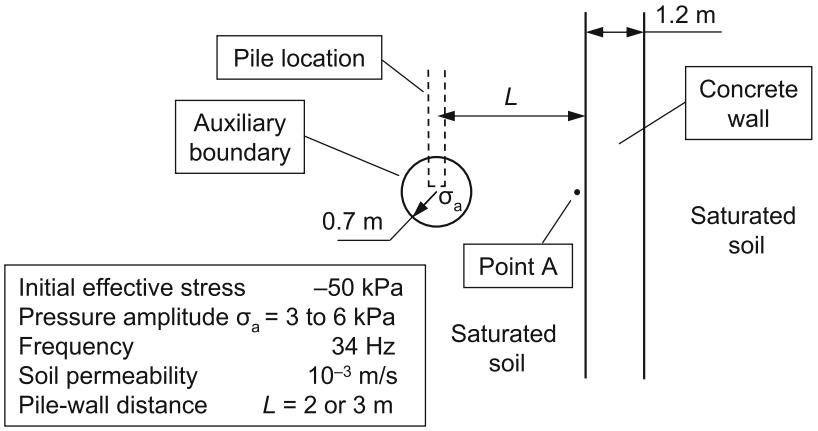

Fig. 6. A spherical auxiliary boundary with a pressure amplitude σ_a approximating the influence of a vibrating pile on the stress state near a concrete wall [11]

instant of resonance depends, besides the constitutive parameters of the soil, on the pressure amplitude, the pile-wall distance, the relative soil density and the permeability. The influence of the permeability on the stress state near the wall is the same as for the vicinity of the pile toe: high permeability does not allow the pore pressure to grow, but does not hinder the effective stress reduction. As a result, the total stress becomes eventually reduced by approximately the same amount as the effective stress. In the cases shown in Fig. 7, the stress state behind the wall remains practically unchanged.

The studies in [7,8,11] were the first to use the high-cycle accumulation model [4,12] for the solution of boundary value problems for saturated soils

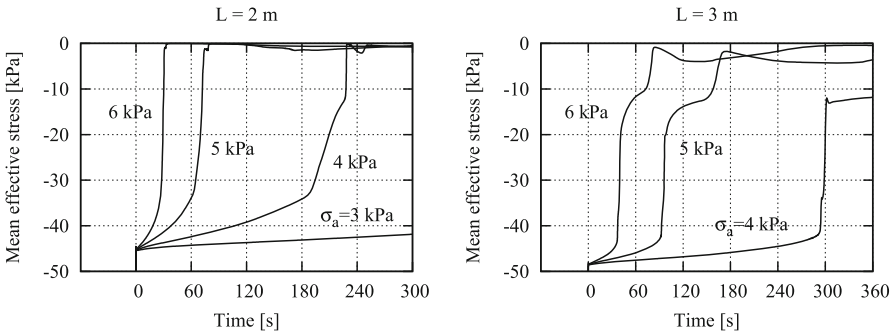

Fig. 7. Mean effective stress near the wall (Point A in Fig. 6) as a function of time for different pressure amplitudes σ_a and two pile-wall distances L, calculated for sand L12 with a relative density of 0.6 [11]

under dynamic loading. Earlier applications of the model dealt with dry or fully drained soils under quasi-static cyclic loading.

The numerical solution of dynamic boundary value problems for saturated soils encountered two kinds of instability. The first instability stems from the property of the high-cycle model to produce, under certain conditions, widely diverging stress responses for slightly different deformation paths. Consider two soil samples with the same initial stress state and density. Let each of them be subjected to a uniaxial compression ε_1 with a constant deformation rate and, at the same time, to small-amplitude cyclic deformation with an increasing amplitude ε^{amp}, as shown in Fig. 8. The deformation of the two samples is slightly different, and it would be natural to expect only a slight difference in the stress paths as well. However, the stress paths diverge markedly, although both finally approach zero, see Fig. 8. The cyclic and monotonic parts of the deformation, when applied individually, would lead, respectively, to the decrease and increase in the absolute value of the mean stress. The result of the superposition depends on the intensity of the two components. Although the decrease due to the cyclic deformation in the present example dominates, the dependence on the monotonic deformation is nevertheless strong. That is why the two stress paths diverge. Another example, in which the compression eventually dominates and the stress increases after a temporary fall, is shown in Fig. 9.

The high sensitivity of the stress response to the variation of the applied deformation exists only for certain combinations of the deformation path, the initial stress state and the density. Exceptional as this phenomenon might seem, it may manifest itself in numerical calculations and completely spoil a spatially continuous solution. Different stress paths, like those shown in Fig. 8, were obtained in neighbouring finite elements or within one element in numerical solutions with the 4-node bilinear axisymmetric quadrilateral elements of Abaqus/Standard. This instability usually leads to the formation of a zone in which the stresses change discontinuously and irregularly from element to element. The zone of irregularity disappears as the stresses in all elements of the zone approach zero. The instability did not arise when using the 8-node biquadratic axisymmetric quadrilateral elements.

While the presence of discontinuous solutions is easy to see, another kind of instability faced in the numerical simulations does not lead to any discontinuity and may not be as easy to notice as the previous one. The instability has been revealed by solving a problem with a spherically symmetric solution as a two-dimensional axisymmetric problem. It was found that the solution may lose spherical symmetry at a certain instant and then remain non-symmetric. The mechanism of this bifurcation cannot yet be clearly explained. The loss of symmetry occurs in the problems with nonzero permeability after the formation of a low-stress zone and is initiated by non-symmetric strain amplitude fields arising in the steady-state problem prior to the loss of symmetry. The non-symmetric strain amplitude fields may be a consequence of instability caused by the very low shear stiffness in the low-stress zone, as compared to the bulk modulus. The latter remains almost unchanged due to the presence of pore water. The fact that the non-reflecting boundary conditions at the remote boundary are

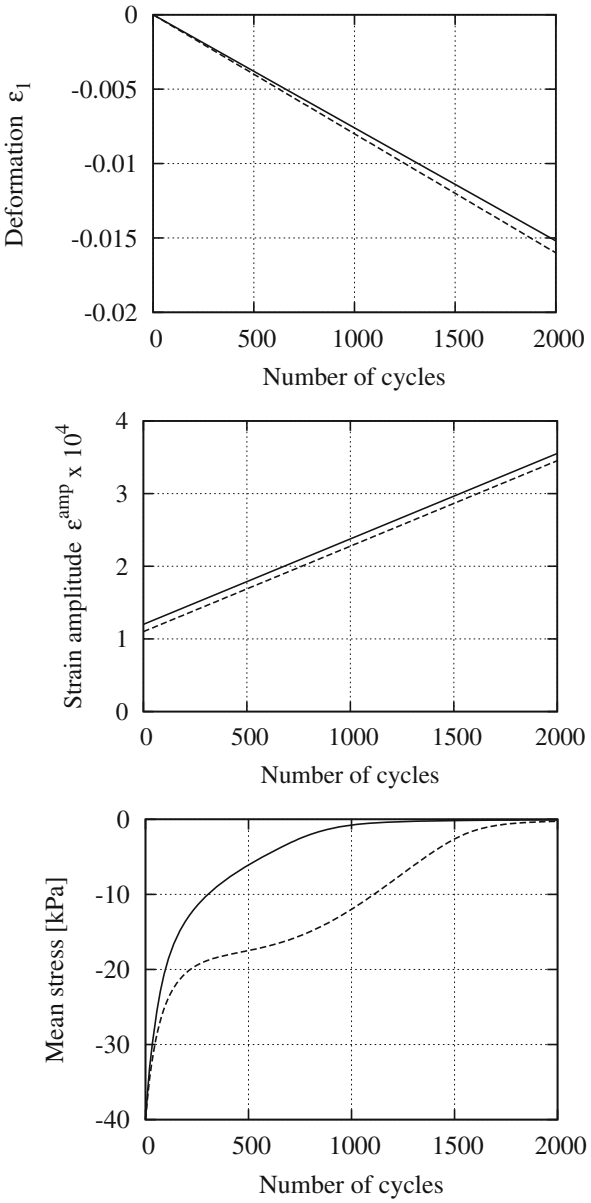

Fig. 8. Superposition of monotonic uniaxial compression ε_1 and cyclic deformation with increasing strain amplitude ε^{amp} calculated with the high-cycle accumulation model for sand L12. Two slightly different deformation paths (solid and dashed lines) produce markedly different stress responses. Initial state: $\sigma_1 = -50\,\text{kPa}$, $\sigma_2 = \sigma_3 = -35\,\text{kPa}$, $I_D = 0.6$

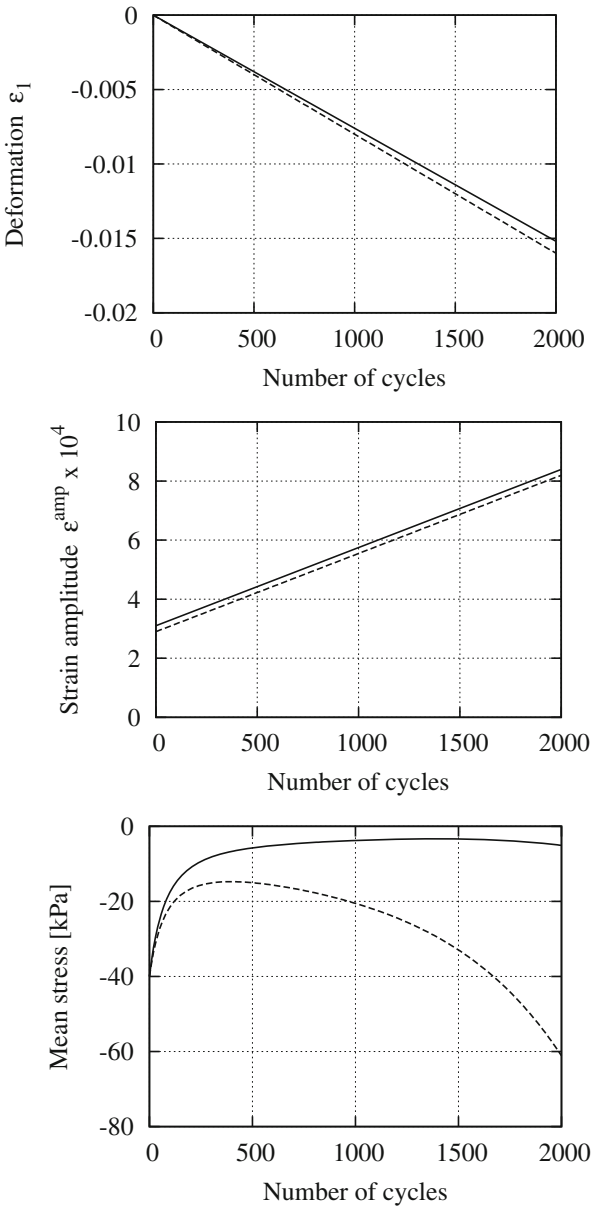

Fig. 9. The same as in Fig. 8 for a different deformation path and $I_D = 0.8$

not exact may also play a role leading to spurious non-symmetric eigenmodes. The non-symmetric disturbance to the stresses and density increases because of some complicated positive feedback. This instability has been eliminated by introducing a small correction stress σ^* in the steady-state problem [11] to prevent too low shear stiffness.

6 Concluding Remarks

Vibratory pile driving or vibro-compaction of soils are high-cycle processes in which the ultimate stress state and density of the soil, except for the immediate vicinity of the vibration source, are determined by the weak accumulation effects at small to medium strain amplitudes. The problem of the large-amplitude vibration of a pile in saturated soil was solved with the hypoplasticity model as a low-cycle problem to find the stress state around the pile toe at the beginning of the vibration. One should proceed with caution when using the hypoplasticity model for the solution of high-cycle problems. As shown in the present paper, the hypoplasticity model has shortcomings in reproducing the accumulation effects. The accumulation of residual stresses and deformations under purely cyclic loading is qualitatively correct but exhibits a lack of adequate dependence on the strain amplitude and the relative soil density. A combination of monotonic and small-amplitude cyclic deformation may lead to physically unrealistic stress states and thus produce an incorrect response. These facts should be taken into account when using the hypoplasticity model for the simulation of cyclic deformation processes such as vibratory pile driving or vibro-compaction, especially with a large number of cycles.

The high-cycle pile vibration problem was solved with the explicit cyclic model. This model is more reliable from the viewpoint of the accumulation effects but is applicable only to small strain amplitudes. Because of this restriction, boundary value problems with the cyclic model require special formulation in order to exclude the zone of large strain amplitudes from the computational domain. The main difficulty in this approach is the indeterminacy of boundary conditions for the reduced computational domain. Resolving this difficulty is crucial for the accuracy of the modelling.

Acknowledgments. The study was financed by the Deutsche Forschungsgemeinschaft as part of the Research Unit FOR 1136 'Simulation of geotechnical construction processes with holistic consideration of the stress strain soil behaviour', Subproject 6 'Soil deformations close to retaining walls due to vibration excitations'.

References

1. Chrisopoulos, S., Osinov, V.A., Triantafyllidis, T.: Dynamic problem for the deformation of saturated soil in the vicinity of a vibrating pile toe. In: Triantafyllidis, T. (ed.) Holistic Simulation of Geotechnical Installation Processes. LNACM, vol. 80, pp. 53–67. Springer, Heidelberg (2016). doi:10.1007/978-3-319-23159-4_3
2. Gudehus, G.: A comprehensive constitutive equation for granular materials. Soils Found. **36**(1), 1–12 (1996)
3. Niemunis, A., Herle, I.: Hypoplastic model for cohesionless soils with elastic strain range. Mech. Cohesive-frict. Mater. **2**(4), 279–299 (1997)
4. Niemunis, A., Wichtmann, T., Triantafyllidis, T.: A high-cycle accumulation model for sand. Comput. Geotech. **32**, 245–263 (2005)
5. Osinov, V.A.: Wave-induced liquefaction of a saturated sand layer. Continuum Mech. Thermodyn. **12**(5), 325–339 (2000)

6. Osinov, V.A.: Large-strain dynamic cavity expansion in a granular material. J. Eng. Math. **52**, 185–198 (2005)
7. Osinov, V.A.: Application of a high-cycle accumulation model to the analysis of soil liquefaction around a vibrating pile toe. Acta Geotech. **8**, 675–684 (2013)
8. Osinov, V.A.: Numerical modelling of the effective-stress evolution in saturated soil around a vibrating pile toe. In: Triantafyllidis, T. (ed.) Holistic Simulation of Geotechnical Installation Processes. LNACM, vol. 77, pp. 133–147. Springer, Heidelberg (2015). doi:10.1007/978-3-319-18170-7_7
9. Osinov, V.A., Gudehus, G.: Dynamics of hypoplastic materials: theory and numerical implementation. In: Hutter, K., Kirchner, N. (eds.) Dynamic Response of Granular and Porous Materials Under Large and Catastrophic Deformations, pp. 265–284. Springer, Berlin (2003)
10. Osinov, V.A., Chrisopoulos, S., Triantafyllidis, T.: Numerical study of the deformation of saturated soil in the vicinity of a vibrating pile. Acta Geotech. **8**, 439–446 (2013)
11. Osinov, V.A., Chrisopoulos, S., Grandas-Tavera, C.: Vibration-induced stress changes in saturated soil: a high-cycle problem. In: Triantafyllidis, T. (ed.) Holistic Simulation of Geotechnical Installation Processes. LNACM, vol. 80, pp. 69–84. Springer, Heidelberg (2016). doi:10.1007/978-3-319-23159-4_4
12. Wichtmann, T.: Explicit accumulation model for non-cohesive soils under cyclic loading. Dissertation, Publications of the Institute of Soil Mechanics and Foundation Engineering, Ruhr-University Bochum, vol. 38 (2005)
13. Wichtmann, T., Private communication (2016)
14. Wichtmann, T., Niemunis, A., Triantafyllidis, T.: On the determination of a set of material constants for a high-cycle accumulation model for non-cohesive soils. Int. J. Numer. Anal. Meth. Geomech. **34**, 409–440 (2010)
15. Wichtmann, T., Niemunis, A., Triantafyllidis, T.: On the 'elastic' stiffness in a high-cycle accumulation model for sand: a comparison of drained and undrained cyclic triaxial tests. Can. Geotech. J. **47**(7), 791–805 (2010)
16. Wichtmann, T., Niemunis, A., Triantafyllidis, T.: On the 'elastic stiffness' in a high-cycle accumulation model - continued investigations. Can. Geotech. J. **50**(12), 1260–1272 (2013)
17. Wichtmann, T., Niemunis, A., Triantafyllidis, T.: Improved simplified calibration procedure for a high-cycle accumulation model. Soil Dyn. Earthq. Eng. **70**, 118–132 (2015)
18. von Wolffersdorff, P.A.: A hypoplastic relation for granular materials with a predefined limit state surface. Mech. Cohesive-frict. Mater. **1**(3), 251–271 (1996)
19. Zienkiewicz, O.C., Chang, C.T., Bettess, P.: Drained, undrained, consolidating and dynamic behaviour assumptions in soils. Géotechnique **30**(4), 385–395 (1980)
20. Zienkiewicz, O.C., Chan, A.H.C., Pastor, M., Schrefler, B.A., Shiomi, T.: Computational Geomechanics with Special Reference to Earthquake Engineering. Wiley, Chichester (1999)

Computer Aided Calibration, Benchmarking and Check-Up of Constitutive Models for Soils. Some Conclusions for Neohypoplasticity

Andrzej Niemunis(✉) and Carlos Eduardo Grandas-Tavera

Institute of Soil Mechanics and Rock Mechanics,
Karlsruhe Institute of Technology, Karlsruhe, Germany
andrzej.niemunis@kit.edu

Abstract. A computer aided calibration, benchmarking and testing of constitutive models is presented. A large collection of test data for Karlsruhe sand is used together with the neohypoplastic model as an example. The essential feature of the procedure is an automatic evaluation of the discrepancies between a test and its simulation. They can be minimized by modifications of material constants or used as a benchmark for different models. Apart from the curve-fitting part one may check whether a constitutive model violates the Second Law. For this purpose several specially designed stress loops are tried out. A shake down of all state variables is established. The neohypoplasticity and the barotropic hypoelasticity are used as examples in the thermodynamic tests. In conclusion several modification to neohypoplastic models are presented.

Keywords: Second law · Material calibration · `umat`

1 Introduction

A constitutive model for soil is given in a form of the user's material subroutine `umat` which is a well established standard of the commercial FE program ABAQUS®. The main subject here is the calibration of the model, i.e. a general method to find the material constants. The FE program is not necessary for the calibration because we assume homogeneous fields of stress and strain in all tests. A small public-domain program INCREMENTALDRIVER, http://www.pg.gda.pl/~aniem/dyd.html, enables numerical *element* tests (a single Gauss point in the FEM). One can use INCREMENTALDRIVER to simulate various loading paths with prescribed stress path $\boldsymbol{\sigma}(t)$ or strain path $\boldsymbol{\epsilon}(t)$ or partly both. It is assumed that numerous test data files containing various stress and strain paths are available for comparisons. For example such data bank for sand is available online, http://www.torsten-wichtmann.de/, and described in detail in [14,15].

INCREMENTALDRIVER can read the test results[1] and perform a computation with `umat`. The prescribed path is followed *in-fly* and one can watch the developing discrepancy between the simulation and the laboratory results.

[1] In different components, e.g. Roscoe or Cartesian.

T. Triantafyllidis (ed.), *Holistic Simulation of Geotechnical Installation Processes*,
Lecture Notes in Applied and Computational Mechanics 82, DOI 10.1007/978-3-319-52590-7_7

At the beginning of each increment `umat` is given the stress $\boldsymbol{\sigma}^n$ and the internal state variables $\boldsymbol{\alpha}^n$. `umat` updates these values depending on the strain increment $\Delta\boldsymbol{\epsilon} = \boldsymbol{\epsilon}^{t+\Delta t} - \boldsymbol{\epsilon}^t$ returning their values $\boldsymbol{\sigma}^{n+1}$ and $\boldsymbol{\alpha}^{n+1}$ at the end of the increment. Moreover `umat` calculates a tangential stiffness matrix[2] $\mathsf{E} = \partial\Delta\boldsymbol{\sigma}/\partial\Delta\boldsymbol{\epsilon}$. The main task of IncrementalDriver is to drive `umat` along a prescribed loading path defined by strain or stress components. The complementary components of $\boldsymbol{\epsilon}^{n+1}$ and $\boldsymbol{\sigma}^{n+1}$ are calculated using constitutive equations and stored (in an output file) together with the collection of all state variables $\boldsymbol{\alpha}^{n+1}$. It is easy to follow a strain path $\boldsymbol{\epsilon}(t)$ feeding `umat` with the strain increments $\Delta\boldsymbol{\epsilon}$ along the path: the update of all state variables[3] is performed by `umat` itself and IncrementalDriver needs just to do some bookkeeping and to output the results. It is more difficult to follow a prescribed stress path $\boldsymbol{\sigma}(t)$ or a combined stress/strain path (=generalized loading path). The essential problem arises from the fact that `umat` accepts only *strain increments* $\overset{\circ}{\Delta}\boldsymbol{\epsilon}$ as input. For a prescribed stress increment $\overset{\circ}{\Delta}\boldsymbol{\sigma}$ IncrementalDriver determines iteratively the components of $\Delta\boldsymbol{\epsilon}$ in a procedure similar to the equilibrium iteration (EI) in the FEM.

The final result obtained from IncrementalDriver is a chronological list of states which is usually plotted and compared with analogous diagrams from the laboratory. We call such list a *history* and the discrete states are called the *records*. A portion of history with roughly proportional prescribed increments is called a *step* and the difference between two consecutive records is an *increment*. IncrementalDriver can read a history from an external file choosing some components (columns) as an input. Such input file can be obtained from laboratory or it can be the output of IncrementalDriver itself, usually generated with a different `umat` or with a different set of material constants.

A fair comparison of several[4] `umat`s should be done basing on a common collection of laboratory tests[5]. However, constitutive models are usually evaluated graphically using different collections of tests and differently *selected* components of the material response. The main objective of this paper is to formulate a fair benchmark, instead. For the *quantification* of the discrepancy between the laboratory results and the simulation we define a scalar functional $\mathcal{F}(C_i, \boldsymbol{\alpha}_0, \boldsymbol{\epsilon}(t))$, possibly with some constraints. In the process of calibration the loading program is fixed, $\boldsymbol{\epsilon}^S(t) = \boldsymbol{\epsilon}^L(t)$, and we can iterpret the scalar discrepancy functional as a *penalty function* $F(C_i, \boldsymbol{\alpha}_0)$ to be minimized by an optimal choice of the material constants C_i and the initial values $\boldsymbol{\alpha}_0$ of state variables.

The functional $\mathcal{F}(\boldsymbol{\epsilon}(t))$ is a promising general-purpose tool in constitutive modeling. It can be helpful:

---

[2] Jacobian matrix.

[3] Except for strain.

[4] Describing different constitutive models or different sets of material constants.

[5] We use triaxial and oedometric tests on the Karlsruhe fine sand [13] here but other types of tests (biaxial, true-triaxial, hollow-cylinder tests) can also be read by IncrementalDriver. For compatibility with `umat` one should convert the nominal stress to the Cauchy stress and the Biot strain to the Hencky strain in each record of the test data files.

- to calibrate a constitutive model (as a penalty function for optimization);
- to compare optimally calibrated models (as a benchmark);
- to evaluate the sensitivity [5] of the response to different material constants;
- to evaluate an admissible range of the material constants;
- to determine what aspect of the constitutive description needs an improvement.

A formulation of a good functional $\mathcal{F}(\boldsymbol{\epsilon}(t))$ is not easy and it may differ depending on the engineering problem at hand. The essential benefit of $\mathcal{F}(\boldsymbol{\epsilon}(t))$ is the objectivity. Although a considerable experience has been gathered in the traditional (graphical) evaluation of the constitutive models for soils, it happens frequently that only "nicely looking" diagrams are selected for publications. Sometimes even the set of material constants for the same material is modified from test to test to render the model more attractive. In order to avoid biased comparisons it seems of great value to have several public-domain benchmarks. Different benchmarks can be suited to different engineering requirements:

a. Settlement: stiffness after shake-down, after reversals, accumulation, creep
b. Strength: Peak strength, dilatancy and contractancy
c. Liquefaction: dilatancy and contractancy upon monotonic or cyclic loading under undrained conditions

Of course, some other features like simplicity, originality and robustness of a model, the uniqueness of the solution or a good simulation of shear banding are also of considerable importance, however we do not consider such qualities here. We assume that all `umats` are formulated in an objective manner and neither the time nor the strain is considered as a state variable.

A serious drawback of a phenomenologically formulated constitutive model can be the violence of the 2nd Law of thermodynamics. Some users may principally reject a "non-physical" model that violates the 2nd Law irrespectively of the quality of the simulations [2,3]. Therefore we propose to allow for some inequality constraints to accompany the functional $\mathcal{F}(\boldsymbol{\epsilon}(t))$. For example, a simple thermodynamical constraint can be based on the inequality $\int \boldsymbol{\sigma} : \mathrm{d}\boldsymbol{\epsilon} > 0$ upon a closed *stress* cycle[6]. No cumulative evolution of $\boldsymbol{\alpha}$ is allowed if we want to conclude a perpetuum mobile (an inadmissible material behaviour) from $\int \boldsymbol{\sigma} : \mathrm{d}\boldsymbol{\epsilon} < 0$.

2 Assumptions for the Evaluation of $\boldsymbol{\sigma}^{L} - \boldsymbol{\sigma}^{S}$

Only rate independent constitutive models are considered (no creep or relaxation). The laboratory values are denoted by $\sqcup^{L}$ and the ones from simulation by $\sqcup^{S}$. We begin with a list of generally desired features of the evaluation algorithm.

[6] Stress is a state variable and strain is not. It is essential to recover all state variables after a cycle to check the 2nd Law.

1. We assume $\boldsymbol{\epsilon}^L(t) = \boldsymbol{\epsilon}^S(t)$ i.e. the deformation prescribed or measured in the laboratory is applied in the simulation. The quality of the simulation is evaluated comparing the stress paths $\boldsymbol{\sigma}^L(t)$ and $\boldsymbol{\sigma}^S(t)$. This assumption excludes tests with incomplete description of the strain path[7].
2. Instead of time t we use the length z of the strain path, $\mathrm{d}z = \|\dot{\boldsymbol{\epsilon}}\|\mathrm{d}t$. The length z grows monotonically so each stress component can be parametrized by a function $\sigma_{ij}(z)$.
3. The frequency of sampling used in comparison $\|\boldsymbol{\sigma}^L - \boldsymbol{\sigma}^S\|$ should not (strongly) affect the evaluation of the quality of the simulation.
4. The calculation is performed in steps understood as sequences of proportional load increments. The discrepancy $\boldsymbol{\sigma}^S - \boldsymbol{\sigma}^L$ resulting from previous steps may accumulate[8]. In order to eliminate the inherited error $\boldsymbol{\sigma}^L - \boldsymbol{\sigma}^S$ from previous steps we set $\boldsymbol{\sigma}^S_B$ to the measured value $\boldsymbol{\sigma}^L_B$ at the beginning of each step. The operation $\boldsymbol{\sigma}^S := \boldsymbol{\sigma}^L = \boldsymbol{\sigma}_B$ is further called the *alignment*.
5. The constitutive routines, `umat`, should be robust enough to survive such alignments. The void ratio needs no reset because of identical deformation program, $\boldsymbol{\epsilon}^L = \boldsymbol{\epsilon}^S$. Other state variables $\boldsymbol{\alpha}$ usually cannot be aligned because they cannot be measured.
6. We apply the alignment of stress at the beginning of each step only. Alignment after individual stress increments (or short sequences thereof) could cause a problem with asymptotic values shown (for the 1D case) in Fig. 1. Slightly overestimated yield stress can result in very different increments

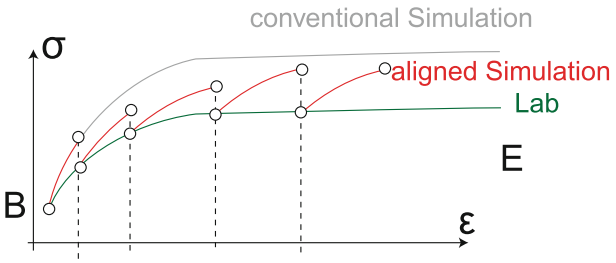

Fig. 1. Calculation of a strain-controlled step B-E using a special constitutive algorithm that aligns the simulated stress $\boldsymbol{\sigma}^S$ to the laboratory value $\boldsymbol{\sigma}^L$ after every increment in order to compare just the increments $\Delta\boldsymbol{\sigma}^S - \Delta\boldsymbol{\sigma}^L$ instead of the whole stress paths $\boldsymbol{\sigma}^S(t) - \boldsymbol{\sigma}^L(t)$

[7] Given drained triaxial test results with full description in axial direction $\epsilon_1(t), \sigma_1(t)$ and partial description in radial direction $\sigma_2(t) = \sigma_3(t)$ one can perform a calculation with IncrementalDriver and compare say $\epsilon_1^S(t)$ with $\epsilon_1^L(t)$ but one cannot use such test for calibrations and for benchmarks because some components of the strain path $\boldsymbol{\epsilon}(t)$ are neither measured nor prescribed.

[8] In some tests such accumulation has a positive feedback. For example, consider an isotropic compression calculated with a barotropic elasticity, $\dot{p} = kp\dot{\varepsilon}_{\mathrm{vol}}$. A small error at the beginning of the test will grow exponentially.

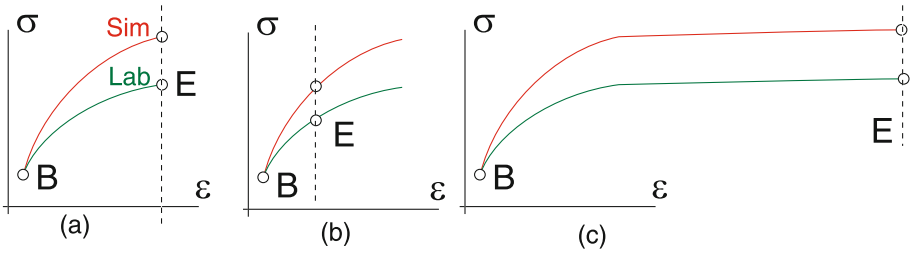

Fig. 2. All 1D tests (a–c) should be evaluated similarly, i.e. the quality of simulation is identical. Tests (a–c) differ by the duration of the step but not from the quality of the simulation.

$\Delta\sigma^S \neq \Delta\sigma^L$ if stress is aligned after each increment. Comparison of longer sequences reveals a good quality of the simulation (Fig. 2).

7. A detection of turning points should be performed using the scalar product of the directions $\vec{\boldsymbol{\epsilon}}^n : \vec{\Delta}\boldsymbol{\epsilon}^{n+1}$, wherein n is the number of increment. We expect that each stress component can be well approximated by a parabolic curve $\sigma_{ij}(z) = \frac{1}{2}\sigma''_{ij}z^2 + \sigma'_{ij}z + \sigma_{ijB}$ (Fig. 3).

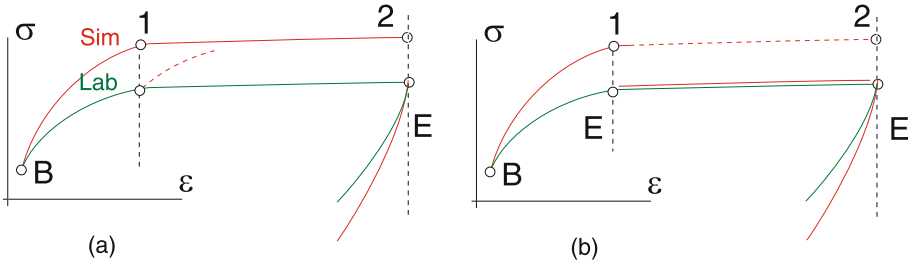

Fig. 3. Simulations with different constitutive models (a) and (b) after the alignment of stress at (1). Upon the continuation of straining 1–2 with the model (a): the discrepancy reappears and hence it cannot be treated as an inherited error. Using model (b): the discrepancy disappears so the alignment of stress is justified: further straining would increase the inherited error although the constitutive response on the strain portion 1–2 is nearly perfect.

3 Detecting Reversals and Kinks in $\epsilon^L(z)$

Due to high frequency of recording the increments may be very small and it may occur that the subsequent strain increments (read from the history) point to very different directions simply due to some noise in measurements. Therefore, it is not a good idea to use $\arccos(\vec{\Delta}\boldsymbol{\epsilon}^n : \vec{\Delta}\boldsymbol{\epsilon}^{n+1}) > \cos\theta_r$ as a definition of a reversal point.

The removal of the noise could be performed by a convolution of the raw data with a discrete Gauss distribution as a smoothing function. This is implemented in the following Mathematica procedure:

```
smoothData[data_, nGlPoints_: 2] := Module[{ker, t, n, i, EPtime, EQtime, smoothD,
   dataExtendB, dataExtendE, smoothDstep},
ker = Table[Exp[-n^2/10.0]/Sqrt[10.0 \[Pi]], {n, -nGlPoints, nGlPoints}]; ker /= (Plus @@ ker);
smoothD = ( ListCorrelate[ker , #] & /@ Transpose[data] ) // Transpose ;
dataExtendB = Array[{0, 0} &, nGlPoints]; dataExtendE = Array[{0, 0} &, nGlPoints];
Do[dataExtendB = {data[[nGlPoints-i + 1,1]], Interpolation[smoothD, data[[nGlPoints-i+1,1]] ]};
 dataExtendE = {data[[Length[data]-nGlPoints+i,1]],
   Interpolation[smoothD,data[[Length[data]-nGlPoints+i,1]]]};
   PrependTo[smoothD, dataExtendB]; AppendTo[smoothD, dataExtendE];
   ,{i, 1, nGlPoints}];
smoothD]
```

However, if the source of noise is the loading device, rather than inaccuracies in measurement, then such noise should not be removed because the material response can be affected by small oscillations that accompany the monotonic loading. Moreover, smoothing across reversals may lead to strong rounding thereof. The test $\vec{\Delta\boldsymbol{\epsilon}}^n : \vec{\Delta\boldsymbol{\epsilon}}^{n+1} > \cos\theta_r$ on smoothed kinks may overlook some rounded ones. Therefore we recommend smoothing between the reversals only.

In order to detect a reversal we propose the following algorithm. A sequence of strain increments is approximated by two consecutive strain spans $\mathbf{a}$ and $\mathbf{b}$ with a predefined length, say $\|\mathbf{a}\| = \|\mathbf{b}\| \approx L = 0.002\%$. The parameter L may be modified depending on the noise, on the size of smallest strain cycles and on the accuracy of the measurement. The spans should connect the existing records of $\boldsymbol{\epsilon}^L(t)$ and they should have a common hinge (a polygon with two segments and three points in strain space). The lengths will be only approximately equal to L (no interpolation). Our polygon is sliding along the strain path and the angle $\theta(z)$ between the arms $\mathbf{a}$ and $\mathbf{b}$ is evaluated. The (discrete) parameter z corresponds to the location of the middle point of the polygon. This angle θ shows whether the directions of strain spans (of length $\approx L$) are very different. Suppose that the strain spans $\mathbf{a}$ and $\mathbf{b}$ (arms of the polygon) point to very different directions at $z = \bar{z}$

$$\arccos(\vec{\mathbf{a}} : \vec{\mathbf{b}}) = \theta(\bar{z}) > \theta_r \tag{1}$$

say with $\theta_r = 30°$.

We do not mark $\bar{z}$ as a reversal of the strain path yet. From $\bar{z}$ on we simply integrate θ and $z\theta$ from $\bar{z}$ to $\bar{z} + L$. The reversal is defined as

$$z_r = A/B \qquad \text{wherein} \qquad A = \int_{\bar{z}}^{\bar{z}+L} z\theta(z)\mathrm{d}z \qquad \text{and} \qquad B = \int_{\bar{z}}^{\bar{z}+L} \theta(z)\mathrm{d}z \tag{2}$$

During the numerical integration the polygon is being pushed along the strain path until $z = \bar{z} + L$ is reached and we assume that beyond the reversal zone the condition (1) is not satisfied anymore. Otherwise we continue the calculation of both integrals A and B until (1) is not satisfied and then use $(2)_1$. The algorithm works reasonably also in the 1-D case (Fig. 4).

If the length of strain increments does not vary significantly, $\Delta z \approx \text{const}$, we may convert L into a particular number of increments.

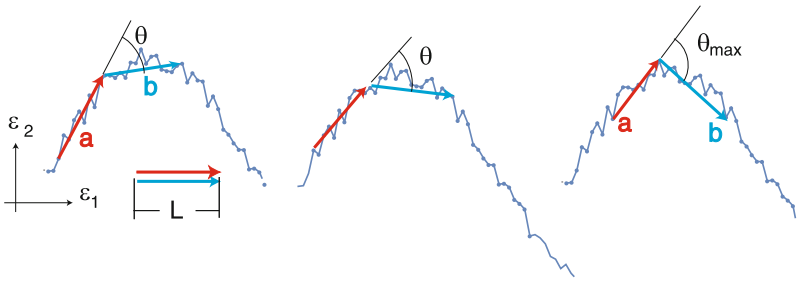

Fig. 4. Two connected strain spans **a** and **b** are used to find maximum θ while being pushed through the strain path $\boldsymbol{\epsilon}^L(z)$ over a reversal zone

4 Quantification of Discrepancies $\boldsymbol{\sigma}^S(z) - \boldsymbol{\sigma}^L(z)$

We propose a simple method to evaluate the quality of the simulations within a single step from t_B to t_E. In the absence of creep and relaxation we can use the length $z(t) = \int_{t_B}^{t} \|\dot{\boldsymbol{\epsilon}}(\tau)\| \mathrm{d}\tau$ of the strain path as the independent material time[9]. Such time grows from $z_B = 0$ to $z_E > 0$. Simulating a step we repeat the strain path obtained from (or prescribed in) the laboratory, i.e. $\boldsymbol{\epsilon}^S(z) = \boldsymbol{\epsilon}^L(z)$. All discrepancies are measured in stress only, $\boldsymbol{\sigma}^S(z) \neq \boldsymbol{\sigma}^L(z)$. We commence each step at the common stress $\boldsymbol{\sigma}^S = \boldsymbol{\sigma}^L = \boldsymbol{\sigma}_B$, i.e. we undo the differences from the previous steps and set $\boldsymbol{\sigma}^S$ to $\boldsymbol{\sigma}^L$ at the beginning of each step. After the step is completed different end-values $\boldsymbol{\sigma}_E^L = \boldsymbol{\sigma}^L(z_E)$ and $\boldsymbol{\sigma}_E^S = \boldsymbol{\sigma}^S(z_E)$ can be obtained. We propose to approximate the stress path components by parabolic curves basing on the Taylor series

$$\boldsymbol{\sigma}(z) = \boldsymbol{\sigma}_B + \boldsymbol{\sigma}' z + \frac{1}{2}\boldsymbol{\sigma}'' z^2 \quad \text{for} \quad \boldsymbol{\sigma} = \boldsymbol{\sigma}^L \quad \text{or} \quad \boldsymbol{\sigma} = \boldsymbol{\sigma}^S, \tag{3}$$

whereas $\sqcup'$ and $\sqcup''$ denote the derivatives with respect to z at $z = 0$. For the evaluation of the quality of the simulation we calculate the

- inclinations $\boldsymbol{\sigma}'_B$ and curvatures $\boldsymbol{\sigma}''_B$ at the beginning of each step s. We do it separately for $\boldsymbol{\sigma}^S(z)$ and $\boldsymbol{\sigma}^L(z)$
- contribution F^s_{raw} to the penalty function basing on differences in inclinations and in curvatures from step s
- total value of penalty function collecting all step contributions weighted by the average stress level in the step

In order to determine σ'_{ij} and σ''_{ij} we may use, apart from σ_{ijE}, the integrals $W_{ij} = \int_0^{z_E} (\sigma_{ij} - \sigma_{ijB}) \mathrm{d}z$, Fig. 5

$$W_{ij} = \int_0^{z_E} [\sigma'_{ij} z + \frac{1}{2}\sigma''_{ij} z^2] \mathrm{d}z = \frac{1}{2}\sigma'_{ij} z_E^2 + \frac{1}{6}\sigma''_{ij} z_E^3 \tag{4}$$

[9] Similarly to the concept of endochronic theory but without fading memory.

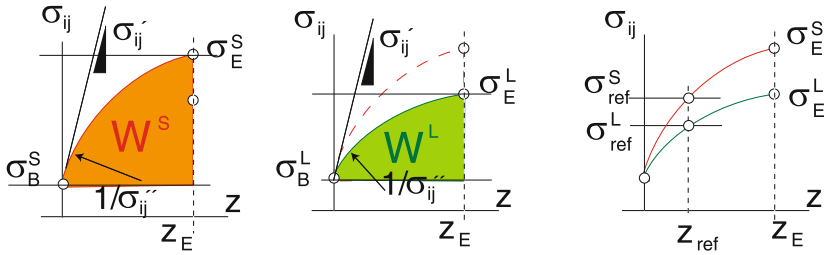

Fig. 5. The stresses $\boldsymbol{\sigma}^S_{\rm ref}$ and $\boldsymbol{\sigma}^L_{\rm ref}$ to be compared in the penalty function are evaluated at $z = z_{\rm ref} = 0.1\%$ using approximation of the step curves $\boldsymbol{\sigma}^S(z)$ and $\boldsymbol{\sigma}^L(z)$ based on Taylor expansion

The values $\sigma_{ijE} = \sigma_{ijB} + \sigma'_{ij} z_E + \frac{1}{2}\sigma''_{ij} z_E^2$ can be directly found from the history produced by IncrementalDriver and from the history obtained in the laboratory. After evaluation of z for each record the integrals W_{ij} can also be easily calculated, say using the numerical trapezoidal rule. Given σ_{ijE} and W_{ij} we may find σ'_{ij} and σ''_{ij} (both at $z = 0$) by solving

$$\left[\begin{array}{c|c} z_E & \frac{1}{2}z_E^2 \\ \hline \frac{1}{2}z_E^2 & \frac{1}{6}z_E^3 \end{array}\right] \cdot \left\{\begin{array}{c} \sigma'_{ij} \\ \sigma''_{ij} \end{array}\right\} = \left\{\begin{array}{c} \sigma_{ijE} - \sigma_{ijB} \\ W_{ij} \end{array}\right\} \tag{5}$$

We need these values for all components σ^L_{ij} and σ^S_{ij} separately. The *raw value* $F^s_{\rm raw}$ of the discrepancy in a single step s is defined as a stress difference at $z_{\rm ref} = 0.1\%$, identical in all steps. The directly determined difference $\|\boldsymbol{\sigma}^S(z_{\rm ref}) - \boldsymbol{\sigma}^L(z_{\rm ref})\|$ is less representative for the whole step than

$$F^s_{\rm raw} = \|\boldsymbol{\sigma}^L_{\rm ref} - \boldsymbol{\sigma}^S_{\rm ref}\| \quad \text{where} \quad \boldsymbol{\sigma}_{\rm ref} = \boldsymbol{\sigma}_B + \boldsymbol{\sigma}' z_{\rm ref} + \frac{1}{2}\boldsymbol{\sigma}'' z^2_{\rm ref} \tag{6}$$

obtained from the parabolic approximations of the whole step[10]. Note that the duration of a step does not influence the evaluation, at least not significantly.

The raw discrepancies $F^s_{\rm raw}$ from different steps could be simply added. However, it would not be fair to add $F_{\rm raw}$ at a very different average stresses over a step, due to the well known barotropy of granular materials. Therefore, we propose to scale $F_{\rm raw}$ in such way as if they were obtained for $p_{\rm ref} = -\frac{1}{3}{\rm tr}\,\boldsymbol{\sigma} = 100\,{\rm kPa}$ and at the critical void ratio e_c. For this purpose a baro-pyknotropic normalization factor $f(e,p)$ is used. The values of e and p should be representative for the current step. The final error is found as

$$F = \frac{1}{n_s}\sum f(e,p) F^s_{\rm raw} \quad \text{with} \quad f(e,p) = \left(\frac{p_{\rm ref}(\frac{1+e}{1+e_c})^{-1/\lambda_B}}{p}\right)^{n_B} \tag{7}$$

wherein e_c is the critical void ratio at $p_{\rm ref} = 100\,{\rm kPa}$ and $p_{\rm ref}(\frac{1+e}{1+e_c})^{-1/\lambda_B}$ is the pressure that renders the actual void ratio e to be the critical one. The constant

[10] Moreover some steps can be shorter than 0.1% and $\boldsymbol{\sigma}_{\rm ref}$ has to be extrapolated in this case.

λ_B is the inclination of the CSL slope in the double logarithmic Butterfield diagram. The exponent $n_B \approx 0.6$ describes the barotropy of stiffness $E \sim (p/p_{\mathrm{ref}})^{n_B}$ The quality of the model can be evaluated from the average value of weighted raw discrepancy from all steps and from all tests. Of course, one may use different weighting factors to favor some tests of importance for a given practical problem. This would lead to another benchmark, however.

5 A Thermodynamic Constraint

We consider an element test (state variables are homogeneous fields) of a soil sample (constant mass) under isothermal condition, $\Theta = \text{const}$. As a thermodynamic constraint we require that the constitutive model implemented as `umat` satisfies the inequality

$$\int \boldsymbol{\sigma} : \mathrm{d}\boldsymbol{\epsilon} > 0 \text{ upon any closed cycle (CC)} \tag{8}$$

By definition, the closed cycle (CC) means that not only stress but also other state variables must return to their initial values at the end of the cycle. We should have $\boldsymbol{\sigma}(T) = \boldsymbol{\sigma}(0)$ and $\boldsymbol{\alpha}(T) = \boldsymbol{\alpha}(0)$ wherein T is period of the loading function. The strain $\boldsymbol{\epsilon}$ is not a state variable in soil mechanics[11]. Hence, the condition $\boldsymbol{\epsilon}(T) = \boldsymbol{\epsilon}(0)$ is not needed in a CC.

The integral $\int \boldsymbol{\sigma} : \mathrm{d}\boldsymbol{\epsilon}$ describes the work input. The heat $s\Theta$ may flow freely from or into the sample. The internal energy is increased by the sum of the heat inflow and work input. We assume that the internal energy is a function of stress and state variables only, $U(\boldsymbol{\sigma}, \boldsymbol{\alpha})$. We may omit the temperature Θ because it is assumed to be constant. The function $U(\boldsymbol{\sigma}, \boldsymbol{\alpha})$ exists although it need not be explicitly formulated by the constitutive model under consideration. Admittedly the arguments of U are somewhat unusual[12] but the Legendre conversion of the internal energy to Gibbs free enthalpy is not necessary because we do not consider any differentials. Our criterion (8) is based solely on the fact that the internal

[11] We assume that the void ratio, which itself is usually an energetically relevant quantity, is stored directly as a component of $\boldsymbol{\alpha}$ and its evolution equation of is of the rate form $\dot{e} = (1+e)\dot{\epsilon}_{kk}$. However, one may memorize just the initial void ratio e_0 (as a kind of material constant) and calculate the current one from the total form $e = (1+e_0)\exp(\epsilon_{kk}) - 1$. In such case the void ratio need not be a state variable because it is a secondary variable to the volumetric strain. This approach renders the volumetric strain a state variable. The deviatoric part of the total strain $\boldsymbol{\epsilon}^*$ is not usually a state variable is soil mechanics. For simplicity we assume that all `umats` use the rate form $\dot{e} = (1+e)\dot{\epsilon}_{kk}$ and no part of strain need to be treated as a state variable.

[12] The caloric function for the density of internal energy is typically $\bar{U}(\boldsymbol{\epsilon}^{\mathrm{el}}, s, \dots)$ with entropy s, (elastic) strain $\boldsymbol{\epsilon}^{\mathrm{el}}$, stress $\boldsymbol{\sigma} = \partial_{\boldsymbol{\epsilon}}\bar{U}$, and temperature $\Theta = \partial_s \bar{U}$. One may resolve the latter two equations for $s(\boldsymbol{\sigma}, \Theta)$ and $\boldsymbol{\epsilon}^{\mathrm{el}}(\boldsymbol{\sigma}, \Theta)$ and substitute these expressions into the caloric equation: $U(\boldsymbol{\sigma}, \Theta, \dots) = \bar{U}(\boldsymbol{\epsilon}^{\mathrm{el}}(\boldsymbol{\sigma}, \Theta), s(\boldsymbol{\sigma}, \Theta), \dots)$. This is the form we are dealing with.

energy cannot change after a CC because $\boldsymbol{\sigma}$ and $\boldsymbol{\alpha}$ do not. If the work input (8) is positive after a CC, that is at the same U, then the heat outflow of the same amount must have occurred. Hence, the work input per CC can be called the density of one-cycle dissipation. If the work input is negative $\int \boldsymbol{\sigma} : \mathrm{d}\boldsymbol{\epsilon} < 0$ after a CC then the heat inflow must have compensated it. In the latter case the material has converted heat inflow into work output, which is known as *perpetuum mobile* of the second kind. Such material contradicts the Second Law. An important assumption in the above criterion is that *all energetically relevant state variables are known*. This means that the internal energy function $U(\boldsymbol{\sigma}, \boldsymbol{\alpha})$, even if not explicitly formulated in the constitutive description, does not depend of anything else but $\boldsymbol{\sigma}, \boldsymbol{\alpha}$ and the temperature Θ.

Of course, it is not possible to check the positiveness of energy input $\int \boldsymbol{\sigma} : \mathrm{d}\boldsymbol{\epsilon} > 0$ over all CCs. We may check only a few CCs upon which we expect this criterion to be endangered. Our test is therefore a necessary condition only. It is not sufficient for the thermodynamic consistency of the model in `umat`. All state variables $\boldsymbol{\alpha}$ may evolve during a CC according to $\boldsymbol{\alpha}(t) = \boldsymbol{\alpha}^{\mathrm{oscil}}(t) + \boldsymbol{\alpha}^{\mathrm{acc}} t/T$. We distinguish in this evolution the oscillatory (=periodic) portion $\boldsymbol{\alpha}^{\mathrm{oscil}}(t)$ with $\boldsymbol{\alpha}^{\mathrm{oscil}}(0) = \boldsymbol{\alpha}^{\mathrm{oscil}}(T)$ and the monotonic accumulation $\boldsymbol{\alpha}^{\mathrm{acc}} t/T$.

A CC tests requires $\boldsymbol{\alpha}^{\mathrm{acc}} = \mathbf{0}$. We assume that the monotonic portion of the evolution of all state variables eventually leads to asymptotic values $\boldsymbol{\alpha}^{\mathrm{asy}}$ for which no further accumulation occurs, i.e. $\int_0^T \dot{\boldsymbol{\alpha}} \mathrm{d}t = \mathbf{0}$. In order to reach such asymptotic state we may need thousands of *conditioning cycles*, however. In order to avoid such tedious calculations an iterative procedure could be used that regards the accumulation $\boldsymbol{\alpha}^{\mathrm{acc}}(\boldsymbol{\alpha}_0)$ as a function of the starting value $\boldsymbol{\alpha}_0$ of all state variables. The stress path is closed and kept unchanged. The correction $\mathbf{c}$ of the initial guess $\boldsymbol{\alpha}_0$ can be found with the Newton iteration solving

$$\boldsymbol{\alpha}^{\mathrm{acc}}(\boldsymbol{\alpha}_0 + \mathbf{c}) \approx \boldsymbol{\alpha}^{\mathrm{acc}}(\boldsymbol{\alpha}_0) + (\partial \boldsymbol{\alpha}^{\mathrm{acc}} / \partial \boldsymbol{\alpha}_0) : \mathbf{c} = \mathbf{0} \tag{9}$$

for $\mathbf{c}$. The derivative $(\partial \boldsymbol{\alpha}^{\mathrm{acc}} / \partial \boldsymbol{\alpha}_0)$ can be found numerically in each iteration. Unfortunately, such non-physical improvement of $\boldsymbol{\alpha}_0$ can easily lead to values of $\boldsymbol{\alpha}$ beyond the admissible range, especially when $\boldsymbol{\alpha}_0$ of the above iteration lied far away from the shake-down values $\boldsymbol{\alpha}^{\mathrm{asy}}$. Therefore in hard cases we preferred to apply thousands of cycles to reach a shake-down state $\boldsymbol{\alpha}$ in a natural (constitutive) manner.

In soil mechanics the usual state variables are stress $\boldsymbol{\sigma}$ and void ratio e. The closedness of stress is guaranteed by the loading program but we need to adjust the initial value e_0 of the void ratio in such way that the accumulation $e^{\mathrm{acc}}(e_0) = \int_0^T \dot{e} \mathrm{d}t = 0$ vanishes after the full stress cycle. The correction c of the initial void ratio e_0 can be found iterative from $e^{\mathrm{acc}}(e_0 + c) \approx e^{\mathrm{acc}}(e_0) + (\partial e^{\mathrm{acc}} / \partial e_0) c = 0$.

Having found the asymptotic state $\boldsymbol{\alpha}^{\mathrm{asy}}$ we may check whether energy can be extracted from the material (a perpetuum mobile of the second kind). Clockwise and counterclockwise circulations should be applied. Note that $\boldsymbol{\alpha}^{\mathrm{asy}}$ may be slightly different in both cases. IncrementalDriver can perform a stress cycle (a loading program with $\int \mathrm{d}\boldsymbol{\sigma} = 0$) whereas the integration $\int \boldsymbol{\sigma} : \mathrm{d}\boldsymbol{\epsilon}$ is performed

using the calculated strain increments. A shake down of $\boldsymbol{\alpha}$ can be easily checked in the history obtained from simulation.

In the above analysis we have assumed that the evolution equations of all variables is bounded, i.e. $\boldsymbol{\alpha}^{\mathrm{asy}}$ exists. In particular, we exclude the situation that the oscillatory portion has a different period than the one of stress. We exclude the periodic stress $\boldsymbol{\sigma}(T_\sigma) = \boldsymbol{\sigma}(0)$ and a periodic state variable $\boldsymbol{\alpha}(T_\alpha) = \boldsymbol{\alpha}(0)$ with different periods $T_\alpha \neq T_\sigma$.

5.1 Identifying All Energetically Relevant State Variables

Technically, umat may store different quantities in the list `statev` of state variables. Some of the components may be just auxiliary variables of no importance for the energy conservation, for example the number of return mapping iterations or a mobilized friction angle. In order to recognize true, i.e. energetically relevant variables α_i from the list `statev` we perform a special identification test, checking whether a variation of a component i of `statev` influences the energy input upon a CC. The relevance test may give different results upon different stress paths and for different circulations. The procedure (9), i.e. establishing of the shake-down values, need to be applied to "energetical" components `statev` only.

If one cannot exclude *a priori* any component of `statev` we check all of them. To check the relevance of the i-th component of `statev` upon a given loop and for a given circulation we proceed as follows.

1. Compute the energy input $D_0 = \int \boldsymbol{\sigma} : \mathrm{d}\boldsymbol{\epsilon}$ upon a CC path commenced from a chosen `statev`.
2. Repeat the same CC but adding a small perturbation β to the ith component of the initial `statev` and compute the energy input D_i.
3. If D_i differs significantly from D_0, then our ith component counts as a true state variable for the current CC and current circulation.

5.2 Examples

Let us consider a 2D Coulomb elastoplastic model for a cohesionless soil with a constant dilatancy angle $\tan\psi = -\dot{\epsilon}/|\dot{\gamma}|$ larger than the friction angle $\tan\varphi = |\tau|/\sigma$, i.e. $\psi > \varphi$ with geotechnical sign convention, $\sigma > 0$. The void ratio is not implemented in the model so the only state variable is stress. After a long monotonic shearing the stress remains constant, Fig. 6. Such shearing can be interpreted as a degenerated case of a CC because $\boldsymbol{\sigma}(T) = \boldsymbol{\sigma}(0)$ with an arbitrarily chosen period T. Moreover, in the asymptotic plastic flow we have $\mathrm{sign}(\dot{\gamma}) = \sigma(\tau)$ and the total mechanical power is negative, viz.

$$\tau\dot{\gamma} + \sigma\dot{\epsilon} = |\sigma\tan\varphi||\dot{\gamma}| - \sigma\tan\psi|\dot{\gamma}| = \sigma(\tan\varphi - \tan\psi)|\dot{\gamma}| < 0 \qquad (10)$$

In Fig. 6 we can interpret the $\sigma\dot{\boldsymbol{\epsilon}}$ scalar product of $\dot{\boldsymbol{\epsilon}}$ and $\boldsymbol{\sigma}$ which is evidently negative for $\psi > \varphi$.

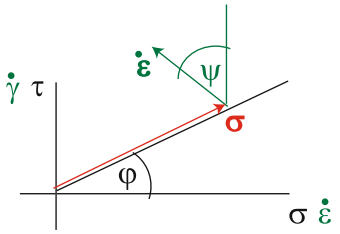

Fig. 6. Frictional material with excessive dilatancy

Declaring e as an energetically relevant state variable we could not consider the monotonic shearing as a CC anymore because of $e^{\mathrm{acc}} \neq 0$. Generally, our test with CC is suitable for materials with bounded state variables only, i.e. all state variables $\boldsymbol{\alpha}$ must reach a steady state $\boldsymbol{\alpha}^{\mathrm{asy}}$ upon a monotonic deformation with $\dot{\boldsymbol{\epsilon}} = \mathrm{const}$. However, it can be shown that such declaration is of no importance because changes in e do not influence $\int \boldsymbol{\sigma} : \mathrm{d}\boldsymbol{\epsilon}$.

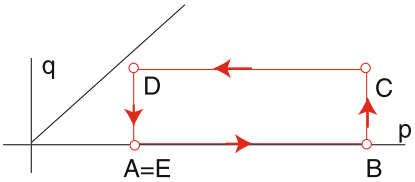

Fig. 7. A CC in stress with a barotropic hypoelastic material.

Let us consider a hypoelastic barotropic model. The bulk modulus is proportional to pressure p, $K = p/\kappa$, similarly as the shear modulus, $G = \mu p/\kappa$ with $\mu = \frac{3-6\nu}{2+2\nu}$. We consider a CC, ABCDA, Fig. 7 consisting of four steps: $\Delta p > 0; \Delta q > 0; -\Delta p; -\Delta q$; starting from the initial stress p_0 and $q_0 = 0$. We find the strain increments from the integration

$$\Delta_{AB}\epsilon_{\mathrm{vol}} = \int_{p_0}^{p_0+\Delta p} \frac{\kappa}{p}\mathrm{d}p = \kappa \ln \frac{p_0+\Delta p}{p_0} \qquad \Delta_{BC}\epsilon_q = \frac{\kappa \Delta q}{3\mu}\frac{1}{p_0+\Delta p} \tag{11}$$

$$\Delta_{CD}\epsilon_{\mathrm{vol}} = \int_{p_0+\Delta p}^{p_0} \frac{\kappa}{p}\mathrm{d}p = \kappa \ln \frac{p_0}{p_0+\Delta p} \qquad \Delta_{DA}\epsilon_q = -\frac{\kappa \Delta q}{3\mu}\frac{1}{p_0} \tag{12}$$

After the CC we obtain an accumulation of strain $\epsilon_q^{\mathrm{acc}} = \frac{\kappa \Delta q}{3\mu}(1/(p_0+\Delta p) - 1/p_0)$ but strain is not considered as an energetically relevant state variable in soils and hence its accumulation does not contradict the definition of CC.

The total work input upon a CC is

$$\int_{t_A}^{t_E} \boldsymbol{\sigma} : \dot{\boldsymbol{\epsilon}}\ \mathrm{d}t = \int_{t_A}^{t_E} \boldsymbol{\sigma} : \mathsf{C} : \dot{\boldsymbol{\sigma}}\mathrm{d}t = \oint \boldsymbol{\sigma} : \mathsf{C} : \mathrm{d}\boldsymbol{\sigma} \quad \text{with} \quad \mathsf{C} = \partial\boldsymbol{\epsilon}/\partial\boldsymbol{\sigma} \tag{13}$$

For triaxial tests p is energetically conjugated with ϵ_{vol}, similarly as q with ϵ_q. Hence, we need just two components of the compliance $C_{pp} = \kappa/p$ and $C_{qq} = \kappa/(3\mu p)$. The total work upon our CC consists of

$$U_{AB} = \int_{p_0}^{p_0+\Delta p} p\kappa/p\mathrm{d}p = \Delta p\kappa \tag{14}$$

$$U_{BC} = \int_{0}^{\Delta q} q\kappa/(3\mu(p_0+\Delta p))\mathrm{d}q = (\Delta q)^2\kappa/(6\mu(p_0+\Delta p)) \tag{15}$$

$$U_{CD} = \int_{p_0+\Delta p}^{p_0} p\kappa/p\mathrm{d}p = -\Delta p\kappa \tag{16}$$

$$U_{DA} = \int_{\Delta q}^{0} q\kappa/(3\mu p_0)\mathrm{d}q = -(\Delta q)^2\kappa/(6\mu p_0) \tag{17}$$

Their sum is negative

$$U_{ABCDA} = \frac{(\Delta q)^2\kappa}{6\mu}\left[\frac{1}{p_0+\Delta p} - \frac{1}{p_0}\right] \tag{18}$$

so the barotropic hypoelasticity is thermodynamically inadmissible.

6 Using MATHEMATICA `NMinimize[]` for Calibration

We can use the discrepancy between simulations and experimental results as described by (7) to calibrate the material constants of a constitutive model. The calibration can be formulated as follows: find the set of material constants $C_1, C_2, \dots$ that minimizes the function $F(C_1, C_2, \dots)$ defined by (7). We have done this using the MATHEMATICA's, https://www.wolfram.com/mathematica/, function `NMinimize`. In general, $F(C_1, C_2, \dots)$ cannot be expressed analytically, and therefore the gradients $\partial F/\partial C_i$ required by some local optimization algorithms can be expensive. Therefore we choose the downhill optimization algorithm (by setting the option `Method -> "NelderMead"`). This algorithm is based on evaluations of F without $\partial F/\partial C_i$.

The minimized function $F(C_i)$ is evaluated in MATHEMATICA by calls to an external Fortran program that wraps the INCREMENTALDRIVER. Hence `NMinimize` evaluates F as an external command. During the minimization procedure, MATHEMATICA writes the current set of constants in a text file, the Fortran program reads those constants from the text file, evaluates the error function F and writes its value in a text file. Finally, MATHEMATICA reads the value of F from that text file and returned that value to `NMinimize`.

To illustrate how a coupling of MATHEMATICA and Fortran works in the context of a minimization problem consider the following Fortran code which evaluates the objective function $F(C_1, C2) = \cos(C_1)\sin(C_2)$

```
      program fun
      implicit none
      character(256) :: workDir, line
      real(8) :: C1,C2,f
      workDir = 'C:\Data\projects\neoHypo\MathematicaUndFortran\'
     &      // 'Console1\Console1\Debug\'
      open(unit=10,file=trim(workDir) // 'constants.txt')
      read(10,*) C1
      read(10,*) C2
      f = cos(C1)*sin(C2)
      open(unit=11,file=trim(workDir) // 'f.txt')
      write(11,*) f
      close(10); close(11)
      end program fun
```

This program is called by the function `f` in MATHEMATICA via

```
workDir = \"C:\\Data\\projects\\neoHypo\\MathematicaUndFortran\\Console1\\Console1\\Debug\\"
f[C1_?NumberQ, C2_?NumberQ] := Module[{fval},
  iter += 1;
  Export[workDir <> "constants.txt", {C1, C2}];
  RunProcess[workDir <> "Console1.exe"] ;
  fval = Import[workDir <> "f.txt", "Table"][[1, 1]];
  fval
  ]
iter = 0;
NMinimize[{f[C1, C2], -1 <= C1 <= 1, -1 <= C2 <= 1}, {C1, C2},  Method -> {"NelderMead"},
MaxIterations -> 1000]
iter
```

Constraints to the parameters $C_1, C_2, \ldots$ can be provided directly in `NMinimize` or by returning large values of F (penalty values) in the Fortran program when the parameters violate the constraints.

7 New Developments in Neohypoplasticity

The neohypoplastic model [8] was presented in detail in the second volume of the "Holistic Simulation" series. We assume that the reader has this volume at hand and hence only some new developments of the model are presented here. Using the procedure described in Sect. 5, we were able to conclude that the evolution of the void ratio in neohypoplasticity requires an improvement. In order to check whether energy can be extracted from material, we attempted in vain to perform a true CC. In the hope of satisfying the condition $\boldsymbol{\alpha}^{\mathrm{acc}} = \mathbf{0}$ we were applying hundreds of stress cycles, see Fig. 8. After some time, $\mathbf{z}^{\mathrm{acc}} = \mathbf{0}$ established itself, but $e^{\mathrm{acc}} \neq 0$ (unlimited densification). As the condition $\boldsymbol{\alpha}^{\mathrm{acc}} = \mathbf{0}$ could not be satisfied for all state variables, the violation of the Second Law by neohypoplasticity could not be properly tested.

In order to keep $e > e_d = e_{\min}$ we proposed a limited range of ω describing the additional contractancy due to rolling and a special dilatancy term $\mathbf{m}^d Y_d$. We include both in the expression for the stress rate

$$\dot{\boldsymbol{\sigma}} = \bar{\mathsf{E}} : \left(\dot{\boldsymbol{\epsilon}} - \mathbf{m}\, Y \|\dot{\boldsymbol{\epsilon}}\| - \omega \mathbf{m}^z \, \langle -\mathbf{z} : \dot{\boldsymbol{\epsilon}} \rangle - \mathbf{m}^d Y_d \|\dot{\boldsymbol{\epsilon}}\|\right) \quad \text{with} \quad \mathbf{m}^d = -\mathbf{m}^z = \vec{\mathbf{1}} \tag{19}$$

The factor ω, initially intended as a material constant, has been rendered a barotropic function $\omega(P)$. It grows at small pressures P in accordance to the

observation that the cyclic accumulation at a constant strain amplitude accelerates with decreasing P. Hence we propose

$$\omega(P) = \frac{P_{\mathrm{ref}} f_e(e)}{z_{\max}(P_{\min}+P)}, \quad \text{where} \quad f_e = 1 - 1/\left[1+\exp(k_d(e-e_d))\right] \tag{20}$$

rapidly suppresses the "rolling" contractancy at $e \approx e_d$ or smaller. The material constants are

$z_{\max}$	$P_{\min}$	P_{ref}	k_d
0.05	3	$100\sqrt{3}$	200

.

Let us consider an extremely dense state $e < e_d$ with $\omega = 0$ due to $f_e \approx 0$ and with $Y \approx Y_{\min}$. The additional dilatancy Y_d should guarantee $\dot{e} - \dot{e}_d > 0$ for any strain rate $\dot{\boldsymbol{\epsilon}}$, i.e.

$$(1+e)\mathbf{1} : \dot{\boldsymbol{\epsilon}} + a e_d n_B (aP)^{n_B-1}\dot{P} > 0 \quad \text{with} \quad a = \sqrt{3}/h_{Bs} \quad \text{and} \quad \mathbf{1} : \dot{\boldsymbol{\epsilon}} = -\sqrt{3}\dot{\epsilon}_P$$

The rate $\dot{e}_d = e_d'(P)\dot{P}$ has been obtained from differentiation of the Bauer's compression line and $\dot{P}$ can be calculated from (19). For the sake of simplicity let us assume isotropic elasticity $\bar{E}$ and hence $\dot{P} = -\vec{\mathbf{1}} : \bar{\mathsf{E}} : (\dot{\boldsymbol{\epsilon}} - \mathbf{m}\dots) = \bar{E}_{PP}(\dot{\epsilon}_P - m_P \dots)$. The resulting inequality allows to derive the necessary Y_d. We use $e = e_d$, $-\vec{\mathbf{1}} : \mathbf{m}^d = -1$ and we overestimate the contractancy with $-\vec{\mathbf{1}} : \mathbf{m} = 1$

$$\begin{aligned} a e_d n_B (aP)^{n_B-1}\bar{E}_{PP}\left(\dot{\epsilon}_P - Y\|\dot{\boldsymbol{\epsilon}}\| + Y_d\|\dot{\boldsymbol{\epsilon}}\|\right) &> (1+e_d)\sqrt{3}\dot{\epsilon}_P \\ \bar{E}_{PP}\left(\dot{\epsilon}_P - Y\|\dot{\boldsymbol{\epsilon}}\| + Y_d\|\dot{\boldsymbol{\epsilon}}\|\right) &> (aP)^{1-n_B}\frac{(1+e_d)}{a n_B e_d}\sqrt{3}\dot{\epsilon}_P \\ \bar{E}_{PP}\left(\dot{\epsilon}_P - Y\|\dot{\boldsymbol{\epsilon}}\| + Y_d\|\dot{\boldsymbol{\epsilon}}\|\right) &> (aP)^{1-n_B}\frac{(1+e_d)}{a n_B e_d}\sqrt{3}\dot{\epsilon}_P \end{aligned} \tag{21}$$

Apart from very low pressures, say $P < 5\,\mathrm{kPa}$ the stiffness $\bar{E}_{PP}$ is significantly larger than the expression at $\dot{\epsilon}_P$ on the r.h.s of (21). Moreover Y is very small at $e = e_d$ and hence the inequality (21) can be endangered for unloading $\dot{\epsilon}_P < 0$, say for $\dot{\epsilon}_P < -1$. The deviatoric component is of no importance if $Y^d > Y$ and hence we take $\dot{\epsilon}_Q = 0$ In this case our inequality takes the form

$$Y_d - Y > 1 - (aP)^{1-n_B}\frac{(1+e_d)}{\bar{E}_{PP} a n_B e_d}\sqrt{3} \tag{22}$$

Let us denote the above value as Y_{dd}, i.e. the maximal value of Y_d. In general

$$Y_d/Y_{dd} = 1 - 1/\left[1+\exp(k_d(e_d-e))\right] \tag{23}$$

As described in [8], Sect. 4.5 there, an asymmetric term had been be added to the elastic stiffness to enable modelling of different peak friction angles under drained and undrained loading. Instead of adding an asymmetric term we propose now to rotate the stiffness, see Sect. 7.1. The advantage of this new approach is its flexibility. It allows just the deviatoric portion of stress to be rotated, which is in agreement with some additional laboratory tests presented also in Sect. 7.1.

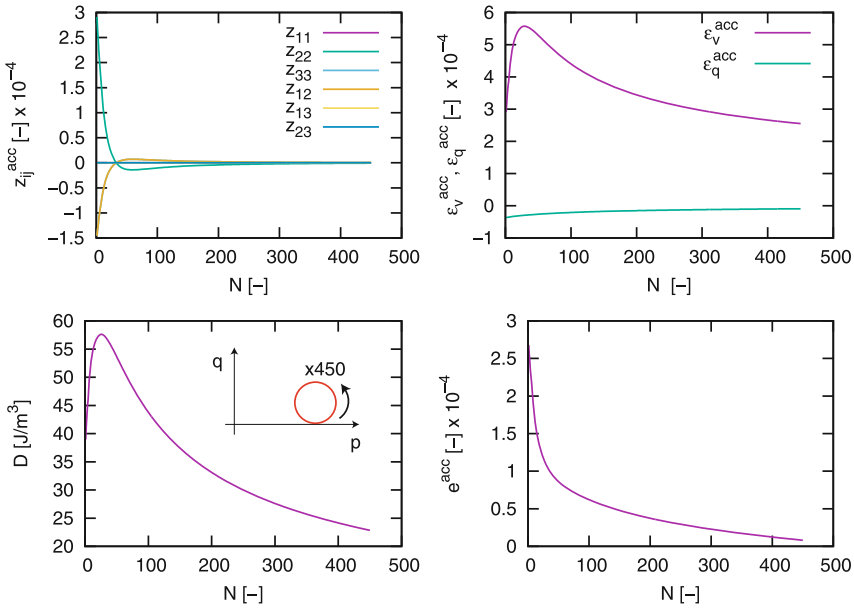

Fig. 8. Work input $D = \int \boldsymbol{\sigma} : \mathrm{d}\boldsymbol{\epsilon}$ upon 450 CC in stress using neohypoplasticity. Since $\mathbf{z}^{\mathrm{acc}}$ vanishes after few cycles, one may use the last CC to check whether energy can be extracted from material. However, this is not possible since void ratio continues decreasing after each CC.

Further, some attempts were made to provide a coupling between the neohypoplasticity and the paraelastic (PE) model for small amplitudes proposed in [9]. The major concern here was the so-called "overshooting" effect, Sect. 7.2. Finally an extension has been proposed in Sect. 7.3 to consider viscous effects (excluded from the calibration procedure).

7.1 Alternative Non-symmetric Elastic Stiffness

Instead of adding $\pm L$ to the off-diagonal terms of the stiffness matrix, as shown in [8], we propose a *rotation* of the stress rate on the $P-Q$ plane. The isometric components of the linear elastic stress $\{\dot{P}^{\mathrm{el}}, \dot{Q}^{\mathrm{el}}\}$ could be rotated using

$$\begin{Bmatrix} \dot{P} \\ \dot{Q} \end{Bmatrix} = \begin{bmatrix} c & -s \\ s & c \end{bmatrix} \cdot \begin{Bmatrix} \dot{P}^{\mathrm{el}} \\ \dot{Q}^{\mathrm{el}} \end{Bmatrix} \quad \text{with} \quad \begin{Bmatrix} \dot{P}^{\mathrm{el}} \\ \dot{Q}^{\mathrm{el}} \end{Bmatrix} = \begin{bmatrix} E_{PP} & E_{PQ} \\ E_{QP} & E_{QQ} \end{bmatrix} \cdot \begin{Bmatrix} \dot{\epsilon}_P \\ \dot{\epsilon}_Q \end{Bmatrix}, \tag{24}$$

wherein $c = \cos\beta$, $s = \sin\beta$ and $\beta > 0$ denotes a ccw rotation of the elastic stress rate on the $P-Q$ plane. It has been shown experimentally, Fig. 9, that just the deviatoric part of the stress rate should be rotated,

$$\begin{Bmatrix} \dot{P} \\ \dot{Q} \end{Bmatrix} = \begin{Bmatrix} \dot{P}^{\mathrm{el}} \\ 0 \end{Bmatrix} + \begin{bmatrix} c & -s \\ s & c \end{bmatrix} \cdot \begin{Bmatrix} 0 \\ \dot{Q}^{\mathrm{el}} \end{Bmatrix} \tag{25}$$

In the general case we need an operator R_{ijkl} that rotates the stress rate $\dot\sigma^*_{ij}$ as if it was a vector in 9 dimensional space, i.e. the Frobenius norm $\|\mathcal{R}:\dot{\boldsymbol\sigma}^*\| = \|\dot{\boldsymbol\sigma}^*\|$ does not change. However, neither the eigenvectors nor the eigenvalues of $\dot\sigma^*_{ij}$ are preserved. The rotation is performed on the plane containing the hydrostatic axis and the current stress[13], i.e. spanned by $-\vec\delta_{ij}$ and $\dot\sigma^*_{ij}$. We start by introducing two operators

$$A_{ijkl} = \vec\delta_{ij}\vec\delta_{kl} \quad \text{and} \quad D_{ijkl} = I_{ijkl} - A_{ijkl} \tag{26}$$

which extract the hydrostatic part $\mathcal{A}:\boldsymbol\sigma$ and the deviatoric part $\mathcal{D}:\boldsymbol\sigma$ from a 2nd rank tensor $\boldsymbol\sigma$, respectively.

The rotation operator $\dot{\boldsymbol\sigma}^*$ is obtained using an analogy to the Rodriguez formula

$$R_{ijkl} = I_{ijkl} + (c-1)(u_{ij}u_{kl} + v_{ij}v_{kl}) - \sqrt{1-c^2}(u_{ij}v_{kl} - v_{ij}u_{kl})\,, \tag{27}$$

wherein $u_{ij} = -\vec\delta_{ij}$ and $v_{ij} = \vec\sigma^*_{ij}$ are perpendicular unit tensors and $c = \cos\beta$ is the cosine of the rotation angle β. Tensor R_{ijkl} rotates from u_{ij} to v_{ij}, i.e. from P-axis via current Q towards $-P$. In particular, the same strain increment is rotated counterclockwise at $Q > 0$ and clockwise at $Q < 0$ in the P,Q plane. The rotation is objective and $\mathcal{R}$ is a 4th rank tensor. The stiffness is rotated for the deviatoric portion only using $\mathsf{E}^{\rm rot} = \mathcal{A}:\mathsf{E} + \mathcal{R}:\mathcal{D}:\mathsf{E}$. In the elastic case

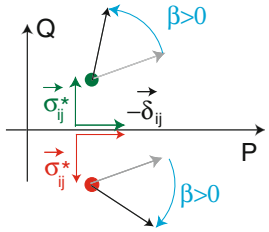

$$\dot{\boldsymbol\sigma} = (\mathcal{A}:\mathsf{E} + \mathcal{R}:\mathcal{D}:\mathsf{E}):\dot{\boldsymbol\epsilon} \tag{28}$$

```
Needs["Tensor`bnova`"]

(* u = -onev; v = onevstar;  c = Cos[a]; s =  Sin[a];  a = -Pi/6;
RR = identity4 + (c - 1) ((u~out~u) + (v~out~v) ) -    s ((u~out~v) - (v~out~u));
aa // voigtE // Inverse // voigtCi  ;   isoPQ[aa]   *)
 elUpdate[state_, de_, params_] := Module[{T, dT  , eps, RR },
    {T , eps} = state[[ 1 ;; 2]];    RR = rotationTensor[-onev, onevstar, -Pi/6];
   aa = (RR~  colon~ (deviatorer  ~colon~  iE[100, 0.2] ))
      +  ((onev~out~ onev) ~colon~  iE[100, 0.2] );
   dT = aa ~colon~ de;   {T + dT, eps + de }
   ];
g4 = stressResponsePQ[elUpdate, {-100*delta, 0*delta}, {}]
```

The objectivity of the rotation can be checked rotating the transformed (with `a`) tensor and then transforming back (with `p`) the result

```
Needs["Tensor`bnova`"]
a=aRot12[40 \[Degree]].aRot23[20 \[Degree]]; p=pRot23[20 \[Degree]].pRot12[40 \[Degree]] ;
s = DiagonalMatrix[{1, 2, 3}];  RR = rotationTensor[-onev, deviator[s], -Pi/6] // N;
Rs = RR ~colon~ s // N
asa = rotateTensor[s, a]  // N;
RRa = rotationTensor[-onev, deviator[asa], -Pi/6] ;   (* or RRa = rotateTensor[RR,a] *)
Rasa = RRa ~colon~ asa // N;  pRasap = rotateTensor[Rasa , p]  // Chop
```

[13] A generalized $\bar P - \bar Q$ plane with $\bar P = -\mathrm{tr}\,\boldsymbol\sigma/\sqrt{3}$ and $\bar Q = \|\boldsymbol\sigma^*\|$.

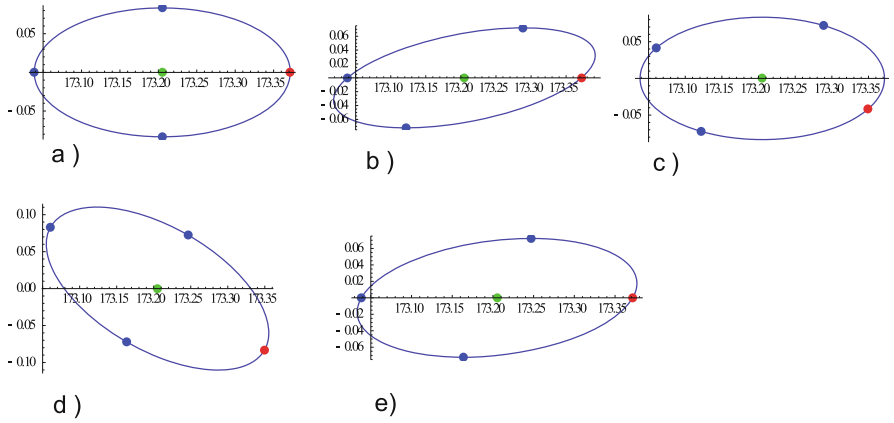

Fig. 9. Modifications of an isotropic elastic (Poisson number 0.2 shown in all pictures) response envelope in the PQ-diagram. Red point corresponds to the isotropic compression. (a) basic response envelope $\dot{\boldsymbol{\sigma}} = \mathsf{E} : \dot{\boldsymbol{\epsilon}}$, (b) deviatoric strain rate rotated CW by 30° i.e. $\dot{\boldsymbol{\sigma}} = \mathsf{E} : (\mathcal{A} + \mathcal{R} : \mathcal{D}) : \dot{\boldsymbol{\epsilon}}$, (c) total strain rate rotated CW by 30° i.e. $\dot{\boldsymbol{\sigma}} = \mathsf{E} : \mathcal{R} : \dot{\boldsymbol{\epsilon}}$, (d) total stress rate rate rotated CW by 30° i.e. $\dot{\boldsymbol{\sigma}} = \mathcal{R} : \mathsf{E} : \dot{\boldsymbol{\epsilon}}$ (e) deviatoric stress rate rate rotated CW by 30° i.e. $\dot{\boldsymbol{\sigma}} = (\mathcal{A} + \mathcal{R} : \mathcal{D}) : \mathsf{E} : \dot{\boldsymbol{\epsilon}}$. The latter modification has been confirmed by the tests.

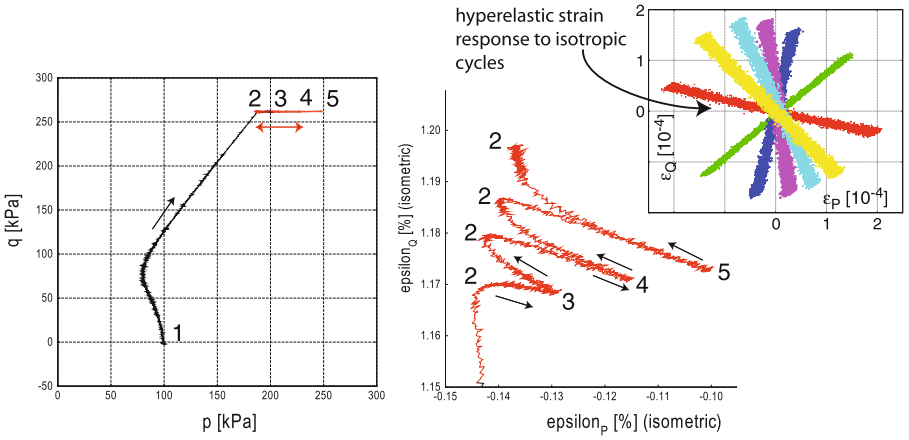

Fig. 10. Left: $p - q$ stress path consisting of several isotropic compression cycles 2-3-2-4-2-5-2 preceded by a long monotonic undrained shearing 1–2. Inclination of the strain response in the middle is similar to Strain paths in the $\varepsilon_{\text{vol}} - \varepsilon_q$ obtained from isotropic compression after conditioning (shake-down). The tests (left) were done by T. Wichtmann and L. Knittel [7].

The rotation of the deviatoric portion of stress rate only is justified by the following triaxial test, Fig. 10-left. Identical dense sand samples as described in [8], Sect. 3.1, are subjected to different isotropic compression cycles 1–2 after a long undrained shearing path 0–1. The corresponding strain increments, Fig. 10-right, are only slightly rotated off the isotropic direction.

Starting from a triaxial compression (state 1) the rotation of the strain increments was counterclockwise in the $\varepsilon_{\mathrm{vol}} - \varepsilon_q$ diagram, that means contrarily to the rotation observed in the hyperelastic part. Hence, we may conclude that the appropriate rotation of the elastic response should involve just the deviatoric stress rate, as shown in Fig. 9e. As yet there is too little systematic experimental data to decide which type of modification of isotropic stiffness is of advantage: the one from Fig. 9b or e.

7.2 Coupling of Neohypoplasticity with Paraelasticity

The paraelastic (PE) [9,11] region has been defined in [9] as a sphere in the strain space that encompass the reversible stress-strain behaviour. The PE sphere undergoes a kinematic hardening, i.e. the middle point $\boldsymbol{\epsilon}_c$ of the root reversal is "dragged" by the current strain $\boldsymbol{\epsilon}$ and rotated by the "headwind" as shown in Fig. 11. Both can be described by

$$\dot{\mathbf{e}} = c_1\,(\mathsf{I} - \vec{\mathbf{e}}\,\vec{\mathbf{e}}) : \dot{\boldsymbol{\epsilon}} \quad \text{with} \quad \mathbf{e} = \boldsymbol{\epsilon} - \boldsymbol{\epsilon}_c \quad \text{or}$$
$$\dot{\boldsymbol{\epsilon}}_c = (1 - c_1)\dot{\boldsymbol{\epsilon}} + c_1 \vec{\mathbf{e}}\,\vec{\mathbf{e}} : \dot{\boldsymbol{\epsilon}} \quad \text{with} \quad \dot{\boldsymbol{\epsilon}}_c = \dot{\epsilon} \quad \text{for} \quad \vec{\mathbf{e}} \sim \dot{\boldsymbol{\epsilon}}$$

Multiplier m_T increases stiffness E_{HP} due to change $\cos\alpha = \vec{\dot{\boldsymbol{\epsilon}}} : \vec{(\boldsymbol{\epsilon} - \boldsymbol{\epsilon}_c)}$ in the direction of straining

$$\mathsf{E} \quad \text{is interpolated between} \quad \begin{cases} \mathsf{E}_{\mathrm{HP}} & \text{for} \quad \cos\alpha > 0 \\ m_T \mathsf{E}_{\mathrm{HP}} & \text{for} \quad \cos\alpha = 0 \end{cases}$$

It turns out that the PE range may protrude beyond the yield surface after neutral loading or after a shakedown on the yield surface. This may lead to the so-called "overshooting" upon resumed monotonic deformation, Fig. 12.

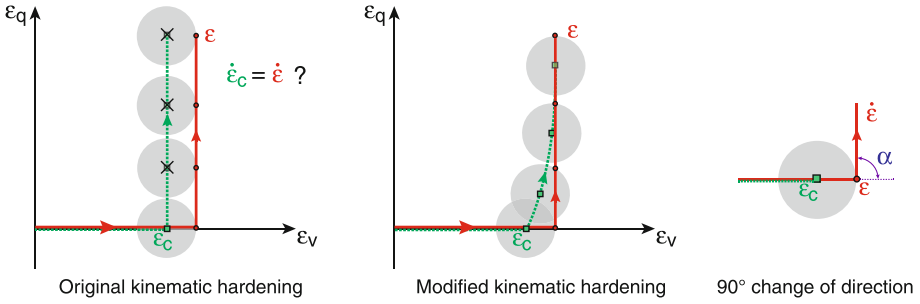

Fig. 11. The "headwind" makes the evolution of $\boldsymbol{\epsilon}_c$ similar to dragging.

A related but more serious deficiency, common to many models including PE or the intergranuar strain, can be revealed upon a slow monotonic shearing overlaid by a high-cycle oscillation[14]. The high-cycle oscillation leads to an elastic shakedown at any stress. In consequence of this, the nonlinear terms are strongly suppressed. Hence, extremely large stress ratios (including tension stress) can be reached resulting from the monotonic portion of loading.

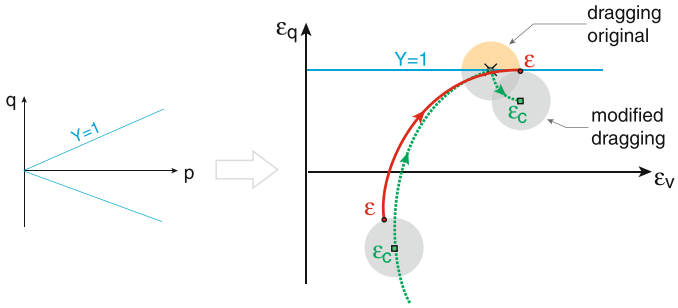

Fig. 12. Modified evolution of $\boldsymbol{\epsilon}_c$ prevents the "overshooting"

In order to circumvent this problem the following modification of the evolution equation

$$\begin{aligned} \dot{\mathbf{e}} &= -c_2 Y^n (\vec{\mathbf{e}} - \mathbf{m}) \|\dot{\boldsymbol{\epsilon}}\| \quad \text{with} \quad \mathbf{e} = \boldsymbol{\epsilon} - \boldsymbol{\epsilon}_c \quad \text{or} \\ \dot{\boldsymbol{\epsilon}}_c &= \dot{\boldsymbol{\epsilon}} + c_2 Y^n (\vec{\mathbf{e}} - \mathbf{m}) \|\dot{\boldsymbol{\epsilon}}\| \quad \text{with} \quad \dot{\boldsymbol{\epsilon}}_c = \dot{\boldsymbol{\epsilon}} \quad \text{for} \quad Y = 0 \end{aligned} \tag{29}$$

is proposed. The main purpose of (29) is to repel the centre $\boldsymbol{\epsilon}_c$ from the yield surface and to mitigate the "overshooting". On the yield surface, $Y = 1$, a state $\vec{\mathbf{e}} = \mathbf{m}$ should establish itself.

Summing up, the kinematic hardening consists of dragging with headwind and of repulsion. The resulting evolution equation has the form

$$\dot{\boldsymbol{\epsilon}}_c = (1 - c_1)\dot{\boldsymbol{\epsilon}} + c_1 \vec{\mathbf{e}}\, \vec{\mathbf{e}} : \dot{\boldsymbol{\epsilon}} + c_2 Y^n (\vec{\mathbf{e}} - \mathbf{m}) \|\dot{\boldsymbol{\epsilon}}\|$$

In the incremental formulation the above rate equation is not exact. However, in the usual projection on the surface $\|\mathbf{e} + \Delta\mathbf{e}\| = r$ we should not correct the strain $\boldsymbol{\epsilon}$ but the centre $\boldsymbol{\epsilon}_c$ of the elastic region. The $\Delta\boldsymbol{\epsilon}$ remains constant in the return mapping iteration. It can change within the equilibrium iteration only.

[14] Cycles of small amplitude but high frequency, say 100 cycles per 0.1 ‰ of monotonic deformation.

7.3 Viscosity

The neohypoplastic model has been supplemented by two rheological effects:

– slow decay of the back strain $\mathbf{e}$, which can be used to simulate aging,
– fast Bagnold viscosity for high rates of shear deformations, which can be of importance during liquefaction (at $\boldsymbol{\sigma} \approx \mathbf{0}$).

Both effects can be deactivated, e.g. for calibration procedures or thermodynamic check-up.

Relaxation of the Back Strain. The constitutive behaviour of sand is time dependent. A slow relaxation of the centre $\boldsymbol{\epsilon}_c$ of the elastic region in strain space is proposed to be described as an evolution of the so-called root reversal in the paraelastic model. The middle point $\boldsymbol{\epsilon}_c$ of the PE root reversal may evolve towards the current strain $\boldsymbol{\epsilon}$ according to

$$\dot{\mathbf{e}} = -\frac{1}{\tau}\mathbf{e} \tag{30}$$

with the relaxation time[15] $\tau(\boldsymbol{\sigma})$. After the deformation is stopped, $\dot{\boldsymbol{\epsilon}} = \mathbf{0}$, the decay $\mathbf{e} \to \mathbf{0}$ leads to $\boldsymbol{\epsilon}_c \to \boldsymbol{\epsilon}$. Hence, (30) may lead to an overshooting (Fig. 12). However, transient overshooting is acceptable for sands, cf. the TESRA model [1]. The overshooting is indeed transient: a subsequent shearing can easily reactivate the repelling mechanism (29). Relaxation (30) is driven by the time alone and repelling (29) is driven by the length of deformation. One should prevent relaxation (30) to dominate over (29) during any combination of monotonic and high-cycle loading in order to avoid problems described in Sect. 7.2. For this purpose, the relaxation time τ is rendered stress-dependent. It simply grows to infinity for large Q/P. In this case the relaxation is practically absent.

Bagnold Viscosity. Another viscous effect is proposed for very fast deformation. It may be of importance for vanishing hypoplastic stress $\boldsymbol{\sigma}^{\mathrm{HP}} = \mathbf{0}$ because the barotropic stiffness may vanish due to $\mathsf{E} \sim P^n$. The Bagnold viscosity is similar to the well known Newtonian viscosity $\boldsymbol{\sigma}^* = \mu\dot{\boldsymbol{\epsilon}}^*$ but beside shear stress $\boldsymbol{\sigma}^*$ it implements the normal stress components which is called *dispersive pressure*. Several models for debris flow or magma flow have been proposed basing on this kind of viscosity, [6]. The total viscous stress is proposed to be calculated from

$$\boldsymbol{\sigma}^{\mathrm{vis}} = \eta_{\mathrm{Bag}} \left[\dot{\boldsymbol{\epsilon}}^* - k_{\mathrm{Bag}} \vec{\mathbf{1}} \|\dot{\boldsymbol{\epsilon}}^*\| \right] , \tag{31}$$

[15] The half-life of $\mathbf{e}$ is $\tau \ln(2)$.

wherein minus is due to the mechanical sign convention. Only linear dependence[16] is used in (31) with[17] dynamic friction $k_{\mathrm{Bag}} \approx 0.7$ and dynamic viscosity $\eta_{Bag} \approx 0.02\,\mathrm{kPa}$. Formally, the stress rate $\mathring{\boldsymbol{\sigma}}^{\mathrm{vis}}$ obtained from time differentiation of (31) can be added (parallel coupling) to the hypoplastic rate $\mathring{\boldsymbol{\sigma}}^{\mathrm{HP}}$

$$\mathring{\boldsymbol{\sigma}} = \mathring{\boldsymbol{\sigma}}^{\mathrm{HP}} + \mathring{\boldsymbol{\sigma}}^{\mathrm{vis}} \quad \text{with} \quad \mathring{\boldsymbol{\sigma}}^{\mathrm{vis}} = \eta_{\mathrm{Bag}} \left[\ddot{\boldsymbol{\epsilon}}^{*} - k_{\mathrm{Bag}} \vec{\mathbf{1}} (\dot{\boldsymbol{\epsilon}}^{*})^{\rightarrow} : \ddot{\boldsymbol{\epsilon}}^{*} \right] \tag{32}$$

In numerical implementation we use (31) rather than the incremental form of (32). For this purpose the viscous stress $\boldsymbol{\sigma}^{\mathrm{vis}\ n}$ from the previous increment need to be memorized. Given the updated stress $\boldsymbol{\sigma} + \overset{\Delta}{\boldsymbol{\sigma}}^{\mathrm{HP}}$ we first subtract $\boldsymbol{\sigma}^{\mathrm{vis}n}$ stored as a state variable and then we add the current viscous stress $\boldsymbol{\sigma}^{\mathrm{vis}}$ from (31). The main argument for using (31) is the accuracy upon sudden strain path reversals. Although such reversals are rare in reality, they may often appear in numerical simulations. Equation (32) may evoke artificial stress jump upon reversals due to $(\dot{\boldsymbol{\epsilon}}^{*})^{\rightarrow} : \ddot{\boldsymbol{\epsilon}}^{*} \neq 0$, especially for small time increments. As an illustrative example

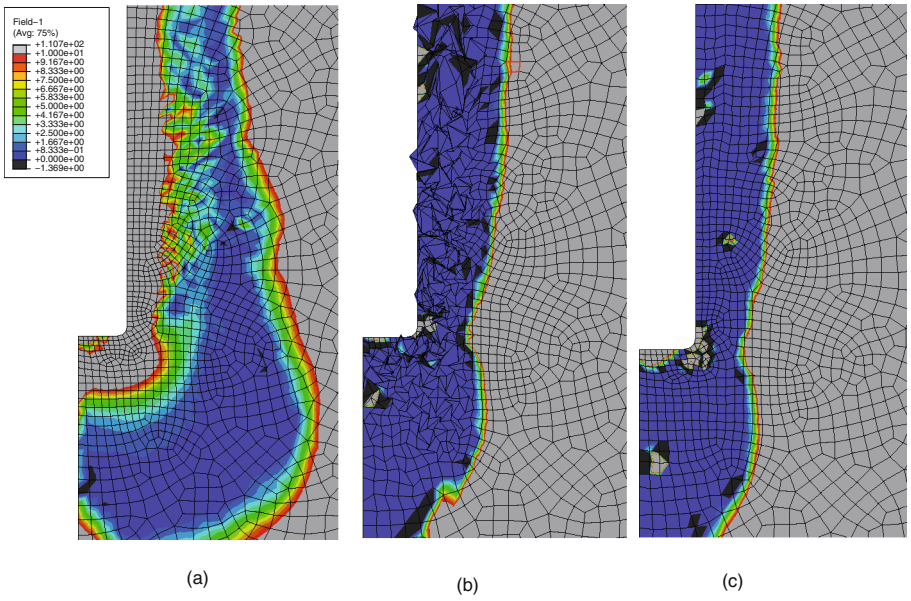

Fig. 13. Liquified zone around a vibrating pile (axial symmetry). The von Wolffersdorff hypoplastic [16] version (a) predicts excessive spreading [10,12] of the this zone, compared to neohypoplasticity (b, c). A strong mesh distortion is observed in the liquefied zone if calculated with neohypoplasticity without viscosity (b). It is evident that the Bagnold viscosity can regularize the calculation with neohypoplasticity (c).

[16] Hunt et al. [4] showed that two velocity ranges, originally proposed by Bagnold, are not necessary.

[17] These parameters are obtained from rough extrapolation of experiments on suspensions with very low density.

let us consider a 180° reversal changing the sign of $\dot{\boldsymbol{\epsilon}}^*$ but keeping $\|\dot{\boldsymbol{\epsilon}}^*\| = \text{const}$. According to (32) the dispersive pressure will jump by $-\eta_{\text{Bag}} k_{\text{Bag}} \vec{\mathbf{1}}(\dot{\boldsymbol{\epsilon}}^*)^{\rightarrow} : \ddot{\boldsymbol{\epsilon}}^* \Delta t$ although it is clear from (31) that it should remain unchanged. The viscous part of stress contributes to the Jacobian matrix as follows

$$\mathcal{D}^{\text{vis}} = \frac{\partial \boldsymbol{\sigma}^{\text{vis}}}{\partial \overset{\triangle}{\boldsymbol{\epsilon}}} = \frac{\eta_{\text{Bag}}}{\Delta t} \left[\mathsf{J}^D - k_{\text{Bag}} \vec{\mathbf{1}} (\overset{\triangle}{\boldsymbol{\epsilon}}^*)^{\rightarrow} \right] \tag{33}$$

with the tensor $J^D_{ijkl} = \delta_{ik}\delta_{jl} - \frac{1}{3}\delta_{ij}\delta_{kl}$ of deviatoric projection, $\sqcup^* = \mathsf{J}^D : \sqcup$.

For isometric components (31) takes the form

$$\begin{cases} P^{\text{vis}} & = \eta_{\text{Bag}} k_{\text{Bag}} |\overset{\triangle}{\epsilon}_Q| / \Delta t \\ Q^{\text{vis}} & = \eta_{\text{Bag}} \overset{\triangle}{\epsilon}_Q / \Delta t \end{cases} \tag{34}$$

and the Jacobian is a 2×2 matrix

$$\left[\mathcal{D}^{\text{vis}}\right] = \left[\begin{array}{c|c} 0 & s k_{\text{Bag}} \\ \hline 0 & 1 \end{array}\right] \frac{\eta_{\text{Bag}}}{\Delta t} \quad \text{with} \quad s = \text{sign}(\overset{\triangle}{\epsilon}_Q) \tag{35}$$

Importance of Bagnold Viscosity. It turns out that Bagnold viscosity can strongly influence the FEM simulations of the installation process of a vibro-injection pile. In an example calculation we tested an axisymmetric FE-model with a dynamic 34 Hz loading under undrained conditions. We used Bagnold to simulate the liquified soil material as an extremely dense suspension. The neo-hypoplasticity results in a much narrower liquefied zone and Bagnold viscosity provides a natural regularization, Fig. 13.

8 Conclusions

The proposed computer-aided calibration and benchmarking of constitutive models is very promising. The essential element of the algorithm is the scalar penalty functional $\mathcal{F}()$ that allows for an objective evaluation of the quality of the constitutive simulation. This functional requires several auxiliary operations like detection of kinks and a so-called alignment that eliminates inherited errors from earlier steps. Other undesired factors, like the length of the path or the stress level, may also endanger the objectivity of the evaluation. They have been mitigated too. The calibration of the material constants is simply a minimization of the penalty functional $\mathcal{F}()$ for a given set of tests with fixed strain paths. This operation, possibly under consideration of additional constraints, is delegated to MATHEMATICA. An important constraint is the consistency with the Second Law. A computer-aided checkup of this aspect of a material model has been developed. This consistency checkup turned out to be very helpful in the development of neohypoplasticity. Basing on its results a modification to the evolution of the volumetric strain has been proposed. Moreover it turned out that the asymmetric portion of stiffness would work better if controlled by the strain

path length z rather than by the the stress obliquity. Finally, several recent developments of the neohypoplastic model have been presented. They replace the asymmetric part of stiffness by a special rotation of stiffness. Optionally, a rheological mechanism has been added for the back stress evolution. Moreover a viscous stress (of Bagnold type) has been implemented in order to improve simulations of liquefied sands.

References

1. Benedetto, H., Tatsuoka, F., Ishihara, M.: Time dependent shear deformation characteristics of sand and their constitutive modelling. Soils Found. **41**, 1–21 (2001)
2. Gudehus, G., Jiang, Y., Liu, M.: Seismo- and thermodynamics of granular solids. Granul. Matter **13**, 319–340 (2010)
3. Houlsby, G.T., Puzrin, A.M.: Principles of Hyperplasticity. Springer, London (2006)
4. Hunt, M.L., Zenit, R., Campbell, C.S., Brennen, C.E.: Revisiting the 1954 suspension experiments of R.A. Bagnold. J. Fluid Mech. **452**, 1–24 (2002)
5. Johansson, H., Runesson, K., Larsson, F.: Parameter identification with sensitivity assessment and error computation. GAMM-Mitteilungen **30**(2), 430–457 (2007). doi:10.1002/gamm.200790026
6. Johnson, A.: A model for grain flow and debris flow. Technical report 96–728, US Department of the Interior, US Geological Survey, Denver, Colorado (1996)
7. Knittel, L.J.: Fortgesetzte quasi-statische Untersuchungen zur Elastizität von Sand als Grundlage eines neuen hypoplastischen Stoffmodells. Bachelorarbeit, Institut für Boden- und Felsmechanik, Karlsruher Institut für Technologie, September 2014
8. Niemunis, A., Tavera, C.E.G., Wichtmann, T.: Peak stress obliquity in drained and undrained sands. simulations with neohypoplasticity. In: Triantafyllidis, T. (ed.) Holistic Simulation of Geotechnical Installation Processes. LNACM, vol. 80, pp. 85–114. Springer, Heidelberg (2016). doi:10.1007/978-3-319-23159-4_5
9. Niemunis, A., Prada-Sarmiento, L.F., Grandas-Tavera, C.E.: Paraelasticity. Acta Geotech. **6**(2), 67–80 (2011)
10. Osinov, V.A., Chrisopoulos, S., Grandas-Tavera, C.: Vibration-induced stress changes in saturated soil: a high-cycle problem. In: Triantafyllidis, T. (ed.) Holistic Simulation of Geotechnical Installation Processes. LNACM, vol. 80, pp. 69–84. Springer, Heidelberg (2016). doi:10.1007/978-3-319-23159-4_4
11. Prada Sarmiento, L.F.: Paraelastic description of small-strain soil behaivour. Ph.D. thesis, IBF, Karlsruher Institut für Technologie, Nr. 173 (2012)
12. Chrisopoulos, S., Osinov, V.A., Triantafyllidis, T.: Dynamic problem for the deformation of saturated soil in the vicinity of a vibrating pile toe. In: Triantafyllidis, T. (ed.) holistic simulation of geotechnical installation processes. LNACM, vol. 80, pp. 53–67. Springer, Heidelberg (2016). doi:10.1007/978-3-319-23159-4_3
13. Wichtmann, T., Niemunis, A., Triantafyllidis, T.: Improved simplified calibration procedure for a high-cycle accumulation model. Soil Dyn. Earthquake Eng. **70**, 118–132 (2015)

14. Wichtmann, T., Triantafyllidis, T.: An experimental data base for the development, calibration and verification of constitutive models for sand with focus to cyclic loading. Part I: tests with monotonic loading and stress cycles. Acta Geotech. **11**(4), 739–762 (2016). doi:10.1007/s11440-015-0402-z
15. Wichtmann, T., Triantafyllidis, T.: An experimental data base for the development, calibration and verification of constitutive models for sand with focus to cyclic loading. Part II: tests with strain cycles and combined loading. Acta Geotech. **11**(4), 763–774 (2016). doi:10.1007/s11440-015-0412-x
16. von Wolffersdorff, P.-A.: Eine neue Version des erweiterten hypoplastischen Stoffgesetzes. Mech. Cohesive Frict. Mater. **1**, 251–271 (1993)

Simulation of Cyclic Loading Conditions Within Fluid-Saturated Granular Media

Wolfgang Ehlers[1], Maik Schenke[1(✉)], and Bernd Markert[2]

[1] Institute of Applied Mechanics (CE), University of Stuttgart, Stuttgart, Germany
Maik.schenke@mechbau.uni-stuttgart.de

[2] Institute of General Mechanics, RWTH Aachen University, Aachen, Germany

Abstract. In civil engineering, the installation of a reliable foundation is essential for the stability of the emerging structure. Already during the foundation process, a comprehensive survey of the mutual interactions between the preliminary established construction pit and the surrounding soil is indispensable, especially, when building in an existing context. In this regard, drawing our attention to the construction site at the Potsdamer Platz in Berlin, which resides within a nearly fully saturated soil and in the immediate vicinity of existing structures, measurements have revealed significant displacements of the retaining walls during the vibratory installation of the foundation piles via a so-called vibro-injection procedure. Herein, due to the gradual plastic strain accumulation and the small pore-fluid permeability of the granular assembly, the rapid cyclic loading conditions gave rise to a gradual pore-pressure build-up, which degraded the load-bearing capacity of the surrounding soil.

Addressing the simulation of cyclic loading conditions within a fluid-saturated soil, the present contribution proceeds from a multi-phasic continuum-mechanical approach based on the Theory of Porous Media (TPM), where the solid scaffold is described as an elasto-(visco)plastic material incorporating both an isotropic and a kinematic hardening model. The properties of the proposed solid-skeleton description are extensively discussed. Moreover, the model response is compared to experimental data.

Keywords: Elasto-plasticity · Soil mechanics · Theory of Porous Media

1 Introduction

A soil is a complex aggregate of several mutual interacting components. On the one hand, it consists of the soil grains composing the solid skeleton and, on the other hand, of a single or multiple pore fluid(s), e.g. pore water or pore gas, occupying the intergranular pore space. Consequently, due to their granular structure, soils cannot be classified as solids or fluids, as their macroscopic observed state (solid- or fluid-like) strongly relies upon the loading conditions and the mutual interactions between the individual constituents. For instance, common failure scenarios, such as slope instabilities or soil liquefactions, can be

T. Triantafyllidis (ed.), *Holistic Simulation of Geotechnical Installation Processes*,
Lecture Notes in Applied and Computational Mechanics 82, DOI 10.1007/978-3-319-52590-7_8

traced back to a pore-pressure build-up. In particular, the contract tendency of the granular assembly gives rise to an excess of pore pressure, which degrades the intergranular normal contact forces and, thereby the intergranular frictional forces. In consequence, the load-bearing capacity of the overall soil compound decreased.

The present contribution is dedicated to the numerical simulation of liquid-saturated granular assemblies, which are subjected to cyclic loading conditions as they occur, for instance, during earthquakes or geotechnical installations processes (e. g. installation of vibro-injection piles). Aiming at the stability analysis of fluid-saturated granular media, there are several models available, see, e. g., [33,44], from which most are based on the phenomenological and somehow ad hoc formulated *Biot*'s theory [4], however, proceeding from different approaches in order to describe the solid-skeleton behaviour. In this regard, special attention needs to be paid to the description of the contractant (densification) and dilatant (loosening) behaviour of the granular assembly under pure shear deformations as a consequence of the micro-structural grain motions, such as grain sliding and grain rolling. Depending on the initial density, the soil exhibits a macroscopically contractant (loose soil) or dilatant behaviour (dense soil) under shear loading, where in the latter, although the dilatant regime is more pronounced, the deformation behaviour is preceded by a slight contractant property at first. However, experimental observations have revealed that with ongoing shear deformation, independent of the initial soil state (loose or dense), the soil reaches a critical state from which on no further volumetric changes occur, see [8]. This observation motivated the development of so-called critical-state-line (CSL) models, see, e. g., [27,34,37]. In this regard, some are associated with the Cam-Clay-based descriptions, see, e. g. [27] or [34], and others with the hypoplasticity framework, see e. g. [41]. Furthermore, it is also worth to mention the more phenomenological approaches, such as [45,46], which employ a direct stress-strain relation that distinguishes between loading and unloading stages. Other approaches account for the hardening (and softening) behaviour through kinematic hardening models. Herein, the yield surface is translated or rotated within the principle stress space through a so-called kinematic back-stress tensor and/or a rotation tensor, respectively. In this connection, further two concepts can be distinguished to handle the nonlinear hardening (or softening) material properties. On the one hand, there are the so-called multiple-yield-surface models, which have been introduced by [23,30]. Herein, various nested yield surfaces are defined, where each subdomain is associated with constant hardening parameters. Upon loading, the individual hardening regimes are gradually activated and the hardening behaviour accumulates. These models suffer from their piece-wise linear hardening properties and theoretically require an infinite number of nested yield surfaces to accurately recover the non-linear behaviour and, in turn, a significant number of material parameters. On the other hand, there are the nonlinear kinematic hardening models, which already propose a non-linear relation for the evolution of the kinematic back-stress tensor, see, e. g., [1], or the evolution of

the rotation tensor, respectively. A comparison between both concepts can be found in [28].

For the purpose of this contribution, the description of the soil aggregate proceeds from the thermodynamically consistent TPM as a suitable modelling approach. Herein, the overall soil is described as an immiscible biphasic aggregate composed of the soil grains and the percolating pore water. The description of the solid skeleton is based on the approach of [13], who proposed an elasto-(visco)plastic formulation incorporating an isotropic hardening model and a stress-dependent failure surface. The model has been validated through the simulation of small-scale slope-failure experiments. Subsequently, the solid-skeleton model was incorporated into a dynamic biphasic formulation by [19,22] to cope with dynamic loading conditions and the related phenomena therein, such as dynamic soil liquefaction, thereby illustrating that the TPM-based modelling approach appropriately accounts for the important solid-skeleton-pore-fluid interaction. For the purpose of this contribution, the formulations of [13] will be further enhanced through a kinematic hardening model based on nonlinear evolution of the kinematic back-stress tensor to overcome its shortcomings under quasi-static cyclic loading conditions.

2 Fluid-Saturated Soil Model

In what follows, a fluid-saturated soil model is presented. In this regard, at first, the theoretical framework namely the TPM is briefly reviewed. For a more detailed insight refer, e. g., to [6,18] and references therein. Subsequently, the governing equations are tailored to describe a fluid-saturated soil, where particular focus is put on the description of the elasto-plastic behaviour of the solid skeleton.

2.1 Preliminaries

With respect to the TPM, the overall aggregate is treated as an immiscible mixture of various interacting components φ^α, which are assumed to be homogeneously distributed within a representative elementary volume (REV) $\mathrm{d}v$. However, addressing the simulation of fluid-saturated soils, the overall aggregate is composed of the solid skeleton ($\alpha = S$), assembled by the soil grains, and of the pore liquid ($\alpha = L$) representing the pore water. The composition of the bulk volume element is defined through the respective volume fractions $n^\alpha = \mathrm{d}v^\alpha / \mathrm{d}v$, where $\mathrm{d}v^\alpha$ is the partial volume of the component φ^α within the REV. Note that the saturation condition $\sum_\alpha n^\alpha = n^S + n^L = 1$ must hold.

Following this, two density functions are defined. The material (realistic or effective) density $\rho^{\alpha R} = \mathrm{d}m^\alpha / \mathrm{d}v^\alpha$ relates the components local mass $\mathrm{d}m^\alpha$ to its volume $\mathrm{d}v^\alpha$, while the partial (global or bulk) density $\rho^\alpha = \mathrm{d}m^\alpha / \mathrm{d}v$ is associated with the bulk volume. Moreover, both density definitions are related to each other through $\rho^\alpha = n^\alpha \rho^{\alpha R}$. As we assume materially incompressible and uncrushable grains, the realistic density of the solid remains constant under the

prescribed isothermal conditions, but the bulk density can still change through a changing volume fraction n^α.

2.2 Kinematics

In the framework of the TPM, the individual components φ^α are treated as superimposed continua, where each spatial point is simultaneously occupied by particles of both components. Moreover, each component is moving according to its own motion function and, thus, has its own velocity field. In this regard, it is convenient to express the solid motion in the *Lagrange*an description through the solid displacement $\mathbf{u}_S$ and the motion of the pore-liquid component φ^L in the *Euler*ian setting relative to the solid motion through the seepage velocities $\mathbf{w}_L$:

$$\begin{aligned} &\bullet \text{ solid:} && \mathbf{u}_S = \mathbf{x} - \mathbf{X}_S,\ (\mathbf{u}_S)'_S = \overset{\prime}{\mathbf{x}}_S, \\ &\bullet \text{ pore liquid:} && \mathbf{w}_L = \overset{\prime}{\mathbf{x}}_L - \overset{\prime}{\mathbf{x}}_S\,. \end{aligned} \tag{1}$$

Therein, $\mathbf{X}_S$ denotes the position of a solid material point in the reference configuration ($t = t_0$), while $\mathbf{x}$ is the position of a point in the current configuration ($t > t_0$). Moreover, $(\cdot)'_S$ and $(\cdot)'_L$ denote the material time derivatives following the motion of the solid skeleton and the pore fluid, respectively.

2.3 Balance Relations

The underlying balance equations proceed from the balance equations of classical continuum mechanics. However, with respect to an efficient solution procedure, the set of governing balance laws is tailored to the particular application scenario of the present contribution by imposing several constraints on the general balance laws. In this regard, the individual constituents are assumed to be materially incompressible, i. e. $(\rho^{\alpha R})'_S = 0$, and mass-exchange processes among them are excluded. Moreover, only quasi-static processes are considered, i. e. the acceleration terms are dropped, and the investigations are restricted to isothermal processes. Note that, in order to obtain a thermodynamically consistent model, the entropy inequality is exploited additionally. However, its lengthy evaluation is not carried out here, instead, only the final results are given. An interested reader is referred, for instance, to [12,16] and references therein. Following these elaborations, the underlying balance laws are the momentum balance and the volume balance both associated with the overall aggregate:

$$0 = \operatorname{div}(\mathbf{T}^S_E - p\,\mathbf{I}) + (\rho^S + \rho^L)\mathbf{g}, \tag{2}$$

$$0 = \operatorname{div}(\mathbf{v}_S + \frac{k^L}{\gamma^{LR}}\{\rho^{LR}\mathbf{b} - \operatorname{grad} p\}). \tag{3}$$

Therein, $\mathbf{g}$ is the unique mass-specific body force (gravity), k^L is the hydraulic conductivity (*Darcy* permeability) and $\gamma^{LR} = g\rho^{LR}$ is the effective fluid weight with $g = |\mathbf{g}| = \text{const.}$ as the scalar gravitational acceleration. Moreover,

$\mathbf{T}_E^S$ is the effective solid stress, which is associated with the intergranular forces, p is the pore-fluid pressure and $\mathbf{I}$ is the second-order identity tensor. The corresponding primary variables of the resulting independent field variables are the solid displacement $\mathbf{u}_S$ and the pore-liquid pressure p.

2.4 Solid Skeleton

Due to its granular microstructure, the solid skeleton exhibits a complex material behaviour. In particular, the macroscopic behaviour of the granular assembly is a result of the microstructural grain motions leading to irreversible (plastic) deformations on the macroscopic level. These plastic deformations are of particular importance during multiple loading-unloading loops, see, for instance, the comprehensive experimental observations of [2], where irreversible deformations have been found during both pure deviatoric and pure isotropic loading conditions. To mimic the gradual accumulation of plastic deformations during cyclic loading, kinematic hardening model are commonly used, thereby usually proceeding either from a rotation or a translation of the yield surface within the principle stress space. An example of the former can be found in [29], where the yield surface is allowed to tilt over the hydrostatic axis of the principle stress space. In contrast, other authors, for instance [1,5], follow the latter approach. For the purpose of this contribution, the latter is used, as it, in contrast to the rotational hardening approach, additional allows for a plastic strain accumulation observed during cyclic isotropic compression see e. g. [2].

For the purpose of this contribution, the constitutive description of the solid skeleton is based on [13], where an elasto-plastic formulation proceeding from comprehensive quasi-static monotonic experiments has been proposed. In particular, the experiments have revealed that the shape of the failure surface, which, in turn, governs all admissible stress states, is not constant but depends on the current isotropic stress state. Moreover, an isotropic hardening formulation has been used to account for material hardening. To additionally account for the hardening properties of granular assemblies under cyclic loading conditions, the given formulation of [13] is extended through a translational kinematic hardening model yielding a mixed isotropic-kinematic hardening model. Following the elasto-plastic modelling framework, this section comprises the individual model components, in particular, the description within the elastic domain, the yield criterion, the evolution of the plastic strains, the isotropic and the kinematic hardening models, and the stress-dependent failure surface.

Preliminaries. The description of the solid skeleton is constrained to the small strain regime. Consequently, the linear solid-strain tensor is given by

$$\varepsilon_S = \frac{1}{2}(\operatorname{grad}\mathbf{u}_S + \operatorname{grad}^T\mathbf{u}_S) \qquad \longrightarrow \qquad \varepsilon_S = \varepsilon_{Se} + \varepsilon_{Sp}, \tag{4}$$

which, in the framework of elasto-plasticity, is additively split into an elastic ε_{Se} and a plastic part ε_{Sp}. Following this, the solid volume fraction can be written as, see [20],

$$n^S = n_{0S}^S(1-\varepsilon_S^V) = n_{0S}^S(1-\varepsilon_{Sp}^V)(1-\varepsilon_{Se}^V) = n_p^S(1-\varepsilon_{Se}^V). \tag{5}$$

Therein, n_{0S}^S denotes the initial solid volume fraction and $\varepsilon_S^V = \operatorname{div} \mathbf{u}_S = \boldsymbol{\varepsilon}_S \cdot \mathbf{I}$ is the volumetric solid strain, which is split into its corresponding elastic part $\varepsilon_{Se}^V = \boldsymbol{\varepsilon}_{Se} \cdot \mathbf{I}$ and plastic part $\varepsilon_{Sp}^V = \boldsymbol{\varepsilon}_{Sp} \cdot \mathbf{I}$. Moreover, with respect to the assumed small strain regime, the effective solid stress tensor is approximated by its linearised formulation $\boldsymbol{\sigma}_E^S$, i. e. $\boldsymbol{\sigma}_E^S \approx \mathbf{T}_E^S$. Note that, as we proceed from a continuum-mechanical framework, volumetric compression corresponds to negative volumetric quantities, i. e. $\boldsymbol{\sigma}_E^S \cdot \mathbf{I} < 0$ and $\varepsilon_S^V < 0$, whereas volumetric expansion corresponds to positive volumetric quantities, i. e. $\boldsymbol{\sigma}_E^S \cdot \mathbf{I} > 0$ and $\varepsilon_S^V > 0$. Within the elasto-plastic setting, the investigation, whether the current stress state yields purely elastic, or elasto-plastic deformations, is made based on the yield criterion $F(\boldsymbol{\sigma}_E^S)$, where the deformation is purely elastic for $F < 0$ and elasto-plastic for $F = 0$. In a graphical representation, the yield limit, $F = 0$, is depicted through the so-called yield surface in the principle stress space. It bounds the elastic domain and, consequently, defines all elastic stress states. Once plastic deformations are commenced, the load cannot increase any further unless the elastic domain is altered through a suitable hardening mechanism. In this regard, in order account for hardening or softening effects, the hardening model has to alter the shape of the yield-surface (isotropic hardening) or translate the yield locus

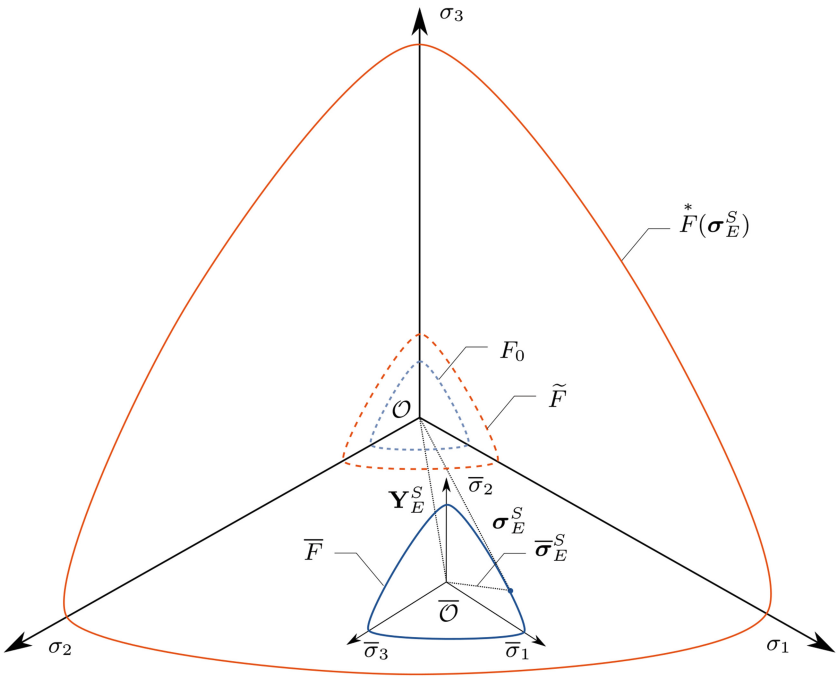

Fig. 1. Illustration of the failure surface $\overset{*}{F}$ and of the isotropic and kinematic hardening concepts.

through the principle stress space (kinematic hardening), where in any case the failure surface bounds the ultimately allowable stress states, see Fig. 1[1].

In this regard, in order account for hardening or softening effects, the hardening model needs to alter the shape of the yield-surface (isotropic hardening) or translate the yield locus through the principle stress space (kinematic hardening), where the failure surface $\overset{*}{F}$ bounds the ultimately allowable stress states, see Figure 1. Note that, following the findings of [13], the failure surface is not constant but depends on the current stress state, i. e. $\overset{*}{F} = \overset{*}{F}(\boldsymbol{\sigma}_E^S)$. Proceeding from the isotropic hardening model, the shape of the yield surface is altered, e. g., via expansion or shrinkage, from its initial state F_0 towards its current state $\widetilde{F}$ through a variation of the yield surface parameters. In case of kinematic hardening, the yield locus is shifted from its initial position $\mathcal{O}$ towards $\overline{\mathcal{O}}$ within the principle stress space $\{\sigma_1, \sigma_2, \sigma_3\}$ via the back-stress tensor $\mathbf{Y}_E^S$ (shifting tensor), viz.

$$\boldsymbol{\sigma}_E^S = \overline{\boldsymbol{\sigma}}_E^S + \mathbf{Y}_E^S \,. \tag{6}$$

Combining both hardening concepts, the yield surface is simultaneously shifted (kinematic hardening) and altered (isotropic hardening) simultaneously, where the latter is described within the shifted principle stress space $\{\overline{\sigma}_1, \overline{\sigma}_2, \overline{\sigma}_3\}$.

Elastic domain. In order to capture the materially non-linear behaviour of sand, in the geometrically linear regime, the following stress-strain relation based on a non-linear elastic potential is introduced [13]:

$$\overline{\boldsymbol{\sigma}}_E^S := \frac{\partial \Psi^{Se}}{\partial \boldsymbol{\varepsilon}_{Se}} = 2\,\mu^S\,\boldsymbol{\varepsilon}_{Se}^D + \left[k_0^S + k_1^S\left(\frac{\varepsilon_{Se\,\mathrm{crit}}^V}{\varepsilon_{Se\,\mathrm{crit}}^V - \varepsilon_{Se}^V} - 1\right)\right] \varepsilon_{Se}^V\,\mathbf{I}. \tag{7}$$

Therein, $\varepsilon_{Se}^D = \varepsilon_{Se} - 1/3\;\varepsilon_{Se}^V\,\mathbf{I}$ denotes the deviator of the elastic strain tensor. Moreover, μ^S is the constant elastic shear modulus, k_0^S and k_1^S are volumetric bulk moduli, and $\varepsilon_{Se\,\mathrm{crit}}^V$ is the critical volumetric strain, which is given by

$$\varepsilon_{Se\,\mathrm{crit}}^V = 1 - \frac{n_{\max}^S}{n_P^S}, \tag{8}$$

where $n_{\max}^S$ is a material parameter defining the densest packing.

Yield surface. Within the framework of elasto-plasticity, the elastic domain is bounded by an appropriate yield surface. For soils, or granular matter in general, a suitable criterion is provided in [17]. It reads:

$$\begin{aligned} \overline{F} &= \sqrt{\Gamma \overline{\mathrm{II}}_\sigma^D + \frac{1}{2}\alpha \bar{\mathrm{I}}_\sigma^2 + \delta^2 \bar{\mathrm{I}}_\sigma^4} + \beta \bar{\mathrm{I}}_\sigma + \varepsilon + \bar{\mathrm{I}}_\sigma^2 - \kappa = 0, \\ \Gamma &= \left(1 + \gamma \frac{\overline{\mathrm{III}}_\sigma^D}{(\overline{\mathrm{II}}_\sigma^D)^{3/2}}\right)^m. \end{aligned} \tag{9}$$

[1] Herein, the stress tensors are interpreted as vectors in the principle stress space.

Therein, $\bar{\mathrm{I}}_\sigma$, $\bar{\mathrm{II}}_\sigma^D$ and $\bar{\mathrm{III}}_\sigma^D$ are the first principal invariant of $\overline{\boldsymbol{\sigma}}_E^S$ and the (negative) second and third principal invariants of the effective stress deviator $(\overline{\boldsymbol{\sigma}}_E^S)^D$ all given in the shifted principle stress space. The material parameter sets $\mathcal{S}_h = (\delta, \varepsilon, \beta, \alpha, \kappa)^T$ and $\mathcal{S}_d = (\gamma, m)^T$ define the shape of the yield surface in the hydrostatic ($\mathcal{S}_h$) and deviatoric plane ($\mathcal{S}_d$) (Fig. 2).

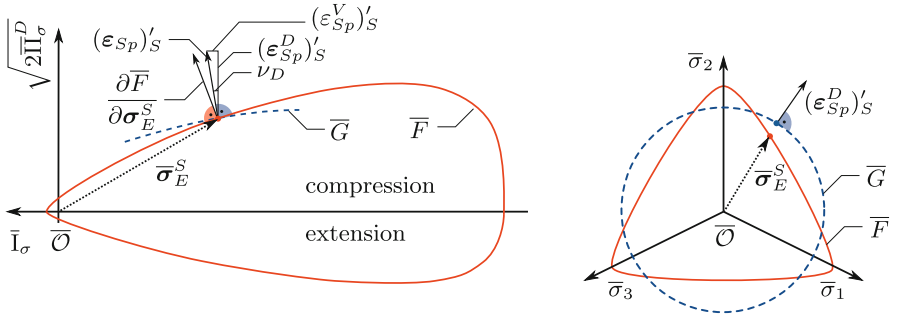

Fig. 2. Sketch of the evolution of the plastic flow in the hydrostatic (left) and deviatoric plane (right).

Evolution of plastic strains. In order to evaluate the evolution of the plastic strains, following the experimental findings of several authors, see, e. g., [26] or [43], the concept of non-associated plasticity needs to be applied for frictional geomaterials as an associated flow rule would overestimate the volumetric deformations. In this regard, a suitable plastic potential, which allows for an adequate description of the contractant and dilatant behaviour of the granular assembly is introduced:

$$\overline{G} = \sqrt{\psi_1 \bar{\mathrm{II}}_\sigma^D + \frac{1}{2}\alpha\, \bar{\mathrm{I}}_\sigma^2 + \delta^2 \bar{\mathrm{I}}_\sigma^4} + \psi_2 \beta\, \bar{\mathrm{I}}_\sigma + \epsilon\, \bar{\mathrm{I}}_\sigma^2 . \tag{10}$$

Therein, ψ_1 and ψ_2 are material parameters, which serve to relate the dilatation angle ν_D to experimental data. The flow rule governing the plastic strain rate $(\varepsilon_{Sp})'_S$ reads

$$(\boldsymbol{\varepsilon}_{Sp})'_S = \Lambda \frac{\partial \overline{G}}{\partial \overline{\boldsymbol{\sigma}}_E^S}, \tag{11}$$

Therein, Λ is the so-called plastic multiplier, which in the framework of viscoplasticity using the overstress concept of *Perzyna* [32] is determined from

$$\Lambda = \frac{1}{\eta} \left\langle \frac{F}{\sigma_0} \right\rangle^r , \tag{12}$$

where $\langle \cdot \rangle$ are the *Macaulay* brackets, η is the relaxation time, σ_0 is the reference stress and r is the viscoplastic exponent. Note that the overstress concept regularises the ill-posed problem, for instance at the onset of shear bands, see [14] and the references therein, through a careful choice of the parameters η and r.

Isotropic and kinematic hardening. In granular assemblies, any macroscopically observed plastic deformation is a result of the microstructural grain motions leading to macroscopic hardening or softening effects. In this regard, experimental observations have revealed an anisotropic material behaviour, see, e. g., [25] or [35], which originates from the preceded loading history, see [5]. This anisotropy is of particular importance upon the stress reversal under cyclic (dynamic and quasi-static) loading conditions. An explanation is found by the similarities between the established theory of dislocation movement in solid materials, e. g. metals, known as the *Bauschinger effect* [3], and the grain motions and the related grain-to-grain interactions. Additionally, a densification or loosening of the granular assembly leads to isotropic hardening or softening, respectively, which needs to be considered as well.

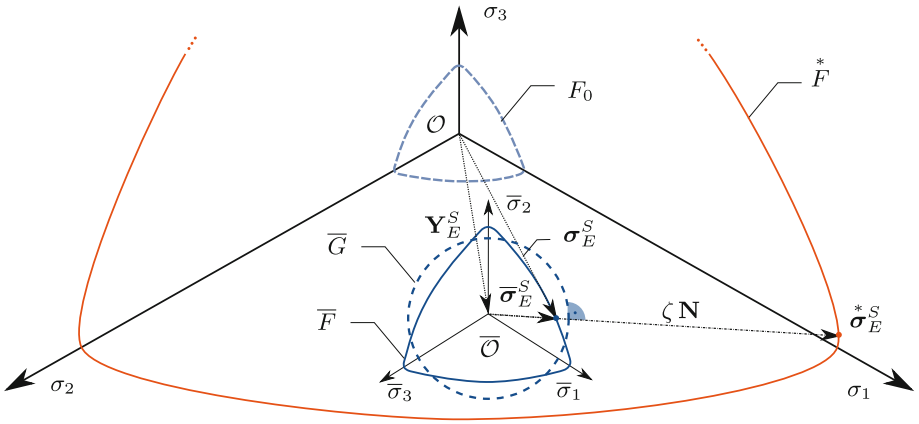

Fig. 3. Sketch of the combined isotropic-kinematic hardening concept considering the failure surface.

Any hardening model needs to ensure that the current stress state is admissible. In particular, it has to satisfy the yield criterion, i. e. $\overline{F}(p_i) \leq 0$, and, in addition, the failure criterion

$$\overset{*}{F} = F(\overset{*}{p}_i) \leq 0 \tag{13}$$

as the ultimate loading boundary, where $\overset{*}{p}_i \in \{\overset{*}{\alpha}, \overset{*}{\beta}, \overset{*}{\delta}, \overset{*}{\epsilon}, \overset{*}{\gamma}\}$ denotes the set of material parameters governing the failure surface. In order to ensure the admissibility of the computed stress state, the commonly used predictor-corrector scheme, see [38], is used. Herein, a preliminary overstress is computed based on the current strain increment (predictor step), which is, subsequently, checked whether the current increment is elastic ($F < 0$) or elasto-plastic ($F \geq 0$). In case of plasticity, the governing equations of the plasticity model are solved such that the resulting stress state lies on the yield surface ($F = 0$) (plastic corrector

step), where, in the scope of the present formulation, the shape of the yield surface is adjusted (isotropic hardening) and the yield locus is shifted through the principle stress space (kinematic hardening). In the scope of the kinematic hardening part, the translation direction is of particular interest. In this regard, Mróz [29] proposed an approach based on the geometric requirement that the tangential plane on the yield surface, which is associated with the current stress state, has to correspond to a tangential plane on the failure surface, thereby defining a second stress state on the failure surface. The evolution of the plastic strain is then governed by the vector defined through the current stress state and the second stress state leading to neither an associated nor a plastic-potential-driven non-associated flow rule. Note that the approach of [29] prevents an intersection of the yield and failure surfaces.

The current model also proceeds from a stress-projection method, but in contrast to [29], following a non-associated flow rule exploiting a plastic potential. In particular, the projection is carried out utilising the current stress state $\boldsymbol{\sigma}_E^S$ and the normalised flow direction $\mathbf{N}$, which proceeds from the plastic potential (10). The projected stress state $\overset{*}{\boldsymbol{\sigma}}{}_E^S$, which lies on the failure surface, is then found with the help of the scaling factor ζ, see Figure 3. In particular, following the concept of the volumetric and deviatoric splitting, the projection is carried out independently along the hydrostatic and the deviatoric direction via

$$(\overset{*}{\boldsymbol{\sigma}}{}_E^S)^V = \boldsymbol{\sigma}_E^S + \zeta^V \mathbf{N}^V, \qquad (\overset{*}{\boldsymbol{\sigma}}{}_E^S)^D = \boldsymbol{\sigma}_E^S + \zeta^D \mathbf{N}^D, \tag{14}$$

where the projected stress tensors $(\overset{*}{\boldsymbol{\sigma}}{}_E^S)^V$ and $(\overset{*}{\boldsymbol{\sigma}}{}_E^S)^D$, the scalar multipliers ζ^V and ζ^D and the normalised projection directions $\mathbf{N}^V$ and $\mathbf{N}^D$ are the corresponding contributions in the hydrostatic and deviatoric direction, respectively. The projection directions are computed through

$$\begin{aligned} \mathbf{N}^V &= \frac{1}{3}\operatorname{sgn}(G^V)\mathbf{I} \quad \text{with } G^V = \frac{\partial \overline{G}}{\partial \overline{\boldsymbol{\sigma}}_E^S} \cdot \mathbf{I}, \\ \mathbf{N}^D &= \frac{1}{\|\mathbf{G}^D\|}\mathbf{G}^D \quad \text{with } \mathbf{G}^D = \frac{\partial \overline{G}}{\partial \overline{\boldsymbol{\sigma}}_E^S} - \frac{1}{3}\left(\frac{\partial \overline{G}}{\partial \overline{\boldsymbol{\sigma}}_E^S} \cdot \mathbf{I}\right)\mathbf{I}, \end{aligned} \tag{15}$$

where $\operatorname{sgn}(\cdot) = (\cdot)/\|\cdot\|$ denotes the signum function with $\|(\cdot)\| = \sqrt{((\cdot)\cdot(\cdot))}$ being the *Euklid*ian norm. Exploiting the relations $(14)_1$ and $(14)_2$, ζ^V and ζ^D can be computed[2] through the requirement that the projected stresses have to lie on the failure surface, i. e.

$$\overset{*}{F}(\zeta^V) \overset{!}{=} 0 \qquad \text{and} \qquad \overset{*}{F}(\zeta^D) \overset{!}{=} 0. \tag{16}$$

[2] Note that under pure hydrostatic or deviatoric loading, the contributions of the plastic flow in the deviatoric or hydrostatic direction, respectively, are not uniquely defined due to $\|\mathbf{G}^D\| = 0$ and $G^V = 0$, respectively. Consequently, arbitrary projection directions $\mathbf{N}^D$ and $\mathbf{N}^V$ are defined in this case in order to keep the formulation computable. In this case, the scaling factors, ζ^V and ζ^D, do not contribute to the hardening, see (18) and (19), due to vanishing plastic strain rates in the corresponding directions.

Consequently, the presented formulation always ensures the admissibility of the resulting stress state. To make this point more clear, lets assume an invalid stress state, i. e. where the current stress point lies outside the domain bound by the failure surface. In this case, at the onset of plastic deformations, the scaling factor ζ will be negative and the plastic strain increment, will be in the opposite direction, thereby leading to a softening material behaviour.

Next, the isotropic and kinematic hardening laws are addressed. In this regard, concerning the isotropic hardening, suitable evolution laws for the parameter subset $p_i \in \{\beta, \delta, \epsilon, \gamma\}$ of the yield surface $\overline{F}$ have been proposed by [15], viz.

$$\begin{aligned} (p_i)'_S &= (p_i^V)'_S + (p_i^D)'_S = (\overset{*}{p}_i - p_i)[\, C_{pi}^V\, (\varepsilon_{Sp}^V)'_S + C_{pi}^D\, \|(\boldsymbol{\varepsilon}_{Sp}^D)'_S\| \,] \\ \text{with} \quad & p_i(t=0) = p_{i0}, \end{aligned} \tag{17}$$

which, however, are adopted to match the present mixed isotropic-kinematic hardening concept and yield

$$\begin{aligned} (p_i)'_S &= (p_i^V)'_S + (p_i^D)'_S = \zeta^V C_{pi}^V (\varepsilon_{Sp}^V)'_S + \zeta^D C_{pi}^D \|(\boldsymbol{\varepsilon}_{Sp}^D)'_S\| \\ \text{with} \quad & p_i(t=0) = p_{i0}. \end{aligned} \tag{18}$$

In both cases, the evolution equation $(p_i)'_S$ for the parameters p_i is separated into volumetric and deviatoric parts, $(p_i^V)'_S$ and $(p_i^D)'_S$, which are driven by the corresponding plastic strain rates, $(\varepsilon_{Sp}^V)'_S$ and $(\varepsilon_{Sp}^D)'_S$, together with the volumetric and the deviatoric evolution constants, C_{pi}^V and C_{pi}^D. Moreover, p_{i0} denotes the initial values of the parameters p_i. Evidently, the deviatoric part only governs plastic hardening, whereas the volumetric part $(p_i^V)'_S$ can take positive or negative values and, therefore, describes both hardening and softening processes [13].

The evolution of the kinematic back-stress tensor $\mathbf{Y}_E^S$ is based on the approach of *Armstrong & Frederick* (AF) [1]. However, it has been modified to match the present framework:

$$\begin{aligned} (\mathbf{Y}_E^S)'_S = \zeta^V (C_0^V - C_1^V |\mathrm{Y}_E^{SV}|)(\varepsilon_{Sp}^V)'_S\, \mathbf{I} \\ + \zeta^D [\, C_0^D (\boldsymbol{\varepsilon}_{Sp}^D)'_S - C_1^D \|(\boldsymbol{\varepsilon}_{Sp}^D)'_S\| \mathbf{Y}_E^{SD} \,]. \end{aligned} \tag{19}$$

Therein, $(\mathbf{Y}_E^S)'_S$ denotes the rate of the kinematic back-stress tensor. Furthermore, $\mathrm{Y}_E^{SV} = \mathrm{Y}_E^S \cdot \mathbf{I}$ and $\mathbf{Y}_E^{SD} = \mathbf{Y}_E^S - 1/3\, \mathrm{Y}_E^{SV} \mathbf{I}$ denote the volumetric and the deviatoric part of the back-stress tensor, and $|(\cdot)|$ is the absolute value of $(\cdot)$. Moreover, C_0^V and C_1^V, and C_0^D and C_1^D are the volumetric and the deviatoric evolution constants, respectively. In contrast to a pure linear kinematic hardening model, which, for instance, was proposed by [5], the nonlinear extension in (19) gives a better representation of the material behaviour. The differences between the linear kinematic, i. e. $C_1^V = 0$ and $C_1^D = 0$, and the AF hardening model are schematically depicted in Fig. 4.

In particular, at the onset of yielding, the nonlinear part is initially inactive. With ongoing (monotonic) loading it becomes more and more pronounced, thereby slowing down the rate of the back-stress tensor. Upon load reversal,

the back-stress tensor and its rate have opposite directions and, therefore, the additional term increases the stress rate. For more details on the AF model, the interested reader is referred, for instance, to the work of [9,10,24] or [31]. where, however, the latter three in particular focus on its extension within the scope of metal-plasticity.

A suitable model for the description of granular media needs to account for the contract and dilatant properties of the granular assembly, which are, within the current setting, driven through the plastic potential. In consequence, the used hardening models adapt, in addition to the yield surface, the plastic potential and, therefore, the direction of the plastic flow as well. The impact on the plastic strain increment proceed from the isotropic and the kinematic hardening model are qualitatively sketched in Fig. 5 (left) and (right), respectively.

Herein, both hardening models are subjected to the same loading scenario starting with an isotropic compression to reach the stress state A and followed up by an pure deviatoric load from A to C. At first, the attention is drawn to the pure isotropic hardening model. Herein, the evolution of the volumetric contribution of the plastic strain increment gradually changes from a contractant behaviour at A towards a dilatant behaviour at C, see Fig. 5 (left). In contrast, in case of the kinematic hardening model, the volumetric part in the plastic strain increment merely exhibits contractant and isochoric properties, see Fig. 5 (right). Consequently, only the isotropic hardening part in the combined isotropic-kinematic hardening model mimics the commonly observed contract-dilatant property of granular matter under pure shear deformation.

Stress-dependent failure surface. To complete the model, the attention is drawn to the stress-dependent failure surface. In this regard, the comprehensive experimental investigations under monotonic quasi-static loading conditions car-

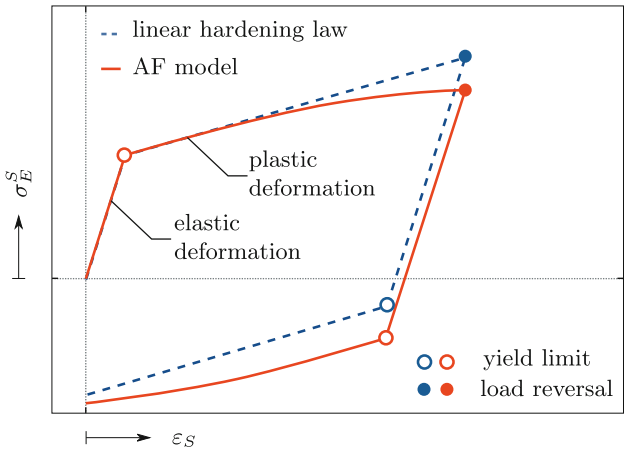

Fig. 4. Comparison between a linear kinematic hardening law and the model of *Armstrong* and *Frederick* [1].

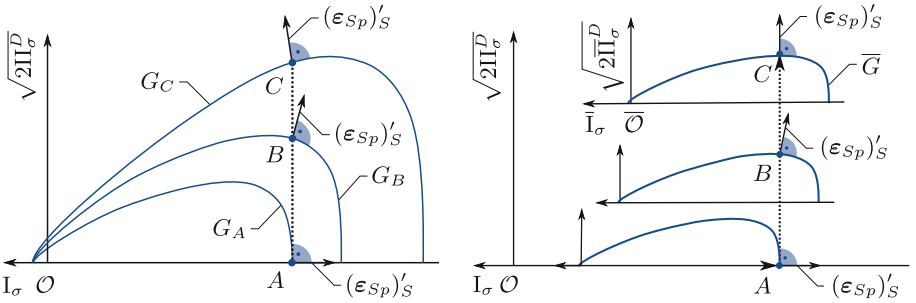

Fig. 5. Comparison of the evolution of the plastic strains in case of pure isotropic (left) and pure kinematic hardening (right).

ried out by [13] have revealed that the failure surface is not constant, but depends on the hydrostatic stress state, i. e. on the confining pressure I_σ. In particular, different confining pressures lead to slightly different granular configurations and, consequently, to different grain movements upon loading. Therefore, at failure the granular configuration and consequently, the corresponding stress states are different. Following [13], the evolution of the stress-dependent failure surface is conducted via

$$\overset{*}{\epsilon}(\mathrm{I}_\sigma) = \overset{*}{\epsilon}_0(1 + \overset{*}{C}_\epsilon \mathrm{I}_\sigma) \qquad \text{with} \qquad \overset{*}{\epsilon} \geq \overset{*}{\epsilon}_{lim}, \tag{20}$$

Therein, $\overset{*}{C}_\epsilon$ is a constant evolution parameter of the failure surface, while $\overset{*}{\epsilon}_0$ theoretically defines the failure surface for the unloaded virgin material, which is adjusted as small as possible but large enough for the smallest confining pressure used in a triaxial experiment. The failure-surface limit is defined by $\overset{*}{\epsilon}_{lim}$.

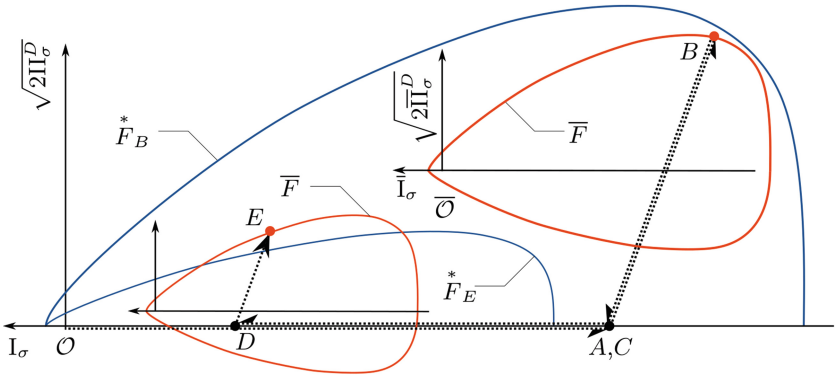

Fig. 6. Schematic sketch of stress path resulting in a not admissible stress state.

Next, the behaviour of the plasticity model and, in particular, its interplay with stress-dependent failure surface is elaborated in terms of a load-unload-reload cycle. For this purposed a possible loading scenario as depicted in Figure 6 is considered. Note that, therein, $\overset{*}{F}_B$ and $\overset{*}{F}_E$ denote the failure surfaces associated with stress states B and E, respectively. In the considered load case, a soil specimen is subjected to a hydrostatic compression and a triaxial load (($\mathcal{O}$-A-B). Next, the specimen is unloaded and the hydrostatic stress level is reduced (B-C-D) and, finally, the specimen is reloaded ($D-E$). Following the considered load path, the stress path $\mathcal{O}$-A-B causes a consolidation and, thereby an load-path-associated granular configuration represented through a shift and an expansion of the elastic domain through the kinematic and isotropic hardening models. During the unloading stage B-C-D, the granular configuration is mainly maintained. However, in the subsequent reload D-E, the stress state violates the yield criterion, thereby representing the interlocked granular configuration and, in consequence, allowing for stresses states violating the failure criterion. However, once the applied load exceeds the yield limit, plastic deformations are commenced and the granular assembly rearranges such that granular configuration and the current hydrostatic stress state match, which is represent in the plasticity model by returning the current stress onto the failure surface.

Summarised solid-skeleton model. With the previous elaborations at hand, two different solid-skeleton descriptions can be summarised, each composed of a set of ordinary differential equations (ODE). In particular, the mixed isotropic-kinematic hardening (IKH) model comprises the Eqs. (11), (12), (18), (19), $(16)_1$ and $(16)_2$ and reads

$$\boldsymbol{\mathcal{L}}_{\text{IKH}} = \begin{bmatrix} (\boldsymbol{\varepsilon}_{Sp})'_S \\ 0 \\ (p_i)'_S \\ (\mathbf{Y}^S_E)'_S \\ 0 \\ 0 \end{bmatrix} - \begin{bmatrix} \Lambda \dfrac{\partial \overline{G}}{\partial \overline{\boldsymbol{\sigma}}^S_E} \\ \Lambda - \dfrac{1}{\eta}\left\langle \dfrac{\overline{F}}{\sigma_0} \right\rangle \\ \zeta^V C^V_{pi}\,(\varepsilon^V_{Sp})'_S + \zeta^D C^D_{pi} \|(\boldsymbol{\varepsilon}^D_{Sp})'_S\| \\ \zeta^V (C^V_0 - C^V_1 |\mathrm{Y}^{SV}_E|)(\varepsilon^V_{Sp})'_S\,\mathbf{I} \\ + \zeta^D [C^D_0 \dot{\boldsymbol{\varepsilon}}^D_p - C^D_1 \|(\boldsymbol{\varepsilon}^D_{Sp})'_S\| \mathbf{Y}^{SD}_E] \\ \overset{*}{F}\left(\zeta^V\right) \\ \overset{*}{F}\left(\zeta^D\right) \end{bmatrix} = \mathbf{0}. \tag{21}$$

The purely isotropic-hardening (IH) model, composed of the relations (11), (12) and (17) is summarised as

$$\boldsymbol{\mathcal{L}}_{\mathrm{IH}} = \begin{bmatrix} (\boldsymbol{\varepsilon}_{Sp})'_S \\ 0 \\ (p_i)'_S \end{bmatrix} - \begin{bmatrix} \Lambda \dfrac{\partial \overline{G}}{\partial \overline{\boldsymbol{\sigma}}^S_E} \\ \Lambda - \dfrac{1}{\eta} \left\langle \dfrac{\overline{F}}{\sigma_0} \right\rangle \\ (\overset{*}{p}_i - p_i)[\, C^V_{pi}\, (\varepsilon^V_{Sp})'_S + C^D_{pi}\, \|(\boldsymbol{\varepsilon}^D_{Sp})'_S\| \,] \end{bmatrix} = \mathbf{0}. \tag{22}$$

Note that, alternatively, $(22)_2$ may be solved for Λ and inserted into $(22)_1$, in order to reduce the number of ODE within the local system on the one hand and to allow for explicit time-discretisation schemes on the other hand.

3 Numerical Treatment

The present section briefly outlines the spatial and temporal discretisation methods as well as the associated solution procedure of the underlying problem. For a more detailed insight into the numerical treatment of elasto-plastic porous materials, the interested reader is referred to, e. g., [13] and references therein.

The spatial discretisation is based on the finite-element method (FEM), thereby following a variational approach of *Bubnov-Galerkin*-type. Note that the ansatz and test functions need to fulfil the *inf-sup* condition (*Ladyshenskaya-Babuška-Brezzi* (LBB) condition) [7] for the sake of a stable solution procedure. In particular, the solid displacements $\mathbf{u}_S$ and their corresponding test functions are approximated by quadratic shape functions, whereas linear shape functions are used for the pore pressure p and its associated test function. Addressing the simulation of quasi-static process, the unconditionally stable backward (implicit) Euler scheme, see e. g. [21], is used for the temporal discretisation.

The resulting system of a non-linear algebraic equations is composed of a global system associated with the finite-element (FE) discretisation and a local system related to the ODE of the elasto-plastic model. The coupled system is solved iteratively through the *Newton-Raphson* method. To be more precisely, in order to obtain an efficient solution strategy, the system is solved in a decoupled manner through a generalisation of the block *Gauss-Seidel-Newton* method, thereby exploiting the block-structured nature of the coupled system. This procedure results in two nested *Newton* iterations, where at each global iteration step, which seeks the solution to the primary variables, the local system is iteratively solved at first for the internal state variables with frozen primary variables. Note that the solution of the local system is found, as usual in elasto-plasticity, through the commonly used *predictor-corrector scheme*, see [38].

Following this, the discrete governing equations are implemented into the coupled FE solver PANDAS, which is then linked to the commercial FE package Abaqus via a general interface, see [36].

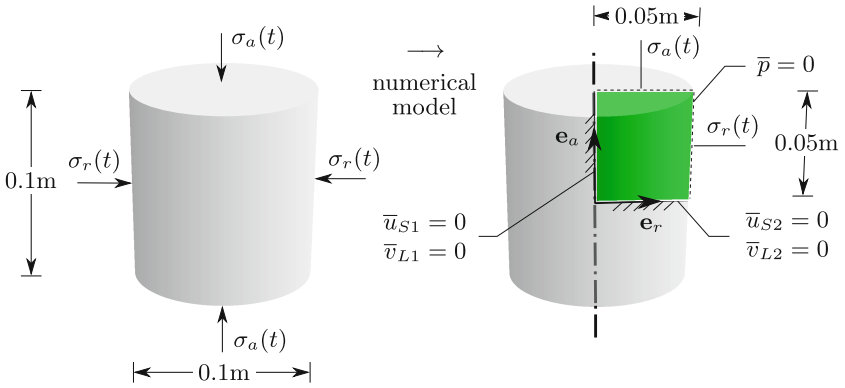

Fig. 7. Geometry and loading of the triaxial test (left) and the deduced IBVP (right).

4 Simulation

The simulations address the investigation of the model responses under quasi-static cyclic loading conditions of the pure isotropic and the mixed isotropic-kinematic hardening model both in comparison to experimental data. In this connection, at first, a triaxial test on a cylindrical sand sample (diameter: 0.1 m, height: 0.1 m) subjected to slow cyclic load cycles is carried out, which will serve as a reference for the subsequent simulations. Herein, on the one hand, the isotropic hardening (IH) model with the material parameters depicted in Appendix A, and, on the other hand, the mixed isotropic-kinematic hardening (IKH) model with the parameters of Appendix B are used. Note that the material constants of the IKH are, in contrast to the IH model, not found through an calibration procedure. Instead, they are adapted from the parameters of the IH model. Therefore, the present investigations merely serve as a proof-of-concept rather than a validation of the material models.

The governing triaxial test and the deduced IBVP are depicted in Fig. 7. Note that in the numerical model, the axial symmetry of the problem is exploited, thereby simplifying the actual three-dimensional problem to a axial-symmetric two-dimensional FE model, which is solely composed of a single axial-symmetric finite element. The solid displacements normal to the symmetry lines (left and bottom edge) are equal to zero, i. e. $\overline{u}_{S1} = \overline{u}_{S2} = 0$, whereas the edges associated with the free surfaces of the specimen, i. e. the top and bottom edge, are free to move and are perfectly drained, i. e. $\overline{p} = 0$. The sample is subjected to a quasi-static cyclic loading, through a prescription of the axial $\sigma_a(t)$ and the radial stresses $\sigma_r(t)$. In particular, the confining pressure, i. e. $\sigma_a(t) = \sigma_r(t) = 0.1$ MPa, is applied in the interval $t \in [\,0\text{ s}, 600\text{ s}\,]$ in a first step. Subsequently, the radial stress is kept constant and the axial stress periodically increases and decreases with an amplitude of $\Delta\sigma_a = 0.05$ MPa, see Fig. 8.

The evolution of the axial solid strain of the experiment, and the computed responses of the IH and IKH model are depicted in Fig. 9. At first, the elabora-

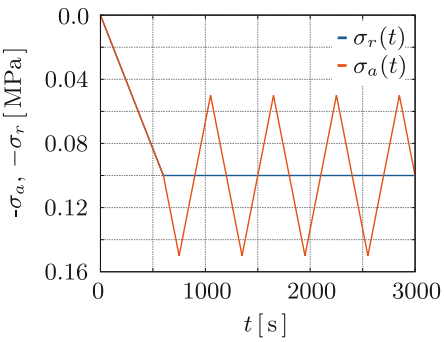

Fig. 8. Evolution of the axial $\sigma_a(t)$ and the radial stress $\sigma_r(t)$ applied on the cylindrical soil specimen.

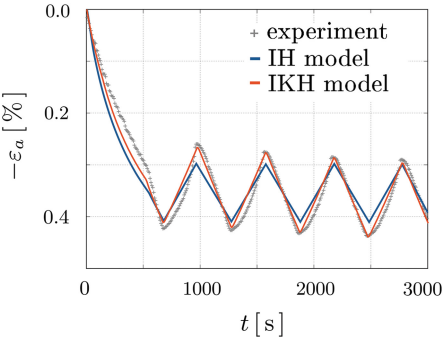

Fig. 9. Evolution of the total axial strain ε_a for the IH and the IKH model in comparison to the experimental records.

tion of the experimental records is addressed. As illustrated by the evolution of the axial strain, the subsequent loading-unloading loops alter the granular configuration, thereby allowing for a gradual axial settlement of the top end of the specimen. These findings are in agreement with the experimental observations of other authors, see, e. g., [11] or [42]. Comparing the experimental observations with the model responses, it can be seen that only the IKH model is capable of predicting the axial settlement under the prescribed quasi-static loading conditions. The predictions of the IKH model are in very good agreement with the test result.

5 Conclusions

The present contribution addressed the simulation of granular assemblies under quasi-static cyclic loading conditions, thereby exploiting the TPM and the elasto-plasticity as suitable modelling frameworks. For the sake of a complete representation, the entire numerical model starting from the governing balance laws, over the constitutive relations towards the numerical treatment has been presented. In particular, two hardening models describing the solid-skeleton behaviour have been elaborated, namely an isotropic and a mixed kinematic-isotropic hardening model. Both formulations have been compared to experimental data, which has been obtained from quasi-static cyclic triaxial tests. It has been shown that the pure isotropic hardening model fails to mimic the axial settlement under slow cyclic loading conditions. In contrast, the mixed isotropic-kinematic hardening model was able to qualitatively reproduce the experimental observations at least to some extent. However, it was also illustrated that the proposed model does not reproduce the exact characteristics of the axial-strain evolution, i. e. the curvature in the zigzag pattern. To trace back the origin of the mismatch, further experimental investigations are necessary to optimise the governing material parameters on the one hand and to identify further physical processes, which might be essential for the mimicking of the experimental observations on the other hand.

Appendix A: Material Parameters of the IH Model

Following the DIN 18196 of the German Institute for Standardisation, the underlying granular material, in particular, the sand[3] of the research unit FOR 1136 "GeoTech", can be classified as closely graded sand with an average grain diameter of $d_{50} = 0.55\,\mathrm{mm}$, see Fig. 10. The density of an individual soil grain, which corresponds to the realistic solid density of the overall aggregate, is $\rho^{SR} = 2\,650\,\mathrm{kg/m^2}$.

In order to identify the solid-skeleton material parameters associated with the FOR1136 sand, the course of actions as described in [13] is followed. Herein, initially several triaxial tests on cylindrical sand specimens (height: 0.1 m, diameter: 0.1 m) have been carried out, from which, subsequently, the materials parameters are identified through a staggered identification scheme, In particular, at first, the elastic shear modulus μ_S is determined straightforward from triaxial loading-unloading loops and the compression-extension-ratio parameter $\overset{*}{\gamma}$ of the failure surface is found from compression and extension experiments at different confining pressures. Subsequently, several triaxial tests at different confining pressure, in particular, $\sigma_{c,1} = 0.1\,\mathrm{MPa}$, $\sigma_{c,2} = 0.2\,\mathrm{MPa}$ and $\sigma_{c,3} = 0.3\,\mathrm{MPa}$, have been carried out, where the axial σ_a and radial stresses σ_r, the axial strain ε_a, and the volumetric strain ε^V have been recorded. The material parameters are then found through a minimisation of the squared error between simulation and experiment, which is known as *Least-Squares* optimisation method. In particular, a gradient-based constrained optimisation is used, in which the *Hesse*an matrix is approximated through the BGFS (Broyden, Fletcher, Goldfarb, Shannon) procedure, see e. g. [39], and the parameter constraints are considered via the sequential-quadratic-programming (SQP) technique, see [40]. The identified solid-skeleton material parameters of the research-unit sand FOR 1136 are summarised in Table 1.

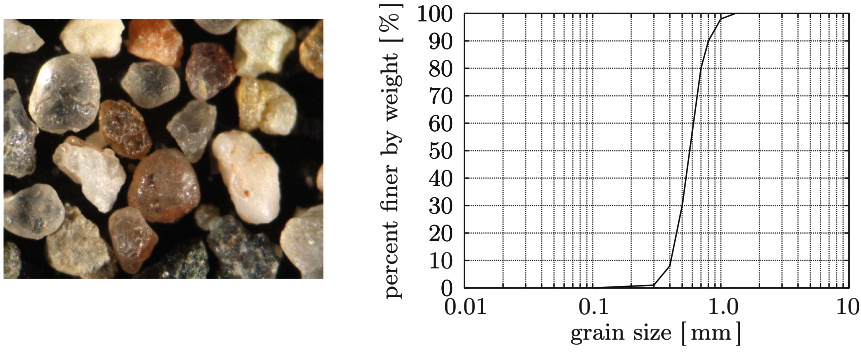

Fig. 10. Microscopic picture of the soil grains (left) and grain size distribution (right) of the sand of the research unit FOR1136.

[3] The sand samples have been provided by the Institute of soil and rock mechanics (Institut für Boden- und Felsmechanik, IBF) of the Karlsruher Institut of Technology (KIT).

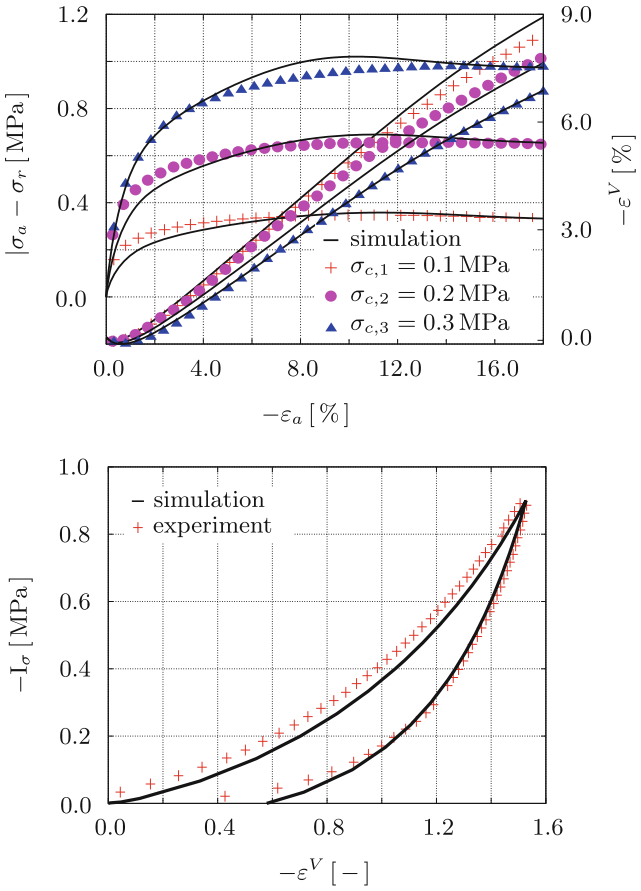

Fig. 11. Comparison of the experimental data with the simulation results of the triaxial tests at different confining pressures (left) and of the isotropic loading-unloading loop (right).

A comparison between the simulation and the experiments for the triaxial experiments at different confining pressures and for the isotropic compression test are depicted in Fig. 11. As can been seen, the model responses are in a quite good agreement with the experimental observations.

Appendix B: Material Parameters of the IKH Model

Proceeding from the material constants of the pure isotropic hardening (IH) model, see Table 1, the governing parameters of the mixed isotropic-kinematic hardening (IKH) model are guessed and the adjustments according to Table 2 are made.

Table 1. Material parameters of the solid skeleton of the sand of the research unit FOR1136.

Parameter	Symbol	Value	Unit
Elastic parameters and solidity			
Initial volume fraction	n^S_{0S}	0.6	-
Maximum volume fraction	$n^S_{\max}$	0.623	-
Shear modulus	μ^S	190	$\mathrm{N/m^2}$
Bulk modulus 1	k^S_1	20	$\mathrm{MN/m^2}$
Bulk modulus 2	k^S_2	47	$\mathrm{MN/m^2}$
Yield-surface parameters			
Yield-surface parameter	α	0.01	$\mathrm{m^2/MN}$
Yield-surface parameter	κ	0.0001	$\mathrm{m^2/MN}$
Yield-surface parameter	m	$0.\overline{54}$	-
Initial yield surface			
Yield-surface parameter	δ_0	0.0009	$\mathrm{m^2/MN}$
Yield-surface parameter	ϵ_0	0.1	$\mathrm{m^2/MN}$
Yield-surface parameter	β_0	0.05	-
Yield-surface parameter	γ_0	0.0	-
Failure surface			
Yield-surface parameter	$\overset{*}{\delta}$	0.09	$\mathrm{m^2/MN}$
Yield-surface parameter	$\overset{*}{\epsilon}_0$	0.01	$\mathrm{m^2/MN}$
Yield-surface parameter	$\overset{*}{\beta}$	0.255	-
Yield-surface parameter	$\overset{*}{\gamma}$	1.75	-
Failure-surface constant	$\overset{*}{C}_\epsilon$	0.4	$\mathrm{m^2/MN}$
iso. hard. evolution constants			
Volumetric constant	C^V_δ	-93	$\mathrm{m^2/MN}$
Volumetric constant	C^V_ϵ	-150	$\mathrm{m^2/MN}$
Volumetric constant	C^V_β	-250	-
Volumetric constant	C^V_γ	-0	-
Deviatoric constant	C^D_δ	23	$\mathrm{m^2/MN}$
Deviatoric constant	C^D_ϵ	200	$\mathrm{m^2/MN}$
Deviatoric constant	C^D_β	180	-
Deviatoric constant	C^D_γ	20	-
Plastic potential			
Parameter 1	ψ_1	1.3	-
Parameter 2	ψ_2	0.53	-
Viscoplasticity			
Reference stress 1	σ_0	0.0001	$\mathrm{MN/m^2}$
Relaxation time	η	0.001	s
Viscoplastic exponent	r	0.001	s

Table 2. Material-parameter adjustments of the solid skeleton for the mixed isotropic-kinematic hardening (IKH) model.

Parameter	Symbol	Value (IH)	→	Value (IKH)	Unit
Yield-surface parameters					
Yield-surface parameter	α	0.01		10^{-5}	m^2/MN
Yield-surface parameter	κ	0.0001		10^{-6}	m^2/MN
Initial yield surface					
Yield-surface parameter	δ_0	0.5		0.0009	m^2/MN
Yield-surface parameter	ϵ_0	0.01		0.1	m^2/MN
Yield-surface parameter	β_0	0.003		0.05	-
Failure surface					
Yield-surface parameter	$\overset{*}{\delta}$	0.09		0.0005	m^2/MN
Yield-surface parameter	$\overset{*}{\epsilon}_0$	0.01		0.00001	m^2/MN
Yield-surface parameter	$\overset{*}{\beta}$	0.255		0.003	-
iso. hard. evolution constants					
Volumetric constant	C_δ^V	-93		-1500	m^2/MN
Volumetric constant	C_ϵ^V	-150		-1500	m^2/MN
Volumetric constant	C_β^V	-250		0	-
Deviatoric constant	C_δ^D	23		-1500	m^2/MN
Deviatoric constant	C_ϵ^D	200		-1500	m^2/MN
Deviatoric constant	C_β^D	180		0	-
Deviatoric constant	C_γ^D	20		0	-
kin. hard. evolution constants					
Volumetric constant	C_0^V	-		0	m^2/MN
Volumetric constant	C_1^V	-		0	m^2/MN
Deviatoric constant	C_0^D	-		300	m^2/MN
Deviatoric constant	C_1^D	-		50	m^2/MN
Plastic potential					
Parameter	ψ_1	1.3		0.001	-
Parameter	ψ_2	0.53		1.0	-

References

1. Armstrong, P.J., Frederick, C.O.: A mathematical representation of the multiaxial bauschinger effect. Report No. RD/B/N 731, Central Electricity Generating Board and Berkeley Nuclear Laboratories (CEGB) (1966)
2. Arslan, U.M.: Zur Frage des elastoplastischen Verformungsverhaltens von Sand. Mitteilungen der Versuchsanstalt für Bodenmechanik und Grundbau 23, TH Darmstadt (1980)
3. Bauschinger, J.: Über die Veränderung der Elastizitätsgrenze und die Festigkeit des Eisens und Stahls durch Strecken und Quetschen, durch Erwärmen und Abkühlen und durch oftmals wiederholte Beanspruchungen. Mitteilungen aus dem mechanisch-technischem Laboratorium 13, Königlich Bayerische Technische Hochschule München (1886)

4. Biot, M.A.: Theory of propagation of elastic waves in a fluid-saturated porous solid. J. Acoust. Soc. Am. **28**, 168–178 (1956)
5. de Boer, R., Brauns, W.: Kinematic hardening of granular materials. Ingenieur-Archiv **60**, 463–480 (1990)
6. de Boer, R., Ehlers, W.: Theorie der Mehrkomponentenkontinua mit Anwendung auf bodenmechanische Probleme. Forschungsberichte aus dem Fachbereich Bauwesen, Heft 40. Universität-GH-Essen (1986)
7. Brezzi, F., Fortin, M.: Mixed and Hybrid Finite Element Methods. Springer, New York (1991)
8. Casagrande, D.R.: Characteristics of cohesionless soils affecting the stability of slopes and earth fills. J. Boston Soc. Civil Eng. **23**, 13–32 (1936)
9. Chaboche, J.L.: Constitutive equations for cyclic plasticity and cyclic viscoplasticity. Int. J. Plast **5**, 247–302 (1989)
10. Chaboche, J.L.: On some modifications of kinematic hardening to improve the description of ratcheting effects. Int. J. Plast **7**, 661–678 (1991)
11. Danne, S., Hettler, A.: Experimental strain response-envelopes of granular materials for monotonous and low-cycle loading processes. In: Triantafyllidis, T. (ed.) Holistic Simulation of Geotechnical Installation Processes. LNACM, vol. 77, pp. 229–250. Springer, Heidelberg (2015). doi:10.1007/978-3-319-18170-7_12
12. Ehlers, W.: Foundations of multiphasic and porous materials. In: Ehlers, W., Bluhm, J. (eds.) Porous Media: Theory, Experiments and Numerical Applications, pp. 3–86. Springer, Berlin (2002)
13. Ehlers, W., Avci, O.: Stress-dependent hardening and failure surfaces of dry sand. Int. J. Numer. Anal. Meth. Geomech. **37**, 787–809 (2013)
14. Ehlers, W., Graf, T., Ammann, M.: Deformation and localization analysis of partially saturated soil. Comput. Methods Appl. Mech. Eng. **193**, 2885–2910 (2004)
15. Ehlers, W., Karajan, N., Wieners, C.: Parallel 3-d simulation of a biphasic porous media model in spine mechanics. In: Ehlers, W., Karajan, N. (eds.) Proceedings of the 2nd GAMM Seminar on Continuum Biomechanics, pp. 11–20. Report No. II-16 of the Institute of Applied Mechanics (CE), University of Stuttgart (2007)
16. Ehlers, W.: Poröse Medien - ein kontinuumsmechanisches Modell auf der Basis der Mischungstheorie. Habilitation Thesis, Forschungsberichte aus dem Fachbereich Bauwesen, Heft 47, Universität-GH-Essen (1989)
17. Ehlers, W.: A single-surface yield function. Arch. Appl. Mech. **65**, 246–259 (1995)
18. Ehlers, W.: Challanges of porous media models in geo- and biomechanical engineering including electro-chemically active polymers and gels. Int. J. Adv. Eng. Sci. Appl. Math. **1**, 1–24 (2009)
19. Ehlers, W., Schenke, M., Markert, B.: Simulation of soils under rapid cyclic loading conditions. In: Triantafyllidis, T. (ed.) Holistic Simulation of Geotechnical Installation Processes. LNACM, vol. 77, pp. 207–228. Springer, Heidelberg (2015). doi:10.1007/978-3-319-18170-7_11
20. Ehlers, W., Scholz, B.: An inverse algorithm for the identification and the sensitivity analysis of the parameters governing micropolar elasto-plastic granular material. Arch. Appl. Mech. **77**, 911–931 (2007)
21. Ellsiepen, P.: Zeit- und ortsadaptive Verfahren angewandt auf Mehrphasenprobleme pröser Medien. Dissertation Thesis, Report No. II-3 of the Institute of Applied Mechanics (CE), University of Stuttgart (1999)
22. Heider, Y., Avci, O., Markert, B., Ehlers, W.: The dynamic response of fluid-saturated porous materials with application to seismically induced soil liquefaction. Soil Dyn. Earthq. Eng. **63**, 120–137 (2014)
23. Iwan, W.D.: On a class of models for the yielding behavior of continuous and composite systems. ASME J. Appl. Mech. **34**, 612–617 (1967)

24. Jirásek, M., Bažant, Z.P.: Inelastic Analysis of Structures. Wiley, New York (2002)
25. Ko, H., Scott, R.F.: Deformation of sand in shear. J. Soil Mech. Found. Div. **93**, 283–310 (1967)
26. Lade, P.V., Duncan, J.M.: Cubical triaxial tests on cohesionless soil. ASCE J. Soil Mech. Found. Div. **99**, 793–812 (1973)
27. Manzari, M.T., Dafalias, Y.F.: A critical state two-surface plasticity model for sands. Geotechnique **47**, 255–272 (1997)
28. Meggiolaro, M.A., Castro, J.T.P., Wu, H.: On the applicability of multi-surface, two-surface and non-linear kinematic hardening models in multiaxial fatigue. Frattura ed Integritá Struttura **33**, 357–367 (2015)
29. Mróz, Z.: An attempt to describe the behavior of metals under cyclic loads using a more general workhardening model. Acta Mech. **7**, 199–212 (1969)
30. Mróz, Z.: On the description of anisotropic workhardening. J. Mech. Phys. Solids **15**, 163–175 (1967)
31. Ohno, N., Wang, J.D.: Kinematic hardening rules with critical state dynamic recovery, part ll - application to experiments of ratcheting behavior. Int. J. Plast **9**, 391–403 (1991)
32. Perzyna, P.: Fundamental problems in viscoplasticity. Adv. Appl. Mech. **9**, 243–377 (1966)
33. Prévost, J.H.: Nonlinear transient phenomena in soil media. Mech. Eng. Mater. **30**, 3–18 (1982)
34. Roscoe, K.H., Burland, J.B.: On the generalized stress-strain behaviour of wet clay. In: Engineering Plasticity, pp. 535–609. Cambridge University Press, Cambridge (1968)
35. Santamarina, J., Klein, K.A., Fam, M.A.: Soils and Waves. Wiley, Chichester (2001)
36. Schenke, M., Ehlers, W.: Parallel solution of volume-coupled multi-field problems using an abaqus-pandas software interface. Proc. Appl. Math. Mech. **15**, 419–420 (2015)
37. Schofield, A.N., Wroth., C.P.: Critical State Soil Mechanics. McGraw-Hill, New York (1968)
38. Simo, J.C., Taylor, R.L.: A return mapping algorithm for plane stress elastoplasticity. Int. J. Numer. Meth. Eng. **22**, 649–670 (1986)
39. Spellucci, P.: Numerische Verfahren der nichtlinearen Optimierung. Birkhäuser, Basel (1993)
40. Spellucci, P.: A new technique for inconsistent QP problems in the SQP-method. Math. Methods Oper. Res. **47**, 335–400 (1998)
41. Wichtmann, T., Niemunis, A., Triantafyllidis, T.: Strain accumulation in sand due to cyclic loading: drained triaxial tests. Soil Dyn. Earthq. Eng. **25**, 967–979 (2005)
42. Wichtmann, T., Triantafyllidis, T.: Behaviour of granular soils under environmental induced cyclic loads. In: Di Prisco, C., Wood, D.M. (eds.) Mechanical Behaviour of Soils Under Environmentally-Induced Cyclic Loads, pp. 1–136. Springer, Wien (2012)
43. Yamada, Y., Ishihara, K.: Anisotropic deformation charateristics of sand under three dimensional stress conditions. Soils Found. **19**, 79–94 (1979)
44. Zienkiewicz, O.C., Bettes, P.: Soil Mechanics - Transient and Cyclic Loads. Wiley, Chichester (1982)
45. Zienkiewicz, O.C., Chan, A.H.C., Pastor, M., Schrefler, B.A., Shiomi, T.: Computational Geomechanics with Special Reference to Earthquake. Wiley, Chichester (2001)
46. Zienkiewicz, O.C., Chang, C.T., Hinton, E.: Non-linear seismic response and liquefaction. Int. J. Numer. Anal. Meth. Geomech. **2**, 381–404 (1978)

Strategies to Apply Soil Models Directly as Friction Laws in Soil Structure Interactions

Christian Weißenfels(✉), Ajay B. Harish, and Peter Wriggers

Institute of Continuum Mechanics, Leibniz Universität Hannover, Hanover, Germany
weissenfels@ikm.uni-hannover.de

Abstract. In this work three different concepts for a direct application of soil models within a frictional contact description are presented. These concepts can be used in conjunction with all different kinds of contact formulations and solution methods. Additionally, all types of plasticity models can be used within these formulations. The advantage of these concepts is shown exemplary in the modeling process of soil-structure interactions where the Ehlers plasticity model for the continuum is now able to describe the soil behavior at the contact surface. The numerical implementation of the new frictional relations is based on the Mortar method and the numerical investigation of a direct shear test shows the reproduction of the typical stress-strain relation of the soil at the contact surface. The work ends with a critical discussion about the different friction formulations and the application of the Ehlers soil model in a direct shear test.

Keywords: Contact mechanics · Finite element method · Mortar method · Friction laws · Projection strategies · Contact layer · Soil mechanics · Soil-structure interactions

1 Introduction

When investigating simulations of sliding contacts, Coulomb's law is mostly preferred to model the frictional behavior. Even within the highly complex modeling process of soil-structure interactions Coulomb's law is applied [1,2], although the simulation of a pile penetration process shows a large difference between numerical and experimental results (Fig. 1, [12]). As a consequence new frictional models were developed in [12] improving the slip behavior. Unfortunately, in this case, a large number of additional material parameters have to be introduced which have to be determined for each individual contact pair.

Within geotechnical installation processes for piles, anchors or sheet pile walls, mostly the surface of the structure has to be viewed as rough. Experimental measurements of a direct shear test between soil and concrete show that for a rough surface of the structure the response behavior is almost equal to the same test case between two soil specimens [20,22,29]. This leads to the conclusion that for soil-rough structure interactions the real contact zone lies

T. Triantafyllidis (ed.), *Holistic Simulation of Geotechnical Installation Processes*,
Lecture Notes in Applied and Computational Mechanics 82, DOI 10.1007/978-3-319-52590-7_9

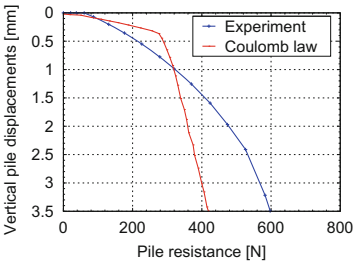

Fig. 1. Comparison of experimental and numerical results of a pile penetration test [12]

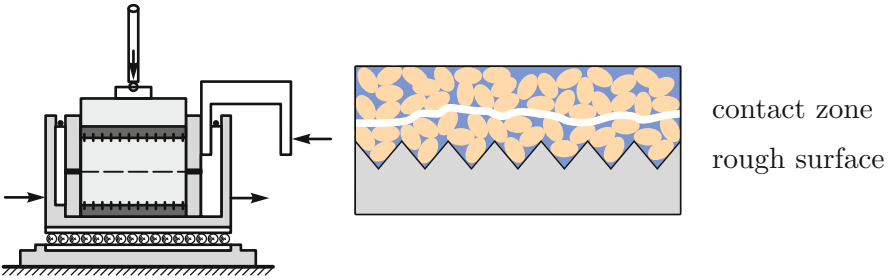

Fig. 2. Development of the contact zone in a direct shear test between soil and a concrete specimen possessing a rough surface

completely within the soil (Fig. 2). Since many soil models are able to represent the three-dimensional geomechanical behavior realistically, the description of the mechanics at the contact layer can be improved by the use of such models. Until now either interface elements [5,36], or special joint elements [10,11] are used to model the contact interface by use of soil models. Additionally, some interface models exists where the rough surface structure is taken into account [14,17]. Unfortunately, these models are limited to small sliding. Only an incorporation into contact formulations makes it possible to simulate the most important situations for engineers, like a pile, anchor or sheet pile wall installations where large relative movements occur.

In order to overcome these limitations in the planing process of foundations three different strategies are presented each able to incorporate soil models directly within any contact formulation. The second advantage of these schemes is the natural outcome that no additional parameters are needed.

A big challenge of any method that includes soil models is the correct reproduction of the dilatant or contractant behavior at the contact surface. A direct integration of these effects into a contact model would lead in the case of contractancy to a penetration of one body into the other, which is not allowed, or in the case of dilatancy to a release of the contact during the sliding process, which is not reasonable. Additionally, yield criteria are often formulated in terms of three stress invariants whereas slip laws are mostly based on the norm of the

tangential stress vector and on the absolute value of the normal pressure. Hence, a direct link between these invariants is not possible. However, in the literature, some relation between contact and continuum are disclosed. For instance, the three-dimensional Mohr-Coulomb yield criterion is the natural extension of the two-dimensional Coulomb slip rule [4]. Using the penalty regularization for the tangential contact formulation the analogue to the elastoplastic theory can be exploited in the modeling process [3,15,33]. In [31] a direct link between the contact and the continuum kinematics is stated which can also be used to incorporate soil models within the contact formulation. All these relations are providing the basis for the presented methods.

If the surface of the structure can be assumed as perfectly smooth, contact takes place directly at the interface of soil and structure and Coulomb's law can be used, as can be seen in the outcomes of experimental tests between steel and soil in [28] or [13]. Only a proper coefficient of friction has to be determined.

A soil model based on the framework of the elastoplastic theory which is able to include the porous structure of the soil [7,9] is stated in Sect. 3. Additionally, two regularization schemes are mentioned shortly at the end of this section which stabilizes numerical algorithm and avoids oscillations between the elastic and plastic state.

Sections 3, 4 and 5 describe the three methods to use soil models as frictions laws in detail. The first one transforms the plasticity equations properly into frictional formulations using the connection between Coulomb slip rule and Mohr-Coulomb yield criterion. The second concept integrates the plasticity model directly into the slip rule formulating a continuum stress dependent coefficient of friction and normal contact force. In the third concept, the two-dimensional contact formulation is extended towards 3D in order to include the plasticity models directly, which leads to a contact layer formulation.

The performance of these concepts are shown in Sect. 6 based on a numerical investigation of a direct shear test. The outcomes are compared with the results of the corresponding three-dimensional setup using interface elements in between of the two contact specimens. The presented work is closed with an evaluation of the projection schemes and of the Ehlers soil model in Sect. 7.

2 Soil Model

The aim of the developed friction laws is the improved prediction of soil structure interactions by an use of soil models directly at the contact surface. Therefore a proper soil description is needed. Among many different models Ehlers developed a generic elasto-plastic formulation [7,9] able to take into account typical effects known in soil mechanics, like the pressure dependency of the friction angle and the dependency of the admissible elastic domain on the Lode angle. The porosity of the soil is considered by the factor c^v given within the linear elastic stress strain relation

$$\boldsymbol{\sigma} = \lambda \, \mathrm{tr}\, \boldsymbol{\varepsilon}^e \, c^v + 2\mu \boldsymbol{\varepsilon}^e. \tag{1}$$

The factor c^v [9] describes the influence of the solid volume ratio which is limited by its initial value n_0^s and its upper bound n_{max}^s

$$c^v = \frac{\operatorname{tr} \boldsymbol{\varepsilon}^c}{(\operatorname{tr} \boldsymbol{\varepsilon}^c - \operatorname{tr} \boldsymbol{\varepsilon}^e)}, \quad \operatorname{tr} \boldsymbol{\varepsilon}^c = \frac{n_p^s}{n_{max}^s} - 1 = \frac{n_0^s}{n_{max}^s (1 + \operatorname{tr} \boldsymbol{\varepsilon}^p)} - 1. \tag{2}$$

The yield criterion bounding the admissible elastic domain is formulated in terms of the first invariant of the stress tensor $\mathrm{I}_{\boldsymbol{\sigma}}$ as well as of the second $\mathrm{II}_{\mathbf{s}}$ and of the third invariant $\mathrm{III}_{\mathbf{s}}$ of the deviatoric stress $\mathbf{s}$

$$f(\boldsymbol{\sigma}) = \sqrt{\left(1 + \gamma \, \mathrm{III}_{\mathbf{s}} \, \mathrm{II}_{\mathbf{s}}^{-\frac{3}{2}}\right)^m \mathrm{II}_{\mathbf{s}} + \frac{1}{2} \alpha \, \mathrm{I}_{\boldsymbol{\sigma}}^2 + \delta^2 \, \mathrm{I}_{\boldsymbol{\sigma}}^4} + \beta \, \mathrm{I}_{\boldsymbol{\sigma}} + \epsilon \, \mathrm{I}_{\boldsymbol{\sigma}}^2 - \kappa = 0. \tag{3}$$

Seven parameters $(\alpha, \beta, \gamma, \delta, \epsilon, \kappa, m)$ have to be determined by proper material tests [7] where the friction angle φ and the cohesion c are linked to the model via $\kappa = c \cos\varphi$ and $\beta = \frac{1}{3}\sin\varphi$. To ensure a correct dilatancy or contractancy behavior of the soil in this model a non associated plasticity formulation is used. Defining a potential $g(\boldsymbol{\sigma})$

$$g(\boldsymbol{\sigma}) = \sqrt{\Psi_1 \mathrm{II}_{\mathbf{s}} + \frac{1}{2}\alpha \mathrm{I}_{\boldsymbol{\sigma}}^2 + \delta^2 \mathrm{I}_{\boldsymbol{\sigma}}^4} + \Psi_2 \beta \mathrm{I}_{\boldsymbol{\sigma}} + \epsilon \mathrm{I}_{\boldsymbol{\sigma}}^2 \tag{4}$$

the evolution equation of the plastic strain is given by the derivative of the potential with respect to the stress tensor multiplied with the plastic rate $\dot{\lambda}$

$$\begin{aligned} \dot{\boldsymbol{\varepsilon}}^p = \dot{\lambda} \frac{\partial \mathrm{g}(\boldsymbol{\sigma})}{\partial \boldsymbol{\sigma}} &= \frac{1}{2 g_{rt}} \left[\Psi_1 \mathbf{s} + \left(\alpha \mathrm{I}_{\boldsymbol{\sigma}} + 4\delta^2 \mathrm{I}_{\boldsymbol{\sigma}}^3\right) \mathbf{1}\right] + \left(\Psi_2 \beta + 2\epsilon \mathrm{I}_{\boldsymbol{\sigma}}\right) \mathbf{1} \\ g_{rt} &= \sqrt{\Psi_1 \mathrm{II}_{\mathbf{s}} + \frac{1}{2}\alpha \mathrm{I}_{\boldsymbol{\sigma}}^2 + \delta^2 \mathrm{I}_{\boldsymbol{\sigma}}^4}. \end{aligned} \tag{5}$$

The dilatancy and contractancy effects of the soil can be controlled by the two additional parameters (Ψ_1, Ψ_2). A measure able to determine the dilatant or contractant behavior is the tangent of the dilatancy angle ν^p. This value is the quotient of the volumetric plastic strain to the norm of its deviatoric part

$$\tan\nu^p = \frac{\dot{\boldsymbol{\varepsilon}}^p \cdot \mathbf{1}}{3 \| \dot{\mathbf{e}}^p \|}. \tag{6}$$

The tensor $\dot{\mathbf{e}}^p = \dot{\boldsymbol{\varepsilon}}^p - 1/3(\dot{\boldsymbol{\varepsilon}}^p \cdot \mathbf{1})\,\mathbf{1}$ used in (6) indicates the deviatoric part of the rate of the plastic strain. Since the soil has a highly nonlinear plastic behavior, an additional equation is needed to take into account hardening and softening effects. In the Ehlers soil model evolution equations for the four parameters $\mathbf{h} = [\beta, \gamma, \delta, \epsilon]^{\mathrm{T}}$ are introduced in order to describe these effects

$$\dot{\mathbf{h}} = \dot{\lambda} \left(\mathbf{h}_{max} - \mathbf{h}\right) \left[\mathbf{C}_{\mathbf{h}}^{\mathbf{v}} \tan\nu^{\mathbf{p}} + \mathbf{C}_{\mathbf{h}}^{\mathbf{d}}\right] \| \dot{\mathbf{e}}^p \| = 0. \tag{7}$$

Therein $\mathbf{h}_{max}$ corresponds to the maximum values of the parameters and $\mathbf{C}_{\mathbf{h}}^{\mathbf{v}}, \mathbf{C}_{\mathbf{h}}^{\mathbf{d}}$ control the volumetric and the deviatoric changes, respectively. The actual stress

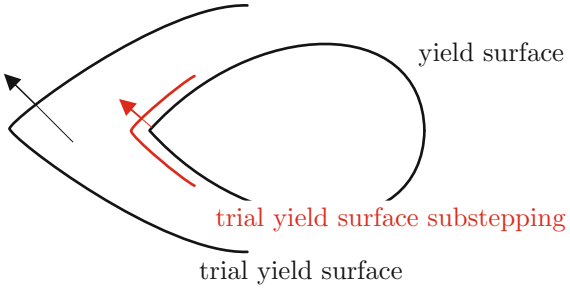

Fig. 3. Difference between standard and substepping back-projection schemes

is computed from the constitutive Eqs. (1)–(7) and the numerical solution is based on the implicit return mapping algorithm [26]. A detailed implementation can be found in [23,30]. Unfortunately, in the case of a plastic response, due to the conical structure of the yield surface in stress space, the back-projection within the return mapping algorithm onto the surface can fail, especially close to the apex. This is especially true when the trial stress and the trial hardening parameters are far away from the projection point (Fig. 3). Hence a projection to different solutions can occur which leads to a non convergence of the algorithm. A possibility to improve the closest point projection algorithm is the use of a substepping scheme [27] which is based on line search techniques. A numerical implementation within the implicit return mapping algorithm can be found in [18]. Another challenge is the oscillation between the elastic and the plastic state due to the kink in the transition between the two states. This can lead also to a non converging of the overall solution algorithm. Remedies to overcome such cases are viscoplastic regularization. The formulation used here is presented in [6] and numerically implemented in [25].

3 Friction Laws by Relating Contact and Continuum Stress Quantities

The formulations and solution techniques related to the elasto-plastic theory have a lot in common with the ones related to the frictional contact behavior. The yield criterion bounding the elastic domain is similar to the slip rule limiting the stick case. Furthermore, an evolution equation is used for the plastic strain in the continuum as well as for the tangential movement between the contacting bodies. Despite all similarities, unfortunately, a direct transition from plasticity to friction is not possible. The stress dependency within the yield criterion is often expressed by means of three invariants whereas friction laws are expressed in terms of the norm of the tangential stress and the normal pressure. Additionally, dilatancy and contractancy effects cannot be directly included in the contact formulation. A positive dilatancy angle would lead to a release of the contact, although the pressure between the bodies is non zero and a negative dilatancy angle would lead to a normal penetration which is not allowed.

Therefore, to incorporate the dilatancy effects at the contact layer an additional contact stress component is introduced.

One of the oldest model describing especially granular materials is the Mohr-Coulomb yield criterion. This criterion

$$f^m = \frac{\sqrt{\mathrm{II_s}}\cos(\Theta)}{\cos\varphi} + \left[\frac{1}{3}\mathrm{I}_{\boldsymbol{\sigma}} - \sqrt{\frac{\mathrm{II_s}}{3}}\sin\Theta\right]\tan\varphi = 0. \tag{8}$$

is actually the three-dimensional extension of the Coulomb friction law

$$f^c = \|\mathbf{t}_\mathrm{T}\| + \mathrm{t_N}\,\tan\varphi = \mathbf{0} \tag{9}$$

see [4] for a derivation. Comparing these two formulations the norm of the tangential contact stress $\|\mathbf{t}_\mathrm{T}\|$ and the normal pressure $\mathrm{t_N}$ between the two contact members can not be directly related to the continuum quantities $\mathrm{I}_{\boldsymbol{\sigma}}$, $\sqrt{\mathrm{II_s}}$, Θ. However, since the tangential contact motion is equivalent to shearing with a load on top, the Lode angle

$$\Theta = -\frac{1}{3}\arcsin\left(\frac{\sqrt{27}}{2}\frac{\mathrm{III_s}}{\mathrm{II_s}^{\frac{3}{2}}}\right) \tag{10}$$

can be assumed to be zero $\Theta = 0°$. With this assumption the stress values mostly used in plasticity models can be directly related to the standard contact stress quantities

$$\mathrm{II_s} := \|\mathbf{t}_\mathrm{T}\|^{\mathbf{2}}\cos^{\mathbf{2}}\varphi, \qquad \mathrm{I}_{\boldsymbol{\sigma}} := \mathbf{3}\,\mathrm{t_N}, \qquad \boldsymbol{\Theta} := \mathbf{0}°. \tag{11}$$

This kind of projection can also be illustratively explained, see Fig. 4 where the friction law is simply obtained by a cut of the yield surface at a Lode angle of 0°. Together with the link between the continuum stress invariants and the contact quantities Eq. (11) the standard algorithms (see [33] for more details) computing the normal and tangential contact stress can be stated. Unfortunately, due to this projection the tangential stress vector is mostly not pointing towards the sliding direction anymore due to the dilatancy effects. In contact cases the dilatancy angle has to be zero. Otherwise either a release of the contact or a penetration of one body into the other would occur which is not allowed. Looking at the graphical illustration in Fig. 5 the projected tangential stress vector $\mathbf{t}^{proj}$ can be subdivided into a part parallel to the sliding direction and a part $\mathrm{t_D}$ perpendicular to it. Thereby the latter part corresponds to the norm of the tangential stress multiplied with the tangent of the dilatancy angle

$$\mathrm{t_D} = -\tan\nu^p\|\mathbf{t}_\mathrm{T}\|. \tag{12}$$

The minus sign has to be added, since the normal stress contributions and not the pressure is considered. Hence in the relation of the contact and continuum stress quantities (11) the dilatancy effects can be considered without influencing the sliding behavior by writing alternatively

$$\mathrm{I}_{\boldsymbol{\sigma}} = 3\mathrm{t_N} - 3\tan\nu^p\,\|\mathbf{t}_\mathrm{T}\|. \tag{13}$$

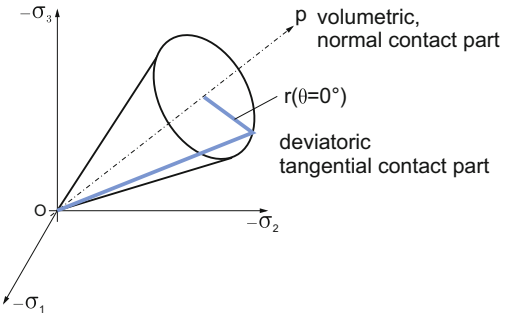

Fig. 4. Cut through the yield surface at a Lode angle of 0°

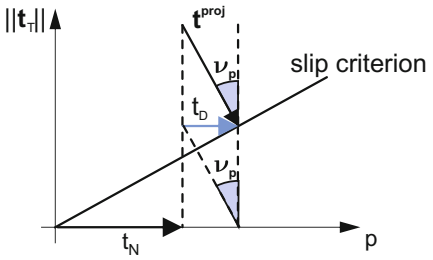

Fig. 5. Graphical illustration of the two constituents of the normal contact stress

4 Friction Laws by Relating Contact and Continuum Kinematics

In many frictional contact models the specific slip behavior is only included into the coefficient of friction within Coulomb's law. The coefficient μ is then a function of the temperature, the pressure, the contact velocity or the surface roughness, for instance. A model based on a pressure and velocity dependent coefficient of friction can be found in [35]. Such a model is also formulated for soil-structure interactions in [12]. Due to the complex behavior in the zone between the soil and the structure many new material parameters are needed. More detailed descriptions of different frictional formulations can be found in [33] and the references therein. Based on this idea a new concept of projecting plasticity models onto the contact surface is developed so that the coefficient of friction and the also the normal contact stress within Coulomb's law depend directly on the three-dimensional stress tensor

$$f^c = \|\mathbf{t}_\mathrm{T}\| + \mu\,(\boldsymbol{\sigma})\,\mathrm{t}_\mathrm{N}\,(\boldsymbol{\sigma}) = \mathbf{0}. \tag{14}$$

As mentioned in the previous section contact can also be considered as shearing with load on top (Fig. 6). Instead of relating the continuum stress invariants to the contact stress as described in Sect. 3 the continuum kinematics are now

Fig. 6. Equivalence of sliding and shear

expressed in terms of the contact quantities. In the case of a penalty regularization, see standard computational contact textbooks like [33] for more information, the tangential stress

$$\mathbf{t}_{\mathrm{T}} = -c_{\mathrm{T}} \left[\mathbf{g}_{\mathrm{T}} - \mathbf{g}_{\mathrm{T}}^{p} \right] \tag{15}$$

is given by the difference of the actual and the plastic slip distance multiplied by a penalty parameter. In standard contact algorithms the actual slip distance is computed by an integration of the slip velocity $\dot{\mathbf{g}}_{\mathrm{T}}$ over time

$$\mathbf{g}_{\mathrm{T}} = \int_{t_0}^{t} \dot{\mathbf{g}}_{\mathrm{T}} \mathrm{d}\tau. \tag{16}$$

The tangential penalty parameter can be chosen arbitrarily and hence it can also be assumed to depend on twice the shear modulus μ divided by an intrinsic virtual height. Applying the penalty regularization a penetration between the contacting bodies is allowed. If the penalty parameter is approaching infinity, the non-penetration condition holds exactly and no height between the bodies arises. Here if the height approaches zero the penalty parameter approaches infinity which verifies the proposed approach. The actual tangential contact stress can now be reformulated

$$\mathbf{t}_{\mathrm{T}} = -2\,\mu \frac{1}{h} \left[\mathbf{g}_{\mathrm{T}} - \mathbf{g}_{\mathrm{T}}^{p} \right], \quad c_{\mathrm{T}} = \frac{2\,\mu}{h}. \tag{17}$$

The second term can be interpreted as the negative shear strain of the contact layer, see also Fig. 6 for a graphical illustration,

$$\varepsilon_{3\alpha}^{e} = \frac{1}{h} \left[g_{\mathrm{T}\alpha} - g_{\mathrm{T}\alpha}^{p} \right]. \tag{18}$$

The negative sign of the tangential gap values in (17) can also explained by means of the different assumptions made in the contact theory compared to the continuum formulations, see [30] for more details. Due to the small intrinsic height h, which is assumed between the two contacting bodies, no membrane strains are taken into account

$$\varepsilon_{\alpha\beta}^{e} \equiv 0. \tag{19}$$

As mentioned in Sect. 3, the dilatancy effects can not be reproduced directly within a contact formulation and an alternative formulation has to be included. Here the normal stress component is already known and corresponds to the pressure resulting from the enforcement of the non penetration condition

$$\sigma_{33} = \mathrm{t}_{\mathrm{N}}. \tag{20}$$

Using a linear stress strain relationship the elastic strain in the normal direction can be reformulated in terms of the normal stress component and the elastic normal strains

$$\varepsilon^e_{33} = \frac{\sigma_{33}}{\lambda + 2\,\mu} + \frac{\lambda}{\lambda + 2\,\mu}\left[\varepsilon^e_{11} + \varepsilon^e_{22}\right]. \tag{21}$$

The stress strain relationship in Voigt notation can now be modified in order to compute the missing stress components

$$\begin{bmatrix}\sigma_{11}\\ \sigma_{22}\\ \sigma_{12}\\ \sigma_{23}\\ \sigma_{13}\end{bmatrix} = \begin{bmatrix} c_{11} & c_{22} & 0 & 0 & 0\\ c_{22} & c_{11} & 0 & 0 & 0\\ 0 & 0 & \mu & 0 & 0\\ 0 & 0 & 0 & \mu & 0\\ 0 & 0 & 0 & 0 & \mu\end{bmatrix} \begin{bmatrix}\varepsilon^e_{11}\\ \varepsilon^e_{22}\\ 2\varepsilon^e_{12}\\ 2\varepsilon^e_{23}\\ 2\varepsilon^e_{13}\end{bmatrix} + \begin{bmatrix}1\\1\\0\\0\\0\end{bmatrix} c_{33}\sigma_{33}. \tag{22}$$

The new coefficients in (22) can be derived directly from Eq. (21)

$$c_{11} = \frac{2\lambda^2 + 4\lambda\mu + 4\mu^2}{\lambda + 2\,\mu}, \quad c_{22} = \frac{2\lambda^2 + 2\lambda\mu}{\lambda + 2\,\mu}, \quad c_{33} = \frac{\lambda}{\lambda + 2\,\mu} \tag{23}$$

Together with the nodal plastic strain at the previous time step all quantities are known and can be used within any three-dimensional plasticity routine delivering the actual continuum stress and the material tangent at contact. Due to the known normal stress component the continuum material routine has to be modified only slightly, but the solution algorithm remains the same. The final step in the overall algorithm is the computation of the coefficient of friction. Based on the analogy of the Coulomb friction law (9) and the Mohr-Coulomb yield criterion (8) the coefficient of friction

$$\mu = \left| \tan\left(\arcsin\left(\frac{\sqrt{\mathrm{II_s}}\cos\Theta}{\frac{1}{3}\mathrm{I}_{\boldsymbol{\sigma}} - \sqrt{\frac{\mathrm{II_s}}{3}}\sin\Theta} \right)\right)\right| \tag{24}$$

as well as the normal stress component follows directly from the invariants of the actual stress tensor

$$\mathrm{t_N} = \frac{1}{3}\mathrm{I}_{\boldsymbol{\sigma}} - \sqrt{\frac{\mathrm{II_s}}{3}}\sin\Theta. \tag{25}$$

Like in Sect. 3 the first term can be characterized as the normal pressure resulting from the enforcement of the non-penetration condition. Since the Lode angle Θ is not zero in case of dilatancy/contractancy, the second term can be interpreted as the contribution to the force acting in normal direction due to dilatancy or contractancy effects, respectively.

5 Friction Laws by Extending Contact Kinematics to 3D

To extend the contact kinematics a relation between continuum kinematics and standard contact formulations has to be stated. This link can be easily established if the solid-shell concept [16,24] is adopted. In analogy to this concept any

point of the continuum is defined in terms of the corresponding position vector of each surface together with a linear interpolation in between. The position vectors of the deformed and of the initial configuration can then be simplified to a description of the position vectors of each contact surface

$$\begin{aligned}\mathbf{x}(\xi^\alpha,\xi) &= \mathbf{x}^2(\xi^{2\alpha}) + \frac{\xi}{h}\left[\mathbf{x}^1(\xi^{1\alpha}) - \mathbf{x}^{\mathbf{2}}(\xi^{\mathbf{2}\alpha})\right] \\ \mathbf{X}(\xi^\alpha,\xi) &= \mathbf{X}^2(\xi^{2\alpha}) + \frac{\xi}{h}\left[\mathbf{X}^{\mathbf{1}}(\xi^{\mathbf{1}\alpha}) - \mathbf{X}^{\mathbf{2}}(\xi^{\mathbf{2}\alpha})\right].\end{aligned} \tag{26}$$

The interpolation between the contacting bodies is regularized by the parameter ξ and by the height of the contact layer h. The index $(\mathrm{a}=1)$ indicates values of the slave surface and the index $(\mathrm{a}=2)$ stands for values of the master surface. Additionally, $\xi^{a\alpha}$ corresponds to the intrinsic coordinates of the two surfaces. In contrast to the shell theory the initial configuration, indicated by the position vector $\mathbf{X}$, is exactly the configuration at the onset of contact. The base vectors directly follows from the derivative of the position vector with respect to the intrinsic coordinates

$$\begin{aligned}\mathbf{G}_\alpha &= \frac{\partial \mathbf{X}}{\partial \xi^\alpha} = \left(1-\frac{\xi}{h}\right)\mathbf{X}^2_{,\alpha} + \frac{\xi}{h}\mathbf{X}^1_{,\alpha} = \left(1-\frac{\xi}{h}\right)\mathbf{A}^2_\alpha + \frac{\xi}{h}\mathbf{A}^1_\alpha = \bar{\mathbf{G}}_\alpha \\ \mathbf{G}_3 &= \frac{\partial \mathbf{X}}{\partial \xi} = \frac{1}{h}\left[\mathbf{X}^1 - \mathbf{X}^2\right] = \mathbf{N} = \bar{\mathbf{G}}_{\mathbf{3}}.\end{aligned} \tag{27}$$

In the initial configuration, the gap vector between the two surfaces conforms to a not normalized normal vector at the contact layer. The derivative of the position vector with respect to the surface coordinates are equal to the two surface base vectors $\mathbf{A}^{\mathbf{1}}_\alpha$, $\mathbf{A}^{\mathbf{2}}_\alpha$. Like in shell theory, in the deformed configuration the gap vector is normally not perpendicular anymore (Fig. 7). The dimensionless gap vector is termed director and indicated by $\mathbf{d}$ and $\mathbf{a}^{\mathbf{1}}_\alpha$, $\mathbf{a}^{\mathbf{2}}_\alpha$ correspond to the surface base vectors of the deformed configuration

$$\begin{aligned}\mathbf{g}_\alpha &= \frac{\partial \mathbf{x}}{\partial \xi^\alpha} = \left(1-\frac{\xi}{h}\right)\mathbf{x}^2_{,\alpha} + \frac{\xi}{h}\mathbf{x}^1_{,\alpha} = \left(1-\frac{\xi}{h}\right)\mathbf{a}^2_\alpha + \frac{\xi}{h}\mathbf{a}^1_\alpha = \bar{\mathbf{g}}_\alpha \\ \mathbf{g}_3 &= \frac{\partial \mathbf{x}}{\partial \xi} = \frac{1}{h}\left[\mathbf{x}^1 - \mathbf{x}^2\right] = \mathbf{d} = \bar{\mathbf{g}}_{\mathbf{3}}.\end{aligned} \tag{28}$$

The base vectors of the contact layer can now be formulated either in terms of the position vectors $\mathbf{g}_i$, $\mathbf{G}_i$ or directly written by means of the surface base vectors. The latter ones are indicated by a bar on top $\bar{\mathbf{g}}_i$, $\bar{\mathbf{G}}_i$. However, both formulations are identical. The connection to the standard contact kinematics can now be derived, if the components of the Green Lagrange strain tensor are computed in terms of the two base vector formulations

$$E_{ij} = \frac{1}{2}\left(\mathbf{g}_i \cdot \bar{\mathbf{g}}_j - \mathbf{G}_i \cdot \bar{\mathbf{G}}_j\right). \tag{29}$$

Within that work Latin letters $i, j = 1, 3$ indicate continuum quantities whereas Greek letters $\alpha, \beta = 1, 2$ are related to quantities of the surface. In order to derive

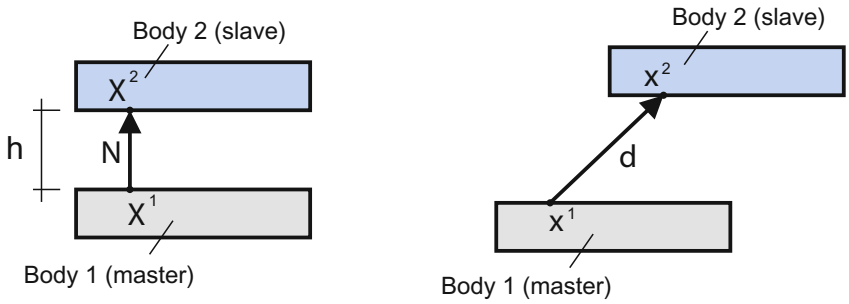

Fig. 7. Initial (left) and deformed configuration (right) of a simple two-dimensional contact layer example

the connection between contact and continuum kinematics these components have to be integrated over the height

$$g_{ij} = \int_0^h E_{ij} \mathrm{d}\xi. \tag{30}$$

In analogy to the shell theory the membrane part indicates the change of the surface base vectors during the deformation. Due to the integration each part is now weighted with fractions of the height

$$\begin{aligned} g_{\alpha\beta} = &\frac{h}{6}\left[\mathbf{x}^1_{,\alpha}\cdot\mathbf{a}^1_\beta + \mathbf{x}^2_{,\alpha}\cdot\mathbf{a}^2_\beta\right] + \frac{h}{12}\left[\mathbf{x}^1_{,\alpha}\cdot\mathbf{a}^2_\beta + \mathbf{x}^2_{,\alpha}\cdot\mathbf{a}^1_\beta\right] \\ &- \frac{h}{6}\left[\mathbf{X}^1_{,\alpha}\cdot\mathbf{A}^1_\beta + \mathbf{X}^2_{,\alpha}\cdot\mathbf{A}^2_\beta\right] + \frac{h}{12}\left[\mathbf{X}^1_{,\alpha}\cdot\mathbf{A}^2_\beta + \mathbf{X}^2_{,\alpha}\cdot\mathbf{A}^1_\beta\right]. \end{aligned} \tag{31}$$

The shear part is characterized by the tangential change of the gap vector. At the beginning of contact the initial surface base vectors $\mathbf{A}^1_\alpha$, $\mathbf{A}^2_\alpha$ are perpendicular to the normal vector $\mathbf{N}$ and thus the double shear components only computes in terms of the current quantities

$$2g_{\alpha 3} = \left(\mathbf{x}^1 - \mathbf{x}^2\right)\cdot\frac{1}{2}\left(\mathbf{a}^1_\alpha + \mathbf{a}^2_\alpha\right). \tag{32}$$

Finally, the normal part describes the change of the norm of the gap vectors during deformation

$$g_{33} = \frac{1}{2}\left(\mathbf{x}^1 - \mathbf{x}^2\right)\cdot\mathbf{d} - \frac{1}{2}\left(\mathbf{X}^1 - \mathbf{X}^2\right)\cdot\mathbf{N}. \tag{33}$$

With the definition of the difference vector $\mathbf{w}$ as the change of the gap vector

$$\mathbf{w} = \left(\mathbf{x}^1 - \mathbf{x}^2\right) - h\mathbf{N}, \quad \mathbf{d} = \frac{1}{h}\mathbf{w} + \mathbf{N} \tag{34}$$

the normal part of the integrated Green Lagrange strain components can be rewritten

$$g_{33} = \mathbf{w}\cdot\mathbf{N} + \frac{1}{2h}\mathbf{w}\cdot\mathbf{w}. \tag{35}$$

Since only small changes are assumed in the normal direction the second, non-linear, part can be neglected. With this assumption the remaining first part of

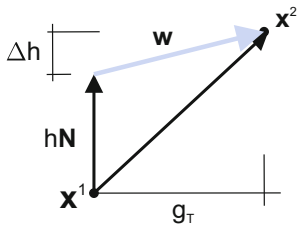

Fig. 8. Split of the gap vector into normal direction and difference vector for the two-dimensional case

Eq. (35) can be considered as the change of the height during the deformation as can be seen as well in Fig. 8

$$g_{33} = \triangle h. \tag{36}$$

The advantage of this formulation is the simple representation of the kinematical deformation in normal direction even in a sinuous movement. The standard contact quantities are obtained if the height in (30) approaches zero

$$g^c_{ij} = \lim_{h \to 0} \int_0^h \mathrm{E}_{ij} d\xi. \tag{37}$$

Since the initial height of the contact layer is zero in standard contact situations, g^c_{33} exactly corresponds to the normal gap

$$g^c_{\alpha\beta} = 0, \quad 2g^c_{\alpha 3} = \left(\mathbf{x}^1 - \mathbf{x}^2\right) \cdot \frac{1}{2}\left(\mathbf{a}^1_\alpha + \mathbf{a}^2_\alpha\right), \quad g^c_{33} = g_{\mathrm{N}}. \tag{38}$$

In standard contact formulations $\mathbf{a}^1_\alpha$ is mostly assumed as the tangential base vector at the contact surface. This means that the surface base vectors of each side are pointing towards the same direction and are equal in length

$$\mathbf{a}^1_\alpha = \frac{1}{2}\left(\mathbf{a}^1_\alpha + \mathbf{a}^2_\alpha\right). \tag{39}$$

This outcome is also in line with the assumptions made in Sect. 4. Neglecting the approach of the height towards zero 3-dimensional contact kinematics can be stated. The corresponding strain can be obtained, if the resulting formulation is divided by the height h

$$E^c_{ij} = \frac{1}{h}\int_0^h E_{ij} \mathrm{d}\xi = \frac{1}{h} g_{ij}. \tag{40}$$

Just as in the previous section this strain can be used within any 3-dimensional plasticity routine using the same solution algorithms which yields the actual continuum stress and the material tangent at the contact layer. A detailed description of this contact layer formulation and its numerical implementation can be found in [31]. In contrast to the previous section the continuum material routine has not to be modified.

6 Numerical Investigations

The performance of the three different formulations to include soil models directly in contact formulations will be demonstrated at a direct shear test. Numerical implementation of the algorithms for standard continuum formulations can be found for instance in [34]. The presented new frictions laws are included into contact formulations based on the Mortar method. This method is at the moment the most robust discretization technique for contact problems and hence it is applied in this work. A more detailed introduction and discussions on application of the Mortar method for contact problems are available in [19,21,30]. The implementation of the presented frition laws of the Sects. 3, 4 and 5 within the Mortar method can be found in [31,32].

Table 1. Material data for GEBA sand

$\lambda = 100\,\frac{\mathrm{MN}}{\mathrm{m}^2}$	$\mu = 150\,\frac{\mathrm{MN}}{\mathrm{m}^2}$	$n_0^s = 0.585$	$n_{max}^s = 0.595$
$\beta_0 = 0.105$	$\beta_{max} = 0.263$	$C_\beta^v = -58$	$C_\beta^d = 350$
$\gamma_0 = 0.0$	$\gamma_{max} = 1.6$	$C_\gamma^v = -10$	$C_\gamma^d = 35$
$\delta_0 = 0.01\,\frac{\mathrm{m}^2}{\mathrm{MN}}$	$\delta_{max} = 0.005\,\frac{\mathrm{m}^2}{\mathrm{MN}}$	$C_\delta^v = 90$	$C_\beta^d = -15.9$
$\epsilon_0 = 0.0805\,\frac{\mathrm{m}^2}{\mathrm{MN}}$	$\epsilon_{max} = 0.008\,\frac{\mathrm{m}^2}{\mathrm{MN}}$	$C_\epsilon^v = -300$	$C_\epsilon^d = 300$
$\alpha = 0.01$	$\kappa = 0.0001\,\frac{\mathrm{MN}}{\mathrm{m}^2}$	$m = 0.5454$	$\eta = 0.005$
$\Psi_1 = 0.97$	$\Psi_2 = 0.48$		

In this direct shear test a soil specimen of dense fine sand slides over a block of steel ($\mathrm{E} = 210 \cdot 10^3\,\mathrm{MN/m^2}$, $\nu = 0.2$). The surface of the steel block is assumed to be rough and hence governing the shear behavior. The direct shear test deliver the same response as the three-dimensional triaxial test which can be seen in experimental investigations [22]. The sand is taken from the Gebenbacher (GEBA) pit with grain diameters between 0.03–0.3 mm, a sieve retention of $\mathrm{d_{10}} = 0.09\,\mathrm{mm}$, $\mathrm{d_{60}} = 0.11\,\mathrm{mm}$ and a coefficient of uniformity of $\mathrm{C}_U = 1.22$. The material parameter are determined in [8] and are given in Table 1. On top of the test apparatus a variable surface pressure is applied. Furthermore, the soil specimen and the block of steel are fixed in the horizontal direction. In order to avoid tension within the soil specimen on the side where the tangential displacement is applied a pressure of $\mathrm{p}_1 = 0.5\,\mathrm{kN/m^2}$ ensures positive stress values within the soil (Fig. 9). For each concept of a friction law based on continuum

soil models a series of different vertical pressure loads is investigated. In order to compare the reproducibility of the continuum behavior at the contact surface all the results are compared with the same direct shear test where now one layer of continuum elements is located in between of the two plates as can be seen in Fig. 10. The evaluation of the continuum case is based on the analogy between the Mohr-Coulomb yield criterion and the Coulomb friction law in Eqs. (8) and (9), respectively.

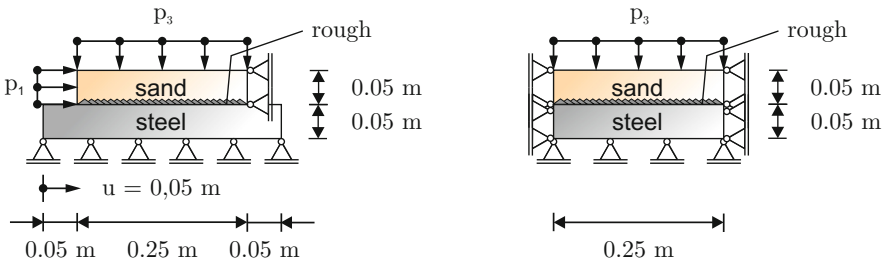

Fig. 9. Side view and front view of the direct shear test with a rough surface

Fig. 10. Finite element mesh of the contact case (left) and of the continuum case with one layer of elements between the two bodies (right)

6.1 Friction Laws by Relating Contact and Continuum Stress Quantities

Comparing the force evaluation along the sliding distance a different behavior is obvious (Fig. 11). In the interface element during the phase when the pressure is imposed a plastic response behavior can be observed already. In the contact model only stick occurs in the first loading situation. Hence the evolution of the hardening behavior starts not before sliding and then in a more moderate fashion. In order to compare the results with the continuum case in normal direction as well, not only the contact pressure, but also the dilatancy part, see Eq. (13), is considered in Fig. 11. This leads to a value slightly larger than the applied contact force on top of the specimen. The Lode angle is not exactly zero in the case of dilatancy or contractancy and leads to a small under-prediction of the force acting in normal direction although dilatancy was included in the formulation. Additionally, it can be seen from Fig. 11 that the change of the

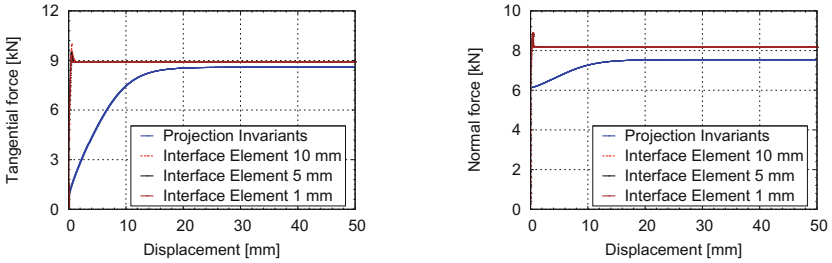

Fig. 11. Comparison of tangential (left) and normal force (right) versus sliding distance at a constant pressure of 100 = kN/m^2

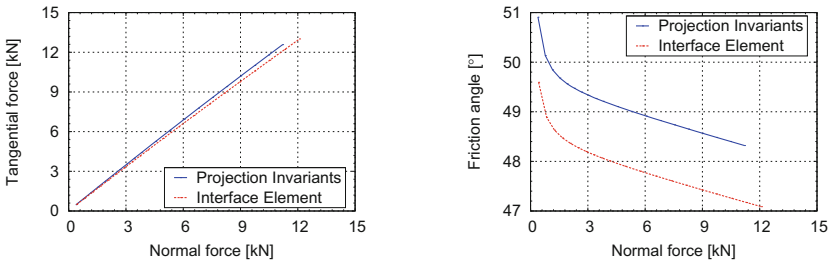

Fig. 12. Comparison of tangential force (left) and friction angle (right) versus normal force

height of the interface element has not a strong influence on the final result. Only the peak behavior is slightly different at the onset of sliding. Nevertheless the evaluation of the final friction angle as well as of the final tangential force over the normal force are qualitatively in a good accordance as can be seen in Fig. 12. Beside the possibility of arbitrary large relative movements between the soil and the structure another advantage of this contact formulation is the reduction of the CPU time with a factor of 10 compared to the corresponding computation of the continuum model.

Remark: Comparing the tangential force evaluation of the projected contact formulation (Fig. 11) with the outcome of a triaxial test [32] the results are qualitatively pretty close. The accordance can be explained with the similar evolution of the hardening parameters in both cases which is different to the corresponding behavior in a direct shear test. Looking at the normal-tangential force evaluation of Fig. 12 the cap structure of the underlying yield criterion cannot be completely reproduced. Only the middle part, which is slightly curved, can be represented leading to the nonlinear behavior in the evaluation of the friction angle over the normal force in Fig. 12. The yield criterion of Eq. (3) and hence the projected slip rule have four roots on the axis of the normal force and on the space diagonal, respectively. However the domain is only defined between the inner two roots. Hence for values beyond the inner roots a unique

back-projection onto the slip line can not be guaranteed anymore. A detailed explanation of these implications can be found in [30].

6.2 Friction Laws by Relating Contact and Continuum Kinematics

For the evaluation of the second strategy the same investigations using the same direct shear test is conducted. In contrast to the first concept now a height has to be introduced. Although this height is artificial it is chosen to consist of 10 mm corresponding to the forced localization zone occurring within the soil structure interaction zone. This height is imposed directly within the continuum simulation using standard elements at the interface and considered intrinsically within the contact formulation.

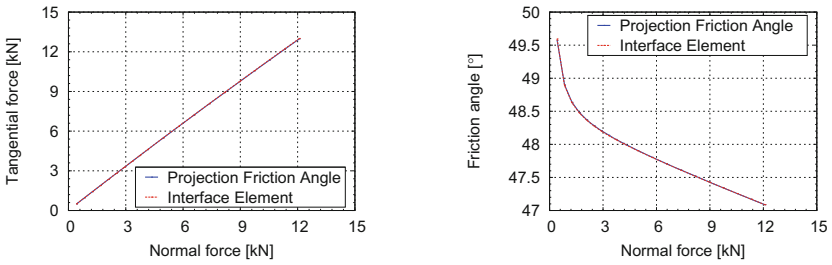

Fig. 13. Comparison of tangential force (left) and friction angle (right) versus normal force

Comparing the final tangential force and the final friction angle of different normal load levels (Fig. 13) both evaluations shows the same outcome.

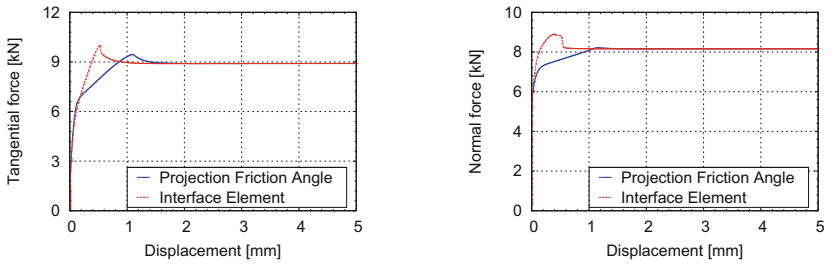

Fig. 14. Comparison of tangential (left) and normal force (right) versus sliding distance of the first 5 mm at a constant pressure of 100 = kN/m^2 (right)

The tangential force of the interface element and of the projected contact formulation end up both with the same force and shows a hardening peak (14).

Only the height of the peak and the time when it occurs are different. The same holds for the normal force evaluation in Fig. 14. As mentioned in Sect. 4 the normal force includes the contact pressure from the enforcement of the non-penetration condition as well as a part resulting from dilatancy/contractancy effects. However replacing the upper specimen by a block of steel and comparing the evaluation of the tangential and of the normal force both outcomes are almost equal (see [32]). The reason for the good accordance is the small normal strain in direction of sliding ($\varepsilon_{11} \approx 10^{-6}$) due to the stiffer upper block which conforms to the assumption made in Eq. (19). In the soil-structure example presented here this normal strain is around $\varepsilon_{11} \approx 10^{-3}$ and can not be disregarded anymore.

As well as for the projection scheme in Sect. 3 the CPU time of this projection method is also around 10 times less as for the pure continuum case with interface elements in between of the upper and lower specimen.

6.3 Friction Laws by Extending Contact Kinematics to 3D

In contrast to the test scenarios before now a real height is introduced between the two contact bodies defining a contact layer. The initial mesh of this contact layer approach and of the corresponding interface element are shown in Fig. 15. As can be seen on the left side of the Fig. 15 in the contact case the upper block seems to hoover over the lower specimen, but in this open space the continuum soil model is embedded. Looking at the tangential and normal force evaluation in Fig. 16, contrary to the friction laws of Sects. 3 and 4, both outcomes are identical, since the membrane strain is now considered at the contact layer. In the frictional behavior of GEBA fine sand a hardening zone at the beginning of loading is obviously accompanied by a small increase of the normal force. Such a behavior is typical for dense sand. The computation of the tangential and the normal force at each time step are based on the analogy between Coulomb and Mohr-Coulomb. The stress values of each soil element in the pure continuum FEM model are evaluated at the mid plane of that element. Another big advantage of the developed element is that the dilatant behavior can now be reproduced at the contact layer. In the evaluation of the height (Fig. 17) it has to be highlighted that in the first few steps a decrease of the height slightly below the initial 10 mm occurs showing a contractant behavior. Afterward the height increases due to dilatancy. This outcome is very typical for

Fig. 15. Finite element mesh of the contact case (left) and of the continuum case with one layer of elements between the two contact bodies (right)

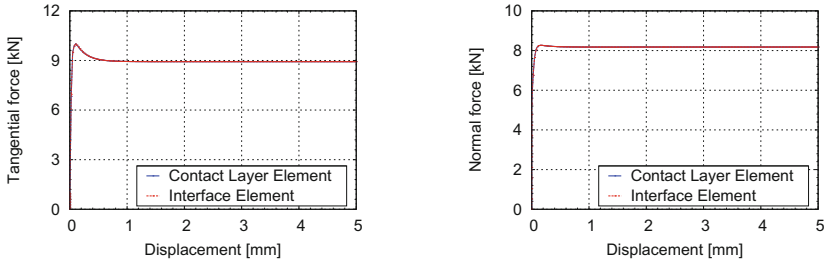

Fig. 16. Tangential force (left) and normal force (right) versus sliding distance at the first 5 mm with a initial contact height of h = 10 mm and with a constant pressure of $p_3 = 100\ kN/m^2$

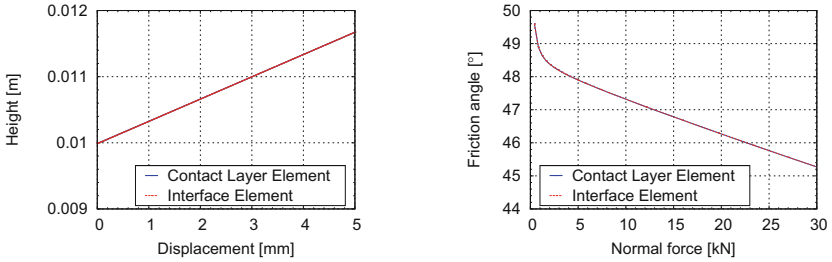

Fig. 17. Height versus sliding distance at the first 5 mm with a initial contact height of h = 10 mm and with a pressure of $p_3 = 100\ kN/m^2$ (left) and friction angle versus normal pressure (right)

dense sand. With standard contact models such characteristics cannot be reproduced. The dilatancy would releases the contact which is not feasible and the contractancy would lead to a penetration which is not allowed. An evaluation at different surface pressures p_3 additionally shows that the friction angle is not linearly depending on the normal force (Fig. 17) if the GEBA fine sand model is used at the contact layer.

7 Conclusion

In this work three different strategies were presented each able to directly use soil models as friction laws. The first concept exploits the natural relation between Coulomb slip rule and Mohr-Coulomb yield criterion to establish a connection between the stress invariants of the continuum and the contact quantities, normal pressure and norm of the tangential stress. To model dilatancy effects properly a new dilatancy stress component was introduced. Since the Lode angle is not zero in the case of dilatancy or contractancy effects, this scheme underpredicts the real stress at the contact surface. If both bodies are sticking together the response behavior is only elastic. However in the continuum case a plastic response is also possible if the relative movement of the two bodies is only small. Both

phenomena reason the slightly different outcome of the first concept compared to the interface element.

The second approach has the advantage of a direct implementation of the plasticity model into the friction equations and constitutes a very robust algorithm. On the other hand the introduced height of the contact layer leads to an additional parameter which has to be determined. Since within soil-structure interactions the height of the contact layer corresponds to the height of a forced localization, a value of 2–3 times the average grain diameter is a reasonable approach.

Finally the last method of a contact layer formulation can reproduce the continuum behavior exactly. Here as well a height has to be introduced which can also be legitimated by the forced localization zone which occurs at the contact layer.

Additionally, as mentioned in this work, the outcome of the triaxial test differs from the corresponding evaluation of the direct shear test using the Ehlers model which should not be the case for proper soil models. The back-projection algorithm can also not deliver feasible results, if the normal pressure is too large or too small due to the double roots at the limits of the slip line. In between the range is imaginary which adds another challenge to the back-projection algorithm. To show the real performance of especially the first two concepts a comparison with other plasticity models has to be done.

It has also to be highlighted that all three contact formulations can be applied in arbitrary large sliding situations. In this work the focus lied on the comparison with interface element. At the end it has to be mentioned that although these concepts were applied only to soil-structure interactions, they can be seen as a generic scheme to include any kind of continuum model within a contact formulation.

Acknowledgments. This research project is supported by the *Deutsche Forschungsgemeinschaft* (German Research Foundation) within the research unit 1136: Simulation of Geotechnical Construction Processes with Holistic Consideration of Constitutive Laws in Soils.

References

1. Anastasopoulos, I., Gazetas, G.: Foundation-structure systems over a rupturing normal fault: part II. Analysis of the Kocaeli case histories. Bull. Earthq. Eng. **5**, 277–301 (2007)
2. Casciati, S., Borja, R.: Dynamic FE analysis of South Memnon Colossus including 3D soil-foundation-structure interaction. Comput. Struct. **82**, 1719–1736 (2004)
3. Curnier, A.: A theory of friction. Int. J. Solids Struct. **20**, 637–647 (1984)
4. Desai, C.S., Siriwardane, H.: Constitutive Laws for Engineering Materials with Emphasis on Geologic Materials. Prentice-Hall, Englewood Cliffs (1984)
5. Desai, C.: Numerical design-analysis for piles in sands. J. Geotechn. Eng. Div. **GT6**, 613–635 (1974)
6. Duvaut, G., Lions, J.: Inequalities in Mechanics and Physics. Springer, Heidelberg (1976)

7. Ehlers, W.: A single-surface yield function for geomaterials. Arch. Appl. Mech. **65**, 246–259 (1995)
8. Ehlers, W., Avci, O., Markert, B.: Computation of slope movements initiated by rain-induced shear bands in small-scale tests and in situ. Vadose Zone J. **10**(2), 512–525 (2011)
9. Ehlers, W., Scholz, B.: An inverse algorithm for the identification and the sensitivity analysis of the paramters governing micropolar elasto-plastic granular material. Arch. Appl. Mech. **77**, 911–931 (2007)
10. Goodman, R., Taylor, R., Brekke, T.: A model for the mechanics of jointed rock. J. Soil Mech. Found. Div. **94**, 637–659 (1968)
11. Gqhaboussi, J., Wilson, E., Isenberg, J.: Finite element for rock joints and interfaces. J. Soil Mech. Found. Div. **10**, 833–848 (1973)
12. Haraldsson, A.: Formulierung und Simulation der Kontaktvorgänge in der Baugrund-Tragwerk-Interaktion. Ph.D. thesis, Universität Hannover, Germany (2003)
13. Hu, L., Pu, J.: Testing and modeling of soil-structure interfaces. J. Geotech. Geoenviron. Eng. **130**, 851–860 (2004)
14. Kucharski, S., Klimczak, T., Polijaniuk, A., Kaczmarek, J.: Finite-elments model for the contact of rough surfaces. Wear **177**, 1–13 (1994)
15. Michalowski, R., Mroz, Z.: Associated and non-associated sliding rules in contact friction problems. Archieve Mech. **30**, 259–276 (1978)
16. Parisch, H.: A continuum-based shell theory for non-linear applications. Int. J. Numer. Meth. Eng. **38**, 1855–1883 (1995)
17. Pei, L., Hyun, S., Molinari, J., Robbins, M.: Finite element modeling of elasto-plastic contact between rough surfaces. J. Mech. Phys. Solids **53**, 2385–2409 (2005)
18. Perez-Foguet, A., Rodriguez-Ferran, A., Huerta, A.: Consistent tangnet matrices for substepping schemes. Comput. Methods Appl. Mech. Eng. **190**, 4627–4647 (2001)
19. Popp, A., Gee, M.W., Wall, W.A.: A finite deformation mortar contact formulation using a primal-dual active set strategy. Int. J. Num. Methods Eng. **79**, 1354–1391 (2009)
20. Potyondy, J.: Skin friction between various soils and construction materials. Géotechnique **11**, 339–353 (1961)
21. Puso, M.A., Laursen, T.A.: A mortar segment-to-segment contact method for large deformation solid mechanics. Comput. Methods Appl. Mech. Eng. **193**, 601–629 (2004)
22. Reul, O.: In-situ Messungen und numerische Studien zum Tragverhalten der kombinierten Pfahl-Plattengründungen. Ph.D. thesis, Technischen Hochschule Darmstadt, Germany (2000)
23. Scholz, B.: Application of a micropolar model to the localization phenomena in granular materials: general model, sensitivity analysis and parameter optimization. Ph.D. thesis, Universität Stuttgart, Germany (2007)
24. Schoop, H.: Oberflächenorientierte Schalentheorie endlicher Verschiebungen. Ingenieur-Archiv **56**, 427–437 (1986)
25. Simo, J.: Numerical analysis and simulation of plasticity. In: Handbook of Numerical Analysis, vol. 6. Elsevier Science B.V (1998)
26. Simo, J., Taylor, R.: Consistent tangent operators for rate-independent elastoplasticity. Comput. Methods Appl. Mech. Eng. **48**, 101–118 (1985)
27. Sloan, S.: Substepping schemes for the numerical integration of elastoplastic stress-strain relations. Int. J. Numer. Meth. Eng. **24**, 893–911 (1987)

28. Tejchman, J., Wu, W.: Experimental and numerical study of sand-steel interfaces. Int. J. Numer. Anal. Meth. Geomech. **19**, 513–536 (1995)
29. Uesugi, M., Kishida, H., Uchikawa, Y.: Friction between dry sand and concrete under monotonic and repeated loading. Soils Found. **30**, 115–128 (1990)
30. Weißenfels, C.: Contact methods integrating plasticity models with application to soil mechanics. Ph.D. thesis, Universität Hannover, Germany (2013)
31. Weißenfels, C., Wriggers, P.: A contact layer element for large deformations. Comput. Mech. **50**, 873–885 (2015)
32. Weißenfels, C., Wriggers, P.: Methods to project plasticity models onto the contact surface applied to soil structure interactions. Comput. Geotech. **65**, 187–198 (2015)
33. Wriggers, P.: Computational Contact Mechanics, 2nd edn. Springer, Heidelberg (2006)
34. Wriggers, P.: Nonlinear Finite Element Methods. Springer, Heidelberg (2008)
35. Wriggers, P., Reinelt, J.: Multi-scale approach for frictional contact of elastomers on rough rigid surfaces. Comput. Methods Appl. Mech. Eng. **198**, 1996–2008 (2009)
36. Zaman, M., Desai, C., Drumm, E.: Interface model for dynamic soil-structure interaction. J. Geotechn. Eng. **110**, 1257–1273 (1984)

A Zero Elastic Range Hypoplasticity Model for Sand

Mahdi Taiebat[1(✉)] and Yannis F. Dafalias[2,3]

[1] Department of Civil Engineering, University of British Columbia, Vancouver, BC, Canada
mtaiebat@civil.ubc.ca
[2] Department of Civil and Environmental Engineering, University of California, Davis, CA, USA
[3] Department of Mechanics, National Technical University of Athens, Zographou, Greece

Abstract. The theory of zero purely elastic range in stress space within the framework of bounding surface plasticity is applied to sand constitutive modelling. With a vanished yield surface, plastic loading occurs for any direction of the stress ratio rate on which the loading and plastic strain rate directions now depend, rendering the model incrementally non-linear. The resulting model falls into the category of hypoplasticity in the sense of dependence of the plastic strain rate direction on the stress rate direction, that is different from another constitutive hypoplasticity theory, which does not involve classical plasticity loading-unloading criteria and additive decomposition of total strain rate into elastic and plastic parts. The simplicity of the conceptual structure of the model is particularly attractive as it consists of only one surface, the bounding/failure surface, and the stress point itself in the deviatoric stress ratio plane. The model follows the basic premises of the SANISAND family of models that unify the description for any pressure and density within critical state theory. Elimination of the classical yield surface concept circumvents the complexity associated with satisfying the consistency condition; however, the incrementally non-linear hypo-plastic nature of the new formulation requires special handling of its numerical implementation. The work shows the simulative capabilities of the model that are comparable with those of the classical model with very small yield surfaces, including simulations under cyclic and rotational shear loading.

Keywords: Sands · Constitutive relations · Hypoplasticity · Zero elastic range · Critical state · Bounding surface

1 Introduction

The idea of zero elastic range in plasticity theory where the yield surface size shrinks to zero and the surface degenerates to the current stress point in stress space was first presented in [3] as a corollary of bounding surface (BS) plasticity where such disappearance of yield surface is compensated by the still finite

T. Triantafyllidis (ed.), *Holistic Simulation of Geotechnical Installation Processes*,
Lecture Notes in Applied and Computational Mechanics 82, DOI 10.1007/978-3-319-52590-7_10

bounding surface that determines now the loading direction and plastic modulus. The physical motivation was the effort to simulate the response of artificial graphite [3,8,9], a material used in nuclear reactor technology and which exhibits zero purely elastic range in loading and unloading.

Several other materials do show either a zero or an extremely limited purely elastic range response described by a very small yield surface, prominent among them being soils, in particular granular soils or sands. In sand constitutive modeling the consequence of this trait was reflected in the adoption by various models of a very small size yield surface (YS) in stress-ratio space $\boldsymbol{r} = \boldsymbol{s}/p$, with $\boldsymbol{s}$ the deviatoric and p the hydrostatic parts of the stress $\boldsymbol{\sigma}$, respectively, obeying a kinematic hardening rule. Among such models the most relevant to the current paper are the two-surface model in [7,21], and its variation in [26] where the name SANISAND was firstly adopted. Such a model is illustrated in Fig. 1(a) where the YS is shown as a very small circle in $\boldsymbol{r}$ space with the back stress-ratio $\boldsymbol{\alpha}$ as its center. The larger surface represents the bounding surface (BS) that varies in size, on which the image stress point $\boldsymbol{r}^b$ is defined as shown by the unit norm deviatoric direction $\boldsymbol{n}$ along $\boldsymbol{r} - \boldsymbol{\alpha}$. The $\boldsymbol{R}'$, normal to the BS at $\boldsymbol{r}^b$, is the plastic deviatoric strain rate direction. As usual with BS plasticity, the plastic modulus K_p depends on the projected on $\boldsymbol{n}$ distance $(\boldsymbol{r}^b - \boldsymbol{r}) : \boldsymbol{n}$ such that $K_p = 0$ when $\boldsymbol{r} = \boldsymbol{r}^b$, i.e., when the stress ratio is on the BS. The θ represents the relevant Lode angle.

It is then natural to consider the possibility that this very small yield surface can be taken in the limit to be of vanishing size becoming identical to the back-stress ratio that is its center, and consequently the YS surface degenerates to the stress point $\boldsymbol{r}$ itself. In passing one can observe that in the counterpart of the above for the classical triaxial $q - p$ space, the yield surface is represented by a very narrow wedge, which for vanishing elastic range collapses onto the stress ratio line $q/p = \eta$. The conceptual framework of the working of the model is illustrated in Fig. 1(b). The stress ratio rate is denoted by $\dot{\boldsymbol{r}}$ (a superposed dot indicates henceforth the rate), and the stress ratio increment $d\boldsymbol{r} = \dot{\boldsymbol{r}}dt$, is shown as an arrow emanating from $\boldsymbol{r}$, with dt the time increment. The extension of $\dot{\boldsymbol{r}}$ direction defines the image (or bounding) stress ratio $\boldsymbol{r}^b$ (mapping rule) at its intersection with the BS, where again $\boldsymbol{n}$ and $\boldsymbol{R}'$ are defined. Figure 1(c) illustrates the process when the Lode angle θ effect on the BS is omitted and the BS becomes circular, but the Lode angle effect on $\boldsymbol{R}'$ is maintained. Notice that whichever is the direction of $\dot{\boldsymbol{r}}$ for $\boldsymbol{r}$ inside or on the BS (see later for the case of $\boldsymbol{r}$ outside the BS), there will be always a unique bounding stress ratio point $\boldsymbol{r}^b$ and associated $\boldsymbol{n}$ for convex BS shape, and furthermore $\boldsymbol{n} : \dot{\boldsymbol{r}} > 0$ guaranteeing there will be always plastic loading. Both $\boldsymbol{n}$ and $\boldsymbol{R}'$ depend on the stress rate direction. Such dependence in conjuction with the mapping rule shown in Figs. 1(b) and (c), while originally proposed in [3,8,9] for artificial graphite, it was also proposed for soils in a qualitative sense in [4], and applied to sands within a full constitutive modeling framework in [2,14,29], and more recently in [12], in constitutive frameworks quite different than the present ones. According to [6] these models, which are also incrementally non-linear (the first

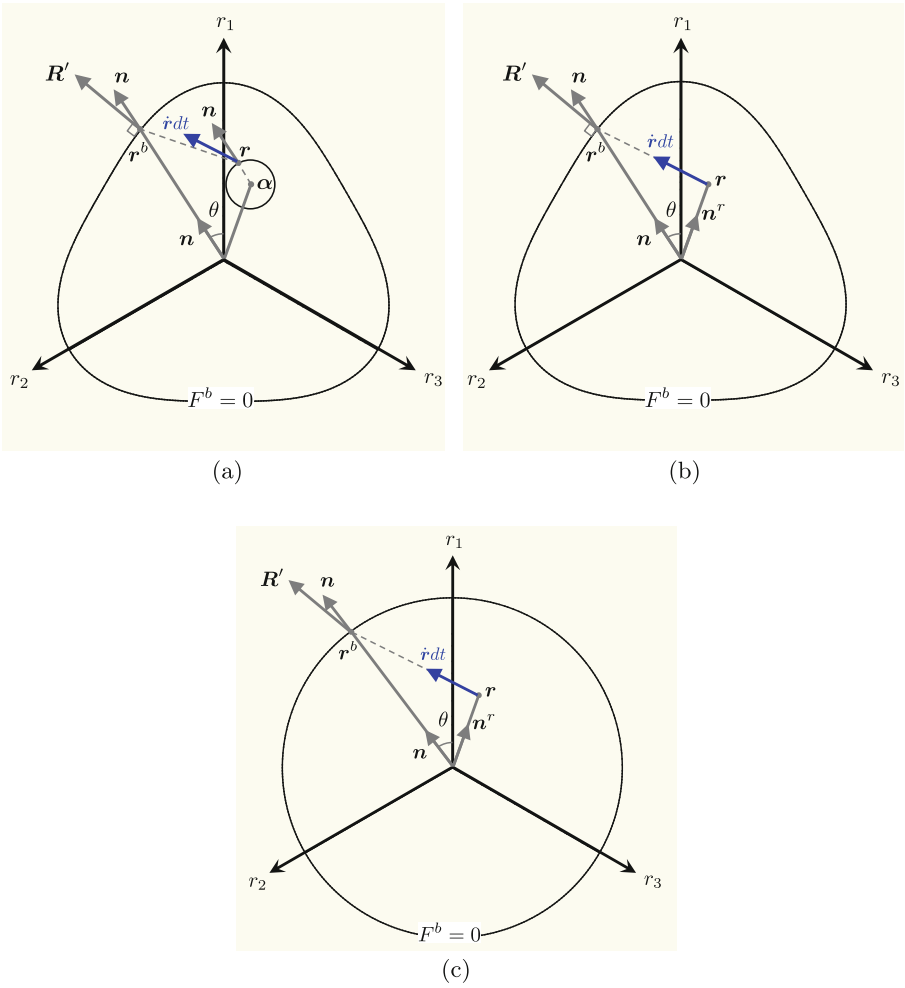

Fig. 1. Illustration of the concept of the SANISAND-Z model (a) small yield surface, bounding surface, mapping rule, loading direction $\boldsymbol{n}$ and deviatoric plastic strain rate direction $\boldsymbol{R}'$, (b) shrinking of the yield surface to the stress ratio point $\boldsymbol{r}$, and (c) elimination of the Lode angle effect on the bounding surface.

such model was proposed in [11] in a different setting) are named hypoplasticity models; the same word hypoplasticity is used for a different class of models (e.g. [15,16]) that do not involve classical plasticity loading-unloading criteria and additive decomposition of total strain rate into elastic and plastic parts. Incorporating the zero elastic range model within the framework of SANISAND models, introduces what has been called the SANISAND-Z model, Z standing for zero elastic range [10]. Its presentation and further elaboration is the objective of this paper.

Before closing this introduction it is instructive to delineate the present zero elastic range model from several other models that claim, erroneously, to be also of zero elastic range. Prominent among them are the stress-reversal surfaces models in [22,23]. This is illustrated in Fig. 2, where after reversal at $\boldsymbol{r}_{in}$ a new loading process begins and the current stress ratio point $\boldsymbol{r}$ is projected at $\boldsymbol{r}^b$ on the BS by a radius emanating from $\boldsymbol{r}_{in}$; at $\boldsymbol{r}^b$ the loading direction $\boldsymbol{n}$ is defined and transferred at $\boldsymbol{r}$. But this projection process creates an implied reversal/loading surface shown by dashed line which is homothetic to the BS with center of homothecy the $\boldsymbol{r}_{in}$ and on which the current $\boldsymbol{r}$ lies. If now the stress rate $\dot{\boldsymbol{r}}$ is in a tangent direction to the created reversal/loading surface, i.e. it is normal to $\boldsymbol{n}$ as shown in Fig. 2, purely elastic response is induced during such neutral loading path, allowing the stress ratio $\boldsymbol{r}$ to move around the loading surface without causing any plastic deformation, thus, violating the concept of zero elastic range. The second large family of erroneously called zero elastic range models is that of generalized plasticity, where a loading direction $\boldsymbol{n}$ and its opposite $\boldsymbol{n'} = -\boldsymbol{n}$ are defined in stress space and plastic loading is postulated for both $\boldsymbol{n} : \dot{\boldsymbol{r}} > 0$ and $\boldsymbol{n} : \dot{\boldsymbol{r}} = -\boldsymbol{n}' : \dot{\boldsymbol{r}} < 0$ with different plastic moduli in each case giving the impression of non existence of purely elastic range. However, again in this scheme a neutral loading path defined by $\boldsymbol{n} : \dot{\boldsymbol{r}} = 0$ causes only elastic deformation around an implied loading surface (the definition of $\boldsymbol{n}$ is tantamount to the definition of such surface), that negates again the zero elastic range character of generalized plasticity. Bottom line is that zero elastic range must be exactly what the name signifies, i.e., a null yield surface that collapses onto the stress point itself, within a scheme that guarantees realistic description of plastic strain rate norm and direction.

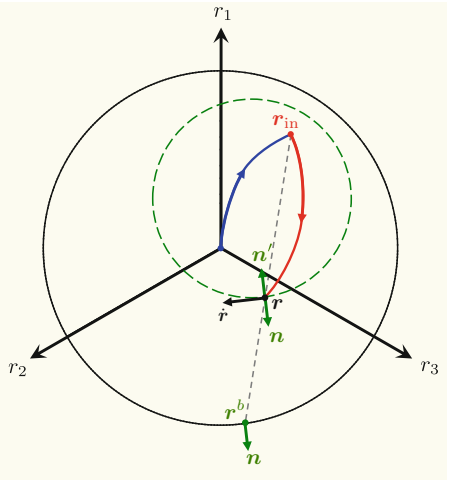

Fig. 2. Geometrical explanation why stress reversal surfaces and generalised plasticity models are not zero elastic range models.

2 The SANISAND-Z Constitutive Model

The sensitivity of sands to stress-ratio changes renders the stress-ratio space the appropriate one for the development of any sand constitutive model. Additional plastic deformation due to a change of stress under constant stress ratio, requires a modified formulation [26], which will not be considered in this work. The additive decomposition of total strain rate into an elastic and plastic part will be assumed, with the former given in terms of shear G and bulk K elastic moduli, and the latter occurring along a direction $\boldsymbol{R} = \boldsymbol{R}' + (1/3)D\boldsymbol{I}$ with $\boldsymbol{R}'$ the deviatoric part of $\boldsymbol{R}$, and D the dilatancy. A deviatoric unit norm loading direction $\boldsymbol{n}$ is defined at stress ratio space as discussed before in conjunction with Fig. 1, such that $\mathrm{tr}\boldsymbol{n} = 0$ and $\mathrm{tr}\boldsymbol{n}^2 = 1$.

According to standard plasticity formulation as shown in [21], and with the loading index (or plastic multiplier) L defined in terms of stress or total strain rates and the plastic modulus K_p, the strain rate - stress rate direct and inverse relations for a stress ratio dependent response are given as follows:

$$\dot{\boldsymbol{\varepsilon}} = \frac{1}{2G}\dot{\boldsymbol{s}} + \frac{1}{3K}\dot{p}\boldsymbol{I} + \langle L\rangle(\boldsymbol{R}' + \frac{1}{3}D\boldsymbol{I}) \tag{1}$$

$$\dot{\boldsymbol{\sigma}} = 2G\dot{\boldsymbol{e}} + K\dot{\varepsilon}_v\boldsymbol{I} - \langle L\rangle(2G\boldsymbol{R}' + KD\boldsymbol{I}) \tag{2}$$

$$\begin{aligned} L &= \frac{1}{K_p}\boldsymbol{n} : p\dot{\boldsymbol{r}} = \frac{1}{K_p}\boldsymbol{n} : (\dot{\boldsymbol{\sigma}} - \frac{\dot{p}}{p}\boldsymbol{\sigma}) = \frac{1}{K_p}\boldsymbol{n} : (\dot{\boldsymbol{s}} - \dot{p}\boldsymbol{r}) \\ &= \frac{2G\boldsymbol{n} : \dot{\boldsymbol{e}} - K(\boldsymbol{n} : \boldsymbol{r})\dot{\varepsilon}_v}{K_p + 2G\boldsymbol{n} : \boldsymbol{R}' - KD(\boldsymbol{n} : \boldsymbol{r})} \end{aligned} \tag{3}$$

where $\langle L\rangle = L$ if $L > 0$, and $\langle L\rangle = 0$ if $L \leq 0$, the latter signifying the event of unloading, $\boldsymbol{\varepsilon}$ denotes the strain tensor, $\boldsymbol{e}$ its deviatoric part and ε_v its volumetric with a superposed dot implying their rates. It is important to notice that for hardening response $K_p > 0$ while for softening and perfectly plastic response $K_p \leq 0$. In the latter case it follows that necessarily $\boldsymbol{n} : \dot{\boldsymbol{r}} \leq 0$ so that $L > 0$. Because for elastic unloading also $\boldsymbol{n} : \dot{\boldsymbol{r}} \leq 0$, the distinction between softening plastic loading and elastic unloading is made based on the sign of L calculated from the last expression of Eq. (3) in terms of the total strain rates.

In addition, since the model is developed within the framework of Critical State Soil Mechanics, the Critical Stress Ratio (CSR) in triaxial p–q space and Critical State Line (CSL) in void ratio e – pressure p space are given by the equations [20]

$$\frac{q}{p} = \eta = \eta_c = M; \qquad e = e_c = e_0 - \lambda(\frac{p}{p_{at}})^{\xi} \tag{4}$$

where the M assumes different values in compression and extension and becomes function of the Lode angle in multiaxial stress space, while e_0, λ and ξ are material constants. The forgoing formulation requires the specification of the hypoelastic moduli G and K, and the plastic constitutive ingredients $\boldsymbol{n}$, $\boldsymbol{R}'$, D, and K_p.

The Hypoelastic Moduli G and K

The G and K are given as functions of p and current void ratio e by the relations

$$G = G_0 p_{at} \frac{(2.97-e)^2}{1+e} \left(\frac{p}{p_{at}}\right)^{1/2}; \qquad K = \frac{2(1+\nu)}{3(1-2\nu)} G \tag{5}$$

where the expression for G is given in [25]. Here G_0 is a model parameter, ν is a constant Poisson's ratio, and p_{at} is the atmospheric pressure for normalization.

Definition of Bounding, Dilatancy and Critical State Surfaces

Excluding for simplicity the Lode angle dependence of M, the BS is shown schematically as a circle $F^b = 0$ in the stress ratio space of Fig. 3. Following [19,21], and denoting by $\boldsymbol{r}^b$ a stress ratio on the BS, its analytical expression is given by

$$F^b = (\boldsymbol{r}^b : \boldsymbol{r}^b)^{1/2} - \sqrt{\frac{2}{3}} M^b = 0; \qquad M^b = M \exp(-n^b \psi) \tag{6}$$

where the value of M is taken as the average between its triaxial compression and extension values, M_c and M_e, respectively, to compensate for the exclusion of Lode angle dependence, $\psi = e - e_c$ is the state parameter [1], n^b a positive model constant and $\sqrt{(2/3)} M^b$ is the variable with ψ radius of the BS.

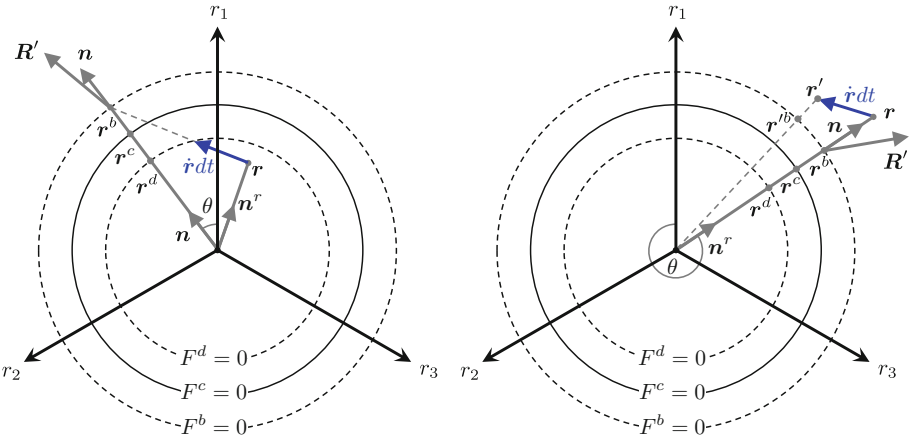

Fig. 3. Illustration of the working of the SANISAND-Z model in conjunction with bounding $F^b = 0$, dilatancy $F^d = 0$ and Critical State $F^c = 0$ surfaces, for (a) stress ratio point $\boldsymbol{r}$ inside the bounding surface, and (b) stress ratio point $\boldsymbol{r}$ outside the bounding surface.

With $\boldsymbol{r}^d$ denoting a stress ratio on the dilatancy surface (DS) $F^d = 0$ which is homocentric to the BS as shown in Fig. 3, its analytical expression is

$$F^d = (\boldsymbol{r}^d : \boldsymbol{r}^d)^{1/2} - \sqrt{\frac{2}{3}} M^d = 0; \qquad M^d = M \exp(n^d \psi) \tag{7}$$

with n^d a positive model constant. At critical state $\psi = 0$ and $M^b = M^d = M$, thus, BS and DS collapse to the Critical State surface (CS) $F^c = 0$, shown in Fig. 3 as a circle of radius $\sqrt{(2/3)}M$. The placement of BS and DS outside and inside CS surface, respectively, can be interchanged due to the value of ψ being negative (denser than critical samples) or positive (looser than critical samples) [21].

The Loading Direction $\boldsymbol{n}$

(i) Stress Ratio Inside or on the BS: Consider first the current stress ratio $\boldsymbol{r}$ inside or on the BS as shown in Fig. 3(a), which implies $(\boldsymbol{r} : \boldsymbol{r})^{1/2} \leq \sqrt{(2/3)}M^b$. For future reference a unit norm deviatoric tensor $\boldsymbol{n}^r = \boldsymbol{r}/|\boldsymbol{r}|$ is defined along $\boldsymbol{r}$. The stress ratio rate $\dot{\boldsymbol{r}} = |\dot{\boldsymbol{r}}|\,\boldsymbol{\nu}$ is defined in terms of its norm $|\dot{\boldsymbol{r}}|$ and its unit norm deviatoric direction $\boldsymbol{\nu}$ such that $\mathrm{tr}\boldsymbol{\nu} = 0$ and $\mathrm{tr}\boldsymbol{\nu}^2 = 1$. As already elaborated, the image stress ratio $\boldsymbol{r}^b$ on the BS is obtained as the intersection of $\dot{\boldsymbol{r}}$ direction with the BS. For a given $\dot{\boldsymbol{r}}$ in the case of a circular BS the $\boldsymbol{r}^b$can be analytically specified by:

$$\boldsymbol{r}^b = \boldsymbol{r} + b\boldsymbol{\nu}; \quad b = -\boldsymbol{r} : \boldsymbol{\nu} + \left[(\boldsymbol{r} : \boldsymbol{\nu})^2 + (2/3)(M^b)^2 - \boldsymbol{r} : \boldsymbol{r}\right]^{1/2} \tag{8}$$

where the foregoing expression for b is obtained by inserting $\boldsymbol{r}^b = \boldsymbol{r} + b\boldsymbol{\nu}$ in Eq. (6) and solving for b in terms of the (non negative) largest real root of the resulting quadratic equation. The loading direction $\boldsymbol{n}$ is defined normal to BS at $\boldsymbol{r}^b$, hence, based on Eq. (6) one has

$$\boldsymbol{n} = \frac{\partial F^b}{\partial \boldsymbol{r}^b} = \frac{\boldsymbol{r}^b}{|\boldsymbol{r}^b|} \tag{9}$$

where $\boldsymbol{n}$ is shown in Fig. 3(a) along the radius $\boldsymbol{r}^b$. The points $\boldsymbol{r}^d$ and $\boldsymbol{r}^c$ are defined as the intersections of $\boldsymbol{n}$ with the dilatancy and critical state surfaces $F^d = 0$ and $F^c = 0$, respectively, as shown in Fig. 3(a).

(ii) Stress Ratio Outside the BS: It is possible that the current stress ratio $\boldsymbol{r}$ finds itself outside the BS, shown in Fig. 3(b), as a result of diminishing radius of the latter due to its dependence on the state parameter ψ, Eq. $(6)_2$, that implies $(\boldsymbol{r} : \boldsymbol{r})^{1/2} \geq \sqrt{(2/3)}M^b$. In this case the plastic modulus becomes negative (see subsequent definition), hence, there are two possibilities: either continued plastic loading with softening response or elastic unloading. In both cases the stress ratio rate $\dot{\boldsymbol{r}}$ points "inwards" of $\boldsymbol{r}$ towards the BS and the distinction of which one of the aforementioned two cases occurs is based on the sign of L according to

Eq. (3). L requires the determination of the image stress ratio $\boldsymbol{r}^b$ to obtain the loading direction $\boldsymbol{n}$ normal to BS at $\boldsymbol{r}^b$. If the $\boldsymbol{r}^b$ is defined as before, i.e., as the intersection of $\dot{\boldsymbol{r}}$ with the BS, the direction of $\dot{\boldsymbol{r}}$ may not intersect the BS for $\boldsymbol{r}$ outside the BS, as implied in the illustration of Fig. 3(b). Thus, a re-definition of the mapping rule for $\boldsymbol{r}^b$ is necessary as the intersection with the BS of the radius connecting the origin to $\boldsymbol{r}$, Fig. 3(b), and $\boldsymbol{n} = \partial F^b/\partial \boldsymbol{r}^b$ as in Eq. (10). Such definition of $\boldsymbol{r}^b$ maintains the continuity of the mapping rule as the $\boldsymbol{r}$ crosses the BS, and becomes independent of $\dot{\boldsymbol{r}}$ when $\boldsymbol{r}$ is outside the BS. Now the process of loading/unloading is as follows. If $L > 0$ according to the last expression of Eq. (3) expressed in terms of the total strain rates, plastic loading with softening occurs; if $L < 0$, it signifies elastic unloading. In either case the direction of $\dot{\boldsymbol{r}}$ points inwards the current $\boldsymbol{r}$, which is updated to the position $\boldsymbol{r}' = \boldsymbol{r} + \dot{\boldsymbol{r}}dt$ as shown in Fig. 3(b). The $\dot{\boldsymbol{r}}dt$ is obtained from the calculation of the $\dot{\boldsymbol{\sigma}}$ from Eq. (2) for either case since $\langle L \rangle = L$ when $L > 0$, and $\langle L \rangle = 0$ when $L < 0$. At $\boldsymbol{r}'$ one has $\boldsymbol{r}'^b$ as shown in Fig. 3(b) and $\boldsymbol{n}' = \partial F^b/\partial \boldsymbol{r}^{b\prime}$. For this new $\boldsymbol{n}'$ the previous process is repeated. The $\boldsymbol{r}$ will reach eventually the BS from outside. Observe that while $\boldsymbol{r}$ is outside the BS no reverse plastic loading can occur according to the above scheme, but this is not expected to cause any problem because the excursion outside the BS is very small.

The Deviatoric Plastic Strain Rate Direction $\boldsymbol{R}'$

The specification of the plastic strain rate direction $\boldsymbol{R} = \boldsymbol{R}' + (1/3)D\boldsymbol{I}$ requires the definition of the deviatoric part $\boldsymbol{R}'$ and the dilatancy D. The total flow rule is non associative.

(i) Deviatoric Associative Flow Rule: If a deviatoric associative flow rule is postulated, then one can set

$$\boldsymbol{R}' = \boldsymbol{n} \tag{10}$$

It follows that $\boldsymbol{n} : \boldsymbol{R}' = \boldsymbol{n} : \boldsymbol{n} = 1$ in the last member of Eq. (3) for L.

(ii) Deviatoric Non-associative Flow Rule: Following [7] the relative inaccuracy of the deviatoric associative flow rule due to independence from the Lode angle θ in Fig. 3, can be corrected by a deviatoric non-associative flow rule obtained from a Lode angle dependent plastic potential surface $F^p = 0$ defined in stress ratio space by

$$F^p = (\boldsymbol{r}^p : \boldsymbol{r}^p)^{1/2} - \sqrt{\frac{2}{3}} M^p(\theta) = 0 \tag{11}$$

$$M^p(\theta) = g(\theta) M_c; \quad g(\theta) = \frac{2c}{(1+c) - (1-c)\cos 3\theta}; \quad c = \frac{M_e}{M_c} \tag{12}$$

where M_c and M_e are the critical stress ratios in triaxial compression and extension, respectively, $g(\theta)$ is the Lode angle-dependent interpolation function, and

$\boldsymbol{r}^p$ is a stress ratio on $F^p = 0$. The $F^p = 0$ is not shown in Fig. 3 for reasons of clarity, but it has the usual rounded triangular shape caused by the θ dependence as shown for the BS in Fig. 1(a) and (b). For any $\boldsymbol{r}^b$ defined according to the mapping rules of the previous subsection, there is a corresponding $\boldsymbol{n}$, and for this $\boldsymbol{n}$ there is a corresponding Lode angle θ defined by $\cos 3\theta = \sqrt{6}\mathrm{tr}\boldsymbol{n}^3$. The $\boldsymbol{R}'$ is defined as the gradient of $F^p = 0$ with respect to the stress, at a point $\boldsymbol{r}^p$ on $F^p = 0$ that is along $\boldsymbol{n}$, which is expressed in [7]:

$$\boldsymbol{R}' = B\boldsymbol{n} - C(\boldsymbol{n}^2 - \frac{1}{3}\boldsymbol{I}); \quad B = 1 + \frac{3}{2}\frac{1-c}{c}g(\theta)\cos 3\theta; \quad C = 3\sqrt{\frac{3}{2}}\frac{1-c}{c}g(\theta) \tag{13}$$

For $c = 1$ Eq. (13) yields as expected the associative deviatoric flow rule $\boldsymbol{R}' = \boldsymbol{n}$ because $F^p = 0$ becomes circular in π-plane. Based on Eq. (13) it follows again that $\boldsymbol{n} : \boldsymbol{R}' = B - C\mathrm{tr}\boldsymbol{n}^3 = 1$ in Eq. (3) for L, where the equality of the last two members of the above equation is based on the expression $\cos 3\theta = \sqrt{6}\mathrm{tr}\boldsymbol{n}^3$.

The Dilatancy D

Following the original suggestion in [21], the dilatancy will depend on the distance $\boldsymbol{r}^d - \boldsymbol{r}$ of the current stress ratio $\boldsymbol{r}$ from its image $\boldsymbol{r}^d$ on the DS, projected on the unit direction $\boldsymbol{n}$, Fig. 3, thus, the following expression holds accounting for $\boldsymbol{r}^d = \sqrt{2/3}M^d\boldsymbol{n}$ and $\boldsymbol{n}^r = \boldsymbol{r}/|\boldsymbol{r}|$:

$$D = A_d(\boldsymbol{r}^d - \boldsymbol{r}) : \boldsymbol{n} = A_d(\sqrt{\frac{2}{3}}M^d - |\boldsymbol{r}|\,\boldsymbol{n}^r : \boldsymbol{n}) \tag{14}$$

with A_d a model parameter and the reminder that M^d depends on the state parameter ψ according to Eq. (7). Equation (14) can yield a positive (contraction) or negative (dilation) value of D, depending on the relative placement of $\boldsymbol{r}^d$ and $\boldsymbol{r}$ in conjunction with $\boldsymbol{n}$. The A_d in the simplest case is constant, but it was found beneficial for the simulation of liquefaction to render it a function of a fabric dilatancy tensor $\boldsymbol{z}$ as $A_d = A_0(1 + \sqrt{(3/2)}\langle \boldsymbol{z} : \boldsymbol{n}\rangle)$, with A_0 a constant, where $\boldsymbol{z}$ evolves according to $\dot{\boldsymbol{z}} = -c_z\langle -\dot{\varepsilon}_v^p\rangle(\sqrt{(2/3)}z_{\max}\boldsymbol{n} + \boldsymbol{z})$. Notice that here the factors $\sqrt{(3/2)}$ and $\sqrt{(2/3)}$ were appropriately added to the original expressions of A_d and $\dot{\boldsymbol{z}}$, respectively, presented in [7], so that the values of the constants A_0, c_z and $z_{\max}$ calibrated from a simpler triaxial formulation and data, can be used directly as input in the multiaxial expressions above.

The Plastic Modulus K_p

Consistent with a BS formulation the value of the plastic modulus K_p will depend on the "distance" $\boldsymbol{r}^b - \boldsymbol{r}$ of the current stress ratio $\boldsymbol{r}$ from its image $\boldsymbol{r}^b$ on the BS, projected on the unit direction $\boldsymbol{n}$. An extension of the proposition made in [7] will be adopted where the back-stress ratio $\boldsymbol{\alpha}$ of their formulation is now

substituted by the stress ratio $\boldsymbol{r}$ (recall that for zero elastic range one obtains $\boldsymbol{r} = \boldsymbol{\alpha}$ as the yield surface shrinks to zero), which then reads:

$$K_p = \frac{2}{3} ph \frac{(\boldsymbol{r}^b - \boldsymbol{r}) : \boldsymbol{n}}{(\boldsymbol{r} - \boldsymbol{r}_{in}) : \boldsymbol{n}} \tag{15}$$

The $\boldsymbol{r}_{in}$ is the value of $\boldsymbol{r}$ at the initiation of a plastic loading event and h is a model parameter which is function of the void ratio e and pressure p according to $h = G_0 h_0 (1 - c_h e)(p/p_{at})^{-0.5}$, with h_0 and c_h model parameters. The factor $2/3$ was placed for maintaining the same value of h calibrated under triaxial conditions. The $\boldsymbol{r}_{in}$ must be updated to a new value at initiation of a new plastic loading event in order to obtain the infinite value of the plastic modulus resulting from Eq. (15) when $\boldsymbol{r} = \boldsymbol{r}_{in}$, expected in such event. Since one has always $L > 0$ when $\boldsymbol{r}$ is inside the BS, a new plastic loading event is defined as follows. When in Eq. (15) the $(\boldsymbol{r} - \boldsymbol{r}_{in}) : \boldsymbol{n} \leq 0$, it means that the current loading direction $\boldsymbol{n}$, defined in terms of $\dot{\boldsymbol{r}}$, forms an angle greater than 90° in the generalized stress ratio space with the tensor $\boldsymbol{r} - \boldsymbol{r}_{in}$, which is a measure of the overall direction of ongoing stress loading path that started at $\boldsymbol{r}_{in}$. But such drastic change of loading direction in regards to ongoing loading path is tantamount to unloading and the beginning of a new loading process. Hence the $\boldsymbol{r}_{in}$ is updated to the current $\boldsymbol{r}$ value when the denominator of Eq. (15) becomes negative, and a new loading process begins with an initially infinite value of the plastic modulus because the denominator becomes zero after the update. In other words the unloading event is followed immediately by a new loading event, without any purely elastic response taking place. The foregoing process is further illustrated in Fig. 4 where a loading process begins at the origin which serves as $\boldsymbol{r}_{in}$ at the start. At $\boldsymbol{r}$ the directions of $\dot{\boldsymbol{r}}dt$ that continue plastic loading and those that signify instantaneous unloading and a new plastic loading event, can

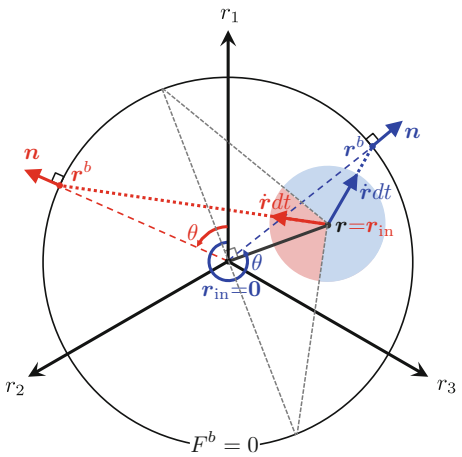

Fig. 4. Illustration of the loading and unloading/reloading domains for the direction of $\dot{\boldsymbol{r}}$ in deviatoric stress space, and the updating of $\boldsymbol{r}_{in}$.

be easily visualized and distinguished by the shaded sectors of the little circle drawn around $\boldsymbol{r}$ in such way that the forward continued loading is defined by all $\boldsymbol{n}$ for which $(\boldsymbol{r}-\boldsymbol{r}_{in}):\boldsymbol{n}=\boldsymbol{r}:\boldsymbol{n}>0$ while the new plastic loading event for all $\boldsymbol{n}$ for which $(\boldsymbol{r}-\boldsymbol{r}_{in}):\boldsymbol{n}=\boldsymbol{r}:\boldsymbol{n}\leq 0$. These two sectors are defined by connecting the point $\boldsymbol{r}$ with the two ends of the diameter of the $F^b=0$ which is perpendicular to $\boldsymbol{r}-\boldsymbol{r}_{in}=\boldsymbol{r}$, because at these two ends the corresponding $\boldsymbol{n}$ is normal to $\boldsymbol{r}-\boldsymbol{r}_{in}=\boldsymbol{r}$ and $\boldsymbol{r}:\boldsymbol{n}=0$. Upon unloading/initiation of new loading, the previous $\boldsymbol{r}_{in}$ at the origin, is updated to the current $\boldsymbol{r}$. Finally, when $\boldsymbol{r}$ moves outside the BS and $\boldsymbol{r}^b$ is defined along $\boldsymbol{r}$ on the BS, Fig. 3(b), the quantity $(\boldsymbol{r}^b-\boldsymbol{r}):\boldsymbol{n}<0$ in Eq. (15), which implies a $K_p<0$, signifying a softening material response as long as $L>0$ according to Eq. (3).

The updating of $\boldsymbol{r}_{in}$ in Eq. (15), necessary to obtain a smooth elasto-plastic transition by rendering $K_p=\infty$ at initiation of a loading event, creates also the so-called overshooting response upon reverse loading/immediate reloading associated with its updating, known since the time of its inception [3]. Overshooting implies a stress-strain curve which unrealistically overshoots the continuation of a previous curve had the event of reverse loading/reloading not taken place. In order to remedy overshooting, [6] outlined a way of updating $\boldsymbol{r}_{in}$, which is implemented in the current model and has been presented in detail in [10]. In this reference one can also find the triaxial counterpart formulation of SANISAND-Z, that will not be presented here. It suffices for illustration purposes to show Fig. 5, which is the counterpart of Fig. 3(a) in triaxial space, where the stress ratio $\boldsymbol{r}$ is now the line $\eta=q/p$ and the bounding, dilatancy and critical state surfaces are represented by the straight lines with slopes M_c^b, M_c^d, M_c^c, in compression and M_e^b, M_e^d, M_e^c, in extension, while loading occurs for any rate of η in the compression or extension directions.

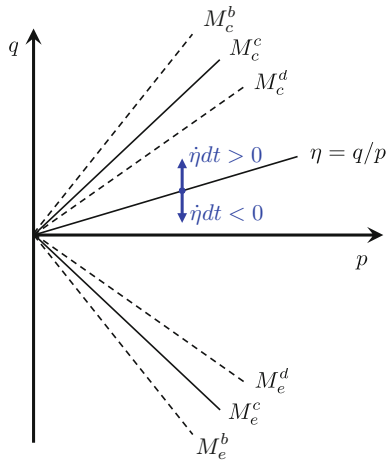

Fig. 5. Illustration of the SANISAND-Z model in triaxial stress space where the deviatoric stress ratio point of Fig. 3 becomes the line $\eta=q/p$, and the bounding, dilatancy and critical state surfaces become the lines M^b, M^d and M^c with subscripts c and e for compression and extension, respectively.

3 Model Performance

Detailed calibration process for the SANISAND models are presented in [27]; their calibrated parameters for Toyoura sand are used in the present study, and shown in Table 1. Simulation results are based on both the SANISAND-Z model with true zero elastic range and the [7] version of SANISAND with a tiny yield surface cone. The trace of the cone on the stress-ratio $\boldsymbol{r}$ plane is a circular deviatoric yield surface with center $\boldsymbol{\alpha}$ and radius $(2/3)\,\mathrm{m}$. A small value of $m = 0.01$ is used for the simulations with [7] model. The SANISAND-Z model uses a constant critical stress ratio M which is set equal to the compression value M_c here, in order to properly capture the main part of the loading which is in triaxial compression in these simulations. The [7] model uses a Lode angle dependent critical stress ratio with M varying between M_c in triaxial compression and $M_e = cM_c$ in triaxial extension, although no extension is relevant to these data.

Performance of the SANISAND-Z model in simulation of selected drained and undrained triaxial loading and unloading paths, in comparison with the data of Toyoura sand from [28], is already reported in [10] and similar to previous models examined in [7,26,27]. In this presentation the response under some more complicated stress paths will be examined. Figures 6, 7, 8, 9 and 10 presented in the following, are in fact variations of corresponding figures in [10].

Figure 6 compares the experimental data [24] and model simulations for drained constant-p cyclic triaxial tests on isotropically consolidated loose samples of Toyoura sand. In this test the amplitude of shear strain $(\varepsilon_a - \varepsilon_r)$ has been increased in different cycles of loading. The simulation with the SANISAND-Z model is done with a constant critical stress ratio M which is set equal to $M_c(1 + c)/2$, in order to properly capture the average response in compression and extension. The simulation results are presented with solid lines in Figs. 6(d–f). The simulations with the [7] model are done in two different ways for the critical stress ratio with: (i) a constant $M = M_c(1 + c)/2$ (for direct comparison with the results from the SANISAND-Z model), and (ii) a Lode angle dependent M. The simulations results for these two choices of M with

Table 1. SANISAND-Z model parameters for Toyoura sand[a]

Model constant	Symbol	Value	Model constant	Symbol	Value
Elasticity	G_0	125	Plastic modulus	h_0	15
	ν	0.05		c_h	0.987
Critical state	M_c	1.25		n^b	1.25
	c	0.712	Dilatancy	A_0	0.704
	e_0	0.934		n^d	2.1
	λ	0.019	Fabric-dilatancy	$z_{\max}$	4
	ξ	0.7		c_z	600

[a]Additional overshooting correction parameters: $\bar{e}^p_{eq} = 0.01\%$ and $n = 1$ (default)

the [7] model are presented with dashed and dot-dashed lines, respectively, in Figs. 6(d–i). The models show almost same results as each other, and very close to those observed in the experiments. Of course the simulations results with [7] and $M(\theta)$ are slightly closer to those observed in the experiments. Accumulation of compressive volumetric strain with cyclic loading can be observed in Fig. 6, and clearly when the stress ratio exceeds a certain value, which varies by the state, the specimen begins to dilate. Additional comparison for cyclic loading of a dense sample of Toyoura sand are presented in [10] showing again very similar trend.

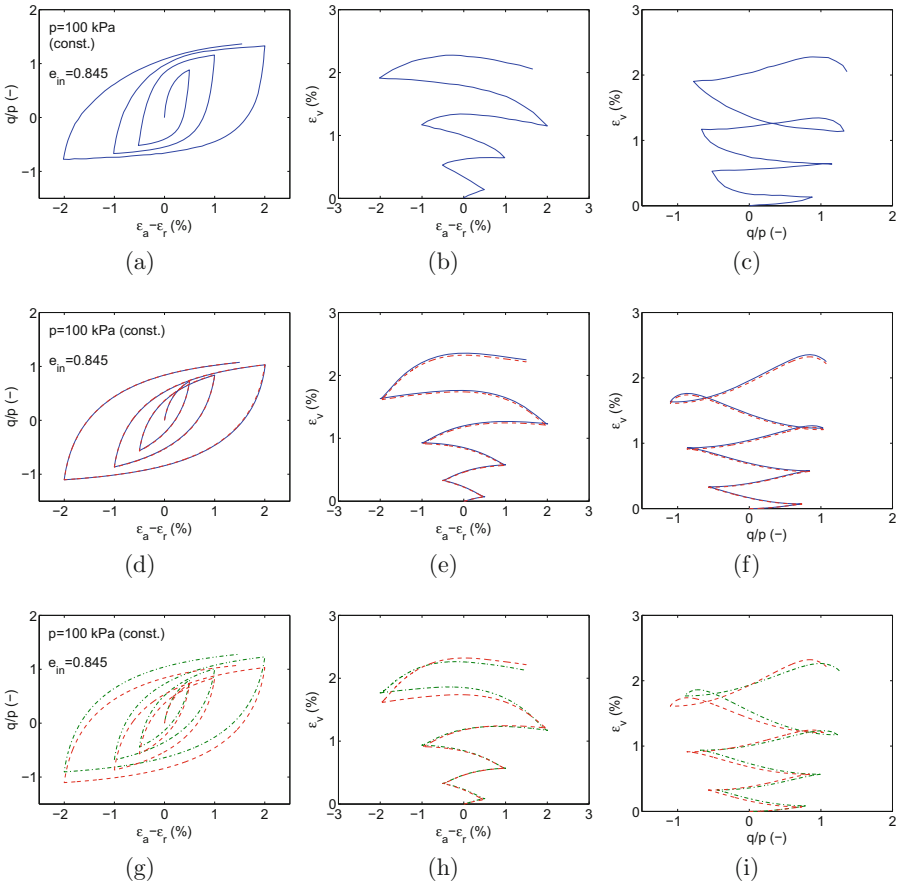

Fig. 6. Simulations vs. experiments in constant-p cyclic drained triaxial tests on isotropically consolidated relatively loose samples of Toyoura sand: experimental data (a–c) are after [24]; simulations (d–f and g–i) are using SANISAND-Z model with $M = M_c(1+c)/2$ (solid lines), [7] model with $M = M_c(1+c)/2$ (dashed lines), and [7] model with $M = M(\theta)$ (dot-dashed lines).

Simulation results under a particular rotational shear path comprising a circular stress path in the π-plane are presented in Figs. 7 and 8. The simulation results exhibit in a very illustrative way the performance of SANISAND-Z for such an unorthodox stress path. While the triaxial simulations can use the much simpler formulation of the triaxial space, the rotational shear requires the full general stress space formulation and numerical implementation, the latter being a problem to reckon with due to the incrementally non-linear feature of the equations. These simulations are intended to be compared with data from Fuji river sand for which no data for calibration were available. However, given the similarity of this sand with Toyoura sand, the model constants of the latter from Table 1 were used, instead. Figure 7 presents details of the simulation results for the following loading scenario: An isotropically consolidated sample with $p_{in} = \sigma_c = 98\,\text{kPa}$ and $e_{in} = 0.822$ is subjected to undrained triaxial compression by increasing the σ_z until reaching $\tau_{oct} = 12.5\,\text{kPa}$, where $\tau_{oct} = (1/3)\left[(\sigma_x - \sigma_y)^2 + (\sigma_x - \sigma_z)^2 + (\sigma_y - \sigma_z)^2\right]^{1/2}$; then keeping the τ_{oct} constant, the sample is subjected to a cyclically varying circular stress path in the π-plane under undrained condition. Three sets of simulation results are presented in Fig. 7 showing performance of SANISAND-Z model with $M = M_c(1 + c)/2$ (dashed lines), [7] model with $M = M_c(1+c)/2$ (dashed lines), and [7] model with $M = M(\theta)$ (dot-dashed lines). The increasing amplitude helicoidal stress path in the stress ratio π-plane plot of Fig. 7(a) is due to the decrease of p, because of pore water pressure increase as shown in Fig. 7(b), hence, the increase of the ratio of stress/p.

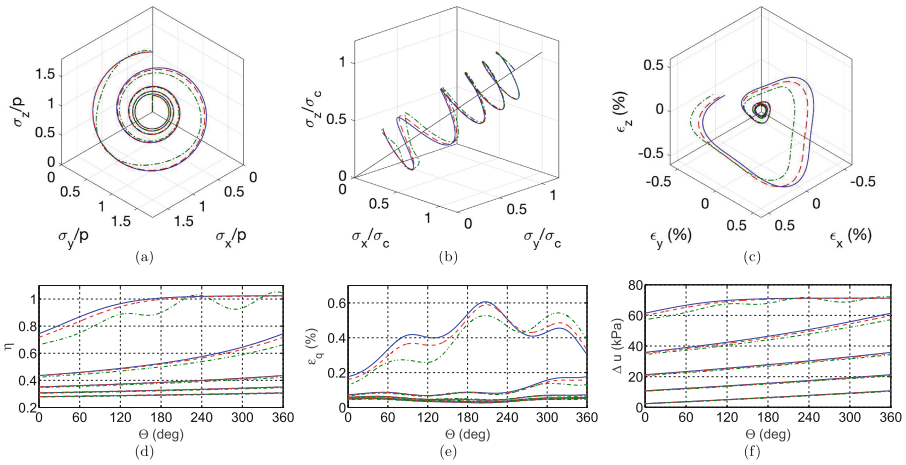

Fig. 7. Extended simulation results for undrained circular cyclic loading with $\tau_{oct} = 12.5\,\text{kPa}$ on Fuji river sand for 5 cycles using model constants for Toyoura sand from Table 1: SANISAND-Z model with $M = M_c(1 + c)/2$ (solid lines), [7] model with $M = M_c(1 + c)/2$ (dashed lines), and [7] model with $M = M(\theta)$ (dot-dashed lines).

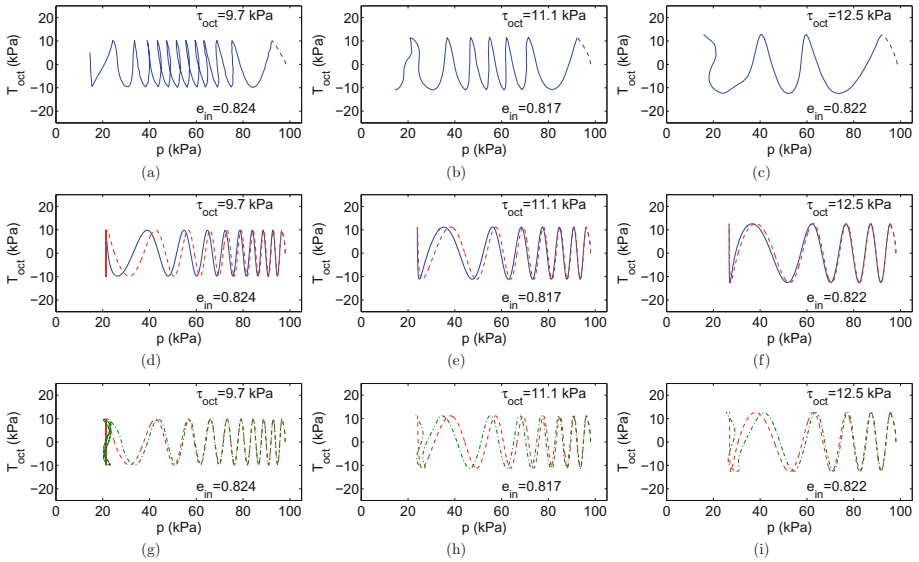

Fig. 8. Simulations vs. experiments in undrained circular cyclic tests on Fuji river sand using model constants for Toyoura sand from Table 1: experimental data (a–c) are after [30]; simulations (d–f and g–i) are using SANISAND-Z model with $M = M_c(1 + c)/2$ (solid lines), [7] model with $M = M_c(1 + c)/2$ (dashed lines), and [7] model with $M = M(\theta)$ (dot-dashed lines).

Figure 8 compares the effective stress path for undrained circular stress loading path between the simulations and the corresponding experimental results in [30] who explored three levels of $\tau_{oct} = 9.7$, 11.1, and 12.5 kPa. In this figure $T_{oct} = \tau_{oct} \cos\Theta$, where Θ determines the angle of rotation of shear stress on the octahedral plane, shown in the original paper of [30]. Very similar general trend of response is observed between the simulation results and the experimental data. It is interesting to compare the plot of Fig. 7(b) with those of Figs. 8(f, i) for $\tau_{oct} = 12.5$ kPa; the former is in fact a three dimensional perspective of the latter two. This is a good indicative of the overall performance of the SANISAND-Z model in such complex loading condition. A more specific calibration of the model parameters for Fuji river sand would likely provide better match between the simulations and experimental results.

Because a stress ratio based model will not induce plastic deformation under constant stress ratio loading, the question arises on how the present model will respond to an oedometric test. Such test imposes a constant total volumetric to total deviatoric strain ratio that in triaxial space is equal to 3/2, which can become soon a constant stress ratio (fixed K_0); before constant stress ratio is reached, plastic deformation is induced by the model. In Fig. 9(a) the response of the model under such oedometric test in loading and unloading is shown in p, q stress space for two initial void ratio values, one for dense ($e_{in} = 0.65$) and the other for loose ($e_{in} = 0.95$) sample, starting at an initial $p = 10$ kPa, using the

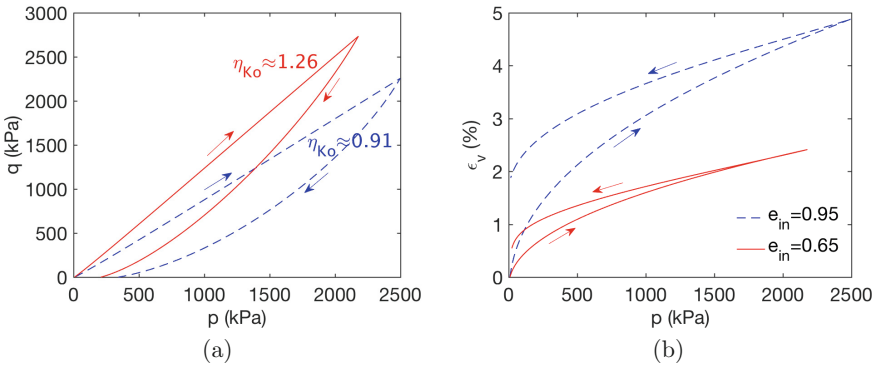

Fig. 9. Numerical simulation results for K_0 compression loading and un-loading on isotropically consolidated (p_{in}=10 kPa) very loose ($e_{in} = 0.95$ in dashed lines) and very dense ($e_{in} = 0.65$ in solid lines) samples using constants of Table 1.

constants of Table 1. The stress path attains a very close to constant value of the stress ratio $q/p = \eta = \eta_{K_0} \approx 1.26$ for the dense and $q/p = \eta = \eta_{K_0} \approx 0.91$ for the loose sample, which based on the relation $K_0 = (3 - \eta_{K_0})/(2\eta_{K_0} + 3)$ yields the values $K_0 = 0.32$ and $K_0 = 0.43$ for dense and loose samples, respectively. Simultaneously Fig. 9(b) shows a volumetric strain ε_v in the order of 2% and 3% at the end of loading, and remaining strain of 0.5% and 2% at the end of unloading, for dense and loose samples, respectively; clearly plastic volumetric deformation takes place also during the unloading phase. The foregoing K_0 and volumetric strain values are realistic, in particular accounting for the fact the model was not calibrated to obtain the K_0 value and strains under oedometric loading and unloading.

The model can simulate general and unusual loading paths such as rotational shear and shows similar simulation capabilities as its dual model with a very small yield surface in [7]. The dependence of the loading direction $\boldsymbol{n}$ and in particular the plastic strain rate direction $\boldsymbol{R}'$ on the stress rate direction $\boldsymbol{\nu}$, although supported qualitatively by experiments and DEM simulations, needs a more thorough investigation to compare the theoretical suggestions to experimental (real or virtual) evidence in a quantitative way. For example the following two response characteristics can be proposed for verification and calibration by DEM in the future, which are particularly suited for a model with zero elastic range. The first is related to the suggestion in [13,17] to plot stress increments around a stress point corresponding to strain probes of same norm in various directions; the tips of the stress increments constitute what we can call the Gudehus' response envelope. Here a conjugate Gudehus' response envelope will be used, where a material sample is loaded till a point in stress space, and then very small stress increments of equal norm are applied in all directions, and the corresponding strain increments are plotted radially around an origin in strain space; the locus of their tips constitutes the aforementioned envelope. In fact this

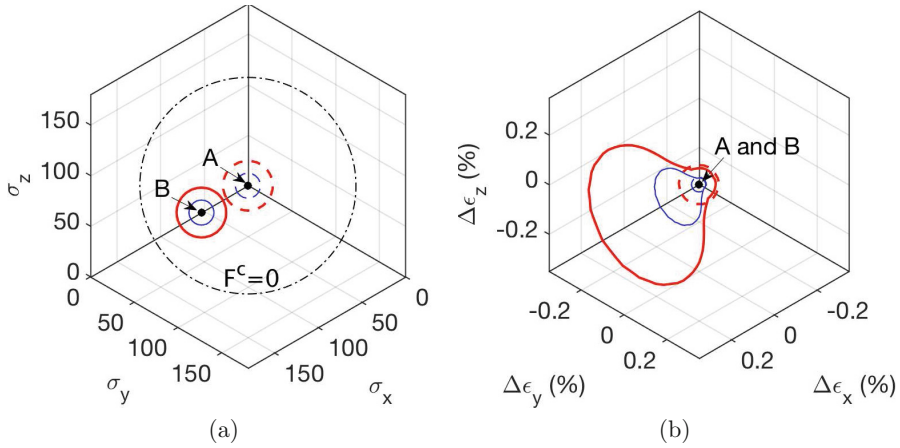

Fig. 10. Numerical simulation results for conjugate Gudehus' response envelopes. The initial state of the sample is $e_{in} = 0.88$, $p = 100\,\text{kPa}$ (point A), then sheared with constant p to $\tau_{oct} = 25\,\text{kPa}$ (point B). At points A and B the sample is subjected to constant norm stress increments of 10 kPa (thin lines) and 20 kPa (thick lines), dashed for point A and solid for point B.

type of response envelope in strain space was first proposed in [18], a fact omitted to be mentioned by mistake in [10], but the option to call it a conjugate Gudehus' response envelope stems from the focus given in [13] to such constitutive modeling features. This is a particularly appropriate test to perform by DEM to check the incremental non-linearity associated with the dependence of the strain increment direction on the stress increment direction. To illustrate this process such a test was performed in drained conditions by the SANISAND-Z model and the results shown on the deviatoric planes for stress and strain increments in Fig. 10(a) and (b), respectively. In Fig. 10(a) the material with initial void ratio $e_{in} = 0.88$ is loaded hydrostatically by $p = 100\,\text{kPa}$, point A, and then sheared at constant p to $\tau_{oct} = 25\,\text{kPa}$, point B. At each position A and B, the sample is probed by stress increments of constant norms 10 kPa and 20 kPa consecutively in various directions, the tips of which are plotted as smaller and larger circular envelopes, respectively, in Fig. 10(a). For each stress probing process the tips of the corresponding strain increments are plotted around the origin of the deviatoric plane for strain increments as shown in Fig. 10(b) for both points A and B, and the resulting shapes are the aforementioned conjugate Gudehus envelopes. The envelopes for the smaller stress probes are included in the envelopes for the larger stress probes at both points, but while at point A on the hydrostatic axis such envelope remains almost circular (there is only Lode angle dependence of the response), at point B the distortion of the envelopes are clearly intense, as a result of the zero elastic range and the plastic modulus dependence on the stress rate direction via the distance from the BS. The second response characteristic which is particular to the zero elastic range feature of the model, is shown by the

plots for a circular rotational shear path in Figs. 7 and 8; these can be repeated by DEM (a 3D DEM code is required) and comparisons made.

4 Conclusion

The SANISAND-Z model is an elastic-plastic constitutive model for sands, which is obtained from a kinematic hardening model when the yield surface size vanishes and the surface shrinks to its back-stress center becoming identical to the stress point itself in the deviatoric stress ratio space. The finite bounding surface is used to define the loading and deviatoric plastic strain rate directions, both of which depend now on the direction of the deviatoric stress ratio rate. Consequently the model is incrementally non linear and falls into the category of hypo-plasticity models in the sense of the term first introduced in [5], and defined in detail in [6].

The non-existing yield surface eliminates the need to satisfy the consistency condition by requiring the stress to remain on the yield surface, but the stability and avoidance of drift of an explicit numerical implementation becomes more difficult to achieve and requires special methodologies. On the other hand the plastic deformation that takes place always for any loading direction (except for elastic unloading at softening regimes for the current formulation when the stress point is outside the bounding surface), renders the model suitable to address bifurcation and localization problems where elastic loading "to the side" is too stiff to accommodate the initiation of a bifurcation process in classical plasticity with neutral loading features, which do not exist in the present model.

Otherwise the simulations of SANISAND-Z are similar in nature to those obtained by its predecessors SANISAND models with small but finite yield surfaces. It is believed that the present model will be very promising in simulations of special loading paths such as multidirectional shear and rotation of principal stress directions, that recently became of importance in various areas, of geotechnical engineering.

Acknowledgment. The research leading to these results has received funding from the European Research Council under the European Union's Seventh Framework Program FP7-ERC-IDEAS Advanced Grant Agreement no. 290963 (SOMEF), and partial support from the Natural Sciences and Engineering Research Council of Canada (NSERC).

References

1. Been, K., Jefferies, M.G.: A state parameter for sands. Géotechnique **35**(2), 99–112 (1985)
2. Cubrinovski, M., Ishihara, K.: State concept and modified elastoplasticity for sand modelling. Soils Found. **38**(4), 213–225 (1998)
3. Dafalias, Y.F.: On cyclic and anisotropic plasticity. Ph.D. thesis, Department of Civil Engineering, University of California, Berkeley, CA, USA (1975)

4. Dafalias, Y.F.: A model for soil behavior under monotonic and cyclic loading conditions. In: Transactions, 5th International Conference on SMiRT, West Berlin, Germany, vol. K, p. K 1/8, August 1979
5. Dafalias, Y.F.: The concept and application of the bounding surface in plasticity theory. In: Hult, J., Lemaitre, J. (eds.) Physical Non-Linearities in Structural Analysis. Springer, Heidelberg (1981)
6. Dafalias, Y.F.: Bounding surface plasticity. I: mathematical foundations and hypoplasticity. J. Eng. Mech. **112**(9), 966–987 (1986)
7. Dafalias, Y.F., Manzari, M.T.: Simple plasticity sand model accounting for fabric change effects. ASCE J. Eng. Mech. **130**(6), 622–634 (2004)
8. Dafalias, Y.F., Popov, E.P.: A simple constitutive law for artificial graphite-like materials. In: 3rd International Conference on Structural Mechanics in Reactor Technology, Transactions, vol. 1, p. C 1/5, London, U.K, September 1975
9. Dafalias, Y.F., Popov, E.P.: Cyclic loading for materials with a vanishing elastic region. Nucl. Eng. Des. **41**(2), 293–302 (1977)
10. Dafalias, Y.F., Taiebat, M.: SANISAND-Z: zero elastic range sand plasticity model. Geotechnique **66**(12), 999–1013 (2016)
11. Darve, F.: Contribution a la Determination de la Loi Rhéologique incrementale des Sols. Ph.D. thesis, Universite de Grenoble, Grenoble, France (1974)
12. Das, S.: Three dimensional formulation for the stress-strain-dilatancy elasto-plastic constitutive model for sand under cyclic behavior. Master's thesis, Department of Civil and National Resource Engineering, University of Canterbury, Christchurch, New Zealand (2014)
13. Gudehus, G.: A comparison of some constitutive laws for soils under radially symmetric loading and unloading. In: Third International Conference on Numerical Methods in Geomechanics, pp. 1309–1323, Aachen, April 2–6 (1979)
14. Gutierrez, M., Ishihara, K., Towhata, I.: Flow theory for sand during rotation of principal stress direction. Soils Found. **31**(4), 121–132 (1991)
15. Herle, I., Kolymbas, D.: Hypoplasticity for soils with low friction angles. Comput. Geotech. **31**, 365–373 (2004)
16. Kolymbas, D.: An outline of hypoplasticity. Arch. Appl. Mech. **61**(3), 143–151 (1991)
17. Kolymbas, D.: Response-envelopes: a useful tool aus hypoplasticity then and now. In: Constitutive Modelling of Granular Materials. pp. 57–105. Springer, Heidelberg (2000)
18. Lewin, P.I., Burland, J.B.: Stress-probe experiments on saturated normally consolidated clay. Géotechnique **20**(1), 38–56 (1970)
19. Li, X.S., Dafalias, Y.F.: Dilatancy for cohesionless soils. Géotechnique **54**(4), 449–460 (2000)
20. Li, X.S., Wang, Y.: Linear representation of steady-state line for sand. J. Geotech. Geoenvironmental Eng. **124**(12), 1215–1217 (1998)
21. Manzari, M.T., Dafalias, Y.F.: A critical state two-surface plasticity model for sands. Géotechnique **47**(2), 255–272 (1997)
22. Mroz, Z., Morris, V.A., Zienkiewicz, O.C.: Application of an anisotropic hardening model in the analysis of elastoplastic deformation of soils. Geotechnique **29**, 1–34 (1979)
23. Mroz, Z., Zienkiewicz, O.C.: Uniform formulation of constitutive equations for clays and sands. In: Mechanics of Engineering Materials, pp. 415–449. Wiley, Chichester (1984)
24. Pradhan, T.B.S., Tatsuoka, F., Sato, Y.: Experimental stress-dilatancy relations of sand subjected to cyclic loading. Soils Found. **29**(1), 45–64 (1989)

25. Richart, F.E., Hall, J.R., Woods, R.D.: Vibrations of soils and foundations. International Series in Theoretical and Applied Mechanics. Prentice-Hall, Englewood Cliffs (1970)
26. Taiebat, M., Dafalias, Y.F.: SANISAND: simple anisotropic sand plasticity model. Int. J. Numer. Anal. Meth. Geomech. **32**(8), 915–948 (2008)
27. Taiebat, M., Jeremić, B., Dafalias, Y.F., Kaynia, A.M., Cheng, Z.: Propagation of seismic waves through liquefied soils. Soil Dynam. Earthq. Eng. **30**(4), 236–257 (2010)
28. Verdugo, R., Ishihara, K.: The steady state of sandy soils. Soils Found. **36**(2), 81–91 (1996)
29. Wang, Z.L., Dafalias, Y.F., Shen, C.K.: Bounding surface hypoplasticity model for sand. J. Eng. Mech. **116**(5), 983–1001 (1990)
30. Yamada, Y., Ishihara, K.: Undrained deformation characteristics of sand in multidirectional shear. Soils Found. **23**(1), 61–79 (1983)

Cyclic Response of Natural Onsøy Clay
Part I: Experimental Analysis

Nina Müthing(✉), Thomas Barciaga, and Tom Schanz

Department of Civil and Environmental Engineering,
Ruhr-Universität Bochum, Universitätsstr. 150, 44780 Bochum, Germany
nina.muething@rub.de

Abstract. In geotechnical applications cyclic loading occurs frequently caused by earthquake shaking, traffic or wind and wave loading. The consideration of cyclic loading effects finds increasing attention nowadays. This particularly holds true for structures, which are of civil importance and involve high investment costs. Sophisticated calculation approaches are applied within the design process of these boundary value problems. However, many of the calculation models assume undrained stress paths, where cyclic loading leads to a continuous generation of excess pore water pressure. When soft, marine clays under slower loading are involved, the dissipation of excess pore water pressure becomes relevant. The transient consolidation process needs to be considered. Thus, in the present paper the consolidation behaviour of Norwegian Onsøy clay as a typical representative of natural, marine clay under cyclic loading is analysed. Part I of this paper presents the experimental study. Testing results from monotonic and cyclic oedometer tests on natural as well as remoulded clay are introduced. The differences in the compression behaviour and pore water pressure dissipation of structured and remoulded clay are illuminated. Furthermore, the effect of cyclic loading characteristics, as e.g. the load amplitude, on consolidation is analysed. Part II of the paper comprises a numerical study. Modelling the cyclic consolidation processes by use of FEM, the focus of the analysis is set on the necessity of different features of a hierarchical model to analyse this type of boundary value problems.

1 Motivation: Natural Clay Behaviour Under Oedometric, Cyclic Loading Conditions

In many geotechnical applications cyclic loading of structures plays an important role and needs to be considered within the design process. Cyclic loading may for example be caused by traffic loads or earthquake shaking. Of cause, it is also of particular importance in the framework of foundation design for offshore installations, as e.g. pipeline or pile foundations, wind turbines and gravity platforms [24]. When dealing with soft soils under slower loading, the dissipation of excess pore water pressure needs to be considered and the transient consolidation of the soil comes into picture.

T. Triantafyllidis (ed.), *Holistic Simulation of Geotechnical Installation Processes*,
Lecture Notes in Applied and Computational Mechanics 82, DOI 10.1007/978-3-319-52590-7_11

Consolidation processes under cyclic loading have been dealt with in a multitude of studies in literature. Analytical solutions considering consolidation under cyclic loading conditions are e.g. available in [18,20,21]. Admittedly, most of these solutions are based on Terzaghi's classical theory assuming geometrical and constitutive linearity. Due to this linearisation only idealized boundary value problems can be analysed. In [16,17,19] an experimental study dealing with cyclic consolidation processes of soft Kaolin clay is introduced. Within this study the excess pore water pressure build-up and dissipation occurring during consolidation is analysed.

Based on this study, the present paper deals with the consolidation of natural, structured clay under cyclic loading. As representative material in the present paper natural, marine Onsøy clay from Norway is considered. Hereby, the focus is set on the behaviour of structured clay loaded to a stress level below and above its yield stress as well as on the difference in consolidation of the natural and identical, but remoulded clay.

Structure of soil includes fabric and bonding. While fabric is the arrangement of soil particles, bonding characterises the connections of the soil skeleton, which are not of frictional kind. When structured clay is subjected to an increasing stress, initially the bonding will procure a relatively stiff behaviour of the soil matrix. Only when the yield stress, the maximum bearable stress, is exceeded the bonding is destroyed and the soil experiences a so-called destructuration. This destructuration is reflected in the stress-strain behaviour by a sudden drop of soil stiffness thus a significant compression caused by a rearrangement of the soil particles [2–4]. Beyond that, the destructuration of natural clay may also be caused by a mechanical destruction of the bonding induced by simple remoulding of the natural clay. From the example of *quick clay* the effect is well known, that sensitive, marine clays subjected to remoulding show a dramatic change in their material behaviour. This effect can be observed in the oedometric compression behaviour of structured clays as due to the mechanical distortion of the structure the remoulded clay shows the same compression behaviour in terms of stiffness in low and high stress ranges [22].

The present paper is subdivided into two parts: Part I presents the experimental study and testing results, while Part II deals with the numerical modelling of the boundary-value problem.

The experimental study, presented in this Part I of the paper, is opened by a characterisation of the tested soil, Onsøy clay. To analyse the compression behaviour of natural and remoulded clay under monotonic loading, stepwise oedometer tests are conducted. To meet the special requirements of the testing, a particular oedometer cell designed and constructed at Ruhr-Universität Bochum is used. This oedometer cell introduced in [16] allows the testing of slurries due to a cell sealing system and enables the measurement of pore water pressure, water in- and outflow, radial stress as well as frictional loss. Regarding the analysis of the settlements differences between natural and remoulded clay are illuminated. The analysis of the compression behaviour of the natural samples additionally allows for determination of the material's yield stress. The knowledge of yield

stress is required for the following cyclic consolidation analysis, as within this study natural and remoulded samples are subjected to cyclic loading with various loading amplitudes below and above yield stress. Thereby, the influence of load amplitude on the cyclic consolidation of structured clay is analysed.

Part II of the paper deals with the numerical modelling. As an important role falls upon the constitutive behaviour of cyclically loaded soils, the necessity of different features of a hierarchical model to analyse this type of boundary value problems is studied.

2 Material Characteristics of Onsøy Clay

The present study was performed using marine, natural Onsøy clay from a site close to Fredrikstad, which is located approximately 100 km south-east of Oslo, Norway. The deposit was formed during glaciation and early post glaciation (Holocene). During the isostatic uplift, caused by the following de-glaciation, the depositional environment changed from marine to estuarine [14]. The material properties of this clay have been characterized in detail by [13,14] as well as other studies at *Norwegian Institute of Technology (NGI)*. The main characteristics are described in the following. A more detailed characterisation can be found in [14,15].

The block sample used for the present study was taken in approx. 10 m depth. For the sampling a Sherbrooke sampler was used in order to prevent disturbance of the sensitive clay material. Details on this sampling procedure can be found in [5,12].

The natural water content of the tested clay was determined to be approximately $w_{nat} = 65\%$ with a mean void ratio of approximately $e_{nat} = 1.77$, as the specific gravity ρ_s was determined according to [1] by pycnometer method to be $\rho_s = 2.77\text{g/cm}^3$. These values coincide with the range for the natural water content given by [14] for samples from similar depths. The pH value was determined by pH probe to be $pH = 7.3$. With reference to tests in [24] on the same material from a different sampling depth, the salt concentration was assumed to be 32.5 g/l, which is in accordance with [14] suggesting an average value of 30 g/l for material from depths larger than 7 m. Table 1 summarises the most important parameters describing the natural state of the sample block used within the present study.

Table 1 additionally gives the plasticity index and Atterberg limits for the tested clay, determined according to [6–8]. With reference to the plasticity diagram after Arthur Casagrande Onsøy clay tested in the present study lies slightly above the A-line and therefore can be characterised as a pronounced plastic clay. The activity I_A can be calculated to $I_A = 1.9$[-].

The grain size distribution was analysed using two different techniques: sedimentation technique according to [9] and laser diffraction method. Figure 1 shows the determined grain size distribution curves. Hereby, Onsøy clay can be characterised as a dark grey clayey silt, with a clay content of 40%. The organic content can be approximated to 0.6% [14].

Table 1. Material characteristics of tested Onsøy clay material

	Onsøy clay
Natural water content, w_{nat}[%]	65
Natural degree of saturation, S_r[%]	96–100
Natural void ratio, e_{nat}[-]	1.77
pH value, pH[-]	7.31
Salt concentration in pore water, Ψ_{Salt}[g/l]	25–29
Liquid limit, w_L[%]	67.4
Plastic limit, w_P[%]	29.6
Plasticity index, I_P[%]	37.8
Shrinkage limit, w_S[%]	28.8
Activity, I_A[-]	1.9

Further material characteristics, e.g. mineralogy, chemical composition, CEC and specific surface area, can be found in [15].

3 Experimental Methods

The experimental study presented in the following covers oedometer tests on natural and remoulded Onsøy clay under monotonic and cyclic loading. All tests were carried out in an oedometer cell designed and constructed at Ruhr-Universität Bochum. The device was introduced in [17,19]. Details on the functionality, construction and calibration of the device in addition can be found in [15]. In the following section the main features of the oedometer device are illustrated together with the applied loading and hydraulic boundary conditions. As sensitive natural and remoulded soil samples are tested, particular consideration is required regarding the sample preparation and installation technique. The description of these closes this chapter.

Oedometer Device

For the experimental study of the consolidation behaviour of clays under cyclic loading an oedometer device was designed and constructed at Ruhr-Universität Bochum, introduced in [17,19].

Figure 2 shows the device, which enables testing of samples with a diameter of 70 mm. For the recent study samples with a height of 20 mm were used. Thereby, the diameter-to-height-ratio of 3.5 follows [10] and limits the friction between sample and oedometer ring to a tolerable extent.

The sample is placed between two filter plates within a stainless-steel oedometer ring, which is fixed in vertical position and sealed against the top and bottom plate of the device by rubber rings. Thus, it allows testing of slurry and paste-like material as required in the present study. The thin-walled oedometer ring is equipped with strain gauges allowing the measurement of radial stresses during

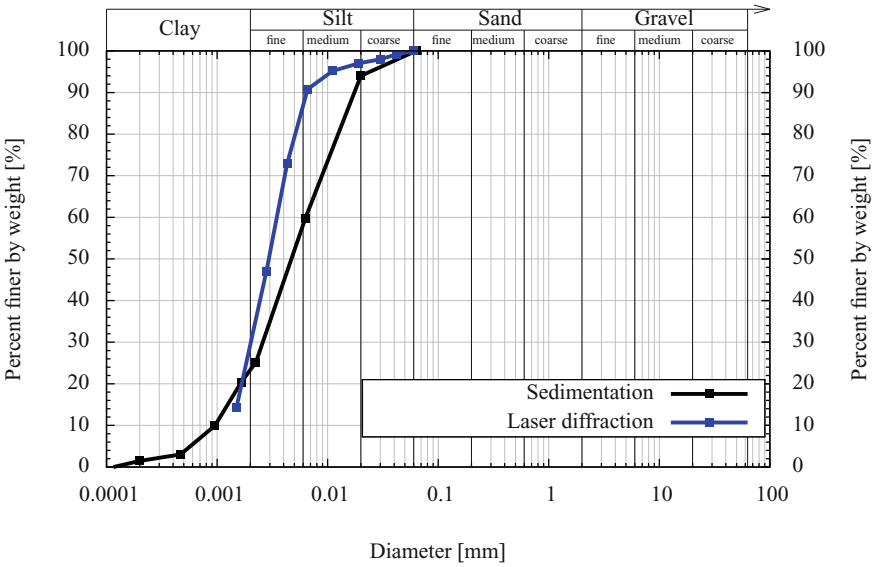

Fig. 1. Grain size distribution of Onsøy clay

the consolidation process. Drainage is allowed through the filter plates embracing the sample. Therefore, in general different drainage conditions are possible. In the present study drainage is executed through the sample top. A pore pressure transducer included in the bottom part of the device is used to measure transient pore water pressure during testing. It is able to measure positive and negative pore water pressures up to 1000/−100 kPa.

A load cell at the top and bottom of the device allows the measurement of vertical force above and below the sample and thereby facilitates the evaluation of frictional loss.

Applied Loading

The present study comprises oedometer tests under monotonic as well as cyclic loading.

In the monotonic loading tests the load is applied stepwise with a magnitude of 10–20–50–100–200–400 kPa during loading phase and 200–100–50–20–10 kPa during unloading phase. The load steps are applied quasi-instantaneously. The vertical stress application is limited to a maximum of 400 kPa due to the measurement range of the strain gauges applied on the oedometer ring.

For the cyclic tests a loading function of sinusoidal type was chosen according to [16,21] as a typical loading pattern in geotechnical applications. The loading function in given in Eq. 1.

$$L(t) = q \ \sin^2 \frac{\pi t}{d} \tag{1}$$

where $L(t) =$ applied loading as a function of time t, $q =$ load amplitude and $d =$ load period.

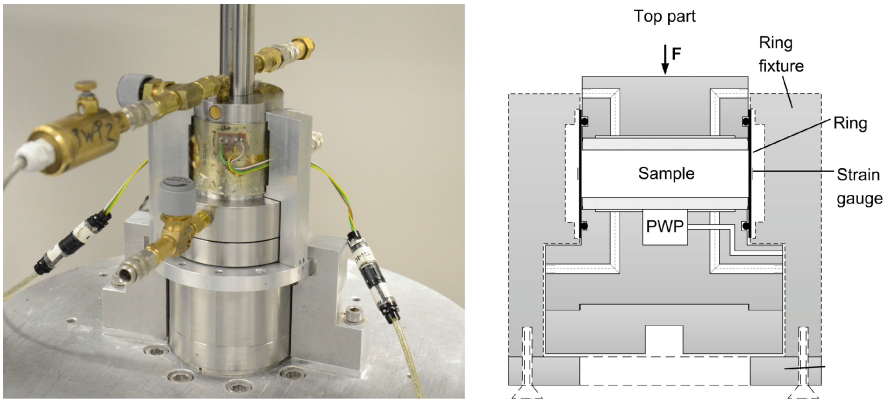

Fig. 2. A Photograph and **B** Sketch of the new oedometer device [17]

Figure 3 shows the haversine loading function over time as applied in the experimental testing.

For cyclic consolidation studies the chosen load period and amplitude are of significant relevance. In the present study the load amplitude was varied with reference to the yield stress of the tested natural material. Details are given in Sect. 5. In agreement with [16] the load period d was chosen to be $d = 120\,\mathrm{s}$. It can be calculated with reference to the time $t^{ref}(T_0 = 1)$. $t^{ref}(T_0 = 1)$ is the time an equivalent sample (identical initial state) under static loading needs to consolidate.

$$d = \frac{T_0 \cdot H^2}{c_v} = \frac{0.0075 \cdot (0.02\,\mathrm{m})^2}{2.5 \cdot 10^{-8}\mathrm{m}^2/\mathrm{s}} = 120\,\mathrm{s} \tag{2}$$

where T_0 is the chosen dimensionless period, c_V is the material-dependent coefficient of consolidation assumed to be a constant, stress-independent value determined from monotonic consolidation tests on equivalent sample material. For details see [17].

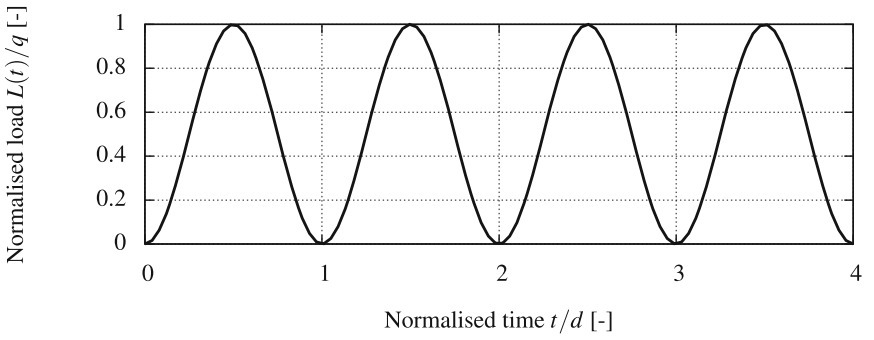

Fig. 3. Haver-sine loading function

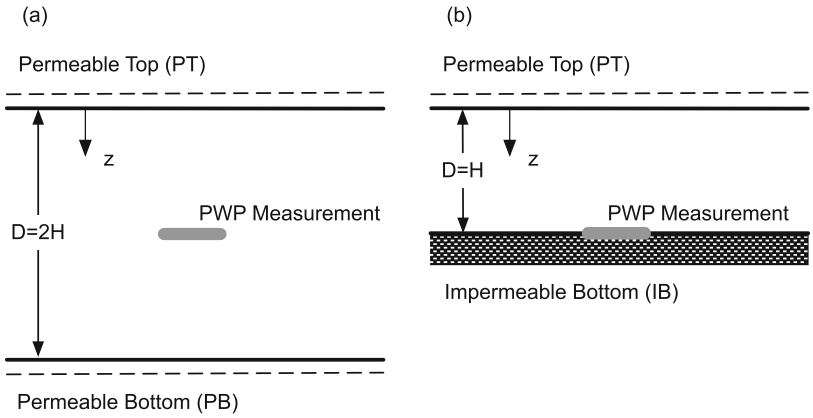

Fig. 4. Equivalence of **(a)** PTPB and **(b)** PTIB oedometer drainage configurations [16]

Hydraulic Boundary Condition

In a standard oedometer configuration usually both top and bottom of the sample are drained (abbreviated PTPB), the maximum pore water pressure occurs in the mid-plane of the sample. In this location, measurement is technically difficult and would cause strong disturbance of the sample and flow paths. Thus, in the present experimental study tests were conducted with permeable top and impermeable bottom (abbreviated PTIB). This configuration is equivalent to a standard PTPB oedometer configuration as illustrated in Fig. 4 [16].

Sample Preparation and Installation

Sample material preparation and installation of the sample in the oedometer ring are distinctly different for remoulded and natural clay. Important details of these procedures are illustrated in the following.

The sample preparation requires particular elaborateness and precision as mainly the natural clay is very sensitive and testing results are susceptible to variations in initial and boundary conditions, e.g. in the initial material state and saturation of the sample. Therefore, throughout the whole installation process, special caution was taken to guarantee homogeneity of the sample, to avoid inclusion of air bubbles and to ensure full saturation of the testing system.

For the tests on natural samples, larger, so-called pre-samples were cut from the block avoiding inclusion of shell fragments, sand inclusions and disturbed boundary areas. The sample itself was then installed by pushing the thin-walled oedometer ring into the pre-trimmed material. This preparation and installation technique was selected to guarantee the least disturbance of the sensitive natural clay as well as close contact between sample and oedometer ring for measurement of horizontal stresses.

The remoulded clay was prepared by mixing soil material at the natural water content of $w_{L,nat} = 65\%$, without prior air or oven drying. The mechanical distortion during mixing is presumed to a cause a complete destruction of the

existing structure in the natural state. Afterwards, the paste-like, remoulded clay was placed in the oedometer ring using a spatula taking special caution to avoid the inclusion of air bubbles during the installation of sample material into the ring.

Pre-moistened filter paper is placed below and above the soil sample to prevent finest particles to be flushed out of the sample into the filter plate clogging its pores.

4 Consolidation Under Monotonic Loading

To analyse the consolidation of Onsøy clay under monotonic loading, stepwise oedometer tests on natural and remoulded samples were carried out. The compression behaviour is analysed regarding the destructuration of the natural clay. A comparison to testing data from literature is drawn in order to evaluate the present test results. Besides, material parameters as for instance compression and swelling index as well as the yield stress are determined from the compression curves. A closer look is taken at the time-dependent settlement evolution and pore water dissipation of natural and remoulded clay. From this comparison conclusions regarding the material behaviour of natural samples before and after exceeding the yield stress can be drawn.

Compression Behaviour

Figure 5 illustrates the compression behaviour of natural and remoulded Onsøy clay from the conducted oedometer tests. The natural clay initially acts very stiff and shows a pronounced destructuration after exceeding the yield stress. Under the applied maximum load of 400 kPa the two materials still show a difference in axial strain or void ratio respectively. However, from tests in a high stress oedometer cell it is known that the compression curves for natural and remoulded clay converge when subjected to a stress of about 1000 kPa [15].

The yield stress σ_y marks the stress at transition point where the compression of natural soil changes from elastic to elasto-plastic. From the test data it is determined to be $\sigma_y \approx 50{-}60\,kPa$. However, additional tests in a high stress oedometer cell suggest a slightly higher yield stress of approx. 80 kPa [15], which is in better accordance with data from literature [14].

The elasto-plastic compression index C_c and elastic swelling index C_s can be calculated from the testing data with reference to Eqs. 3 and 4 to be $C_c = 0.425$ and $C_s = 0.055$.

$$C_{\mathrm{c}} = -\frac{\Delta e}{\Delta \log\left(\sigma'_v\right)} \tag{3}$$

$$C_{\mathrm{s}} = -\frac{\Delta e^{\mathrm{e}}}{\Delta \log\left(\sigma'_v\right)} \tag{4}$$

The compression ratio CR according to [11] is defined as

$$CR = \frac{C_c}{(e_0 + 1)} \tag{5}$$

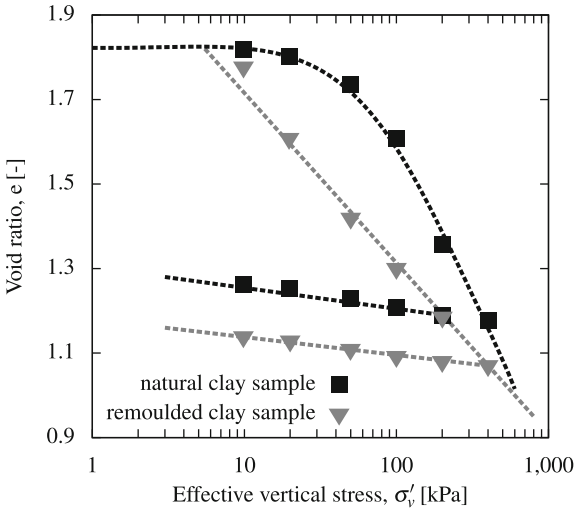

Fig. 5. Compression behaviour of natural and remoulded Onsøy clay

and can be calculated to be $CR = 0.15$. It is in good agreement with data from literature [11].

Figure 6 compares the present test data with test data given in [14] for samples from 6.10 m and 6.23 m depth. In general, the present results are in good agreement with data from literature. The slightly higher yield stress corresponds to the higher sampling depth of the clay tested within the present study.

Settlements

Figure 7 (top) shows the normalised time-dependent settlements of a natural clay sample under oedometric compression. It can be recognised that in the first three load steps from 1–10 kPa, from 10–20 kPa and from 20–50 kPa settlements occur fast compared to the later load steps. In Terzaghi's theory [23] the material's ability to consolidate and the consolidation rate are characterised by the consolidation coefficient c_v. The consolidation coefficient can be described by the following equation

$$c_v = \frac{k \cdot E_s}{\gamma_w} \tag{6}$$

where k is the hydraulic permeability, E_s is the stiffness and γ_w is the unit weight of water. Using c_v the time where 99% of the consolidation settlement has been reached from Terzaghi's theory can be calculated to be

$$t_{99\%} = \frac{2 \cdot H^2}{c_v} \tag{7}$$

where H is the drainage length.

In the first three load steps the natural soil is structured. The high permeability due to high void ratio together with a high stiffness due to intact bonding

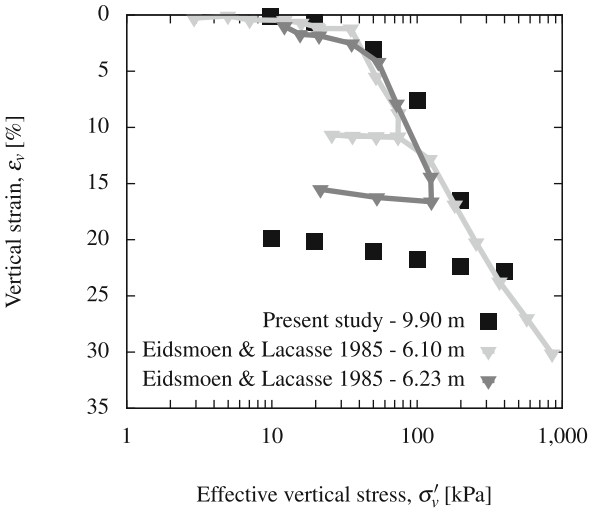

Fig. 6. Compression behaviour of natural and remoulded Onsøy clay - comparison with literature

result in a high c_v and in a fast consolidation respectively. After exceeding the yield stress, the stiffness suddenly drops due to the destructuration of the soil, while the void ratio and permeability experience a slower change. This significantly retards the consolidation process or in terms of c_v causes a decrease in c_v. In the higher load steps the soil matrix is compressed. The decrease in void ratio causes a decrease in permeability. However, the increase in stiffness is more dominant, so that for higher loading the consolidation occurs faster. This can also be observed in Fig. 7 (bottom) illustrating the normalized time-dependent settlements of the remoulded clay sample under oedometric compression. Here, for all load steps it holds true that with ongoing compression the consolidation is accelerated.

Figure 8 compares the normalized time-dependent settlements of natural and remoulded clay experiencing oedometric decompression. It can be observed that due to the experienced destructuration and elastic decompression stress path both clays show an equivalent decompression. Caused by the higher stiffness the swelling deformation occurs faster in the higher than in the lower stress ranges. As the change in stress-dependent stiffness is congruent for remoulded and natural sample (reflected in almost identical inclination of the decompression branch C_S), the swelling rate in the particular load steps likewise is the same.

A detailed study on the evolution of c_v during soil compression and its dependency on changing permeability and stiffness can be found in [15].

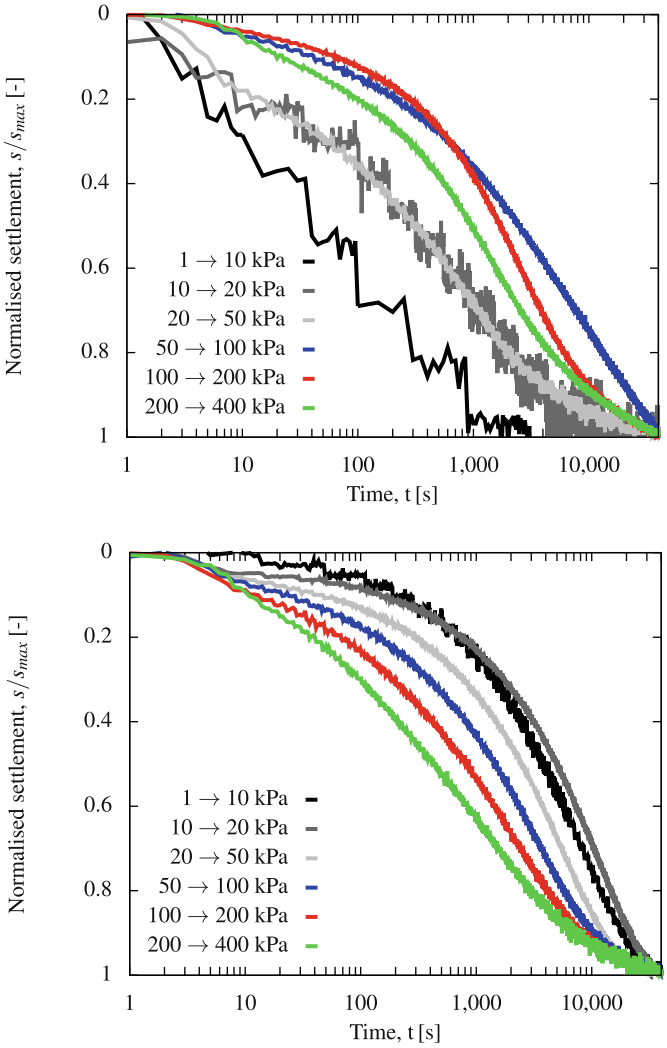

Fig. 7. Time-dependent settlements of natural (top) and remoulded (bottom) Onsøy clay

Pore Water Dissipation

The pore water dissipation during the monotonic load steps reflects the typical behaviour in terms of stiffness and permeability changes found from the time-dependent settlements. A detailed study of the measured pore water pressures during monotonic load application and consolidation phase is beyond the scope of this paper, but can be found in [15].

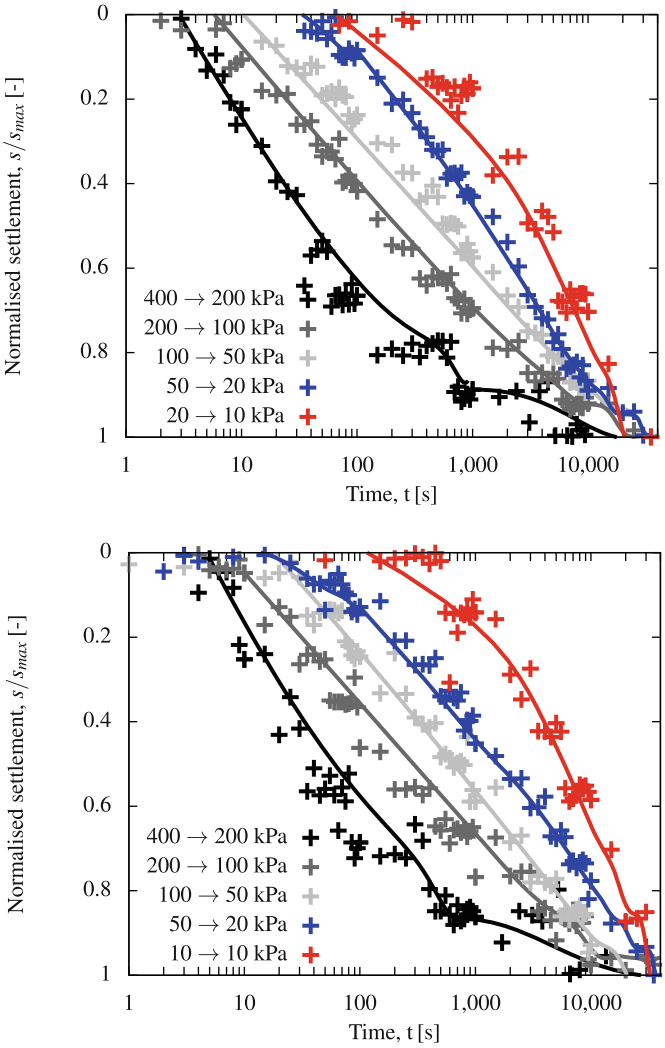

Fig. 8. Time-dependent decompression of natural (top) and remoulded (bottom) Onsøy clay

5 Cyclic Consolidation

For the present study on the consolidation of marine Onsøy clay under cyclic loading six oedometer tests are evaluated to analyse the influence of the applied load amplitude on the consolidation. Thereby, the load amplitude is chosen with reference to the yield stress. While one load amplitude was set to 50 kPa and hence chosen to be smaller than the yield stress, the other two amplitudes were set to be 100 kPa and 200 kPa exceeding the yield stress. The influence of the

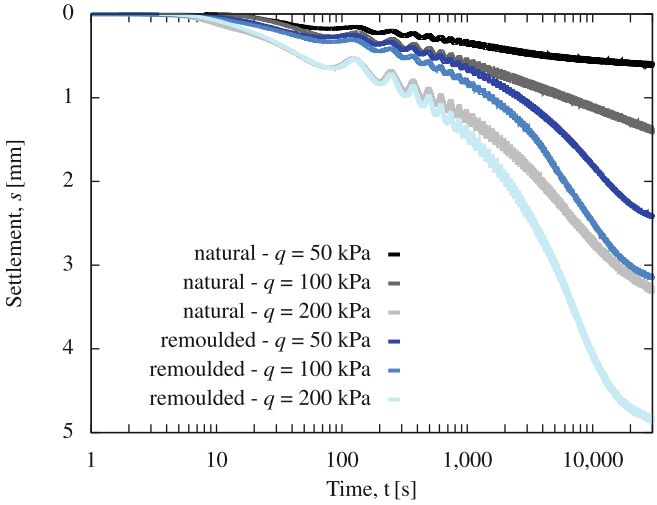

Fig. 9. Time-dependent settlements of natural and remoulded Onsøy clay under cyclic loading

load amplitude on the destructuration and thus on the consolidation process is analysed in terms of time-dependent settlements and pore water dissipation. Other loading characteristics, as e.g. the loading frequency, have an additional influence on the consolidation. A study on these influences can be found in [15], but is not considered in the present paper.

Compressibility and Time-Dependent Settlements

Figure 9 compares the time-dependent settlements of natural and remoulded samples under haversine loading with different amplitudes.

During the cyclic consolidation process the settlements accumulate and after a finite number of load steps reach a quasi stationary state. The number of cycles required for accomplishment of steady state is material and load dependent and accounts for approx. 200–250 cycles in the present testing. The increment of settlement accumulation is significantly decreasing from larger values in the first cycles to smaller ones in quasi stationary state.

Comparing the final settlements after 250 cycles or 500 min to the results from the monotonic oedometer tests (see Fig. 10), it can be observed that the compression under cyclic loading corresponds with the compression under monotonic loading. The generally slightly smaller settlement in cyclic tests can be explained by remaining pore water pressures and a corresponding smaller effective compression stress. Details can be found in [15].

However, it can be observed that compression of all tests on remoulded clay exceed the settlements of the natural samples significantly under loading with same load amplitude. This corresponds to the compression behaviour in monotonic oedometer tests.

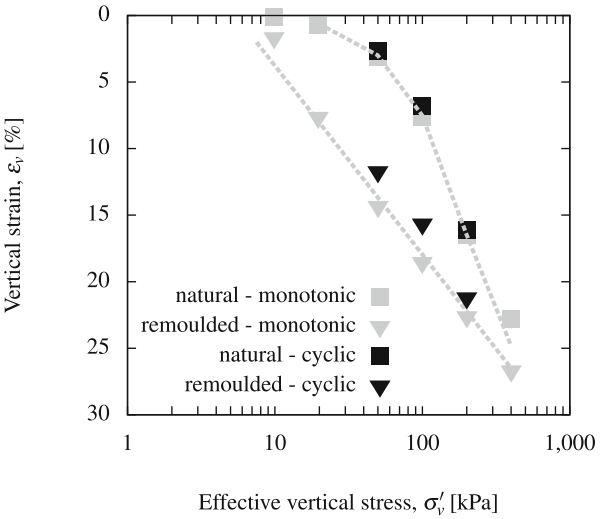

Fig. 10. Compression behaviour of natural and remoulded Onsøy clay under monotonic and cyclic loading

Figure 11 illustrates the normalized time-dependent settlements under cyclic loading. It becomes obvious, that the remoulded samples all show a similar time-dependent behaviour, while the time-dependent compression behaviour of the natural clay depends on the applied load amplitude. The natural sample loaded

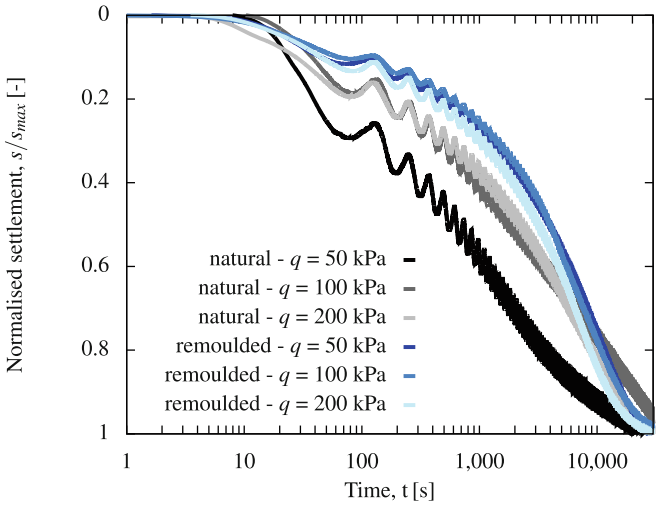

Fig. 11. Normalised time-dependent settlements of natural and remoulded Onsøy clay under cyclic loading

with a load amplitude below yield stress shows a much faster consolidation than the natural samples loaded with a load amplitude above yield stress. This also corresponds to the findings shown for consolidation under monotonic loading. However, it was to be expected from the monotonic testing results that the test under 100 kPa consolidates slower than the test under 200 kPa. This is assumed to be the case as the shape of the settlement curve for 100 kPa suggests that full consolidation is not yet reached.

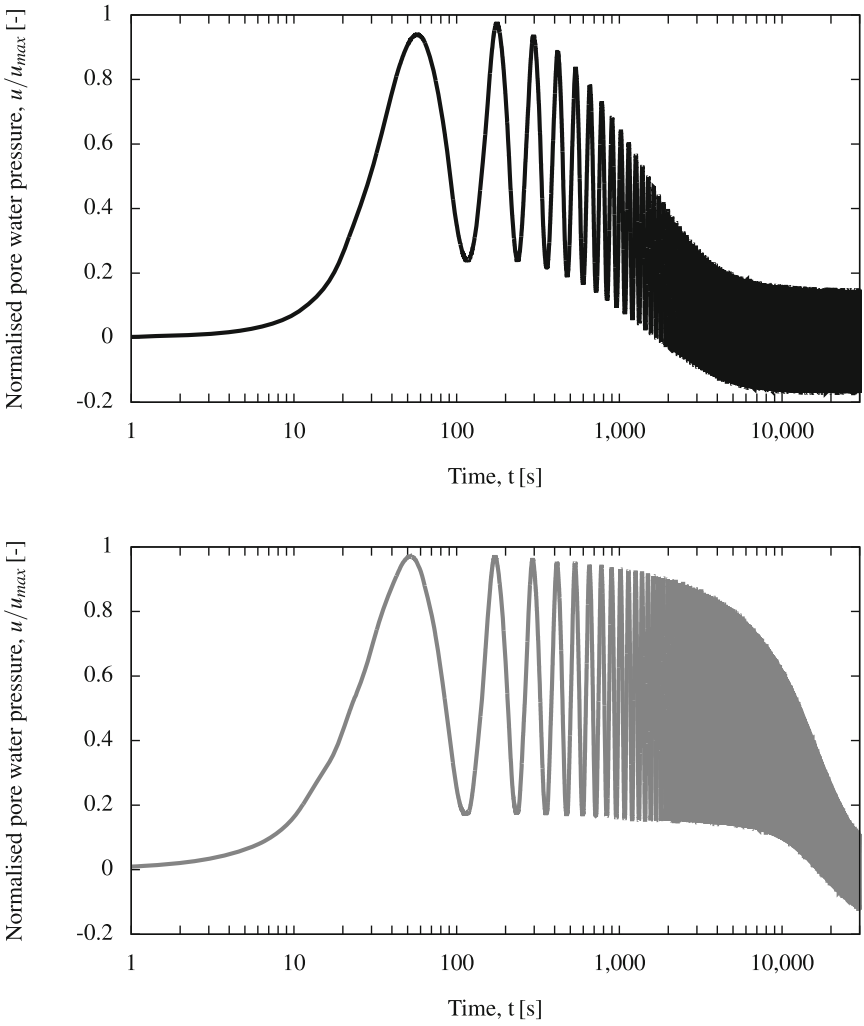

Fig. 12. Pore Water Dissipation of natural (top) and remoulded (bottom) Onsøy clay under cyclic loading of 50 kPa amplitude

Pore Water Dissipation

The difference in consolidation rate for natural and remoulded clay tested with a load amplitude below yield stress is clearly reflected in the pore water dissipation. Figure 12 compares the normalised time-dependent dissipation of pore water pressures for the two tests with a load amplitude of 50 kPa.

Generally, it can be seen that within the first cycles the excess pore water is build up. With ongoing consolidation time the excess pore water pressure dissipates, reaching a quasi stationary state after a finite number of cycles. This number of cycles is equal to the number of cycles necessary to reach a steady settlement state. It is important to notice that the amplitude of excess pore water pressures u is strongly damped during the consolidation process. Moreover, the pore water pressures in the quasi stationary state reach slight negative values at the beginning and end of a loading cycle cycling around 0.

A significantly faster decay of mean pore water pressure is observed for natural than for remoulded clay. Analogue to the monotonic loading the bonding in the soil structure of the natural clay causes a higher stiffness of the material and thus a must faster consolidation. The effect is even more pronounced in the cyclic testing as here due to the alternating loading the effective stress increases slower and thus seems to have a less distinct effect on the destructuration.

6 Conclusion and Outlook

In the present paper the consolidation of Norwegian Onsøy clay as a typical representative of natural, marine clay is analysed.

Part I of this paper comprises the experimental study. To analyse the material behaviour of natural and remoulded clay, Onsøy clay was characterised regarding its soil mechanical properties. In a specially designed oedometer cell tests under monotonic as well as cyclic loading were conducted. Particular considerations and elaborateness are required for sample preparation, installation as well as for the choice and measurement of the hydraulic and mechanical boundary conditions.

The consolidation in terms of compression, time-dependent settlements and pore water dissipation was analysed. From the experimental data it was shown, that Onsøy clay under monotonic loading behaves as a typical structured clay, showing destructuration after reaching its yield stress of approximately 60 kPa. From the cyclic oedometer tests it becomes clear that the monotonic compression is reflected in the cyclic behaviour as well. The influence of structure and loading conditions on the behaviour of natural and remoulded clay was scrutinized by comparing both material types under cyclic loading with load amplitudes below and above yield stress.

The following Part II of this paper comprises a numerical study modelling the cyclic oedometer tests on Onsøy clay. In geotechnical design processes the need for sophisticated constitutive models allowing the simulation of complex boundary value problems is growing. Therefore, the necessity and ability of different features of a hierarchical model to analyse this type of cyclic consolidation boundary value problems are studied.

Acknowledgement. The material characterisation and parts of the experimental testing program were performed within the framework of a master's thesis prepared by Wolfgang Lieske, M.Sc. supervised by the first author. The authors would like to thank Wolfgang Lieske for his contribution. The second author acknowledges financial support provided by the German Science Foundation (DFG) in the framework of the Collaborative Research Centre SFB 837 (subproject A5).

References

1. ASTM D854–14: Standard Test Methods for Specific Gravity of Soil Solids by Water Pycnometer (2014)
2. Burland, J.B.: On the compressibility and shear strength of natural clays. Géotechnique **40**(3), 329–378 (1990)
3. Cotecchia, F., Chandler, R.J.: The influence of structure on the pre-failure behaviour of a natural clay. Géotechnique **47**(3), 523–544 (1997)
4. Cotecchia, F., Chandler, R.J.: A general framework for the mechanical behavior of clays. Géotechnique **50**(4), 431–447 (2000)
5. DIN EN 22475–1: Geotechnische Erkundung und Untersuchung Probenentnahmeverfahren und Grundwassermessungen Teil 1: Technische Grundlagen der Ausfhrung (ISO 22475–1:2006); Deutsche Fassung EN ISO 22475–1:2006, January 2007
6. DIN ISO, TS 17892–6 (Vornorm): Geotechnische Erkundung und Untersuchung - Laborversuche an Bodenproben - Teil 6: Fallkegelversuch (ISO/TS 17892–6:2004), January 2005
7. DIN: 18122–1: Baugrund Untersuchung von Bodenproben Zustandsgrenzen (Konsistenzgrenzen) - Teil 1: Bestimmung der Flie- und Ausrollgrenze, July 1997
8. DIN: 18122–2: Baugrund Untersuchung von Bodenproben Zustandsgrenzen (Konsistenzgrenzen) - Teil 1: Bestimmung der Schrumpfgrenze, September 2000
9. DIN: 18123: Baugrund Untersuchung von Bodenproben Bestimmung der Korngrenverteilung, November 1996
10. DIN: 18135: Baugrund Untersuchung von Bodenproben Eindimensionaler Kompressionsversuch, April 2012
11. Lambe, T.W., Whiteman, R.V.: Soil Mechanics. Wiley, New York (1969)
12. Lefebvre, G., Poulin, C.: A new method of sampling in sensitive clay. Can. Geotech. J. **16**(1), 226–233 (1979)
13. Lunne, T., Berre, T., Andersen, K.H., Strandvik, S., Sjursen, M.: Effects of sample disturbance and consolidation procedures on measured shear strength of soft marine Norwegian clays. Can. Geotech. J. **44**(1), 111 (2007)
14. Lunne, T., Long, M., Forsberg, C.F.: Characterisation and engineering properties of Onsøy clay. In: Tan, T.S. (ed.) Characterisation and Engineering Properties of Natural Soils, vol. 1, pp. 395–427. CRC Press, Boca Raton (2003)
15. Müthing, N.: On the consolidation behaviour of fine-grained soils under cyclic loading. Dissertation, Schriftenreihe des Lehrstuhls für Grundbau, Boden- und Felsmechanik, Ruhr-Universität Bochum (2017). Under preparation
16. Müthing, N., Barciaga, T., Schanz, T.: On the use of isotropic hardening plasticity to model cyclic consolidation of fine grained soils. In: Triantafyllidis, T. (ed.) Holistic Simulation of Geotechnical Installation Processes. LNACM, vol. 80, pp. 131–147. Springer, Heidelberg (2016). doi:10.1007/978-3-319-23159-4_7

17. Müthing, N., Datcheva, M., Schanz, T.: On the influence of loading frequency on the pore-water dissipation behavior during cyclic consolidation of soft soils. In: Oka, F., Murakami, A., Uzuoka, R., Kimoto, S. (eds.) Computer Methods and Recent Advances in Geomechanics, pp. 441–445. CRC Press, Boca Raton (2014)
18. Müthing, N., Razouki, S.S., Datcheva, M., Schanz, T.: Rigorous solution for 1-D consolidation of a clay layer under haversine cyclic loading with rest period. SpringerPlus **5**(1), 1987 (2016)
19. Müthing, N., Röchter, L., Datcheva, M., Schanz, T.: Cyclic consolidation of soft soils. Bochum, Aktuelle Forschung in der Bodenmechanik, Tagungsband zur 1. Deutschen Bodenmechanik Tagung Bochum (2013)
20. Razouki, S.S., Bonnier, P., Datcheva, M., Schanz, T.: Analytical solution for 1D consolidation under haversine cyclic loading. Int. J. Numer. Anal. Meth. Geomech. **37**(14), 2367–2372 (2013)
21. Razouki, S.S., Schanz, T.: One-dimensional consolidation under haversine repeated loading with rest period. Acta Geotech. **6**(1), 13–20 (2011)
22. Skempton, A.W., Northey, R.D.: The sensitivity of clays. Géotechnique **3**(1), 30–53 (1952)
23. Terzaghi, K.: Erdbaumechanik auf bodenphysikalischer Grundlage. Deuticke (1925)
24. Wichtmann, T., Andersen, K.H., Sjursen, M., Berre, T.: Cyclic tests on high-quality undisturbed block samples of soft marine. Can. Geotech. J. **412**, 400–412 (2013)

Cyclic Response of Natural Onsøy Clay
Part II: Constitutive Modeling

Thomas Barciaga[1], Nina Müthing[1(✉)], Maria Datcheva[2], and Tom Schanz[1]

[1] Chair of Foundation Engineering, Soil and Rock Mechanics, Ruhr-Universität Bochum, Universitätsstr. 150, 44780 Bochum, Germany
{thomas.barciaga,Nina.Muething}@rub.de
[2] Institute of Mechanics, Bulgarian Academy of Sciences, Acad Bonchev St, bl 4, 1113 Sofia, Bulgaria

Abstract. Geotechnical csonstruction projects in natural clay deposits are challenging because of the complex constitutive features of these clays (e.g. inherent and stress-induced anisotropy and destructuration). Cyclic loading, on the other hand, is typical for various geotechnical applications where natural clay deposits are involved such as wind and wave loads in relation to onshore and offshore foundations, ship locks or dams. This makes important to consider cyclic loads in the numerical simulations for geotechnical applications in natural clay deposits. Therefore, in case of natural clays it is essential to have proper constitutive models accounting for the clay material response to the cyclic nature of the loading in order to have reliable predictions of the time-dependent consolidation behavior and the corresponding development of the ground settlements. Within the present study the influence of the constitutive model on the numerical simulation of the natural clay consolidation under cyclic loading is qualitatively investigated employing the experimental results for a typical natural clay reported in the companion paper *Cyclic response of natural Onsøy clay – Part I: Experimental analysis*. The approach followed in this paper employs an adequate hierarchical constitutive soil model based on the bounding surface plasticity (BSP) concept. The hierarchical structure of the constitutive model makes it possible to investigate the importance of a particular feature of the model such as the inherent and the stress-induced anisotropy, the structure and the destructuration by activation/deactivation of the associated constitutive parameters. Finally, the model responses (such as the evolution of the excess pore-pressure and the settlement during cyclic loading) of each model of the hierarchical family are compared and discussed with respect to the necessity of the model complexity level. In order to calibrate the constitutive parameters a number of geotechnical experiments are numerically simulated considering natural and reconstituted Onsøy clay samples under drained and undrained hydraulic conditions. Moreover, the significant influence of the destructuration and the features of the BSP concept on the model response under consolidation induced by cyclic loading is highlighted. In conclusion, it is shown that the presented constitutive model based on the BSP concept is generally capable to predict the consolidation behavior of natural clay induced by cyclic loading. The model is suitable to simulate the main phenomena such as the pore-water pressure dissipation behavior and the associated but retarded evolution of the settlement.

T. Triantafyllidis (ed.), *Holistic Simulation of Geotechnical Installation Processes*,
Lecture Notes in Applied and Computational Mechanics 82, DOI 10.1007/978-3-319-52590-7_12

1 Introduction

For the purposes of a reliable geotechnical construction on natural clay deposits due to clay's low stiffness and permeability it is essential to understand the clay consolidation behavior induced by cyclic loading. The consolidation under cyclic loading is characterized by the time-dependent evolution of the excess pore-water pressure, the corresponding development of the effective stress and the associated settlement.

The required adequate constitutive model has to account for the complex constitutive behavior governed by the initial and current stress states, the stress-strain history and the structure of the natural clay. The structure of natural clays consists of two parts [4,20,22]: The anisotropic fabric formed during geological processes such as sedimentation or consolidation and the inter-particle bonding which is related to several different time-dependent physico-chemical processes. The anisotropy effects the rotation of the yield stress with respect to the stress path history and the inter-particle bonding imparts additional strength to the clay before yielding. To capture the complex hydro-mechanical behavior of natural clays the present study is focused on modeling the inherent and the stress-induced anisotropic fabric and the stress-induced destructuration associated with a progressive damage of the inter-particle bonding. Furthermore, the importance of the realistic modeling of the constitutive behavior induced by cyclic loading is emphasized. Special attention is given to the smooth elastoplastic behavior inside the bounding surface, the degradation of the stiffness and the accumulation of plastic strains induced by cyclic loading.

Consequently, a series of hierarchical constitutive SANICLAY models which were introduced in [10,30,34] based on the BSP concept are employed and efficiently implemented in a three-dimensional state-of-the-art finite element code using a robust time integration scheme. The explicit integration scheme with an automatic error control and sub-stepping algorithm originally proposed by [32,33] has been modified to be applicable for the integration of the more complex constitutive equations in the BSP framework. The time integration scheme is out of the scope of the present study.

The Onsøy clay is chosen as a representative for a typical natural clay exhibiting certain anisotropy and destructuration. The constitutive parameters are calibrated against several geotechnical laboratory tests on reconstituted and natural Onsøy clay under oedometric and triaxial mechanical boundary conditions, different loading paths and drained and undrained hydraulic conditions.

The main focus in this study is set on the understanding of the influence of the hierarchical complexity of the constitutive model on the one-dimensional consolidation behavior of natural clay induced by cyclic loading. The aim of the qualitative study is the evaluation of the necessity of certain typical features of the natural clay behavior (e.g. anisotropy, destructuration, elastoplastic behavior during unloading-reloading path) in consolidation analysis rather than a quantitative comparison with the experimental results.

In this study the focus is set on the consolidation behavior under oedometric boundary conditions. Accordingly, qualitative numerical analysis by use of finite

element simulations are carried out. The experimental setup of the oedometer device, the initial conditions and the mechanical and hydraulic boundary conditions are chosen in accordance with the experimental study on *Cyclic response of natural Onsøy clay – Part I: Experimental analysis*. To assess the need and the influence of hierarchical modeling the evolution of the excess pore-water pressure and the settlements are evaluated.

2 A Hierarchical Model Within the Framework of the Bounding Surface Plasticity

The hierarchical structure of the adequate constitutive model in the framework of the BSP is described in the following section. The model is generally formulated in the multiaxial stress space. Firstly, the non-linear elastic model response is introduced followed by the general description of the bounding surface plasticity concept. The model in its simplest form is based on the elastoplastic critical state soil mechanics concept using the Modified Cam-Clay approach incorporating isotropic hardening and softening. Some model extensions allow to capture more sophisticated soil mechanical features of natural clay such as the anisotropy covered by rotational hardening and the destructuration. Concluding, some special features of the BSP model concerning a more appropriate cyclic model response are presented.

2.1 Elasticity

The elastic stress-strain behavior is described by a non-linear stress-dependent isotropic hypo-elastic relation. The stress and the strain tensors can be presented as the sum of the deviatoric and the volumetric part. The formulations in the multiaxial stress and strain space are given in the following: the mean effective stress $p = 1/3 \operatorname{tr} \boldsymbol{\sigma}$, the deviatoric stress tensor $\boldsymbol{s} = \boldsymbol{\sigma} - p\,\boldsymbol{I}$. The elastic stress-strain relationship is given by Eq. 1.

$$\dot{\boldsymbol{\varepsilon}}^{\mathrm{e}} = \frac{\dot{p}}{3\,K}\,\boldsymbol{I} + \frac{\dot{\boldsymbol{s}}}{2\,\mu} \tag{1}$$

The bulk modulus K (see Eq. 2) is assumed to be dependent on the stress state expressed by the effective mean stress p. Furthermore, the bulk modulus K is defined by the specific volume $1 + e$ and the elastic swelling index κ. In this study the definition of the specific volume $v = 1 + e$ is related to the current void ratio e. The shear modulus μ is expressed in terms of the bulk modulus K and a constant Poisson's ratio ν (see Eq. 3).

$$K = \frac{1+e}{\kappa}\,p \tag{2}$$

$$\mu = \frac{3\,(1-2\,\nu)}{2\,(1+\nu)}\,K \tag{3}$$

2.2 Bounding Surface Plasticity

2.2.1 Concept

The BSP concept developed by [1,6,8,9,17–19] allows for a more sophisticated modeling of the behavior inside the yield surface to account for complex stress paths, cyclic loading and accumulation of strains. The multiaxial formulations of the plastic potential surface G and the bounding surface F are given by Eqs. 4 and 5 respectively. The constitutive features incorporated in the plastic potential surface and the bounding surface such as critical state soil mechanics, isotropic hardening and softening, anisotropy and destructuration, non-associated flow rule and Lode angle dependence and the corresponding constitutive parameters will be explained in the following sections.

$$G = \frac{3}{2}\,\{\bar{\boldsymbol{s}} - \bar{p}\,\boldsymbol{\alpha}\} : \{\bar{\boldsymbol{s}} - \bar{p}\,\boldsymbol{\alpha}\} - \left\{M^2 - \frac{3}{2}\,\boldsymbol{\alpha} : \boldsymbol{\alpha}\right\}\,\bar{p}\,\{p_\alpha - \bar{p}\} = 0 \tag{4}$$

$$F = \frac{3}{2}\,\{\bar{\boldsymbol{s}} - \bar{p}\,\boldsymbol{\alpha}\} : \{\bar{\boldsymbol{s}} - \bar{p}\,\boldsymbol{\alpha}\} - \left\{N^2 - \frac{3}{2}\,\boldsymbol{\alpha} : \boldsymbol{\alpha}\right\}\,\bar{p}\,\{p_{\mathrm{s},0} - \bar{p}\} = 0 \tag{5}$$

The bounding surface F indicates the maximum stress state which the clay has been experienced during the stress-strain history and an additional elastic nucleus f_{eln} homologous to the bounding surface defines the elastic range (see Figs. 1 and 2). The bounding surface, the plastic potential surface and the elastic nucleus in the p, q effective mean vs. deviatoric stress space are schematically illustrated in Fig. 1. The main feature of the BSP model is that the plasticity modulus K_{p} at the current stress state $\boldsymbol{\sigma}$ is related to the plasticity modulus $\bar{K}_{\mathrm{p}}$ at the corresponding image stress state $\bar{\boldsymbol{\sigma}}$ on the bounding surface indicated with a bar via a distance function and an additional shape hardening function $\hat{h}$ (see Eq. 6).

$$K_{\mathrm{p}} = \bar{K}_{\mathrm{p}} + \hat{h}\,\frac{\delta}{\langle r - s_{\mathrm{eln}}\,\delta\rangle} = \bar{K}_{\mathrm{p}} + \hat{h}\,\left\langle\frac{b-1}{b - \{b-1\}\;s_{\mathrm{eln}}}\right\rangle \tag{6}$$

This approach ensures a smooth elastoplastic transition and enables the occurrence of elastoplastic deformations for stress paths from the outside of the elastic nucleus to the bounding surface. The plasticity modulus at the image stress state is determined from the consistency condition of the bounding surface $\dot{F} = 0$. This yields to Eq. 7 where $\boldsymbol{q}$ is the vector of the internal hardening variables derived from the hardening rules with respect to the image stress state on the bounding surface.

$$\bar{K}_{\mathrm{p}} = -\frac{\partial F}{\partial \boldsymbol{q}} : \tilde{\boldsymbol{q}} \tag{7}$$

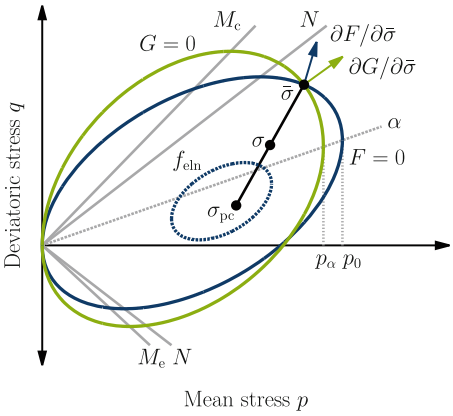

Fig. 1. Schematic illustration of the bounding surface, the plastic potential surface and the elastic nucleus in the p, q effective stress space

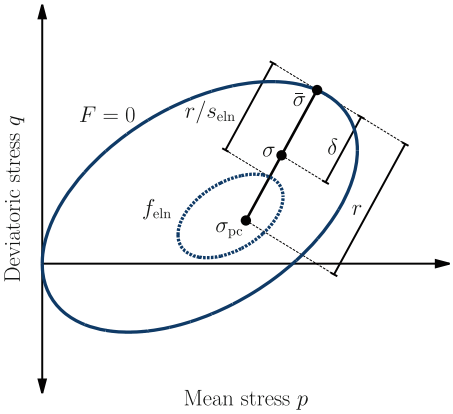

Fig. 2. Schematic illustration of the BSP concept

The image stress is obtained by a radial projection rule (see Eq. 8) where $(1 \leq b < \infty)$ is the similarity ratio between an imaginary loading surface through the current stress state to the bounding surface through the image stress state and $\boldsymbol{\sigma}_{pc}\,(p_{pc}, \boldsymbol{s}_{pc})$ is the projection center. The projection center serves as the center of homology for the loading surface as well as for the elastic nucleus. The similarity ratio can be obtained from inserting the projection rule for the image stress in the bounding surface formulation.

$$\bar{\boldsymbol{\sigma}} = b\ \{\boldsymbol{\sigma} - \boldsymbol{\sigma}_{pc}\} + \boldsymbol{\sigma}_{pc} \tag{8}$$

The generalized scalar distances $\delta = |\bar{\boldsymbol{\sigma}} - \boldsymbol{\sigma}|$ and $r = |\bar{\boldsymbol{\sigma}} - \boldsymbol{\sigma}_{pc}|$ are schematically illustrated in the p, q effective stress space in Fig. 2. Moreover, the constitutive parameter s_{eln} is an indirect measure of the size of the elastic nucleus. For a

stress point inside the elastic nucleus with $r/s_{\mathrm{eln}} < \delta$ the latter term in Eq. 6 and correspondingly the plastic modulus converge to infinity indicating a purely elastic behavior. By setting a huge value for s_{eln} the model response reduces from bounding surface plasticity to conventional elastoplasticity. For a stress point on the bounding surface with $\delta = 0$ or $b = 1$ the latter term in Eq. 6 converges to zero and $K_{\mathrm{p}} = \bar{K}_{\mathrm{p}}$. Hence, the bounding surface acts like a yield surface in conventional elastoplasticity. For all other loading paths having a positive scalar plastic loading index L elastoplastic strains will be induced in accordance with Eq. 9 as a function of the plasticity index K_{p} of the current stress state. Whereat, the scalar plastic loading index L which defines the magnitude of the plastic strain rate is derived from combining the flow rule and the consistency condition on the bounding surface by use of the image stress state. All induced plastic strains result in an update of the yield surface such as expansion, shrinkage or rotation due to isotropic hardening and softening, anisotropy or destructuration.

$$L = \frac{1}{K_{\mathrm{p}}} \frac{\partial F}{\partial \bar{\boldsymbol{\sigma}}} : \dot{\boldsymbol{\sigma}} \tag{9}$$

2.2.2 Critical State

To describe the mechanical stress-strain behavior of natural clays the BSP model is generally formulated in the framework of the critical state soil mechanics. [14, 24] gave an overview of critical state models developed and used in computational geomechanics. The constitutive model employed in the current study is based on the concept of the critical state soil mechanics by use of the Modified Cam-Clay (MCC) formulation. The critical state defines a unique but material dependent relationship between the volumetric stress and the deviatoric stress at failure and the void ratio e_{cs} (or the specific volume) at the critical state independent of the initial state [27–29]. At the critical state in the triaxial stress space the deviatoric plastic strain develops continuously while the triad of the volumetric stress, the deviatoric stress and the void ratio (no total volumetric strain) remains constant. The original Cam-Clay model was initially proposed by [27–29] determining the formulation of the plastic potential from a plastic work rate equation including the dilatancy as the coupling between the plastic volumetric and deviatoric strain rates. The slope of the critical state line projected to the p, q effective stress space is defined as the critical state stress ratio M. Afterward, [3,26] modified the Cam-Clay model having an elliptical plastic potential surface and associated yield surface to overcome the discontinuity of the Cam-Clay surface at the tip.

2.2.3 Isotropic Hardening and Softening

The BSP model incorporates a classical isotropic hardening as used in the Cam-Clay models. The internal hardening variable p_0 is controlling the evolution of the size of the yield surface as a function of the plastic volumetric strain rate $\dot{\varepsilon}_{\mathrm{v}}^{\mathrm{p}}$. Furthermore, the model is suitable to model the softening behavior of heavily

overconsolidated clays on the dry side of the critical state. The evolution of the internal hardening variable p_0 is given by the rate Eq. 10.

$$\dot{p}_0 = \left\{ \frac{1+e}{\lambda - \kappa} \right\} p_0 \, \dot{\varepsilon}_{\mathrm{v}}^{\mathrm{p}} = \langle L \rangle \left\{ \frac{1+e}{\lambda - \kappa} \right\} p_0 \, \mathrm{tr} \left\{ \frac{\partial G}{\partial \bar{\boldsymbol{\sigma}}} \right\} \tag{10}$$

To sum up, the BSP model includes six constitutive parameters which are directly related to the critical state soil mechanics concept. The elastoplastic compression index λ and the elastic swelling index κ define the natural logarithmic effective mean stress-void ratio behavior in loading and unloading-reloading respectively. In addition to this, the Poisson's ratio ν, the critical state stress ratio M in the p, q effective stress space, the isotropic hardening variable p_0 which defines the initial size of the yield surface and the initial void ratio e_0.

2.2.4 Anisotropy

The inherent anisotropy leads to an initial rotation of the yield surface. Induced stresses and corresponding plastic strains result in a evolution (expansion, shrinkage, rotation) of the yield surface with respect to the loading direction. To capture the inherent and stress-induced anisotropy [7] extended the isotropic to an anisotropic formulation of the plastic potential by proposing a new rate expression of the plastic work. This formulation results in a rotated and distorted elliptical plastic potential surface. The anisotropy is introduced to Eq. 4 by a rotational tensor $\boldsymbol{\alpha}$ coupling the plastic volumetric and deviatoric strain rates and by p_α visualized in Fig. 1. The stress-induced evolution of the rotational hardening variable $\boldsymbol{\alpha}$ is controlled using sophisticated rotational hardening rules [7,10–12,36] as a function of the plastic volumetric and deviatoric strain rates and the stress path history. The chosen evolution of the internal hardening variable $\boldsymbol{\alpha}$ is given by the rate Eq. 11.

$$\dot{\boldsymbol{\alpha}} = \langle L \rangle \; c \, p_{\mathrm{atm}} \, \frac{p}{p_0} \, \{ \boldsymbol{\alpha}_{\mathrm{b}} - \boldsymbol{\alpha} \} \tag{11}$$

$$\boldsymbol{\alpha}_{\mathrm{b}} = \frac{\boldsymbol{r}}{x_\alpha} \tag{12}$$

The rate of evolution of anisotropy and rotation is controlled by the constitutive parameter c. The ratio p/p_0 slows down the rate of the evolution for heavily overconsolidated clays and the atmospheric pressure p_{atm} is used for reasons of dimensional consistency. The rate equation includes a proper equilibrium value $\boldsymbol{\alpha}_{\mathrm{b}}$ (see Eq. 12) for the rotational tensor $\boldsymbol{\alpha}$ with respect to various stress paths indicated by the deviatoric stress ratio tensor $\boldsymbol{r} = \boldsymbol{s}/p$. Consequently, employing a less complex rotational hardening rule (out of the sophisticated ones) is sufficient in this study since the oedometric model response is less sensitive to the stress-induced anisotropy due to the almost constant effective stress ratio. The constitutive parameter x_α controls the equilibrium values of the rotational tensor. This allows for a correct modeling of the K_0 loading path (for example in an oedometer test).

In the current study the yield surface and the plastic potential surface have the same rotational tensor $\boldsymbol{\alpha}$ governed by the same rotational hardening rule.

2.2.5 Non-associated Flow Rule and Lode Angle Dependence

To account for a more accurate modeling of the softening behavior of clay under undrained shearing and of the softening behavior of heavily overconsolidated clay under drained shearing [10,15,16] introduced a non-associated flow rule. The formulation of the yield surface in terms of non-associated flow rule is achieved by replacing M and p_α in the formulation of the plastic potential surface by N and p_0.

Furthermore, [10,15,16] added a Lode angle dependence of the plastic potential surface and the yield surface to capture the different behavior in compression and extension. It is to be mentioned that in this study for the sake of simplicity of the time integration of the constitutive equations only the plastic potential surface is considered as Lode angle dependent. Whereat, the critical state stress ratio $M(\theta)$ for the plastic potential surface is a function of the Lode angle θ which is defined as the third stress invariant [31,39] given by Eqs. 13–15 where $m = M_\mathrm{e}/M_\mathrm{c}$ and $\bar{\boldsymbol{r}} - \boldsymbol{\alpha}$ is the effective stress ratio.

$$M(\theta) = \frac{2\,m}{\{1+m\} - \{1-m\}\,\cos(3\,\theta)}\,M_\mathrm{c} \tag{13}$$

$$\cos(3\,\theta) = \sqrt{6}\,\mathrm{tr}(\boldsymbol{n}_{\mathrm{r}\alpha}^3) \tag{14}$$

$$\boldsymbol{n}_{\mathrm{r}\alpha} = \frac{\bar{\boldsymbol{r}} - \boldsymbol{\alpha}}{|\bar{\boldsymbol{r}} - \boldsymbol{\alpha}|} \tag{15}$$

2.2.6 Excessive Rotation and Uniqueness of Critical State

The rate equation of the rotational tensor (see Eq. 11) avoids an excessive rotation of the plastic potential in the vicinity of the critical state by applying a certain restrictive condition for the maximum value of $\boldsymbol{\alpha}$ for η-values exceeding a multiple of M_r defined by an internal model variable ξ given by Eqs. 16–21. Moreover, the uniqueness of the critical state line is guaranteed. The ratio of the rotational tensor at the critical state to the critical state stress ratio $\boldsymbol{\alpha}_\mathrm{cs}/M$ must be independent of the Lode angle θ.

$$\text{if } \eta > \xi\,M_\mathrm{r} \rightarrow \boldsymbol{\alpha}_\mathrm{b} = \frac{\sqrt{\frac{2}{3}}\,\xi\,M_\mathrm{r}\,\boldsymbol{n}_\mathrm{r}}{x_\alpha} \tag{16}$$

$$\eta = \sqrt{\frac{3}{2}\,\boldsymbol{r} : \boldsymbol{r}} \tag{17}$$

$$\xi = x_\alpha\,\frac{\min(M_\mathrm{e}, M_\mathrm{c}, N)}{M_\mathrm{c}} \tag{18}$$

$$M_\mathrm{r} = \frac{2\,m}{\{1+m\} - \{1-m\}\,\cos(3\,\theta_\mathrm{r})}\,M_\mathrm{c} \tag{19}$$

$$\cos(3\,\theta_\mathrm{r}) = \sqrt{6}\,\mathrm{tr}(\boldsymbol{n}_\mathrm{r}^3) \tag{20}$$

$$\boldsymbol{n}_\mathrm{r} = \frac{\boldsymbol{r}}{|\boldsymbol{r}|} \tag{21}$$

2.2.7 Destructuration

The initial structure due to the bonding of the natural clay increases the yield stress compared to the reconstituted clay at the same void ratio allowing for loading paths with a higher effective mean stress without causing yielding. The stress-volumetric strain behavior of a natural clay until the yield stress is reached seems to be predominantly elastic having nearly the same slope and therefore the same swelling index as the reconstituted clay during unloading-reloading paths. After exceeding the yield stress destructuration abruptly occurs causing a reduction of the stiffness and the strength of the natural clay resulting in a large compression. Consequently, the elastoplastic compression index is high. Due to the progressive nature of the destructuration the compression index of the natural clay is gradually decreased until the stress-void ratio curve of the natural clay converges at higher stress states to the corresponding curve of the reconstituted clay. The destructuration is completed and almost no structure remains.

In the constitutive modeling the initial structure and the destructuration are considered by applying the general approach of [13]. A homologous reference surface F_{i} is introduced to describe the size of the yield surface of the reconstituted clay having intrinsic properties independent on the natural state (see Fig. 3). [34,35] incorporated the concept of an intrinsic yield surface in the SANICLAY model introduced by [10]. The concept is based on the assumption that the size of the yield surface of a natural clay depends on the current amount of the structure. The difference in size of both yield surfaces (intrinsic vs. structured) indicates the amount of structural effects and inter-particle bonding forces. Consequently, the degree of structuring is specified by the internal structure variable $S_{\mathrm{i}} = p_{0,\mathrm{s}}/p_{0,\mathrm{i}}$ defined as the ratio of the internal hardening variable $p_{0,\mathrm{i}}$ for the reconstituted clay to $p_{0,\mathrm{s}}$ for the natural structured clay. The initial structure is

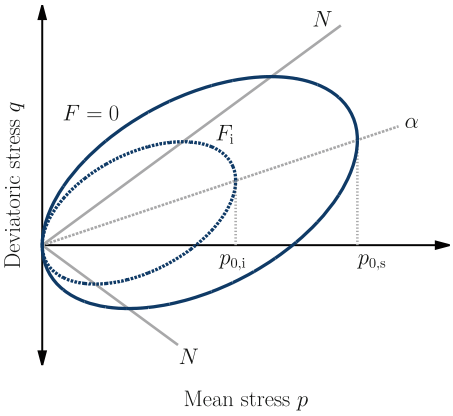

Fig. 3. Schematic illustration of the bounding surface for the natural clay and the intrinsic reference surface for the reconstituted clay in the p, q effective stress space

specified by the constitutive parameter $S_{\mathrm{i},0}$. For reasons of quantification of the structure of a natural clay with respect to the reconstituted state, [5] introduced the stress sensitivity. In brief, the stress sensitivity S_σ is defined as the ratio of the axial effective yield stress $\boldsymbol{\sigma}_{\mathrm{axial,yield}}$ for the natural state to the axial effective stress $\boldsymbol{\sigma}_{\mathrm{axial,yield,\,rec}}$ for the reconstituted state at the same intrinsic void index and can be directly related to the internal structure variable S_i. The internal hardening variable $p_{0,\mathrm{s}}$ is introduced to the formulation of the yield surface in Eq. 5. The evolution of the internal hardening variable $p_{0,\mathrm{s}}$ given by the rate Eq. 22 is divided into the classical isotropic hardening in accordance with Eq. 10 and the counteracting evolution of the structure variable S_i as a decaying function of the plastic volumetric and deviatoric strain rates. The evolution of the structure variable S_i is given by Eqs. 23 and 24. Whereat, the constitutive parameter k_i specifies the rate of destructuration and the constitutive parameter A describes the fraction of the volumetric and the deviatoric plastic strain rates $\dot{\varepsilon}_\mathrm{v}^\mathrm{p}$ and $\dot{\boldsymbol{e}}^\mathrm{p}$ respectively influencing the destructuration. The initial void ratio and the compression and the swelling index are introduced to ensure consistency with the classical isotropic hardening.

$$\dot{p}_{0,\mathrm{s}} = S_\mathrm{i}\,\dot{p}_{0,\mathrm{i}} + \dot{S}_\mathrm{i}\,p_{0,\mathrm{i}} \tag{22}$$

$$\dot{S}_\mathrm{i} = -k_\mathrm{i}\left\{\frac{1+e}{\lambda-\kappa}\right\}\,\{S_\mathrm{i}-1\}\,\dot{\varepsilon}_{\mathrm{destr}}^\mathrm{p} \tag{23}$$

$$\dot{\varepsilon}_{\mathrm{destr}}^\mathrm{p} = \sqrt{\{1-A\}\,\{\dot{\varepsilon}_\mathrm{v}^\mathrm{p}\}^2 + A\left\{\frac{2}{3}\,\dot{\boldsymbol{e}}^\mathrm{p}:\dot{\boldsymbol{e}}^\mathrm{p}\right\}} \tag{24}$$

2.2.8 Shape Hardening Function

Furthermore, for stress paths inside the bounding surface the plasticity modulus K_p in Eq. 6 is also dependent on the shape hardening function $\hat{h}$ given by Eq. 25. The shape hardening function controls the degradation of the stiffness, the accumulation of plastic strains and accordingly the evolution of the stress-strain response loops during cyclic loading. Whereat, h_0 is a constitutive parameter defining the initial value of the shape hardening function. The accumulation of the plastic strains is captured by the internal damage variable d. The evolution of the damage variable is given by the rate Eq. 26 as a function of the deviatoric plastic strain rate and the constitutive parameter a_dam controlling the rate of evolution. The term $\{p_{0,\mathrm{s}}\}^3$ is added for reasons of stress-dependency and dimensional consistency of the shape hardening function. With increasing plastic deviatoric strain rate during cyclic loading the internal damage variable increases, the shape hardening function decreases and consequently the plasticity modulus and the stiffness reduce as well.

$$\hat{h} = \{p_{0,\mathrm{s}}\}^3\;\frac{h_0}{1+d} \tag{25}$$

$$\dot{d} = a_\mathrm{dam}\left\{\frac{2}{3}\,\dot{\boldsymbol{e}}^\mathrm{p}:\dot{\boldsymbol{e}}^\mathrm{p}\right\}^{1/2} \tag{26}$$

2.2.9 Projection Center

The projection center is always updated to the last point of stress reversal to allow for a more accurate simulation of the evolution of the plastic strains during unloading paths. A stress reversal is revealed by the condition for the plastic loading function $L \leq 0$. That means the next stress increment is pointing inside the imaginary loading surface. After updating the projection center a new image stress on the opposite side of the bounding surface is determined resulting initially in a stiff and predominantly elastic model response. Because the projection center serves as the center of homology for the elastic nucleus the position of the elastic nucleus is updated in a analogue manner. Accordingly, the initial part of the next stress increment yields to purely elastic behavior depending on the size of the elastic nucleus.

Moreover, the projection center has to be updated because it must not be outside the bounding surface when the latter one is updated due to isotropic or rotational hardening, destructuration or softening. This requirement arises from the condition of the uniqueness of the image stress for a given projection center and stress state. The evolution of the projection center $\dot{\boldsymbol{\sigma}}_{\mathrm{pc}}(\dot{p}_{\mathrm{pc}}, \dot{\boldsymbol{s}}_{\mathrm{pc}})$ as a function of the evolution of the internal hardening variables $\dot{\boldsymbol{q}}$ is given by Eqs. 27–30. To ensure the proper position of the projection center the ratio X in Eq. 29 should be kept constant. Whereat $\boldsymbol{s}_\alpha = p_{\mathrm{pc}}\,\boldsymbol{\alpha}$ and $\boldsymbol{s}_{\mathrm{bs}}$ is the stress state on the bounding surface which is closest to the projection center.

$$\dot{p}_{\mathrm{pc}} = \frac{p_{\mathrm{pc}}}{p_{0,\mathrm{s}}}\,\dot{p}_{0,\mathrm{s}} \tag{27}$$

$$\dot{\boldsymbol{s}}_{\mathrm{pc}} = \frac{\boldsymbol{s}_{\mathrm{pc}}}{p_{0,\mathrm{s}}}\,\dot{p}_{0,\mathrm{s}} + \left\{ p_{\mathrm{pc}}\,\dot{\boldsymbol{\alpha}} - X\,\sqrt{\frac{2}{3}}\,\frac{p_{\mathrm{pc}}\,\{p_{0,\mathrm{s}} - p_{\mathrm{pc}}\}\,\frac{3}{2}\,\{\boldsymbol{\alpha} : \dot{\boldsymbol{\alpha}}\}}{\{N^2 - \frac{3}{2}\,\{\boldsymbol{\alpha} : \boldsymbol{\alpha}\}\}\;p_{\mathrm{pc}}\,\{p_{0,\mathrm{s}} - p_{\mathrm{pc}}\}^{1/2}}\,\boldsymbol{n}_{\mathrm{pc}} \right\} \tag{28}$$

$$\begin{aligned} X &= \frac{\sqrt{\frac{3}{2}\,\{\boldsymbol{s}_{\mathrm{pc}} - \boldsymbol{s}_\alpha\} : \{\boldsymbol{s}_{\mathrm{pc}} - \boldsymbol{s}_\alpha\}}}{\sqrt{\frac{3}{2}\,\{\boldsymbol{s}_{\mathrm{bs}} - \boldsymbol{s}_\alpha\} : \{\boldsymbol{s}_{\mathrm{bs}} - \boldsymbol{s}_\alpha\}}} \\ &= \frac{\sqrt{\frac{3}{2}\,\{\boldsymbol{s}_{\mathrm{pc}} - \boldsymbol{s}_\alpha\} : \{\boldsymbol{s}_{\mathrm{pc}} - \boldsymbol{s}_\alpha\}}}{\left\{\{N^2 - \frac{3}{2}\,\{\boldsymbol{\alpha} : \boldsymbol{\alpha}\}\}\;p_{\mathrm{pc}}\,\{p_{0,\mathrm{s}} - p_{\mathrm{pc}}\}\right\}^{1/2}} \end{aligned} \tag{29}$$

$$\boldsymbol{n}_{\mathrm{pc}} = \frac{\{\boldsymbol{s}_{\mathrm{pc}} - \boldsymbol{s}_\alpha\}}{|\boldsymbol{s}_{\mathrm{pc}} - \boldsymbol{s}_\alpha|} \tag{30}$$

Finally, it is to be mentioned that the viscoplastic and strain-rate dependent material behavior is not considered in the present study [18,19,23,25].

3 Calibration of the Constitutive Parameters

For the calibration of the constitutive parameters geotechnical tests under oedometric and triaxial mechanical conditions and drained and undrained hydraulic

conditions are numerically simulated. In the following figures the experimental results are indicated by symbols and the numerical results are indicated by lines. It is to be mentioned that the experimental data are provided by different research groups. However, the testing materials originate from similar site and depths but manifesting slightly different in situ conditions such as void ratio, stress state, degree of structure. Further differences may occur due to disturbance by sampling and due to sample preparation. In spite of these differences, the calibration of the constitutive parameters results in just one parameter set.

The oedometer tests under static loading on reconstituted and natural Onsøy clay from a depth of 9.9–10.3 were conducted at Ruhr-Universität Bochum and described in the study *Cyclic response of natural Onsøy clay – Part I: Experimental analysis*. The void ratio-axial stress behavior is visualized in Fig. 4. The elastic swelling index κ and the elastoplastic compression index λ are determined from the oedometer test on the reconstituted material. The initial value of the internal structure variable $S_{\mathrm{i},0}$ is measured according to the stress sensitivity concept and the constitutive parameters k_{i} and A are used to fit the post-yield destructuration behavior. The bounding surface constitutive parameter s_{eln}, h_0 and a_{dam} are calibrated to capture the elastoplastic behavior during the unloading paths which is similar for the reconstituted and the natural clay. In this study, the elastic nucleus is reduced to a single point by setting the constitutive parameter $s_{\mathrm{eln}} = 1$ in order to have no purely elastic material behavior. The damage parameter a_{dam} is set to a small number because the accumulation of plastic strains is not that distinct in the consolidation analysis afterward.

The Poisson's ratio ν is taken from [21] based on a K_0 loading test followed by an elastic K_0 unloading.

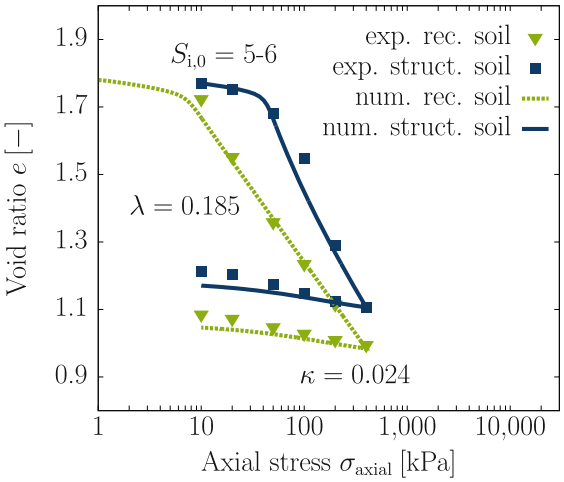

Fig. 4. Axial stress vs. void ratio behavior obtained from oedometer tests on reconstituted and natural Onsøy clay from a depth of 9.9–10.3 m conducted at Ruhr-Universität Bochum

The triaxial test data on natural Onsøy clay are taken from literature. [21] investigated the drained triaxial behavior of anisotropically consolidated Onsøy clay from a depth of 11.4–11.5 m by considering several constant loading paths in compression and extension. Special emphasis is given to the determination of the yield stress with respect to the loading direction. The yield stress different from the in situ stress indicates the initial structure and the multitude of yield stresses from different loading conditions specifies the inherent anisotropy. Consequently, the shape (given by N), the initial size ($p_{0,s}$) and the initial rotation (α_0) of the bounding surface can be derived from the drained triaxial test data by fitting the rotated and distorted ellipse (see Fig. 5).

Furthermore, [37,38] analyzed the undrained triaxial behavior of anisotropically consolidated Onsøy clay from a depth of 10.5–10.9 m in compression and extension. The effective stress paths in Fig. 6 allow for the identification of the critical state stress ratios M_c in compression and M_e in extension. It is to be mentioned that the undrained triaxial test results of [37,38] on different samples show a certain scatter of the stress-strain behavior such as a variation of the value of the peak deviatoric stress. Furthermore, the tests were conducted having faster rate of strain. An increase in strain rate is correlated to a higher deviatoric peak stress. The proposed model in this study is not able to cover strain rate effects.

The constitutive parameter x_α can be calculated based on the closed-form relation for a drained K_0 loading path introduced by [10] shown in Eqs. 31–33. It is to be noted that the initial value of α_0 is derived from the drained triaxial tests as described above and not calculated by $\alpha_{K_0} = \eta_{K_0}/x_\alpha$. This underlies the assumption that the stable state due to the rotation of the plastic potential

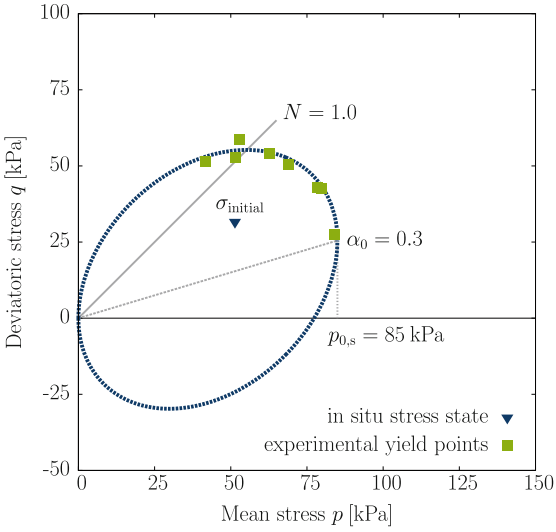

Fig. 5. Rotated bounding surface in p, q effective stress space obtained from anisotropically consolidated drained triaxial tests in compression and extension on natural Onsøy clay from a depth of 11.4–11.5 m [21]

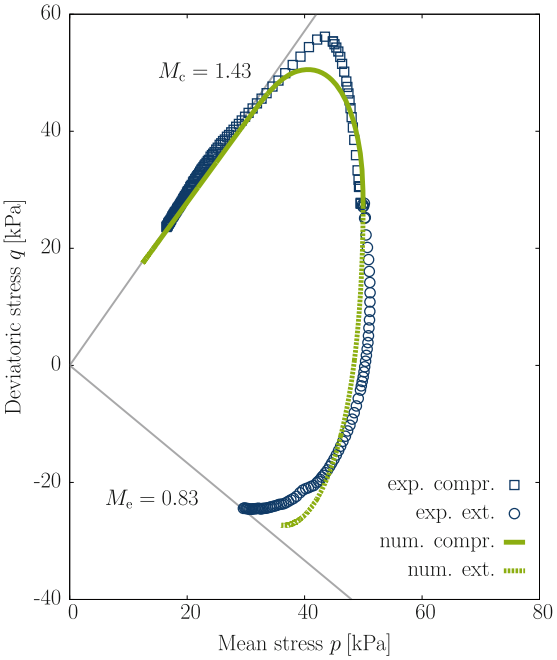

Fig. 6. Effective stress path obtained from anisotropically consolidated undrained triaxial tests in compression and extension on natural Onsøy clay from a depth of 10.5–10.9 m [37,38]

and the bounding surface under K_0 loading is not reached yet. During further loading under a constant η the surfaces will adjust themselves.

$$\alpha_{\mathrm{K}_0} = \frac{\eta_{\mathrm{K}_0}}{x_\alpha} = \frac{3/2\, B\, \eta_{\mathrm{K}_0}^3 + \eta_{\mathrm{K}_0}^2 + \left\{2\, \{1 - \{\kappa/\lambda\}\} - B\, M_c^2\right\} 3/2\, \eta_{\mathrm{K}_0} - M_c^2}{3\, \{1 - \{\kappa/\lambda\}\}} \tag{31}$$

$$B = -\frac{2\, \{1+\nu\}}{9\, \{1-2\,\nu\}}\, \frac{\kappa}{\lambda} \tag{32}$$

$$\eta_{\mathrm{K}_0} = \frac{3\, \{1 - K_0\}}{\{1 + 2\, K_0\}} \tag{33}$$

The constitutive parameter for the evolution of the rotation of the plastic potential and the yield surface is calibrated by fitting against the effective stress path in Fig. 6 and the axial strain-deviatoric stress behavior and the axial strain-excess pore-water pressure behavior illustrated in Fig. 7. The calibration leads to a low value of the constitutive parameter c. This implies that due to a slow rotation the undrained stress path almost follows the shape of the bounding surface both in compression and extension. Furthermore, the bounding surface constitutive parameter s_{eln}, h_0 and a_{dam} can be adjusted.

An overview of the calibrated constitutive parameters is shown in Table 1.

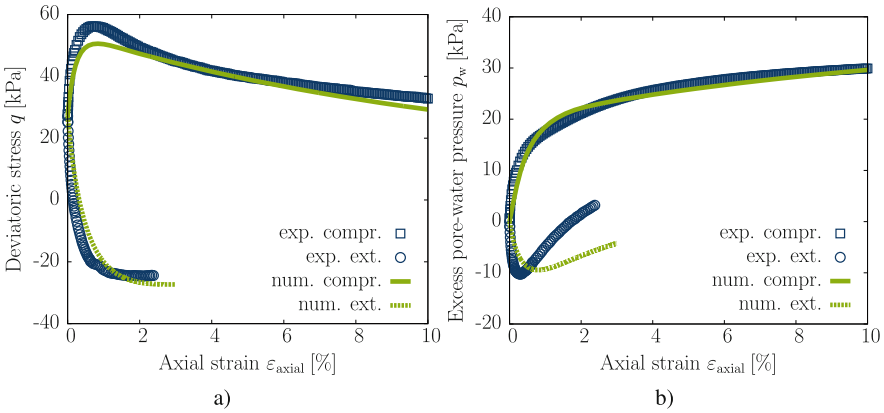

Fig. 7. (a) Axial strain vs. deviatoric stress and (b) axial strain vs. excess pore-water pressure behavior obtained from anisotropically consolidated undrained triaxial tests in compression and extension on natural Onsøy clay from a depth of 10.5–10.9 m [37,38]

Table 1. Constitutive parameters

		MCC	SANICLAY	SANICLAY D	SANICLAY BSP+D
Critical state soil mechanics MCC	κ	0.024	0.024	0.024	0.024
	ν	0.2	0.2	0.2	0.2
	λ	0.185	0.185	0.185	0.185
	M_c	1.43	1.43	1.43	1.43
	M_e	0.83	0.83	0.83	0.83
	N	1.0	1.0	1.0	1.0
Anisotropy rotational hardening	α_0	0	0.3	0.3	0.3
	c	0	10	10	10
	x_α	-	12.2	12.2	12.2
Structure destructuration	S_{i0}	1	1	5	5
	k_i	-	-	0.7	0.7
	A	-	-	0.5	0.5
BSP	s_{eln}	100	100	100	1
	h_0	10,000	10,000	10,000	100
	a_{dam}	0	0	0	1

4 Numerical Modeling of the Consolidation Behavior of Natural Clays Induced by Cyclic Loading

4.1 Concept

In the following section the influence and the necessity of the hierarchical complexity of the constitutive model on the consolidation behavior of natural clays induced by cyclic loading is investigated by use of the finite element method (FEM). Moreover, the numerical results are qualitatively compared with the experimental results. The analysis is conducted by employing the hierarchical structure of the constitutive model. Accordingly, the importance of a certain feature of the model can be elaborated by activation/deactivation of the corresponding constitutive parameters described in the following. In brief, the inherent and the stress-induced anisotropy are deactivated by reducing the constitutive parameters for the initial rotation $\alpha_0 = 0$ and for the evolution of the rotation $c = 0$ respectively. Likewise, the destructuration is disabled by setting the constitutive parameter for the initial structure $S_{\mathrm{i0}} = 1$. Furthermore, the bounding surface is switched to conventional elastoplasticity by increasing the values of the constitutive parameters for the size of the elastic nucleus $s_{\mathrm{eln}} = 100$ and for the initial value of the shape hardening function $h_0 = 10,000$. Add to this, by setting the constitutive parameter $a_{\mathrm{dam}} = 0$ no accumulation of plastic strains induced by cyclic loading is allowed. Consequently, the hierarchical model family is divided into four models listed below. The corresponding constitutive parameters are shown in Table 1. It is to be noted that all models exhibit a Lode angle dependence of the plastic potential and a non-associated flow rule.

- MCC → isotropic hardening and softening
- SANICLAY → additional anisotropy
- SANICLAY D → additional destructuration
- SANICLAY D + BSP → additional bounding surface plasticity

The necessity of the degree of complexity of the constitutive model is evaluated based on the comparison of the model responses of each constitutive model of the hierarchical model family. As the most important model responses in consolidation tests under cyclic loading the evolution of the excess pore-water pressure and the development of the settlements are numerically analyzed.

4.2 Boundary and Initial Conditions

The FEM is an adequate tool for solving geotechnical boundary value problems such as the one-dimensional consolidation induced by cyclic loading. Within the coupled hydro-mechanical consolidation analysis both displacement and pore-water pressure are nodal degrees-of-freedom. The consolidation process is numerically solved according Biot's theory [2]. The geometry (diameter of 7 cm and height of 2 cm) and the mechanical and hydraulic boundary conditions of the simulation model are chosen in accordance with the experimental setup of the

oedometer device introduced in the study *Cyclic response of natural Onsøy clay – Part I: Experimental analysis*. Consequently, the bottom of the sample is vertically fixed and the sample is laterally constraint. The cyclic haversine loading is applied at the top of the sample as a mechanical stress boundary condition, whereat the load amplitude be 200 kPa and the load period be 120 s. Furthermore, the applied hydraulic boundary conditions allow for the drainage of the pore-water at the top of the sample and restricts the sides and the bottom to be impermeable.

In the present study the natural clay sample is chosen and considered as a homogeneous and fully saturated two-phase material composed of solids and pore-water. The effective stresses at the beginning of the simulation are initialized based on the coefficient of lateral earth pressure at rest $K_0 = 0.55$ which is taken from [21]. Moreover, all models initially manifest the same preconsolidation pressure $p_{0,\,\mathrm{s}} = 35$ kPa according to the yield stress derived in the oedometer test under static loading. The initial void ratio $e_0 = 1.783$ is determined in compliance with the experimental data and used to initialize the density. The permeability of the natural clay is assumed to be isotropic in this study. The coefficient of permeability $k = 10^{-8}$ m/s is calibrated against the dissipation behavior of the excess pore-water pressure from the oedometer tests on reconstituted and structured Onsøy clay conducted at Ruhr-Universität Bochum. The void ratio dependence of the permeability following a logarithmic relation is not considered in this study.

4.3 Discussion

In the discussion on the results of the numerical simulations and model predictions data for normalized excess pore-water pressure and settlements will be used. The excess pore-water pressure is normalized by the total stress amplitude 200 kPa, while the settlements are normalized by the maximum value for the

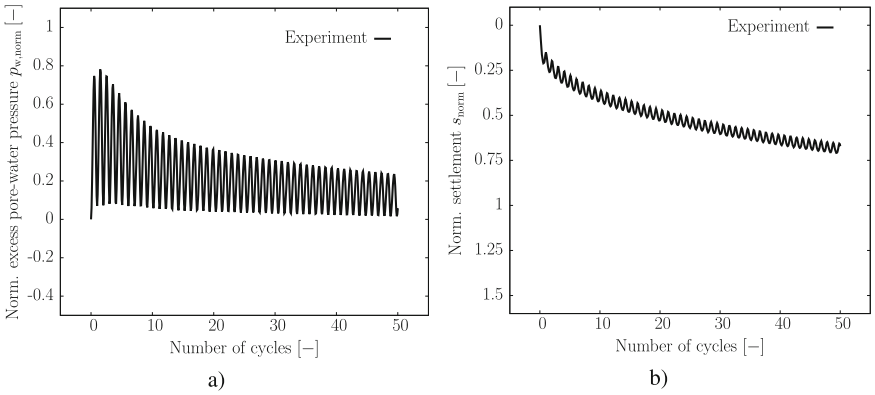

Fig. 8. Experimental data for natural Onsøy clay: (a) normalized excess pore-water pressure and (b) normalized settlement

settlement s in the experiments after 250 cycles where mean value of the excess pore-water pressure oscillates around zero (in our case $s = 3.5\,\text{cm}$).

Figure 8 shows the evolution of the normalized excess pore-water pressure over cycles and the evolution of the normalized settlement over cycles from the consolidation experiment under cyclic loading on natural Onsøy clay using a load amplitude of 200 kPa and a load period of 120 s. The comparison of the experimental results for the evolution of the normalized excess pore-water pressure and the corresponding results from the numerical simulations after employing the four considered constitutive models (Fig. 9) reveals that all models underestimate the reduction in the excess pore-water pressure amplitude and predict negative pore-water pressure fast after first 5–10 cycles. Therefore, there is a need in further analysis of the experimental set-up and the numerical model

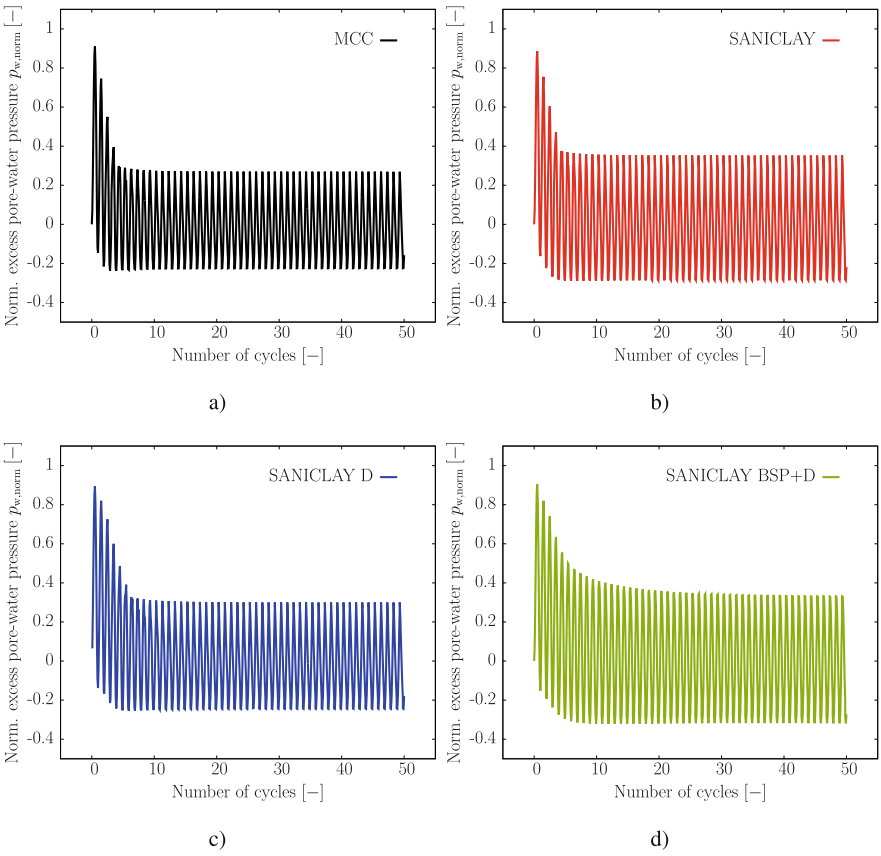

Fig. 9. Evolution of the normalized excess pore-water pressure over cycles from the numerical simulation of consolidation tests under cyclic loading on natural Onsøy clay using a load amplitude of 200 kPa and a load period of 120 s – (a) MCC (b) SANICLAY (c) SANICLAY D (d) SANICLAY BSP+D

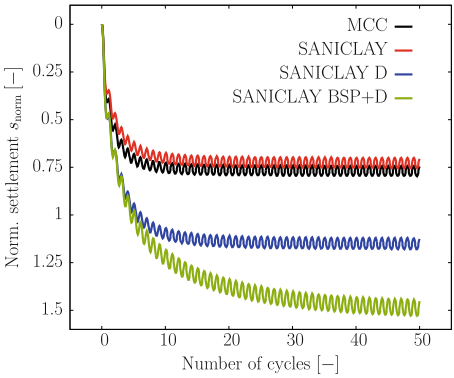

Fig. 10. Evolution of the normalized settlement over cycles from the numerical simulation of consolidation tests under cyclic loading on natural Onsøy clay using a load amplitude of 200 kPa and a load period of 120 s – (a) MCC (b) SANICLAY (c) SANICLAY D (d) SANICLAY BSP+D

including careful check of the consistency of the initial and boundary conditions in the experiment and the corresponding numerical simulation.

Regarding the model predictions for the settlements (Fig. 10) the normalized settlements are most pronounced for the simulations employing the constitutive models with destructuration (SANICLAY D and SANICLAY BSP+D). However, it is to be mentioned that in the experiment (see figure Fig. 8b) approximately just 75% of the maximum settlements are reached after 50 cycles. Similarly like for the normalized pore-water pressure the numerical simulations predict the maximum settlements to be achieved after much less cycles compared to the case in the experiment. While SANICLAY D gives results for the maximum settlements close to those from the experiment, the less complex MCC and SANICLAY models underestimate the corresponding maximum experimental values. Furthermore, due to the accumulation of the plastic strains during cyclic loading the BSP+D model overestimates the corresponding maximum settlements observed in the experiments. It is evident that the complexity in the constitutive mechanical model brings mainly difference in the magnitude of the settlements. It has to be mentioned that a model parameter sensitivity analysis to be made as a future work can give an explanation on the importance of the internal model parameters that are difficult to be identified directly from the available experimental data. Despite these discrepancies the simulations qualitatively well explain the evolution of the settlements with cyclic loading and the reduction of the mean excess pore-water pressure with the increase of the cycle number.

5 Conclusion and Outlook

The objective of the present study is a qualitative numerical analysis of the influence of the hierarchical complexity of a constitutive model on the one-

dimensional consolidation behavior of natural clay induced by cyclic loading. A hierarchical constitutive model based on the BSP concept is introduced and the constitutive parameters are calibrated against various geotechnical element tests on Onsøy clay as a representative for a typical natural clay. The importance of an enriched constitutive model is assessed based on the comparison of the model responses of each constitutive model of the hierarchical model family incorporating different features of the natural clay behavior. The qualitative numerical analysis confirms that the constitutive model is suitable to simulate the one-dimensional consolidation behavior of natural clay induced by cyclic loading. The model is capable to simulate the main phenomena of one-dimensional consolidation induced by cyclic loading. Especially, the ability for simulating the reduction of the mean value of the excess pore-water pressure cycling around zero in the quasi-stationary state, the predominant elastic cycling of the settlements in the quasi-stationary state and the damping of the amplitude of the excess pore-water pressure with an increasing number of cycles are emphasized. Moreover, the importance of an adequate numerical model is pointed up by the significant influence of the destructuration and the features of the BSP concept (such as elastoplastic material behavior in unloading-reloading stress paths) on the model response in one-dimensional consolidation induced by cyclic loading.

The deeper understanding of the one-dimensional consolidation process needs a more sophisticated analysis of the effective stress-strain behavior and especially the evolution of the internal state variables with respect to the cyclic loading. Furthermore, the qualitative analysis presented in the current study has to be continued by investigating the influence of the constitutive parameters on the model responses during cyclic loading by use of a global sensitivity analysis in order to quantitatively compare the numerical with the experimental results.

Acknowledgements. The authors acknowledge the financial support provided by the German Science Foundation (DFG) in the framework of the Collaborative Research Centre SFB 837 (subproject A5).

References

1. Anandarajah, A., Dafalias, Y.F.: Bounding surface plasticity III: application to anisotropic cohesive soils. J. Eng. Mech. **112**(12), 1292–1318 (1986)
2. Biot, M.A.: General theory of three dimensional consolidation. J. Appl. Phys. **12**(2), 155–165 (1941)
3. Burland, J.B.: The yielding and dilation of clay. Géotechnique **15**(2), 211–214 (1965)
4. Burland, J.B.: On the compressibility and shear strength of natural clays. Géotechnique **40**(3), 329–378 (1990)
5. Cotecchia, F., Chandler, R.J.: A general framework for the mechanical behavior of clays. Géotechnique **50**(4), 431–447 (2000)
6. Dafalias, Y.F.: Bounding surface plasticity I: mathematical foundation and hypoplasticity. J. Eng. Mech. **112**(EM9), 966–987 (1986a)

7. Dafalias, Y.F.: An anisotropic critical state soil plasticity model. Mech. Res. Commun. **13**(6), 341–347 (1986c)
8. Dafalias, Y.F., Herrmann, L.R.: Bounding surface formulation of soil plasticity. In: Pande, G.N., Zienkiewicz, O.C. (eds.) Soil Mechanics - Transient and Cyclic Loads, pp. 253–282 (1982)
9. Dafalias, Y.F., Herrmann, L.R.: Bounding surface plasticity II: application to isotropic cohesive soils. J. Eng. Mech. **112**(12), 1263–1291 (1986b)
10. Dafalias, Y.F., Manzari, M.T., Papadimitriou, A.G.: SANICLAY: simple anisotropic clay plasticity model. Int. J. Numer. Anal. Meth. Geomech. **30**, 1231–1257 (2006)
11. Dafalias, Y.F., Taiebat, M.: Anatomy of rotational hardening in clay plasticity. Géotechnique **63**(16), 1406–1418 (2013)
12. Dafalias, Y.F., Taiebat, M.: Rotational hardening with and without anisotropic fabric at critical state. Géotechnique **64**(6), 507–511 (2014). Technical Note
13. Gens, A., Nova, R.: Conceptual bases for a constitutive model for bonded soils and weak rocks. In: International Symposium on Geotechnical Engineering of Hard Soils-Soft Rocks, pp. 485–494. Balkema (1993)
14. Gens, A., Potts, D.M.: Critical state models in computational geomechanics. Eng. Comput. **5**(3), 178–197 (1988)
15. Jiang, J., Ling, H.I.: A framework of an anisotropic elastoplastic model for clays. Mech. Res. Commun. **37**, 394–398 (2010)
16. Jiang, J., Ling, H.I., Kaliakin, V.N.: An associative and non-associative anisotropic bounding surface model for clay. J. Appl. Mech. **79**(3), 031010 (2012)
17. Kaliakin, V.N., Dafalias, Y.F.: Simplifications to the bounding surface. Int. J. Num. Anal. Methods Geomech. **13**, 91–100 (1989). Short communication
18. Kaliakin, V.N., Dafalias, Y.F.: Theoretical aspects of the elastoplastic-viscoplastic bounding surface model for cohesive soils. Soils Found. **30**(3), 11–24 (1990a)
19. Kaliakin, V.N., Dafalias, Y.F.: Verification of the elastoplastic-viscoplastic bounding surface model for cohesive soils. Soils Found. **30**(3), 25–36 (1990b)
20. Lambe, T.W., Whitman, R.Y.: Soil Mechanics. Wiley, New York (1969)
21. Lunne, T., Long, M., Forsberg, C.F.: Characterisation and engineering properties of Onsøy clay. In: Tan, T.S., Phoon, K,K., Hight, D.W., Leroueil, S. (eds.) Characterisation and Engineering Properties of Natural Soils, vol. 1, pp. 395–427. Swets & Zeitlinger (2003)
22. Mitchell, J.K., Soga, K.: Fundamentals of Soil Behavior, 3rd edn. Wiley, Hoboken (2005)
23. Perzyna, P.: Fundamental problems in viscoplasticity. Adv. Appl. Mech. **9**, 243–377 (1966)
24. Potts, D.M., Zdravkovic, L.: Finite Element Analysis in Geotechnical Engineering - Theory. Telford, London (1999)
25. Rezania, M., Taiebat, M., Poletti, E.: A viscoplastic SANICLAY model for natural soft soils. Comput. Geotech. **73**, 128–141 (2016)
26. Roscoe, K.H., Burland, J.B.: On the generalized stress strain behaviour of wet clay. In: Engineering Plasticity, pp. 535–609 (1968)
27. Roscoe, K.H., Schofield, A.N., Thurairajah, A.: Yielding of clays in states wetter than critical. Géotechnique **13**(3), 211–240 (1963)
28. Roscoe, K.H., Schofield, A.N., Wroth, C.P.: On the yielding of soils. Géotechnique **8**(1), 22–53 (1958)
29. Schofield, A.N., Wroth, C.P.: Critical State Soil Mechanics. McGraw-Hill, New York (1968)

30. Seidalinov, G., Taiebat, M.: Bounding surface SANICLAY plasticity model for cyclic clay behavior. Int. J. Numer. Anal. Meth. Geomech. **38**(7), 702–724 (2014)
31. Sheng, D., Sloan, S.W., Yu, H.S.: Aspects of finite element implementation of critical state models. Comput. Mech. **26**, 185–196 (2000)
32. Sloan, S.W.: Substepping schemes for the numerical integration of elastoplastic stress-strain relations. Int. J. Numer. Meth. Eng. **24**, 893–911 (1987)
33. Sloan, S.W., Abbo, A.J., Sheng, D.: Refined explicit integration of elastoplastic models with automatic error control. Eng. Comput. **18**(1–2), 121–194 (2001)
34. Taiebat, M., Dafalias, Y.F., Peek, R.: A destructuration theory and its application to SANICLAY model. Int. J. Numer. Anal. Meth. Geomech. **34**(10), 1009–1040 (2010)
35. Taiebat, M., Kaynia, A.M., Dafalias, Y.F.: Application of an anisotropic constitutive model for structured clay to seismic slope stability. J. Geotech. Geoenviron. Eng. **137**(5), 492–504 (2011)
36. Wheeler, S., Näätänen, A., Karstunen, M., Lojander, M.: An anisotropic elastoplastic model for soft clays. Can. Geotech. J. **40**(2), 403–418 (2003)
37. Wichtmann, T.: Soil behaviour under cyclic loading - experimental observations, constitutive description and applications. Habilitationsschrift, Karlsruher Institut für Technologie (2016)
38. Wichtmann, T., Andersen, K.H., Sjursen, M.A., Berre, T.: Cyclic tests on high-quality undisturbed block samples of soft marine Norwegian clay. Can. Geotech. J. **50**(4), 400–412 (2013)
39. Zienkiewicz, O.C., Pande, O.C.: Some useful forms of isotropic yield surfaces for soil and rock mechanics. In: Finite Elements in Geomechanics, pp. 179–198. Wiley, New York (1977)

Numerical Investigations of the Effects of Dynamic Construction Processes on Deep Excavation Walls

Carla Henning(✉), Andrea Thom, and Achim Hettler

Chair of Mechanics, Structural Analysis and Dynamics, Chair of Soil Mechanics and Foundation Engineering, TU Dortmund University, Dortmund, Germany
carla.henning@tu-dortmund.de

Abstract. Within the scope of the research group FOR 1136 GEOTECH the main objective of subproject 8 (TP 8, part II) was the development of a holistic three-dimensional finite-element model as a framework for further model extensions from other subprojects. Enhanced methods and models for example specific material descriptions, contact element formulations and process approximations should be easily implementable without a loss of reliability of the simulation results. During model development, Thom and Hettler showed that capturing the construction processes and their effects on deep excavation walls by use of dynamic calculation exceeds present storage and computation capacities [1]. The adaptability of the existing model is used to pursue another approach. A more efficient method was developed which nevertheless incorporates the decisive effects of the dynamic influences. Additionally, the advantages and disadvantages of different material models are discussed.

Keywords: Finite-element modelling · Construction-induced deformations · Material modelling

1 Introduction

The excavation of the Potsdamer Platz in Berlin in 1993 is a suitable base for theory and method development, because of comprehensive measurements which were necessary for monitoring and quality management, cf. [2]. Its large dimensions with spans of up to 200 m and depths of up to 25 m required a high construction precision and continuous control. Since the ground water level is 3 m below ground level, the pits were constructed with an anchored underwater concrete bottom slab and tied-back diaphragm walls, see Fig. 1(a). The unexpected additional horizontal displacements of the deep excavation wall, as shown for two measurement points in Fig. 1(b) and (c) are caused by the installation of vibrated RI-piles. The significant difference between the horizontal displacements of the cross sections can be explained by the dynamical installing direction of the RI-piles: construction of RI-piles parallel to the wall (Fig. 1(b)) and orthogonally (Fig. 1(c)).

T. Triantafyllidis (ed.), *Holistic Simulation of Geotechnical Installation Processes*,
Lecture Notes in Applied and Computational Mechanics 82, DOI 10.1007/978-3-319-52590-7_13

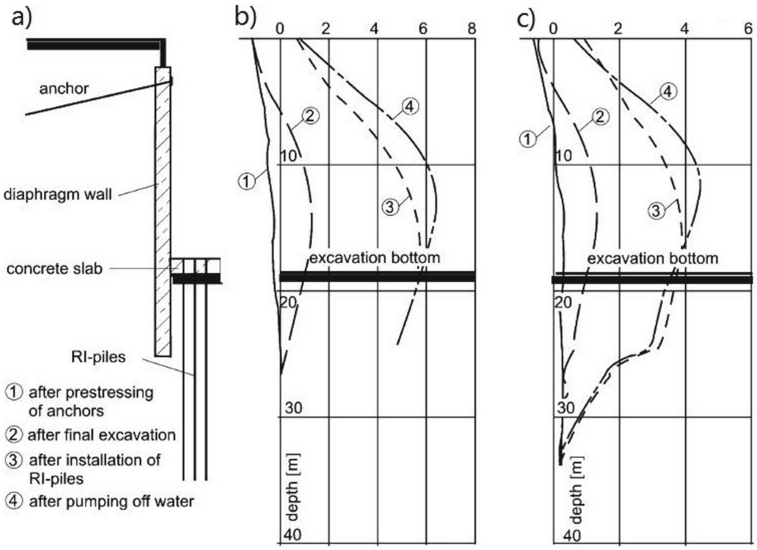

Fig. 1. Debis excavation at Potsdamer Platz (a) cross-section of excavation, (b) horizontal displacements in cs MV1, (c) horizontal displacements in cs MV2, cf. [2]

Thom and Hettler introduced the following model in detail in [1]. The evaluation for a dynamic simulation of installing the vibrated RI-piles is also discussed, but the calculation method exceeded present computation capacities. Section 2 provides an overview of the geometrical model as well as the quasi-static process approximations and Sect. 3 shows an alternative approach for the computation of the dynamic vibration step. The material model impact is shown by means of two examples. Concluding remarks are discussed in Sect. 4.

2 Numerical Model

The finite-element-program ABAQUS was used to create the 3D-model. The chronological order of the construction process can be classified roughly by the 'wished-in-place' installation of the diaphragm wall, an initial excavation by deactivating the corresponding elements, prestressing of anchors, realized by the definition of the feather rigidity at the corresponding places, the second excavation to the bottom of the pit and finally, the installation of the vibrated RI-piles. Figure 2 shows an exploded view of the conclusive FE-model with information about the material layers, contact definitions and geometric divisions. The latter is necessary for the controlling of the FE-mesh structure (refinement of the elements towards the diaphragm wall; element deactivation has to correspond to the actual excavation depth). An established material model for the numerical description of soil is the enhancement of the classical hypo-plasticity (von Wolffersdorff [3]) by Niemunis and Herle [4], which additionally takes the elastic strain range into account. This is used for the first calculation example,

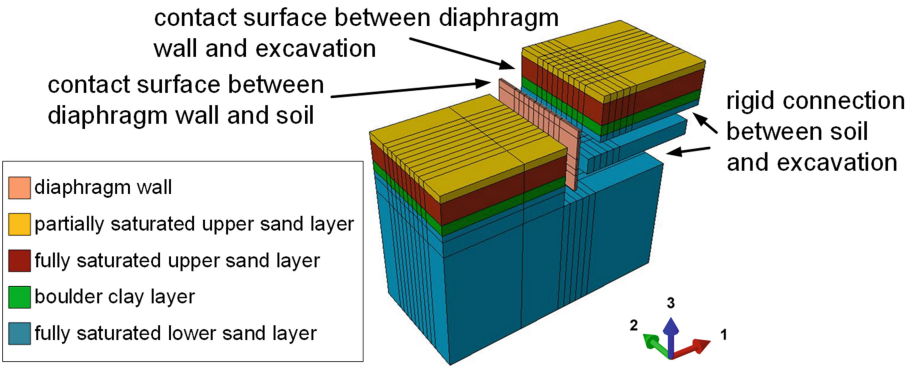

Fig. 2. Overview of the 3D finite element model

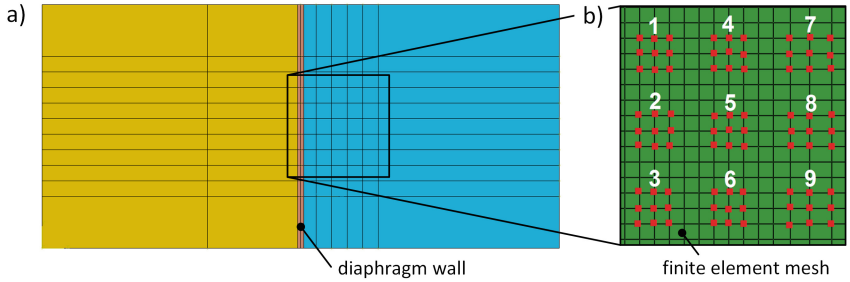

Fig. 3. (a) Model top view (b) RI-pile field and numbering

the classical hypo-plasticity for the second one. The new approach for reducing the computational effort of the dynamic vibration process by applying a pore water overpressure in close vicinity of the piles instead, is motivated by Osinov, cf. [5,6]. He analyzed the effect of soil liquefaction in consequence of RI-pile construction in detail. Here, the soil is approximated by multi-phase C3D8P-elements, which take the solid as well as the liquid phase into account. Through additional mass and interaction terms, the pore pressure λ is solved simultaneously and can be used to apply the overpressure during the vibration process as a boundary condition instead of the dynamic loading. The top view in Fig. 3(a) shows the location of the representative field of nine RI-piles. The construction of each pile is approximated by an assembly of nodes with a depth of 22 m corresponding to the pile length. The numbering in Fig. 3(b) complies with the activation of the boundary conditions.

3 Numerical Solutions

The enhanced hypo-plasticity by Niemunis and Herle is used to approximate the dynamic vibration process of the RI-piles by a quasi-static pore water overpressure, see Sect. 3.1. Due to insufficient accordance with the measured data,

also the classical formulation of hypo-plasticity by von Wolffersdorff is implemented through the USER-interface of the model in Sect. 3.2, to enable an assessment of advantages and disadvantages of the elastic strain range consideration.

3.1 Example 1: Consideration of the Elastic Strain Range

The first modification of the dynamic approximation of the vibration process was to change the method into a static one, as described earlier. Accordingly, the enhanced hypo-plasticity was used likewise. Figure 4 shows the displacement solutions u_1 for the whole geometry after the completed excavation process (a), the application of pore water overpressure (b) as well as the diaphragm wall deformations compared with the measurement data in both cases (c). After the excavation process, the global soil displacements (a) as well as the horizontal deformation of the diaphragm wall (c) correspond to earlier solutions and match the measured values quite well. The only exception is the upper section, where the effected assumptions for the anchors neglect the wall movement because of prestressing forces. As a result of this, the maximum displacements are overestimated. A striking fact is the very small increase of deformations due to the pore water overpressure. That is probably the consequence of the overestimation of stiffness increase by the material model. Strain evaluation of soil elements close to the wall suggests an elastic material response, so the strain and displacement accumulation through cyclic loading is not possible.

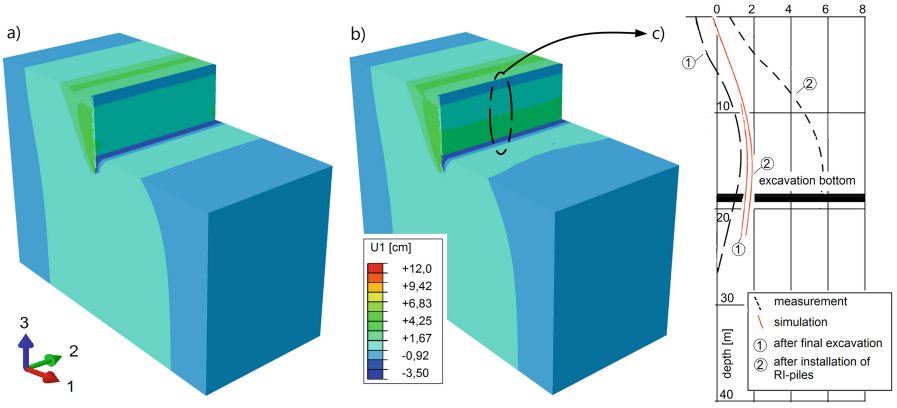

Fig. 4. Horizontal displacements u_1 soil and diaphragm wall (a) after excavation (b) after applying pore water overpressure λ (c) wall displacements at both points in time

3.2 Example 2: Neglect of the Elastic Strain Range

The second example uses the initial formulation of hypo-plasticity without consideration of the elastic strain range to verify the presumption of Sect. 3.1.

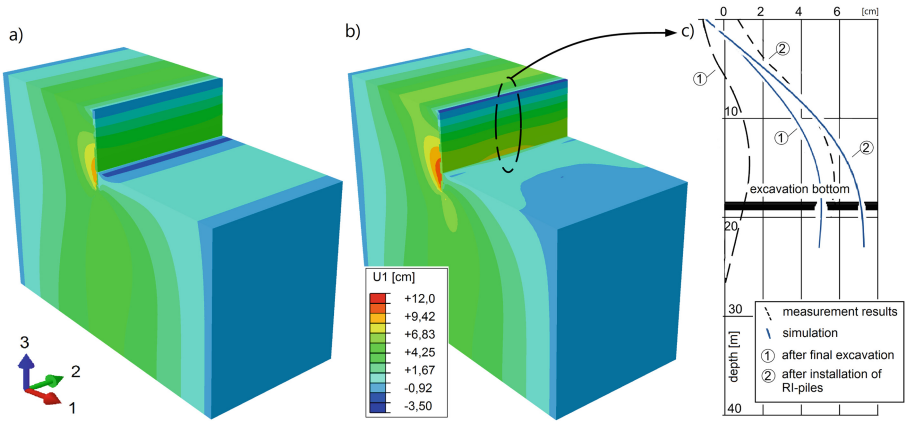

Fig. 5. Horizontal displacements u_1 soil and diaphragm wall (a) after excavation (b) after applying pore water overpressure λ (c) wall displacements at both points in time

Figure 5(a), (b) and (c) show the same evaluations as Fig. 4, but for the simplified material model. The difference in magnitude is significant. Unlike the first example, the increase of deformation Δu due to pore water overpressure close to the RI-piles, achieves realistic dimensions considering that there is just a small field of RI-piles in contrast to the real excavation pit. Whereas an obvious deficiency is the deviation of the first solution state from the measured data. The deformations of the diaphragm wall after the completed excavation process are highly overestimated.

3.3 Comparison of the Variants

While the modified hypo-plasticity is able to map all static processes of the excavation precisely, it fails to capture the influence of pore water overpressure λ in combination with the two-phase C3D8P elements. Whereas the classical formulation captures the static approach for the installation of the vibrated RI-piles, but totally overestimates the construction process of the excavation.

4 Discussion

A comprehensive FE-model was used to capture an alternative approach for cyclic and dynamic loading. For this aim, two different material formulations were used to get the structure response of the interaction between soil and earth structures. Both material models are insufficient for the whole construction process, because their results just partially match to available measurements. Generally, the FE-model is a good framework, because it captures all processes including all simplifications and approaches. It can be used for further investigations on enhancements of material or process modeling, because individual

components can easily be exchanged, for example the material model through the USER-surface.

Acknowledgment. The work presented in this paper was supported by the German Research Foundation (DFG) as subproject 8 "Numerical investigations of the effects of dynamic construction processes on deep excavation walls" of the interdisciplinary research group FOR 1136 "Simulation of geotechnical construction processes with holistic consideration of the stress strain soil behavior (GeoTech)". The authors appreciate the financial support from the DFG. The authors also like to thank their colleagues of Karlsruhe Institute of Technology (KIT) who supported the authors by providing the material models for the numerical calculations.

References

1. Thom, A., Hettler, A.: Prediction of construction-induced deformations of deep excavation walls by the use of a holistic 3D-finite-element model. In: Triantafyllidis, T. (ed.) Holistic Simulation of Geotechnical Installation Processes. LNACM, vol. 80, pp. 231–239. Springer, Heidelberg (2016). doi:10.1007/978-3-319-23159-4_11
2. Triantafyllidis, T.: Neue Erkenntnisse aus Messungen an tiefen Baugruben am Potsdamer Platz in Berlin. Bautechnik **75**, 133–154 (1998). Heft 3
3. von Wolffersdorff, P.-A.: A hypoplastic relation for granular materials with a predefined limit state surface. Mech. Cohesive-Frictional Mater. **I**, 251–271 (1996)
4. Niemunis, A., Herle, I.: Hypoplastic model for cohesionless soils with elastic strain range. Mech. Cohesive-Frictional Mater. **II**, 279–299 (1997)
5. Osinov, V.A., Chrisopoulos, S., Triantafyllidis, T.: Numerical study of the deformation of saturated soil in the vicinity of a vibrating pile. Acta Geotechnica **8**, 439–446 (2013)
6. Osinov, V.A.: Application of a high-cycle accumulation model to the analysis of soil liquefaction around a vibrating pile toe. Acta Geotechnica **8**, 675–684 (2013)

Total and Quasi-Elastic Strains Due to Monotonous and Low-Cycle Loading by Means of Experimental and Numerical Element Tests

Stefanie Danne(✉) and Achim Hettler

Chair of Soil Mechanics and Foundation Engineering,
TU Dortmund University, Dortmund, Germany
Stefanie.Danne@tu-dortmund.de

Abstract. It is known that some common constitutive models show deficits when predicting elastic and plastic deformations due to low cycle loading resulting for example from geotechnical installation processes. The aim of part I of subproject 8 within the DFG research group FOR 1136 (GeoTech) is to show the performance of different constitutive models and to compare them with experimental results and between each other.

Series of drained, stress-controlled triaxial-tests are carried out. The strains from monotonous and low-cycle loading are investigated systematically, regarding total and quasi-elastic strains as well as strain accumulation.

All experiments are recalculated numerically with different constitutive models, amongst them some common as well as advanced constitutive models, which have been developed recently and partly within the aforementioned research group GeoTech. By comparing the experimental and numerical results systematically, an attempt is made to show the model's advantages and deficits and to give hints for the application in boundary value problems.

Keywords: Low-cycle loading · Triaxial tests · Strain response envelopes · Incremental stress-strain behaviour · Granular soils

1 Introduction

In practical applications soil elements can be subject to monotonous as well as to stress or strain cycles with different magnitudes of amplitudes. Constitutive equations used to solve boundary value problems (BVPs) should generally be able to model all these loading situations and predict resulting stresses and deformations realistically.

Especially when it comes to cyclic loading, occurring for example during geotechnical installation processes, it is well known, that some common constitutive models show deficits when predicting elastic and plastic deformations with regard to magnitude as well as to accumulation.

Cyclic loading processes can be divided into high-cycle and low-cycle loading, depending on the number of cycles. To avoid numerical errors and high computing time, it is often useful to calculate deformations due to high-cycle loading by means of

T. Triantafyllidis (ed.), *Holistic Simulation of Geotechnical Installation Processes*,
Lecture Notes in Applied and Computational Mechanics, 82, DOI 10.1007/978-3-319-52590-7_14

explicit models, where irreversible strains are treated similar to creep deformations under constant loads, Niemunis et al. (2005). In Wichtmann's High Cycle Accumulation model e.g. the strain amplitudes are limited to $\Delta\varepsilon \leq 10^{-3}$. So it is appropriate to use other constitutive equations for low number of cycles N, when the magnitude of strains is $\geq 10^{-3}$. Low-cycle loading processes can be roughly defined with $N \leq 50$, Danne and Hettler (2013). In these cases, an implicit calculation of deformations may be appropriate.

In this paper the performance of five common and advanced constitutive models is examined by experimental and numerical element tests with monotonous and low-cycle loading.

After describing some fundamentals in Sect. 2, the resulting strains from experimental and numerical element tests are evaluated separately and divided into

- total strains by monotonous loading (Sect. 3),
- strain accumulation during low cycle loading (Sect. 4) and
- quasi-elastic strains due to low cycle loading (Sect. 5)

The summary at the end of this paper contains some preliminary recommendations which of the considered constitutive equations might be most suitable for application in BVPs.

2 Fundamentals

2.1 Triaxial Device and Testing Procedure

The triaxial device used for the experiments is equipped with high-resolution measurement- and control-technology. The confining pressure as well as the axial force can be controlled independently, so that stress paths in different directions from any initial stress-state can be carried out.

The tested soil is a fine grained sand with a low uniformity-index ($C_U = 1.25$, $d_{50} = 0.15$ mm), having a positive impact when it comes to avoid effects from membrane penetration, investigated e.g. from Nicholson et al. (1993). Height and diameter of the soil specimen are 10 cm.

The soil sample is fabricated by pluviating dry sand thereby maintaining a constant height. This specimen-preparation-method was kept constant for all tests. The achieved relative densities I_D were well reproducible with small deviation (± 0.1). Starting at isotropic stress, the predefined initial stress-state was reached, either by increasing the vertical stress σ_1 (for stress-states in compression) or the horizontal stress σ_3 (for stress-states in extension). Then the soil sample was consolidated.

The experiments are carried out with dense soil samples ($I_D \approx 0.75$). Corresponding results from loose samples are described in Danne (2017). The investigated initial stress-states are shown in Table 1.

The stress controlled experiments are carried out under drained conditions. Therefore stresses are effective stresses ($\sigma = \sigma'$). Cyclic loading is performed at low frequency during low-cycle loading to avoid pore water pressure and maintain pure drained conditions.

Table 1. Initial stress-states in terms of mean pressure p and deviatoric stress q

Stress state	p [kPa]	q [kPa]	Stress–Ratio η = q/p [–]	
A	200	150	0.75	Compression
I	200	0	–	Isotropic
J	200	–100	–0.5	Extension

A detailed description of experimental fundamentals can be found in Danne and Hettler (2015) and Danne (2017).

2.2 Stresses and Strains

The definition of a stress or increment is described in Eqs. (1) and (2).

$$\Delta\sigma = \sqrt{\Delta\sigma_1^2 + 2\Delta\sigma_3^2} \tag{1}$$

$$\Delta\varepsilon = \sqrt{\Delta\varepsilon_1^2 + 2\Delta\varepsilon_3^2} \tag{2}$$

The stress vector can be quantified by plotting the strains in the rendulic plane, see e.g. Gudehus (1979). In this plane, the direction of stress increment can be described by the angle α_σ between stress vector and the positive $\sqrt{2}\ \sigma_3$-axis.

2.3 Constitutive Equations

The following constitutive equations are investigated:

- Hardening Soil-model (HS)
- elasto-plastic model based on the theory of porous media (TPM)
- Hypoplasticity with intergranular strain (IS)
- Intergranular Strain Anisotropy-model (ISA)
- Simple Anisotropic Sand Plasticity model (Sanisand)

2.3.1 Hardening Soil-Model

The Hardening Soil-model ("HS-model") developed by Schanz (1998) is formulated in the framework of classical theory of plasticity. Total strains are calculated using a stress-dependent stiffness, different for first loading and un-/reloading. Plastic strains are calculated by introducing a multi-surface yield criterion. Hardening is assumed to be isotropic depending on both the plastic shear and the volumetric strain. For the frictional hardening a non-associated and for the cap hardening an associated flow rule is assumed.

The numerical calculations have been carried out with the programme Plaxis 2D. The required parameters have been determined experimentally with standard laboratory tests.

2.3.2 TPM-Model

The theory of porous media (TPM) is a general thermodynamically consistent continuum mechanic concept to macroscopically describe common multiphase materials. The theory describes systems, which consist of a porous solid, whose pores are filled by one or more fluids, e.g. liquids or gases. The different parts are not regarded separately; instead a certain volume part is allocated to each part at each point. In soil mechanic applications it is assumed, that a partly saturated soil consists of a solid phase (incompressible grains), a liquid phase (incompressible pore water) and a gas phase (compressible pore gas or air), Ehlers (1996). The considered constitutive equation was developed by Ehlers et al. (2011) within the framework of TPM. It determines deformations by a single yield criterion with isotropic hardening and a yield surface, depending from hydrostatic stress state.

The 29 required parameters for a fine sand, which is very similar to the fine sand used by the authors, were determined and provided by the institute of applied mechanics at Stuttgart University.

2.3.3 Hypoplastic Model with IS

The hypoplastic constitutive model describes the stress-strain behaviour of non-cohesive soils in rate form. Its present version was formulated by von Wolffersdorff (1996). Small strain stiffness formulation (so-called intergranular strain "IS" concept) was added by Niemunis and Herle (1997). All hypoplastic calculations have been carried out with the IS extension.

The parameter set for the tested fine sand has been determined and provided by colleagues of the Karlsruhe Institute of Technology (KIT). The numerical calculations have been carried out with Niemunis' "incremental driver" Niemunis (2008), which has also been provided by the KIT.

2.3.4 Sanisand-Model

The Sanisand-model was developed within the framework of critical state soil mechanics and bounding surface plasticity Taiebat and Dafalias (2008). As analytical description of a narrow but closed cone-type yield surface, that obeys rotational and isotropic hardening, an 8-curve equation is used.

Here too, the colleagues of the KIT have determined the parameters for the tested sand and provided them to the authors. Niemunis' "incremental driver" has been used for the numerical calculations.

2.3.5 Intergranular Strain Anisotropy-Model

The elastoplastic ISA-model recently introduced by Fuentes (2014) is based on the intergranular strain concept, but contrary to the existing formulations it proposes a yield function describing a surface within the intergranular strain space. It includes an elastic locus in the intergranular strain space.

The numerical calculations have been carried out with Niemunis' "incremental driver"; the required parameters for this model have been determined by colleagues of the KIT and provided to the authors.

3 Monotonous Loading

The experimental and numerical results for monotonous loading are evaluated by means of so called "strain response envelopes" (SRE), first mentioned in Lewin and Burland (1970) and Gudehus (1979). Some important and often-cited experiments including a detailed description of the test procedure can be found e.g. in Doanh (2000), Calvetti (2003) or Costanzo et al. (2006). Further results see Danne (2017).

After the soil sample is consolidated at a predefined stress state, stresses are in- or decreased in a certain loading direction until a limit state is reached. For all loading directions one equally prepared and consolidated sample is used.

3.1 Triaxial Compression (Stress State A)

Figure 1 shows the experimental and numerical results determined for stress state A, see Table 1. Apart from the hypoplastic and the ISA-model, all envelopes are approximately symmetrical to their long axis. Best qualitative agreements with the experiments can be found using both elastoplastic models, the HS- and TPM-model, Fig. 2c and d.

Comparing the strains due to the stress increment $\Delta\sigma = 50\,\text{kPa}$ for example (bold line in Fig. 1) best agreements with the experiments concerning the magnitude of the strains can be obtained with the elastoplastic TPM- and the hypoplastic model. Strains calculated with the ISA- and with HS-model are too small. For deviatoric unloading – leading to positive radial and negative axial strains – the strains predicted with the hypoplastic and the ISA-model seem to be too small and the unloading stiffness too large respectively. The shapes of the SREs derived from hypoplastic calculations show a small bulge due to the strain response for isotropic compression ($\alpha_\sigma = 35°$). This cannot be observed experimentally.

Plotting the absolute value of strains depending on the loading direction, a better quantitative evaluation of the results is possible, Fig. 2.

All models show the largest strains due to deviatoric loading. The experimental results lie between the numerical curves. Strains from hypoplasticity and the TPM-model are equal or larger than the experiments. Strains calculated with the Sanisand and the ISA-models are significantly smaller for both stress increments, Fig. 2.

Considering the results for $\Delta\sigma = 50\,\text{kPa}$ in Fig. 2b, the total strains calculated with the hypoplastic model match very well with experiments. Hypoplastic strains due to a smaller stress increment $\Delta\sigma = 20\,\text{kPa}$ however are almost twice as large as the experimental ones at deviatoric unloading ($\alpha_\sigma \approx 315°$), Fig. 2a. For the smaller stress increment, best agreements between the HS-model and the experiments can be observed.

At deviatoric unloading there are better agreements between constitutive equations and experiments, for the differences of the magnitudes of strains are not that significant. The largest unloading-stiffness however can be observed for the hypoplastic model, which is almost twice as large as the ones observed experimentally.

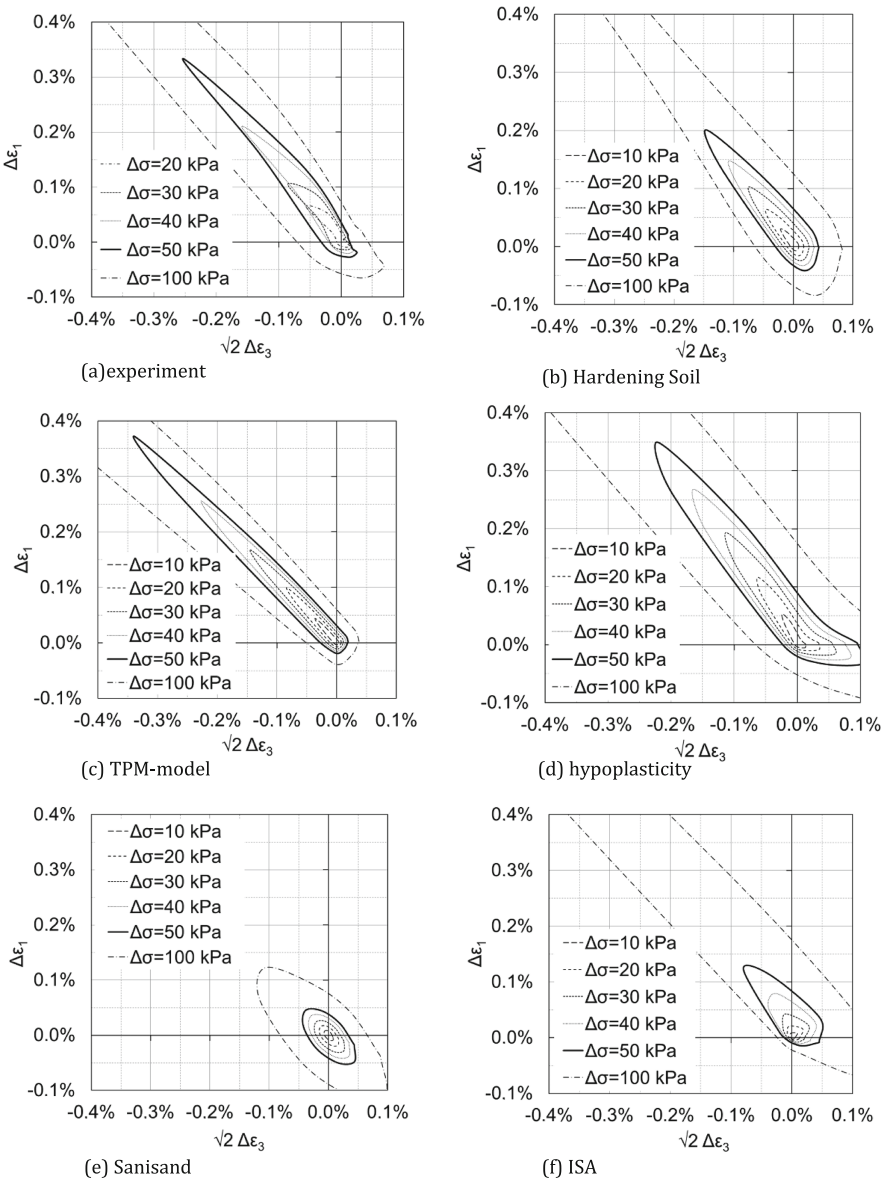

Fig. 1. Strain response envelopes due to monotonous loading for stress state *A*, $I_D \approx 0.75$

3.2 Isotropic Stress State (I)

Starting from the isotropic axis (stress state I, see Table 1), the shapes of the SREs for stress increments $\Delta\sigma \leq 50$ kPa are almost symmetrical for the two elastoplastic models and the experiments, Fig. 3a, b, and c. For larger stress increments the envelopes become elongated towards extension. This might be explained by the fact, that unloading in extension is closer to the failure line than in triaxial compression.

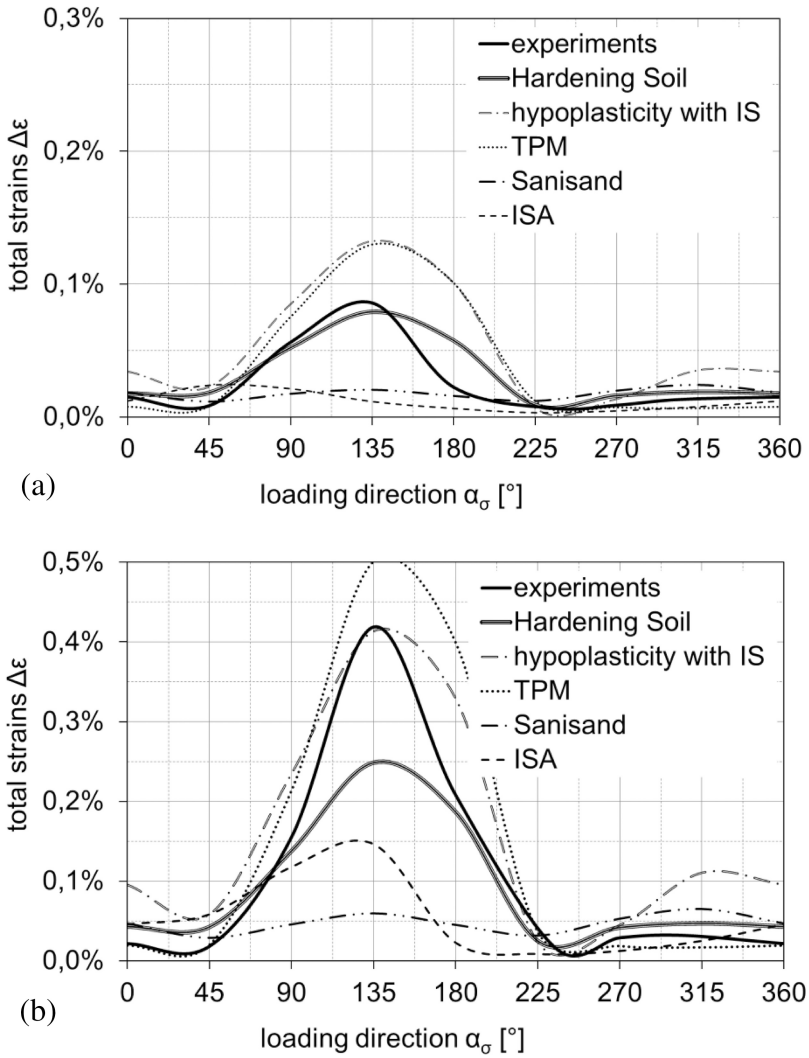

Fig. 2. Absolute value of total strains $\Delta\varepsilon$ due to monotonous loading depending on loading direction α_σ, stress state *A*, $I_D \approx 0.75$: (a) $\Delta\sigma = 20\,\text{kPa}$, (b) $\Delta\sigma = 50\,\text{kPa}$

The hypoplastic and the ISA-model in Fig. 3d and f show significant differences – already observed in compression – between strains due to isotropic compression with positive radial and axial strains and isotropic extension with negative radial and axial strains.

Strains due to this stress increment calculated with the ISA- and the TPM-model seem to be too small for almost all loading directions. For the hypoplastic and the ISA-model it can once again be observed that deviatoric unloading, leading to positive radial and negative axial strains, cannot be reproduced correctly, because the envelopes

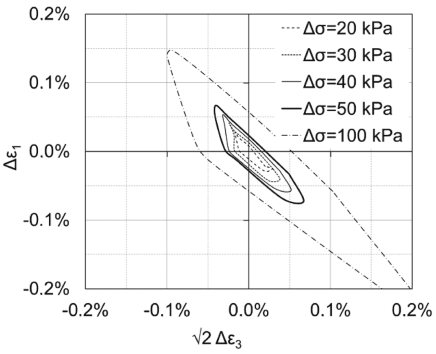

(a) experiment

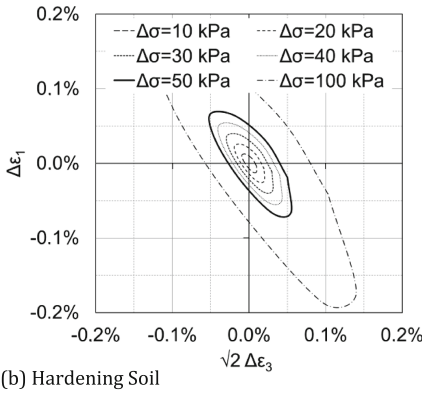

(b) Hardening Soil

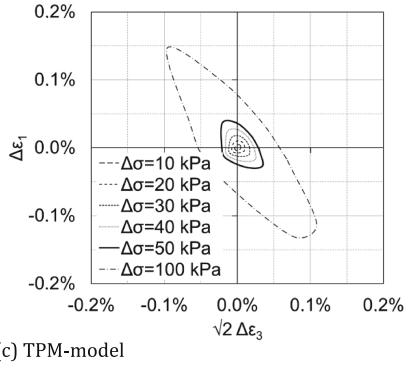

(c) TPM-model

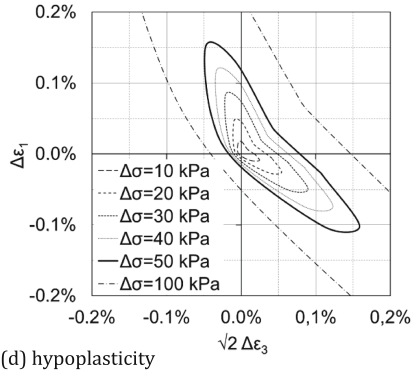

(d) hypoplasticity

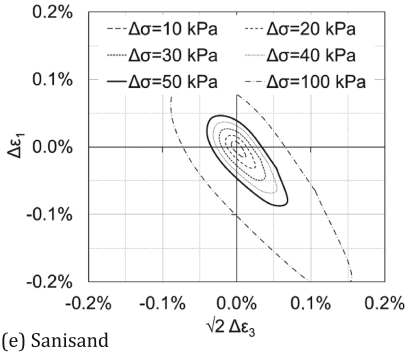

(e) Sanisand

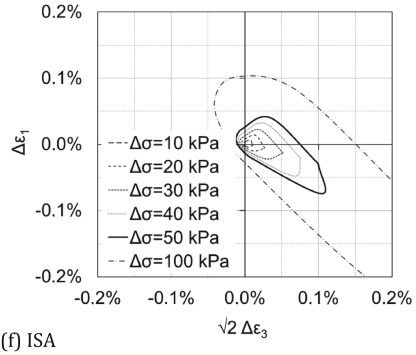

(f) ISA

Fig. 3. Strain response envelopes due to monotonous loading for stress state *I*, $I_D \approx 0.75$

are too small and the stiffness is too large respectively. For the hypoplastic SREs a little bulge within the envelope's shape can be observed, resulting from the strain response due to isotropic compression ($\alpha_\sigma = 35°$).

Figure 4 shows the absolute values of total strains due to a constant strain increment depending on the loading direction. It is obvious that the agreements between the ISA-model and the experiments and all other models are rather poor.

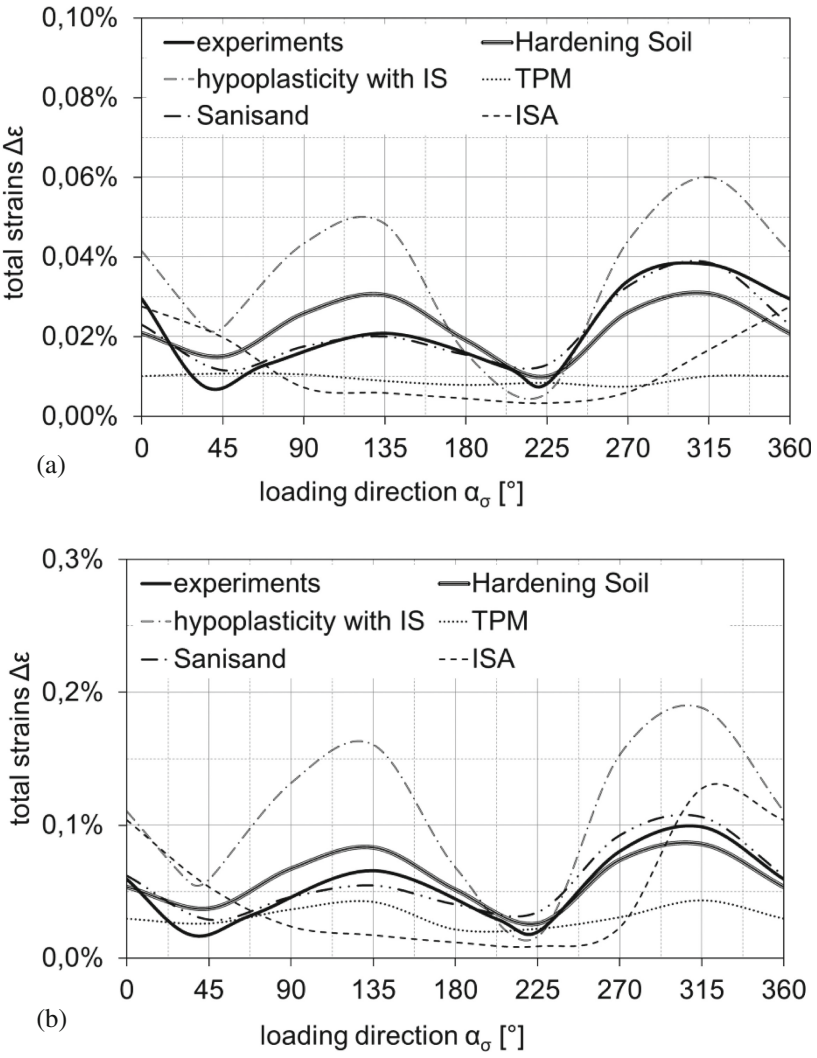

Fig. 4. Absolute value of total strains $\Delta\varepsilon$ due to monotonous loading depending on loading direction α_σ, stress state *I*, $I_D \approx 0.75$: (a) $\Delta\sigma = 20\,\text{kPa}$, (b) $\Delta\sigma = 50\,\text{kPa}$

This is also the case for the hypoplastic strains at deviatoric loading ($\alpha_\sigma \approx 125°$), where strains are almost three times larger than the experimental results.

For both stress increments the strains from the HS-model are closest to the experimental results. However, this is not the case for extension; here the strains from the Sanisand- and hypoplasticity-model are the largest and fit the experimental results best.

3.3 Triaxial Extension (Stress State J)

In Fig. 5 it can be noticed that the agreements between experimental and numerical results in extension are less than in compression.

While the experiments lead to relatively slim SREs, all numerical SREs are wider. The hypoplastic strains are the largest, followed by the ISA-model. Like in the

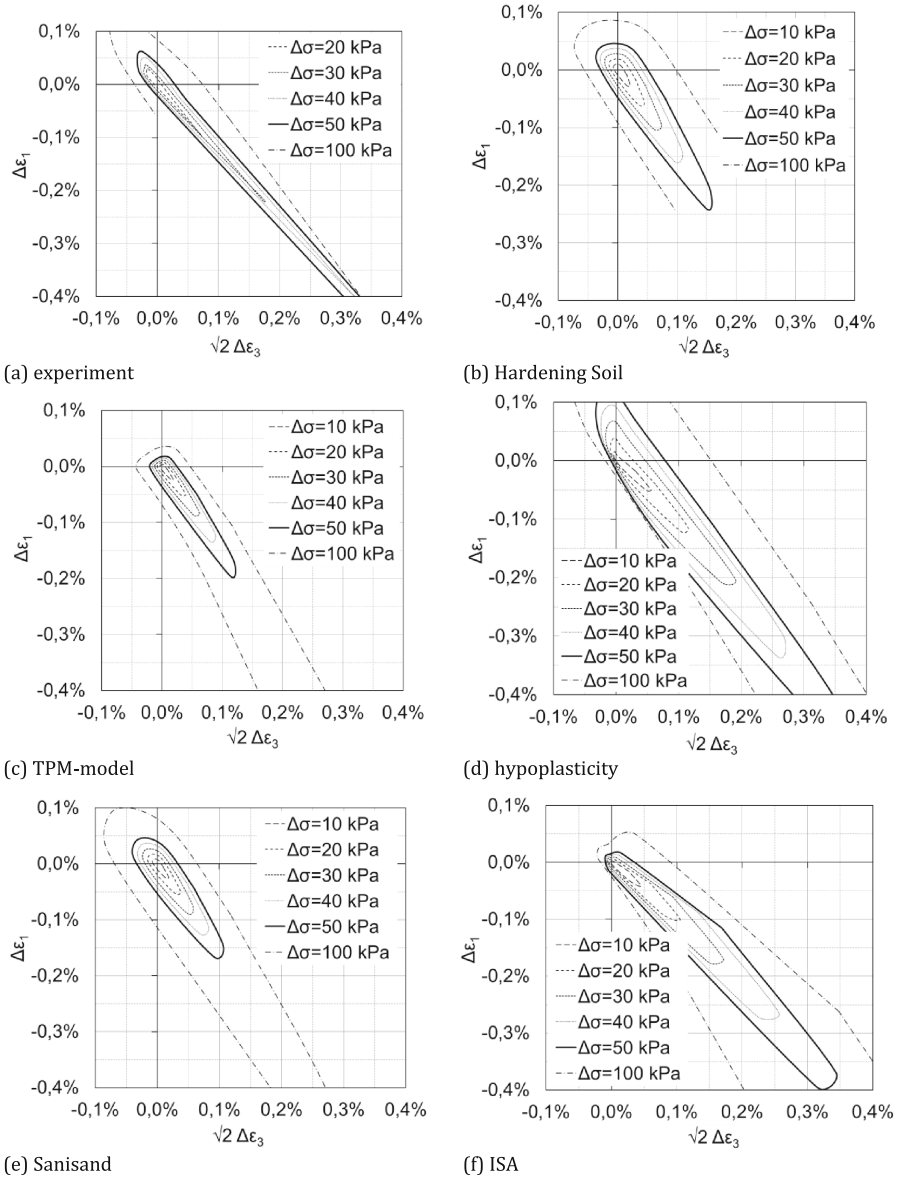

(a) experiment (b) Hardening Soil

(c) TPM-model (d) hypoplasticity

(e) Sanisand (f) ISA

Fig. 5. Strain response envelopes due to monotonous loading for stress state *J*, $I_D \approx 0.75$

experiments the stress increment $\Delta\sigma = 100\,\text{kPa}$ cannot fully be applied with the HS-model in all directions; the outer envelope is not closed.

For a constant stress increment ($\Delta\sigma = 20\,\text{kPa}$ and $\Delta\sigma = 50\,\text{kPa}$), Fig. 6 shows the absolute values of total strains depending on the loading direction. It can be observed that the experimental strains due to loading directions towards the failure line in extension ($\alpha_\sigma \approx 225° \cdots 315°$) are much larger than the numerical results.

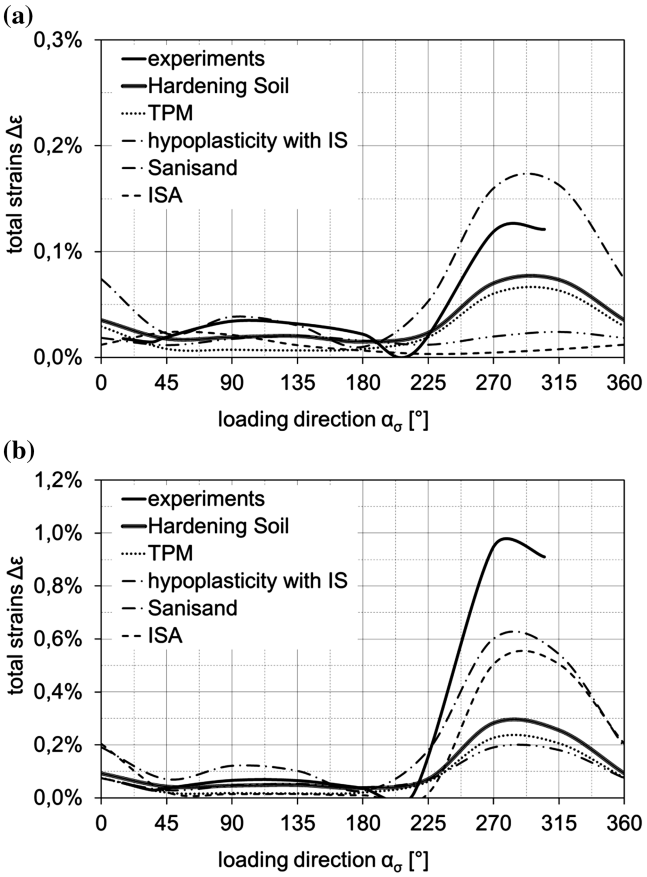

Fig. 6. Absolute value of total strains $\Delta\varepsilon$ due to monotonous loading depending on loading direction α_σ, stress state *J*, $I_D \approx 0.75$: (a) $\Delta\sigma = 20\,\text{kPa}$, (b) $\Delta\sigma = 50\,\text{kPa}$

4 Low Cycle Loading with Regard to Total Strain Accumulation

The strain accumulation during low-cycle loading is investigated by applying deviatoric stress cycles with $\Delta p = 0$ and $\Delta q \neq 0$ on a soil element at the isotropic stress-state I (Table 1).

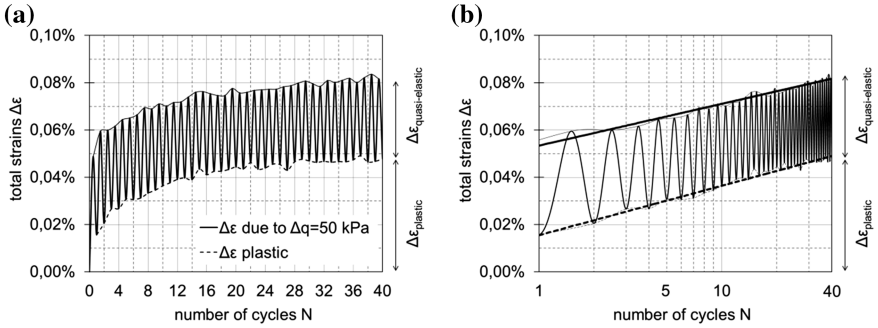

Fig. 7. Strain accumulation due to 40 deviatoric stress cycles $\Delta q = 50\,\text{kPa}$, stress state *I*, $I_D \approx 0.75$: (a) linear x-axis, (b) logarithmic x-axis

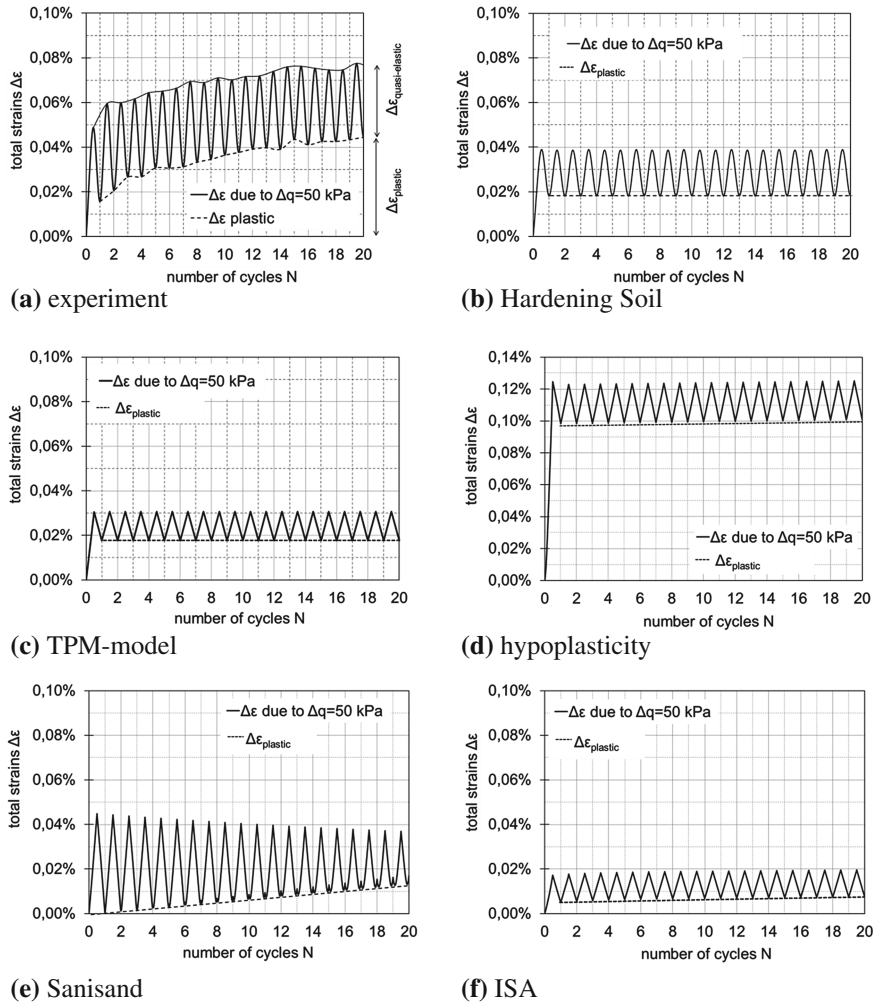

(a) experiment

(b) Hardening Soil

(c) TPM-model

(d) hypoplasticity

(e) Sanisand

(f) ISA

Fig. 8. Strain accumulation $\Delta\varepsilon$ due to 20 pure deviatoric stress cycles $\Delta q = +50\,\text{kPa}$, stress state *I*, $I_D \approx 0.75$

As shown in Fig. 7, the experimentally observed strain accumulation of total strains Δε versus the number of cycles N can be described in this case with a logarithmic approach

$$\varepsilon_{pl,N} = a_1(1 + a_2 \cdot \ln(N)) \tag{3}$$

see e.g. Goldscheider (1977), Hettler (1981), Hettler and Gudehus (1985). It also turns out, that the quasi-elastic strains, i.e. the difference between loading and unloading, remains already constant after a low number of cycles.

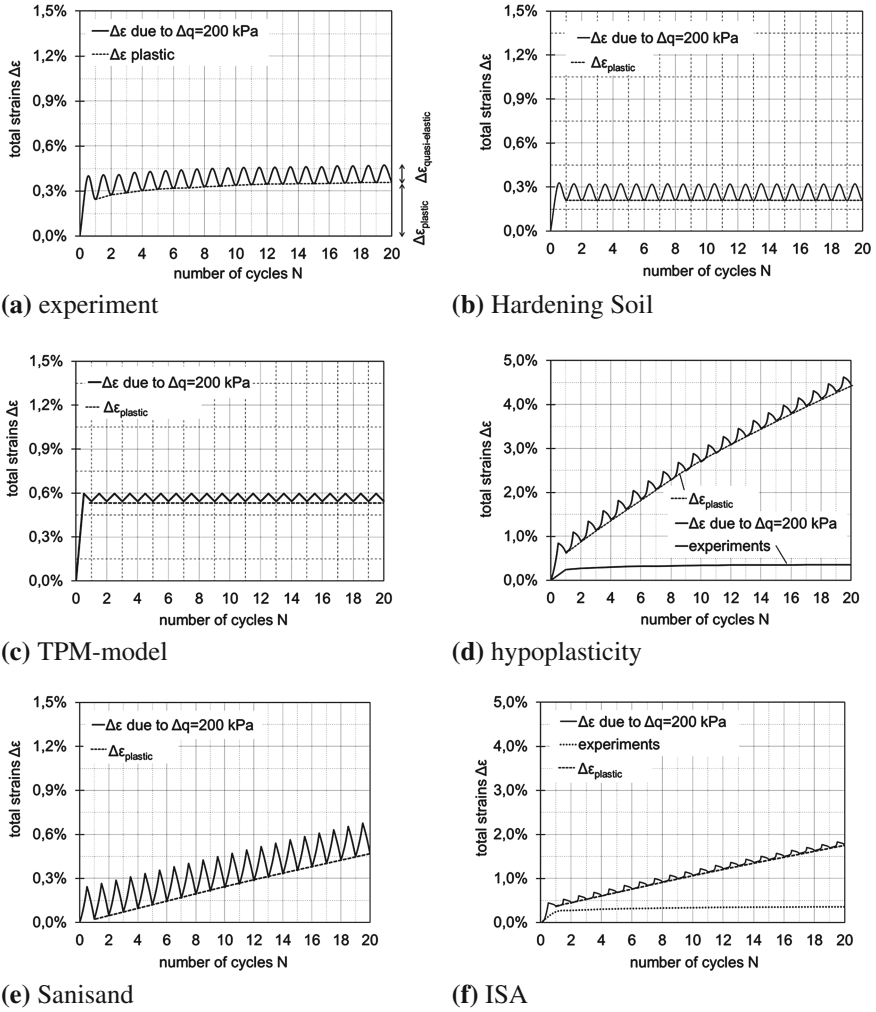

(a) experiment **(b)** Hardening Soil

(c) TPM-model **(d)** hypoplasticity

(e) Sanisand **(f)** ISA

Fig. 9. Strain accumulation $\Delta\varepsilon$ due to 20 pure deviatoric stress cycles $\Delta q = +200$ kPa, stress state *I*, $I_D \approx 0.75$

The comparison between experimental and numerical strain accumulation is shown in Figs. 8 $\Delta q = +50\,\text{kPa}$ and 9 $\Delta q = +200\,\text{kPa}$ with dashed lines for plastic strains. None of the considered constitutive models is able to describe the logarithmic increase, because there is either total elastic behaviour after the first unloading or an approximately linear increase of strains.

For small stress amplitudes $\Delta q = +50\,\text{kPa}$ in Fig. 8 the linear increase observed from the Sanisand-, ISA- and the hypoplastic model is low and the plastic strains after

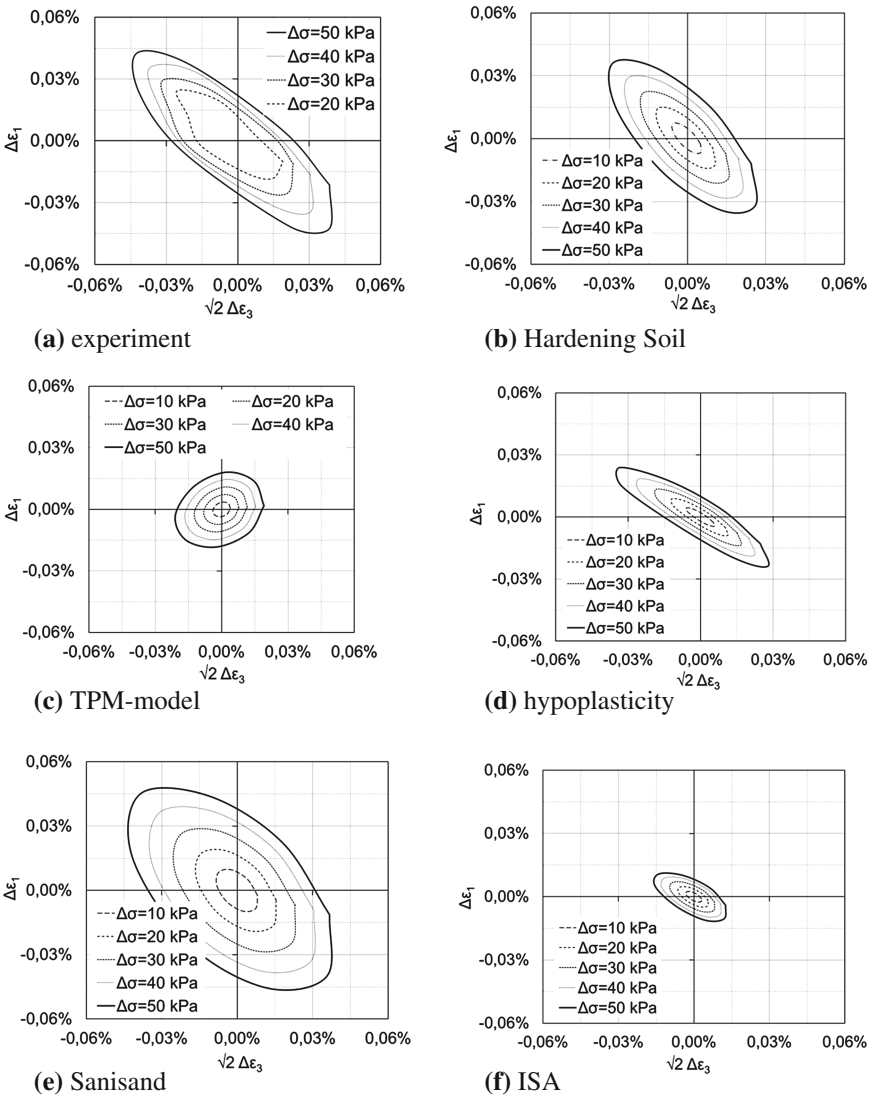

Fig. 10. Quasi-elastic strain response envelopes at low-cycle loading, stress state *A*, $I_D \approx 0.75$: comparison of constitutive equations and experiments

20 cycles of almost all constitutive equations lie at least in an approximately realistic range with $\Delta\varepsilon^{pl} \approx 0.01 \cdots 0.10\%$ and experimental strains $\Delta\varepsilon^{pl,exp} \approx 0.045\%$. The strains after the first unloading of both elastoplastic models almost exactly match the experiments ($\Delta\varepsilon^{pl,exp,N=1} \approx 0.018\%$). These models' elastic behaviour, starting already from the 2nd cycle and the triplication of experimental strains during low cycle loading at the same time to $\Delta\varepsilon^{pl,N=20} \approx 0.043\%$, lead to deviations from the experiments.

Regarding the strain accumulation due to a larger deviatoric stress amplitude $\Delta q = +200\,\text{kPa}$ in Fig. 9, with the same set of parameters results in an unrealistic strain increase ("ratcheting") for the hypoplastic and the ISA-models, as the strains at the end of the low-cycle loading are much larger than in the experiments. The strains calculated with all other constitutive equations at the end of cyclic loading are between $\Delta\varepsilon^{pl,N=20} \approx 0.1\ldots0.5\%$ and are of the same magnitude as the experimental results with $\Delta\varepsilon^{pl,N=20} \approx 0.35\%$.

Similar observations can be made for isotropic stress cycles and different initial densities, see Danne and Hettler (2016) and Danne (2017).

5 Low Cycle Loading with Regard to Quasi-Elastic Strains

Quasi-elastic strains have been investigated in detail e.g. in Danne and Hettler (2016) and Danne (2017). Considering stress amplitudes $\Delta\sigma \leq 50\,\text{kPa}$ it seems to be a good approximation to assume constant elastic behaviour already after a few cycles. While monotonous or low-cycle preloading and the initial density have little influence on the quasi-elastic strains, this is not the case for the mean pressure and the initial stress-state, Danne and Hettler (2013) and Hettler and Danne (2013).

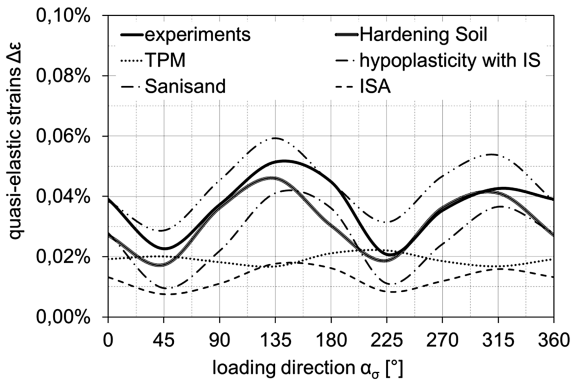

Fig. 11. Absolute value of quasi-elastic strains $\Delta\varepsilon$ due to low-cycle loading with $\Delta\sigma = 50\,\text{kPa}$ depending on loading direction α_σ, stress state *A*, $I_D \approx 0.75$

5.1 Triaxial Compression (Stress State A)

Figure 10 shows the SREs for compression stress state A (Table 1). The envelopes derived from calculations with the TPM- and the ISA-model are too small and the quasi-elastic stiffness too large respectively. In addition, the envelopes from TPM-model have the shape of a circle, which is not realistic. The SREs calculated with hypoplasticity are – in contrast to those observed for monotonic loading – too slim; especially the stiffnesses at isotropic loading and unloading are too large.

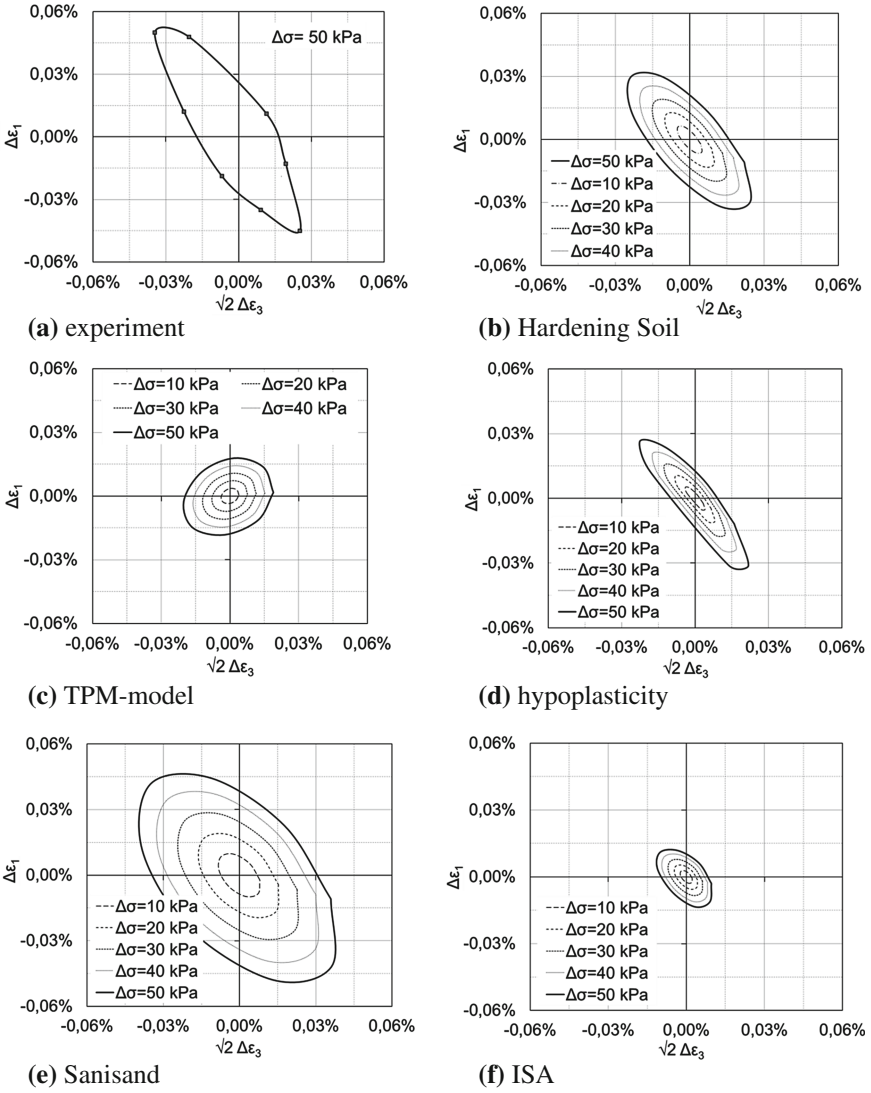

(a) experiment **(b)** Hardening Soil

(c) TPM-model **(d)** hypoplasticity

(e) Sanisand **(f)** ISA

Fig. 12. Quasi-elastic strain response envelopes at low-cycle loading at stress state *I*, $I_D \approx 0.75$: comparison of constitutive equations with experiments

Plotting the absolute value of quasi-elastic strains due to the same stress increment (here: $\Delta\sigma = 50\,\text{kPa}$) depending on the loading direction in Fig. 11 it can be noticed that there are no agreements between the elastoplastic TPM-model and the other models at all, for the envelopes are a circle-shaped, Fig. 10c.

For the other models at least the loading directions, which lead to the largest and the smallest strains respectively are in good accordance. Except for the elastoplastic TPM- and the ISA-model, all models predict absolute values of strains in an approximately correct range.

5.2 Isotropic Stress State (I)

The quasi-elastic SREs from an initial isotropic stress state in Fig. 12 show rather different shapes and sizes. The experimental SREs cannot be reproduced with the TPM- and ISA-model; neither shape nor size match.

Figure 13 shows the absolute value of quasi-elastic strains for a stress increment of 50 kPa depending on the loading direction. All models lead to equal strains due to deviatoric loading and unloading. This is not the case for the experiments, where the strains due to deviatoric unloading are larger than those from deviatoric loading.

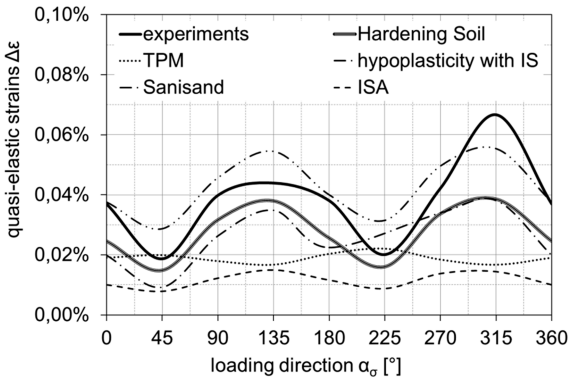

Fig. 13. Absolute value of quasi-elastic strains $\Delta\varepsilon$ due to low-cycle loading with $\Delta\sigma = 50\,\text{kPa}$ depending on loading direction α_σ, stress state *I*, $I_D \approx 0.75$

5.3 Triaxial Extension (Stress State J)

Figure 14 shows the quasi-elastic SREs from stress state J. The experiments lead to the largest quasi-elastic strains for deviatoric loading and unloading.

The absolute values of quasi-elastic strains as a function of the loading direction are shown in Fig. 15.

The experiments lead to the largest quasi-elastic strains, followed by the Sanisand-Model and hypoplasticity. The only constitutive equation which is able to predict larger quasi-elastic strains due to deviatoric unloading (α_σ = 315°) than deviatoric loading (α_σ = 125°) is the hypoplastic model. A stress-induced anisotropy is observed experimentally. It becomes visible by the rotation of the envelopes' main axis for different stress ratios and can also be reproduced best with hypoplastic calculations.

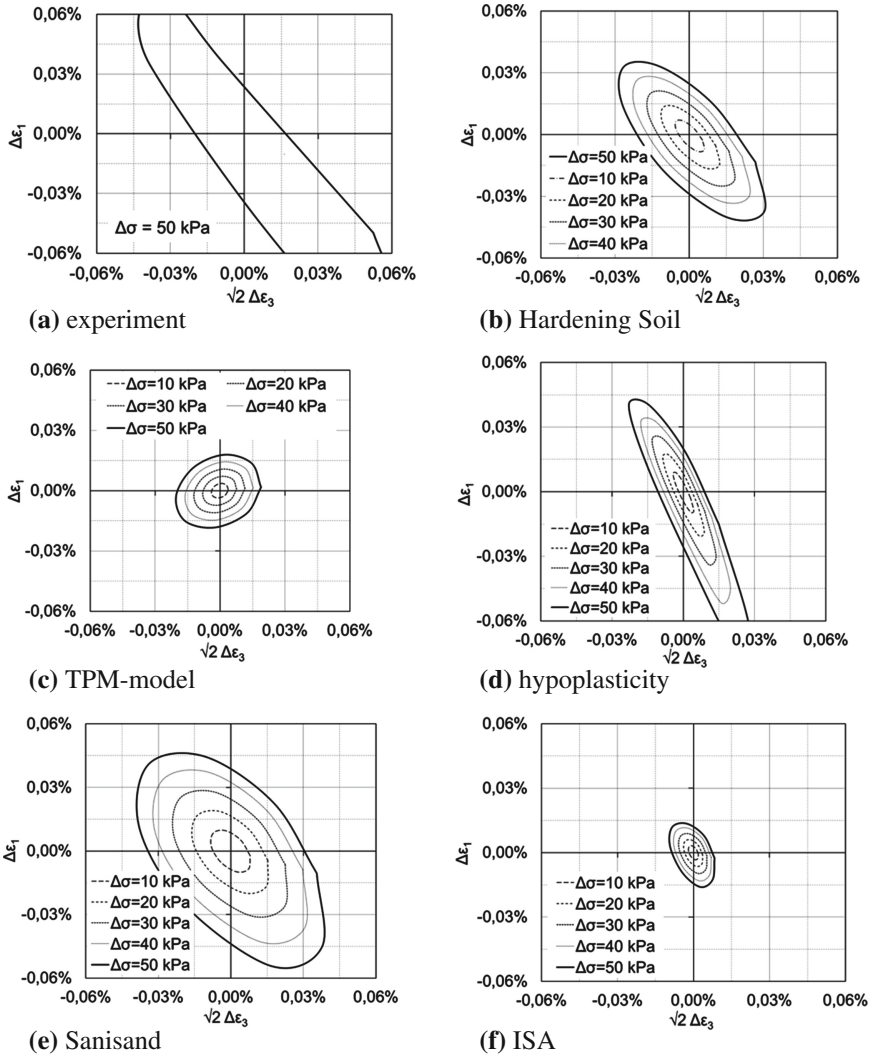

Fig. 14. Quasi-elastic strain response envelopes at low-cycle loading, stress state *J*, $I_D \approx 0.75$: comparison of constitutive equations with experiments

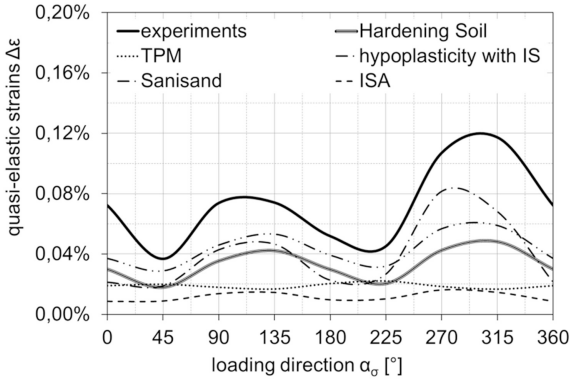

Fig. 15. Absolute value of quasi-elastic strains $\Delta\varepsilon$ due to low-cycle loading with $\Delta\sigma = 50\,\text{kPa}$ depending on loading direction α_σ, stress state *J*, $I_D \approx 0.75$

6 Summary and Recommendations

In the detailed and systematical investigation of the incremental stress-strain behaviour at monotonous and low-cycle loading, no constitutive equation can be identified able to describe the experimental results for all kinds of loading directions appropriately.

In Table 2 an attempt is made to summarise the results evaluating, how the stress-strain behaviour at a certain loading condition can be reproduced by the investigated constitutive equation.

Table 2. Agreements and differences of the considered constitutive equations with the experiments

Constitutive equation	Hardening soil	Elastoplastic model (based on TPM)	Hypoplasticity with interg. strain	Sanisand-Model	ISA-Model
Stress paths with…					
…monotonous loading only	++	+	+	+	+
…monotonous un- and reloading	+	+	–	–	–
Low-cycle loading					
strain accumulation with small stress amplitudes	–	–	+	+	+
strain accumulation with large stress amplitudes	–	–	– –	–	– –
Quasi-elastic strains	++	– –	+	+	–

+(+) (very) good agreements
–(–) (some) differences

Despite of the comprehensive analysis it is very difficult to derive recommendations for practical purposes such as the models' application in BVPs. Beside the fact, that the results are derived from experiments with axially symmetrical stress states under drained conditions, it also has to be kept in mind, that in contrast to element tests, cyclic loading in BVPs does not immediately lead to a cyclic stress field right from the beginning.

Nevertheless Table 2 may be helpful to select a suitable constitutive equation for application in BVPs, but should be complemented by sensitivity analyses, where the influence of the model's parameters on the numerical results is identified, see e.g. Saltelli et al. (2008), Miro et al. (2014).

Despite of the extensive investigations, not all possible influences on the incremental stress-strain behaviour have been considered. Further aspects like grain size distribution, inherent anisotropy may also play a role. Continuative investigations seem appropriate.

Acknowledgment. The work presented in this paper was supported by the German Research Foundation (DFG) as subproject 8 "Incremental stress-strain-behaviour of sand at low-cycle loading and application on excavation-models" of the interdisciplinary research group FOR 1136 "Simulation of geotechnical construction processes with holistic consideration of the stress strain soil behaviour (GeoTech) "Incremental stress-strain behaviour". The authors appreciate the financial support from the DFG.

The authors also like to thank their colleagues of Karlsruhe Institute of Technology (KIT) and of the institute of applied mechanics of Stuttgart University, who supported the authors by providing parameter sets of the fine sand and programmes to carry out the numerical calculations.

References

Costanzo, D., Viggiani, G., Tamagnini, C.: Directional response of a reconstituted fine-grained soil - part I: experimental investigation. Int. J. Numer. Anal. Methods Geomech. **13**, 1283–1301 (2006)

Calvetti, F., Viggiani, G., Tamagnini, C.: A numerical investigation of the incremental behavior of granular soils. Revista di Italiana Geotecnica, pp. 11-29 (2003)

Danne, S., Hettler, A.: Verhalten von nichtbindigen Böden bei niederzyklischer Belastung. Geotechnik **36**, 19–29 (2013)

Danne, S., Hettler, A.: Experimental strain response-envelopes of granular materials for monotonous and low-cycle loading processes. In: Triantafyllidis, T. (ed.) Holistic Simulation of Geotechnical Installation Processes. LNACM, vol. 77, pp. 229–250. Springer, Heidelberg (2015). doi:10.1007/978-3-319-18170-7_12

Danne, S., Hettler, A.: Experimental and numerical element tests for granular soils: performance of different constitutive models for monotonous and low-cycle loading. In: Triantafyllidis, T. (ed.) Holistic Simulation of Geotechnical Installation Processes. LNACM, vol. 80, pp. 149–162. Springer, Heidelberg (2016). doi:10.1007/978-3-319-23159-4_8

Danne, S.: Experimentelle und numerische Untersuchungen zum Verhalten von Sand bei monotoner und niederzyklischer Belastung, Ph. D thesis, Technische Universität Dortmund, Germany (2017, publication in progress)

Doanh, T.: Strain response envelope: a complementary tool for evaluating hostun sand in triaxial compression and extension: experimental observations. In: Kolymbas, D. (ed.) Constitutive Modeling of Granular Materials, pp. 375–396. Springer, Berlin (2000)

Ehlers, W., Avci, O.: Stress-dependent hardening and failure surfaces of dry sand. International Journal for Numerical and analytical Methods in Geomechanics, pp. 1-23 (2011). John Wiley and Sons, Hrsg.

Ehlers, W.: Grundlegende Konzepte in der Theorie poröser Medien. Technische Mechanik, **16**(1), 63–76 (1996)

Fuentes Lacouture, W.M.: Contributions in Mechanical Modeling of Fill Materials. Veröffentlichung des Institutes für Bodenmechanik und Felsmechanik am Karlsruher Institut für Technologie (KIT) (2014)

Goldscheider, M.: Shakedown and incremental collapse of structures in dry sand bodies. In: Proceedings of Dynamical Methods Soil and Rock Mechanics - Plastic and Long-Term Effects. Balkema, Rotterdam (1977)

Gudehus, G.: A comparison of some constitutive laws for soils under radially symmetric loading and unloading. In: Wittke, W. (ed.) Proceedings of the 3rd International Conference on Numerical Methods in Geomechanics, Balkema, pp. 1309–1323 (1979)

Hettler, A.: Verschiebungen starrer und elastischer Gründungskörper in Sand bei monotoner und zyklischer Beanspruchung (Bd. 90). (G. Gudehus, Hrsg.) Karlsruhe: Veröffentlichung des Institutes für Bodenmechanik und Felsmechanik der Universität Fridericana in Karlsruhe (1981)

Hettler, A., Gudehus, G.: A pressure dependent correction for displacement results from 1 g model tests. Géotechnique **35**(4), 497–510 (1985)

Hettler, A., Danne, S.: Strain response envelopes for low-cycle loading processes. In: Proceedings of the 18th International Conference on Soil Mechanics and Geotechnical Engineering, Paris, pp. 1491–1494 (2013)

Lewin, P., Burland, J.: Stress-probe experiments on saturated normally consolidated clay. Géotechnique **20**(1), 38–56 (1970)

Miro, S., Hartmann, D., Schanz, T.: Global sensitivity analysis for subsoil parameter estimation in mechanized tunnelling. Comput. Geotech. **56**, 80–88 (2014)

Nicholson, P., Seed, R., Anwar, H.: Elimination of membrane compliance in undrained triaxial testing: i measurement and evaluation. Can. Geotech. J. **30**, 727–738 (1993)

Niemunis, A., Herle, I.: Hypoplastic model for cohesionless soils with elastic strain range. Mech. Cohesive-Frictional Mater. **2**, 279–299 (1997)

Niemunis, A.: Incremental Driver. User's manual. University of Karlsruhe, Germany (2008)

Niemunis, A., Wichtmann, T., Triantafyllidis, T.: A high-cycle accumulation model for sand. Comput. Geotech. **32**(4), 245–263 (2005)

Saltelli, A., Ratto, M., Andres, T., Campolongo, F., Cariboni, J., Gatelli, D., et al.: Global Sensitivity Analysis: The Primer. Wiley, Chichester (2008)

Schanz, T.: Zur Modellierung des mechanischen Verhaltens von Reibungsmaterialien. In: Vermeer, P. (ed.) Stuttgart: Habilitationsschrift am Institut für Geotechnik, Universität Stuttgart, Germany (1998)

Taiebat, M., Dafalias, Y.: Sanisand, simple anisotropic sand plasticity model. Int. J. Numer. Anal. Methods Geomech. **32**(8), 915–948 (2008)

von Wolffersdorff, P.-A.: A hypoplastic relation for granular materials with a predefined limit state. Mech. Cohesive-Frictional Mater. **1**(3), 251–271 (1996)

Constitutive Model for Viscous Clays Under the ISA Framework

Merita Tafili(✉) and Theodoros Triantafyllidis

Institute of Soil Mechanics and Rock Mechanics,
Karlsruhe Institute of Technology, Karlsruhe, Germany
Merita.tafili@kit.edu

Abstract. The ISA-plasticity is a novel approach based on the intergranular strain concept. It introduces a yield surface within the intergranular strain space. The intergranular strain is related to the recent strain history, which is used to improve the model performance for cyclic loading. This paper proposes an ISA model for the simulation of saturated clays incorporating also possible viscous effects that clays may have. These rate-dependent phenomena are described within a viscous strain rate, which is added to the model besides the elastic and (hypo)plastic one. Possessing the plastic strain rate independent from the viscous strain rate the model is able to describe both viscous and non-viscous clays. At the beginning the formulation of the model is described. Subsequently, some explanation about the numerical implementation and the required parameters is given. Finally, the model is evaluated through some simulations with a Kaolin clay, which are compared with experimental results of laboratory tests. The simulations include oedometric and triaxial tests under monotonic and cyclic loading. The monotonic tests include also strain rate variation to evaluate the rate dependence of the proposed model.

Keywords: Viscous clays · Unsaturated clays · Constitutive model · ISA plasticity · Intergranular strain

1 Introduction

A realistic description of the behavior of viscous and non-viscous clays under monotonic and cyclic loading is of great importance for the evaluation of the performance of geotechnical structures dealing with these materials [2,12]. Researches have found that the clay behaves elastically only under very small strain amplitudes, of about $\|\Delta\varepsilon\| < 10^{-4}$. Subsequently, small strain effects take place including the reduction of the plastic strain rate and the stiffness increase due to reversal loading under medium strain amplitudes in the order of strain magnitude of about $10^{-4} < \|\Delta\varepsilon\| < 10^{-2}$ [17]. Under continuing shearing the material stiffness degradates and under very large deformations, $\|\Delta\varepsilon\| >> 10^{-2}$, it reaches asymptotically the critical state, which indicates the failure. These theoretical and practical observations should pursue every realistic and competent constitutive model.

T. Triantafyllidis (ed.), *Holistic Simulation of Geotechnical Installation Processes*,
Lecture Notes in Applied and Computational Mechanics 82, DOI 10.1007/978-3-319-52590-7_15

In the literature, the usage of different models for each particular simulation problem is recommended. For example for simulations regarding non-viscous clays one would choose an elastoplastic model like [24] or a hypoplastic model like [10,16]. Dealing with a clay that shows a high plasticity, a viscous model is necessary. One could than use an elasto-visco-plastic model [27,28] or a visco-hypoplastic model [17,18]. The mentioned models simulate the behavior of clays under monotonic loading well. Yet, for geotechnical structures dealing with the cyclic behaviour of clays, like for example urban excavations with retaining walls with a low number of cycles due to the excavation and backfilling processes or offshore foundations with a large number of cyclic loading, other models are recommended [13,15]. Thus, to describe different effects several contitutive models are required.

A new constitutive approach has been proposed by Fuentes and Triantafyllidis [8], the ISA-plasticity, which introduces a yield and a bounding surface within the intergranular strain space. Within the yield surface the model accounts for the elastic behavior under very small strain amplitudes. Once the material state reaches the yield and proceeds towards the bounding surface, the effects of intermediate strain amplitudes are considered. Finally, reaching the bounding surface the plastic strain rate reduction and the stiffness increase ceases. The first ISA model was proposed for sands [5,8] and than coupled with the hypoplastic model of Wolffersdorff [26] with extensions to simulate multi-dimensional loading [20]. In [6], the ISA model was reformulated to simulate non-viscous clays. Only qualitative simulations have been performed in [6] and no strain-rate dependency has been introduced into the model.

In this article, a viscous ISA model for clays is proposed. In contrast to other viscous models the time-dependent phenomena are described through an additional strain rate, which can vanish if simulations with non-viscous clays are required. The structure of this article is as follows: at the beginning the formulation of the model is explained. Afterwards, some comments about its numerical implementation and the required parameters are given. Finally, some simulations with a Kaolin clay are discussed in order to evaluate the model performance. The conducted experiments include monotonic and cyclic loading under oedometric and triaxial conditions. Whereby, some tests include the variation of the vertical strain rate to evaluate the performance of the rate dependent component of the model.

The notation of this article is as follows: scalar quantities are denoted with italic fonts (e.g. a,b), vectors and second rank tensors with bold fonts (e.g. $\mathbf{v}$, $\mathbf{A}$, $\boldsymbol{\sigma}$), and fourth rank tensors with Sans Serif type (e.g. E, L). Multiplication with two dummy indices, also known as double contraction, is denoted with a colon ":" (e.g. $\mathbf{A} : \mathbf{B} = A_{ij}B_{ij}$). When the symbol is omitted, it is then interpreted as a dyadic product (e.g. $\mathbf{AB} = A_{ij}B_{kl}$). The deviatoric component of a tensor is symbolized with an asterisk as superscript $\mathbf{A}^* = \mathbf{A} - (\mathrm{tr}\mathbf{A}/3)\,\boldsymbol{I}$. The brackets $\| \quad \|$ denote the Euclidean norm $\| \mathbf{v} \| = \sqrt{v_i\, v_i}$ or $\| \mathbf{A} \| = \sqrt{\mathbf{A} : \mathbf{A}}$. The effective stress tensor is denoted with $\boldsymbol{\sigma}$ and the strain tensor with $\boldsymbol{\varepsilon}$. The Roscoe invariants are defined as the mean stress $p = -\mathrm{tr}\boldsymbol{\sigma}/3$, the deviatoric

stress $q = \sqrt{3/2} \parallel \boldsymbol{\sigma}^* \parallel$, the volumetric strain $\varepsilon_v = -\mathrm{tr}\dot{\boldsymbol{\varepsilon}}$ and the deviatoric strain $\varepsilon_s = \sqrt{2/3}\|\boldsymbol{\varepsilon}^*\|$.

2 Intergranular Strain Model

The intergranular strain concept was first introduced in hypoplasticity by Niemunis and Herle [19] in order to improve the simulation of soil's behaviour under cyclic loading. Based on this idea and in order to incorporate the elastic locus of the material response, known as the threshold strain [1,23], Fuentes and Triantafyllidis [5] proposed an entirely reformulated intergranular strain model, the ISA-plasticity. It presents an elastoplastic model with the yield surface within the intergranular strain space. The intergranular strain $\mathbf{h}$ is a state variable related to the strain amplitude $\boldsymbol{\varepsilon}$ through the following evolution equation:

$$\dot{\mathbf{h}} = \dot{\boldsymbol{\varepsilon}} - \dot{\lambda}_H \mathbf{N}. \tag{1}$$

According to the elastoplastic terminology, $\dot{\lambda}_H \geq 0$ is the consistency parameter defined later on and $\mathbf{N}$ is the intergranular strain flow rule. The yield surface reads:

$$\text{IS yield surface:} \quad F_H = \|\mathbf{h} - \mathbf{c}\| - R/2 = 0. \tag{2}$$

Under elastic conditions, i.e. $F_H < 0$, the consistency parameter takes $\dot{\lambda}_H = 0$. Obviously, the model delivers an elastic response only for very small strain amplitudes $\|\Delta\boldsymbol{\varepsilon}\| < R$, inside the yield surface $F_H = 0$. The tensor $\mathbf{c}$ is the hardening variable describing the center of the yield surface consisting of a sphere and the material parameter R represents the diameter of the sphere, i.e. it determines the size of the elastic range. As visualized in Fig. 1, in the space spaned by the volumetric invariant and deviator invariant the yield surface takes the form of a circle, which explains many interrelationships. The volumetric invariant is described by $h_v/\sqrt{3} = -\mathrm{tr}(\mathbf{h})/\sqrt{3}$ and the deviator invariant by $\sqrt{3/2}h_s = \|\mathbf{h}^*\|$.

As illustrated in Fig. 1(a) the flow rule is normal to the yield surface and is defined by:

$$\mathbf{N} = (\mathbf{h} - \mathbf{c})/(R/2) = (\mathbf{h} - \mathbf{c})^{\rightarrow} \tag{3}$$

For sake of simplicity it is proposed to consider the norm of $\mathbf{N}$, i.e. $\|\mathbf{N}\| = 1$. As $\mathbf{N}$ is defined only for $F_H = 0$ the distance between $\mathbf{h}$ and $\mathbf{c}$ can take the value $R/2$ as a maximum.

Considering the plastic case in which the intergranular strain "touches" the yield surface $F_H = F_H(\mathbf{h}, \mathbf{c}) = 0$, $\dot{\lambda}_H > 0$, it is desired that after a reversal loading, the material exhibits smoothly the appearance of a plastic strain rate. Brittle materials would present a very rapid change of the stiffness when changing from elastic to plastic behavior, but most soils and some other materials show actually a smooth stiffness transition when it turns from the elastic into plastic regime. This effect can be well simulated through a hardening mechanism of the yield surface described with the tensor $\mathbf{c}$, termed also as "back-intergranular strain". For the ISA platform, some simple relations of the bounding surface plasticity have been adopted to simulate this behavior. Thus, the model considers

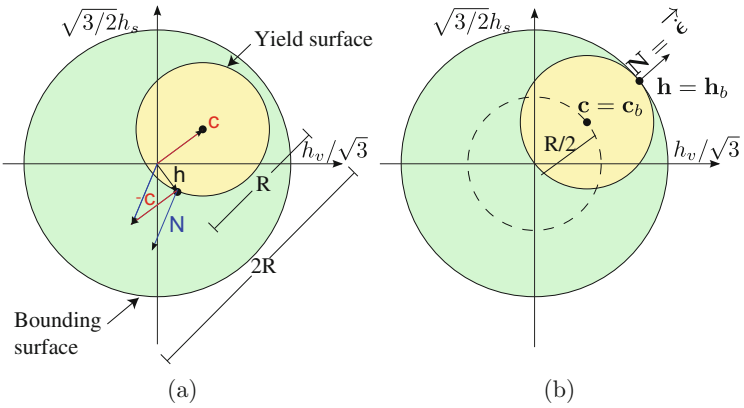

Fig. 1. Yield and bounding surface of the intergranular strain model [5]. (a) Geometry, (b) Example of the bounding condition $F_{Hb} = 0$.

besides the yield surface a bounding surface within the intergranular strain space, which is illustrated in Fig. 1(a) and follows the relation:

$$\text{IS bounding surface: } F_{Hb} = \|\mathbf{h}\| - R = 0 \tag{4}$$

It presents also a sphere (in 3D) with twice the size of the yield surface (for simplicity reasons). The evolution equation of $\mathbf{c}$ describes the hardening of the yield surface towards the bounding surface. By the means of elastoplasticity the general form of this equation reads:

$$\dot{\mathbf{c}} = \dot{\lambda}_H \bar{\mathbf{c}} \tag{5}$$

whereby $\dot{\lambda}_H = 0$ renders $\dot{\mathbf{c}} = 0$, i.e. under elastic conditions no hardening is produced. Therefore, under plastic conditions $\dot{\lambda}_H > 0$ the hardening is determined by the proposed function $\bar{\mathbf{c}}$. In order to fulfill the bounding surface constraint $\|\mathbf{h}\| \leq R$, the hardening variable should be bounded by $\|\mathbf{c}\| = R/2$, see also Fig. 1(a). For this purpose, the "image" of the tensor $\mathbf{c}$ is introduced:

$$\mathbf{c}_b = R/2\,(\dot{\boldsymbol{\varepsilon}})^{\rightarrow}. \tag{6}$$

Hence, the hardening function $\bar{\mathbf{c}}$ reads:

$$\bar{\mathbf{c}} = \beta\,(\mathbf{c}_b - \mathbf{c})/R. \tag{7}$$

Hereby β is a material parameter defining the hardening rate. Note that for $\beta = 0$ no hardening is experienced and the intergranular strain model gets perfect plastic. Of course, Eq. 7 is only defined under plastic conditions $F_H = 0$.

The consistency parameter is derived by means of elastoplasticity to:

$$\dot{\lambda}_H = \frac{\langle \mathbf{N} : \dot{\boldsymbol{\varepsilon}} \rangle}{\mathbf{N} : \mathbf{N} + \mathbf{N} : \bar{\mathbf{c}}} = \frac{\langle \mathbf{N} : \dot{\boldsymbol{\varepsilon}} \rangle}{1 + H_H} \tag{8}$$

whereby $H_H = \mathbf{N} : \bar{\mathbf{c}} = -(\partial F_H / \partial \mathbf{c}) : \bar{\mathbf{c}}$ defines the hardening modulus.

The presented model defines the elastoplastic evolution of the intergranular strain concept proposed by Fuentes [5]. It presents an associated flow rule $\mathbf{N} = \partial F_H / \partial \mathbf{h}$ and a single hardening mechanism.

As will be highlighted in the next section, the proximity of the intergranular strain to the bounding surface is important to quantify if the plastic strain is whether fully mobilized or not. For this purpose an image tensor of the intergranular strain at the bounding surface is introduced:

$$\mathbf{h}_b = R\mathbf{N}. \tag{9}$$

and the proximity of $\mathbf{h}$ to $F_{Hb} = 0$ is described by $\|\mathbf{h}_b - \mathbf{h}\|$. According to Fuentes model, the bounding surface should be asymptotically reached after applying large strains in a constant direction $(\dot{\boldsymbol{\varepsilon}})^{\rightarrow}$. In order to interpolate between the fully mobilized state and strain reversal after fully mobilized state the scalar function ρ is introduced:

$$\rho = 1 - \frac{\|\mathbf{h}_b - \mathbf{h}\|}{2R}. \tag{10}$$

This scalar function provides two important and illustrative cases. For $\|\mathbf{h}_b - \mathbf{h}\| = 2R$ it yields $\rho = 0$ viz. strain reversal after fully mobilized state and for $\mathbf{h} = \mathbf{h}_b$ it renders $\rho = 1$ viz. fully mobilized state, for more details see Fig. 2. The last case is very useful when formulating relations of the mechanical model under medium and large strain amplitudes. Thus, this scalar function is used to interpolate between the elastoplastic and hypoplastic mechanical model formulation as will be shown in the next section.

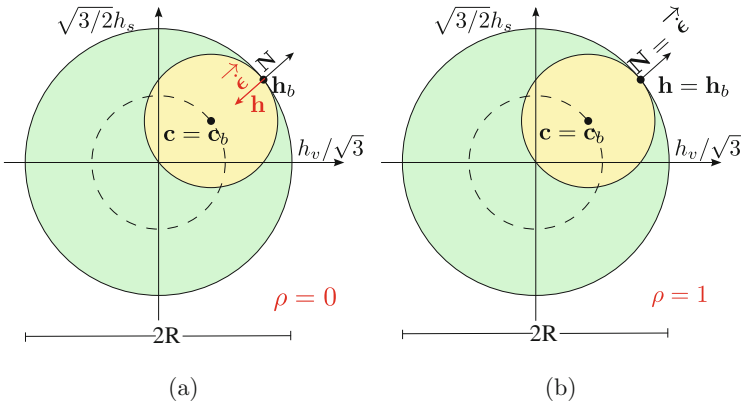

Fig. 2. The interpolation function ρ and its limit values: (a) $\rho = 0$ for $\|\mathbf{h}_b - \mathbf{h}\| = 2R$, (b) $\rho = 1$ for $\mathbf{h} = \mathbf{h}_b$.

3 Mechanical Model Formulation

As mentioned before, the stress-strain-time behavior of clayey soils is of primary concern for the evaluation of long-time performance in geotechnical engineering.

The phenomena associated with the viscosity of soils such as strain creep, stress relaxation and rate-dependence, may be important especially for calculations in soft soils, i.e. at low overconsolidation ratios (OCR).

Contrary to visco-plastic models, the proposed visco-ISA model assumes the "decomposition" of the strain rate into elastic $\dot{\boldsymbol{\varepsilon}}^e$, plastic $\dot{\boldsymbol{\varepsilon}}^p$ and viscous $\dot{\boldsymbol{\varepsilon}}^v$ portion:

$$\dot{\boldsymbol{\varepsilon}} = \dot{\boldsymbol{\varepsilon}}^e + \dot{\boldsymbol{\varepsilon}}^p + \dot{\boldsymbol{\varepsilon}}^v \tag{11}$$

with the constitutive equation:

$$\dot{\boldsymbol{\sigma}} = \mathsf{E} : \dot{\boldsymbol{\varepsilon}}^e = \mathsf{E} : (\dot{\boldsymbol{\varepsilon}} - \dot{\boldsymbol{\varepsilon}}^p - \dot{\boldsymbol{\varepsilon}}^{vis}) = m\,\bar{\mathsf{E}} : (\dot{\boldsymbol{\varepsilon}} - y_h\,\bar{\dot{\boldsymbol{\varepsilon}}}^p - \dot{\boldsymbol{\varepsilon}}^{vis}) \tag{12}$$

whereby $\bar{\mathsf{E}}$ is the residual stiffness and the tensor $\bar{\dot{\boldsymbol{\varepsilon}}}^p$ is the residual plastic strain rate. The stress rate continuity between the elastic and plastic response is established through the scalar functions m and y_h.

The plastic strain rate factor y_h reduces the plastic strain rate upon unloading or cyclic loading $y_h < 1$ and guarantees a smooth transition between elastic and plastic response through the relation:

$$y_h = \rho^{\chi} \langle \mathbf{N} : \dot{\boldsymbol{\varepsilon}}^{\rightarrow} \rangle. \tag{13}$$

Obviously for $y_h = 0$ the model response is elastic and $y_h = 1$ implies fully mobilized states thus no plastic strain rate reduction is required. χ is a material parameter, which can be calibrated through a cyclic undrained triaxial test.

The stiffness increase upon cyclic loading or unloading is produced through the factor m [5]:

$$m = m_R + (1 - m_R)\, y_h. \tag{14}$$

At fully mobilized states $y_h = 0$ and $m = m_R$ and under neglection of the viscous strain rate $\dot{\boldsymbol{\varepsilon}}^v$ the model can simply be adjusted by adopting $\bar{\mathsf{E}}$ and $\bar{\dot{\boldsymbol{\varepsilon}}}^p$ to a conventional elastoplastic model for example the MCC model for clays or to a hypoplastic model for clays like the one developed by Masin [16]. For the definition of the stiffness tensor, plastic and viscous strain rate some basic modifications regarding the characteristic void ratios and stress surfaces are required. These are explained within the next sections.

3.1 Normal Consolidation and Critical State Line

The normal consolidated line for clays, well known also from the MCC model, is identifed at isotropic stress states $q = 0$ when the void ratio is equal to the maximum void ratio $e = e_i$:

$$e_i = e_{i0} - \lambda \log(p/p_{\text{ref}}) \tag{15}$$

whereby e_{i0} is a parameter describing the value of the maximum void ratio e_i at $p = p_{\text{ref}} = 1$ kPa, the scalar λ is the compression index and $p_{\text{ref}} = 1$ kPa is the reference mean stress. The Hvorslev pressure $p = p_{ei}$ is the maximum pressure at constant void ratio, which is obtained from Eq. 15 for $e = e_i$:

$$p_{ei} = \exp\left((e_{i0} - e)/\lambda\right) \tag{16}$$

The critical void ratio e_c follows also from the relations of the modified Cam Clay model:

$$e_c = (e_{i0} - \lambda \log(2)) - \lambda \log(p/p_{\text{ref}}) \tag{17}$$

where $e_{c0} = e_{i0} - \lambda \log(2)$ is the critical void ratio at $p_{ref} = 1$ kPa. The term $\lambda \log(2))$ in Eq. 17 comes from the fact, that once the critical state is reached, the mean pressure yields accordingly to a value of $p = p_{ei}/2$ [6].

3.2 Critical State Surface and Bounding Surface

The model is based on the bounding surface plasticity [4] and on the critical state plasticity [14], incorporating a bounding and a critical surface. The critical surface determines the soil behavior at large deformations ($\|\boldsymbol{\varepsilon}\| > 25\%$) and reads [9]:

$$\text{Critical state surface:} \quad F_c \equiv \mathbf{r} : \mathbf{r} - r_c = 0, \quad r_c = \sqrt{2/3} M_c g(\theta_{\mathbf{n}}) \tag{18}$$

with the current stress ratio $\mathbf{r} = \boldsymbol{\sigma}^*/p$ and the critical state slope M_c for triaxial compression in the $p - q$ space. The scalar function $g = g(\theta)$ governs the shape of the critical state surface seen from a deviator plane and is evaluated with the Lode's angle θ:

$$c \leq g(\theta) = \frac{2c}{(1+c) - (1-c)\cos(3\theta)} \leq 1 \tag{19}$$

with the ratio between the critical state slope M_c for triaxial extension and triaxial compression $c = M_e/M_c = 3/(3 + M_c)$.

At the bounding surface holds the condition $\|\bar{\dot{\boldsymbol{\varepsilon}}}\|/\|\dot{\boldsymbol{\varepsilon}}\| = Y = 1$ and under neglection of the viscous strain in Eq. 12, the stress rate would vanish $\dot{\boldsymbol{\sigma}} = \mathbf{0}$. This implies that the bounding surface can be also used to describe the peak stress ratio of the material. The bounding surface incorporated in this work is similar to the one incorporated in [6]:

$$\text{Bounding surface:} \quad F_b \equiv \mathbf{r} : \mathbf{r} - r_c f_b = 0 \quad \text{with} \quad f_b = f_{b0} \left(1 - \left(\frac{e}{e_i}\right)^{n_F}\right)^{1/2} \tag{20}$$

with the material parameter $f_{b0} > 1$ used to define the maximum stress ratio $\|\mathbf{r}\|$ at overconsolidated states and the exponent n_F, which reads:

$$n_F = \frac{\log\left(\left(f_{b0}^2 - 1\right)/f_{b0}^2\right)}{\log\left(e_c/e_i\right)}. \tag{21}$$

This exponent controlls the intersection between the bounding and critical state surface [6].

3.3 Stiffness Tensor

The ISA stiffness tensor proposed by Fuentes is computed via multiplying the residual stiffness tensor with a scalar function, which Niemunis introduced likewise in [17]:

$$\mathsf{E} = m\bar{\mathsf{E}} \tag{22}$$

whereby $1 \leq m \leq m_R$ is the scalar function responsible for the stiffness increase upon reversal loading:

$$m = m_R + (1 - m_R)\, y_h. \tag{23}$$

Note, that for elastic conditions in the intergranular strain space $y_h = 0$ and thus $m = m_{max} = m_R$. Hence, the requirement of the maximum value for the stiffness under elastic conditions is fulfilled.

Otherwise, for $y_h = 1$, which implies fully mobilized states the interpolation function m renders its minimum value $m = 1$. The residual stiffness tensor $\bar{\mathsf{E}}$ obeys the relation [5,6]:

$$\bar{\mathsf{E}} = K\mathbf{1} \otimes \mathbf{1} + 2G\mathsf{I}^{dev} - \frac{K}{\sqrt{3}M_c}(\mathbf{1} \otimes \mathbf{r} + \mathbf{r} \otimes \mathbf{1}). \tag{24}$$

The bulk modulus K and shear modulus G are adjusted to the behavior of clays:

$$K = \frac{p\,(1+e)}{\lambda}\frac{1}{1 - Y_{0min}} \tag{25}$$

$$G = \frac{p\,(1+e)}{\lambda}\frac{1}{1 - Y_{0min}}\frac{3\,(1-2\nu)}{2\,(1+\nu)} \tag{26}$$

whereby ν is the Poisson ratio and the scalar function $Y_{0min} = (r_k - 1)/(r_k + 1)$ with the compression and swelling index λ and κ respectively.

3.4 Plastic Strain Rate

The plastic strain rate is proposed to account for small strain effects through the relation:

$$\dot{\boldsymbol{\varepsilon}}^p = y_h \bar{\dot{\boldsymbol{\varepsilon}}}^p \tag{27}$$

whereby y_h from Eq. 13 implies three fundamental cases for the plastic strain rate:

- $y_h = 0$: the response is elastic and no plastic strain rate is required.
- $0 < y_h < 1$: a smooth transition between elastic and plastic response is produced. A reduction of the plastic strain rate is implied.
- $y_h = 1$: the response is (hypo)plastic and no reduction of the plastic strain rate is required. The plastic strain rate takes its residual value.

The residual plastic strain rate $\bar{\dot{\boldsymbol{\varepsilon}}}^p$ is formulated by means of hypoplasticity [17] and adjusted to account for the material behavior of soft soils:

$$\bar{\dot{\boldsymbol{\varepsilon}}}^p = Y\mathbf{m}\|\dot{\boldsymbol{\varepsilon}}\| \tag{28}$$

with the proposed flow rule:

$$\mathbf{m} = (-1/2\,F\,\mathbf{1} + \mathbf{r})^{\rightarrow}. \tag{29}$$

The scalar F is a function of the critical state and the deviator stress ratio tensor $F(g(\theta), \mathbf{r})$. The degree of nonlinearity is adjusted to the material behavior of clays with different overconsolidation ratios OCR ≥ 1:

$$Y = Y_0 + (1 - Y_0) \left(\frac{\|\mathbf{r}\|}{f_b} \right)^2, \quad Y_0 = \left(\frac{r_k - 1}{r_k + 1} \right) \left(\frac{p}{p_{ei}} \right)^2, \quad r_k = \frac{\lambda}{\kappa}. \tag{30}$$

The degree of nonlinearity takes its minimum value $Y = Y_0$ at isotropic states $\mathbf{r} = \mathbf{0}$ and its maximum value $Y = 1$ at the bounding surface.

3.5 Viscous Strain Rate

The time-dependent phenomena in the proposed model are treated through the viscous part of the strain rate $\dot{\boldsymbol{\varepsilon}}^{vis}$. For the viscous strain rate the well known relation used in several visco-plastic models [17,18,22] is adopted for the proposed visco ISA model:

$$\dot{\boldsymbol{\varepsilon}}^{v} = C_\alpha \left(\frac{1}{\mathrm{OCR}_{3D}} \right)^{1/I_v} \mathbf{m} \tag{31}$$

whereby $C_\alpha = I_v \lambda$ is the parameter first introduced by Buisman [3] and I_v the viscosity index. Note that by calibrating the viscosity index I_v and the compression index λ the constant C_α can be mathematically evaluated. A special feature of this formulation is that by setting $I_v = 0$ the viscous strain rate vanishes avoiding so the exponent discontinuity. Moreover, the proposed model can be used for both viscous $I_v \neq 0$ and non viscous $I_v = 0$ soft soils.

The overconsolidation ratio OCR_{3D} should be evaluated for three dimensional stress states. Thus it is necessary to consider both, the mean stress p and the deviatoric stress q for the calculation and in order to be consistent with the one dimensional relation $\mathrm{OCR} = p_{ei}/p$, at isotropic states the overconsolidation ratio should yield the value $\mathrm{OCR}_{3D} = p_{ei}/p$. In this work, a similar formulation as the one used to determine the degree of nonlinearity (see Eq. 30) is proposed:

$$\mathrm{OCR}_{3D} = \frac{p_{ei}}{p} + \left(1 - \frac{p_{ei}}{p} \right) \left(\frac{\|\mathbf{r}\|}{\|\mathbf{r}_b\|} \right)^2. \tag{32}$$

The undrained strength c_u of viscous soft soils is rate dependent and every competent constitutive model should be able to simulate this important feature for geotechnical problems. Some qualitative undrained triaxial simulations with the proposed model for several strain rates are represented in Fig. 3, whereby the rate dependence of the undrained shear strength can be observed: slower strain rates return a lower shear strength (see Fig. 3(a) and (b)) and a higher pore water pressure development or reduction of effective stress (see Fig. 3(b)).

The lateral earth pressure $K_0 = \sigma_{22}/\sigma_{11} = \sigma_{33}/\sigma_{11}$, used to calculate the earth pressure distribution for example on retaining walls, tunnel lining, deep foundations etc., is an important feature of every constitutive model. Refering to

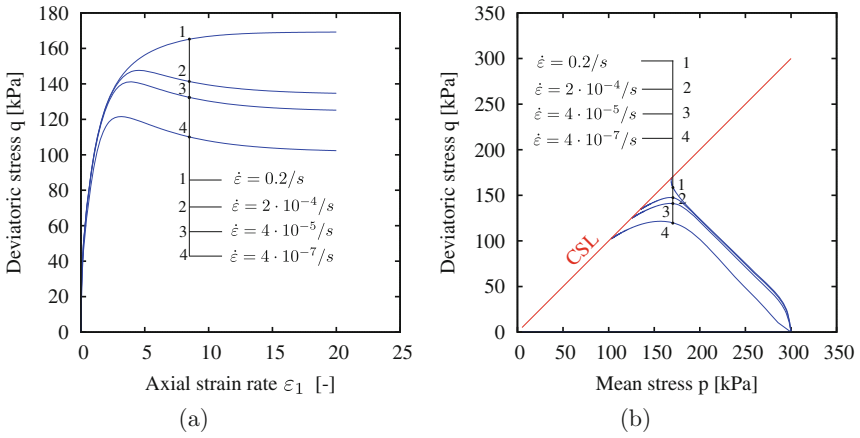

Fig. 3. Isochoric shearing illustrating the dependence of strength $c_u = q_{max}/2$ on the applied deformation rate $\dot{\varepsilon}$

normal consolidated states, Jaky [11] proposed an empirical relation for the coefficient $K_0 = 1 - \sin(\varphi_c)$ which depends on the residual friction angle φ_c. Figure 4 represents the model's performance for two oedometric tests $\Delta\boldsymbol{\varepsilon}_{11} = 0.1$ with different deformation rates $\dot{\varepsilon} = 6 \cdot 10^{-4}\,/s$ and $\dot{\varepsilon} = 6 \cdot 10^{-6}\,/s$, respectively. The identical response for both strain rates can be observed in Fig. 4(b) whereby also the coincidence between the simulations and the empirical relation is evident.

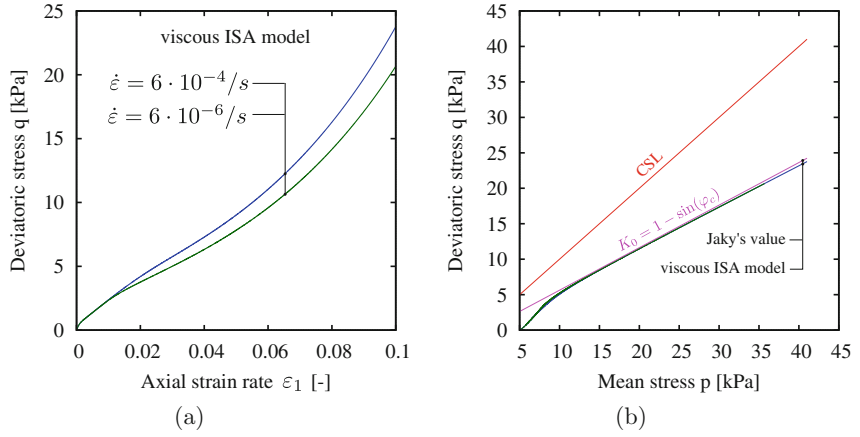

Fig. 4. Oedometric test. Verification of models performance comparing the simulated K_0 value with Jaky's $K_0 = 1 - \sin(\varphi_c)$ value.

4 Numerical Implementation and Parameters

In general, the integration of constitutive models using an explicit algorithm and possibly substepping is precise enough. Yet, the viscous models require a special numerical treatment, because the viscous strain rate is very sensitive to changes in the void ratio and in particular in the stress or for larger time increments. These effects were not existent in non-viscous models, because they are not dependent on time and the overconsolidation ratio is not used with a power law in the order of 20. Niemunis [17] recommended the substepping as well as the implicit updating of stress and the implicit integration of the intergranular strain $\mathbf{h}$.

The proposed model has been implemented with the programming language FORTRAN, whereby the well known "elastic predictor" scheme has been used [21]. The terms associated with non viscous clays were explicitly implemented. For the viscous strain rate, the semi-implicit scheme proposed by [17] has been implemented. In order to avoid numerical problems, a substepping scheme with small strain increments overlapped the described integrations. The subroutine follows the syntax of the subroutine UMAT from the software ABAQUS Standard.

The model requires the calibration of 12 material parameters. All parameters with the required routine tests for their calibration are listed in Table 1.

Table 1. Material constants of the proposed viscous ISA model

	Description	Units	Approx. range	Kaolin		Useful experiments
Hypo-elasticity				monotonic	cyclic	
λ	Compression index	[-]	$10^{-6} - 1$	0.12	0.12	IC*
κ	Swelling index	[-]	$10^{-6} - 1$	0.03	0.03	IC*
e_{i0}	Maximum void ratio	[-]	$0.5 - 2$	1.72	1.72	IC*
ν	Poisson ratio	[-]	$0 - 0.5$	0.352	0.352	UTC**
Characteristic surfaces						
M_c	CS slope	[-]	$0.7 - 1.5$	1.0	1.0	UTC**, DTC***
f_{b0}	Bounding surface factor	[-]	$1 - 2$	1.25	1.5	UTC**, DTC***
Viscosity						
I_v	Viscosity index	[-]	$0 - 0.05$	0.015	0.015	IC* ($2 \times \dot{\varepsilon}$)
Intergranular strain						
m_R	Stiffness factor	[-]	$1 - 7$	5	5	CUTC****
R	IS yield surface radius	[-]	$10^{-5} - 10^{-4}$	10^{-4}	1.8×10^{-4}	-
β	IS hardening parameter	[-]	$0 - 1$	0.2	0.076	CUTC****
χ	IS exponent	[-]	$1 - 10$	7	20	CUTC****

(*) IC: Isotropic test (loading-unloading)
(**) UTC: Undrained triaxial test
(***) DTC: Drained triaxial test
(****) CUTC: Cyclic undrained triaxial test

5 Simulations with Kaolin Clay

This section presents some simulations with the proposed model for the Kaolin clay. The performance of the model is compared with the experiments performed on this medium plasticity clay with a viscosity index of $I_v = 0.015$ by Wichtmann [25]. The parameter set calibrated for the Kaolin clay is listed in Table 1. In all simulations the intergranular strain $\mathbf{h}$ has been initialized with $h = -R\ \vec{\mathbf{1}}$ corresponding to a fully mobilized state after isotropic compression.

Figure 5 presents an oedometer test and the model's prediction. The experiment consists of several constant rate-of-strain stages, various creep phases and some unloading-reloading cycles showing hysteretic behavior. Both, experiment and simulation conducted from the oedometric normal consolidated state were

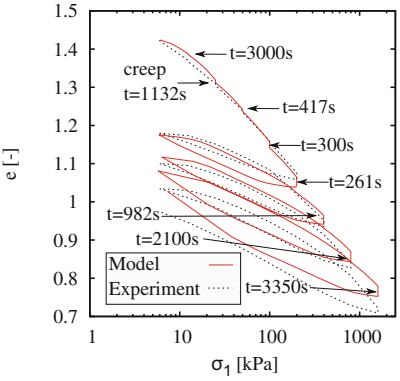

Fig. 5. Oedometer test with loading, unloading-reloading and creep steps

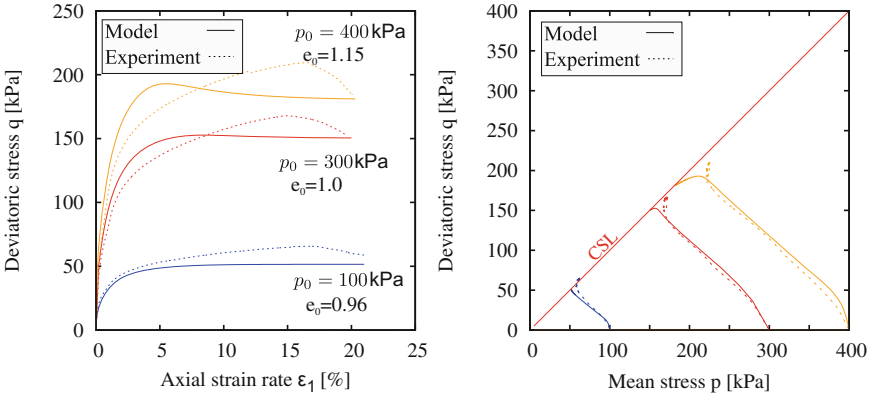

(a) q vs. ε_1 space (b) p vs. q space

Fig. 6. Undrained triaxial tests on normal consolidated samples

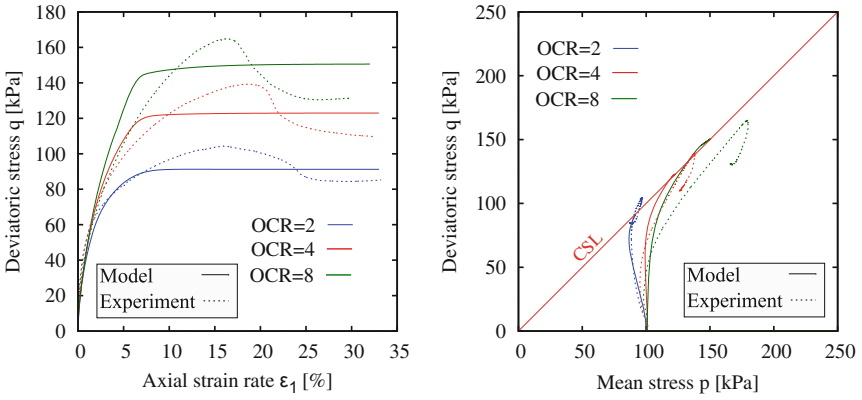

(a) q vs. ε_1 space (b) p vs. q space

Fig. 7. Undrained triaxial tests on over consolidated samples

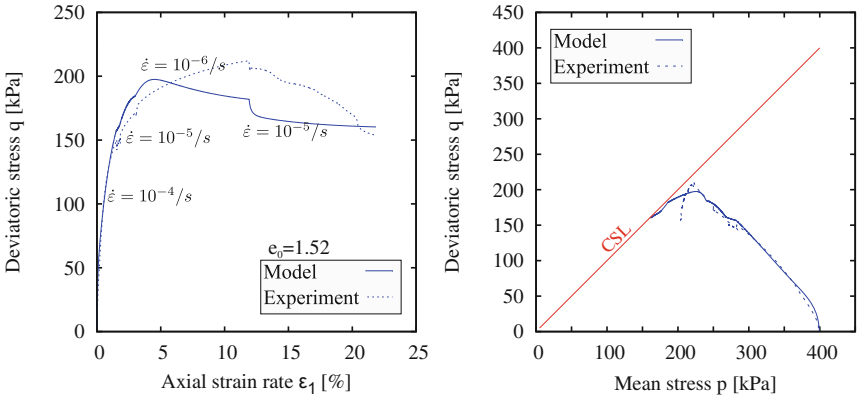

(a) q vs. ε_1 space (b) p vs. q space

Fig. 8. Undrained triaxial test with strain rate jumps

stress-controlled. The simulation with the viscous ISA model captures all effects observed in the experiment.

Figure 6 represents undrained monotonic triaxial tests conducted on normal consolidated samples of Kaolin clay with different confining pressures $p_0 = 100\,\text{kPa}$, $p_0 = 200\,\text{kPa}$ and $p_0 = 300\,\text{kPa}$ and the same axial strain rate $\dot{\varepsilon}_1 = 10^{-8}\,1/s$. The experimental data (dashed lines) and the simulations (solid lines) depicted in both $q-\varepsilon_1$ space and $p-q$ space show satisfactory coincidence, with some small discrepancies regarding the peak stress.

The undrained behavior of over consolidated samples is presented in Fig. 7. The samples were consolidated to mean pressures of $p_0 = 200\,\text{kPa}$, $p_0 = 400\,\text{kPa}$ and $p_0 = 800\,\text{kPa}$ and then unloaded to $p_0 = 100\,\text{kPa}$, hence three over consolidation ratios were obtained $OCR = 2$, $OCR = 4$ and $OCR = 8$, respectively.

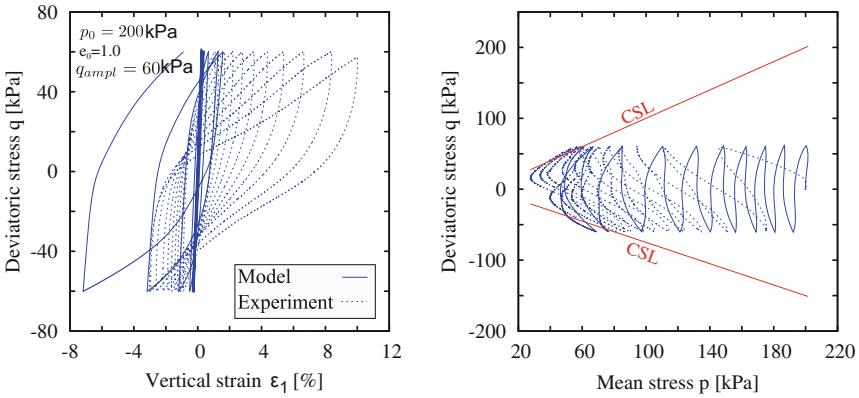

(a) q vs. ε_1 space (b) p vs. q space

Fig. 9. Cyclic undrained triaxial test on normally consolidated sample with stress cycles of $q_{ampl} = 60$ kPa and displacement rate of $\dot{\varepsilon}_1 = 0.1$ mm/min

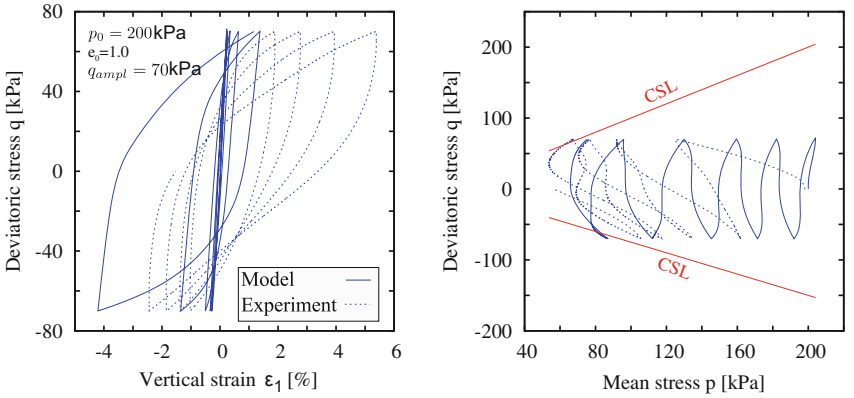

(a) q vs. ε_1 space (b) p vs. q space

Fig. 10. Cyclic undrained triaxial test on normally consolidated sample with stress cycles of $q_{ampl} = 70$ kPa and displacement rate of $\dot{\varepsilon}_1 = 0.1$ mm/min

The simulations represented with solid lines Fig. 7(a) show a similar pattern with the peak stress as for OCR = 1, Fig. 6(a).

Figure 8 presents a multi stage constant-rate-of-strain undrained triaxial test according to the following sequence: $\dot{\varepsilon}_1 = 10^{-4} \rightarrow \dot{\varepsilon}_1 = 10^{-5} \rightarrow \dot{\varepsilon}_1 = 10^{-6} \rightarrow \dot{\varepsilon}_1 = 10^{-5}\, 1/s$. The simulation shows satisfactory coincidence with experimental results.

The cyclic performance of the proposed model is presented in Figs. 9 and 10 for undrained triaxial compression tests with symmetric deviatoric stress cycles of amplitude $q_{ampl} = 60$ kPa and $q_{ampl} = 70$ kPa, respectively. The simulations with the set of parameters given in Table 1 for monotonic loading showed

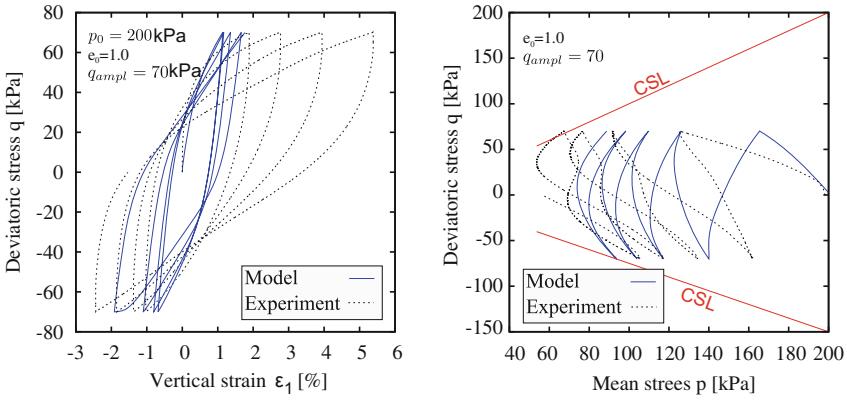

(a) q vs. ε_1 space (b) p vs. q space

Fig. 11. Cyclic undrained triaxial test on normally consolidated sample with stress cycles of $q_{ampl} = 70$ kPa and displacement rate of $\dot{\varepsilon}_1 = 0.1$ mm/min simulated with the extended model from [9]

excessive accumulation of stress and strain (ratcheting). Therefore, a new parameter set has been used in Figs. 9 and 10 in order to improve the prediction of the model upon cyclic loading. The simulations with this parameter set capture well the experimental observations for both deviatoric stress amplitudes.

In [9] the cyclic extension introduced by Poblete et al. [20] was implemented in the proposed visco ISA model. The model requires 3 additional parameters and is able to describe both monotonic and cyclic loading of clays with only one parameter set [7,9], an example of cyclic loading simulations is given in Fig. 11. The parameter set used for these simulations can be found in [7,9].

6 Closure and Outlook

In the present work, a constitutive model for the simulation of saturated clays within the ISA-plasticity has been proposed. The main feature of the model is its generality for viscous and non-viscous clays, thus different properties of clays can be evaluated with the same model. Furthermore, the model can describe also the cyclic behavior of clays due to its intergranular strain concept. The simulations for the Kaolin clay showed a good prediction for monotonic and cyclic loading in undrained triaxial tests and oedometer tests compared to experimental results. Also the strain rate dependency was successfully investigated, whereby the variation of the vertical strain rate was implemented. Some other experimental observations are left out for future model improvement, such as the inherent anisotropy, cementation, dilatancy and partial saturation.

References

1. Anderson, D., Richart, F.: Effects of straining on shear modulus of clays. J. Geotech. Eng. ASCE **102**(9), 975–987 (1976)
2. Avgerinos, V., Potts, D.M., Standing, J.: The use of kinematic hardening models for predicting tunnelling-induced ground movements in London clay. Géotechnique **66**(2), 106–120 (2016)
3. Buisman, K.: Results of long duration settlement test. In: 1st ICSMFE, pp. 103–107, Cambridge (1936)
4. Dafalias, Y.: Bounding surface plasticity. I: mathematical foundation and hypoplasticity. J. Eng. Mech. **112**(9), 966–987 (1986)
5. Fuentes, W.: Contributions in Mechanical Modelling of Fill Materials. Ph.D. thesis, Institute of Soil Mechanics and Rock Mechanics, Karlsruhe Institute of Technology, Karlsruhe, vol. 179 (2014)
6. Fuentes, W., Hadzibeti, M., Triantafyllidis, T.: Constitutive model for clays under the ISA framework. In: Triantafyllidis, T. (ed.) Holistic Simulation of Geotechnical Installation Processes. LNACM, vol. 80, pp. 115–129. Springer, Heidelberg (2016). doi:10.1007/978-3-319-23159-4_6
7. Fuentes, W., Tafili, M., Triantafyllidis, T.: An ISA-plasticity based model for viscous and non-viscous clays. Sent, Acta Geotechnica (2016)
8. Fuentes, W., Triantafyllidis, T.: ISA model: a constitutive model for soils with yield surface in the intergranular strain space. INJAMG **39**(11), 1235–1254 (2015)
9. Hadzibeti, M.: Formulation and calibration of a viscous ISA model for clays. Masterthesis. Institute of Soil Mechanics and Rock Mechanics, Karlsruhe Institute for Technology, Karlsruhe (2016)
10. Herle, I., Kolymbas, D.: Hypoplasticity for soils with low friction angles. Comp. Geotech. **31**(5), 365–373 (2004)
11. Jaky, J.: Pressure in silos. In: 2nd ICSMFE, pp. 103–107, London (1948)
12. Karstunen, M., Yin, Z.: Modelling time-dependent behavior of murro test embankment. Géotechnique **60**(10), 735–749 (2010)
13. Manzari, M., Akaishi, M., Dafalias, Y.: A simple anisotropic clay plasticity model. Mech. Res. Commun. **29**(4), 241–245 (2002)
14. Manzari, M., Dafalias, Y.: A critical state two-surface plasticity model for sands. GEOT **47**(2), 255–272 (1997)
15. Manzari, M., Papadimitriou, A., Dafalias, Y.: SANICLAY: simple anisotropic clay plasticity model. IJNAMG **30**(4), 1231–1257 (2006)
16. Masin, D.: Hypoplastic models for fine-grained solid. Ph.D. thesis, Charles University, Prague (2006)
17. Niemunis, A.: Extended hypoplastic models for soils. Habilitation, Monografia 34, Ruhr-University Bochum (2003)
18. Niemunis, A., Grandas-Tavera, C.E., Prada-Sarmiento, L.F.: Anisotropic viscohypoplasticity. Acta Geotech. **4**(4), 293–314 (2009)
19. Niemunis, A., Herle, I.: Hypoplastic model for cohesionless soils with elastic strain range. MCFM **4**(2), 279–299 (1997)
20. Poblete, M., Fuentes, W., Triantafyllidis, T.: On the constitutive modeling of multidimensional cyclic loading. Sent, Acta Geotechnica (2016)
21. Simo, J.C., Hughes, T.J.R.: Computational Inelasticity. Springer, New York (1998)
22. Stolle, D., Bonnier, P., Vermeer, P.: A soft soil model and experiences with two integration schemes. In: 6th International Symposium on Numerical Models in Geomechanics (NUMOG VI), pp. 123–128, Amsterdam, The Netherlands (1999)

23. Tsai, C., Mejia, L., Meymand, P.: A strain-based procedure to estimate strength softening in saturated clays during earthquakes. Soils Dynam. Earthquake Eng. **66**, 191–198 (2014)
24. Whittle, A.J., Kavvadas, M.J.: Formulation of MIT-E3 constitutive model for over consolidated clays. J. Geotech. Engi. Div. ASCE **120**(1), 173–198 (1994)
25. Wichtmann, T.: Soil behaviour under cyclic loading - experimental observations, constitutive description and applications. Habilitation, Karlsruhe Institute for Technology, Institute of Soil Mechanics and Rock Mechanics, vol. 181 (2016)
26. Wolffersdorff, P.: A hypoplastic relation for granular materials with a predefined limit state surface. Mech. Cohesive Frictional Mater. **1**(3), 251–271 (1996)
27. Yao, Y., Kong, L., Hu, J.: An elastic-viscous-plastic model for overconsolidated clays. Sci. China Technol. Sci. **56**(2), 441–457 (2013)
28. Yin, J., Graham, J.: Elastic viscoplastic modelling of the time-dependent stress-strain behavior of soils. Can. Geot. J. **36**(4), 736–745 (1999)

Evaluating the Performance of an ISA-Hypoplasticity Constitutive Model on Problems with Repetitive Loading

William Fuentes[1(✉)], Theodoros Triantafyllidis[2], and Carlos Lascarro[1]

[1] University del Norte, Barranquilla, Colombia
fuentes@uninorte.edu.co
[2] Institute of Soil Mechanics and Rock Mechanics, Karlsruhe Institute of Technology, Karlsruhe, Germany

Abstract. The ISA-plasticity is a useful theory to propose constitutive models for soils accounting for small strain effects. It uses the intergranular strain concept, previously proposed by Niemunis and Herle (1997) to enhance the capabilities of some existing hypoplastic models under cyclic loading. In contrast to its predecessor, the ISA-plasticity presents a completely different formulation to incorporate an elastic locus depending on a strain amplitude. However, it keeps similar advantages and brings other new ones such as the elastic locus and improved simulations of the plastic accumulation upon a number of cycles. In the present article, some numerical investigations are made to evaluate the performance of an ISA-plasticity based model on simulations with repetitive loading. We have chosen to couple the ISA-plasticity with the hypoplastic model by Wolfferdorff to simulate some experiments. At the beginning of the article, the theory of the ISA-plasticity is briefly explained. Subsequently, its numerical implementation is step by step detailed. A semi-explicit algorithm is proposed and some hints are given to allow the coupling with other models. At the end, some simulations of experiments with the Karlsruhe fine sand are shown in which the performance of the model under repetitive loading is evaluated. The behavior of the plastic accumulation is examined upon a number of cycles and some remarks are given about the current investigation.

Keywords: ISA model · Plastic accumulation · Repetitive loading · Hypoplasticity

1 Introduction

The ISA-Plasticity is a useful mathematical platform to develop constitutive models for the simulation of cyclic loading in soils. This theory considers the fact that the simulation of cyclic behavior is improved when accounting for the effect of the recent strain history [16,17]. Therefore, it incorporates the intergranular strain concept, originally proposed by Niemunis and Herle [13] to consider this

T. Triantafyllidis (ed.), *Holistic Simulation of Geotechnical Installation Processes*, Lecture Notes in Applied and Computational Mechanics 82, DOI 10.1007/978-3-319-52590-7_16

information. The mathematical formulation of the ISA-Plasticity is however different from the one of Niemunis and Herle [13]: to start, the evolution equation of the intergranular strain is elastopolastic, and its formulation is based on a simple bounding surface approach. Furthermore, it considers an elastic locus related to a specific strain amplitude which can be adjusted to the elastic threshold strain amplitude [18,20]. Finally, its yield surface presents a kinematic hardening similar to some "bubble" models for clay (e.g. [1]) to simulate a smooth transition between the elastic and plastic behavior.

Since the work of Fuentes and Triantafyllidis [6], the ISA-plasticity has been used to extend some existing models. Recently, an ISA-plasticity model was coupled with the hypoplastic model by Wolffersdorff [21] to examine its behavior under complex loading [15]. It was concluded that the model needed to be extended in order to simulate well the plastic accumulation under repetitive loading. The proposed extension in [15] is based on a simple mechanism: if the model experiences subsequent cycles away from the critical state line, it reduces the rate of plastic accumulation. With this, the proposed extension achieved a good performance in some simulations with cyclic loading. However, this version is recent and should be carefully inspected with additional examples in order to study its advantages and disadvantages. Beside this, the procedure for its numerical integration has not been well detailed and discussed. Hence, more description is expected by some users for the implementation of an ISA-plasticity based model on finite element codes to solve boundary value problems.

In the present work, we evaluate an ISA-plasticity based model under repetitive loading. We include some simulations of element test under monotonic and cyclic loading to analyze the behavior of the plastic accumulation upon a number of cycles. Furthermore, we analyze the performance of the model in a finite element simulation of a shallow foundation subjected to cyclic loading. Additional descriptions for the numerical implementation of the model were also included. The structure of the present article is as follows. We begin with an outline of the ISA-plasticity and give some hints to link it with some existing models. Then, a numerical integration scheme is detailed. Finally, the mentioned simulations are shown and carefully analyzed. The notation of this article is as follows. Scalar quantities are denoted with italic fonts (e.g. a, b), second rank tensors with bold fonts (e.g. $\mathbf{A}$, $\boldsymbol{\sigma}$), and fourth rank tensors with Sans Serif type (e.g. E, L). Multiplication with two dummy indices, also known as double contraction, is denoted with a colon ":" (e.g. $\mathbf{A} : \mathbf{B} = A_{ij}B_{ij}$). A dyadic product between two second rank tensors is symbolized with $\mathbf{A} \otimes \mathbf{B}$ and results in a fourth order tensor $C_{ijkl} = A_{ij}B_{kl}$. The deviatoric component of a tensor is symbolized with an asterisk as superscript $\mathbf{A}^*$. The effective stress tensor is denoted with $\boldsymbol{\sigma}$ and the strain tensor with $\boldsymbol{\varepsilon}$. The Roscoe invariants are defined as $p = -\mathrm{tr}\boldsymbol{\sigma}/3$, $q = \sqrt{3/2}\,\|\boldsymbol{\sigma}^*\|$, $\varepsilon_v = -\mathrm{tr}\boldsymbol{\epsilon}$ and $\varepsilon_s = \sqrt{2/3}\,\|\boldsymbol{\epsilon}^*\|$.

1.1 Brief Description of the ISA-plasticity

In this section the formulation of the ISA-plasticity is outlined. Details and additional information of the model are found in [5,6]. We use the same notation of the variables as in former publications [5,6].

According to this theory, cycles under small strain amplitudes ($\|\Delta\boldsymbol{\varepsilon}\| < 10^{-4}$) deliver an elastic response while those with larger strain amplitudes render plastic behavior. The transition from elastic to plastic is demarcated by the strain amplitude $\|\Delta\boldsymbol{\varepsilon}\| = R \approx 10^{-4}$. To capture this, the ISA-plasticity uses the information of the intergranular strain which is a strain-type state variable, proposed by Niemunis and Herle [13] to detect recent changes of the strain rate direction. Having this information, we may improve existing models for the simulation of cyclic loading and eliminate the excessive plastic accumulation (racheting). The ISA-plasticity featured an alternative evolution equation for the intergranular strain $\mathbf{h}$, with a special characteristic: under elastic conditions, the intergranular strain $\mathbf{h}$ evolves identically with the strain $\boldsymbol{\varepsilon}$:

$$\dot{\mathbf{h}} = \dot{\boldsymbol{\varepsilon}} \qquad \text{(under elastic conditions)} \tag{1}$$

The latter condition makes simple the formulation of a yield surface with the desired property. It should present a spherical shape within the principal space of the intergranular strain to guarantee an elastic locus with a specific strain amplitude $\|\Delta\boldsymbol{\varepsilon}\| = R$. Therefore, the yield function denoted with F_H, is defined as:

$$F_H = \|\mathbf{h} - \mathbf{c}\| - \frac{R}{2} \tag{2}$$

whereby R is a material parameter representing the strain amplitude and $\mathbf{c}$ is a tensor representing the center of the yield surface and therefore called the back-intergranular strain. The value of R may be adjusted to the elastic amplitude observed on shear modulus degradation curves, with typical values around $R \approx 10^{-5}$–10^{-4}. The yield surface presents a kinematic hardening which follows some hardening rules from the bounding surface plasticity. Therefore, the model considers an additional bounding surface as depicted in Fig. 1. Its movement is ruled by the kinematic hardening of its center, i.e. the back-intergranular strain $\mathbf{c}$.

The evolution law of the intergranular strain $\mathbf{h}$ is elastoplastic. Its formulation was basically proposed considering two facts: the first is that under elastic conditions its evolution equation gives $\dot{\mathbf{h}} = \dot{\boldsymbol{\varepsilon}}$. The second is the assumption of an associated flow rule $\mathbf{N} = (\partial F_H/\partial \mathbf{h})$ to make its formulation simple. Hence, the following evolution law has been proposed [6]:

$$\dot{\mathbf{h}} = \dot{\epsilon} - \dot{\lambda}_H \mathbf{N} \tag{3}$$

whereby $\lambda_H \geq 0$ is the consistency parameter (or plastic multiplier) and $\mathbf{N}$ is the flow rule ($\|\mathbf{N}\| = 1$) which reads:

$$\mathbf{N} = \frac{\partial F_H}{\partial \mathbf{h}} = \frac{\mathbf{h} - \mathbf{c}}{R/2} \tag{4}$$

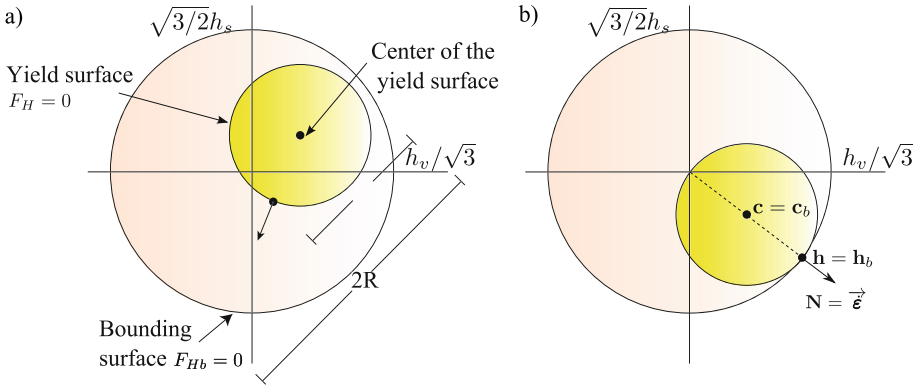

Fig. 1. Yield surface and bounding surface within the intergranular strain principal space. (a) Names and notation. (b) Example of a bounding condition for the intergranular strain

The consistency parameter vanishes under elastic conditions $\lambda_H = 0$ and takes its maximum value $\dot{\lambda}_H = \|\dot{\epsilon}\|$ at the bounding surface of the intergranular strain. The shape of the bounding surface is also spherical but with fixed center at $\mathbf{h} = \mathbf{0}$ and diameter equal to $2R$, i.e. it presents twice the size of the yield surface. The bounding surface function F_{Hb} reads:

$$F_{Hb} = \|\mathbf{h}\| - R \tag{5}$$

The hardening rule for the back-intergranular strain $\mathbf{c}$ uses similar ideas to the bounding surface plasticity. For this purpose, we project an image tensor of $\mathbf{c}$ at the bounding surface with the following mapping rule:

$$\mathbf{c}_b = (R/2)\overrightarrow{\dot{\boldsymbol{\varepsilon}}} \tag{6}$$

whereby $\mathbf{c}_b$ is the projected tensor. The hardening function $\bar{\mathbf{c}} = \dot{\mathbf{c}}/\dot{\lambda}$ reads:

$$\bar{\mathbf{c}} = \beta_h(\mathbf{c}_b - \mathbf{c})/R \quad \text{with} \quad \dot{\mathbf{c}} = \dot{\lambda}_H \bar{\mathbf{c}} \tag{7}$$

where β_h is an additional parameter to control the rate of $\mathbf{c}$. Notice that if $\mathbf{c}_b = \mathbf{c}$ then the rate $\bar{\mathbf{c}} = \mathbf{0}$ vanishes. Hence for very large strains, the model gives $\mathbf{h} = \mathbf{h}_b$, $\mathbf{c} = \mathbf{c}_b$, see Fig. 1b. The expression for the consistency parameter is deduced by simple plasticity relations from the consistency equation $\dot{F}_H = 0$ and reads:

$$\dot{\lambda}_H = \frac{\langle \mathbf{N} : \dot{\varepsilon} \rangle}{1 - \left(\dfrac{\partial F_H}{\partial \mathbf{c}} \right) : \bar{\mathbf{c}}} \tag{8}$$

whereby the operator $\langle x \rangle = x$ when $x > 0$ and $\langle x \rangle = 0$ if $x \leq 0$. The Eqs. 2–8 conform the model of the intergranular strain alone. This model evolves in parallel with the mechanical model but independently because it does not depend on

the stress tensor $\boldsymbol{\sigma}$. The ISA-plasticity introduces some additional scalar factors to use the information provided by the intergranular strain model. These scalar factors depend on the projection of the intergranular strain $\mathbf{h}$ at the bounding surface using the flow rule $\mathbf{N}$ as the mapping tensor:

$$\mathbf{h}_b = R\mathbf{N} \tag{9}$$

where $\mathbf{h}_b$ is the projected tensor. Aided by tensor $\mathbf{h}_b$, one may detect some recent movements in the loading history. For example, if $\|\mathbf{h}_b - \mathbf{h}\| = 0$, it means that the current intergranular strain lies at its bounding condition. According to the model, this condition is only reached under large strain amplitudes and is therefore called "mobilized states". On the other hand, greater values of $\|\mathbf{h}_b - \mathbf{h}\| > 0$ represent a reversal loading which has been recently performed. Hence, the model proposes the function ρ as:

$$\rho = 1 - \frac{\|\mathbf{h}_b - \mathbf{h}\|}{2R} \tag{10}$$

In this manner, $\rho = 0$ implies reversal loading while $\rho = 1$ implies "mobilized states". In the next section, the mechanical model will be briefly described.

1.2 Description of the Mechanical Model

The mechanical model relates the stress rate $\dot{\boldsymbol{\sigma}}$ with the strain rate $\dot{\boldsymbol{\varepsilon}}$ through a constitutive equation. For this theory, the constitutive equation presents the following general form:

$$\dot{\boldsymbol{\sigma}} = m\bar{\mathsf{E}} : (\dot{\boldsymbol{\varepsilon}} - y_h\dot{\bar{\boldsymbol{\varepsilon}}}^p) \tag{11}$$

where m and y_h are scalar functions, $\bar{\mathsf{E}}$ and $\dot{\bar{\boldsymbol{\varepsilon}}}^p$ are called "mobilized" stiffness tensor and "mobilized" plastic strain rate respectively. Tensors $\bar{\mathsf{E}}$ and $\dot{\bar{\boldsymbol{\varepsilon}}}^p$ can be adjusted to existing relations of hypoplastic models, e.g. [8,10,21]. Actually, when the intergranular strain lies under mobilized states, the scalar functions render $m = 1$ and $y_h = 1$ and the model yields to:

$$\dot{\boldsymbol{\sigma}} = \bar{\mathsf{E}} : (\dot{\boldsymbol{\varepsilon}} - \dot{\bar{\boldsymbol{\varepsilon}}}^p) \qquad \text{(for mobilized states)} \tag{12}$$

This mathematical form is actually not recognized as a formal hypoplastic model [9]. Users of the Hypoplasticity family are rather familiar with the equation:

$$\dot{\boldsymbol{\sigma}} = \mathsf{L}^{\text{hyp}} : \dot{\boldsymbol{\varepsilon}} + \mathbf{N}^{\text{hyp}}\,\|\dot{\boldsymbol{\varepsilon}}\| \qquad \text{(for mobilized states)} \tag{13}$$

whereby L^{hyp} is the "linear" stiffness and $\mathbf{N}^{\text{hyp}}$ is the "non-linear" stiffness [8,10,21,22]. The existing relations for tensors L^{hyp} and $\mathbf{N}^{\text{hyp}}$ can be adopted for the present theory when setting the following equivalencies:

$$\mathsf{L}^{\text{hyp}} = \bar{\mathsf{E}} \tag{14}$$

$$\mathbf{N}^{\text{hyp}} = -(\mathsf{E} : \dot{\bar{\boldsymbol{\varepsilon}}}^p)/\|\dot{\boldsymbol{\varepsilon}}\| \tag{15}$$

We have selected the hypoplastic model by Wolffersdorff [21] for the present work considering that our interest is the simulation of sand.

The scalar function y_h is a factor which ranges between $0 \leq y_h \leq 1$ and aims to reduce the plastic strain rate after reversal loading. The function y_h reads:

$$y_h = \rho^{\chi} \langle \mathbf{N} : \overrightarrow{\dot{\boldsymbol{\varepsilon}}} \rangle \tag{16}$$

where χ is an exponent which can be set as a material constant [6], or improved to account for the effect of repetitive loading within the plastic accumulation rate [14]. The function m aims to increase the stiffness upon reversal loading. This function reads:

$$m = m_R + (1 - m_R) y_h \tag{17}$$

where m_R is a material constant to increase the stiffness under elastic conditions. The consideration of these equations allows to illustrate schematically the response of the ISA model under different strain amplitudes, as depicted in Fig. 1. For instance, let us suppose an elastic strain amplitude of $R = 10^{-4}$. For small strain amplitudes ($\|\Delta\boldsymbol{\varepsilon}\| < 10^{-4}$), the behavior is elastic and the constitutive equation yields to $\dot{\boldsymbol{\sigma}} = m_R \bar{\mathsf{E}} : \dot{\boldsymbol{\varepsilon}}$. For very large strain amplitudes ($\|\Delta\boldsymbol{\varepsilon}\| > 10^{-2}$), also called "mobilized states", the intergranular strain lies at its bounding condition $\mathbf{h} = \mathbf{h}_b$ and the scalar factors give $y_h = 1$ and $m = 1$. Therefore, the model coincides with the hypoplastic equation $\dot{\boldsymbol{\sigma}} = \bar{\mathsf{E}} : (\dot{\boldsymbol{\varepsilon}} - \dot{\tilde{\boldsymbol{\varepsilon}}}^p)$ or $\dot{\boldsymbol{\sigma}} = \mathsf{L}^{\text{hyp}} : \dot{\boldsymbol{\varepsilon}} + \mathbf{N}^{\text{hyp}} \|\dot{\boldsymbol{\varepsilon}}\|$. Between these two states, a "transition" phase exists in which the model operates with the equation $\dot{\boldsymbol{\sigma}} = m\bar{\mathsf{E}} : (\dot{\boldsymbol{\varepsilon}} - y_h \dot{\tilde{\boldsymbol{\varepsilon}}}^p)$, see Fig. 2.

The recent modification by Poblete et al. [15] included the modification of exponent χ to improve the simulations under repetitive loading. In order to detect whether a few or a number of subsequent cycles have been performed, they proposed an additional state variable ε^{acc} with the following evolution law:

$$\dot{\varepsilon}_{\text{acc}} = \frac{C_a}{R}(1 - y_h - \varepsilon_{\text{acc}}) \|\dot{\boldsymbol{\varepsilon}}\| \tag{18}$$

whereby C_a is a material parameter controlling the rate of $\dot{\varepsilon}_{\text{acc}}$ [15]. Notice that if one performs subsequent cycles, the function y_h reduces its value $y_h \to 0$ and the state variable ε_{acc} starts to increase. Hence, one can use this information to reduce the plastic strain rate upon subsequent cycles which are now detected with the condition $\varepsilon_{\text{acc}} > 0$. To achieve this, the exponent χ is reduced according to the relation:

$$\chi = \chi_0 + \varepsilon_{\text{acc}}(\chi_{\max} - \chi_0) \tag{19}$$

whereby χ_0 and $\chi_{\max}$ are material constants. The first should be adjusted for small number of cycles $N < 3$ and the other for large number of cycles (e.g. $N > 15$).

We now end this section with the deduction of the continuum (explicit) stiffness $\mathsf{M} = (\partial\dot{\boldsymbol{\sigma}}/\partial\dot{\boldsymbol{\varepsilon}})$ of the model. This can be deduced after derivation of the constitutive equation such that it reduces to:

$$\dot{\boldsymbol{\sigma}} = \mathsf{M} : \dot{\boldsymbol{\varepsilon}} \tag{20}$$

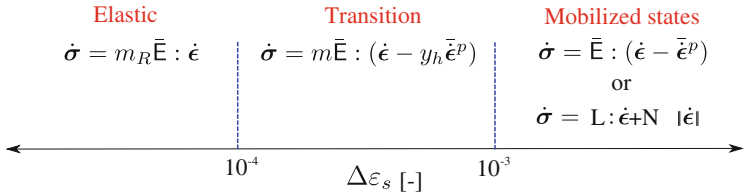

Fig. 2. For cycles under small strain amplitudes $\|\dot{\varepsilon}\| < R$, the behavior is elastic. At mobilized states, the constitutive equation turns into hypoplastic. Between these two states, a smooth transition is simulated through the functions $0 \leq m \leq m_R$ and $0 \leq y_h \leq 1$

whereby the continuum stiffness M reads:

$$\mathsf{M} = \begin{cases} [m_R + (1 - m_R) y_h](\mathsf{L}^{\text{hyp}} + \rho^{\chi} \mathbf{N}^{\text{hyp}} \otimes \mathbf{N}) & \text{for } F_H \geq 0 \\ m_R \mathsf{L}^{\text{hyp}} & \text{for } F_H < 0 \end{cases} \tag{21}$$

1.3 Numerical Implementation

A numerical implementation for finite element codes has been performed in a FORTRAN subroutine following the syntax of ABAQUS. The simulations were made using the open-source software INCREMENTAL DRIVER [12] created by Niemunis but modified by the authors of this work to improve the code for cyclic loading. The algorithm is semi-explicit, meaning that most equations were solved explicitly except by a few which will be mentioned in the sequel. The integration strategy is similar to classical implementations of elastoplastic models, in which an elastic predictor is made to detect whether an elastic or plastic step should be performed. For this implementation, a subincrementation algorithm is recommended to avoid numerical convergence difficulties. A subincrement size of about $\|\Delta\varepsilon\| \approx 10^{-5}$ is recommended. The implementation is split in two parts, the first related to the intergranular strain model and the second to the mechanical model. The subroutine structure is typical of finite elements code, in which the strain increment together with the current state (stress, state variables) are given as input and the subroutine delivers the state at the end of the increment, see Table 1. The jacobian $J_{ijkl} = \partial \Delta\sigma_{ij} / \partial \Delta\varepsilon_{kl}$ is provided at the end of the implementation for its use in the global finite element matrix. The integration presented in the subsequent sections is based on the equations from Sect. 1.1.

1.4 Integration of the Intergranular Strain Model

The implementation begins with the intergranular strain model. The fact that the model does not depend on the stress $\boldsymbol{\sigma}$ makes its implementation easier because is not coupled with the mechanical model. In other words, the intergranular strain may be integrated independently from the mechanical model. The integration scheme begins with the computation of a trial elastic step to

Table 1. Input and ouput variables of the numerical implementation.

Symbol name	
Input variables	
ε_{ij}	Strain (beginning of increment)
$\Delta\varepsilon_{ij}$	Strain increment
σ_{ij}	Stress (beginning of increment)
Δt	Time increment
h_{ij}	Intergranular strain (beginning of increment)
c_{ij}	Back-intergranular strain (beginning of increment)
$\varepsilon^{\mathrm{acc}}$	State variable (beginning of increment)
Output variables	
σ_{ij}	Stress (end of the increment)
J_{ijkl}	Jacobian (end of increment)
h_{ij}	Intergranular strain (end of increment)
c_{ij}	Back-intergranular strain (end of increment)
$\varepsilon^{\mathrm{acc}}$	State variable (end of increment)

evaluate the yield function. In the following lines, a step-by-step guide is given using the index notation to make simpler the interpretation of the tensorial operations.

The first step is to define the strain rate $\dot{\varepsilon}_{ij}$ and the unit strain rate $\hat{\dot{\varepsilon}}_{ij}$:

$$\begin{aligned} \dot{\varepsilon}_{ij} &= \Delta\varepsilon_{ij}/\Delta t \\ \hat{\dot{\varepsilon}}_{ij} &= \frac{\dot{\varepsilon}_{ij}}{\sqrt{\dot{\varepsilon}_{ij}\dot{\varepsilon}_{ij}}} \end{aligned} \tag{22}$$

Then, the trial intergranular strain variable h_{ij}^{trial} and trial back-intergranular strain c_{ij}^{trial} are computed assuming elastic conditions:

$$\begin{aligned} h_{ij}^{\mathrm{trial}} &= h_{ij} + \Delta\varepsilon_{ij} \\ c_{ij}^{\mathrm{trial}} &= c_{ij} \end{aligned} \tag{23}$$

The trial yield surface F^{trial} is then computed:

$$F^{\mathrm{trial}} = [(h_{ij}^{\mathrm{trial}} - c_{ij}^{\mathrm{trial}})(h_{ij}^{\mathrm{trial}} - c_{ij}^{\mathrm{trial}})]^{1/2} - \frac{R}{2} \tag{24}$$

In case that $F^{\mathrm{trial}} < 0$, an elastic step is performed. For that case, we take the trial variables h_{ij}^{trial} and c_{ij}^{trial} as the solution:

$$\begin{aligned} h_{ij} &= h_{ij}^{\mathrm{trial}} \\ c_{ij} &= c_{ij}^{\mathrm{trial}} \end{aligned} \tag{25}$$

In case that $F^{\text{trial}} \geq 0$, a plastic step is performed. In the plastic case, we begin with the computation of the flow rule. For our implementation, we use the approximation $N_{ij} \approx N_{ij}^{\text{trial}}$:

$$N_{ij} = \frac{(h_{ij}^{\text{trial}} - c_{ij}^{\text{trial}})}{\sqrt{(h_{ij}^{\text{trial}} - c_{ij}^{\text{trial}})(h_{ij}^{\text{trial}} - c_{ij}^{\text{trial}})}} \tag{26}$$

Subsequently, the consistency parameter is computed $\dot{\lambda}$ as a function of the image tensor $c_{ij}^{\max}$ and the hardening function $\bar{c}_{ij}$:

$$\begin{aligned} c_{ij}^{\max} &= \frac{R}{2}\hat{\varepsilon} \\ \bar{c}_{ij} &= \frac{\beta_R}{R}(c_{ij}^{\max} - c_{ij}) \\ \dot{\lambda} &= \frac{N_{ij}\dot{\varepsilon}_{ij}}{\bar{c}_{ij}N_{ij} + 1} \end{aligned} \tag{27}$$

Finally, the back-intergranular strain c_{ij} and the intergranular strain h_{ij} are deduced implicitly from Eqs. 3 and 7 respectively:

$$\begin{aligned} c_{ij} &= c_{ij} + \frac{\beta_R/R(c_{ij}^{\max} - c_{ij})\dot{\lambda}\Delta t}{1 + \beta_R/R\dot{\lambda}\Delta t} \\ h_{ij} &= h_{ij} + \frac{\left[\dot{\varepsilon}_{ij}\Delta t - \dfrac{\dot{\lambda}\Delta t}{R/2}(h_{ij} - c_{ij})\right]}{\left(1 + \dfrac{\dot{\lambda}\Delta t}{R/2}\right)} \end{aligned} \tag{28}$$

At the end of the plastic step, we recommend to use a simple correction to ensure the condition $F_H = 0$. We compute the flow rule N_{ij} with the actualized variables of the tensors h_{ij} and c_{ij} and then we correct c_{ij} as follows:

$$\begin{aligned} N_{ij} &= \frac{(h_{ij} - c_{ij})}{\sqrt{(h_{ij} - c_{ij})(h_{ij} - c_{ij})}} \\ c_{ij} &= h_{ij} - \frac{R}{2}N_{ij} \end{aligned} \tag{29}$$

Notice that with the latter correction the yield function gives $F_H = 0$. Some minor refinements may be introduced to the code to ensure that h_{ij} and c_{ij} never cross beyond the bounding surface, but these corrections are not discussed in the present work. In the next section, the numerical integration of the mechanical model is detailed.

1.5 Integration of the Mechanical Model

We now present an integration procedure for the mechanical model. In contrast to the previous section, the mechanical model is coupled with the response of the

intergranular strain. An implicit implementation is troublesome in view of the large amount of derivatives to be considered. Therefore, we perform an explicit integration and let the numerical convergence to be achieved by selecting an appropiated subincrement size. In the following lines, the code sequence for the mechanical model is explained.

We begin with the computation of exponent χ according to Eq. 19:

$$\chi = \chi_0 + \varepsilon_{\text{acc}}(\chi_{\max} - \chi_0) \tag{30}$$

Then, the flow rule N_{ij} is once more actualized with the variables h_{ij} and c_{ij} calculated within the intergranular strain model:

$$N_{ij} = \frac{(h_{ij} - c_{ij})}{\sqrt{(h_{ij} - c_{ij})(h_{ij} - c_{ij})}} \tag{31}$$

Subsequently, the scalar factors ρ and y_h are evaluated:

$$\begin{aligned} \rho &= 1 - \frac{\sqrt{(RN_{ij} - h_{ij})(RN_{ij} - h_{ij})}}{2R} \\ y_h &= \rho^{\chi}\langle N_{ij}\hat{\dot{\varepsilon}}_{ij}\rangle \end{aligned} \tag{32}$$

Once the scalar functions and the intergranular model are actualized, we proceed to compute the stiffness tensor M_{ijkl}. For this purpose, tensors N_{ij}^{hyp} and L_{ijkl}^{hyp} ought to be defined. For our code, we have used some additional FORTRAN subroutines to compute these tensors according to the hypoplastic equation by Wolfferdorff [21], see Appendix A. We recall that the user is free to select the hypoplastic model with its respective definitions for tensors N_{ij}^{hyp} and L_{ijkl}^{hyp}. In general, these tensors do not depend on the intergranular strain model variables, but only on the current stress $\boldsymbol{\sigma}$ and void ratio e. Hence, we recommend their implementation with a simple explicit procedure with the appropriate subincrement size. The user may improve this integration with automatic subincrementation with error control [3,4].

Having tensors N_{ij}^{hyp} and L_{ijkl}^{hyp} defined, we compute the stiffness tensor M_{ijkl}. The computation of the stiffness tensor M_{ijkl} depends whether an elastic ($F^{\text{trial}} \geq 0$) or plastic step ($F^{\text{trial}} < 0$) has been performed within the intergranular strain model and reads:

$$M_{ijkl} = \begin{cases} [m_R + (1 - m_R)y_h](L_{ijkl}^{\text{hyp}} + \rho^{\chi} N_{ij}^{\text{hyp}} N_{kl}) & \text{for } F^{\text{trial}} \geq 0 \\ m_R L_{ijkl} & \text{for } F^{\text{trial}} < 0 \end{cases} \tag{33}$$

The stress σ_{ij} is actualized with the equation:

$$\sigma_{ij} = \sigma_{ij} + M_{ijkl}\Delta\epsilon_{kl} \tag{34}$$

Finally, the void ratio e and the state variable ε_{acc} are actualized:

$$\begin{aligned} \varepsilon_{\text{acc}} &= \varepsilon_{\text{acc}} + \frac{C_a}{R}(1 - y_h - \varepsilon_{\text{acc}})\sqrt{\Delta\varepsilon_{ij}\Delta\varepsilon_{ij}} \\ e &= e + (1 + e)(\Delta\varepsilon_{ii}) \end{aligned} \tag{35}$$

For the sake of simplicity, we approximate the jacobian with $J_{ijkl} \approx M_{ijkl}$ at the end of the subroutine. Simulations have shown that this approximation leads to numerical convergence.

1.6 Material Parameters

In this section a brief description of the material parameters is given. A summary of the model parameters with their respective names is given in Table 2. In this table, we have also included their suggested range and some useful experiments for their determination.

We basically distinguish three types of parameters: the first related to the behavior of the material under monotonic loading. These parameter are the one from tensors $\mathsf{L}^{\mathrm{hyp}}$ and $\mathbf{N}^{\mathrm{hyp}}$, see Appendix A. The hypoplastic model by Wolfferdorff adopted incorporates 8 parameters very well studied in the literature [7,11]. They correspond to h_s, n_B, e_{i0}, e_{c0}, e_{d0}, α and β and are calibrated using routine tests under monotonic loading, especially oedometric and triaxial tests. A comprehensive guide for their determination can be found in [7,15]. The second group corresponds to those incorporated in the evolution law of the intergranular strain model. They correspond to m_R, R, β_h and χ_0 and can be adjusted with cyclic triaxial test. Notice that some of these parameters, such as m_R and R, were already introduced in the intergranular strain model by Niemunis and Herle [11,13] and therefore their calibration experience can be also used for the present model. A procedure for their determination is explained in some recent works [5,6,15]. Lastly, the parameters C_a and $\chi_{\max}$ are aimed to control the behavior of the model for a large number of repetitive cycles (e.g. $N > 15$). They were explained in the work of [15] including some remarks for their calibration. In order to analyze the influence of the parameter C_a, we have included some simulations of a cyclic undrained triaxial test in Figs. 3 and 4. These simulations borrow the parameters of the Karlsruhe fine sand (see Table 2) but vary the parameter $C_a = \{0.005, 0.015, 0.025\}$. The void ratio was set to $e = 0.8$ and the initial consolidation pressure to $p_0 = 100\,\mathrm{kPa}$. Cycles with a stress amplitude of $q^{\mathrm{amp}} = 50\,\mathrm{kPa}$ were applied. The results shows how increasing values of C_a increases the number of cycles required to reach the critical state line, see e.g. Fig. 4. Hence, in some way the parameter C_a represents how fast the model increases its stiffness due to the application of subsequent cycles. We will show that a similar pattern is observed in finite element simulations of cyclic phenomena.

2 Simulations of Experiments

In this section, we present the simulations of some triaxial tests to analyze the model. These simulations consider an element test condition, meaning that homogeneous fields of stress and strain are assumed. The selected material corresponds to the Karlsruhe fine sand, which has been previously calibrated in a

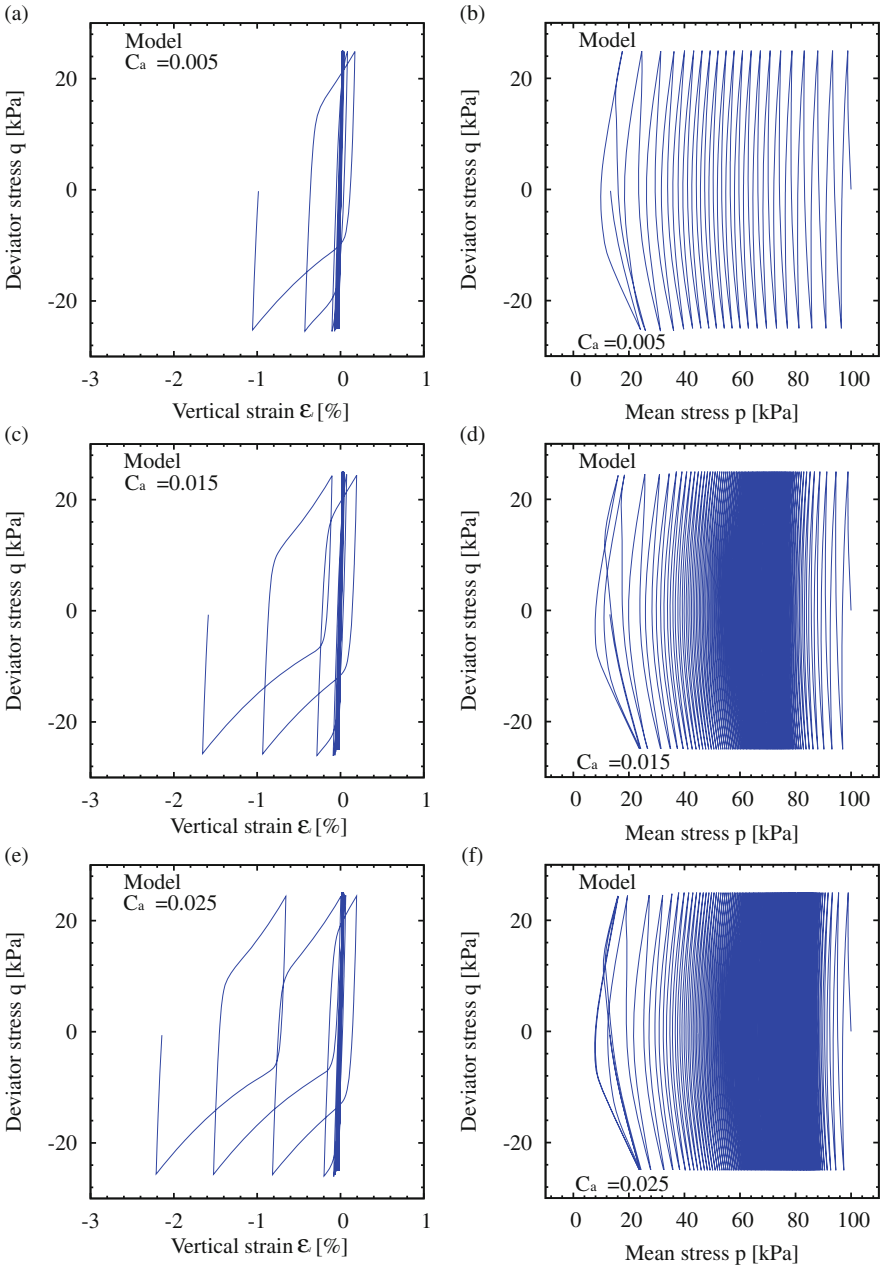

Fig. 3. Simulations of cyclic undrained triaxial test. Parameters of Karlsruhe fine sand. Variation of parameter C_a

Table 2. Material constants of the model

	Description	Units	Approx. range	Value	Useful experiments
Wolffersdorff hypoplaticity					
φ_c	Critical state friction angle	[°]	0°−50°	33	UTC[a]
h_s	Granular hardness	[-]	$10-10^7$	86260	OC[b]
n_B	Barotropy exponent	[-]	$10^{-6}-1$	0.32	OC
e_{i0}	Maximum void ratio	[-]	0.1−2	1.21	$e_{\max}$ test
e_{c0}	Critical void ratio	[-]	0.1−2	1.09	$e_{\max}$ test, UTC, DTC[c]
e_{d0}	Minimal void ratio	[-]	0.1−2	0.67	
α	Dilatancy exponent	[-]	0−2	0.21	UTC, DTC
β	Exponent	[-]	0−10	1.5	UTC, OC, UTC, DTC
ISA parameters					
m_R	Stiffness factor	[-]	1−7	5	CUTC[d]
R	IS yield surface radius	[-]	$10^{-5}-10^{-4}$	1.4×10^{-4}	–
β_h	IS hardening parameter	[-]	0−1	0.35	CUTC
χ_0	Minimum value of χ	[-]	1−10	7	CUTC
Extension by [15]					
C_a	Controls the rate of ε^{acc}	[-]	0−1	0.025	CUTC
$\chi_{\max}$	Maximum value of χ	[-]	1−50	15	CUTC

[a]UTC: Undrained triaxial test
[b]OC: Oedometric compression test
[c]DTC: Drained triaxial test
[d]CUTC: Cyclic undrained triaxial test

former work [15]. This sand presents a mean grain size of $d_{50} = 0.14$ and a uniformity coefficient equal to $C_u = d_{60}/d_{10} = 1.5$. The grain size is catalogued as sub-angular, and seems not to produce an inherent anisotropy on air pluviated samples due to its roundness [5]. The minimum and maximum void ratios are $e_{\min} = 0.677$ and $e_{\max} = 1.054$ respectively and a specific gravity of $G_s = 2.65$ has been determined.

The first simulations correspond to six different undrained triaxial tests under monotonic loading. All these tests were consolidated isotropically to the same initial mean stress $p = 200\,\text{kPa}$ and sheared under triaxial conditions. Three of them were sheared under compression while the other three under extension. The void ratios e range between $e = 0.698-0.964$ and are indicated in Fig. 5. All tests were simulated with the proposed model and showed in general a good agreement, except by the lack of a quasi-steady state in the simulations. The latter shortcoming is related to the performance of the Wolffersdorff hypoplastic model.

The next experiments consist on two different cyclic undrained triaxial tests. The first is shown in Fig. 6. The sample was isotropically consolidated to a mean stress of $p_0 = 200\,\text{kPa}$ and ended with a void ratio of $e = 0.800$. Then, stress cycles with an amplitude of $q^{\text{amp}} = 120\,\text{kPa}$ were applied. The experiment exhibited 8 cycles before reaching failure at the critical state line. The simulations

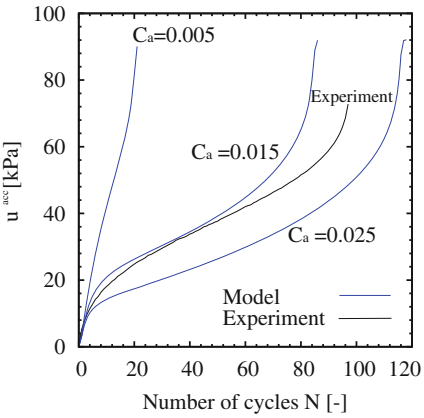

Fig. 4. Simulations of cyclic undrained triaxial test. Parameters of Karlsruhe fine sand. Variation of parameter C_a

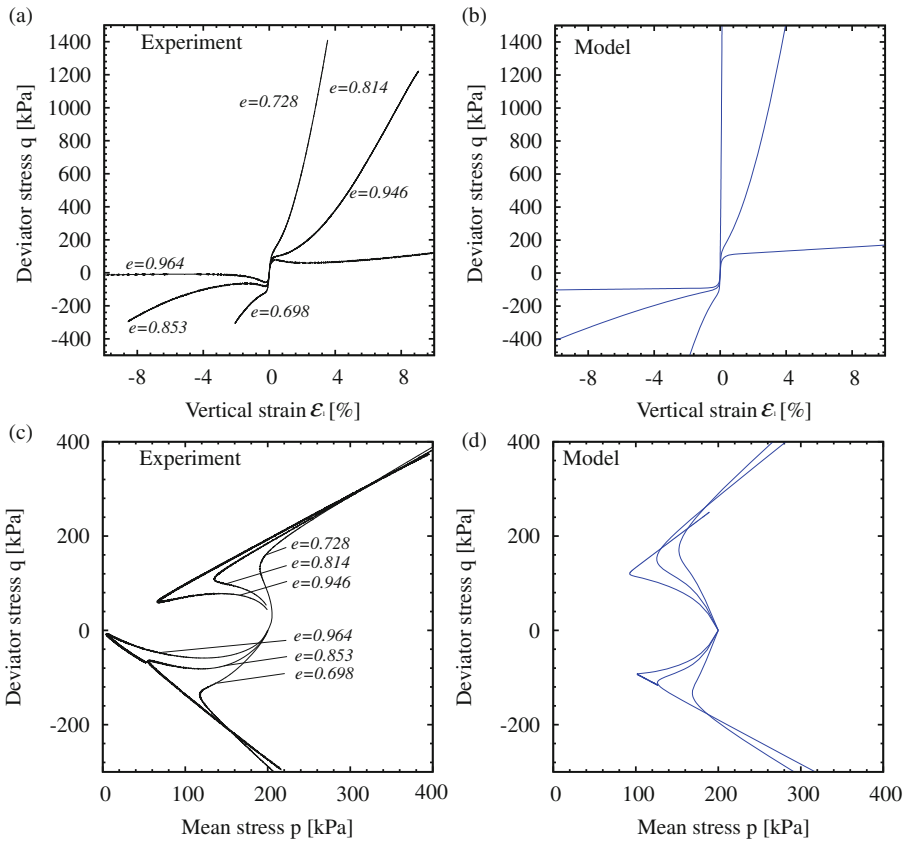

Fig. 5. Undrained triaxial test under compression and extension. Variation of initial void ratios. Experiments using Karlsruhe fine sand, data from [19]

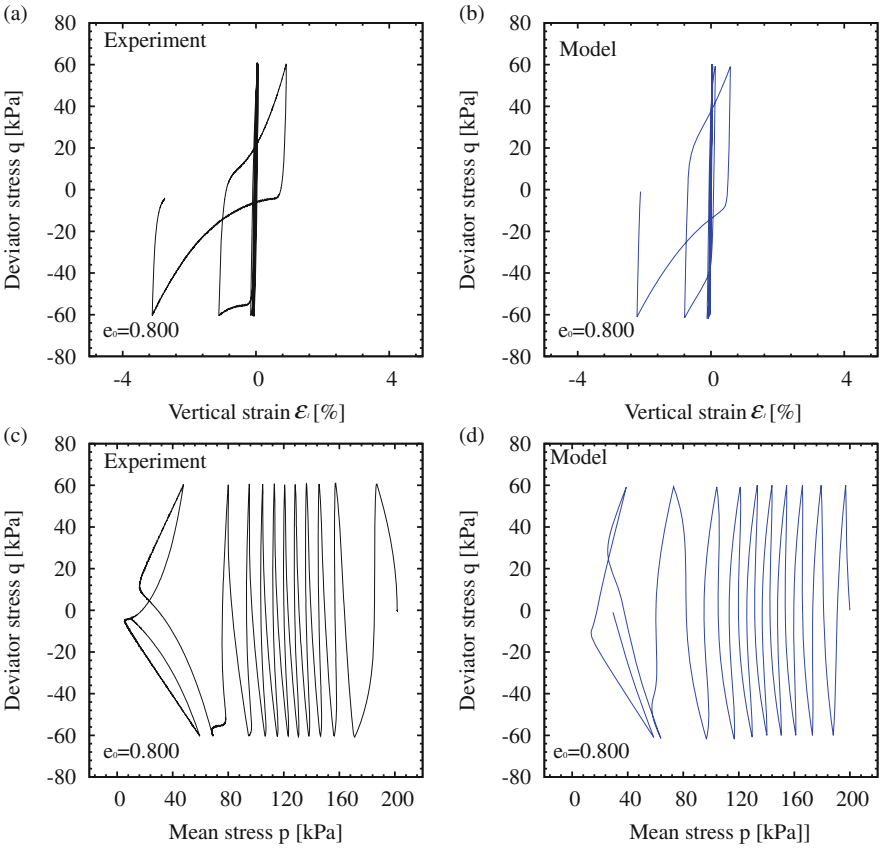

Fig. 6. Undrained triaxial test under cyclic loading. Deviator stress amplitude of $q^{\text{amp}} = 120\,\text{kPa}$. Experiment using Karlsruhe fine sand, data from [19]

also showed the same number of cycles. The post-failure behavior may present some discrepancies. At that state, some other effects such as the cyclic mobility are of importance, but this analysis is out of the scope of the present article. The second cyclic test presents a similar density $e = 0.798$ after consolidation but a different stress amplitude $q^{\text{amp}} = 50\,\text{kPa}$. The sample has been isotropically consolidated to a pressure of $p = 100\,\text{kPa}$. Considering the smaller value of the stress amplitude, a larger number of cycles before reaching failure is expected. The experiment showed about 90 cycles while the simulation showed about 83 cycles (Fig. 7). This is discrepancy is somehow small and may be improved by selecting more appropriated parameters. The accumulated pore pressure u^{acc} against the number of cycles N of the two cyclic triaxial tests are plotted in Fig. 8.

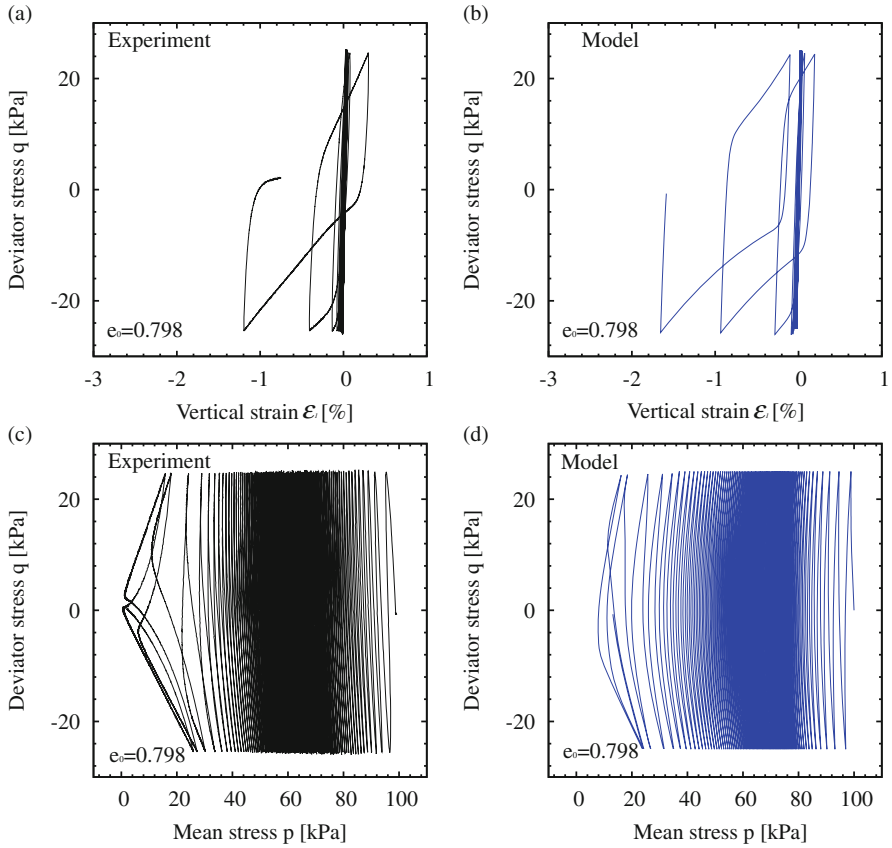

Fig. 7. Undrained triaxial test under cyclic loading. Deviator stress amplitude of $q^{\text{amp}} = 50\,\text{kPa}$. Experiment using Karlruhe fine sand, data from [19]

3 Simulations with Finite Elements

We now evaluate the constitutive model in a boundary value problem solved with finite elements. The problem corresponds to a circular shallow foundation subjected to cyclic loading. The finite element model was made by [23] to simulate a scaled model of a shallow foundation constructed in the laboratory of the Institute of Soil Mechanics and Rock Mechanics from the Karlsruhe Institute of Technology [23]. The geometry and the boundary conditions are depicted in Fig. 9. The main objective is to analyze the influence of the parameter C_a in the simulations. Axial-symmetric finite elements with two degrees of freedom per node (only displacements) were employed. The soil corresponds to the Karlsruhe fine sand in dry conditions, i.e. no pore water pressure were included. The problem has been simulated using the software ABAQUS Standard. A contact formulation solved by the penalty method has been employed to simulate the frictional interaction between the foundation and the soil with a friction coefficient of 0.5.

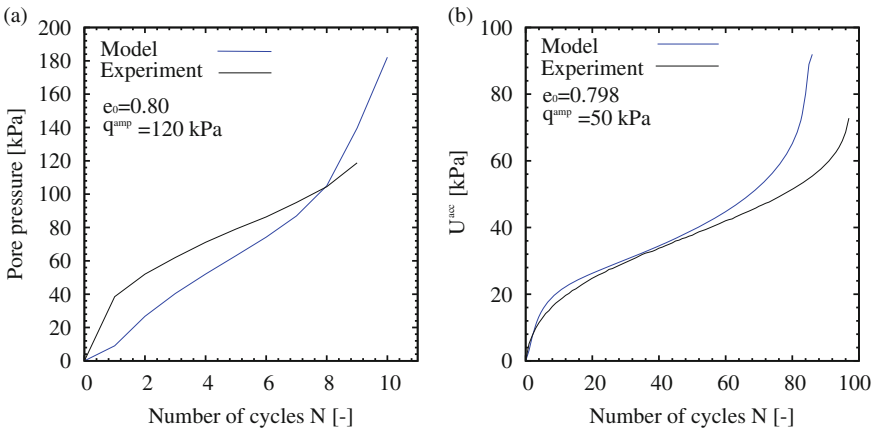

Fig. 8. Accumulated pore pressure u^{acc} against number of cycles N. Experiment using Karlruhe fine sand, data from [19]

The foundation material is steel and is simulated with an isotropic elastic model with a Young modulus equal to $E = 2.1 \times 10^8$ kPa and Poisson ratio $\nu = 0.3$. The density of the foundation has been neglected on the current analysis.

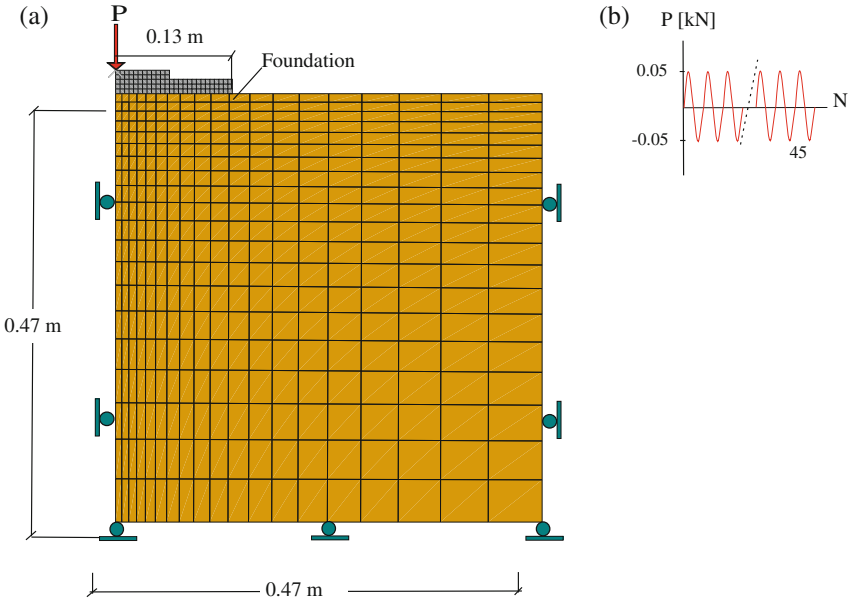

Fig. 9. Geometry and boundary conditions of the finite element simulation

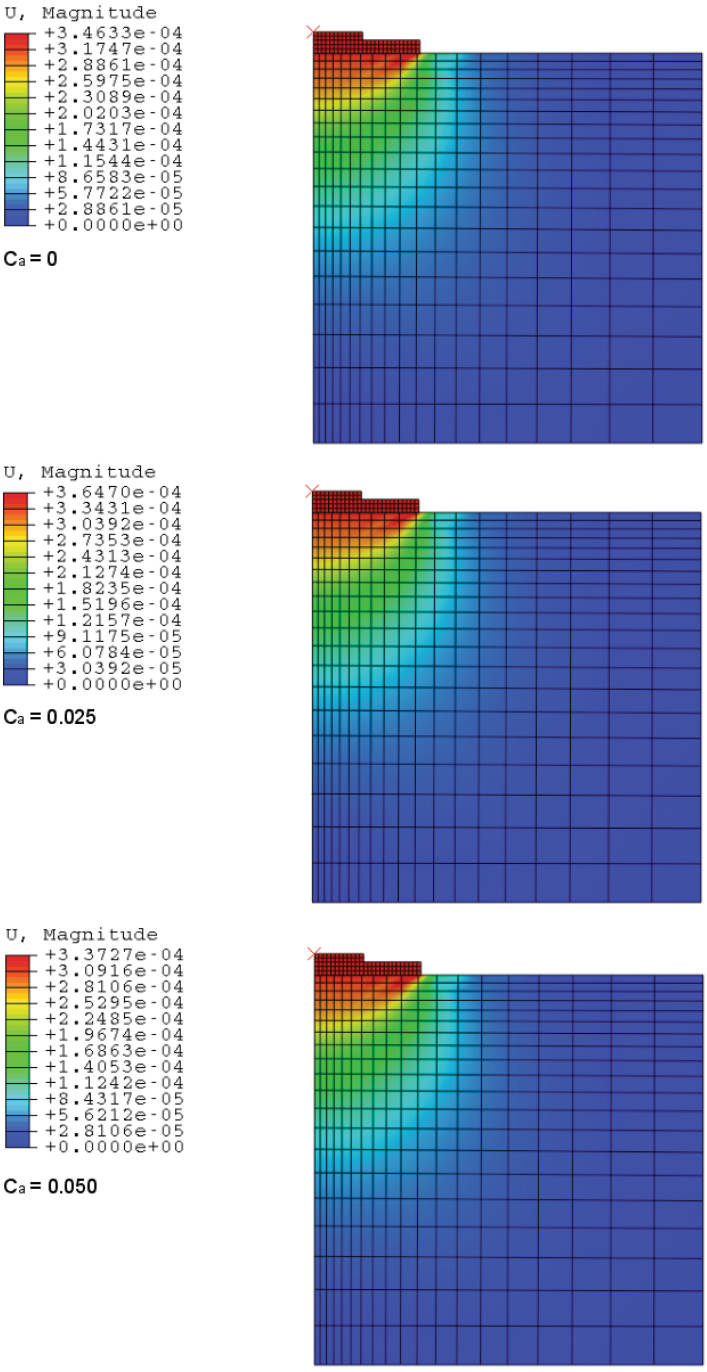

Fig. 10. Displacements contours for each case ($C_a = 0$, $C_a = 0.025$ and $C_a = 0.05$)

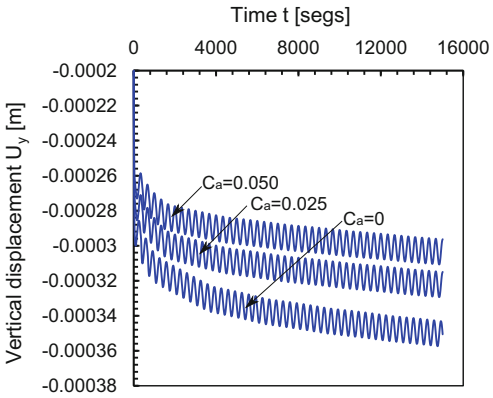

Fig. 11. Vertical displacement of the foundation ($C_a = 0$, $C_a = 0.025$ and $C_a = 0.05$)

A geostatic condition has been initially applied assuming a lateral earth coefficient of $K_0 = 0.5$ and a dry density of the sand equal to $\rho_d = 1500\,\mathrm{kg/m^3}$. The initial void ratio has been set to $e = 0.8$ and the intergranular strain has been initialized assuming mobilized states in the vertical direction, i.e. $h_{22} = -R$ and $c_{22} = -R/2$, where the subindex 2 points in the vertical direction.

After the geostatic step, a sinusoidal load is applied on the top of the foundation. The load is schematized in Fig. 9 and presents 45 cycles with maximum value equal to $P = 0.5\,\mathrm{kN}$. We consider a very slow load velocity to ignore any dynamic effect. Three different simulations were performed considering the variation of parameter $C_a = \{0, 0.025, 0.05\}$. The cases with $C_a > 0$ consider the extension proposed in [15] to account for repetitive loading. The Fig. 10 presents the contours of the displacements for the three cases at the end of the simulation. The results clearly show an increasing settlement of the foundation with decreasing value of C_a. Hence in some way, the parameter C_a simulates the overall increase of the stiffness upon the subsequent cycles. The plots of the vertical displacements U_y on the top of the foundation are shown in Fig. 11.

4 Closure

We have performed some simulations of some experiments to evaluate the accuracy of an ISA-plasticity based model. For large strain ampltiudes $\|\delta\boldsymbol{\varepsilon}\| > 10^{-2}$, the model delivers the hypoplastic relation by Wolffersdorff [21]. The extension by [15] was herein considered to simulate the reduction of the plastic accumulation for increasing number of subsequent cycles. The simulations of element test with cyclic loading under undrained triaxial conditions showed satisfactory results. The model was able to capture approximately the number of cycles required to reach the critical state line. We have also inspected the performance of the model in a boundary value problem of scaled shallow foundation subjected to cyclic loading. With the simulations, we have proved that the current model is

able to increase its overall stiffness when it experiences repetitive loading. Currently, some other issues are investigated to improve the model, as for example the cyclic mobility effect and the post-liquefaction behavior.

A Hypoplastic Model from Wolffersdorff

The hypoplastic model by Wolffersdorff has been explained in several works [7,11,15,21]. We outline here the equations required to implement the model. The general equation reads:

$$\dot{\boldsymbol{\sigma}} = \mathsf{L}^{\text{hyp}} : \dot{\boldsymbol{\varepsilon}} + \mathbf{N}^{\text{hyp}} \, \|\dot{\boldsymbol{\varepsilon}}\| \tag{36}$$

whereby L^{hyp} is the "linear" stiffness and $\mathbf{N}^{\text{hyp}}$ is the "non-linear" stiffness. The linear stiffness L^{hyp} reads [21]:

$$\dot{\boldsymbol{\sigma}} = \mathsf{L}^{\text{hyp}} = f_b f_e \frac{1}{\hat{\boldsymbol{\sigma}} : \hat{\boldsymbol{\sigma}}} (F^2 \mathsf{I} + a^2 \hat{\boldsymbol{\sigma}} \hat{\boldsymbol{\sigma}}) \tag{37}$$

whereby $\hat{\boldsymbol{\sigma}} = \boldsymbol{\sigma}/\text{tr}\boldsymbol{\sigma}$ is the relative stress [11], I is a unit fourth order tensor for symmetric tensors and the other quantities f_b, f_e, F and a are scalar functions. The scalar function F is defined as:

$$F = \sqrt{\frac{1}{8}\tan^2(\psi) + \frac{2 - \tan^2(\psi)}{2 + 2\sqrt{2}\tan(\psi)\cos(3\theta)}} - \frac{1}{2\sqrt{2}\tan(\psi)} \tag{38}$$

whereby the factors a, θ and ψ are defined as:

$$\begin{aligned} a &= \frac{\sqrt{3}(3 - \sin(\varphi_c))}{2\sqrt{2}\sin(\varphi_c))} \\ \tan\psi &= \sqrt{3}\|\hat{\boldsymbol{\sigma}}^*\| \\ \cos(3\theta) &= \sqrt{6}\frac{\text{tr}(\hat{\boldsymbol{\sigma}}^*\hat{\boldsymbol{\sigma}}^*\hat{\boldsymbol{\sigma}}^*)}{(\hat{\boldsymbol{\sigma}}^* : \hat{\boldsymbol{\sigma}}^*)^{3/2}} \end{aligned} \tag{39}$$

and depends on the deviator stress $\boldsymbol{\sigma}^*$ and the critical state friction angle φ_c. The remaining scalar functions f_b, f_e and f_d are dependent on the characteristic void ratios proposed by Bauer [2]:

$$\begin{aligned} e_i &= e_{i0} \exp\left(-\left(3p/h_s\right)^{n_B}\right) \\ e_d &= e_{d0} \exp\left(-\left(3p/h_s\right)^{n_B}\right) \\ e_c &= e_{c0} \exp\left(-\left(3p/h_s\right)^{n_B}\right) \end{aligned} \tag{40}$$

These curves introduces the parameters e_{i0}, e_{d0}, e_{c0}, h_s and n_B. The scalar functions f_e and f_b are called picnotropy and barotropy factors and read:

$$\begin{aligned} f_e &= \left(\frac{e_c}{e}\right)^{\beta} \\ f_b &= \frac{h_s}{n_B}\left(\frac{1+e_i}{e_i}\right)\left(\frac{e_{i0}}{e_{c0}}\right)^{\beta}\left(-\frac{\text{tr}\boldsymbol{\sigma}}{h_s}\right)^{1-n_B}\left[3 + a^2 - \sqrt{3}a\left(\frac{e_{i0} - e_{d0}}{e_{c0} - e_{d0}}\right)^{\beta}\right]^{-1} \end{aligned} \tag{41}$$

with the parameter β. The non-linear stiffness is defined as:

$$\mathbf{N}^{\text{hyp}} = f_d f_b f_e \frac{Fa}{\hat{\boldsymbol{\sigma}} : \hat{\boldsymbol{\sigma}}} (\hat{\boldsymbol{\sigma}} + \hat{\boldsymbol{\sigma}}^*) \tag{42}$$

with the density factor:

$$f_d = \left(\frac{e - e_d}{e_c - e_d} \right)^{\alpha} \tag{43}$$

with the parameter α controlling the model dilatancy.

References

1. Al-Tabbaa, A., Wood, D.: An experimentally based bubble model for clay. In: Pietruszczak, S., Pande, G.N. (eds.) Conference on Numerical Models in Geomechanics NUMOG 3, Balkema, pp. 91–99 (1989)
2. Bauer, E.: Zum mechanischem Verhalten granularer Stoffe unter vorwiegend ödometrischer Beanspruchung. In: Veröffentlichungen des Institutes für Bodenmechanik und Felsmechanik der Universität Fridericiana in Karlsruhe, Heft 130, Karlsruhe, Germany, pp. 1–13 (1992)
3. Fellin, W., Mittendorfer, M., Ostermann, A.: Adaptive integration of constitutive rate equations. Comput. Geotech. **36**(5), 698–708 (2009)
4. Fellin, W., Ostermann, A.: Consistent tangent operators for constitutive rate equations. Int. J. Numer. Anal. Meth. Geomech. **26**(12), 1213–1233 (2002)
5. Fuentes, W.: Contributions in mechanical modelling of fill materials, Issue 179. Institute of Soil Mechanics and Rock Mechanics (IBF), Karlsruhe Institute of Technology (KIT) (2014)
6. Fuentes, W., Triantafyllidis, T.: ISA model: a constitutive model for soils with yield surface in the intergranular strain space. Int. J. Numer. Anal. Meth. Geomech. **39**(11), 1235–1254 (2015)
7. Herle, I., Gudehus, G.: Determination of parameters of a hypoplastic constitutive model from properties of grain assemblies. Mech. Cohesive Frict. Mater. **4**(5), 461–486 (1999)
8. Herle, I., Kolymbas, D.: Hypoplasticity for soils with low friction angles. Comput. Geotechn. **31**(5), 365–373 (2004)
9. Kolymbas, D.: Introduction to Hypoplasticity, 1st edn. A.A. Balkema, Rotterdam (2000)
10. Masin, D.: A hypoplastic constitutive model for clays. Int. J. Numer. Anal. Meth. Geomech. **29**(4), 311–336 (2005)
11. Niemunis, A.: Extended hypoplastic models for soils. In: Habilitation, Heft 34, Schriftenreihe des Institutes für Grundbau und Bodenmechanik der Ruhr-Universität Bochum, Germany (2003)
12. Niemunis, A.: Incremental driver, user's manual. Karlsruhe Institute of Technology KIT, Germany, March 2008
13. Niemunis, A., Herle, I.: Hypoplastic model for cohesionless soils with elastic strain range. Mech. Cohesive Frict. Mater. **2**(4), 279–299 (1997)
14. Poblete, M.: Behaviour of cyclic multidimensional excitation of foundations structures, University of Karlsruhe. Institute of Soil and Rock Mechanics (2016)

15. Poblete, M., Fuentes, W., Triantafyllidis, T.: On the simulation of multidimensional cyclic loading with intergranular strain. Acta Geotech. **11**(6), 1263–1285 (2016)
16. Simpson, B.: Retaining structures: displacement and design. Géotechnique **42**(4), 541–576 (1992)
17. Viggiani, G., Atkinson, J.H.: Stiffness of fine-grained soil at very small strains. Géotechnique **45**(2), 245–265 (1995)
18. Wichtmann, T.: Explicit accumulation model for non-cohesive soils under cyclic loading, Heft 38. Dissertation, Schriftenreihe des Institutes für Grundbau und Bodenmechanik der Ruhr-Universität Bochum (2005). http://www.rz.uni-karlsruhe.de/~gn97/
19. Wichtmann, T.: Experiments with Karlsruhe fine sand. Technical report, Institute of Soil and Rock Mechanics (IBF), Karlsruhe Institute of Technology (KIT) (2013)
20. Wichtmann, T., Niemunis, A., Triantafyllidis, T.: On the "elastic" stiffness in a high-cycle accumulation model for sand: a comparison of drained and undrained cyclic triaxial test. Can. Geotech. J. **47**(7), 791–805 (2010)
21. Wolffersdorff, V.: A hypoplastic relation for granular materials with a predefined limit state surface. Mech. Cohesive Frict. Mater. **1**(3), 251–271 (1996)
22. Wu, W., Niemunis, A.: Failure criterion, flow rule and dissipation function derived from hypoplasticity. Mech. Cohesive Frict. Mater. **1**(2), 145–163 (1996)
23. Zachert, H.: Untersuchungen zur Gebrauchstauglichgkeit von Grundugen für Offshore-Windenergieanlagen, Issue 180. Institute of Soil Mechanics and Rock Mechanics (IBF), Karlsruhe Institute of Technology (KIT) (2014)

Author Index

T. Triantafyllidis (ed.), *Holistic Simulation of Geotechnical Installation Processes*,
Lecture Notes in Applied and Computational Mechanics, 82, DOI 10.1007/978-3-319-52590-7